이학박사학위논문

Probing interactions between earth materials and fluids at the atomic and micrometer scale: Insights from quantum chemical calculations and NMR micro-imaging

지구물질과 유체의 상호작용에 대한 원자 단위와 마이크로미터 단위의 관찰: 양자화학계산과 핵자기공명 현미영상 연구

A dissertation in partial fulfillment of the requirements for the degree of Doctor of Philosophy

2011년 2월

서울대학교 대학원
지구환경과학부

이 범 한

Abstract

Probing interactions between earth materials and fluids at the atomic and micrometer scale: Insights from quantum chemical calculations and NMR micro-imaging

Bum Han Lee
School of Earth and Environmental Sciences
The Graduate School
Seoul National University

Interactions between earth materials and fluids is one of the most important processes in the Earth's surface and interior, and thus, the probing and understanding the interaction play an important role in the estimation and prediction of industrial and environmental processes in the Earth's surface and geophysical processes in the Earth's interior. In this study, the structure, property, and structure-property relationships for interactions between earth materials and fluids were estimated by quantum chemical calculations at the atomic scale and probed by NMR micro-imaging at the micrometer scale.

In quantum chemical calculations study, the effect of the lattice topology (ideal hexagonal rings vs. ditrigonal rings) and cluster size of

model clusters (three-ring *vs.* seven-ring clusters) on the nature of benzyl alcohol adsorption on kaolinite surfaces were investigated with an emphasis on the equilibrium configuration, binding energy, and NMR chemical shielding tensors. The optimized structure of benzyl alcohol adsorbed on the tetrahedral layer of kaolinite is characterized by a weak hydrogen bond and dispersion force, and that on the octahedral layer of kaolinite is characterized by two hydrogen bonds. The results for the binding energies indicate a stronger binding energy between benzyl alcohol and octahedral surfaces than that between benzyl alcohol and tetrahedral layers. Although the calculated binding energies for seven-member rings with varying lattice topologies are rather similar, the detailed optimized structures are distinct, demonstrating the effect of lattice topology on the nature of adsorption. The calculated ^{17}O isotropic chemical shieldings of some basal oxygens decrease up to approximately 4–5 ppm after the adsorption, suggesting that the NMR technique may be useful in exploring the nature of adsorption between organic molecules and silicate surfaces.

In the first NMR micro-imaging study, relationships among porosity, specific surface area, structural parameters (D_{cc} and lacunarity), and the corresponding macroscopic properties (configurational entropy and permeability) were established. The D_{cc} of the 3D porous networks increases with increasing specific surface area at constant porosity and with increasing porosity at constant specific surface area. Lacunarity at the intermediate box size (~0.47 mm in the current model sands) was

δ

reproduced well with specific surface area. The maximum configurational entropy increases with increasing porosity, and the entropy length of the pores decreases with increasing specific surface area and was used to calculate the average connectivity among the pores. The correlation among porosity, specific surface area, and permeability is consistent with the prediction from the Kozeny-Carman equation. From the relationship between the permeability and the D_{cc} of pores, permeability can be expressed as a function of the D_{cc} of pores and porosity. This study provides improved insights into the nature of porous media and has useful geophysical implications for elasticity and shear viscosity of complex composites of rock, glasses, melt, and fluids.

In the second NMR micro-imaging study, high resolution images of water distribution in porous media initially saturated with silicone oil were obtained with varying durations of water flows using NMR micro-imaging with up to 50 μm resolution, and the effect of the size and shape of the particles which make up the porous media on the distribution of water was investigated. Volume fractions, specific surface areas, and cube counting fractal dimension of water phase for each sample obtained from 3D spin echo images with increasing duration of water injection and were well fitted to single-exponential recovery functions. Asymptotic values for the samples of glass beads were much larger than those for the silica gel samples, mostly because the pore structures of the silica gel are different from those of the glass beads. Convergence rates of all the properties were inversely proportional to the permeability, indicating that the convergence

δ

rates were correlated to the transport property of the porous media. This study shows that the pore structure of particles which make up the porous media plays an important role in the water distribution of porous media which was initially saturated with an immiscible fluid.

High resolution NMR micro-imaging of the fluids in porous media may shed some light on diverse applications in hydrogeology and geophysics. However, it is difficult to obtain high resolution images of fluids in porous media using NMR micro-imaging due to the low amounts of fluids and short spin-spin relaxation times. In the final NMR micro-imaging study, the possibility of high resolution images of fluids in porous media were investigated using Mongolian desert sandstone, natural pisolite, and samples of glass beads with a small sample size, high porosity, strong magnetic field (18.8 T), and strong field gradient (300 G/cm). The results show that NMR micro-imaging can be used to obtain images of the porous media comprised of grain sizes down to 75 μm with resolutions of up to 19.5 μm/pixel for highly porous media.

……

Keywords: quantum chemical calculations, NMR micro-imaging, earth materials, fluids, structure-property relationship,

Student Number: 2000-20668

Table of Contents

List of Figures

δ

List of Tables

δ

Chapter 1. Introduction

Diverse geological processes in the Earth's surface and interior depend on the macroscopic properties of earth materials which are determined by their microscopic scale (from Å to μm) local structures. For example, coordination environments and topological disorder of atoms in silicate melts and glasses play an crucial role in the generation, migration, and dynamics of magma (Lee, 2005; Lee et al., 2008), and those of germanate glasses may explain the large compressibility and nonlinear changes in density (Lee and Lee, 2006; Lee et al., 2010). Therefore, probing microscopic scale configuration is essential in understanding and predicting macroscopic properties and diverse geological processes.

The interactions between earth materials and fluids are one of the most important processes in the Earth's surface and interior. In the Earth's surface, the processes include pollutant migration, bioavailability, and biodegradation in soils (Knezovich et al., 1987; Kowalska et al., 1994), oil recovery from reservoir rocks (Lake, 1989), and underground storage of CO_2 and nuclear waste (Hendriks and Blok, 1993). In the Earth's interior, the processes take place in rock-melt-fluid composites (Takei, 1998), and affect the elastic properties, viscosity, and seismic wave attenuation of the composites. Therefore, probing and understanding these interactions play an important role in the estimation and prediction of processes in the Earth's surface and interior.

Interactions between earth materials and fluids can be probed at diverse length scales. For example, hydrologic cycle is estimated on a global length scale (hundreds of kilometers) (Dirmeyer and Brubaker, 2007), and the relationship between the variability of the topography, soil, and rainfalls and the storm response can be seen at the catchment scale (in the order of kilometers) (Wood et al., 1990). In this study, the interactions between earth materials and fluids were probed using quantum chemical calculations and NMR micro-imaging at the atomic and micrometer scale, respectively.

In the research area for silicate glasses and melts, there are three fundamental questions: the atomic and nano-scale structures and the extent of disorder of these systems, the effects of variation in atomic-scale disorder on the macroscopic properties of melts, and the effect of these properties on geological processes, such as generation, migration, and dynamics of magmas (Lee, 2005). The structure, the property, and the structure-property relationship are also key questions on the interactions between earth materials and fluids. This study's aim was for the systematic exploration of the structures, properties, and structure-property relationships for the interactions between earth materials and fluids from the information obtained at the atomic and micrometer scale.

This thesis is composed of 7 chapters including this introduction and appendix. In chapter 2, summary of the principles of quantum chemical calculations and NMR micro-imaging and pulse sequences of the NMR micro-imaging used in this study are presented. In chapter 3, probing

the interactions between kaolinite and benzyl alcohol at the atomic length scale using quantum chemical calculations and the detailed equilibrium configuration of the adsorption (for the microscopic structure), binding energies (for the macroscopic properties), and NMR parameters (for the parameter manifesting the structure-property relationship) are presented (Lee and Lee, 2009). In chapter 4, imaging of 3D porous networks filled with fluids at micrometer length scale using NMR micro-imaging (for the structure), quantifying them with parameters including cube counting fractal dimension, lacunarity, and configurational entropy (for the properties), and exploring the relationship between structural parameters and hydrological property such as permeability (for the structure-property relationship) are presented (Lee and Lee, submitted). In chapter 5, imaging of the water distribution in porous media initially saturated with silicone oil at the micrometer length scale using NMR micro-imaging (for the structure), quantification of the water distribution with structural parameters (for the property), and investigation of the relationship between a parameter characterizing the water distribution and permeability (for the structure-property relationship) are presented (Lee and Lee, in preparation). In chapter 6, in order to extend NMR micro-imaging to diverse applications in porous media research, high resolution images of fluid distribution in porous sandstone, natural pisolite, and glass beads column are presented (Lee et al., in preparation). In chapter 7, geophysical implications of this study are discussed. This thesis suggests that the parameters including configurational entropy and cube counting fractal dimension are also

useful in describing the processes in the Earth's interior in addition to the processes in the Earth's surface. Finally, in the appendix, abstracts of papers published in domestic journals are presented. They include a quantum chemical calculations study on Mulliken charges and magnetic shielding tensor for benzyl alcohol adsorption on kaolinite tetrahedral surfaces (Lee and Lee, 2007), a NMR micro-imaging study on porous media composed of glass beads, silica gel, and porous sandstone (Lee and Lee, 2009), and a random packing simulations study on geophysical implications for configurational entropy and cube counting fractal dimension of porous networks (Lee and Lee, 2010)..

d

References

Dirmeyer, P. A. and Brubaker, K. L. (2007) Characterization of the global hydrologic cycle from a back-trajectory analysis of atmospheric water vapor. Journal of Hydrometeorology, 8, 20-37.

Hendriks, C. A. and Blok, K. (1993) Underground storage of carbon dioxide. Energy Conversion and Management, 34, 945-957.

Knezovich, J. P., Harrison, F. L. and Wilhelm, R. G. (1987) The bioavailability of sediment-sorbed organic chemicals: A review. Water, Air, snd Soil Pollution, 32, 233-245.

Kowalska, M., Guler, H. and Cocke, D. L. (1994) Interactions of clay minerals with organic pollutants. The Science of the Total Environment, 141, 223-240.

Lake, L. W. (1989) Enhanced Oil Recovery. Old Tappan, Prentice Hall Inc.

Lee, B. H., Cho, J. H. and Lee, S. K. (in preparation) High resolution NMR micro-imaging of fluids in porous media.

Lee, B. H. and Lee, S. K. (2007) The effect of lattice topology on benzyl alcohol adsorption on kaolinite surfaces: Quantum chemical calculations of Mulliken charges and magnetic shielding tensor. Journal of Mineralogical Society of Korea, 20(4), 313-325.

Lee, B. H. and Lee, S. K. (2009) 3-dimensional μm-scale pore structures of porous earth materials: NMR micro-imaging study. Journal of Mineralogical Society of Korea, 22(4), 313-324.

Lee, B. H. and Lee, S. K. (2010) Geophysical implications for configurational entropy and cube counting fractal dimension of porous networks: insights from random packing simulations. Journal of Mineralogical Society of Korea, 23(4), 367-375.

Lee, B. H. and Lee, S. K. (2009) Effect of lattice topology on the adsorption of benzyl alcohol on kaolinite surfaces: Quantum chemical calculations of geometry optimization, binding energy, and NMR chemical shielding. American Mineralogist, 94, 1392-1404.

Lee, B. H. and Lee, S. K. (in preparation) Probing of water distribution in porous model sands with immiscible fluids: Nuclear magnetic resonance micro-imaging study.

Lee, B. H. and Lee, S. K. (submitted) Effects of specific surface area and porosity on cube counting fractal dimension, lacunarity, and configurational entropy of porous networks of model sands: insights from random packing simulations and NMR micro-imaging. Journal of Geophysical Research.

Lee, S. K. (2005) Microscopic origins of macroscopic properties of silicate melts and glasses at ambient and high pressure: Implications for melt generation and dynamics. Geochimica et Cosmochimica Acta, 69(14), 3695-3710.

Lee, S. K., Kim, H. N., Lee, B. H., Kim, H. I. and Kim, E. J. (2010) Nature of chemical and topological disorder in borogermanate glasses: insights from B-11 and O-17 solid-state NMR and quantum chemical calculations. Journal of Physical Chemistry B, 114, 412-420.

Lee, S. K. and Lee, B. H. (2006) Atomistic origin of germanate anomaly in GeO_2 and Na-germanate glasses: Insights from two-dimensional ^{17}O NMR and quantum chemical calculations. Journal of Physical Chemistry B, 110, 16408-16412.

Lee, S. K., Lin, J. F., Cai, Y. Q., Hiraoka, N., Eng, P. J., Okuchi, T., Mao, H. K., Meng, Y., Hu, M. Y., Chow, P., Shu, J. F., Li, B. S., Fukui, H., Lee, B. H., Kim, H. N. and Yoo, C. S. (2008) X-ray Raman scattering study

of $MgSiO_3$ glass at high pressure: Implication for triclustered $MgSiO_3$ melt in Earth's mantle. Proceedings of the National Academy of Sciences of the United States of America, 105(23), 7925-7929.

Takei, Y. (1998) Constitutive mechanical relations of solid-liquid composites in terms of grain-boundary contiguity. Journal of Geophysical Research, 103(B8), 18183-18203.

Wood, E. F., Sivapalan, M. and Beven, K. (1990) Similarity and scale in catchment storm response. Reviews of Geophysics, 28, 1-18.

δ

Chapter 2. Methods

2.1. Quantum Chemical Calculations

Quantum chemical calculations can provide complementary information to experiments or estimate data that cannot be obtained by experimental methods due to limitations. In quantum chemical calculations, the energy and other related properties of a system are obtained by solving the Schrödinger equation (Foresman and Frisch, 1996; McQuarrie and Simon, 1997);

$$H\Psi = E\Psi . \qquad (2.1)$$

where H is the Hamiltonian operator, E is the energy (an eigen value of the Hamiltonian operator), and Ψ is the wave function. However, exact solutions to the Schrödinger equation for a multi-electron molecule are not computationally practical, and therefore, quantum chemical calculations use approximation methods for its solutions (Foresman and Frisch, 1996; McQuarrie and Simon, 1997). One of the most popular approximation methods is the Hartree-Fock method where the solution is obtained by self-consistent field for multi-electron wave function (Fukutome, 1981). Another popular approximation method is the density functional theory where electron correlations are treated by density functional of electrons. Among density functional theory methods, B3LYP (Becke, 3 parameters, Lee-Yang-Parr) is the most frequently used method (Lee et al., 1988; Becke, 1993). By using these approximation methods, various properties including single

δ

point energy, optimized geometry, transitional state geometry, and vibrational frequency of a system can be obtained (Foresman and Frisch, 1996). With the improvement of computation speed, it can use large clusters with hundreds of atoms. Therefore, it might be a suitable tool for probing the interaction between earth materials and fluids at the atomic length scale.

2.2. NMR Micro-imaging

NMR micro-imaging refers to NMR imaging in which a high spatial resolution (100 μm <) is obtained. The difference between NMR micro-imaging and MRI (magnetic resonance imaging) which is widely used in clinical purposes is the size of the samples and the strength of the magnetic field; in MRI, human bodies and animals are objectives in which the diameters are generally tens of centimeters and the magnetic field generally ranges from 0.2 to 3 Tesla, and in NMR micro-imaging, the size of samples ranges from a few millimeters to a few centimeters and the magnetic field generally ranges from 4.7 to 21.1 Tesla.

2.2.1. Principles of NMR imaging

A key to understanding NMR imaging is a field gradient (Callaghan, 1991; Blümich, 2000). The linear relationship between NMR frequency and space coordinate is obtained by restricting the space dependence of the magnetic field to the field gradient (Levitt, 2001),

δ

$$G_x = \frac{\partial B_z}{\partial x}. \qquad (2.2)$$

In this case, each point along the x-axis of the sample is characterized by a different resonance frequency. Figure 2-1 shows the schematic diagram of field gradient in the x-direction and the corresponding NMR signals.

In general, the components $\boldsymbol{G}_{kl}$ of the magnetic-field gradient tensor **G** are defined as the spatial derivatives of the magnetic field,

$$G_{kl} = \frac{\partial B_k}{\partial x_l} \qquad (2.3)$$

Because the magnetic field $\boldsymbol{B}$ is a vector with components B_x, B_y, and B_z, the magnetic-field gradient is a second-rank tensor with nine components. It can be written as the dyadic product of the gradient operator ∇ and the magnetic field,

$$\mathbf{G} = \nabla B = \begin{bmatrix} G_{xx} & G_{xy} & G_{xz} \\ G_{yx} & G_{yy} & G_{yz} \\ G_{zx} & G_{zy} & G_{zz} \end{bmatrix} \qquad (2.4)$$

The gradient field is generated by an extra set of coils and is added to the homogeneous magnetic fields B_0 in the z-direction and the weak time-dependent field B_{rf} perpendicular to B_0,

$$B = B_0 + B_{rf} + \mathbf{G}r \qquad (2.5)$$

where r is the space vector with components x, y, and z. When $B_{rf} = 0$, the NMR frequency is dependent on space,

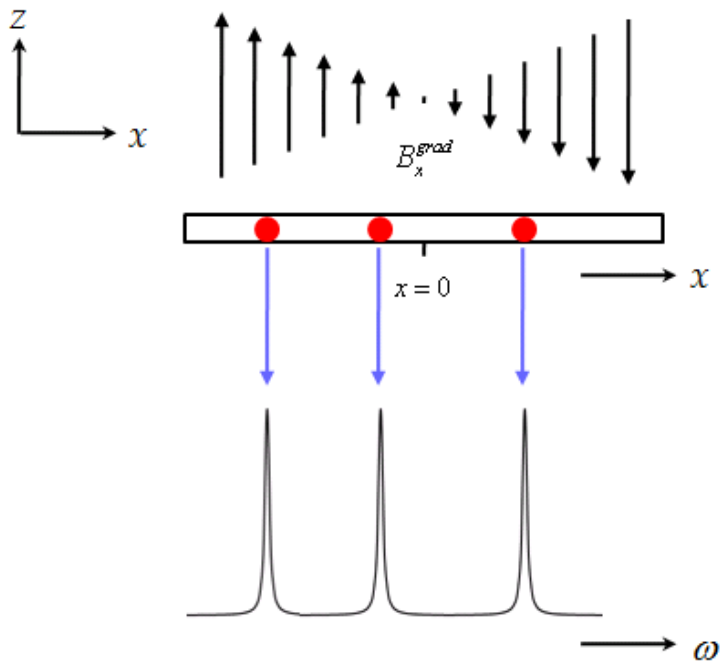

Figure 2-1. A diagram showing field gradient, nuclei lying in x-direction, and the corresponding NMR signals which are different in frequency domain because Larmor frequencies varied due to the field gradient (modified from Levitt (2001)).

δ

$$\begin{aligned}\varpi_0(r) &= \gamma\left|\boldsymbol{B}\right| = \gamma\left|B_0 + \mathbf{G}r\right| \\ &= \gamma[(B_{0x} + G_{xx}x + G_{xy}y + G_{xz}z)^2 \\ &+(B_{0y} + G_{yx}x + G_{yy}y + G_{yz}z)^2 \\ &+(B_{0z} + G_{zx}x + G_{zy}y + G_{zz}z)^2]^{1/2}\end{aligned} \tag{2.6}$$

Because $B_{0x} = B_{0y} = 0$, the terms dominating the resonance frequency are given in the last row. Thus only three elements of the gradient tensor determine the resonance frequency in first order. The three relevant terms are often used to form the gradient vector *G*,

$$\begin{pmatrix} G_{zx} \\ G_{zy} \\ G_{zz} \end{pmatrix} \equiv \boldsymbol{G} = \begin{pmatrix} G_x \\ G_y \\ G_z \end{pmatrix}. \tag{2.7}$$

In NMR imaging, the equilibrium magnetization M_0 depends on space *r*. For a 90 degree pulse, the magnetization from the volume element at position *r* is given by

$$M^+(t) = M_0(r)\exp\{\mathrm{i}\varpi_0(r)t\}, \tag{2.8}$$

where $\omega_0(r)$ is the space-dependent NMR frequency. The sum of signals originating from the nuclei at all position *r* is observed, so that Eq. (2.8) needs to be integrated,

$$M^+(t) = \int_{-\infty}^{\infty} M_0(r)\exp(\mathrm{i}\gamma \mathrm{G}rt)dr\,. \tag{2.9}$$

If in addition the gradient is time dependent, the phase of the exponential in (2.9) is determined by the time integral of G,

δ

$$M^{+}(t) = \int_{-\infty}^{\infty} M_0(r)\exp\left(\mathrm{i}\gamma r\int_0^t G(t')dt'\right)dr \equiv \int_{-\infty}^{\infty} M_0(r)\exp\{-\mathrm{i}k(t)r\}dr \tag{2.10}$$

where the wave vector k is the Fourier conjugate variable to the space coordinate r,

$$k(t) = -\gamma\int_0^t G(t')dt' . \tag{2.11}$$

Transverse magnetization will be in phase at all space coordinates immediately after the pulse. But in the presence of a magnetic field gradient the precession frequency varies in space, and a different precession phase is accumulated over time at each space coordinate.

To obtain an image, the gradient $G(t)$ must be varied in such a way that all values of k are sampled which are relevant to the image. The image itself is then derived by Fourier transformation of the NMR signal. There are two ways to encode the space information to the NMR signal. First, the gradients can be turned on to a constant value G_x during data acquisition (frequency encoding). In this case, k_x scales with the acquisition time t_2, and the space information in x-direction is frequency encoded. Second, the gradient G_y can be turned on for a fixed time t_1 before data acquisition to yield a certain value of the gradient integral k_y at the start (phase encoding). In this case, the space information in y-direction is encoded in the phase of the signal acquired during t_2, and the experiment needs to be repeated for different initial phases obtained by varying G for fixed t_1. A 2D image is typically obtained by a combination of both phase encoding in one

dimension and frequency encoding in the other.

2.2.2. Pulse sequences used in this study

Figure 2-2 shows a timing diagram of 3D imaging with the gradient echo method (GE3D) which is used in chapter 4 for obtaining various 3D pore structure data of the samples of glass beads and silica gel. In this method, echo signal is obtained by sinc3 shaped pulse in F1 channel and gradient echo in Phase direction. Frequency encoding is applied by a gradient in Phase direction during the acquisition of echo signal. Phase encoding is applied to two orthogonal directions; Phase and Slice directions. In this way, three orthogonal space information is obtained; frequency encoding in one direction, phase encoding in two directions. The two gradient pulses are applied at the same time and are cycled through all possible combinations. The frequency encoding gradient has its dephasing negative lobe to cause the spins to be in phase at the center of the acquisition, and then, the frequency encoding gradient is applied and a signal recorded

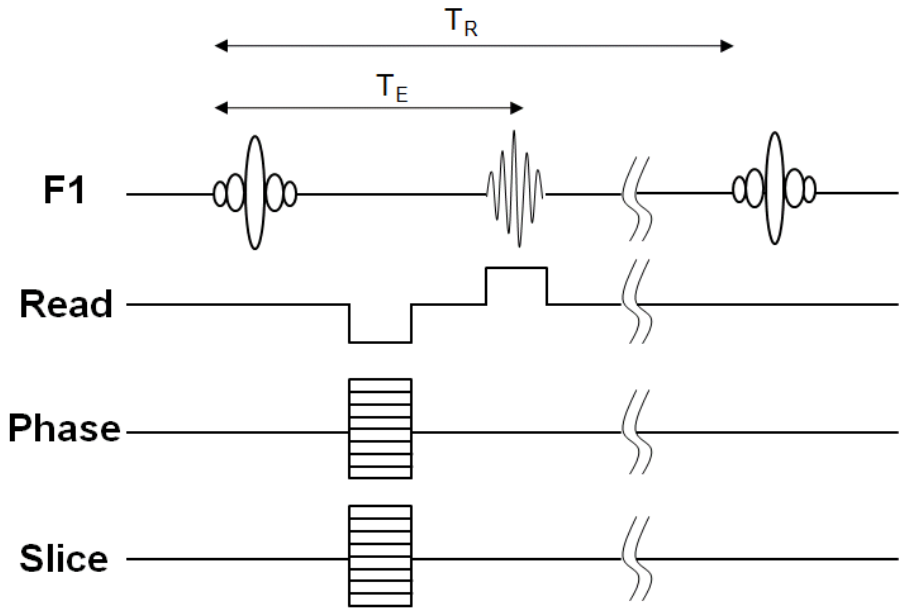

Figure 2-2. A timing diagram for 3D imaging with the gradient echo method (GE3D). Echo time (T_E) and repetition time (T_R) are also shown.

Figure 2-3 shows a timing diagram of chemical shift selective excitation pulse sequence (CHESS) used in chapter 5 for obtaining 2D images of two phase fluids. In this method, echo signal is obtained by Gaussian excitation and refocusing pulses in F1 channel. Gaussian excitation pulse with a flip angle of 90 degree is applied for excitation of a specific frequency, followed by a dephasing gradient (homogeneity spoiling gradient). The spoiling gradient leaves the spin system in a state where no net magnetization of the unwanted component remains entirely unaffected in the form of z-magnetization (Haase et al., 1985). A period of time equal to $T_E/2$ elapses and a 180 degree slice selective pulse is applied in conjunction with the slice selection gradient. Phase encoding gradients are applied after the 180 degree pulse, and after the echo signal. The frequency encoding gradient is applied in Read direction after the 180 degree pulse during the time that echo is collected.

Figure 2-4 shows a timing diagram of 3D imaging with the spin echo method (SE3D) used in chapter 5 for obtaining 3D images of water distribution in porous media comprised of glass beads and silica gel which are initially saturated with silicone oil. In this method, echo signal is obtained by sinc3 shaped excitation and refocusing pulses in F1 channel. A slice selective 90 degree RF pulse is applied, followed by a dephasing spoiler gradient which plays the same role in the CHESS protocol. A period of time equal to $T_E/2$ elapses and a 180 degree slice selective pulse is applied. Phase encoding is applied to two directions; Phase and Slice directions as in GE3D protocol. The frequency encoding gradient is applied

in Read direction after the 180 degree pulse during the time that echo is collected.

Figure 2-5 shows a timing diagram of 2D imaging with the spin echo method (SE2D) used in chapter 6 for obtaining high resolution images of porous media. In this method, echo signal is obtained by sinc3 shaped excitation and refocusing pulses in F1 channel. A slice selective 90 degree RF pulse is applied in conjunction with a slice selection gradient. A period of time equal to $T_E/2$ elapses and a 180 degree slice selective pulse is applied in conjunction with the slice selection gradient. Phase encoding gradients are applied after the 180 degree pulse, and after the echo signal. The frequency encoding gradient is applied in Read direction after the 180 degree pulse during the time that echo is collected.

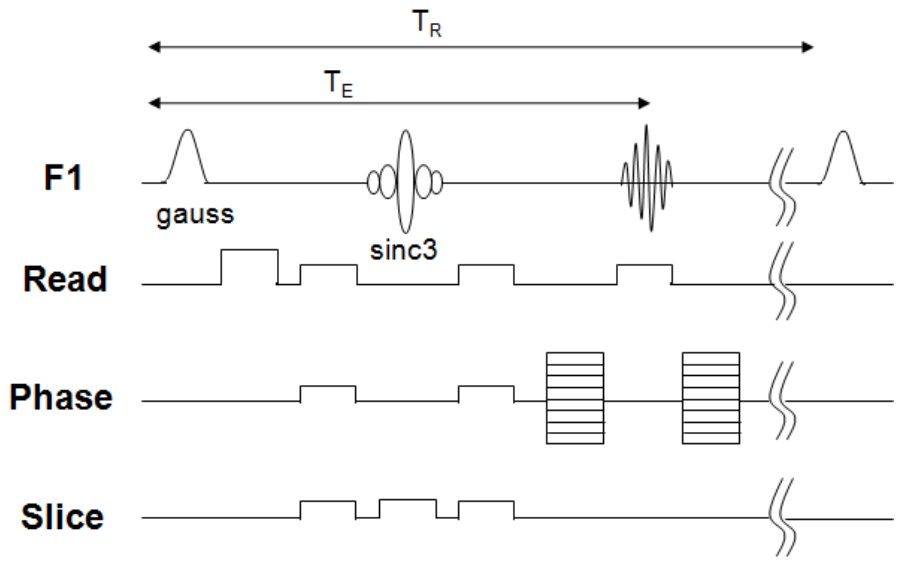

Figure 2-3. A timing diagram for chemical shift selective excitation pulse sequence (CHESS). Echo time (T_E) and repetition time (T_R) are also shown.

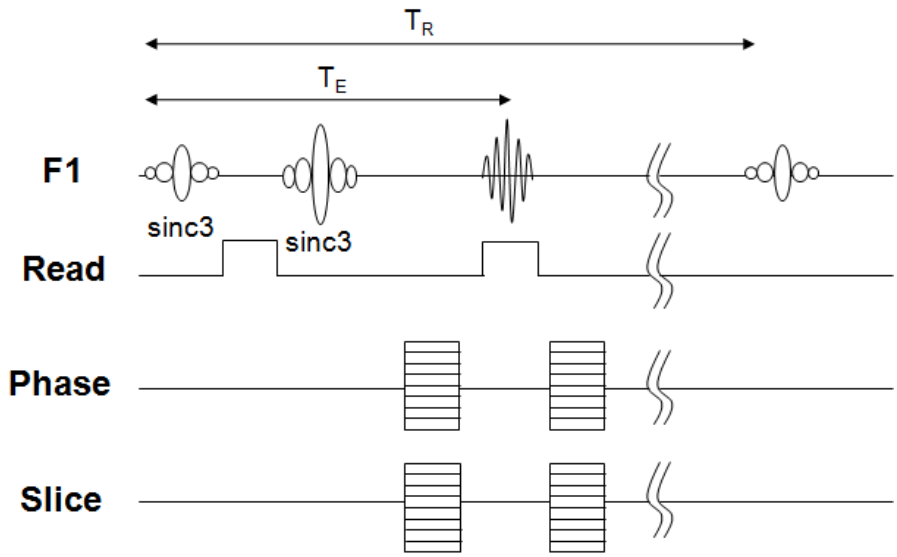

Figure 2-4. A timing diagram for spin echo 3D imaging pulse sequence (SE3D). Echo time (T_E) and repetition time (T_R) are also shown.

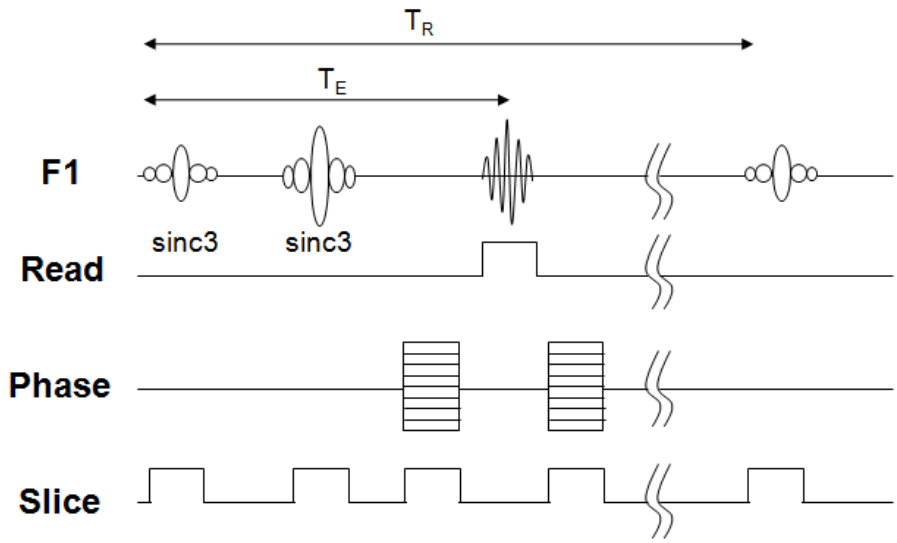

Figure 2-5. A timing diagram for spin echo 2D imaging pulse sequence (SE2D). Echo time (T_E) and repetition time (T_R) are also shown.

References

Becke, A. D. (1993) A new mixing of Hartree-Fock and local density-functional theories. Journal of Chemical Physics, 98(2), 1372-1377.

Blümich, B. (2000) NMR Imaging of Materials. Oxford, Clarendon Press, 541 p.

Callaghan, P. T. (1991) Principles of Nuclear Magnetic Resonance Microscopy. Oxford, Clarendon Press, 492 p.

Foresman, J. B. and Frisch, Æ. (1996) Exploring Chemistry with Electronic Structure Methods. Pittsburgh, PA, Gaussian, Inc., 302 p.

Fukutome, H. (1981) Unrestricted Hartree-Fock theory and its applications to molecules and chemical reactions. International Journal of Quantum Chemistry, 20, 955-1065.

Haase, A., Frahm, J., Hanicke, W. and Matthaei, D. (1985) ^{1}H NMR chemical shift selective (CHESS) imaging. Physics in Medicine and Biology, 30, 341-344.

Lee, C., Yang, W. and Parr, R. G. (1988) Development of the Colle-Salvetti correlation-energy formula into a functional of the electron density. Physical Review B, 37(2), 785-789.

Levitt, M. H. (2001) Spin Dynamics. Chichester, John Wiley & Sons Ltd, 686 p.

McQuarrie, D. A. and Simon, J. D. (1997) Physical Chemistry: A Molecular Approach. Sausalito, University Science Books, 1360 p.

Chapter 3. Effect of lattice topology on the adsorption of benzyl alcohol on kaolinite surfaces: Quantum chemical calculations of geometry optimization, binding energy, and NMR chemical shielding

Abstract

The effect of the lattice topology (ideal hexagonal rings vs. ditrigonal rings) and cluster size of model clusters (three-ring vs. seven-ring clusters) on the nature of benzyl alcohol adsorption on kaolinite surfaces using quantum chemical calculations were investigated with an emphasis on the equilibrium configuration, binding energy, and NMR chemical shielding tensors. The optimized structure of benzyl alcohol adsorbed on the tetrahedral layer of kaolinite varies according to the type and size of model cluster. While the calculated binding energy varies with the level of theory and the basis sets used for the calculations, the binding energies between benzyl alcohol and seven-ring clusters are smaller than those between benzyl alcohol and three-ring clusters partly due to the edge hydrogen for the latter. The results also indicate a stronger binding energy between benzyl alcohol and octahedral surfaces than that between benzyl alcohol and tetrahedral layers. Although the calculated binding energies for seven-member rings with varying lattice topologies are rather similar, the detailed optimized structures are distinct, demonstrating the effect of lattice topology on the nature of adsorption. The optimized structures and binding energies indicate that an intermediate degree of hydrogen bonding

is dominant for the three-member silicate rings and that the interaction between the benzene ring and basal oxygens in the seven-member rings is characterized by a weak hydrogen bond and dispersion force. The calculated ^{17}O isotropic chemical shieldings of some basal oxygens decrease up to approximately 4–5 ppm after the adsorption (with an estimated uncertainty of approximately 2 ppm). Since the high-resolution ^{17}O 3QMAS NMR spectroscopy of layer silicates yielded a resolution of 1–2 ppm for the basal oxygen sites in the layer silicates (e.g., Lee et al. 2003), the NMR technique may be useful in exploring the nature of adsorption between organic molecules and silicate surfaces, while further computational studies on the effect of the basis sets, the surface coverage, and the types of diverse organic molecules with larger model clusters for surfaces remain to be explored.

3.1. Introduction

Interactions between layer silicates and organic molecules play an important role in pollutant migration, bioavailability, and biodegradation in soils (Knezovich et al., 1987; Kowalska et al., 1994; Brown et al., 1999). The knowledge of their interactions can give improved insights into their applications as catalysts and nano-composites and into the enhanced oil recovery (Ogawa and Kuroda, 1995; Tunney and Detellier, 1996; Pinnavaia and Beall, 2000). An understanding of the process of benzyl alcohol adsorption on kaolinite surfaces can offer better insights into the adsorption of a benzene ring with alcohol functionality on mineral surfaces

and account for the wettability of reservoir rocks (Anderson, 1986; Madsen et al., 1996). The adsorption of benzyl alcohol on kaolinite surfaces renders the surfaces functional for many applications including polymer reinforcement (Bayer et al., 2010), and thus batch experiments were performed for the determination of the adsorption isotherm (Førland et al., 1995; Førland, 2001). Despite the importance and implications of this process, little is known about the detailed equilibrium configuration and binding energy for the adsorption of benzyl alcohol on kaolinite surfaces, which are essential to understand the nature of the interactions. The objective of this study is to investigate the nature of the interactions between kaolinite and benzyl alcohol theoretically using quantum chemical calculations.

Kaolinite is one of the dioctahedral 1:1 layer silicates. The nature of organic molecule adsorption on kaolinite has been studied using diverse experimental techniques, such as batch adsorption isotherm experiments (e.g., Førland 2001; Førland et al. 1995; Lee and Kim 2002; Li and Gupta 1994), X-ray absorption spectroscopy (e.g., Bantignies et al. 1998; Brown et al. 1988; Kelleher and O'Dwyer 2002; Olejnik et al. 1970), nuclear magnetic resonance (e.g., Feng et al. 2005; Jurkiewicz and Maciel 1995; Murray et al. 2005; Seger and Maciel 2006; Tao and Maciel 1998; Wang and Xing 2005; Xie and Hayashi 1999), and infrared and Raman spectroscopy (e.g., Johansson et al. 1999; Kubicki et al. 1999; Thomas and Kelley 2008; Yariv 1996; Yariv and Lapides 2000). Molecular dynamics (MD) simulation has also been useful in revealing the nature of the interactions between kaolinite and

organic molecules (e.g., Murgich et al. 1998; Teppen et al. 1998; Tunega et al. 2002a; Tunega et al. 2004; van Duin and Larter 2001). While these experimental and theoretical studies have provided insights into the nature of adsorption, the detailed atomic configuration of adsorbed molecules and the binding energies between the adsorbed molecules and surfaces have not yet been fully understood.

Quantum chemical calculations, which are effective tools for obtaining detailed microscopic information on the adsorption behavior of organic molecules, are complementary to other experimental and MD studies (Foresman and Frisch, 1996; Boulet et al., 2006), and have been utilized in diverse geological applications (e.g., see Cygan and Kubicki 2001 and the references therein). A few recent applications include studies of the atomic structures of silicate glasses and melts (e.g., Lee 2004; Lee 2006; Lee et al. 2001; Lee and Stebbins 2006; Tossell 2001; Xue and Kanzaki 1998), isotope fractionation in natural systems (Schauble et al., 2001; Schauble et al., 2003; Schauble et al., 2004; Ottonello and Zuccolini, 2005; Tossell, 2005; Suh et al., 2007), and the adsorption of organic species onto mineral surfaces (e.g., Aquino et al. 2007; Kwon et al. 2006; Plant et al. 2006; Viruela-Martín et al. 1993; Yoon et al. 2004; Zhanpeisov et al. 1999).

Quantum chemical calculations have been used to study the adsorption of various organic molecules on kaolinite surfaces, including formamide, N-methylformamide and dimethylsulfoxide (Michalkova et al., 2002), sarin and soman (Michalkova et al., 2004), thymine and uracil (Robinson et al., 2007), acetic acid and acetate ion (Tunega et al., 2002),

nitrobenzene (Pelmenschikov and Leszczynski, 1999; Michalkova et al., 2005; Gorb et al., 2006), and benzene (Castro and Martins, 2005) (see Table 3-1). Previous theoretical studies on the adsorption of organic molecules on kaolinite surfaces have reported that the more the hydrogen bonds formed between the surface oxygen and the hydrogen in organic molecules, the stronger the overall interaction between the organic molecules and the surfaces (Michalkova et al., 2002). It has also been shown that organic molecules on the octahedral layer are more strongly adsorbed than those on the tetrahedral layer of kaolinite (Michalkova et al., 2002; Tunega et al., 2002; Michalkova et al., 2004; Robinson et al., 2007).

Previous studies have often used relatively small clusters, and their results may have been somewhat affected by the terminal hydrogens (See Table 3-1 below). Although the actual lattice surfaces of layer silicates consist of ditrigonal rings, some of the previous studies have used ideal (hexagonal) rings (Pelmenschikov and Leszczynski, 1999; Hong et al., 2001; Hong et al., 2002; Gorb et al., 2006). Therefore, the effect of the cluster size and lattice topology of the model clusters on the binding energy and equilibrium configuration has not yet been fully understood. For example, previous quantum chemical calculations for the adsorption of sarin ($C_4H_{10}FO_2P$) and soman ($C_7H_{16}FO_2P$) on kaolinite (dickite) surfaces and the adsorption of 25 small organic molecules on zeolite surfaces showed that the optimized structures were not significantly affected by the size of the model clusters but the binding energy between the molecules and the surfaces increases with an increase in the size of the clusters, up to 33

kJ/mol (Michalkova et al., 2004; Solans-Monfort et al., 2005). However, the orientations of nitrobenzene molecules on layer silicates were found to be dependent on the surface area of the tetrahedral layers (Pelmenschikov and Leszczynski, 1999; Michalkova et al., 2004). Other earlier theoretical studies also showed that the lattice topology and the size of the model cluster affect the nature of the interaction: the enthalpy of hydrolysis for crystalline silicates was reported to significantly vary with the size and topology (bond angle) of the silicate clusters (Pelmenschikov et al., 2000). These studies suggest that the effects of cluster size (taking long-range interaction into consideration) and lattice topology on the equilibrium geometry and the strength of the interactions between organic molecules and mineral surfaces should be carefully examined. In this study, four different model clusters for kaolinite were prepared in order to improve our understanding of the interaction between benzyl alcohol and kaolinite and to systematically investigate the effects of the lattice topology and surface area of the model clusters on the atomic configuration and binding energy. NMR parameters, including chemical shielding, are effective in determining local electronic structures because the parameters are sensitive to changes in the electron distribution around the nuclides of interest (Mehring, 1983; Tossell, 2001). The NMR chemical shielding tensors of the nuclides (e.g., ^{1}H, ^{13}C, ^{15}N) in adsorbates have been estimated using quantum chemical calculations in order to give insights into the hydrogen bonding and van der Waals' bondings between organic molecules and inorganic substrates, such as zeolite (Haase and Sauer, 1994; Haase and

Sauer, 1995; Krossner and Sauer, 1996; Simperler et al., 2002; Simperler et al., 2004). Most NMR experiments have explored the adsorption of organic molecules on clay minerals by probing the atomic configurations around the nuclides in the adsorbates (Feng et al., 2005; Wang and Xing, 2005; Winkler et al., 2007). Because ^{17}O NMR chemical shielding is also sensitive to local electronic structures, and thus the atomic configuration around oxygen (see Stebbins 1995 and the references therein), the changes in atomic environments due to adsorption can potentially be investigated by exploring the changes in the ^{17}O NMR chemical shift for oxygens in the layer silicates before and after the adsorption. Recent ^{17}O triple-quantum magic-angle spinning (3QMAS) NMR studies have shown that in chemically distinct O environments, a resolution of up to several ppm can be achieved for phyllosilicates (e.g., ^{17}O enriched natural kaolinite and synthetic complex 2:1 layer silicates) (Lee and Stebbins, 2003; Lee et al., 2003; Lee and Weiss, 2008). Quantum chemical calculations of ^{17}O NMR chemical shielding for model layer silicates before and after adsorption can, therefore, test the utility of the 3QMAS NMR technique as an experimental probe of adsorption on kaolinite.

In this study, optimized structures, binding energies, and NMR chemical shieldings of the interactions between benzyl alcohol and kaolinite surfaces are estimated by performing quantum chemical calculations. Then, the nature of the interactions and the importance of model clusters used to simulate clay minerals are discussed.

Table 3-1. BSSE corrected binding energies (kJ/mol) between the tetrahedral layer (T) or octahedral layer (O) of kaolinite and other organic molecules, as reported in previous studies of quantum chemical calculations applying cluster approximation.

Model Cluster*	Organic Molecule†	Binding Energy‡	Level of Theory and Basis Set§	Reference‖
1 ring T + 1 ring O	Acetatic acid (T)	-17.2 ~ -10.9	B3LYP/SVP+sp:MNDO ~ B3LYP/SVP	(1)
	Acetate ion (O)	-280.9 ~ -305.6	B3LYP/SVP+sp ~ B3LYP/SVP:MNDO	
1 ring O	Formamide (O)	-60.9	B3LYP/3-21G*	(2)
	N-methylformamide (O)	-15.4	B3LYP/3-21G*	
	Dimethylsulfoxide (O)	-11.1	B3LYP/3-21G*	
7 ring T + 7 ring O	Sarin (T)	-31.0	B3LYP/6-31G(d,p):PM3	(3)
	Soman (T)	-38.1	B3LYP/6-31G(d,p):PM3	
	Sarin (O)	-69.1	B3LYP/6-31G(d,p):PM3	
	Soman (O)	-63.6	B3LYP/6-31G(d,p):PM3	
1 ring T + 1 ring O	Sarin (T)	-20.5 ~ -16.3	B3LYP/6-31G(d,p):HF/3-21G ~ B3LYP/6-31G(d,p):PM3	
	Soman (T)	-23.9 ~ -16.7	B3LYP/6-31G(d,p):HF/3-21G ~ B3LYP/6-31G(d,p):PM3	
	Sarin (O)	-54.4 ~ -53.6	B3LYP/6-31G(d,p):HF/3-21G ~ B3LYP/6-31G(d,p):PM3	
	Soman (O)	-41.4 ~ -31.0	B3LYP/6-31G(d,p):HF/3-21G ~ B3LYP/6-31G(d,p):PM3	
1 ring T	Thymine (T)	-17.2 ~ -5.9	B3LYP/6-31++G(d,p) ~ B3LYP/6-31G(d)	(4)
1 ring O	Thymine (O)	-88.3	B3LYP/6-31G(d)	
1 ring T	Uracil (T)	-17.6 ~ -15.1	B3LYP/6-31++G(d,p) ~ B3LYP/6-31G(d)	
1 ring O	Uracil (O)	-126.9	B3LYP/6-31G(d)	
ideal 1 ring T	1,3,5-trinitrotoluene (T)	-15	B3LYP//SCF/6-31G(d)	(5)
3 ring T + 3 ring O	1,3,5-trinitrotoluene (T)	-29.7 ~ -13.0	MP2/6-31G(d): HF/6-31G(d): HF/3-21G ~ HF/6-31+G(d):HF/6-31G(d):HF/3-21G	(6)
ideal 3 ring T	1,3,5-trinitrotoluene (T)	-60.7 ~ -16.3	MP2/6-31G(d)(0.25)//HF/6-31G(d) ~ B3LYP/6-31G(d)//HF/6-31G(d)	(6)
3 ring T	2,4-dinitrotoluene (T)	-27.2	HF/3-21G	(7)
1 ring O	2,4-dinitrotoluene (O)	-74.1	HF/3-21G	
1 ring T + 1 ring O	Benzene (O)	-19.0	RHF/3-21G* using the Morokuma–Kitaura correction	(8)
	Benzene (O)	-21.6	RHF/3-21G* using the Counterpoise correction	

* T and O refer to the tetrahedral layer and octahedral layer of kaolinite, respectively. The number refers to the number of tetrahedral or octahedral rings in each layer. Thus, "1 ring T + 1 ring O" indicates that the model cluster comprises a sheet of kaolinite on both layers. A model cluster represented as "ideal" indicates that the tetrahedral layer is an ideal hexagonal ring, and a model cluster not represented as "ideal" indicates that the atomic position of the model cluster is obtained from its structural data.

† T and O in parentheses refer to the tetrahedral and octahedral surfaces, respectively, on which the organic molecule is adsorbed.

‡ The lowest and highest energies, respectively, obtained in each study.

§ Each method refers to the level of theory and basis set used in the calculation of the binding energy. The method with a colon refers to ONIOM (high level: (medium level:) low level). The lower and upper limits correspond to the methods for determining the lowest and highest binding energies, respectively, in each study.

‖ (1) Tunega et al. 2002b; (2) Michalkove et al. 2002; (3) Michalkove et al. 2004; (4) Robinson et al. 2007; (5) Pelmenschikov and Leszczynski 1999; (6) Gorb et al. 2006; (7) Michalkove et al. 2005; (8) Castro and Martins 2005.

3.2. Methods

3.2.1. Model clusters

Figure 3-1 shows the model clusters used to simulate kaolinite surfaces. All of the dangling bonds were saturated with hydrogens for charge balance. Model cluster 1 ($Si_{24}O_{66}H_{36}$) consists of seven ideal (hexagonal) silicate rings (Figure 3-1A). Symmetry constraints in this model cluster are as follows: basal and apical Si-O bond lengths are fixed at 1.616 Å and 1.618 Å, respectively (Bish, 1993), and Si-O-Si and O-Si-O angles are maintained at 140° and 109.5°, respectively, which are the average values for silica (Sauer et al., 1994). The O-H bond length, Si-O-H angle, and O-Si-O-H dihedral angle for the dangling hydrogen atoms are fixed at 0.96 Å, 140°, and 0°, respectively (Pelmenschikov et al., 1992; Sauer et al., 1994; Zhanpeisov et al., 1999). Model cluster 2 ($Si_{24}O_{66}H_{36}$) is composed of seven ditrigonal silicate rings and the atomic positions are obtained from crystallographic data (Bish and von Dreele, 1989) (Figure 3-1B). Kaolinite has three distinct basal oxygen sites (O3, O4, and O5), as shown in Figure 3-1B, and two apical oxygen sites (O1 and O2). Model cluster 3 ($Al_{13}Si_{13}O_{63}H_{35}$) is a sheet of kaolinite that consists of three rings of tetrahedral silicate and octahedral aluminum layers (Figure 3-1C). This model cluster consists of seven inner hydrogens 19 interlayer hydrogens (Hobbs et al., 1997), and nine dangling hydrogens. Model cluster 4 ($Si_{13}O_{37}H_{22}$), which consists of three ditrigonal silicate rings, is obtained by removing the octahedral layer from model cluster 3 (Figure 3-1D).

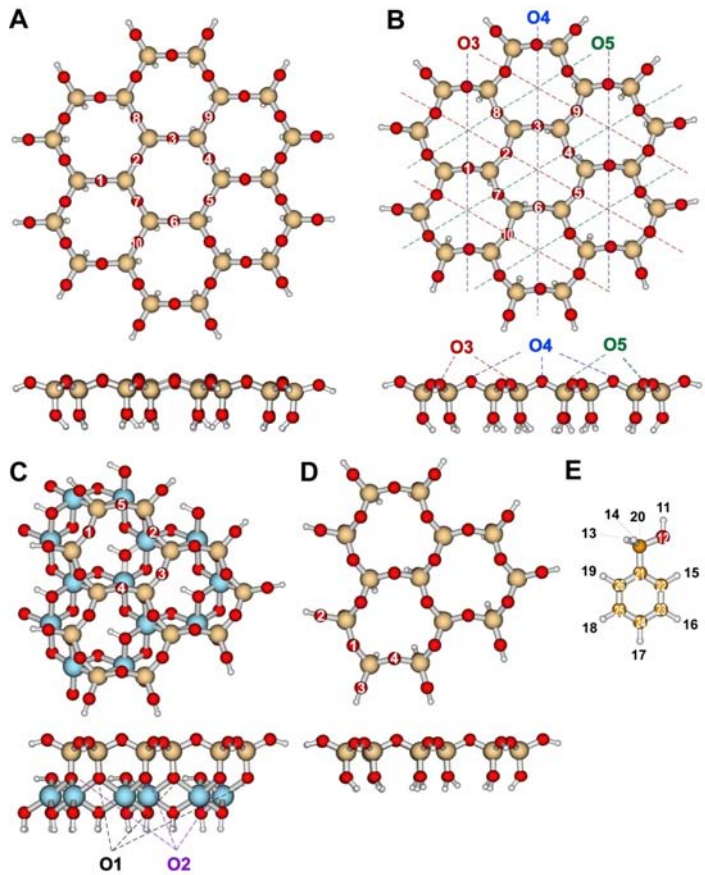

Figure 3-1. Four different model clusters for simulating kaolinite: (A) Model cluster 1; (B) model cluster 2 with three distinct basal oxygen sites—O3, O4, and O5 (indicated by red, blue, and green dashed lines, respectively); (C) model cluster 3 with two distinct apical oxygen sites—O1 and O2 (indicated by black and purple dashed lines, respectively); and (D) model cluster 4; and (E) the optimized molecular structure of benzyl alcohol calculated at the HF level with a 6-31G basis set. The top view (top) and side view (bottom) are shown in (A)-(D). In all of the clusters, the oxygen, silicon, hydrogen, aluminum, and carbon atoms are represented by red, wheat-colored, white, blue, and gold spheres, respectively.

It should be noted that a model cluster with a single siloxane ring is too small to be used for describing the interaction between the layer silicates and benzyl alcohol and that the results would be largely affected by the terminal hydrogens. Three-ring clusters have often been used to simulate layer silicate surfaces (e.g., Gorb et al. 2006; Michalkova et al. 2005). It would be difficult to carry out quantum chemical calculations for clusters larger than seven silicate rings without using the ONIOM method, which utilizes multilevel calculation for computational efficiency (Svensson et al., 1996). In this study, a seven member ring cluster without ONIOM, which was more thorough and precise in reproducing the potential energy of the electrons in the interaction between the silicates and organic molecules, but necessitated a moderate computational cost, was used. Thus, the three-ring cluster represents a relatively small silicate surface and seven-ring cluster a larger surface. This study serves as a starting point to explore the effects of cluster size and lattice topology on the adsorption of organic molecules on kaolinite surfaces. Surfaces with intermediate sizes (i.e., four, five, and six ring clusters) remain to be explored because the current study only provides the results for two model end members.

3.2.2. Computational methods

Geometry optimization, binding energy, and NMR chemical shielding calculations involving quantum chemical calculations were performed using Gaussian 03 (Frisch et al., 2004). Whereas a much larger cluster can be studied using MD simulations, the potential fields used for

MD simulations are greatly simplified compared with those based on the detailed electron interactions used in the current quantum chemical calculations. Quantum chemical calculations can be performed with either a Gaussian atomic orbital basis set or plane wave basis set. Quantum chemical calculations using Gaussian basis sets, where it is essential to select an appropriate cluster choice to obtain the desired results were performed.

A cluster of benzyl alcohol ($C_6H_5CH_2OH$) molecules was optimized without molecular symmetry constraints at the Hartree-Fock (HF) level of theory with a 6-31G basis set. Figure 3-1E shows the optimized molecular structure of benzyl alcohol. The geometry optimization of the intermolecular structure of benzyl alcohol adsorbed on each model cluster was performed at the HF level of theory with the 6-31G basis set, and additionally, on model clusters 1 and 2, at the Becke, three-parameter, Lee-Yang-Parr (B3LYP) hybrid functional level of theory with the 6-31G and 6-31G(d) basis sets (Lee et al., 1988; Becke, 1993; Becke, 1993). The benzyl alcohol molecule was located at the same position on each siloxane surface with the same initial configurations of inter-molecular distances, angles, and dihedral angles.

It should be noted that only the distances, angles, and dihedral angles between benzyl alcohol and each model cluster could be varied, while the internal variables for benzyl alcohol and each model cluster were fixed upon optimizing the geometry of benzyl alcohol adsorption on the tetrahedral layer of the model cluster. Because the orientation of the

δ

hydroxyl groups could play an important role in the adsorption of the kaolinite on the octahedral layer, the hydrogen atoms of the interlayer and inner hydroxyl groups of model cluster 3 were also varied upon geometry optimization.

Binding energy (E_{bind}) is defined as

$$E_{bind} = (E_A + E_B) - E_{AB} . \qquad (3.1)$$

where E_{AB} is the total energy of AB molecule, and E_A and E_B are the energies of molecules A and B, respectively. The binding energies between benzyl alcohol and model clusters 1 and 2 were calculated at the HF level with a 6-31G basis set; at the B3LYP level with 6-31G, 6-31G(d), and 6-311+G(2d,p) basis sets; and at the MP2 level with a 6-31G basis set for the optimized geometries at HF/6-31G. In addition to these, the binding energies between benzyl alcohol and model clusters 1 and 2 were also calculated at the B3LYP level with the 6-31G and 6-31G(d) basis sets for the optimized geometries determined at each level [i.e., B3LYP/6-31G//B3LYP/6-31G and B3LYP/6-31G(d)//B3LYP/6-31G(d)]. The binding energies between benzyl alcohol and model clusters 3 and 4 were calculated at the HF level with a 6-31G basis set and at the B3LYP level with 6-31G, 6-31G(d), and 6-311+G(2d,p) basis sets for the optimized geometries at HF/6-31G. Basis set superposition errors (BSSE) in the binding energies were corrected using the counterpoise method (Boys and Bernardi, 1970).

The NMR chemical shielding tensors of the hydrogens (^{1}H),

carbons (^{13}C) in benzyl alcohol, and basal oxygens (^{17}O) were calculated using the gauge-including atomic orbital (GIAO) method, the individual gauges for atoms in molecules (IGAIM) method, and the continuous set of gauge transformations (CSGT) method at the B3LYP level of theory with a 6-31G(d) basis set for benzyl alcohol and all model clusters before and after the adsorption. Because the calculated NMR chemical shielding tensors depend on the choice of basis sets, energy level of theory, and cluster size (Foresman and Frisch, 1996; Xue and Kanzaki, 1998; Tossell, 2001; Frisch et al., 2004)], the ^{17}O NMR chemical shielding tensors of the basal oxygens were also calculated at the B3LYP level with a 6-311+G(2d,p) basis set for model clusters 1 and 2 to check the effect of the basis sets. As for the ^{17}O chemical shielding tensors of the basal oxygens, the calculated ^{17}O NMR chemical shifts of the basal oxygens using the IGAIM and the CSGT methods ranged approximately from 20 to 34 ppm [referenced to $H_2O(l)$ with an absolute chemical shielding value of 287.5 $\pm$ 0.6 ppm, see Wasylishen and Bryce 2002], and are not consistent with the experimental ^{17}O NMR results for bridging oxygen in layer silicates [ranging from 43 to 56 ppm (Lee and Stebbins, 2003)] and in other silicates [ranging approximately from 40 to 87 ppm (Stebbins, 1995)]. The ^{17}O isotropic chemical shifts for basal oxygens [referenced to $H_2O(l)$], calculated using the GIAO method, range from 42.5 to 51.1 ppm [B3LYP/6-31G(d)] and from 58.6 to 68.5 ppm [B3LYP/6-311+G(2d,p)]; thus, the experimental ^{17}O isotropic chemical shifts were reasonably well-reproduced (see Results and Discussion below). As the GIAO method has also been successful in

δ

calculating the ^{17}O chemical shifts for diverse oxide materials (e.g., Lee 2004; Lee and Lee 2006; Xue and Kanzaki 1998), and the IGAIM and CSGT methods have been used mostly to calculate the ^{1}H and ^{13}C NMR chemical shielding tensors in organic molecules (e.g., Huang et al. 2005; Simion and Sorensen 1996; Wiberg et al. 1999), the O-17 NMR *chemical shieldings* that were found using the GIAO method are reported (see below for more discussion). The ^{17}O quadrupolar coupling constants (C_q) and asymmetry parameters (η) were calculated at the B3LYP level of theory with a 6-31G(d) basis set using the Gaussian 03 and were extracted using the EFGshield (Adiga et al., 2007).

3.3. Results and Discussion

3.3.1. Optimized structures

Figure 3-2 shows the optimized structures of benzyl alcohol adsorbed on model clusters; the structures are calculated at the HF level of theory with a 6-31G basis set. The optimized structures on the tetrahedral layer have various configurations depending on the topology and size of the model clusters. The planes of benzene rings on model clusters 1 and 2 are subparallel to the siloxane surfaces, with a slight inclination toward the center of the tetrahedral surface due to hydrogen bonding between alcohol hydrogen [H(11) in the benzyl alcohol molecule, Figure 3-1E] and basal oxygens and the dispersion forces between the benzene rings and basal oxygens (Figures 3-2A and 2B, see below for further discussion). Since the benzyl alcohol molecule is located at the center of the siloxane ring, it is

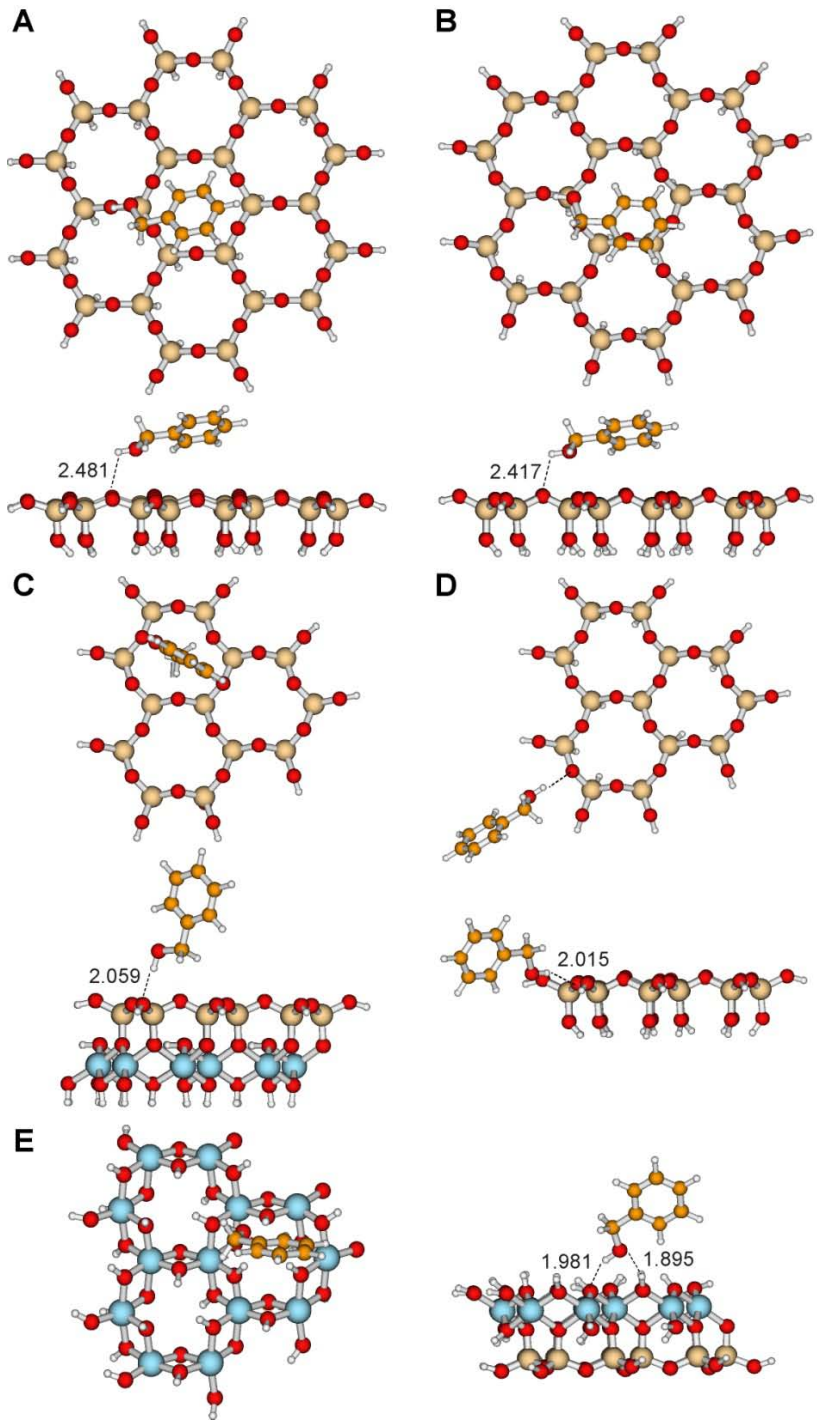

Figure 3-2. (caption on next page)

Figure 3-2. Optimized structures of benzyl alcohol adsorbed on (A) model cluster 1, (B) model cluster 2, (C) the tetrahedral layer of model cluster 3, (D) model cluster 4, and (E) the octahedral layer of model cluster 3, calculated at HF/6-31G. The top view and side view of the optimized structure are shown for each of the clusters. The oxygen, silicon, hydrogen, aluminum, and carbon atoms are represented by red, wheat-colored, white, blue, and gold spheres, respectively. In the top views of (C) and (E), the bottom layers [the octahedral layer in (C) and the tetrahedral layer in (E)] have been removed for visual clarity. Dashed lines indicate the hydrogen bonding in each model cluster and the numbers indicate the hydrogen bonding distances (the unit is Å).

unlikely that the optimized structures are significantly affected by the terminal hydrogens. The optimized structures of benzyl alcohol adsorbed on the tetrahedral layer of model clusters 3 and 4 are different from those on model clusters 1 and 2: the plane of the benzene ring is perpendicular to the siloxane surface for model cluster 3, and the benzyl alcohol molecule is located outside the basal surface of model cluster 4. The configurations for model clusters 3 and 4 are probably due to the small cluster size where the interaction between the terminal hydrogen and the hydrogens of the benzene ring is apparently dominant. The optimized geometries of clusters with (model cluster 3) and without (model cluster 4) the octahedral layer are also different, demonstrating the effect of the octahedral layer on the adsorption. Figure 3-2E shows the optimized structure of benzyl alcohol adsorbed on the octahedral layer of model cluster 3. The plane of the benzene ring is also normal to the octahedral surface of model cluster 3 (as is the case for the tetrahedral layer, as shown in Figure 3-2C): hydrogen bonds are formed between the oxygen in the alcohol group [O(12) in the benzyl alcohol molecule, Figure 3-1E] and the hydrogen in the hydroxyl group of the octahedral surface, and between the hydrogen in the alcohol group [H(11) in the benzyl alcohol molecule, Figure 3-1E] and the oxygen in the hydroxyl group of the octahedral surface. Note that the basal surface at the octahedral layer consists of only interlayer hydrogens, and therefore, the octahedral layer of model cluster 3 is free from perturbations caused by the terminal hydrogens. Figure 3-3 shows the optimized structures of benzyl alcohol adsorbed on model clusters 1and 2 calculated at the B3LYP

energy level of theory. Whereas the optimized structures are clearly dependent on the lattice topology, the optimized configurations at the B3LYP level of theory and varying basis sets are rather similar to those calculated at the HF level of theory (Figure 3-2), suggesting that the optimized geometry are not much dependent on the energy level of theory or the basis set [Figures 3-2A, 3- 3A, and 3-3C show model cluster 1 calculated at HF/6-31G, B3LYP/6-31G, and B3LYP/6-31G(d), respectively, and Figures 3-2B, 3-3B, and 3-3D show model cluster 2 calculated at HF/6-31G, B3LYP/6-31G, and B3LYP/6-31G(d), respectively]. Table 3-2 shows the interatomic distances between benzyl alcohol and the tetrahedral layer of each model cluster. Figure 3-2 (and Figure 3-3) further indicates that the detailed optimized structures of model clusters 1 and 2 are different. For instance, the distances between the hydrogen in the alcohol group [H(11) in Figure 3-1E] and the basal oxygen in model cluster 1 are longer than those in model cluster 2, regardless of the calculation method used [HF/6-31G, B3LYP/6-31G, and B3LYP/6-31G(d)]. The distances between the basal oxygens and the hydrogens in benzene ring [H(15), H(16), H(17), H(18), and H(19) in the benzyl alcohol molecule, Figure 3-1E] for model cluster 1 are generally shorter than those for model cluster 2 (Table 3-2).

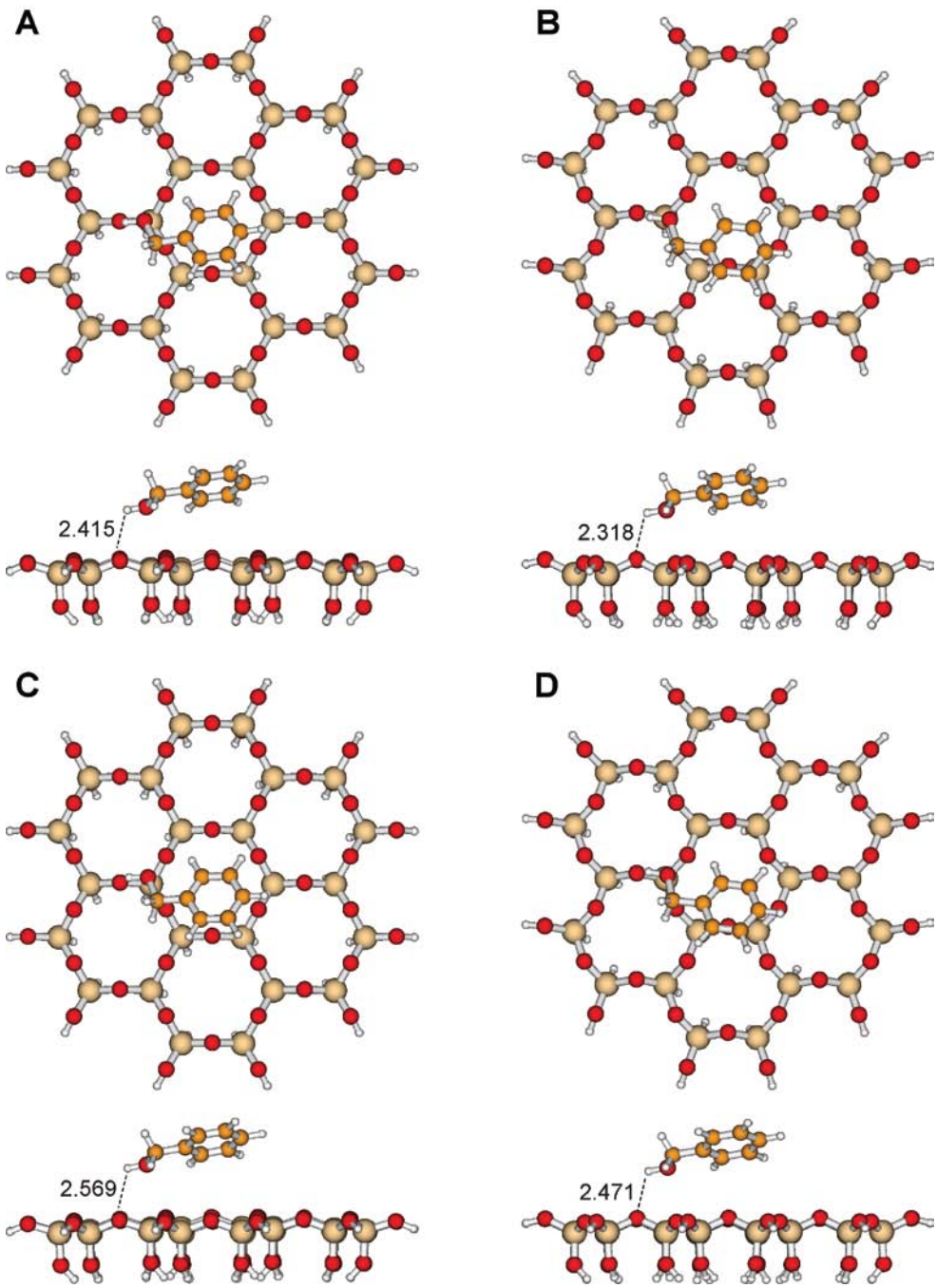

Figure 3-3. (caption on next page)

Figure 3-3. Optimized structures of benzyl alcohol adsorbed on (A) model cluster 1 and (B) model cluster 2, calculated at B3LYP/6-31G, and on (C) model cluster 1 and (D) model cluster 2, calculated at B3LYP/6-31G(d). The top view and side view of the optimized structure are shown for each of the clusters. The oxygen, silicon, hydrogen, aluminum, and carbon atoms are represented by red, wheat-colored, white, blue, and gold spheres, respectively. Dashed lines indicate the hydrogen bonding in each model cluster and the numbers indicate the hydrogen bonding distances (the unit is Å).

Table 3-2. Interatomic distances (Å) in the optimized structures of benzyl alcohol adsorbed on the tetrahedral layer of each model cluster of kaolinite; the distances are calculated at the HF (all clusters) and B3LYP (model clusters 1 and 2) levels of theory with 6-31G and 6-31G(d) basis sets.

Atom in kaolinite (atom number in Figures 3-1A-D) - Atom in benzyl alcohol (atom number in Figure 3-1E)	HF/6-31G (Å)		B3LYP/6-31G (Å)		B3LYP/6-31G(d) (Å)	
	Cluster 1	**Cluster 2**	**Cluster 1**	**Cluster 2**	**Cluster 1**	**Cluster 2**
O(1)-H(11)	2.481	2.417	2.415	2.318	2.569	2.471
O(2)-H(15)	2.746	2.896	2.702	2.890	3.044	3.194
O(4)-H(16)	3.089	3.215	2.930	2.994	3.296	3.425
O(5)-H(17)	4.112	4.451	3.890	3.926	4.174	4.417
O(6)-H(18)	4.976	5.059	4.796	4.706	4.948	5.084
O(6)-H(19)	4.459	4.318	4.360	4.388	4.557	4.713
O(7)-H(13)	2.789	2.755	2.716	2.694	2.828	2.881
O(7)-H(14)	4.264	4.268	4.183	4.212	4.330	4.418
	Cluster 3	**Cluster 4**				
O(1)-H(11)	2.059	2.015				
O(2)-H(13)	2.780	4.124				
O(3)-H(19)	4.038	3.144				
O(4)-H(14)	2.529					

The shortest distances between the hydrogen in the alcohol group [H(11) in Figure 3-1E] and the basal oxygen of the tetrahedral layer of model clusters 1, 2, 3, and 4, calculated at HF/6-31G, are 2.481 Å, 2.317 Å, 2.059 Å, and 2.015 Å, respectively, and the two hydrogen bond distances in the case of the octahedral layer of model cluster 3, calculated at HF/6-31G, are 1.895 Å and 1.981 Å (Figure 3-2). The relative strength of hydrogen bonding is estimated by considering the distance between hydrogen and the acceptor atom (i.e., oxygen); the distance ranges of 1.2–1.5, 1.5–2.2, and 2.2–3.0 Å correspond to strong, medium, and weak hydrogen bonds, respectively (Parthasarathi and Subramanian, 2006; Rozas, 2007). On the basis of this correspondence, the hydrogen bond for model clusters 1 and 2 can be categorized as weak (note that this classification was based on the interatomic distance only, see below for further discussion). The adsorption on the tetrahedral layer of model clusters 3 and 4 and on the octahedral layer of model cluster 3 are characterized by medium hydrogen bonding.

3.3.2. Binding energies

Table 3-3 and Figure 3-4 show the binding energies between each model cluster and benzyl alcohol. The binding energies calculated at the HF level of theory are larger than those calculated at the B3LYP level of theory and decrease with an increase in the number of basis set functions (Foresman and Frisch, 1996; Pelmenschikov and Leszczynski, 1999). The binding energies calculated at MP2/6-31G for model clusters 1 and 2 are smaller than those calculated at HF/6-31G, but larger than those based on

Table 3-3. BSSE corrected binding energies (kJ/mol) between each model cluster and benzyl alcohol. The BSSE values are shown in parentheses. BSSE uncorrected binding energies can be calculated by subtracting the BSSE values from the BSSE corrected binding energy values.

	Cluster 1	**Cluster 2**	**Cluster 3 (tetrahedral layer)**	**Cluster 3 (octahedral layer)**	**Cluster 4**
HF/6-31G	-33.4 (29.9)	-37.1 (26.8)	-52.8 (24.2)	-92.7 (22.1)	-71.3 (15.4)
B3LYP/6-31G//HF/6-31G	1.5 (26.7)	-0.6 (30.4)	-16.8 (19.0)	-62.7 (27.7)	-29.1 (17.3)
B3LYP/6-31G(d)//HF/6-31G	8.9 (25.4)	13.0 (30.4)	-1.2 (16.7)	-52.5 (23.8)	-19.8 (14.6)
B3LYP/6-311+G(2d,p)//HF/6-31G	9.4 (16.7)	7.5 (17.0)	-2.7 (11.4)	-43.9 (7.7)	-16.6 (5.1)
MP2/6-31G//HF/6-31G	-4.2 (42.4)	-8.6 (39.6)			
B3LYP/6-31G	3.3 (33)	3.4 (34.1)			
B3LYP/6-31G(d)	13.3 (30.7)	6.9 (25.4)			

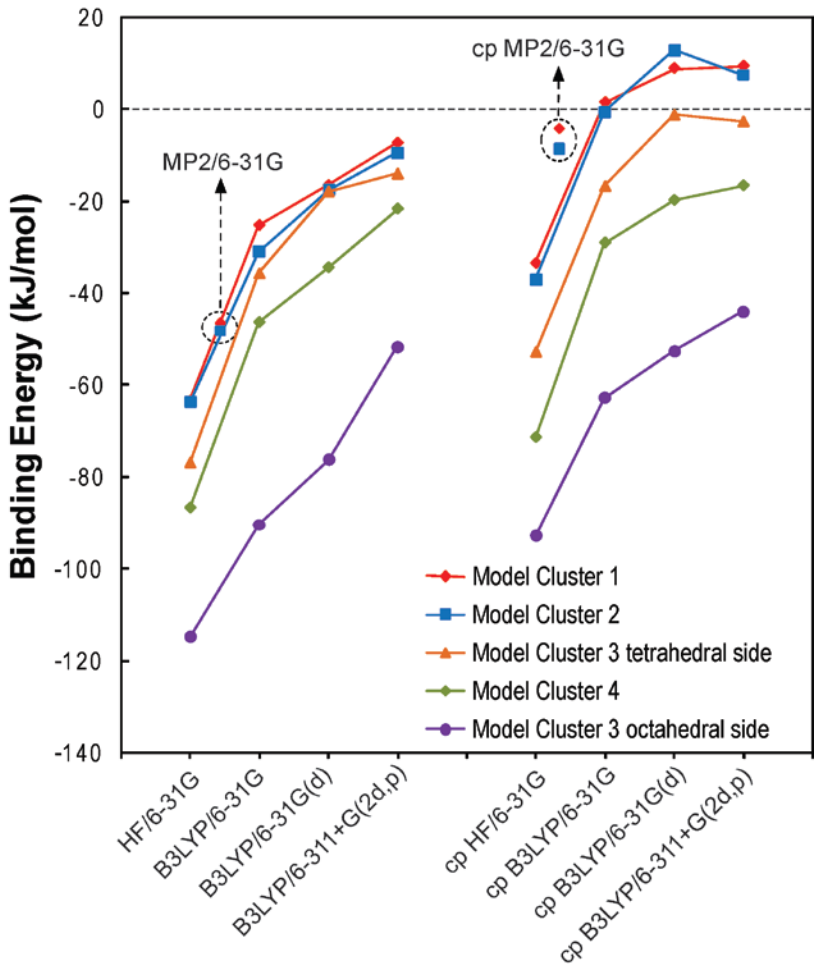

Figure 3-4. Binding energies between benzyl alcohol and each model cluster for the optimized structures at HF/6-31G. The level of theory and the basis set for each binding energy are given in the x-axis label. A basis set with the prefix "cp" indicates counterpoise correction. Dashed ellipses indicate binding energies calculated at MP2/6-31G for model clusters 1 and 2.

B3LYP/6-31G. The BSSE corrected binding energies are systematically smaller than the binding energies without counterpoise correction.

While the calculated binding energy varies significantly with the energy levels of theory and the types of basis sets, the binding energy differences among the clusters are fairly constant, regardless of the calculation method (from the weakest to the strongest binding energy: model cluster 1 < model cluster 2 < tetrahedral layer of model cluster 3 < model cluster 4 < octahedral layer of model cluster 3). The BSSE corrected binding energies (uncorrected values are shown in parentheses) are –33.4 to +9.4 (–63.3 to –7.3) kJ/mol (model cluster 1), –37.1 to +13.0 (–63.8 to -9.5) kJ/mol (model cluster 2), –52.8 to –1.2 (–77.0 to –14.0) kJ/mol (tetrahedral layer of model cluster 3), -92.7 to -43.9 (–114.8 to -51.6) kJ/mol (octahedral layer of model cluster 3), and –71.3 to –16.6 (–86.7 to –21.7) kJ/mol (model cluster 4). The basis set superposition error values range from 5.1 to 42.4 kJ/mol and are similar to the values reported for interactions between organic molecules and clay minerals or oxide fragments (Pelmenschikov and Leszczynski, 1999; Michalkova et al., 2002; Tunega et al., 2002; Castro and Martins, 2005; Gorb et al., 2006; Granqvist et al., 2007; Robinson et al., 2007). Whereas the BSSE is comparable to the calculated binding energy difference, it should be noted that the *differences* in the binding energies among the model clusters are rather constant regardless of the level of theory and the basis sets. At identical levels of theory and with similar basis sets, the differences between the binding energies for model cluster 1 and those for model cluster 2 are relatively insignificant (0.1 to 6.4 kJ/mol)

(Table 3-3). However, the optimized structures are rather different (Table 3-2 and Figures 3-2 and 3-3), which indicates the effect of the lattice topology (i.e., ideal hexagonal rings vs. ditrigonal rings) on the atomic arrangement of the molecules on the kaolinite surfaces.

As shown in Table 3-3 and Figure 3-4, the binding energies for model clusters 1 and 2 at the B3LYP level of theory are observed to be positive in the current study. A positive binding energy for the interactions between kaolinite and other organic molecules has not been reported in previous studies. However, positive binding energies have been reported for weakly bonded systems at the density functional theory, including B3LYP, after counterpoise corrections. Examples include diatomic rare gas molecules (Pérez-Jordá and Becke, 1995), van der Waals complexes between hydrogen peroxide and nitrogen, helium, neon, and argon (Molina et al., 2002), and $H_3C–H \cdots [NO]$ complexes (Crespo-Otero et al., 2005). Thus, the positive values may be due to the underestimation of the weak interatomic interactions, including dispersion forces, in the calculations based on B3LYP. Because the dispersion force arises from the correlation of excited electrons between molecules (i.e., inter-molecular electronic interaction) (Stone, 1996), molecular orbital methods involving electron correlation, such as the MP2 method, may better describe non-primary bonding, such as hydrogen bonding, and the dispersion force (Møller and Plesset, 1934; Cremer, 1998). This is because the second-order perturbation term explicitly includes a contribution from the dispersion force term (Stone, 1996). Because MP2 calculation for large clusters, as in the current

study, is computationally expensive, the binding energies were calculated using a relatively small basis set (i.e., 6-31G) for benzyl alcohols adsorbed on model clusters 1 and 2. Calculation with an extended basis set at the MP2 level needs to be examined.

The calculated binding energy at MP2/6-31G with counterpoise correction is found to be negative (–4.2 kJ/mol for model cluster 1 and –8.6 kJ/mol for model cluster 2). Therefore, the current results (weak positive or nearly zero binding energies calculated at the B3LYP level and weak negative binding energies at the MP2 level for model clusters 1 and 2) indicate that B3LYP may not completely reproduce weak interactions, such as dispersion force interactions, as suggested by other studies (Pérez-Jordá and Becke, 1995; Stone, 1996; Molina et al., 2002; Crespo-Otero et al., 2005). The results also indicate the contribution of the dispersion force potential to the interactions between the benzene ring and basal oxygens.

Table 3-1 shows the binding energies between kaolinite and other organic molecules reported in previous quantum chemical calculations using cluster approximation. The BSSE corrected binding energies for the octahedral layer of kaolinite are generally larger than those for the tetrahedral layer (in absolute value), which is consistent with the current results for benzyl alcohol. While a direct comparison would be difficult due to differences in the calculation methods and cluster sizes, the binding energy, which depends on the size of the clusters, the energy levels of theory, and the basis sets, calculated for benzyl alcohol on the tetrahedral layer of model clusters 1 and 2 is somewhat smaller than that calculated for

other molecules. The binding energy for benzyl alcohol on the octahedral layer of model cluster 3 is comparable to that calculated for other molecules.

3.3.3. NMR chemical shielding

Table 3-4 shows the isotropic magnetic shieldings of the hydrogens (^{1}H) and carbons (^{13}C) in benzyl alcohol. While the absolute isotropic magnetic shieldings calculated using the GIAO method are slightly larger than those estimated by the IGAIM and the CSGT methods, the differences in the chemical shielding before and after adsorption is largely identical regardless of the calculation method (Table 3-4). The calculated ^{1}H isotropic magnetic shielding for hydrogen forming a hydrogen bond with surface oxygen decreases upon adsorption. The isotropic magnetic shielding of the hydrogens forming hydrogen bonds [H(11) in Figure 3-1E], calculated using the GIAO method, decreases up to 0.31 ppm for model cluster 1, 0.49 ppm for model cluster 2, 1.14 ppm for model cluster 3, and 1.99 ppm for model cluster 4 after the adsorption (Table 3-4). This trend and the magnitude of the changes in the ^{1}H chemical shielding are consistent with the previous experimental and theoretical studies of organic molecule adsorption on layer silicate surfaces (e.g., Chu et al. 1990; Xie and Hayashi 1999; Yesinowski and Eckert 2009). While further study is necessary, a stronger hydrogen bond and thus a shorter H···O distance (cluster 4) apparently leads to a larger change in the isotropic chemical shielding after the adsorption.

Table 3-4. Isotropic magnetic shieldings (ppm) of hydrogens and carbons in benzyl alcohol before and after the adsorption on the tetrahedral surface of each model cluster.

	Atom in benzyl alcohol (atom number in Figure 3-1E)	Isotropic magnetic shielding (ppm)				
		before	after* (Cluster 1)	after* (Cluster 2)	after* (Cluster 3)	after* (Cluster 4)
GIAO	H(11)	32.71	32.40 (-0.31)	32.22 (-0.49)	31.56 (-1.14)	30.71 (-1.99)
	H(13,14)	27.55	27.46 (-0.08)	27.36 (-0.18)	26.95 (-0.60)	27.46 (-0.09)
	H(15,16,17,18,19)	25.24	25.07 (-0.17)	25.01 (-0.23)	25.00 (-0.24)	25.24 (0.00)
	C(20)	128.86	128.91 (0.05)	128.87 (0.02)	130.00 (1.15)	129.6 (0.72)
	C(21)	59.14	58.55 (-0.59)	58.47 (-0.68)	56.67 (-2.47)	56.7 (-2.44)
	C(22,26)	74.34	73.93 (-0.40)	73.8 (-0.54)	73.48 (-0.86)	73.9 (-0.46)
	C(23,24,25)	71.61	71.52 (0.09)	71.49 (-0.12)	72.37 (0.77)	72.1 (0.51)
IGAIM	H(11)	32.03	30.83 (-1.19)	30.82 (-1.21)	30.49 (-1.53)	30.29 (-1.73)
	H(13,14)	26.37	25.52 (-0.85)	25.54 (-0.92)	25.32 (-1.05)	26.13 (-0.23)
	H(15,16,17,18,19)	24.84	23.90 (-0.94)	-23.92 (-0.92)	24.18 (-0.66)	24.82 (0.02)
	C(20)	126.65	126.12 (-0.53)	126.32 (-0.33)	127.81 (1.15)	127.99 (1.33)
	C(21)	58.75	57.38 (-1.38)	57.42 (-1.33)	55.71 (-3.04)	56.28 (-2.48)
	C(22,26)	70.99	69.70 (-1.29)	69.79 (-1.20)	69.64 (-1.35)	70.58 (-0.41)
	C(23,24,25)	69.00	68.02 (-0.98)	68.08 (-0.92)	69.39 (0.39)	69.55 (0.56)
CSGT	H(11)	32.00	30.83 (-1.18)	30.81 (-1.20)	30.50 (-1.51)	30.29 (-1.71)
	H(13,14)	26.34	25.50 (-0.84)	25.53 (-0.81)	25.31 (-1.03)	26.11 (-0.23)
	H(15,16,17,18,19)	24.81	23.88 (-0.93)	23.91 (-0.91)	24.15 (-0.66)	24.79 (-0.02)
	C(20)	126.65	126.12 (-0.53)	126.33 (-0.32)	127.81 (1.16)	127.99 (1.33)
	C(21)	58.76	57.39 (-1.37)	57.44 (-1.32)	55.72 (-3.04)	56.28 (-2.48)
	C(22,26)	70.98	69.70 (-1.28)	69.79 (-1.19)	69.63 (-1.35)	70.56 (-0.41)
	C(23,24,25)	68.98	68.01 (-0.97)	68.07 (-0.91)	69.37 (0.39)	69.54 (0.55)

***** The number in parentheses is the difference in the isotropic magnetic shielding [(after the adsorption) – (before the adsorption)].

The calculated differences in the ^{13}C isotropic magnetic shielding for benzyl alcohol are insignificant, with the exception of those for C(21) (in Figure 3-1E) in model clusters 3 and 4, where the differences are approximately 2-3 ppm. While the ^{13}C isotropic magnetic shielding differences calculated using the GIAO method are slightly smaller than those estimated using the IGAIM and the CSGT methods (up to approximately 0.9 ppm), the differences in chemical shielding calculated using the IGAIM and the CSGT methods are almost identical. The relatively larger decrease in chemical shielding for C(21) in model clusters 3 and 4 may also stem from the stronger hydrogen bonding between benzyl alcohol and those clusters (Table 3-4).

The ^{17}O isotropic chemical shieldings of basal oxygens before the adsorption (without benzyl alcohol) in model cluster 1 calculated at B3LYP/6-31G(d), range from 243.8 ppm to 253.2 ppm, apparently depending on the distance from the center of the model cluster. They are also slightly affected by the configurations of dangling hydrogens attached to apical oxygens (note that the oxygen sites in model cluster 1 are not crystallographically distinct). These results demonstrate that the ^{17}O NMR chemical shielding strongly depends on the atomic configuration around the second and higher coordination environments as well as on the nearest-neighbor atomic arrangements (e.g., Lee 2004; Tossell 2001). The isotropic chemical shieldings of the basal oxygens in the other model clusters calculated at B3LYP/6-31G(d) range from 236.4 ppm to 245.0 ppm (for model cluster 2), from 242.7 ppm to 251.7 ppm (for model cluster 3), and

from 243.7 ppm to 250.2 ppm (for model cluster 4). Those of the oxygens in model cluster 2 are dependent on the crystallographic positions (i.e., O3, O4, and O5 in Figure 3-1B): the average Si-O-Si bond angles are 130.6° (O3), 142.6° (O4), and 132.6° (O5), and the average Si-O bond lengths are 1.608 and 1.614 Å (O3), 1.597 and 1.628 Å (O4), and 1.611 and 1.618 Å (O5) (Bish and von Dreele, 1989). The isotropic chemical shifts [referenced to $H_2O(l)$] for the O3, O4, and O5 sites in model cluster 2 calculated at B3LYP/6-31G(d) are 43.8 ± 1.2, 45.6 ± 0.7, and 49.9 ± 1.0 ppm, respectively. While there is a noticeable basis set effect (see Computational methods above), the ^{17}O chemical shielding calculated at B3LYP/6-311+G(2d,p) show a similar trend with respect to cluster size variation and crystallographically distinct oxygen environments. The trend in the average chemical shielding for oxygen sites in the current study is somewhat different from the trend suggested in a previous O-17 3QMAS NMR study of kaolinite, where the isotropic chemical shifts for the O3, O4, and O5 sites were 54.3 ± 1, 46.5 ± 1, and 51.3 ± 1 ppm, respectively (Lee and Stebbins, 2003), suggesting that a larger cluster may be necessary to reveal the relatively small difference in chemical shift in crystallographically distinct atomic sites.

Table 3-5 shows the calculated ^{17}O isotropic magnetic shieldings for the basal oxygens on the surfaces. Figure 3-5 (showing model clusters 1 and 2 only) also presents the isotropic magnetic shielding differences between the oxygen sites before and after the adsorption [(isotropic magnetic shielding after the adsorption) – (isotropic magnetic shielding before the adsorption)], where several oxygens close to benzyl alcohol are shown (see

Table 3-5. Isotropic magnetic shieldings (ppm) of several basal oxygens close to the benzyl alcohol.

	Cluster 1	Isotropic magnetic shielding (ppm)		Cluster 2	Isotropic magnetic shielding (ppm)	
	Atom*	before	after†	Atom*	before	after†
B3LYP/6-31G(d) GIAO	**O(1)**	**244.3**	**241.4 (-2.9)**	**O(1)**	**242.1**	**240.8 (-1.6)**
	O(2)	252.4	247.7 (-4.7)	O(2)	242.2	238.4 (-3.8)
	O(3)	252.7	252.2 (-0.5)	O(3)	245.0	245.0 (0)
	O(4)	252.8	251.4 (-1.4)	O(4)	238.1	236.5 (-1.6)
	O(5)	253.0	252.2 (-0.8)	O(5)	242.1	242.4 (0.3)
	O(6)	252.8	253.3 (0.6)	O(6)	243.7	244.0 (0.3)
	O(7)	252.7	251.2 (-1.5)	O(7)	238.7	238.6 (-0.1)
	O(8)	243.9	243.5 (-0.4)	O(8)	237.2	236.8 (-0.4)
	O(9)	243.9	243.1 (-0.8)	O(9)	242.4	242.2 (-0.2)
	O(10)	244.4	244.5 (0.1)	O(10)	241.0	241.3 (0.3)
B3LYP/6-311+G(2d,p) GIAO	**O(1)**	**230.4**	**226.7 (-3.7)**	**O(1)**	**226.2**	**224.7 (-1.5)**
	O(2)	239.1	233.7 (-5.4)	O(2)	227.6	222.1 (-5.5)
	O(3)	238.9	237.0 (-1.9)	O(3)	228.9	228.9 (0)
	O(4)	239.0	235.7 (-3.3)	O(4)	221.3	217.9 (-3.4)
	O(5)	239.7	237.7 (-2.0)	O(5)	227.9	228.1 (0.2)
	O(6)	239.0	237.5 (-1.5)	O(6)	226.8	225.6 (-1.2)
	O(7)	239.0	235.9 (-3.1)	O(7)	222.0	220.6 (-1.4)
	O(8)	229.9	228.4 (-1.5)	O(8)	220.5	218.9 (-1.6)
	O(9)	230.3	227.9 (-2.4)	O(9)	228.8	228.3 (-0.5)
	O(10)	230.8	228.5 (-2.3)	O(10)	225.2	225.3 (0.1)
	Cluster 3	Isotropic magnetic shielding (ppm)		Cluster 4	Isotropic magnetic shielding (ppm)	
	Atom*	before	after†	Atom*	before	after†
B3LYP/6-31G(d) GIAO	**O(1)**	**245.0**	**243.6 (-1.4)**	**O(1)**	**237.1**	**236.9 (-0.2)**
	O(4)	242.7	241.1 (-1.6)	O(4)	246.5	245.1 (-1.4)

* The number in parentheses refers to the atom number in model clusters 1, 2, 3, and 4, as indicated in Figures 3-1A, B, C, and D, respectively. O(1) forms the hydrogen bond. See Figure 3-5 for the position of each oxygen atom. Note that the atom number in Figure 3-1 (white font) is for labeling the basal oxygens only.

† The number in parentheses is the difference in the isotropic magnetic shielding [(after the adsorption) – (before the adsorption)].

δ

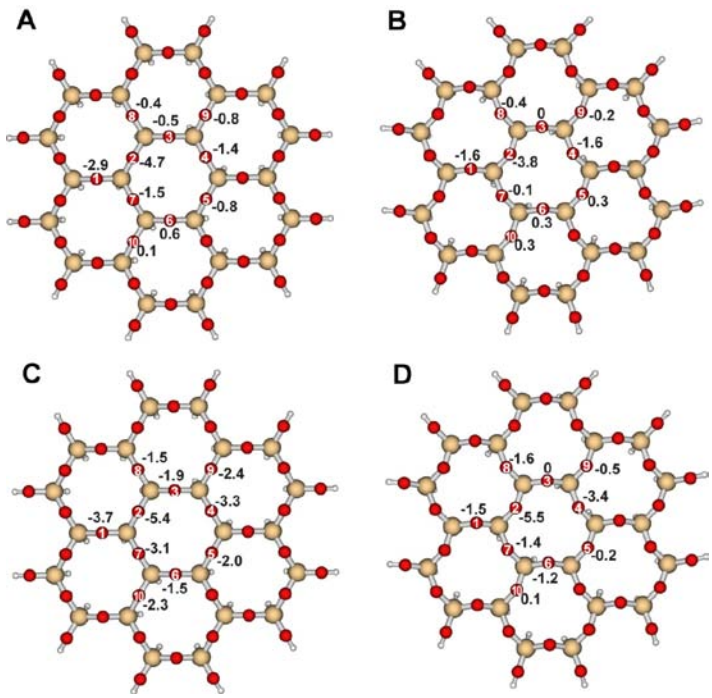

Figure 3-5. Model cluster 1 (A and C) and model cluster 2 (B and D) with the differences in chemical shielding for several oxygens close to benzyl alcohol. (A) and (B) are calculated at B3LYP/6-31G(d), and (C) and (D) are calculated at B3LYP/6-311+G(2d,p). The oxygen, silicon, and hydrogen are represented by red, wheat-colored, and white spheres, respectively. Refer to Figure 3-2 for the location of benzyl alcohol on each model cluster. The numbers on the oxygen atom are identical to those shown in Figure. 3-1. Note that the chemical shift in the oxygen site (δ_{shift}) can be described as follows: δ_{shift} = isotropic chemical shielding of oxygen in reference molecule (σ_{ref}) – isotropic chemical shielding of oxygen sites in layer silicates (σ_{oxy}). The chemical shift difference before and after the adsorption is $\Delta\delta_{shift} = \delta_{shift}$ (after adsorption) – δ_{shift} (before adsorption) = [$\sigma_{ref} - \sigma_{oxy}$ (after adsorption)] – [$\sigma_{ref} - \sigma_{oxy}$ (before adsorption)] = – [σ_{oxy} (after adsorption) - σ_{oxy} (before adsorption)] = - $\Delta\ \sigma_{oxy}$. Therefore, $\Delta\ \delta_{shift} = -\ \Delta\ \sigma_{oxy}$.

figure caption 3-5). Whereas the model clusters used in this study may not be sufficiently large to accurately estimate the NMR chemical shielding values for basal oxygens, *the differences* in the ^{17}O NMR chemical shieldings before and after the adsorption are important, revealing the effect of the adsorption. In systematically controlled calculations, as shown in the computational method section above, the difference in the chemical shift is due only to the adsorption of benzyl alcohol on the surfaces. The ^{17}O chemical shielding of the basal oxygens mostly decreases after the adsorption (see Table 3-5). The largest chemical shielding differences calculated at B3LYP/6-31G(d) are –4.7, –3.8, –1.6, and –1.4 ppm for model clusters 1, 2, 3, and 4, respectively, and those calculated at B3LYP/6-311+G(2d,p) are 5.4 and -5.5 ppm for model clusters 1 and 2, respectively. The ^{17}O chemical shift differences calculated at B3LYP/6-311+G(2d,p) are somewhat larger (from -0.1 to +2.4 ppm) than those calculated at B3LYP/6-31G(d) (Figure 3-5). This discrepancy indicates that the calculated uncertainty in the O-17 NMR chemical shielding could be as large as 2.4 ppm. Some of the oxygens in the model clusters [e.g., O(1) and O(2) in model cluster 1 and O(1) in model cluster 2] have chemical shielding differences that were larger than the maximum uncertainty, and these calculated differences stem from the adsorption. It should be noted that the oxygens that formed hydrogen bonds with benzyl alcohol did not show the largest chemical shielding differences after the adsorption [O(1) in Figure 3-5 and Table 3-1]. This may be due to the fact that the ^{17}O NMR chemical shielding is dependent, not only on the O···H distance but also on the

δ

atomic configurations beyond the first coordination environments (i.e., the entire atomic arrangement of the molecule on the surface) (Lee, 2004).

The calculated differences in the ^{17}O C_q and η of the key basal oxygen before and after the adsorption were 0.088 MHz and 0.015 [O(1) in Figure 3-1A] (model cluster 1), 0.081 MHz and 0.033 [O(1) in Figure 3-1B] (model cluster 2), 0.171 MHz and 0.024 [O(1) in Figure 3-1C] (model cluster 3), and 0.215 MHz and 0.125 [O(1) in Figure 3-1D] (model cluster 4), respectively. These differences, with the exception of the C_q for model clusters 3 and 4, are insignificant. Thus, it is difficult to investigate these changes experimentally. The relatively large changes in C_q for the oxygen sites in model cluster 4 may have resulted from the stronger hydrogen bond between the alcohol hydrogen and basal oxygen [O(1)] compared to the other clusters.

While additional theoretical NMR chemical shielding tensor calculations using larger coordination spheres for the model clusters for clay surfaces are certainly necessary, the calculated ^{17}O isotropic chemical shieldings of some basal oxygens generally decrease up to approximately 4–5 ppm after the adsorption. Since the experimental high-resolution ^{17}O 3QMAS NMR spectroscopy of layer silicates yielded a resolution of 1–2 ppm among the basal oxygen sites in the layer silicates (Lee and Stebbins, 2003; Lee et al., 2003; Lee and Weiss, 2008), the advanced ^{17}O 3QMAS may be useful in exploring the nature of the adsorption between organic molecules and silicate surfaces. Whereas the oxygen sites were well resolved in our previous ^{17}O NMR spectra for natural Georgia kaolinite

with negligible Fe content and synthetic 2:1 layer silicates without Fe (Lee and Stebbins, 2003; Lee et al., 2003; Lee and Weiss, 2008), the presence of paramagnetic impurity (e.g., Fe) in other natural layer silicates can broaden the NMR peaks. Also note that the adsorption of organic molecules may result in a broadening of the resonance peaks (in addition to the shift), making it difficult to resolve the adsorption induced changes in the chemical shift. As the current study only explores the effect of a single benzyl alcohol molecule on the surface, the additional effects of surface coverage and other diverse organic molecules on NMR chemical shielding remain to be investigated.

3.4. Conclusion

The effect of lattice topology and cluster size of four different kaolinite model clusters on the adsorption of benzyl alcohol were investigated by performing quantum chemical calculations of the optimized structure, binding energy, and NMR chemical shielding. The optimized geometry of benzyl alcohol adsorbed on the tetrahedral surface of kaolinite show that the adsorption on three-ring clusters is affected by the edge hydrogens due to relatively small surface area, while that on seven-ring clusters is not affected. The results also show that the geometry of adsorption on ideal hexagonal rings is different from that of adsorption on ditrigonal rings, demonstrating the topology dependence of adsorption. The optimized structure and binding energy calculations suggest that adsorption on the tetrahedral surface is dominated by weak hydrogen

bonding and dispersion force, while that on the octahedral surface is mostly governed by hydrogen bonding. The NMR chemical shielding calculations show that the weak interaction on the tetrahedral surface can be potentially resolved by high-resolution solid-state ^{17}O 2D NMR. The results obtained and trends observed in the present manuscript suggest that a model cluster simulating clay surfaces should be carefully designed using quantum chemical calculations, particularly when the adsorption is weak and the adsorbate is fairly large.

References

Adiga, S., Aebi, D. and Bryce, D. L. (2007) EFGShield - A program for parsing and summarizing the results of electric field gradient and nuclear magnetic shielding tensor calculations. Canadian Journal of Chemistry, 85, 496-505.

Anderson, W. G. (1986) Wettability literature survey - Part 1: Rock-oil-brine interactions and the effects of core handling on wettability. Journal of Petroleum Technology, 38(11), 1125-1144.

Aquino, A. J. A., Tunega, D., Haberhauer, G., Gerzabek, M. H. and Lischka, H. (2007) Quantum chemical adsorption studies on the (110) surface of the mineral goethite. Journal of Physical Chemistry C, 111(2), 877-885.

Bantignies, J. L., Moulin, C. C. D. and Dexpert, H. (1998) Asphaltene adsorption on kaolinite characterized by infrared and X-ray absorption spectroscopies. Journal of Petroleum Science and Engineering, 20(3-4), 233-237.

Bayer, I. S., Steele, A., Martorana, P. J. and Loth, E. (2010) Fabrication of superhydrophobic polyurethane/organoclay nano-structured composites from cyclomethicone-in-water emulsions. Applied Surface Science, 257, 823-826.

Becke, A. D. (1993) Density-functional thermochemistry. III. The role of exact exchange. Journal of Chemical Physics, 98, 5648-5652.

Becke, A. D. (1993) A new mixing of Hartree-Fock and local density-functional theories. Journal of Chemical Physics, 98(2), 1372-1377.

Bish, D. L. (1993) Rietveld refinement of the kaolinite structure at 1.5 K. Clays and Clay Minerals, 41, 738-744.

Bish, D. L. and von Dreele, R. B. (1989) Rietveld refinement of non-hydrogen atomic positions in kaolinite. Clays and Clay Minerals, 37, 289-296.

Boulet, P., Greenwell, H. C., Stackhouse, S. and Coveney, P. V. (2006) Recent advances in understanding the structure and reactivity of clays using electronic structure calculations. Journal of Molecular Structure: THEOCHEM, 762, 33-48.

Boys, S. F. and Bernardi, F. (1970) The calculation of small molecular interactions by the differences of separate total energies. Some procedures with reduced errors. Molecular Physics, 19, 553-566.

Brown, G. E. J., Calas, G., Waychunas, G. A. and Petiau, J. (1988) X-ray absorption-spectroscopy and its applications in mineralogy and geochemistry. Spectroscopic Methods in Mineralogy and Geology. F. C. Hawthorne. Chelsea, Michigan, Mineralogical Society of America, 18, 431-512 p.

Brown, G. E. J., Henrich, V. E., Casey, W. H., Clark, D. L., Eggleston, C., Felmy, A., D.W., G., Grätzel, M., Maciel, G., McCarthy, M. I., Nealson, K. H., Sverjensky, D. A., Toney, M. F. and Zachara, J. M. (1999) Metal oxide surfaces and their interactions with aqueous solutions and microbial organisms. Chemical Reviews, 99, 77-174.

Castro, E. A. S. and Martins, J. B. L. (2005) Theoretical study of benzene interaction on kaolinite. Journal of Computer-Aided Materials Design, 12, 121-129.

Chu, P.-J., Potrzebowski, M. J., Gao, Y. and Scott, A. I. (1990) Conformational studies of N-benzoyl-L-phenylalanine by combined rotation and multiple-pulse spectroscopy ^{1}H nuclear magnetic resonance. Journal of the American Chemical Society, 112, 881-883.

Cremer, D. (1998) Møller–Plesset Perturbation Theory. Encyclopedia of Computational Chemistry. P. von Rague-Schleyer. New York, John Wiley, 3, 1706-1735 p.

Crespo-Otero, R., Montero, L. A., Stohrer, W.-D. and de la Vega, J. M. G. (2005) Basis set superposition error in MP2 and density-functional theory: A case of methane-nitric oxide association. Journal of Chemical Physics, 123, 134107.

Cygan, R. T. and Kubicki, J. D., Eds. (2001) Molecular Modeling Theory: Applications in the Geosciences. Reviews in Mineralogy & Geochemistry. Washington DC, Mineralogical Society of America, 531 p.

Førland, G. M. (2001) Adsorption of benzyl alcohol onto alumina and kaolinite surfaces from a nonaqueous solution. Journal of Colloid and Interface Science, 242(2), 477-479.

Førland, G. M., Borve, K. J., Hoiland, H. and Skauge, A. (1995) Adsorption of short-chain alcohols from decane solutions onto kaolinite. Journal of Colloid and Interface Science, 171(2), 261-269.

Feng, X. J., Simpson, A. J. and Simpson, M. J. (2005) Chemical and mineralogical controls on humic acid sorption to clay mineral surfaces. Organic Geochemistry, 36(11), 1553-1566.

Foresman, J. B. and Frisch, Æ. (1996) Exploring Chemistry with Electronic Structure Methods. Pittsburgh, PA, Gaussian, Inc., 302 p.

Frisch, M. J., Trucks, G. W., Schlegel, H. B., Scuseria, G. E., Robb, M. A., Cheeseman, J. R., J.A. Montgomery, J., Vreven, T., Kudin, K. N., Burant, J. C., Millam, J. M., Iyengar, S. S., Tomasi, J., Barone, V., Mennucci, B., Cossi, M., Scalmani, G., Rega, N., Petersson, G. A., Nakatsuji, H., Hada, M., Ehara, M., Toyota, K., Fukuda, R.,

Hasegawa, J., Ishida, M., Nakajima, T., Honda, Y., Kitao, O., Nakai, H., Klene, M., Li, X., Knox, J. E., Hratchian, H. P., Cross, J. B., Bakken, V., Adamo, C., Jaramillo, J., Gomperts, R., Stratmann, R. E., Yazyev, O., Austin, A. J., Cammi, R., Pomelli, C., Ochterski, J. W., Ayala, P. Y., Morokuma, K., Voth, G. A., Salvador, P., Dannenberg, J. J., Zakrzewski, V. G., Dapprich, S., Daniels, A. D., Strain, M. C., Farkas, O., Malick, D. K., Rabuck, A. D., Raghavachari, K., Foresman, J. B., Ortiz, J. V., Cui, Q., Baboul, A. G., Clifford, S., Cioslowski, J., Stefanov, B. B., Liu, G., Liashenko, A., Piskorz, P., Komaromi, I., Martin, R. L., Fox, D. J., Keith, T., Al-Laham, M. A., Peng, C. Y., Nanayakkara, A., Challacombe, M., Gill, P. M. W., Johnson, B., Chen, W., Wong, M. W., Gonzalez, C. and Pople, J. A. (2004) Gaussian 03. Wallingford CT, Gaussian, Inc.

Gorb, L., Lutchyn, R., Zub, Y., Leszczynska, D. and Leszczynski, J. (2006) The origin of the interaction of 1,3,5-trinitrobenzene with siloxane surface of clay minerals. Journal of Molecular Structure: THEOCHEM, 766(2-3), 151-157.

Granqvist, B., Sandberg, T. and Hotokka, M. (2007) Adsorption of organic probes on silica through Lewis interactions: A comparison of experimental results and quantum chemical calculations. Journal of Colloid and Interface Science, 310, 369-376.

Haase, F. and Sauer, J. (1994) H-1 NMR chemical-shifts of ammonia, methanol, and water-molecules interacting with Brönsted acid sites of zeolite catalysts - Ab-initio calculations. Journal of Physical Chemistry, 98(12), 3083-3085.

Haase, F. and Sauer, J. (1995) Interaction of methanol with Brönsted acid sites of zeolite catalysts - An ab-initio study. Journal of the

American Chemical Society, 117(13), 3780-3789.

Hobbs, J. D., Cygan, R. T., Nagy, K. L., Schultz, P. A. and Sears, M. P. (1997) All-atom ab initio energy minimization of the kaolinite crystal structure. American Mineralogist, 82(7-8), 657-662.

Hong, H. L., Fu, Z. Y. and Min, X. M. (2001) The adsorption of $[Au(HS)_2]^-$ on kaolinite surfaces: Quantum chemistry calculations. Canadian Mineralogist, 39, 1591-1596.

Hong, H. L., Min, X. M. and Fu, Z. Y. (2002) Study on adsorption of submicrometer gold on kaolinite by quantum chemistry calculations. American Mineralogist, 87(1), 1-4.

Huang, M. J., Lee, K. S. and Hurley, S. J. (2005) Nuclear magnetic resonance spectral analysis and molecular properties of berberine. International Journal of Quantum Chemistry, 105(4), 396-409.

Johansson, U., Holmgren, A., Forsling, W. and Frost, R. L. (1999) Adsorption of silane coupling agents onto kaolinite surfaces. Clay Minerals, 34(2), 239-246.

Jurkiewicz, A. and Maciel, G. E. (1995) Solid-state ^{13}C NMR studies of the interaction of aceton, carbon tetrachloride and trichloroethylene with soil components. The Science of the Total Environment, 164, 195-202.

Kelleher, B. P. and O'Dwyer, T. F. (2002) Intercalation of benzamide into expanded kaolinite under ambient environmental conditions. Clays and Clay Minerals, 50(3), 331-335.

Knezovich, J. P., Harrison, F. L. and Wilhelm, R. G. (1987) The bioavailability of sediment-sorbed organic chemicals: A review. Water, Air, snd Soil Pollution, 32, 233-245.

Kowalska, M., Guler, H. and Cocke, D. L. (1994) Interactions of clay

minerals with organic pollutants. The Science of the Total Environment, 141, 223-240.

Krossner, M. and Sauer, J. (1996) Interaction of water with Brönsted acidic sites of zeolite catalysts. Ab initio study of 1:1 and 2:1 surface complexes. Journal of Physical Chemistry, 100(15), 6199-6211.

Kubicki, J. D., Schroeter, L., M., Itoh, M. J., Nguyen, B. N. and Apitz, S. E. (1999) Attenuated total reflectance Fourier-transform infrared spectroscopy of carboxylic acids adsorbed onto mineral surfaces. Geochimica et Cosmochimica Acta, 63(18), 2709-2725.

Kwon, K. D., Vadillo-Rodriguez, V., Logan, B. E. and Kubicki, J. D. (2006) Interactions of biopolymers with silica surfaces: Force measurements and electronic structure calculation studies. Geochimica et Cosmochimica Acta, 70(15), 3803-3819.

Lee, C., Yang, W. and Parr, R. G. (1988) Development of the Colle-Salvetti correlation-energy formula into a functional of the electron density. Physical Review B, 37(2), 785-789.

Lee, S. K. (2004) Structure of silicate glasses and melts at high pressure: Quantum chemical calculations and solid-state NMR. Journal of Physical Chemistry B, 108, 5889-5900.

Lee, S. K. and Lee, B. H. (2006) Atomistic origin of germanate anomaly in GeO_2 and Na-germanate glasses: Insights from two-dimensional ^{17}O NMR and quantum chemical calculations. Journal of Physical Chemistry B, 110, 16408-16412.

Lee, S. K., Musgrave, C. B., Zhao, P. and Stebbins, J. F. (2001) Topological disorder and reactivity of borosilicate glasses: Quantum chemical calculations and ^{17}O and ^{11}B NMR. Journal of Physical Chemistry B, 105, 12583-12595.

Lee, S. K. and Stebbins, J. F. (2003) O atom sites in natural kaolinite and muscovite: O-17 MAS and 3QMAS NMR study. American Mineralogist, 88(4), 493-500.

Lee, S. K. and Stebbins, J. F. (2006) Disorder and the extent of polymerization in calcium silicate and aluminosilicate glasses: O-17 NMR results and quantum chemical molecular orbital calculations. Geochimica et Cosmochimica Acta, 70, 4275-4286.

Lee, S. K., Stebbins, J. F., Weiss Jr., C. A. and Kirkpatrick, R. J. (2003) O-17 and Al-27 MAS and 3QMAS NMR study of synthetic and natural layer-silicates. Chemistry of Materials, 15, 2605-2613.

Lee, S. K. and Weiss, C. A. J. (2008) Multiple oxygen sites in synthetic phyllosilicates with expandable layers: ^{17}O solid-state NMR study. American Mineralogist, 93, 1066-1071.

Lee, S. Y. and Kim, S. J. (2002) Adsorption of naphtalene by HDTMA modified kaolinite and halloysite. Applied Clay Science, 22, 55-63.

Li, Y. C. and Gupta, G. (1994) Adsorption of hydrocarbons by clay-minerals from gasoline. Journal of Hazourdous Materials, 38(1), 105-112.

Møller, C. and Plesset, M. S. (1934) Note on an approximation treatment for many-electron systems. Physical Review 46, 618-622.

Madsen, L., Grahl-Madsen, L., C. Gron, Lind, I. and Engell, J. (1996) Adsorption of polar aromatic hydrocarbons on synthetic calcite. Organic Geochemistry, 24(12), 1151-1155.

Mehring, M. (1983) Principles of High Resolution NMR in Solids. Berlin Heidelberg New York, Springer-Verlag, 342 p.

Michalkova, A., Gorb, L., Ilchenko, M., Zhikol, O. A., Shishkin, O. V. and Leszczynski, J. (2004) Adsorption of sarin and soman on dickite: An ab initio ONIOM study. Journal of Physical Chemistry B, 108(6),

1918-1930.

Michalkova, A., Martinez, J., Zhikol, O. A., Gorb, L., Shishkin, O. V., Leszczynska, D. and Leszczynski, J. (2006) Theoretical study of adsorption of Sarin and Soman on tetrahedral edge clay mineral fragments. Journal of Physical Chemistry B, 110(42), 21175-21183.

Michalkova, A., Szymczak, I. J. and Leszczynski, J. (2005) Adsorption of 2,4-dinitrotoluene on dickite: The role of H-bonding. Structural Chemistry, 16(3), 325-337.

Michalkova, A., Tunega, D. and Nagy, L. T. (2002) Theoretical study of interactions of dickite and kaolinite with small organic molecules. Journal of Molecular Structure: THEOCHEM, 581, 37-49.

Molina, J. M., Dobado, J. A., Daza, M. C. and Villaveces, J. L. (2002) Structure and bonding of weak hydrogen peroxide complexes. Journal of Molecular Structure: THEOCHEM, 580, 117-126.

Murgich, J., Rodriguez M., J., Izquierdo, A., Carbognani, L. and Rogel, E. (1998) Interatomic interactions in the adsorption of asphaltenes and resins on kaolinite calculated by molecular dynamics. Energy & Fuels, 12, 339-343.

Murray, D. K., Harrison, J. C. and Wallace, W. E. (2005) A ^{13}C CP/MAS and ^{31}P NMR study of the interactions of dipalmitoylphosphatidylcholine with respirable silica and kaolin. Journal of Colloid and Interface Science, 288, 166-170.

Ogawa, M. and Kuroda, K. (1995) Photofunctions of intercalation compounds. Chemical Reviews, 95, 399-438.

Olejnik, S., Posner, A. M. and Quirk, J. P. (1970) The interaction of polar organic compounds into kaolinite. Clay Minerals, 8(4), 421-434.

Ottonello, G. and Zuccolini, M. V. (2005) Ab-initio structure, energy and

δ

stable Cr isotopes equilibrium fractionation of some geochemically relevant H-O-Cr-Cl complexes. Geochimica et Cosmochimica Acta, 69, 851-874.

Pérez-Jordá, J. M. and Becke, A. D. (1995) A density-functional study of van der Waals forces: rare gas diatomics. Chemical Physics Letters, 233, 134-137.

Parthasarathi, R. and Subramanian, V. (2006) Characterization of hydrogen bonding: From van der Waals interactions to covalency Hydrogen Bonding - New Insights. S. J. Grabowski. Dordrecht Springer, 3, 1-50 p.

Pelmenschikov, A. and Leszczynski, J. (1999) Adsorption of 1,3,5-trinitrobenzene on the siloxane sites of clay minerals: Ab initio calculations of molecular models. Journal of Physical Chemistry B, 103(33), 6886-6890.

Pelmenschikov, A., Strandh, H., Pettersson, L. G. M. and Leszczynski, J. (2000) Lattice resistance to hydrolysis of Si-O-Si bonds of silicate minerals: Ab initio calculations of a single water attack onto the (001) and (111) β-cristobalite surfaces. Journal of Physical Chemistry B, 104, 5779-5783.

Pelmenschikov, A. G., Morosi, G. and Gamba, A. (1992) Quantum chemical molecular models of oxides. 2. Methanol adsorption on silica and zeolites. Journal of Physical Chemistry, 96, 2241-2246.

Pinnavaia, T. J. and Beall, G. W., Eds. (2000) Polymer-clay nanocomposites. New York, John Wiley & Sons, 349 p.

Plant, D. F., Simperler, A. and Bell, R. G. (2006) Adsorption of methanol on zeolites X and Y. An atomistic and quantum chemical study. Journal of Physical Chemistry B, 110, 6170-6178.

Robinson, T. L., Michalkova, A., Gorb, L. and Leszczynski, J. (2007) Hydrogen bonding of thymine and uracil with surface of dickite: An ab initio study. Journal of Molecular Structure: THEOCHEM, 844-845, 48-58.

Rozas, I. (2007) On the nature of hydrogen bonds: An overview on computational studies and a word about patterns. Physical Chemistry Chemical Physics, 9, 2782-2790.

Sauer, J., Ugliengo, P., Garrone, E. and Saunders, V. R. (1994) Theoretical study of van der Waals complexes at surface sites in comparison with the experiment. Chemical Reviews, 94, 2095-2160.

Schauble, E. A., Rossman, G. R. and Taylor, J. H. P. (2001) Theoretical estimates of equilibrium Fe-isotope fractionation from vibrational spectroscopy. Geochimica et Cosmochimica Acta, 65(2487-2497).

Schauble, E. A., Rossman, G. R. and Taylor, J. H. P. (2003) Theoretical estimates of equilibrium chlorine-isotope fractionation. Geochimica et Cosmochimica Acta, 67, 3267-3281.

Schauble, E. A., Rossman, G. R. and Taylor, J. H. P. (2004) Theoretical estimates of equilibrium chromium-isotope fractionation. Chemical Geology, 205, 99-114.

Seger, M. R. and Maciel, G. E. (2006) NMR investigation of the behavior of an organothiophosphate pesticide, chlorpyrifos, sorbed on soil components. Environmental Science & Technology, 40, 791-796.

Simion, D. V. and Sorensen, T. S. (1996) A theoretical computation of the aromaticity of (benzene)Cr(CO)(3) compared to benzene using the exaltation of magnetic susceptibility criterion and a comparison of calculated and experimental NMR chemical shifts in these compounds. Journal of the American Chemical Society, 118(31),

7345-7352.

Simperler, A., Bell, R. G. and Anderson, M. W. (2004) Probing the acid strength of Brønsted acidic zeolites with acetonitrile: Quantum chemical calculaton of ^{1}H, ^{15}N, and ^{13}C NMR shift parameters. Journal of Physical Chemistry B, 108, 7142-7151.

Simperler, A., Bell, R. G., Philippou, A. and Anderson, M. W. (2002) Theoretical study of toluene adsorbed on zeolites X and Y: Calculation of ^{13}C NMR parameters. Journal of Physical Chemistry B, 106, 10944-10954.

Solans-Monfort, X., Sodupe, M., Mó, O., Yáñez, M. and Elguero, J. (2005) Hydrogen bond vs proton transfer in HZSM5 zeolite. A theoretical study. Journal of Physical Chemistry B, 109, 19301-19308.

Stebbins, J. F. (1995) Nuclear magnetic resonance spectroscopy of silicates and oxides in geochemistry and geophysics. Handbook of Physical Constants. T. J. Ahrens. Washington D.C., American Geophysical Union, 2, 303-332 p.

Stone, A. J. (1996) The Theory of Intermolecular Forces. Oxford, Clarendon Press, 264 p.

Suh, J. H., Lee, S. K. and Lee, I. (2007) Quantum chemical calculations of equilibrium copper (I) isotope fractionations in ore-forming fluids. Chemical Geology, 243, 225-237.

Svensson, M., Humbel, S., Froese, R. D. J., Matsubara, T., Sieber, S. and Morokuma, K. (1996) ONIOM: A multilayered integrated MO + MM method for geometry optimizations and single point energy predictions. A test for diels-alder reactions and $Pt(P(t\text{-}Bu)_3)_2 + H_2$ oxidative addition. Journal of Physical Chemistry 100, 19357-19363.

Tao, T. and Maciel, G. E. (1998) ^{13}C NMR study of co-contamination of clays

with carbon tetrachloride and benzene. Environmental Science & Technology, 32, 350-357.

Teppen, B. J., Yu, C. H., Miller, D. M. and Schafer, L. (1998) Molecular dynamics simulations of sorption of organic compounds at the clay mineral/aqueous solution interface. Jounal of Computational Chemistry, 19(2), 144-153.

Thomas, J. E. and Kelley, M. J. (2008) Interaction of mineral surfaces with simple organic molecules by diffuse reflectance IR spectroscopy (DRIFT) Journal of Colloid and Interface Science, 322(2), 516-526.

Tossell, J. A. (2001) Calculating the NMR properties of minerals, glasses, and aqueous species. Molecular Modeling Theory: Applications in the Geosciences. R. T. Cygan and J. D. Kubicki. Washington, DC, The Mineralogical Society of America, 42, 437-458 p.

Tossell, J. A. (2005) Calculating the partitioning of the isotopes of Mo between oxidic and sulfidic species in aqueous solution. Geochimica et Cosmochimica Acta, 69(2981-2993).

Tunega, D., Benco, L., Haberhauer, G., Gerzabek, M. H. and Lischka, H. (2002) Ab initio molecular dynamics study of adsorption sites on the (001) surfaces of 1 : 1 dioctahedral clay minerals. Journal of Physical Chemistry B, 106(44), 11515-11525.

Tunega, D., Haberhauer, G., Gerzabek, M. H. and Lischka, H. (2002) Theoretical study of adsorption sites on the (001) surfaces of 1 : 1 clay minerals. Langmuir, 18(1), 139-147.

Tunega, D., Haberhauer, G., Gerzabek, M. H. and Lischka, H. (2004) Sorption of phenoxyacetic acid herbicides on the kaolinite mineral surface - an ab initio molecular dynamics simulation. Soil Science, 169(1), 44-54.

Tunney, J. J. and Detellier, C. (1996) Aluminosilicate nanocomposite materials. Poly(ethylene glycol)-kaolinite intercalates. Chemistry of Materials, 8, 927-935.

van Duin, A. C. T. and Larter, S. R. (2001) Molecular dynamics investigation into the adsorption of organic compounds on kaolinite surfaces. Organic Geochemistry, 32, 143-150.

Viruela-Martín, P., Zicovich-Wilson, C. M. and Corma, A. (1993) Ab initio molecular orbital calculations of the protonation reaction of propylene and isobutene by acidic OH groups of isomorpbously substituted zeolites. Journal of Physical Chemistry, 97, 13713-13719.

Wang, K. J. and Xing, B. S. (2005) Structural and sorption characteristics of adsorbed humic acid on clay minerals. Journal of Environmental Quality, 34(1), 342-349.

Wasylishen, R. E. and Bryce, D. L. (2002) A revised experimental absolute magnetic shelding scale for oxygen. Journal of Chemical Physics, 117(22), 10061-10066.

Wiberg, K. B., Hammer, J. D., Zilm, K. W. and Cheeseman, J. R. (1999) NMR chemical shifts. 3. A comparison of acetylene, allene, and the higher cumulenes. Journal of Organic Chemistry, 64(17), 6394-6400.

Winkler, P., Novoszad, M., Gerzabek, M. H., Haberhauer, G., Tunega, D. and Lischka, H. (2007) Interaction of naphthalene derivatives with soil: an experimental and theoretical case study. European Journal of Soil Science, 58(4), 967-977.

Xie, X. and Hayashi, S. (1999) NMR study of kaolinite intercalation compounds with formamide and its derivatives. 1. Structure and orientation of guest molecules. Journal of Physical Chemistry B, 103, 5949-5955.

Xue, X. and Kanzaki, M. (1998) Correlations between ^{29}Si, ^{17}O and ^{1}H NMR properties and local structures in silicates: An ab initio calculation. Physics and Chemistry of Minerals, 26, 14-30.

Yariv, S. (1996) Thermo-IR-spectroscopy analysis of the interactions between organic pollutants and clay minerals Thermochimica Acta, 274, 1-35.

Yariv, S. and Lapides, I. (2000) The effect of mechanochemical treatments on clay minerals and the mechanochemical adsorption of organic materials onto clay minerals. Journal of Materials Synthesis and Processing, 8(3-4), 223-233.

Yesinowski, J. P. and Eckert, H. (2009) Hydrogen environments in calcium phosphates: ^{1}H MAS NMR at high spinning speeds. Journal of the American Chemical Society, 109(21), 6274-6282.

Yoon, T. H., Johnson, S. B., Musgrave, C. B. and Brown, G. E. (2004) Adsorption of organic matter at mineral/water interfaces: I. ATR-FTIR spectroscopic and quantum chemical study of oxalate adsorbed at boehmite/water and corundum/water interfaces. Geochimica et Cosmochimica Acta, 68(22), 4505-4518.

Zhanpeisov, N. U., Adams, J. W., Larson, S. L., Weiss, C. A., Zhanpeisova, B. Z., Leszczynska, D. and Leszczynski, J. (1999) Cluster quantum chemical study of triaminotoluene interaction with a model clay surface. Structural Chemistry, 10(4), 285-294.

Chapter 4. Effects of specific surface area and porosity on cube counting fractal dimension, lacunarity, and configurational entropy of porous networks of model sands: insights from random packing simulations and NMR micro-imaging

Abstract

Despite the importance of understanding and quantifying the microstructure of porous networks in diverse geologic settings, the effect of specific surface area and porosity on the key structural parameters of the networks have not been fully understood. Cube-counting fractal dimension (D_{cc}) and lacunarity analyses of 3D porous networks of model sands and configurational entropy analysis of 2D cross sections of model sands were performed using random packing simulations and nuclear magnetic resonance (NMR) micro-imaging. Relationships among porosity, specific surface area, structural parameters (D_{cc} and lacunarity), and the corresponding macroscopic properties (configurational entropy and permeability) were established. The D_{cc} of the 3D porous networks increases with increasing specific surface area at constant porosity and with increasing porosity at constant specific surface area. Predictive relationships correlating D_{cc}, specific surface area, and porosity were also obtained. Lacunarity at the minimum box size decreases with increasing porosity, and the calculated lacunarity at the intermediate box size (~470

δ

μm in the current model sands) was reproduced well with specific surface area. The maximum configurational entropy increases with increasing porosity, and the entropy length of the pores decreases with increasing specific surface area and was used to calculate the average connectivity among the pores. The correlation among porosity, specific surface area, and permeability is consistent with the prediction from the Kozeny-Carman equation. From the relationship between the permeability and the D_{cc} of pores, permeability can be expressed as a function of the D_{cc} of pores and porosity. The current methods and these newly identified correlations among structural parameters and properties provide improved insights into the nature of porous media and have useful geophysical implications for elasticity and shear viscosity of complex composites of rock, glasses, melt, and fluids.

4.1. Introduction

Quantification of the porous networks in porous media is important for understanding and predicting their macroscopic properties, including permeability of fluids in partially molten rocks (Takei and Holtzman, 2009), transport behavior of ground water (Sahimi, 1993; Gladden et al., 1995), and seismic wave attenuation (Bourbié et al., 1987; Li et al., 2001; Takei, 2002; Takei, 2005). Such quantification also provides essential information that can be used for improving oil recovery from reservoir rocks, predicting pollutant migration in soil, and underground storage of CO_2 and nuclear waste. To quantify and characterize irregular

and disordered porous networks, diverse structural parameters other than porosity have been introduced. These include fractal dimension (e.g., Hansen and Skjeltorp, 1988; Ghilardi et al., 1993; Giménez et al., 1997; Dathe and Thullner, 2005; Tarquis et al., 2008), generalized dimensions (multifractals) (e.g., Muller et al., 1995; Posadas et al., 2003), and lacunarity (e.g., Pendleton et al., 2005). Often, more than two parameters of the porous networks were used to gain insights into the nature of porous media. For example, fractal and multifractal (e.g., Bird et al., 2006), fractal and lacunarity (e.g., Armatas et al., 2002), multifractal and configurational entropy (e.g., Tarquis et al., 2006), and lacunarity and configurational entropy (e.g., Chun et al., 2008) analyses were used to characterize diverse natural porous networks. Despite these key previous studies, the systematic relationships among the structural parameters have not yet been established because most fractal, lacunarity, and configurational entropy analyses of porous networks have been carried out on natural systems (e.g., soil) characterized by intrinsic heterogeneity in density, composition, and phase. Consequently, the general relationship among these parameters for random networks with well-controlled particle sizes and shapes have not been available thus far. Studies of model porous networks prepared by random packing simulations or model glass beads can facilitate easy control of the diameter and shape of the particles in porous media (Schwartz and Banavar, 1989; Coelho et al., 1997; Garcia et al., 2009). The potential results enable us to establish the much anticipated systematic and quantitative relationships among these structural parameters. Furthermore,

macroscopic properties of porous media, such as permeability, depend on specific surface area (Bear, 1972; Dullien, 1979). Because previous studies often used 2D images of porous networks rather than complete 3D networks, the effect of specific surface area on these structural parameters remains unknown. The objective of this study is to investigate the relationships among 3D porous networks, structural parameters, and transport properties, such as permeability, with emphasis on the effect of specific surface area on these parameters.

Nuclear magnetic resonance (NMR) imaging or magnetic resonance imaging (MRI) is a nondestructive technique used to obtain 3D distributions of porous networks in porous media. NMR imaging enables imaging of different chemical species of fluid phases (as opposed to solid skeletons probed by X-ray based techniques), exploring species with varying relaxation times (e.g., spin-lattice relaxation time and spin-spin relaxation time), and mapping of the flow velocity vectors in porous media (see Callaghan, 1991; Blümich, 2000 and references therein). Hence, this method has been used for porous media research such as the distribution of fluids in rocks (e.g., Dereppe et al., 1991; Davies et al., 1994; Doughty and Tomutsa, 1996), chemical reactors (e.g., Gladden, 2003; Lysova et al., 2005, and cements (e.g., Balcom et al., 2003; Gussoni et al., 2004; Faure et al., 2005). NMR method including NML (NMR logging) also has been used to study the relationships between porous media and fluids. It measures relaxation times or diffusion coefficients of fluids in porous media (Kleinberg, 2001; Song et al., 2008). The major difference between NMR imaging and NMR

d

method for probing the porous media is that the former directly obtains the information of pore structure or fluid distribution from the imaging data and the latter indirectly obtains the information from the relaxation times or diffusion coefficients. While both methods enabled us to provide useful information of porous media, a link between the distribution of relaxation times and the measurements from the indirect method needs to be explored. The study will be possible with the ability of 3D imaging of relaxation times and the development of high resolution NMR imaging. NMR micro-imaging refers to NMR imaging in which a high spatial resolution (<100 μm) is obtained. A few NMR micro-imaging studies of porous media have been conducted, including flow velocity in computer-generated percolation clusters (Kossel and Kimmich, 2005), fluid flow and dispersion in random packing of spheres (Manz et al., 1999), self-diffusion maps through chemical products (Gladden et al., 2004), and a fixed bed of ion-exchange resin saturated with methanol (Gladden, 2003). However, little attention has been paid to 3D characterization of porous networks using NMR micro-imaging. It is demonstrated that NMR micro-imaging can be used to obtain 3D images of fluids in various porous media composed of model sands with a spatial resolution of less than ~50 μm. Model sands can also be generated using random packing simulations where the particle sizes, shapes, and packing density of porous networks can be controlled (Jia and Williams, 2001). This would allow us to systematically explore unambiguous relationships between changes in network structures and the corresponding macroscopic properties.

δ

In this study, the nature of diverse structural parameters, such as cube-counting fractal dimension, lacunarity of 3D model porous networks, and configurational entropy of model sands, is explored using their 2D cross-sectional porous network images from NMR micro-imaging and random packing simulations. On the basis of these analyses, the current results aim to provide the previously unknown systematic relationships among the porous networks, these key structural parameters, and the corresponding transport and macroscopic properties. Before describing the methods and discussing the results of this study, a brief introduction of the parameters considered in the current study in the following subsections is provided.

4.1.1. Cube-counting fractal dimension of model porous networks

Fractal dimension—a measure of the degree of complexity of an object—is a noninteger dimension that originates from the power-law relationship between the length scale and the types of objects (e.g., pore space, solid mass, and interface) (Mandelbrot, 1982). 3D box counting fractal dimension (D_{cc}) used in this study can be described as follows (Mandelbrot, 1982):

$$\ln N = D_{cc} \ln\left(1/r\right) + \ln k\,, \tag{4.1}$$

where N is the number of cubes covering the object, r is the side of a cube, and k is a constant. The absolute value of the slope of the linear part within the cutoff lengths in the log-log plot is estimated as D_{cc}.

In the percolation theory, the fractal dimension of the cluster is defined for the regime where the length scale is smaller than the correlation length (Sahimi, 1993). In this regime the cluster is statistically self similar, and its mass M scales with the length scale L as $M \sim L^{D_p}$, where D_p is the fractal dimension of the cluster (Sahimi, 1993). Previous studies assumed that this fractal dimension of the cluster is the same with the fractal dimension obtained by box counting method (Thompson, 1991; Sahimi, 1993). However, the relationship between the fractal dimension obtained from the percolation theory (mass-radius relation) and the cube counting fractal dimension for the 3D objects needs to be explored.

Table 4-1 presents the results of fractal dimension analysis obtained in previous studies for pore space in 3D images of various porous media. 3D images have been obtained mostly by X-ray computed tomography (CT) and NMR imaging. Fractal dimension values obtained for 3D images of soil ranged from 2.05 to 2.94 (Moreau et al., 1999; Perret et al., 2003; Tarquis et al., 2008), and those for glass beads, body-centered cubic (bcc) packed spheres, or glass ballotini ranged from 2.42 to 2.52 (Müller et al., 1995; Klemm et al., 1997; Sederman et al., 1997). Fractal dimension values obtained for 3D images for percolation clusters, pumice stone, and quartz sand were 2.53, 2.90, and 2.70, respectively (Müller et al., 1995; Klemm et al., 1997). It has been shown that an increase in the fractal dimension may indicate an increase in the complexity of the network structure (Perret et al., 2003), irregularity of the fractal objects (Muller and McCauley, 1992; Xu and Sun, 2005), porosity (pore fractal) or area fraction

Table 4-1. Fractal dimension of 3D images of various porous networks from previous studies.

Porous Media	Image Size	Grain Size	Analysis Method	Imaging Method	Fractal Dimension	Reference
soil	2 ~ 6 cm		box counting	Photograph	2.44 ~ 2.84	(Moreau et al., 1999)
soil	19.5 ~ 40 mm		box counting	CT	2.05 ~ 2.16	(Perret et al., 2003)
soil	11.5 mm		box counting	CT	2.20 ~ 2.94	(Tarquis et al., 2008)
sponge	8 mm		porosity-radius	MRI	2.91	(Müller et al., 1995)
sponge	4 mm		porosity-radius	MRI	2.90	(Klemm et al., 1997)
glass beads	8 mm	1 mm	porosity-radius	MRI	2.52	(Müller et al., 1995)
glass beads	4 mm	1 mm	porosity-radius	MRI	2.50	(Klemm et al., 1997)
bcc packed spheres			porosity-radius	Simulation	2.48	(Muller et al., 1995)
percolation cluster	16 mm		porosity-radius	MRI	2.53	(Muller et al., 1995)
pumice stone	13 mm		porosity-radius	MRI	2.90	(Klemm et al., 1997)
quartz sand	4 mm	0.45 ~ 1 mm	porosity-radius	MRI	2.70	(Klemm et al., 1997)
glass ballotini	4.6 cm	5 mm	volume-area	MRI	2.42 ~ 2.44	(Sederman et al., 1997)

(for solid mass fractal) (Perret et al., 2003; Yu and Liu, 2004; Tang and Maragoni, 2008), and the fraction of smaller grains (Avnir et al., 1985; Bartoli et al., 1999; Xu and Dong, 2004).

The fractal object was characterized by self-similarity. Natural objects (including porous media) exhibit linearity within the lower and upper cutoff lengths in log (box counts)-log (box size) plots (Foroutan-pour et al., 1999; Maria and Carey, 2002). Fractal dimension analysis can also be applied to simple structures without apparent self-similarity, such as dilute sets of single-sized spheres (Hamburger et al., 1996; Foroutan-pour et al., 1999; Ciccotti and Mulargia, 2002) and porous networks of model sands, including single-sized spheres (Müller et al., 1995; Klemm et al., 1997; Klemm et al., 2001; Sederman et al., 2001). In this study, D_{cc} analysis was applied to the porous networks of model sands without much pronounced self-similarity (for a network composed of single-sized spheres) and those model sands in which self-similarity existed within a relatively narrow range of cube sizes (see 4.2.4 below for further details).

4.1.2. Lacunarity of model porous networks

Lacunarity—a scale-dependent measure of heterogeneity or texture of an object— can indicate differences between structures that have the same fractal dimensions (Mandelbrot, 1982). In lacunarity analysis, a box (or a cube, as used in this study) of side r is allowed to move over the entire image, and the number of boxes [$n_k(r)$] is counted whenever the box mass

δ

equals k. This procedure is repeated by varying k from 0 to a value equal to the total number of boxes [$N(r)$]. Then, the probability distribution function, $Q(k, r)$, is defined as (Allain and Cloitre, 1991)

$$Q(k,r) = \frac{n_k(r)}{N(r)}. \tag{4.2}$$

The lacunarity [$\Lambda(r)$] is then defined as (Allain and Cloitre, 1991)

$$\Lambda(r) = \sum_{k=0}^{r^2} k^2 Q(k,r) \Bigg/ \left[\sum_{k=0}^{r^2} kQ(k,r) \right]^2, \tag{4.3}$$

where the denominator is the square of the first moment of the probability distribution, and the numerator is the second moment of the probability distribution, which is thus a measure of the variance to mean ratio of box mass (Plotnick et al., 1996).

Lacunarity analysis has recently been used to describe the 2D spatial distribution of natural soil systems (e.g., Pendleton et al., 2005; Kim et al., 2007; Chun et al., 2008). Because of the computational difficulties of lacunarity analysis using the gliding box algorithm, as far as I know, there have been no previous studies using lacunarity analysis in 3D porous networks. Thus the first lacunarity analysis of 3D porous networks of model sands is reported and the relationship among lacunarity, porosity, and specific surface area is explored.

4.1.3. Configurational entropy of model porous networks

Configurational entropy is effective in describing the degree of

δ

disorder in amorphous networks, including oxide glasses and melts with geophysical and geochemical implications (e.g. Lee and Stebbins, 1999; Lee, 2005; Lee et al., 2010). In the current image analysis, configurational entropy analysis was performed using the gliding box algorithm. The probability of a pore pixel number k, $p_k(r)$, is calculated as (Andraud et al., 1994)

$$p_k(r) = \frac{N_k(r)}{N}, \tag{4.4}$$

where $N_k(r)$ is the total number of boxes containing the number of pore pixels of k, and N is the total number of visited boxes. Configurational entropy is defined as

$$H^*(r) = \frac{H(r)}{H_M(r)} = \frac{1}{\log\left(r^2+1\right)} \sum_{k=0}^{r^2} p_k(r) \log p_k(r), \tag{4.5}$$

where $H_M(r) = \log(r^2 + 1)$ is the maximum possible entropy for boxes with an area of r^2. The entropy length refers to a box size at which the configurational entropy reaches its maximum value (i.e., maximum configurational entropy; see Section 3.3 for further details). Entropy length is regarded as an accurate measure of the characteristic size of pores and/or constituent particles (Andraud et al., 1997). Although the maximum configurational entropy is reported to be positively correlated with the porosity of soil networks (Chun et al., 2008), the configurational entropy of the porous networks of model sands and the relationship between configurational entropy and other pore-structure properties have not yet been systematically studied. In this study, the relationships among the

configurational entropy, entropy length, and other parameters of porous networks in model sands were explored.

4.2. Methods

4.2.1. Random packing simulations

Random packing simulations of single-sized spheres were performed using DigiPac software (Structure Vision Ltd.) where particles move according to a predefined stochastic settling process governed by the rebounding probability (Jia and Williams, 2001). The particles and the container were digitized and mapped onto a lattice grid, and then the particles moved on the grid. In the simulation process employed in this study, particles were added from randomly selected points to a circular area directly above the packing. Random packing of spheres was simulated under the influence of gravity. To reproduce a glass-bead packing in a column (see below for glass bead sample preparation for NMR micro-imaging experiment), a tube container and solid wall boundary conditions were used. At a constant tube container diameter of 252 pixels, the particle diameters of the porous media composed of single-sized spheres used for our simulations were varied from 8 to 20 pixels, which corresponded to the approximate diameters of the small and large grains of the glass beads, respectively (see Section 4.2.2 for details). The porous media with diameters ranging from 25 to 30 pixels that corresponded to approximately the maximum size of the sphere in the simulated box were also simulated. The

number of particles in the simulation box was set to decrease with increasing particle diameters; for example, 200, 100, 50, and 10 particles were used for sphere diameters of 8, 10, 15, and 20, respectively.

Porous media with varying porosities were prepared by increasing the number of particles in the fixed container volume while keeping the diameters of the spherical particles constant. The resulting porosity of the simulated porous media ranges from 0.34 to 0.46 (see Table 4-2 for the number of samples for the same sphere diameter and the porosity of each sample). Figure 4-1 shows the 3D isosurface images (Figures 4-1A, 1C, and 1E) and 2D cross-sectional images (Figures 4-1B, 1D, and 1F) of the porous networks of the porous media composed of single-sized spheres with diameters of 20 pixels (Figures 4-1A and 1B), 15 pixels (Figures 4-1C and 1D), and 10 pixels (Figures 4-1E and 1F) obtained by random packing simulations.

δ

Table 4-2. Structural parameters and properties for porous networks obtained by random packing simulations.

Sample name[a]	ϕ[b]	SSA[c]	Perm[d]	EL[e]	MCE[f]	$\Lambda_{0.047}$[g]	$\Lambda_{0.47}$[h]	D_{cc}[l]
8-1	0.41	8.11	194	0.19	0.98	2.41	1.02	2.94
8-2	0.36	8.27	103	0.19	0.95	2.81	1.02	2.93
9-1	0.42	7.56	233	0.19	0.98	2.38	1.02	2.93
9-2	0.43	7.54	250	0.19	0.98	2.34	1.03	2.93
9-3	0.35	7.81	116	0.19	0.95	2.88	1.02	2.90
9-4	0.39	7.69	179	0.19	0.97	2.53	1.02	2.92
10-1	0.43	6.53	325	0.23	0.99	2.31	1.03	2.88
10-2	0.39	7.06	204	0.23	0.97	2.57	1.03	2.87
10-3	0.38	7.08	188	0.23	0.97	2.61	1.03	2.87
10-4	0.41	6.82	242	0.23	0.98	2.45	1.03	2.88
11-1	0.38	6.27	240	0.28	0.95	2.63	1.04	2.82
11-2	0.35	6.33	182	0.28	0.96	2.83	1.05	2.81
11-3	0.42	6.12	425	0.28	0.97	2.34	1.06	2.84
11-4	0.33	6.16	153	0.28	0.94	3.01	1.08	2.79
12-1	0.38	6.07	245	0.28	0.97	2.63	1.06	2.79
12-2	0.43	5.77	801	0.28	0.98	2.19	1.08	2.84
13-1	0.41	5.70	421	0.33	0.99	2.42	1.09	2.81
14-1	0.40	5.23	423	0.38	0.97	2.52	1.12	2.76
14-2	0.36	5.23	291	0.38	0.97	2.75	1.12	2.73
14-3	0.44	5.05	738	0.38	0.98	2.25	1.13	2.79
15-1	0.40	5.09	499	0.38	0.98	2.44	1.14	2.76
16-1	0.40	4.87	521	0.42	0.99	2.48	1.17	2.75
16-2	0.43	4.76	739	0.42	0.99	2.31	1.17	2.77
17-1	0.39	4.81	510	0.42	0.97	2.58	1.19	2.72
17-2	0.40	4.58	571	0.42	0.97	2.51	1.20	2.73
17-3	0.43	4.51	732	0.42	0.98	2.33	1.19	2.75
18-1	0.40	4.34	676	0.47	0.98	2.49	1.23	2.72

δ

18-2	0.39	4.43	565	0.47	0.98	2.58	1.23	2.70
18-3	0.44	4.23	924	0.47	0.99	2.29	1.22	2.75
19-1	0.44	4.06	1108	0.47	0.98	2.26	1.25	2.74
19-2	0.39	4.14	662	0.47	0.97	2.56	1.26	2.70
19-3	0.40	4.16	715	0.47	0.98	2.52	1.26	2.71
20-1	0.40	3.86	755	0.52	0.97	2.51	1.28	2.71
20-2	0.37	3.94	730	0.47	0.97	2.60	1.30	2.68
25-1	0.39	3.21	1144	0.66	0.98	2.56	1.44	2.68
25-2	0.43	3.17	1675	0.61	0.98	2.30	1.42	2.71
26-1	0.42	3.09	1591	0.66	0.99	2.36	1.44	2.70
26-2	0.43	3.13	1613	0.66	0.99	2.34	1.43	2.71
27-1	0.44	3.01	1832	0.70	0.99	2.29	1.44	2.71
27-2	0.42	3.01	1714	0.70	0.97	2.39	1.46	2.69
28-1	0.45	2.91	2138	0.75	0.99	2.22	1.44	2.72
28-2	0.42	3.08	1512	0.70	0.98	2.38	1.44	2.71
29-1	0.44	2.76	2333	0.80	0.98	2.29	1.48	2.71
30-1	0.45	2.48	2924	0.80	0.98	2.24	1.50	2.72
30-2	0.41	2.77	1701	0.75	0.98	2.45	1.54	2.69

[a] The number in front of the hyphen indicates the sphere diameter (pixels), and the number behind the hyphen is used to differentiate the samples by different porosities with the same sphere diameter.

[b] Porosity

[c] Specific surface area (mm^2/mm^3)

[d] Permeability (Darcy, D)

[e] Entropy length

[f] Maximum configurational entropy

[g] Lacunarity value for a box size of 0.047 mm

[h] Lacunarity value for a box size of 0.47 mm

[l] Cube-counting fractal dimension of 3D porous networks

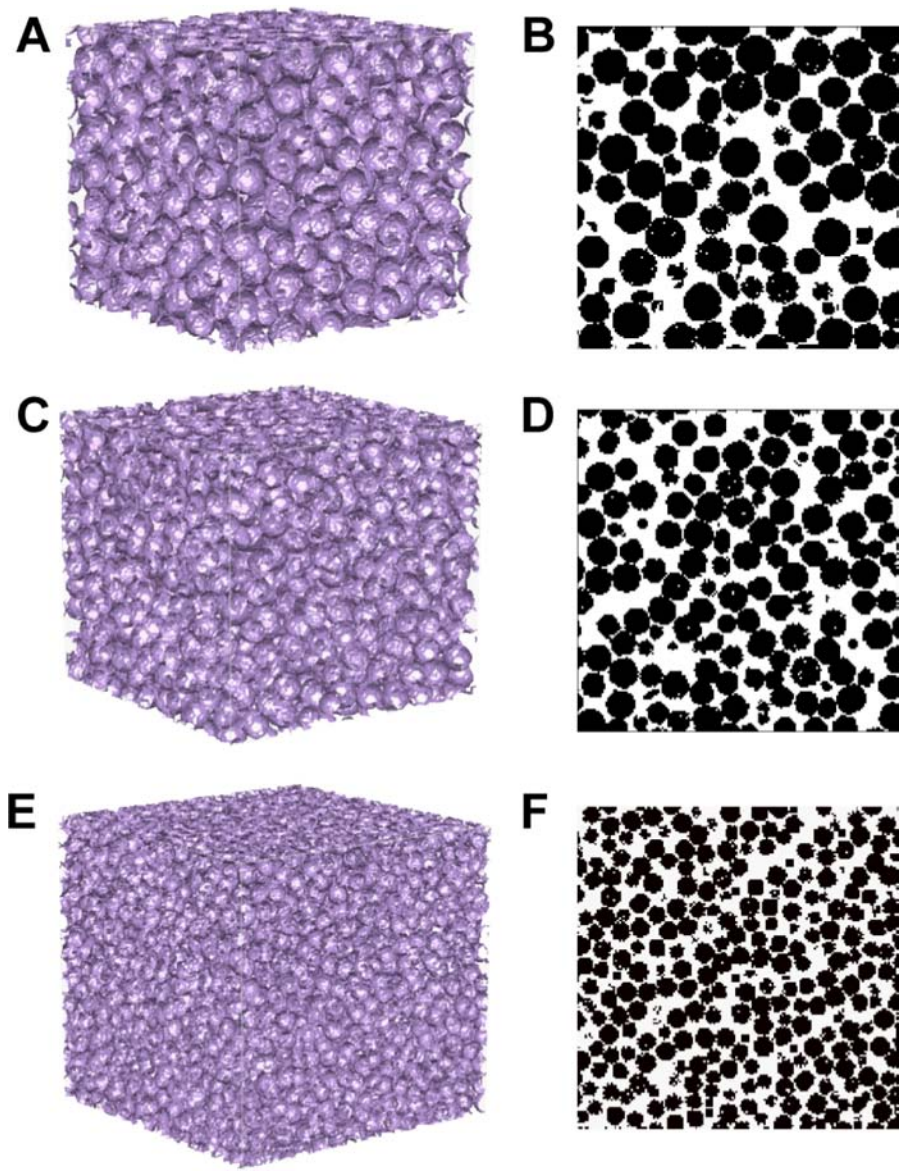

Figure 4-1. Isosurface images of 3D porous networks (A, C, and E) and 2D cross-sectional images (B, D, and F) of porous model sands composed of single-sized spheres with the diameter of 20 pixels (A and B), 15 pixels (C and D) and 10 pixels (E and F) obtained by random packing simulations.

4.2.2. Sample preparation

The glass beads (GBs) and crushed silica gel (SG) particles were spherical and irregularly shaped grains, respectively, and were used for investigating the effect of particle shape and diameter on the porous networks. The samples used for our NMR micro-imaging experiments were divided into six groups: GB1, GB2, GB3, SG1, SG2, and SG3, depending on the average particle size. The particle sizes (diameters) of the GBs (Sigma, acid-washed) were 0.71–1.18 mm (GB1, average 0.95 mm) and 0.21–0.30 mm (GB3, average 0.26 mm) and those of silica gels (SG) were 0.86–1.30 mm (SG1) and 0.25–0.60 mm (SG3). The values of the particle sizes were provided by vendors. It should be noted that the majority of the diameters of GB particles in GB1 and GB3 were mostly the average diameters of the groups and those for SG particles were randomly distributed within the ranges of particle diameters within the groups. Hybrid samples (GB2 and SG2 groups) were obtained by mixing two types of GBs or SG particles (weight ratio of GB1 and GB3 = 1:1 for GB2, and weight ratio of SG1 and SG3 = 1:1 for SG2) to investigate the effect of grain size heterogeneity and diameter on the porous networks and the corresponding properties. Each sample was put in a column that was 10.0 mm in diameter and 24.0 mm in length. Various samples with different porosities within a group by varying packing density of the grains were prepared (see Table 4-3 for the number of samples in each group and the porosity of each sample). Packing density was controlled by shaking the column filled with grains and subsequently checking the weight of the column. For example, the net weight of each

δ

Table 4-3. Structural parameters and properties for porous networks obtained by NMR micro-imaging.

Sample name[a]	ϕ[b]	SSA[c]	Perm[d]	EL[e]	MCE[f]	$\Lambda_{0.047}$[g]	$\Lambda_{0.47}$[h]	D_{cc}[l]
GB 1-1	0.29	2.98	274	0.47	0.93	3.64	1.51	2.60
GB 1-2	0.28	3.12	331	0.60	0.89	3.52	1.51	2.61
GB 1-3	0.28	2.74	318	0.56	0.90	3.58	1.58	2.61
GB 1-4	0.26	2.74	257	0.66	0.88	3.85	1.62	2.59
GB 1-5	0.25	2.68	196	0.66	0.88	3.95	1.61	2.58
GB 1-6	0.23	2.54	169	0.66	0.85	4.45	1.81	2.58
GB 1-7	0.28	3.84	247	0.56	0.92	3.54	1.46	2.55
GB 2-1	0.31	4.98	131	0.28	0.88	3.19	1.17	2.75
GB 2-2	0.29	4.82	125	0.28	0.88	3.42	1.19	2.71
GB 2-3	0.38	6.03	166	0.19	0.96	2.63	1.12	2.86
GB 2-4	0.36	6.05	158	0.19	0.95	2.83	1.10	2.86
GB 2-5	0.32	5.85	111	0.19	0.91	3.16	1.17	2.82
GB 3-1	0.26	9.33	19	0.14	0.86	3.82	1.06	2.90
SG 1-1	0.36	3.25	668	0.75	0.96	3.31	1.46	2.69
SG 1-2	0.31	2.48	700	0.75	0.93	3.19	1.76	2.67
SG 1-3	0.28	2.32	444	0.66	0.90	3.61	1.93	2.66
SG 1-4	0.37	2.76	593	0.75	0.95	3.70	1.56	2.71
SG 1-5	0.31	2.54	766	0.75	0.94	3.21	1.77	2.68
SG 1-6	0.37	2.75	892	0.75	0.95	4.45	1.81	2.71
SG 2-1	0.26	6.25	38	0.42	0.88	3.78	1.39	2.68
SG 3-1	0.27	6.99	30	0.33	0.90	3.75	1.23	2.67

[a] GB and SG indicate glass beads and silica gel samples, respectively. The number in front of the hyphen indicates the group with a similar average grain diameter (see Section 3.2), and the number behind the hyphen is used to differentiate the samples by different porosities within the same group (see text).

δ

[b] Porosity

[c] Specific surface area (mm^2/mm^3)

[d] Permeability (Darcy, D)

[e] Entropy length

[f] Maximum configurational entropy

[g] Lacunarity value for a box size of 0.047 mm

[h] Lacunarity value for a box size of 0.47 mm

[l] Cube-counting fractal dimension of 3D porous networks

d

sample in the column varied from 2.78 g to 3.12 g with decreasing porosity from 0.29 to 0.23 (GB1), from 3.05 g to 3.32 g with decreasing porosity from 0.38 to 0.29 (GB2), and from 1.42 g to 1.68 g with decreasing porosity from 0.36 to 0.28 (SG1). Both ends of the column were loosely covered during the mixing to provide space for grain mixing. The column was saturated with silicone oil (polydimethylsiloxane, Baysilone M30000, density of 0.98 g/cm^3 and viscosity of 30000 mPa·s). A vacuum pump was used to saturate the pore space with silicone oil and to eliminate air bubbles. Both ends of the column were covered with Teflon and membrane filters. Saturation time depended on the grain size. The time taken was approximately 5 min (GB1 and SG1 groups) to ~30 min (GB2, GB3, SG2, and SG3 groups) with a pump pressure of 1.45 torr to saturate the columns. Both ends of the column were sealed with parafilm after saturation.

4.2.3. NMR micro-imaging

NMR micro-imaging experiments were performed at Seoul National University using a Bruker DMX 400 NMR spectrometer with a 9.4 T vertical, wide-bore superconducting magnet, and Korea Basic Science Institute, Ochang using a Bruker DMX 600 NMR spectrometer with a 14.1 T vertical, standard bore superconducting magnet. A micro-2.5 probe head providing a gradient strength of 2.5 G/cm/A for DMX 400 NMR spectrometer and a micro-5 probe head providing a gradient strength of 5.0 G/cm/A for DMX 600 NMR spectrometer were used. As for the scan conditions for 3D volume imaging, a 3D gradient echo (ge3D) imaging

d

pulse sequence was used with a matrix size of the 3D images being 256 × 256 × 256, the field of view being 12 mm × 12 mm × 12 mm, and the spatial resolution being 46.9 μm × 46.9 μm × 46.9 μm. The sinc3-shaped pulse was used with an echo time of 1.781 ms and a repetition time of 1 s. The imaging time for one sample was approximately 18 h for one scan, and the number of scans varied from 1 to 4, depending on the signal-to-noise ratio of the spectra. Figures 4-2 and 4-3 show 3D isosurface images (Figures 4-2A, 2C, 2E, 3A, 3C, and 3E) and 2D cross-sectional images (Figures 4-2B, 2D, 2F, 3B, 3D, and 3F) of the porous networks of GBs (Figure 4-2) and SGs (Figure 4-3) obtained by NMR micro- imaging. Here, the differences in the porous networks among various porous media, such as GB1 (Figures 4-2A and 2B), GB2 (Figures 4-2C and 2D), GB3 (Figures 4-2E and 2F), SG1 (Figures 4-3A and 3B), SG2 (Figures 4-3C and 3D), and SG3 (Figures 4-3E and 3F), were clearly demonstrated. It should be noted that pores that were not accessible to silicone oil were not probed.

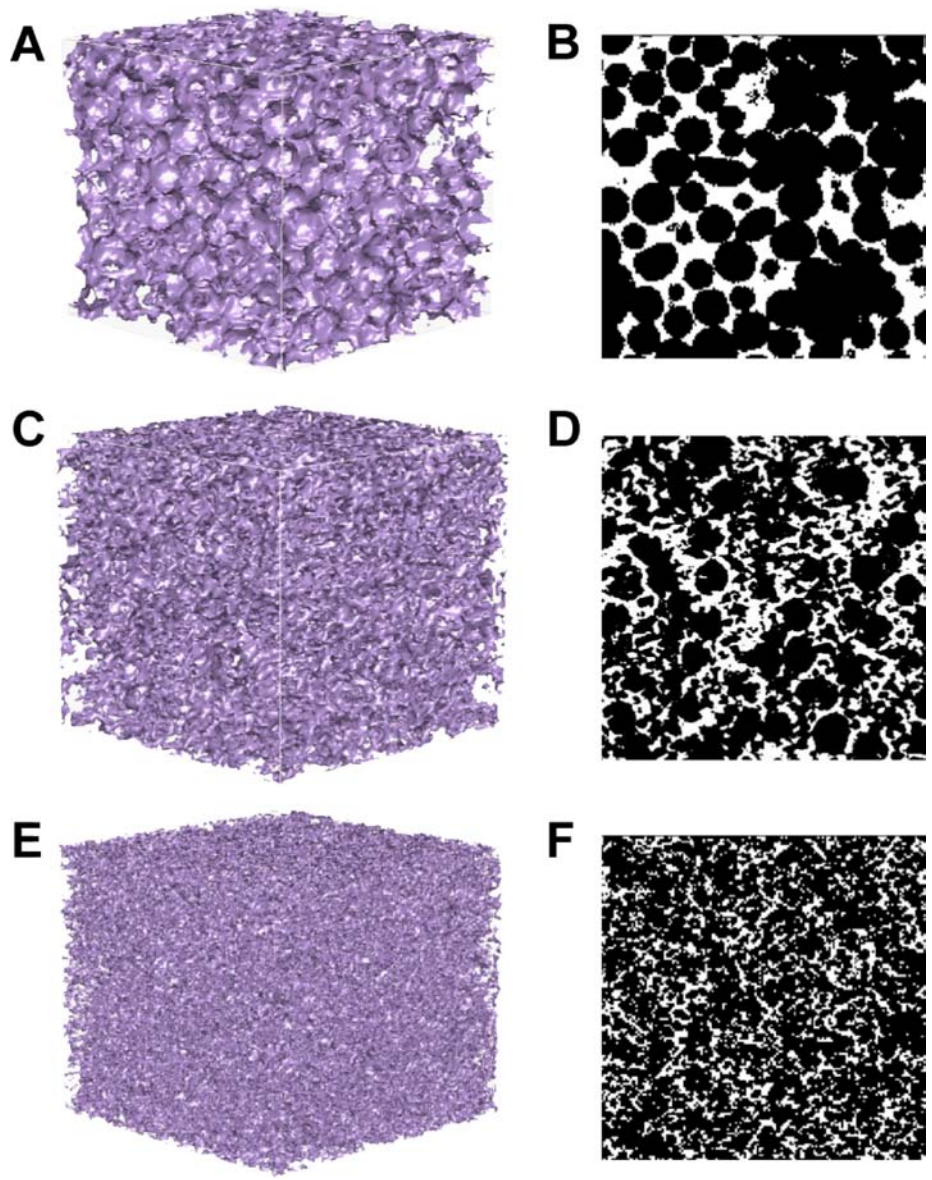

Figure 4-2. Isosurface images of 3D porous networks (A, C, and E) and 2D cross-sectional images (B, D, and F) of GB1 (A and B), GB2 (C and D) and GB3 (E and F) obtained by NMR micro-imaging experiments.

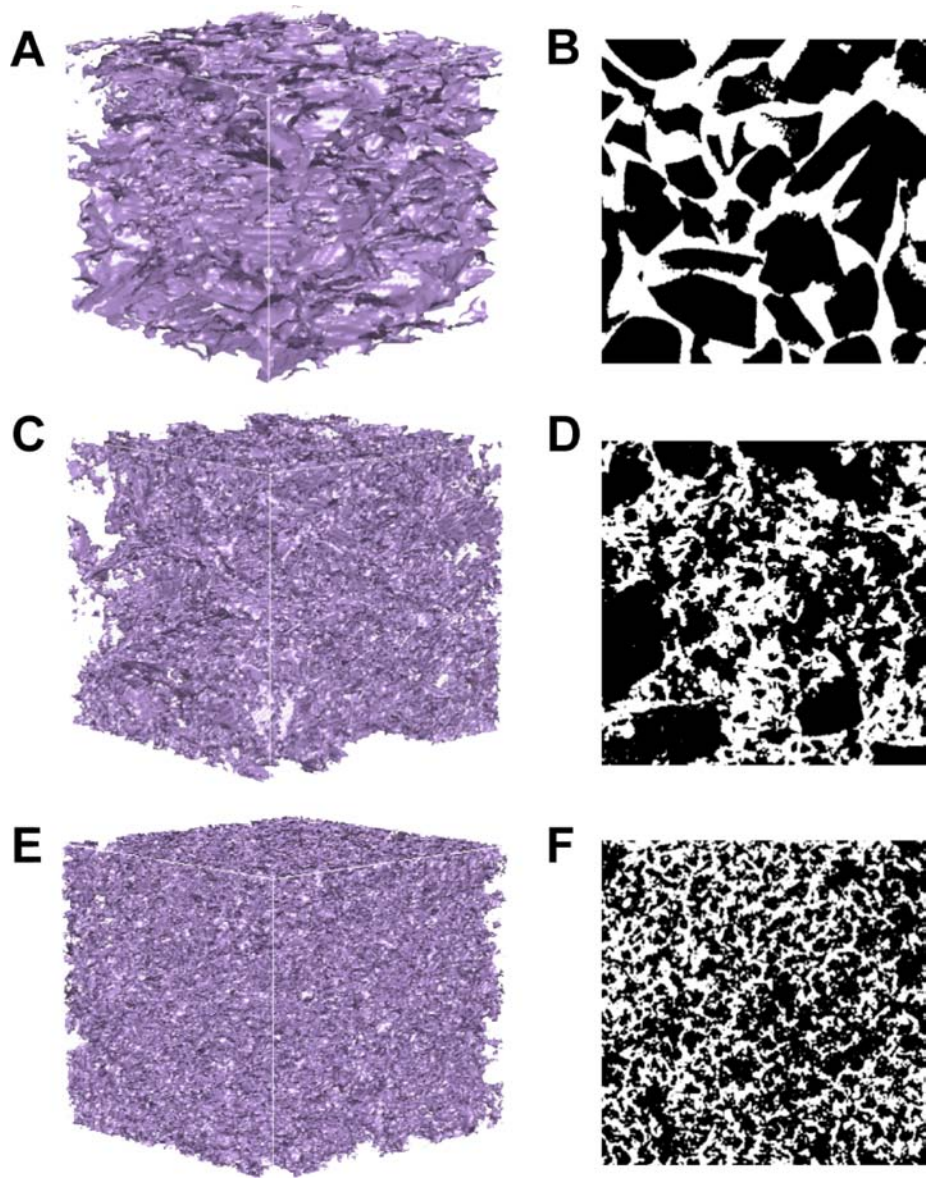

Figure 4-3. Isosurface images of 3D porous networks (A, C, and E) and 2D cross-sectional images (B, D, and F) of SG1 (A and B), SG2 (C and D) and SG3 (E and F) obtained by NMR micro-imaging experiments.

4.2.4. Data analysis

Data analysis of the porous networks was performed using the pixel vs. intensity histogram showing a bimodal distribution. The intensity value at the minimum point between the two peaks was set as the threshold value. Pixels having a larger value than the threshold were set to 1, and those having a smaller value than the threshold were set to 0. These resulting binary data were used for the analysis. To exclude the data outside the column and to suppress wall effects, a sub-volume dataset having a matrix size of 160 × 160 × 160 was extracted from the center of the 3D image having a matrix size of 256 × 256 × 256. The maximum cube size for the entire sample was ~178 × 178 × 178, and 9 pixels from the exterior were excluded.

4.2.4.1. Cube-counting fractal dimension of model porous networks

To obtain D_{cc} from the 3D images for the model porous networks, a 640 × 640 × 640 matrix obtained by fourfold expansion of the original 160 × 160 × 160 matrix was used; thus, the box sizes used for the assessment of D_{cc} were smaller than those for the original data matrix. D_{cc} analysis was conducted by covering the 3D pore volume data with increasing cube size (r). Then, box sizes of 1, 2, 4, 5, 8, 10, 16, 20, 32, 40, 80, 160, 320, and 640 (divisors of 640) were used to avoid border effects (Buczkowski et al., 1998). Then, the number of cubes (N) required to cover the object completely was evaluated. Figure 4-4 shows the log-log plots of box counts vs. box sizes for

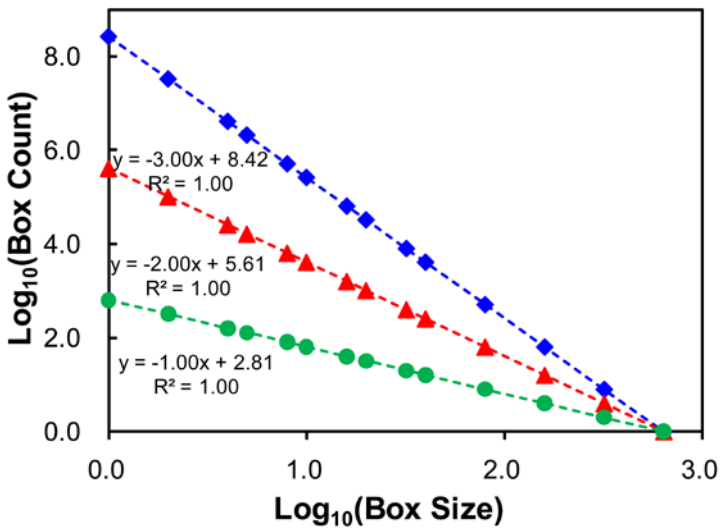

Figure 4-4. Relationship between box counts and box size in log-log plot for a straight line (green circles), a plane (red triangles), and a cube (blue diamonds).

a line, a plane, and a cube using the D_{cc} analysis. The calculated dimensions were the Euclidean dimensions for the line, plane, and cube (1, 2, and 3, respectively), and the data points fit perfectly on each straight line (R^2 = 1.00), indicating that the current cube-counting method with the aforementioned box size selection worked well.

Figure 4-5 shows the log-log plots of the relationship between box counts and box size for the simulated porous networks composed of randomly packed spheres (samples 8-1 and 30-2 had the minimum and maximum grain diameters, respectively; the number in front of the hyphen indicates the sphere diameter (pixels), and the number behind the hyphen refers to the samples with varying porosities for the same sphere diameter, as shown in Table 4-2). As shown in Figure 4-5A, data was grouped into 3 distinct regions with varying box size; the box size ranges for those regions were from 4 to 16 pixels, corresponding to 0.05-0.19 mm (for region I), from 16 to 40 pixels (for region II) pixels, corresponding to 0.19-0.47 mm, and from 40 to 80 pixels, corresponding to 0.47-0.94 mm (for region III), respectively. Region II was then used to estimate the D_{cc} value of the model sands: note that in order to determine the suitable region for the estimation of D_{cc}, the relationship between box counts and box size in log-log plot was plotted with varying box sizes from 4 to 128 pixels, and the region where the box counting is simply counting the object volume, and the region where boxes for counting the object covered the entire volume of the data matrix were excluded (*Bourke*, 2003) (see Supplementary Information 4-S1 for further details). The range of non-integer fractal dimension (i.e., cutoff

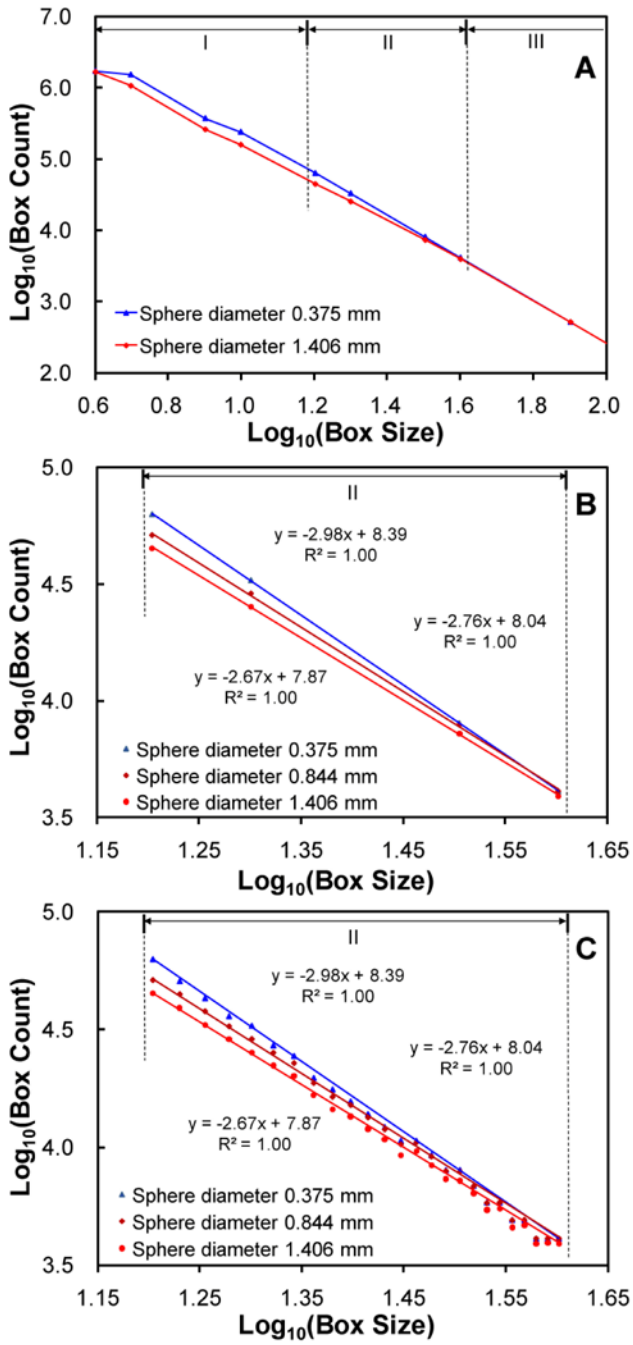

Figure 4-5. (caption on next page)

Figure 4-5. Relationship between box counts and box size in log-log plot for porous networks obtained by random packing simulations of single sized spheres. Each figure is grouped by the following box size ranges: (A) 4-80 pixels (corresponding to 0.047-0.94 mm) with the box sizes of 4, 5, 8, 10, 16, 20, 32, 40, and 80 (divisors of 640) to avoid border effects, (B) 16-40 pixels (corresponding to 0.19-0.47 mm) for sphere diameters of 8, 16, and 30 pixels (corresponding to 0.38, 0.75, and 1.41 mm) with the box sizes of 16, 20, 32, and 40, and (C) 16-40 pixels (corresponding to 0.19-0.47 mm) for sphere diameters of 8, 16, and 30 pixels (corresponding to 0.38, 0.75, and 1.41 mm) with the box sizes from 16 to 40 (16, 17, 18, ….40). In (A), Region I (from 4 to 16 pixels, corresponding to 0.047-0.19 mm), Region II (from 16 to 40 pixels, corresponding to 0.19-0.47 mm), and Region III (from 16 to 80 pixels, corresponding to 0.47-0.94 mm) are shown. Trend lines that are used to estimate the D_{cc} values are also shown in (B) and (C) (see supplementary information for further details).

lengths) in the porous networks may have varied with grain size, but the range for the estimation of D_{cc} in the current study did not vary significantly with grain size because the variation in grain size in this study was not significant within the range used for the estimation of D_{cc}. Thus, the self-similarity of the object was achieved within this relatively narrow range of box sizes that were characterized by power-law behavior in all the 3D porous network data of the model sands (see Supplementary Information 4-S1 for further details). Note that if the grain diameter becomes smaller and the voxel size can be more reduced than the current matrix, the range of the cutoff lengths in the porous networks will be shifted to the smaller scale of box sizes. Then, the corresponding fractal dimension can be different from that obtained from the current cutoff lengths. The estimated uncertainty of D_{cc} value is obtained by varying ranges of pixel size for estimation and is not larger than 0.07 (see Supplementary Information 4-S2 for further details).

The fractal dimension of porous media can be obtained by analyzing solid mass, pore volume, and surface area. The fractal dimension of soil has often shown that the values of the three abovementioned parameters are not identical because the analyzed objects differ from one another even in an image (Crawford and Matsui, 1996; Giménez et al., 1997; Giménez et al., 1997; Stallmach et al., 2002). The D_{cc} of pores, solid mass, and the surfaces of model sands prepared by simulations and experiments were analyzed. For the D_{cc} of solid mass, binary data were generated inversely by the threshold procedure in which values 1 and 0 were used for

solid mass and pores, respectively (see Supplementary Information , Figure 4-S2). For the D_{cc} of the surface, cubes covering only the interface between the pore and the solid mass were considered in box counting (see Supplementary Information , Figure 4-S3).

4.2.4.2. Other parameters

Lacunarity of the 3D porous networks was calculated for 160 × 160 × 160 sub-volume data by the gliding box algorithm by varying the box size from 1 to 48 pixels. The relationship between the lacunarity of all samples at a specific box size and porosity or specific surface area was investigated. Among the various algorithms used for estimating lacunarity (Gefen et al., 1983; Allain and Cloitre, 1991), the gliding box algorithm was suitable to 3D data analysis of porous networks.

Configurational entropy analysis was performed for the 2D cross sections (slices) chosen from the 160 × 160 × 160 sub-volume data; five slices perpendicular to the vertical z-direction (at z = 30, 60, 90, 120, and 150 from the top of the sub-volume data) were selected. The average of the configurational entropies of these five slices is reported. The estimated maximum error was ~0.05 for configurational entropy. Configurational entropy analysis was performed by the gliding box algorithm; the box sizes in this case ranged from 1 to 32 pixels.

Because the binary data was 0 for solid mass and 1 for pores, porosity was estimated by the sum of the pore data divided by the volume

of the matrix. Specific surface area can be defined as the total surface area of the interstitial voids divided by the total mass of the solid grains, total surface area divided by the volume of the solid grains, and that divided by the total bulk volume of the porous medium (Bear, 1972; de Marsily, 1986). In the current study, the third definition of specific surface area - sum of the surface area of clusters composed of connected pixels divided by the volume of the matrix – was used. Surface area was calculated by directly counting the number of pixels corresponding to interfaces from 3D images (Lindquist et al., 1996; Song et al., 2001). Then specific surface area is expressed as surface area (mm^2) divided by volume (mm^3). The unit of specific surface area ($pixel^2/pixel^3$) in the packing simulations was converted to mm^2/mm^3 by setting the field of view of the entire matrix size (256 × 256 × 256) to a dimension used for NMR micro-imaging experiments (12 mm × 12 mm × 12 mm). In the Appendix, the multi-fractal analysis of the model porous networks is described. Supplementary Information also describes relationships among various parameters and properties in which the correlations were not significant and were thus not included in the manuscript.

4.2.4.3. Permeability calculations

The lattice Boltzmann method (LBM) (McNamara and Zanetti, 1988) has been used for simulating fluid flow in porous media and for estimating the permeability of complex 3D porous networks (e.g., Keehm, 2003; Keehm et al., 2004, see Chen and Doolen, 1998 for more detailed

δ

information). In this study, the permeability of model sands was estimated using the LBM, and the relationships between the determined permeability and other structural parameters, including D_{cc}, were investigated. Permeability was estimated for 160 × 160 × 160 sub-volume data with the LBM using DigiFlow software (Structure Vision Ltd.). The D3Q18 scheme was applied in a 3D cubic lattice grid with each grid cell interacting with 18 (out of 26) of its closest neighbors.

4.3. Results and Discussion

Tables 4-2 and 4-3 summarize the calculated structural parameters for the simulated porous networks obtained by random packing simulations and the model sands made of glass beads and silica gel probed using NMR micro-imaging, respectively. Detailed interpretations of the characteristic features of these parameters and the relationships among these parameters are presented below.

4.3.1. Cube-counting fractal dimension of model porous networks

Figure 4-6 shows the relationships between the specific surface area and the D_{cc} of pores, solid mass, and surfaces for single-sized spheres obtained by random packing simulations. Our results indicate that D_{cc} is systematically correlated with the specific surface area (S) and porosity (ϕ) of the porous media. The D_{cc} of pores increases from 2.68 (±0.05) to 2.96 (±0.05) with increasing specific surface area (Figure 4-6A and Table 4-2).

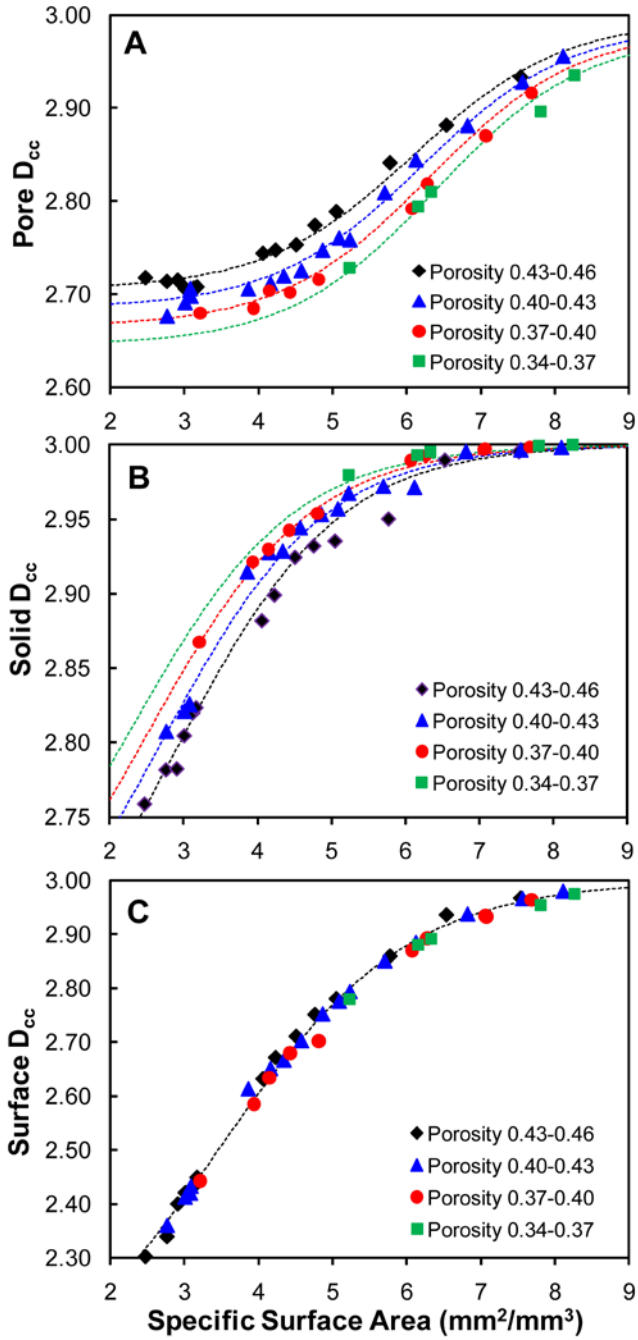

Figure 4-6. (caption on next page)

Figure 4-6. Relationships between cube counting fractal dimension of (A) pore, (B) solid mass, (C) and surface (interface) and specific surface area for porous networks obtained by random packing simulations. Black diamonds, blue triangles, red circles, and green squares correspond to each group of simulation data for porosities 0.43–0.46, 0.40–043, 0.37–0.40, and 0.34–0.37, respectively. Black, blue, red, and green dashed lines in (a) and (b) are obtained from equation (4.6) at the median of the corresponding range of porosity. Each median (the range of porosity is shown in the parentheses) is as follows; 0.445 (0.43-0.46), 0.415 (0.40-0.43), 0.385 (0.37-0.40), 0.355 (0.34-0.37). The fitting parameters for D_{cc} of pore and D_{cc} of solid mass are shown as equations (4.7) and (4.8), respectively, and a, b, c, and d (the fitting parameters) for D_{cc} of surface are 3, 2, 3.455, and 1.28, respectively.

δ

The available data in the figure based on the varying porosity ranges were grouped: 0.43 to 0.46 (group 1), 0.40 to 0.43 (group 2), 0.37 to 0.40 (group 3), and 0.34 to 0.37 (group 4) for visual clarity in the figure. To fit the data and demonstrate the correlation among D_{cc}, specific surface area, and porosity, the Boltzmann sigmoidal function was used as given below:

$$D_{cc}(S) = b + \frac{a-b}{1+\exp[-(S-c)/d)]}, \qquad (4.6)$$

where S is the specific surface area. a, b, c, and d are fitting parameters; a and b are the upper and lower limits of D_{cc}, respectively; c is the median specific surface area; d is a slope parameter. Each dashed line corresponds to the $D_{cc}(S)$ curve where the porosity is the median in each group. Table 4-4 shows the resulting fitting parameters and the corresponding coefficient of determination (R^2) for each group. The high R^2 values (0.99, 1.00, 0.99, and 0.95 for groups 1, 2, 3, and 4, respectively) indicate that the current Boltzmann sigmoidal functions reproduce the data well. From the fitting parameters of pore D_{cc}, the following relations were obtained:

$$a = \tfrac{1}{6}\phi + 2.9, \qquad (4.7a)$$

$$b = \tfrac{2}{3}\phi + 2.4, \qquad (4.7b)$$

$$c = -\tfrac{10}{3}\phi + 7.6, \text{ and} \qquad (4.7c)$$

$$d = 1.0 \quad \text{(constant)}. \qquad (4.7d)$$

δ

The D_{cc} of solid mass also increases from 2.76 (±0.05) to 3.00 (±0.05) with increasing specific surface area and decreasing porosity (Figure 4-6B), consistent with the trend observed for the D_{cc} of pores. Each dataset is fitted with equation (4.6) again. From the fitting parameters of solid mass D_{cc}, the following relations were established (Table 4-4):

$$a = 3.0 \text{ (constant)}, \tag{4.8a}$$

$$b = -\frac{1}{3}\phi + 1.7, \tag{4.8b}$$

$$c = \frac{20}{3}\phi, \text{ and} \tag{4.8c}$$

$$d = 1.1 \text{ (constant)}. \tag{4.8d}$$

The degree of space filling for the D_{cc} of pores and that of solid mass shows opposite signs for fitting parameters; for example, the coefficient of porosity for D_{cc} of pores and that of solid mass in b were 2/3 and -1/3, respectively, and those in c were -10/3 and 20/3, respectively.

The D_{cc} of surfaces increases from 2.30 (±0.05) to 2.98 (±0.05) with increasing specific surface area from 2.48 to 8.27 mm^2/mm^3 (Figure 4-6C). The D_{cc} of surfaces for the specific surface area of 2.48 mm^2/mm^3 (2.3) was much smaller than those for pores and solid mass (2.72 and 2.76, respectively) because the space filling of surfaces was intrinsically much smaller than that of pores and solid mass. Unlike the pores and solid mass, the D_{cc} of surfaces does not depend on the porosity, which is consistent with the previous study on soils (Dathe and Thullner, 2005).

Table 4-4. Parameters and coefficient of determination (R^2) values for fitting functions (equation 4.6) of the relationships between D_{cc} (of pore, solid mass, and surface) and specific surface area with varying porosities for sphere random packing.

	Porosity	a	B	x_0	W	R^2
Pore	0.43-0.46	2.995	2.705	6.1	1.0	0.99
	0.40-0.43	2.990	2.685	6.2	1.0	1.00
	0.37-0.40	2.985	2.665	6.3	1.0	0.99
	0.34-0.37	2.980	2.645	6.4	1.0	0.95
Solid mass	0.43-0.46	3.00	2.59	2.90	1.10	0.99
	0.40-0.43	3.00	2.60	2.70	1.10	0.99
	0.37-0.40	3.00	2.61	2.50	1.10	1.00
	0.34-0.37	3.00	2.62	2.30	1.10	0.96
Surface	-	3.00	2.00	3.455	1.28	1.00

Taking into consideration the experimental results obtained by NMR micro-imaging, Figure 4-7 shows the relationship between the D_{cc} of pore and specific surface area. D_{cc} increases from 2.54 (±0.05) to 2.99 (±0.05) with increasing specific surface area and depended on porosity (Figure 4-7A). Although experimental data showed a similar trend as compared to the results of random packing simulations with single-sized spheres, data for SG (black and red squares in Figures 4-7A and 7B) and hybrid samples of GB (black and red circles in Figures 4-7A and 7B) slightly deviates from the fitted lines (gray and red shaded areas that correspond to the $D_{cc}(S)$ where the porosity ranges from 0.29–0.38 and 0.20–0.29, respectively), indicating that the grain shape and the heterogeneity of the grain size affect the overall trend in $D_{cc}(S)$. Figure 4-7B also shows the D_{cc} of pores for model sands composed of SG (red circle) with heterogeneity in particle shape and size and those for GBs (blue circle) composed of spherical grains. The D_{cc} of pores for model sands composed of SG slightly increases from 2.66 (±0.05) to 2.79 (±0.05) with increasing specific surface area from 2.32 to 8.66 mm^2/mm^3. The D_{cc} for GBs increased rapidly from 2.58 (±0.05) to 2.86 (±0.05) with increasing specific surface area from 2.54 to 6.05 mm^2/mm^3 and then increased gradually to 2.90 (±0.05) with a further increase in specific surface area from 6.05 to 9.33 mm^2/mm^3. The results for GB1 and GB3, composed of uniform spherical grains, were reproduced well using equation (4.6), indicating that the trend obtained from random packing simulations can be extended to the lower porosity regime. The results for SG and GBs for D_{cc} of solid mass and surface were also reproduced well

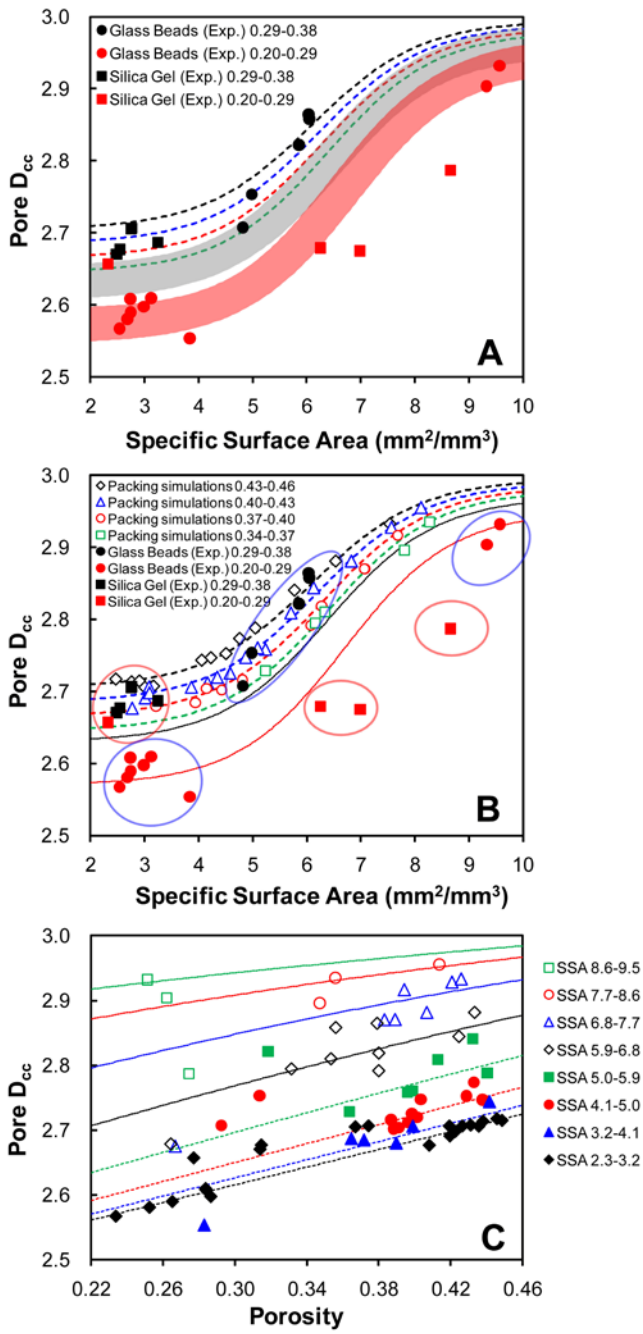

Figure 4-7. (caption on next page)

Figure 4-7. (A) Relationship between cube counting fractal dimension of pore and specific surface area for porous networks obtained by the NMR micro-imaging experiments only with sigmoidal curves for porosity of 0.20-0.29 (red shaded area) and 0.29-0.38 (gray shaded area). (B) Relationship between cube counting fractal dimension of pore and specific surface area for porous networks obtained by NMR micro-imaging experiments indicated by blue large circles for glass beads and red large circles for silica gel samples together with simulation data (open points). Black and red circles correspond to glass bead samples for the porosities of 0.29–0.38 and 0.20–029, respectively. Black and red squares correspond to silica gel samples for the porosities of 0.29–0.38 and 0.20–0.29, respectively. Black diamonds, blue triangles, red circles, and green squares correspond to each group of simulation data for the porosities of 0.43– 0.46, 0.40–043, 0.37–0.40, and 0.34–0.37, respectively. (C) Relationship between cube counting fractal dimension of pore and porosity for porous networks obtained by the random packing simulations and by the NMR micro-imaging experiments. Each line is obtained from equations (4.6) and (4.7) at the median of the corresponding range of specific surface area. Each median (the range of specific surface area is shown in the parentheses) is as follows; from bottom to top, 2.75 (2.3-3.2), 3.65 (3.2-4.1), 4.55 (4.1-5.0), 5.45 (5.0-5.9), 6.35 (5.9-6.8), 7.25 (6.8-7.7), 8.15 (7.7-8.6), and 9.05 (8.6-9.5).

using equation (4.6) (see Supplementary Information, Figure 4-S5). The model sands with pronounced heterogeneity in particle shapes and sizes (e.g. SGs and GB2) may slightly deviate from the prediction from equations (4.6). Figure 4-7C presents the relationship between the D_{cc} of pores and porosity. While the relationship among parameters can be complicated, the trend clearly shows that D_{cc} increases with increasing porosity if it is scaled with specific surface area of the networks. The overall trend is consistent with the trends reported previously (Perret et al., 2003; Yu and Liu, 2004; Tang and Maragoni, 2008).

These results suggest systematic relationships among specific surface area, porosity, the D_{cc} of pores, and average particle diameter. For example, Figure 4-8A shows that the specific surface area of the network decreases with increasing porosity at constant D_{cc} of pores. The D_{cc} does not linearly vary with porosity because of the non-linear relationships among the D_{cc} of pores, specific surface area, and porosity (Figures 4-6 and 4-7). Figures 4-8B and 4-8C show a variation in specific surface area and the D_{cc} of pores as a function of average particle diameter. Both the specific surface area and the D_{cc} of pore apparently decrease with increasing average particle diameter, particularly for the random packing simulations. Note that a variation in specific surface area and the D_{cc} of pore at a specific value of average particle diameter for glass beads and silica gels is also observed, as expected from the experimental condition of varied porosity with fixed diameters of spheres. The correlation between porosity and average particle diameter was weak (see Supplementary Information,

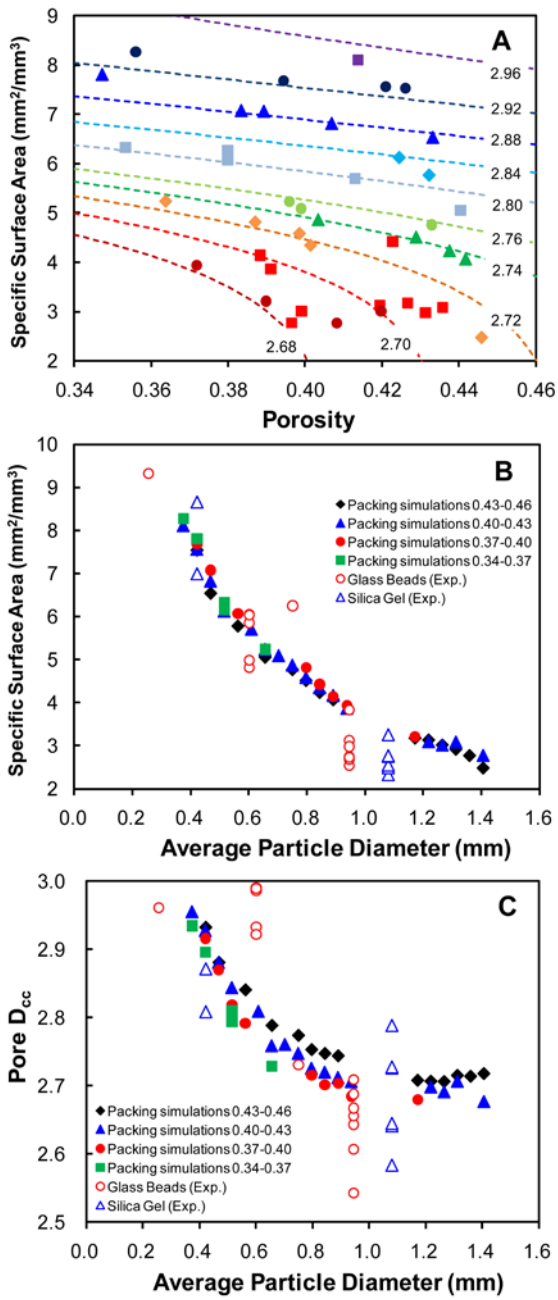

Figure 4-8. (caption on next page)

Figure 4-8. (A) Relationship between specific surface area (mm^2/mm^3) and porosity at identical cube-counting fractal dimension. Each cube-counting fractal dimension value is shown as the numeral on each corresponding dash-dot line obtained using equations (4.6) and (4.7). Data points represented by the same color as each dash-dot line were obtained by random packing simulations for the nearest cube-counting fractal dimension value of each dash-dot line. (B) Relationship between specific surface area (mm^2/mm^3) and average particle diameter. (C) Relationship between cube-counting fractal dimension of pores and average particle diameter. Data in (B) and (C) were obtained by random packing simulations and by NMR micro-imaging experiments.

Figure 4-S6); however, for random packing simulations, porosity increases slightly with increasing particle diameter.

4.3.2. Lacunarity of model porous networks

Figure 4-9 shows the effect of box size on the calculated lacunarity with varying porosity (0.26–0.27, 0.35–0.36, 0.41, and 0.43–0.44) of model porous networks in log (lacunarity)-log (box size) plots. The lacunarity at constant porosity decreases to zero with increasing box size in the log (lacunarity)-log (box size) plot. The log (lacunarity) values at constant box size decrease from ~0.6 to ~0.35 with increasing porosity from 0.26–0.27 to 0.43–0.44. The lacunarity for a porous network composed of larger particle diameters (e.g., GB1-4, 30-2) is larger than that for smaller particle diameters (e.g., GB3-1, 8-1). For porous networks composed of large particle diameters, including GB1-4 (Figure 4-9A), SG1-1 (Figure 4-9B), 30-2 (Figure 4-9C), and 29-1 (Figure 4-9D), the trend in the log (lacunarity)-log (box size) plot produces a peculiar pattern that was initially concave downward. Porous networks composed of intermediate and small particle diameters produce curves that are initially linear at smaller box sizes. The former and the latter corresponded to the moderately clustered pores and the randomly distributed pores in the lacunarity, respectively (Plotnick et al., 1993; Plotnick et al., 1996).

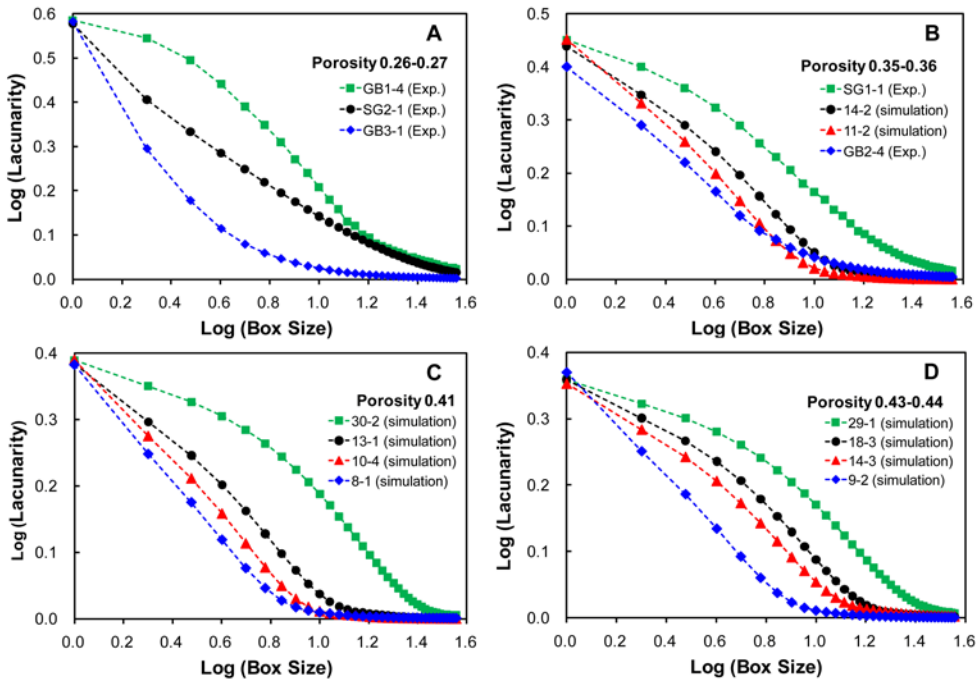

Figure 4-9. Relationship between lacunarity and box size in the log-log plot for porous networks obtained by random packing simulations and by NMR micro-imaging experiments. Each figure is grouped by the following porosity ranges: (A) 0.26–0.27, (B) 0.35–0.36, (C) 0.41, and (D) 0.43–0.44. Each legend indicates the sample names of corresponding data (refer to Tables 4-2 and 4-3).

Because lacunarity can bring out the differences between structures that have the same fractal dimension (Mandelbrot, 1982), the lacunarity of porous networks with identical cube-counting fractal dimension was investigated. Figure 4-10 shows that the effect of box size on lacunarity was distinct for porous networks with identical D_{cc} in the log (lacunarity)-log (box size) plot. In Figure 4-10A, although all porous networks have a D_{cc} of 2.68, the trend in the log (lacunarity)-log (box size) plot for SG2-1 and the trends of the simulation data (20-2 and 25-1) are classified into two distinct groups of networks (i.e., a random distribution of pores and a moderate degree of clustering) (Plotnick et al., 1996). Similarly, in Figure 4-10B, the porous networks have a D_{cc} of 2.79, but the trend in the log (lacunarity)-log (box size) plot for SG3-2 and the trends of the simulation data (12-1 and 14-3) are categorized into random and slightly clustered pores, respectively (Plotnick et al., 1996).

The current results show that the lacunarity of porous networks systematically depends on box size, sphere diameter, and porosity. Figure 4-11A shows the lacunarity of 3D porous networks at the minimum box size (corresponding to 0.047 mm in this study) as a function of porosity. As expected from the definition given in equation (4.3), lacunarity at the minimum box size (r = 1) is inversely proportional to the fraction of occupied sites (Plotnick et al., 1996). The current data (lacunarity vs. porosity) also clearly show that lacunarity decreases with increasing porosity. Figure 4-11B shows the lacunarity of 3D porous networks at a box size of 0.47 mm as a function of specific surface area. Lacunarity of 3D

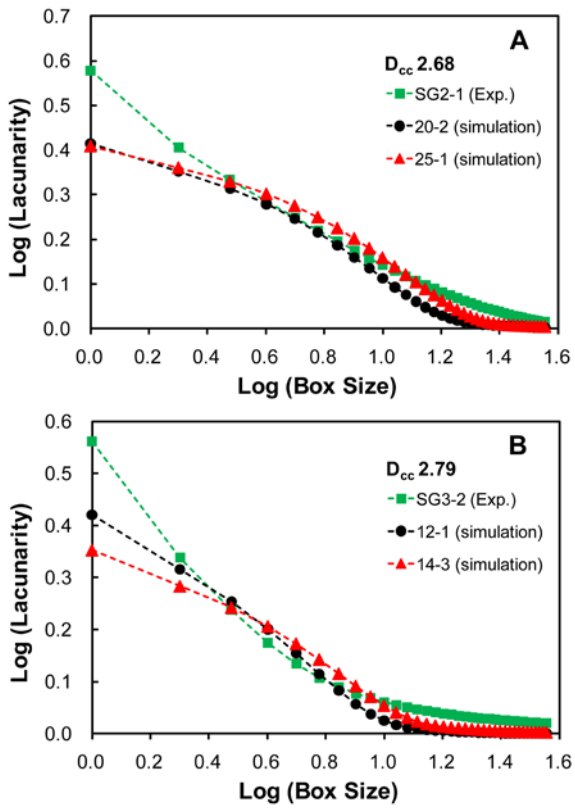

Figure 4-10. Relationship between lacunarity and box size in the log-log plot for porous networks with identical cube-counting fractal dimension (D_{cc}): (A) at D_{cc} = 2.68 and (B) at D_{cc} = 2.79. Each legend indicates the sample names for corresponding data (refer to Tables 4-2 and 4-3).

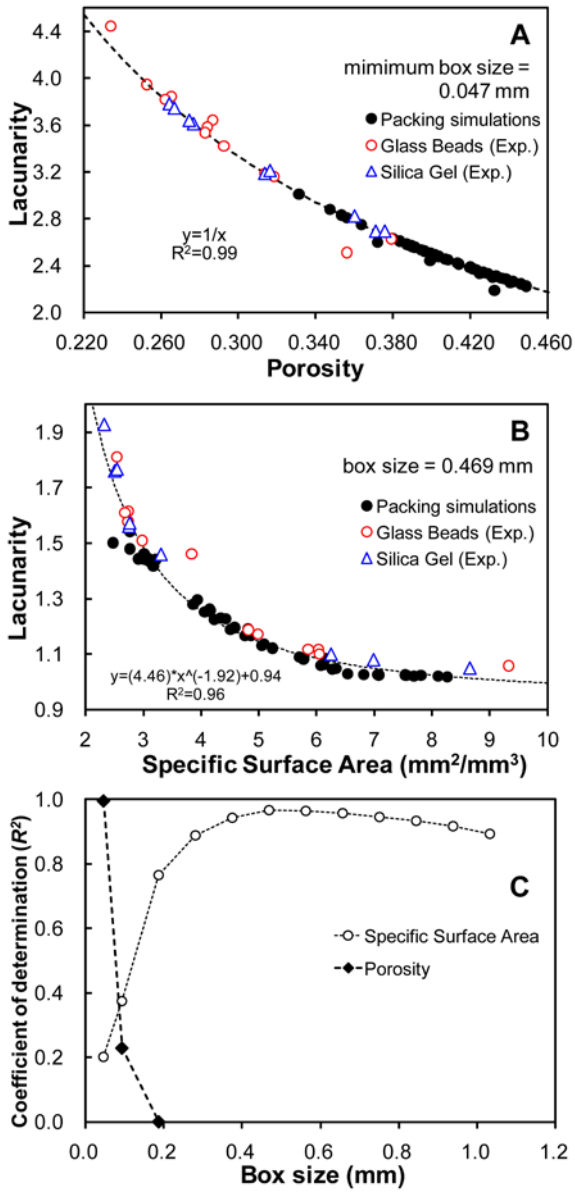

Figure 4-11. (caption on next page)

Figure 4-11. (A) Relationship between lacunarity at the minimum box size and porosity. (B) Relationship between lacunarity at a box size of 0.47 mm and specific surface area. (C) Relationship between coefficient of determination (R^2) and box size for porous networks obtained by random packing simulations and by NMR micro-imaging experiments. The R^2 value of each fitting curve was obtained for the relationship between lacunarity at a specific box size and porosity (black closed diamonds) and between lacunarity at a specific box size and specific surface area (black open circles). Each dashed line in (A) and (B) is a fitting curve obtained using the equation shown in each plot.

δ

porous networks decreases from 1.93 to 1.02 with increasing specific surface area from 2.32 to 8.27 mm^2/mm^3. The relationship between the calculated lacunarity at a box size of 0.47 mm and specific surface area ($\Lambda_{0.469}$) is fitted well with the simple power-law equation:

$$\Lambda_{0.47} = aS^b + c, \tag{4.9}$$

where $\Lambda_{0.469}$ is the lacunarity value at the box size of 0.469 mm, S is the specific surface area, and a, b, and c are fitting parameters and are shown in Figure 4-11B. Figure 4-11C shows R^2 values as a function of box size, showing the effect of box size on porosity and specific surface area; the R^2 values were obtained for lacunarity values of all samples at a specific box size as a function of porosity and specific surface area. Lacunarity at the minimum box size shows the best correlation with porosity (closed diamonds in Figure 4-11C), which is consistent with the correlation reported previously (Plotnick et al., 1996). Furthermore, lacunarity was well correlated with specific surface area when the box size ranged from 8 to 14 pixels (0.38 to 0.66 mm), with the best correlation at 0.47 mm (Figure 4-11B, Equation 4.9 above). The lacunarity at this intermediate box size also had a positive correlation with the average particle diameter (see Figure 4-S7B in Supplementary Information).

d

4.3.3. Configurational entropy of cross sections of model porous networks

Figure 4-12 shows the configurational entropy [$H^*(r)$] of porous networks as a function of box size, r. As previously mentioned (Section 4.1.3), the maximum configurational entropy and the corresponding entropy length can be obtained from $H^*(r)$ (see Figure 4-12A inset). For example, the calculated maximum configurational entropy and the entropy length for porous networks composed of single-sized spheres of diameter 0.656 mm are ~0.96 and 0.4 mm, respectively (Figure 4-12A). The configurational entropy apparently increases with increasing porosity from 0.34–0.37 (Figure 4-12A) to 0.43–0.46 (Figure 4-12D).

Figure 4-13 shows the entropy length of porous networks as a function of average particle diameter (d_p) and specific surface area. The entropy length of the network increased linearly with increasing average particle diameter with a slope of ~0.57 for porous networks obtained by random packing simulations of single-sized spheres and NMR micro-imaging of SG and GBs (red dashed line in Figure 4-13A) and a slope of ~0.54 for porous networks obtained by random packing simulations of single-sized spheres only (black dashed line in Figure 4-13A). Thus, entropy length = ~0.57 $d_p \approx (1/\sqrt{3})d_p$, indicating that the characteristic length of the porous network was ~0.57 times the average particle diameter of the solid grains comprising the porous media. Assuming that the entropy length measures the average diameter of the inscribed spheres in

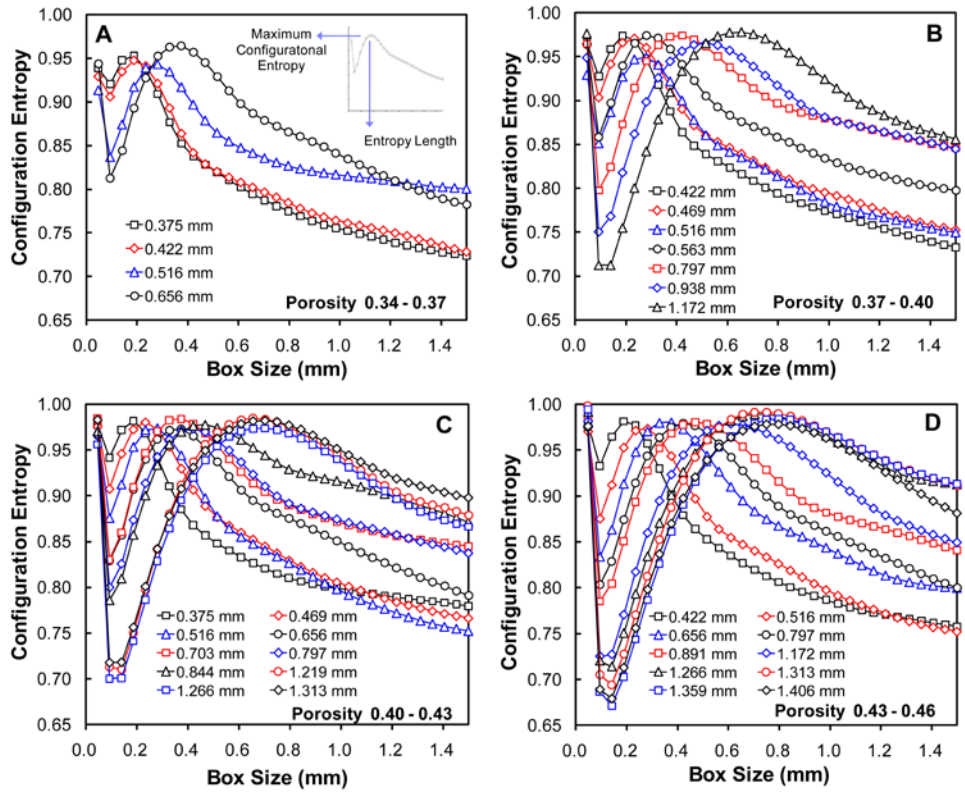

Figure 4-12. Relationship between configurational entropy and box size. Each plot corresponds to the following porosity ranges: (A) 0.34 to 0.37, (B) 0.37 to 0.40, (C) 0.40 to 0.43, and (D) 0.43 to 0.46. Inset in (A) shows the maximum configurational entropy and the corresponding entropy length.

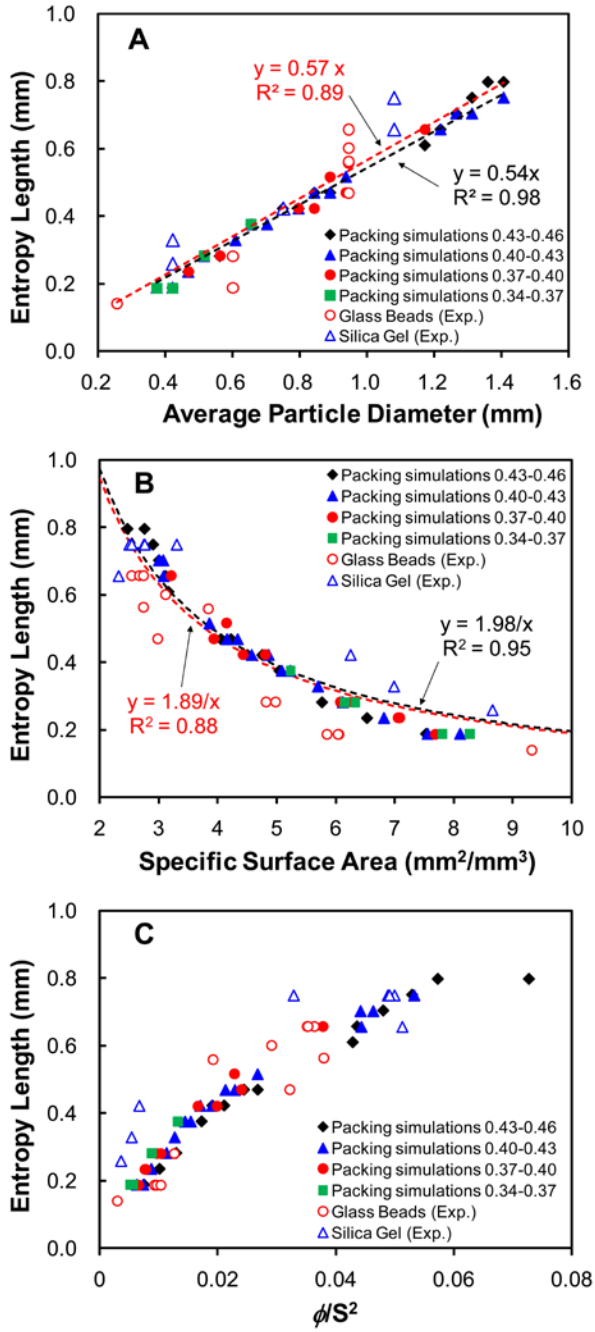

Figure 4-13. (caption on next page)

Figure 4-13. (A) Relationship between entropy length and average particle diameter (mm). (B) Relationship between entropy length and specific surface area (mm^2/mm^3). (C) Relationship between entropy length and (porosity)/(specific surface area)^2. Data in (A, B, and C) were obtained both experimentally and by calculations.

δ

pore bodies, the average coordination number of the pore body can be predicted and is likely to be ~6; the radius ratio of the coordination polyhedra for an octahedron ranges from 0.414 to 0.732 (Nesse, 2000). The current correlation between the average particle diameter and entropy length for porous networks has not been reported previously. As expected from the relationship between specific surface area and the D_{cc} of pores at an average particle diameter (e.g., Figures 4-8B and 8C), there is a variation in entropy length at a specific average particle diameter (Figure 4-13A). In particular, the variation is more significant for the SG than for GBs, indicating that entropy length is sensitive to the heterogeneity of grain size in porous media. Because the specific surface area decreases with increasing average particle diameter, entropy length also decreases (from 1.02 to 0.19 mm) with increasing specific surface area (from 2.32 to 8.27 mm^2/mm^3) (Figure 4-13B). Although the correlation between entropy length and porosity is not significant (see Figure 4-S8 in Supplementary Information) in the samples studied here, it is found that entropy length also increased with increasing (porosity)/(specific surface area)^2 (Figure 4-13C).

Figure 4-14 shows the effect of porosity (ϕ) on configurational entropy. The maximum configurational entropy increases from 0.85 to 0.99 with increasing porosity from 0.23 to 0.45. In addition to the maximum configurational entropy, configurational entropy due to total porosity (S^{config}) can also be calculated from the following simple expression:

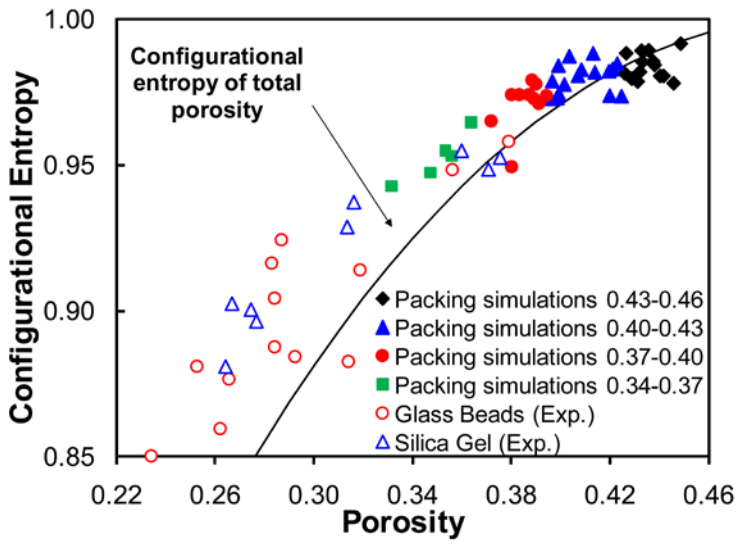

Figure 4-14. Relationship between maximum configurational entropy and porosity. The solid line denotes configurational entropy of total porosity (see text for details).

δ

$$S^{config} = k\left[\phi \ln \phi + (1-\phi)\ln(1-\phi)\right], \qquad (4.10)$$

where k is a constant used to normalize the S^{config} to be a maximum configurational entropy (=1) at $\phi = 0.5$ (In the current study, k = ~ -1.4, black curve in Figure 4-14). Equation (4.10) is equivalent to the configurational entropy, $H^*(r)$, at a box size of 1. Configurational entropy due to total porosity increases with increasing porosity up to 0.5. Although the overall trend is similar, the difference between the configurational entropy of total porosity and the maximum configurational entropy apparently decreases with decreasing porosity. The difference is due to the fact that the former is obtained from the total structure of porous media, whereas the latter is obtained from the local porous networks at the box size of maximum disorder (Andraud et al., 1994) and should thus be larger than the configurational entropy due to total porosity. The clear correlations between configurational entropy and average particle diameter and between configurational entropy and specific surface area were not demonstrated (see Figures 4-S9 in Supplementary Information). By considering the 1:1 correspondence between porosity and configurational entropy, the latter can be predicted and used for the modeling of properties of porous networks and multi-phase rock-melt-fluid composites (see further discussion below). The above correlations revealed the previously unknown nature of entropy length and configurational entropy and their relationships with other key structural parameters in porous networks. Configurational entropy analyses in the current analysis have been limited

δ

to cross sections of porous networks; however, it would be necessary to compare these analyses with future results of configurational entropy for 3D structures of porous networks.

4.3.4. Relationship among structural parameters, cube-counting fractal dimension, and permeability

Structural relationships allowed us to establish a link between the structure and properties of porous networks and conventional structural parameters such as specific surface area, porosity, and average diameter. Permeability for the current dataset was estimated and its relationship with other structural parameters was investigated. Figure 4-15 shows the effects of average particle diameter (Figure 4-15A), specific surface area (Figure 4-15B), and porosity (Figure 4-15C) on calculated permeability for the current dataset obtained by random packing simulations and NMR micro-imaging experiments. The calculated permeability shows a general trend of increasing with increasing average particle diameter and decreasing with increasing specific surface area. Permeability apparently increases with increasing porosity. Figure 4-16A also shows the relationships among permeability, specific surface area (S), and porosity (ϕ) of model sands. The results show that the relationships among the parameters for the model sands are well described with the Kozeny-Carman equation (e.g., de Marsily, 1986)

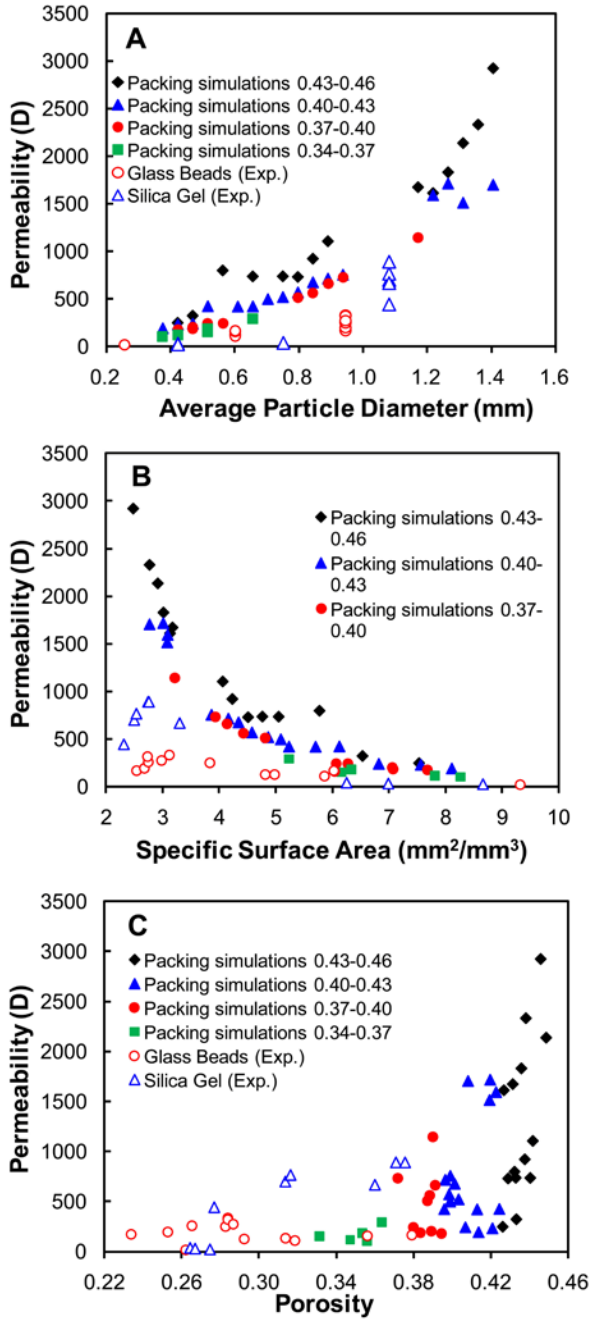

Figure 4-15. (caption on next page)

Figure 4-15. (A) Relationship between permeability and average particle diameter (mm). (B) Relationship between permeability and specific surface area (mm^2/mm^3). (C) Relationship between permeability and porosity. The data in this figure were obtained by random packing simulations and by NMR micro-imaging experiments.

δ

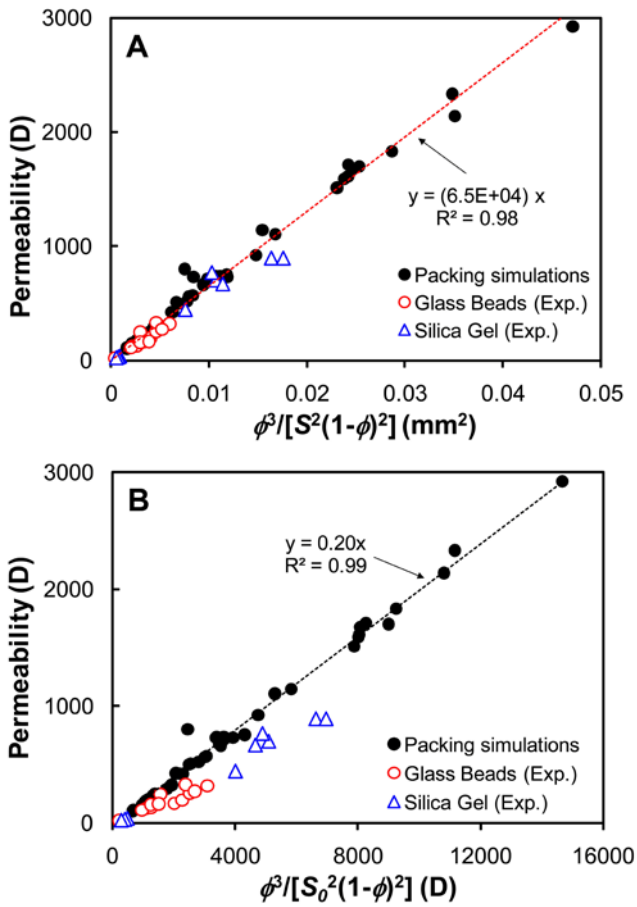

Figure 4-16. (A) Relationship between permeability and (porosity)^3/[(specific surface area)^2(1-porosity)^2] (unit in mm^2). Here the specific surface area refers to total surface area of the interstitial voids divided by the total bulk volume. (B) Relationship between permeability and $\phi^3/[S_0^2(1-\phi)^2]$ (unit in Darcy). Here, S_0 is the total surface area of the interstitial voids divided by the volume of the solid grains. Black closed circles correspond to packing simulation data, and red open circles and blue open triangles correspond to experimental data for glass beads and silica gel samples, respectively.

δ

$$k(\phi, S) = \frac{\phi^3}{C_0 S^2 (1-\phi)^2}, \qquad (4.11)$$

where C_0 is the pore shape factor. Permeability can be well explained by this equation, regardless of grain shape (e.g., sphere or shaped particles studied in the current study) and the heterogeneity in particle size (see Figure 4-S10 in Supplementary Information for correlations among the parameters based on the Kozeny equation).

Upon utilizing total surface area of the interstitial voids divided by the volume of the solid grains (S_0, see Section 4.2.4.2 above) instead of the current definition of the specific surface area, Figure 4-16B also shows the relationship between permeability and $\phi^3/[(S_0)^2 (1-\phi)^2]$ (unit in Darcy). The slope of the relationship for porous media composed of single-sized spheres is approximately 0.2, and that for porous media composed of diverse grain shapes and particle diameters (GB2 and SG2) is slightly smaller than 0.2. The correlation between surface area per unit bulk volume and surface area per unit solid volume is described in Supplementary Information, Figure 4-S11.

Previous studies have suggested that the fractal dimension of porous networks can be used to account for macroscopic transport properties of porous media. For instance, permeability has often been described as a function of porosity and fractal dimension (Jacquin and Adler, 1987; Hansen and Skjeltorp, 1988; Muller and McCauley, 1992; Ghilardi et al., 1993; Costa, 2006) and as a function of pore fractal

δ

dimension and tortuosity fractal dimension (Yu and Cheng, 2002). These results offer useful insights into the nature of permeability in porous networks. The relationships obtained in the current study can also provide further and improved generalization of the relationships between permeability, fractal dimension, and porosity on the basis of newly identified relationships among the structural parameters. For example, by combining equations (4.6) and (4.11) and replacing specific surface area in equation (4.11) with the D_{cc} of pores from equation (4.6), the following equation can be obtained:

$$k(\phi, D_{cc}) = \phi^3 / \left[C_0 \left\{ c - d \ln\left(\frac{a - D_{cc}}{D_{cc} - b} \right) \right\}^2 (1-\phi)^2 \right]. \qquad (4.12)$$

where coefficients *a, b,* and *c* are functions of porosity, as described in equation (4.7), and C_0 is the pore shape factor in the Kozeny-Carman equation. Figure 4-17 shows the relationships among permeability, the D_{cc} of pores, and porosity. Permeability decreases with increasing D_{cc} at constant porosity and increases with increasing porosity at constant D_{cc}. Thus, permeability can be expressed on the basis of the D_{cc} of pores and porosity in porous media composed of sand-sized particles. Note that D_{cc} of pore can be expressed as a function of specific surface area at constant porosity or a function of porosity at constant specific surface area (Figure 4-7). For the geophysical applications, it is more useful that specific surface area is replaced by D_{cc} of pore, and therefore equation (4.12) which is a function of porosity and D_{cc} of pore is suggested. Furthermore, because

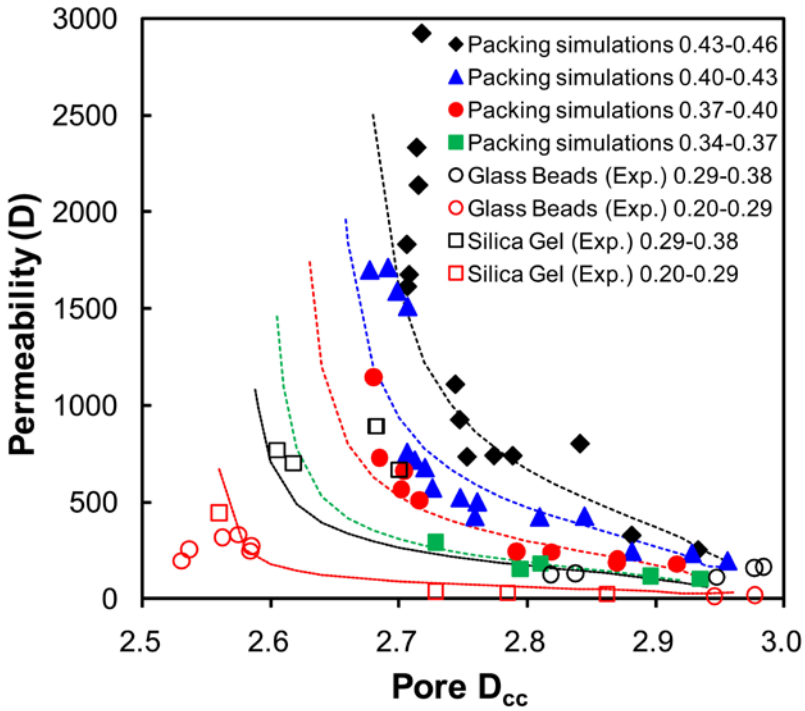

Figure 4-17. Relationship between permeability and cube-counting fractal dimension of porous networks. The equation for each curve is shown as equation (4.12) in the text. Black diamonds, blue triangles, red circles, and green squares correspond to each group of simulation data for porosities 0.43–0.46, 0.40–043, 0.37–0.40, and 0.34–0.37, respectively. Black and red open circles correspond to glass bead samples for porosities 0.29–0.38 and 0.20–029, respectively. Black and red open squares correspond to silica gel samples for the porosities 0.29–0.38 and 0.20–0.29, respectively. Black, blue, red, and green dashed lines and black and red dotted lines are curves for equation (4.12) corresponding to the median porosities in each group: 0.445, 0.415, 0.385, 0.355, 0.335, and 0.245, respectively.

δ

equation (4.12) yielded high correlations among the key structural parameters and properties, it can be applied to diverse natural porous networks (see Supplementary Information, Figure 4-S12 for relationship between permeability and D_{cc} of solid mass, and that between permeability and D_{cc} of surface). In order to generalize equation (4.12), a scaling factor that has the dimension of the square of the length should be included in equation (4.12) (note that permeability has the dimension of the square of the length). A scaling factor would be, for example, the volume of the object divided by the average cutoff lengths. However, as D_{cc} may depend on the length scale of observation, the investigation on D_{cc} for a wider range of volume is necessary for the estimation of the scaling factor. As shown in equation (4.11), permeability has been expressed as a function of porosity and specific surface area (i.e., $k = f(\phi)f(S)$) by Kozeny-Carman equation. In this study, it is suggested that permeabity can be expressed as a function of porosity and D_{cc} (i.e., $k = f(\phi)f(D_{cc})$) by equation (4.12). In Supplementary Information, the effects of $(\text{porosity})^3/(\text{surface area})^2$ and $(\text{porosity})^3/[(\text{surface area})^2(1\text{-porosity}^2)]$ on cube-counting fractal dimension (Figure 4-S13), configurational entropy (Figure 4-S14), and entropy length (Figure 4-S15) have been provided.

In addition to their obvious applications and implications for ground water transport and fluid distribution in natural porous networks, the newly identified relationships among structural parameters and properties may provide additional implications for characterizing and understanding fluid-rock-melts composites and glass-vesicles-rock

δ

composites regardless of the length scale of heterogeneity (from microscopic to mesoscopic). For example, previous studies have shown that shear viscosity of rock-melt composites (η) in the earth's interior is inversely proportional to the exponential of liquid volume fraction (ϕ) in partially saturated porous media [e.g., $\eta^{-1} \propto \exp(\phi)$] (Takei, 1998; Takei, 2005; Takei and Holtzman, 2009). Therefore, on the basis of the inverse correlation between the liquid volume fraction (i.e., porosity) and configurational entropy [equation 4.10], the shear viscosity (η) in the melts can be simply expressed using the configurational entropy (S_c)

$$\eta^{-1} \propto \exp(S_C). \qquad (4.13)$$

The results suggest that shear viscosity decreases with increasing configurational entropy of fluids that are partially saturated in rocks. Thus, configurational entropy can be a complementary parameter for describing elastic properties and shear viscosity of porous media. Note that equation (4.13) shows remarkable similarity to the fundamental microscopic relationship between configurational entropy of supercooled liquids and the viscosity of melts on the basis of the Adam-Gibbs theory (Adam and Gibbs, 1965; Richet, 1984; Lee, 2005), suggesting that a relationship derived from equation (4.13) is robust and can be applied to diverse networks, regardless of the length scale of the constituent objects.

Additionally, the 3D fractal dimension was used to describe P-wave attenuation and velocity in partially saturated rocks. For example, P-wave attenuation at high-frequencies is expressed as

δ

$$Q^{-1} \propto \omega^{-\nu}, \tag{4.14}$$

where Q^{-1} is the P-wave attenuation, and ν is a Hurst exponent (= 3 - fractal dimension of fluid patches in the mesoscopic scale) (Pride and Masson, 2006). Since the fractal dimension (3–Hurst exponent) can be directly calculated by considering fluid patches of partially saturated rocks, P-wave attenuation can also be estimated. 3D fractal dimension would be a more accurate parameter for describing complex networks than the conventional fractal dimension obtained from 2D images.

Although the current analyses are focused on simple porous networks to establish the correlations among the structural and transport properties, the results will be helpful for characterizing more complex porous networks with broader distributions of grain sizes and particle shapes. The methodology and results systematically analyze the structures of diverse porous networks and complex geologic media and have elucidated previously unknown details of the nature of those structural parameters. Further generalization of the relationships identified in the current study using diverse particle sizes and heterogeneity remains to be explored.

4.4. Conclusions

Relationships among the structural parameters and properties for porous media composed of model sands from random packing simulations and NMR micro-imaging experiments were established. The D_{cc} of 3D

δ

porous networks increases with increasing specific surface area at constant porosity and increases with increasing porosity at constant specific surface area. The first lacunarity of 3D porous networks was also reported. The lacunarity at intermediate box size (~ 0.469 mm in the current study) decreases with increasing specific surface area with data showing the power-law relationship between the two parameters. The entropy length of the porous networks decreases linearly with decreasing average particle diameter and can be used to constrain the characteristic length scale of the pores in the networks. The maximum configurational entropy increases with increasing porosity, showing a similar trend with the configurational entropy of the total porosity. Based on this newly identified correlation and the Kozeny-Carman equation, a predictive relationship among permeability as a function of porosity and D_{cc} was proposed. The correlations among the structural and transport parameters analyzed in this study are helpful for understanding complex porous networks and can be used to explain the geometrical and transport properties of porous media.

It was also demonstrated that 3D porous networks can be successfully obtained by NMR micro-imaging with a spatial resolution of ~50 μm, which allowed us to obtain 3D images of porous media composed of particles as small the silt-sized grains. The availability of high spatial resolution images together with other advantages highlighted by its capability of directly probing of fluid phases using NMR micro-imaging will be useful to visualize micrometer scale distributions of two-phase

δ

fluids in porous media and to image melts and fluids in rocks.

Appendix: Multifractal analysis of cross sections of model porous networks

Multifractal analysis of cross sections of porous networks has been applied to characterize the complex geometry that exhibits local fluctuations in density (see below). In that sense, the model sands studied here may not be a favorable system for the multifractal analysis. Multifractal analysis on relatively simple porous networks, however, can reveal useful correlations among their structural parameters and properties; thus, the analysis on porous networks composed of single-sized spheres or model sands was performed to reveal the relationships between generalized dimensions and other key structural parameters.

4.A.1. Summary of theoretical background and data analysis

In multifractal analysis, probability $\mu_i(r)$ in a box i of size r covering a pore space is defined as (Hentschel and Procaccia, 1983)

$$\mu_i(r) = \frac{M_i(r)}{M}, \qquad (4.A1)$$

where $M_i(r)$ is the number of pore pixels included in a square box, and M is the total mass of the object. For every box i, the partition function $[X(q.r)]$ was obtained for different moments q (varying from $-\infty$ to $+\infty$) using

$$X(q,r) = \sum_{i=1}^{N(r)} \mu_i^q(r) = r^{(q-1)D_q}, \qquad (4.A2)$$

δ

where $N(r)$ is the number of boxes covering the entire image. For each q, generalized dimensions (D_q) can be obtained from equation (4.A2) given by

$$D_q = \frac{1}{q-1}\lim_{r\to 0}\frac{\log X(q,r)}{\log r}. \qquad (4.A3)$$

The geometric meaning of D_q can be understood as the dimensions of the set, which leads to divergence of moments of the order of q or higher (Farmer et al., 1983). The generalized dimensions for q = 0, q = 1, and q = 2 (capacity, information, and correlation dimension, respectively), are often used to characterize complex porous networks (e.g., Muller and McCauley, 1992; Muller et al., 1995; Muller, 1996). Multifractal analysis of porous media has been extended to pore space in soils (e.g., Posadas et al., 2003; Bird et al., 2006; Dathe et al., 2006; Grau et al., 2006) and rocks (e.g., Muller and McCauley, 1992; Muller, 1996; Saucier and Muller, 1999). Recently, multifractal analysis was applied to characterize the 3D images of soil samples (Tarquis et al., 2009). Generalized dimensions of 2D cross-sectional images of the porous networks of model sands were calculated and the effect of specific surface area on the generalized dimensions was explored.

Multifractal analysis was carried out using a box-counting algorithm where 2D data with a matrix size of 160 × 160 were expanded to 400 × 400 data using ImageJ software (Rasband, 1997-2009). The box-counting algorithm was performed for every box size from 2 to 256 pixels in steps of 2^k. The generalized dimensions were estimated from the slope of the log-log plot of the partition function [$X(q,r)$] over box size (r).

4.A.2. Results and discussion

Figure 4-A1 shows partition functions [$X(q,r)$] over box sizes (r) in log-log plots ranging from 2 to 256 pixels for 2D cross-sectional images of model porous media by random packing simulations. For $q \geq 0$, the partition functions show linear relationships in the log-log plots. For $q < 0$, two distinct regions were distinguished by a breakpoint at ~log(r) of ~2.8 for [$X(q,r)$] for a sphere diameter of 468.75 mm [break points (BP) in Figure 4-A1]. The box size at the breakpoint increased with increasing grain size.

Figure 4-A2 shows the generalized dimensions of 2D model porous networks studied here as a function of q. The generalized dimension (D_q) was obtained from the trend line corresponding to each q value from –10 to +10 in log [$X(q,r)$] over log [box sizes (r)] (Figure 4-A1). For $q \leq 0$, D_q values decreased with increasing q. For $q > 0$, and they showed relatively constant D_q values. This behavior was consistent with the trend reported for the pore space of soils (Dathe et al., 2006; Grau et al., 2006; Tarquis et al., 2006). In general, D_q values increase with decreasing grain diameter.

Figure 4-A3 shows the relationship between generalized dimensions and specific surface area. Figures 4-A3A and 4-A3B were obtained from the porous networks composed of spheres grouped by porosity ranges of 0.40–0.46 and 0.34–0.40, respectively. Figures 4-A3C and 4-A3D were obtained from GBs and SG samples, respectively. Although it was not clear whether D_q (with varying specific surface area) was dependent on porosity or type of particles (SG or GB) generalized dimensions for $q \leq 0$ increases with increasing specific surface area for

δ

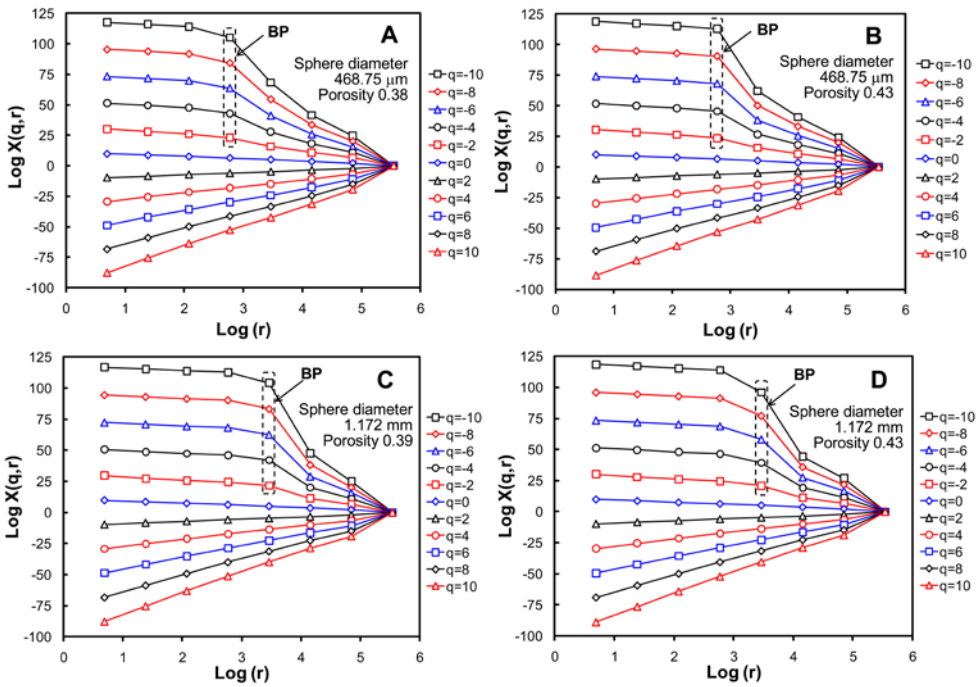

Figure 4-A1. Relationship between partition functions in multifractal analysis and box size in the log-log plots when moment q was varied from –10 to +10. (A) and (B) correspond to the porous networks obtained by random packing simulations for sphere diameters of 468.75 μm and porosities of 0.38 and 0.43, respectively, and (C) and (D) correspond to the porous networks obtained by random packing simulations for sphere diameters of 1.172 mm and porosities of 0.39 and 0.43, respectively.

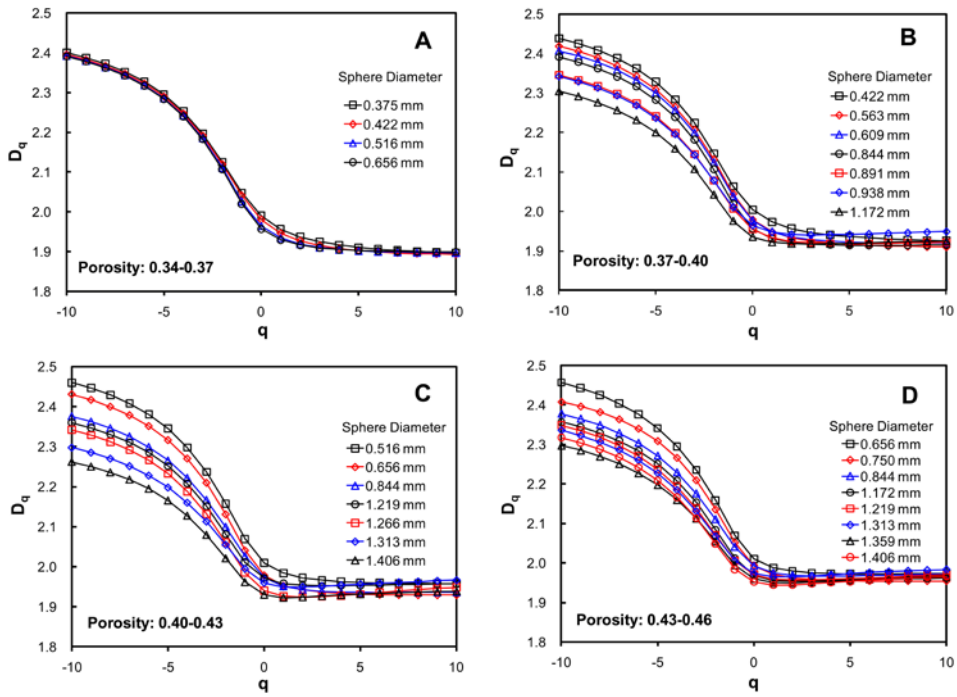

Figure 4-A2. Relationship between generalized dimensions and moment q. Each plot corresponds to the following porosity ranges: (A) 0.34 to 0.37, (B) 0.37 to 0.40, (C) 0.40 to 0.43, and (D) 0.43 to 0.46.

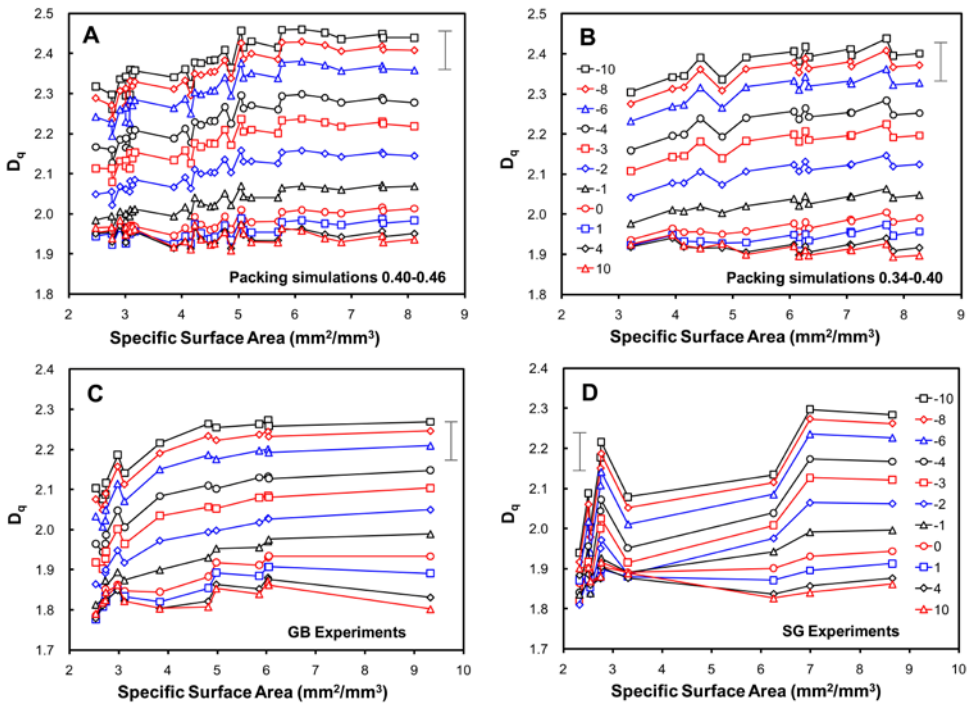

Figure 4-A3. Relationship between generalized dimensions and specific surface area (mm^2/mm^3) when moment q was varied from –10 to +10 (curves for q = –9, –7, –5, 2, 3, 5, 6, 7, 8, and 9 that had trends similar to the other curves are not shown for the sake of clarity). (A) and (B) correspond to the results obtained by random packing simulations of the following porosity ranges: (A) 0.34 to 0.40 and (B) 0.40 to 0.46. (C) and (D) correspond to the results obtained by NMR micro-imaging experiments; (C) glass beads and (D) silica gel. Maximum error is shown as an error bar in each plot. The legend for all figures is shown in (B) and (D).

every data group (Figures 4-A3A-A3D). The difference between the largest and the smallest generalized dimensions at a specific q value was as large as 0.2. The estimated maximum errors (depicted by error bars in Figures 4-A3A–A3D) were smaller than 0.1.

Figure 4-A4 shows the relationships among generalized dimensions, specific surface area, and porosity. While the relationship was not clear in Figure 4-A3, the generalized dimension at a constant specific surface area increases with increasing porosity. This trend is similar to the trends among D_{cc}, specific surface area, and porosity (see Section 4.3.1).

Figure 4-A5 shows the differences between D_0, D_1, and D_2 (i.e., D_0-D_2, D_0-D_1, and D_1-D_2) as a function of specific surface area. The difference functions increase with increasing specific surface area, whereas D_1 and D_2 are not correlated with specific surface area, as shown in Figures 4-A4E and A4F. Among the difference functions, D_0-D_2 shows the largest difference between the maximum and minimum differences between D_0, D_1, and D_2. It was previously reported that D_0-D_1 is a measure of the degree of heterogeneity of a particle size distribution (Posadas et al., 2001). The current relationship between D_0-D_2 and specific surface area has not been reported so far. The fine correlation between the difference function and specific surface area suggests that multifractal analysis may be useful to characterize relatively simple porous networks.

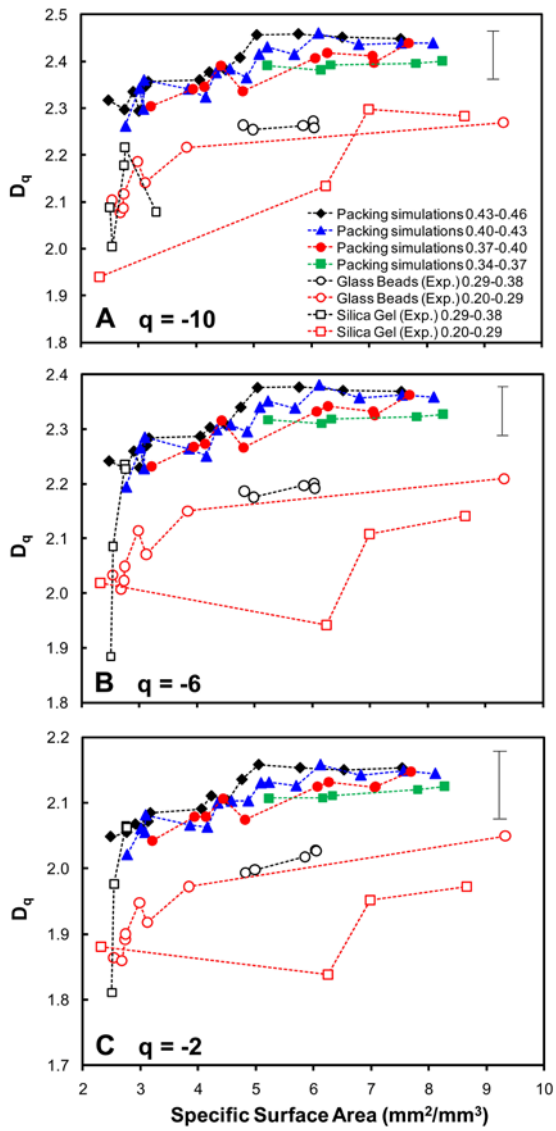

Figure 4-A4. Relationship between generalized dimension and specific surface area (mm^2/mm^3) at a specific moment, q. (A, B, C, D, E, and F) correspond to moment q of –10, –6, –2, 0, 1, and 2, respectively. Maximum error is shown as an error bar in each plot. The legend for all figures is shown in (A) and (D).

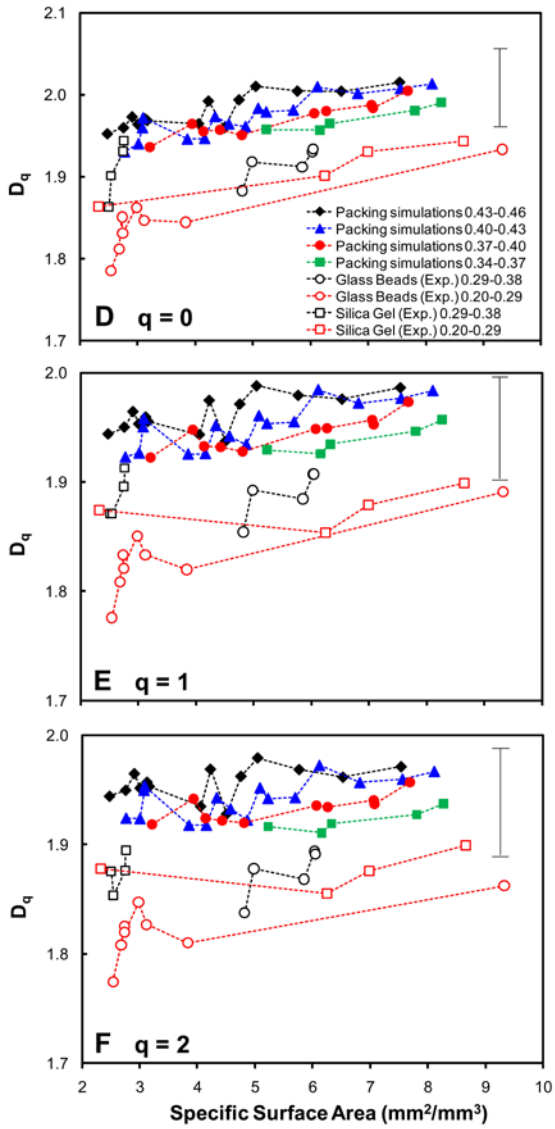

Figure 4-A4. (continued)

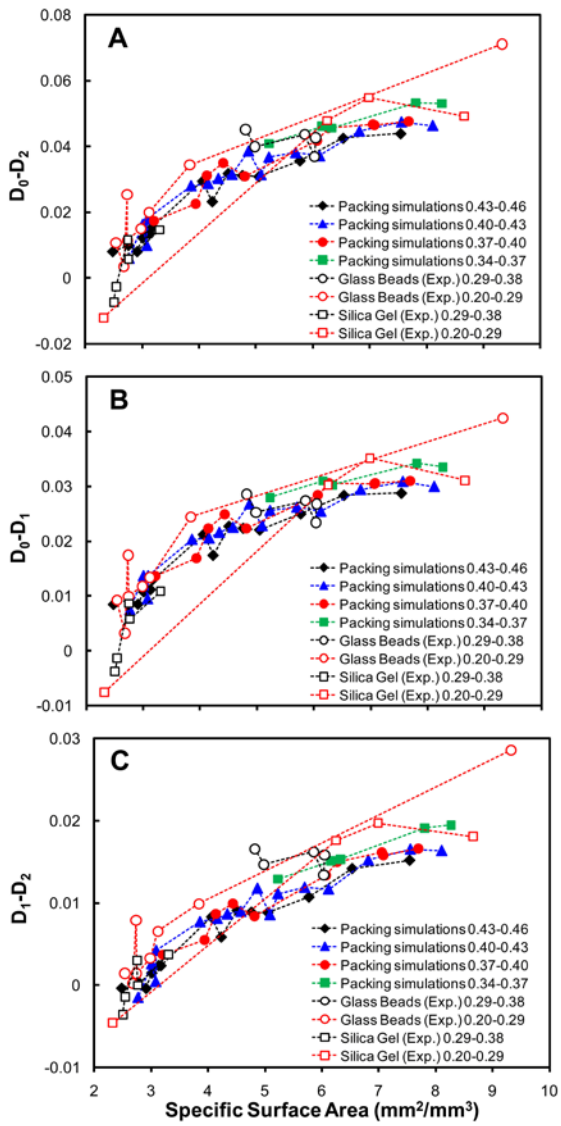

Figure 4-A5. (A) Relationship between D_0-D_2 and specific surface area (mm²/mm³). (B) Relationship between D_0-D_1 and specific surface area (mm²/mm³). (C) Relationship between D_1-D_2 and specific surface area (mm²/mm³).

Supplementary Information

4.S1. Selection of box sizes for estimation of D_{cc}

Figures 4-S1-3 show the relationship between box counts and box size for the simulated pores (Figure 4-S1), solid grains (Figure 4-S2), and surface (Figure 4-S3) composed of randomly packed spheres for sphere diameters of 8 pixels (0.38 mm) (Figure 4-S1A, 4-S2A, and 4-S3A), 15 pixels (0.70 mm) (Figure 4-S1B, 4-S2B, and 4-S3B), and 30 pixels (1.41 mm) (Figure 4-S1C, 4-S2C, and 4-S3C) with varying box size from 4 to 128 pixels (corresponding to 0.047-1.50 mm). Trend lines with three characteristic slopes can be drawn from ~4 to ~10 pixels (red line), from ~11 to ~40 pixels (dark blue line), and from ~40 to ~128 pixels (blue line). These ranges are roughly consistent with region I, II, and III, respectively (see Figure 4-5).

As specifically mentioned in the text, the box size range for non-integer fractal dimension in the porous networks only slightly varies with grain size because the variation in grain size in this study was not significant within the range used for the estimation of D_{cc}. The pixel sizes included in this range (among the divisors of 640) are 16, 20, 32, and 40 pixels (corresponding to 0.19, 0.23, 0.38, and 0.46 mm, respectively).

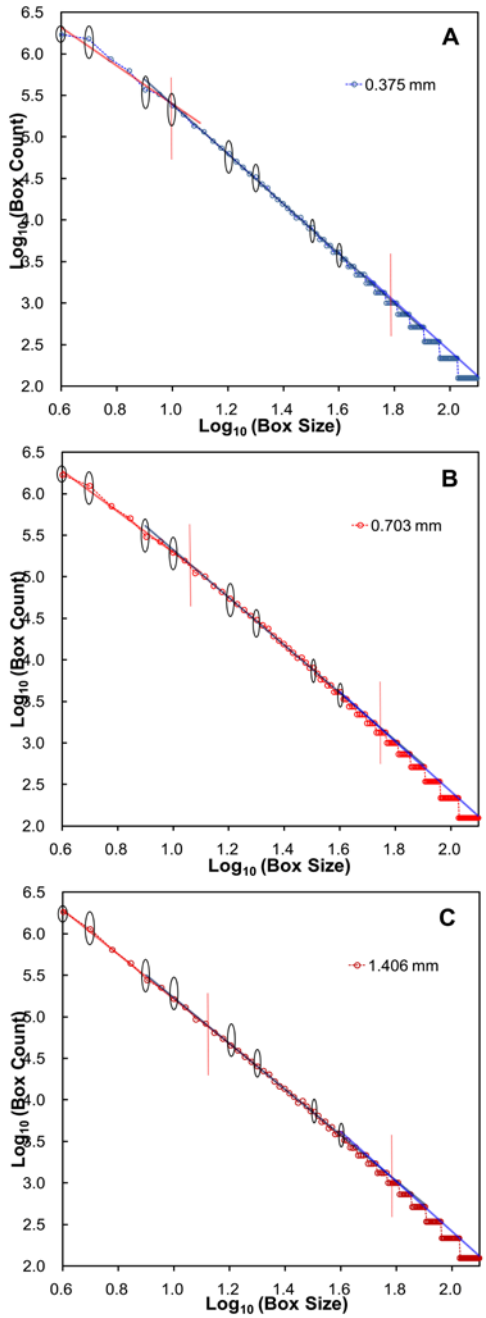

Figure 4-S1. (caption on next page)

Figure 4-S1. Relationship between box counts and box size (from 4 to 128 pixels, corresponding to 0.047-1.50 mm) in log-log plot for porous networks obtained by random packing simulations of single sized spheres with the diameters of (A) 8 pixels (corresponding to 0.38 mm), (B) 15 pixels (corresponding to 0.70 mm), and (C) 30 pixels (corresponding to 1.41 mm). Black ellipsoids indicate the data points that correspond to divisors of 640.

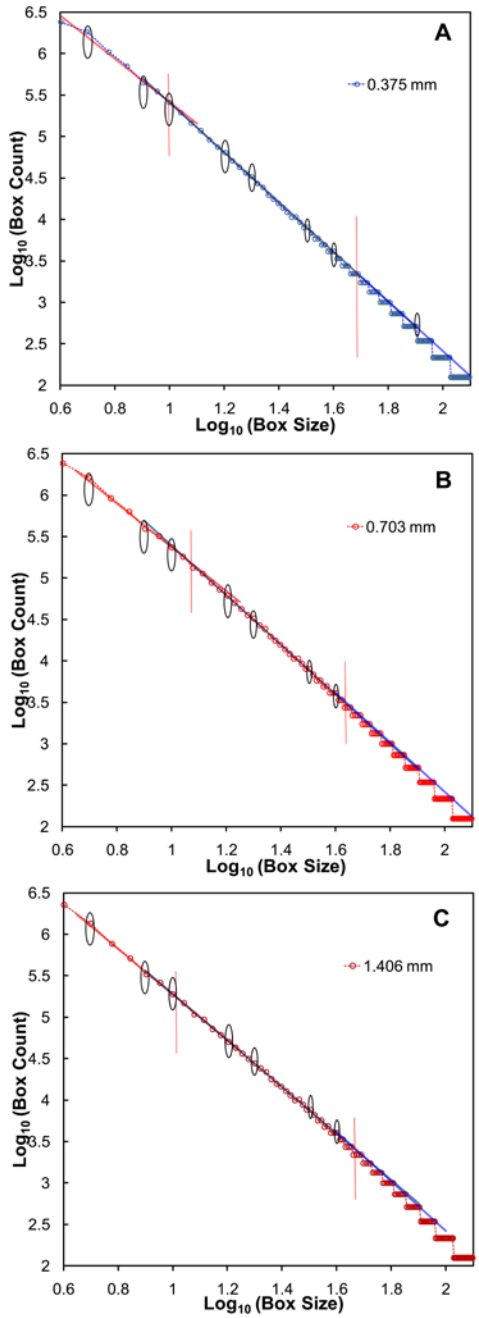

Figure 4-S2. (caption on next page)

Figure 4-S2. Relationship between box counts and box size (from 4 to 128 pixels, corresponding to 0.047-1.50 mm) in log-log plot for solid grains obtained by random packing simulations of single sized spheres with the diameters of (A) 8 pixels (corresponding to 0.38 mm), (B) 15 pixels (corresponding to 0.70 mm), and (C) 30 pixels (corresponding to 1.41 mm). Black ellipsoids indicate the data points that correspond to divisors of 640.

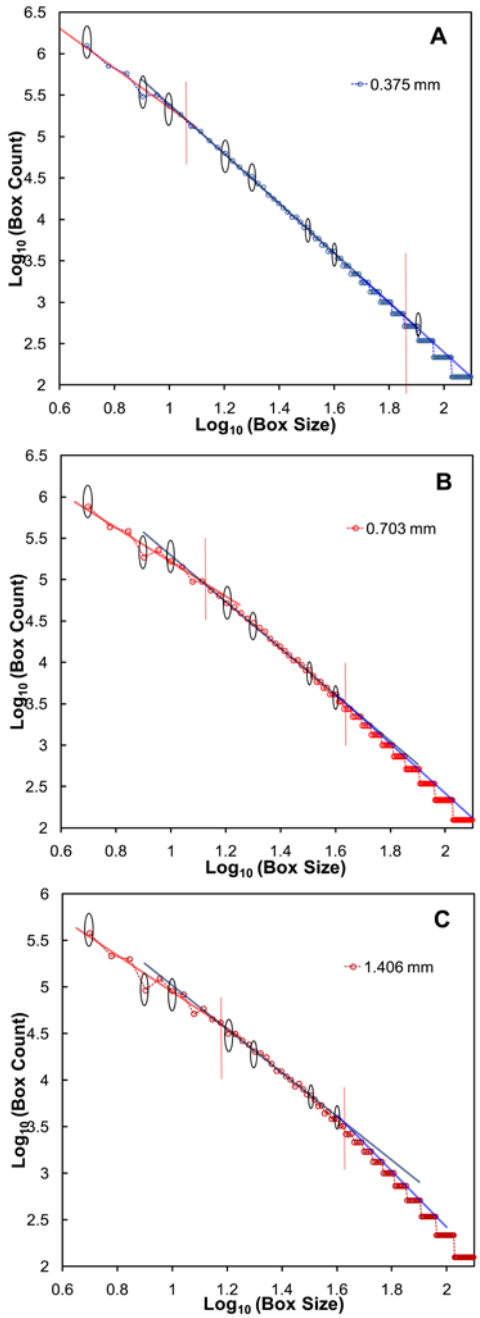

Figure 4-S3. (caption on next page)

Figure 4-S3. Relationship between box counts and box size (from 4 to 128 pixels, corresponding to 0.047-1.50 mm) in log-log plot for solid grains obtained by random packing simulations of single sized spheres with the diameters of (A) 8 pixels (corresponding to 0.38 mm), (B) 15 pixels (corresponding to 0.70 mm), and (C) 30 pixels (corresponding to 1.41 mm). Black ellipsoids indicate the data points that correspond to divisors of 640.

4.S2. Uncertainty in D_{cc}

The estimated D_{cc} in the current study may also depend on the choice of the ranges of box size. In order to estimate the uncertainty in the D_{cc} value, D_{cc} with two distinct box size ranges along the region II was estimated. Figure 4-S4 shows the log-log plots of the relationship between box counts and box size for the simulated porous networks composed of randomly packed spheres for sphere diameters of 8 pixels (0.38 mm) and 30 pixels (1.41 mm) with varying the box size. Two trend lines drawn from ~10 to ~32 pixels (blue line) and from 20 to 64 pixels (red line) for sphere diameters of 8 pixels (0.38 mm) and 30 pixels lead to similar D_{cc} values. The result shows that differences in the estimated D_{cc} are insignificant. The estimated uncertainty in D_{cc} value is thus smaller than ~ 0.07.

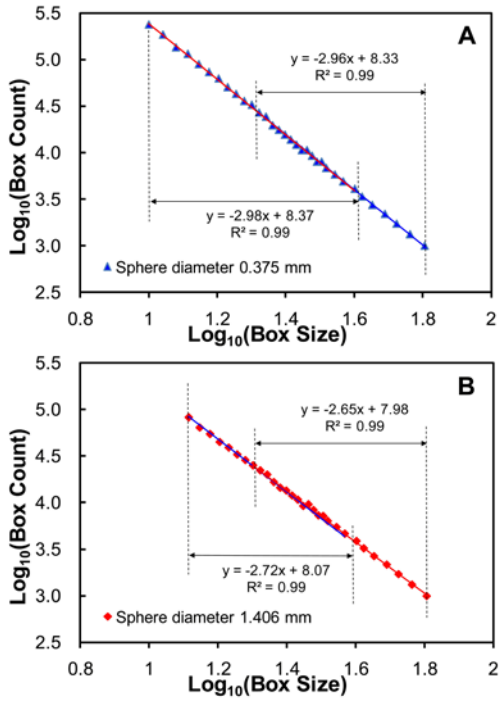

Figure 4-S4. Relationship between box counts and box size in log-log plot for porous networks obtained by random packing simulations of single sized spheres with the diameters of (A) 8 pixels, corresponding to 0.38 mm with the box sizes from 10 to 64 pixels (corresponding to 0.12-0.75 mm), and (B) 30 pixels, corresponding to 1.41 mm with the box sizes from 13 to 64 pixels (corresponding to 0.15-0.75 mm, respectively).

S3. The D_{cc} of solid mass, surface, and specific surface area

Taking into consideration the experimental results obtained by NMR micro-imaging, Figure 4-S5 shows the relationship between the D_{cc} of solid mass, surface, and specific surface area. Figure 4-S5A shows the D_{cc} of solid mass for model sands composed of SG (red circle) with heterogeneity in particle shape and size and those for GBs (blue circle) composed of spherical grains. The D_{cc} of solid mass for model sands composed of SG increases from 2.76 (±0.05) to 3.00 (±0.05) with increasing specific surface area from 2.84 to 8.66 mm^2/mm^3. The D_{cc} of solid mass for GBs increased slightly from 2.94 (±0.05) to 3.00 (±0.05) with increasing specific surface area from 2.74 to 9.57 mm^2/mm^3. Figure 4-S5B shows that D_{cc} of surface increases from 2.30 (±0.05) to 3.00 (±0.05) with increasing specific surface area and does not depend on porosity. The results for SG and GBs for D_{cc} of solid mass and surface were reproduced well using equation (4.6).

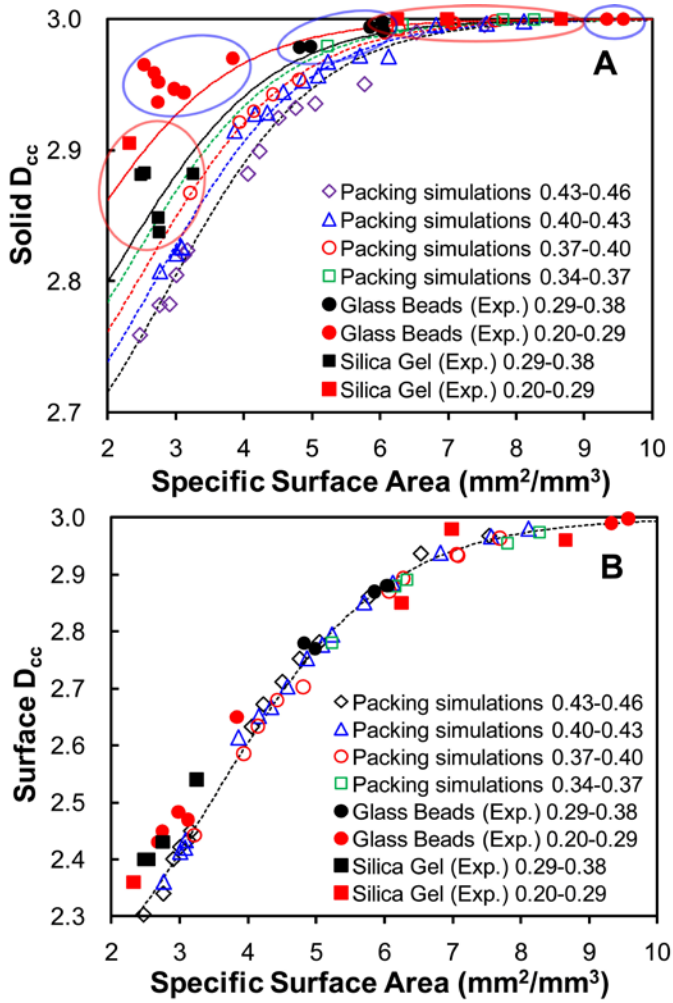

Figure 4-S5. (caption on next page)

Figure 4-S5. Effect of specific surface area on cube counting fractal dimension of (A) solid mass and (B) surface (interface) of model sands. Black and red circles correspond to glass bead samples for the porosities of 0.29–0.38 and 0.20–029, respectively. Black and red squares correspond to silica gel samples for the porosities of 0.29–0.38 and 0.20–0.29, respectively. Black diamonds, blue triangles, red circles, and green squares correspond to each group of simulation data for the porosities of 0.43– 0.46, 0.40–043, 0.37–0.40, and 0.34–0.37, respectively. Black, blue, red, and green dashed lines, and black and red dotted lines in (A) are curves for equation (4.6) corresponding to the median porosities in each group: 0.445, 0.415, 0.385, 0.355, 0.335, and 0.245. The coefficients *a, b, c,* and *d* for D_{cc} of solid mass are shown as equation (4.8). Black dashed line in (B) is curve for equation (4.6) with the coefficients *a, b, c,* and *d* for D_{cc} of surface of 3, 2, 3.455, and 1.28, respectively.

4.S4. Effect of average particle diameter on porosity

Figure 4-S6 shows the effect of average particle diameter on porosity. The general trend is increasing porosity with increasing average particle diameter. However, the trend is not clear because there are several values of porosity for a given average particle diameter used in the synthesis of GB and SG samples.

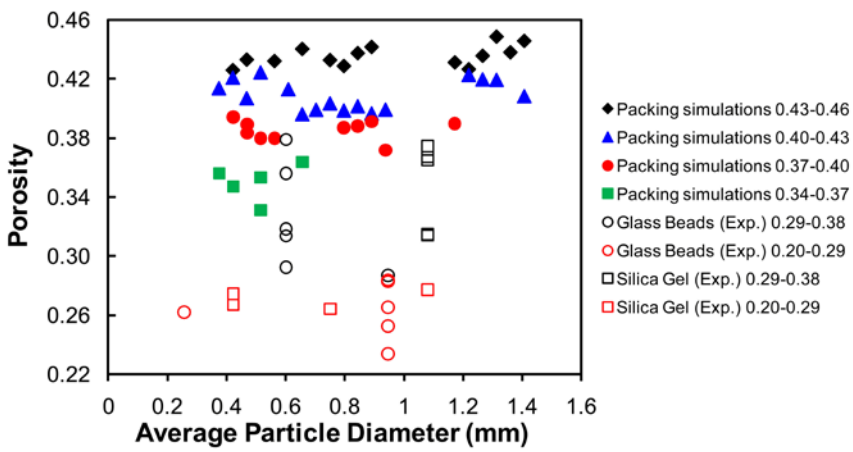

Figure 4-S6. Relationship between porosity and average particle diameter for porous networks obtained by random packing simulations and NMR micro-imaging experiments.

4.S5. Effect of average particle diameter on lacunarity

Figure 4-S7 shows the effect of average particle diameter on lacunarity. Although the lacunarity values at the minimum box size were grouped by their porosity range, the trend for the relationship between lacunarity at the minimum box size and the average particle diameter is not clear (Figure 4-S7A). The lacunarity values at a box size of 0.47 mm are also grouped by their porosity range. While the grouping for simulation data is not noticeable, the lacunariy values apparently increase with increasing average particle diameter (Figure 4-S7B).

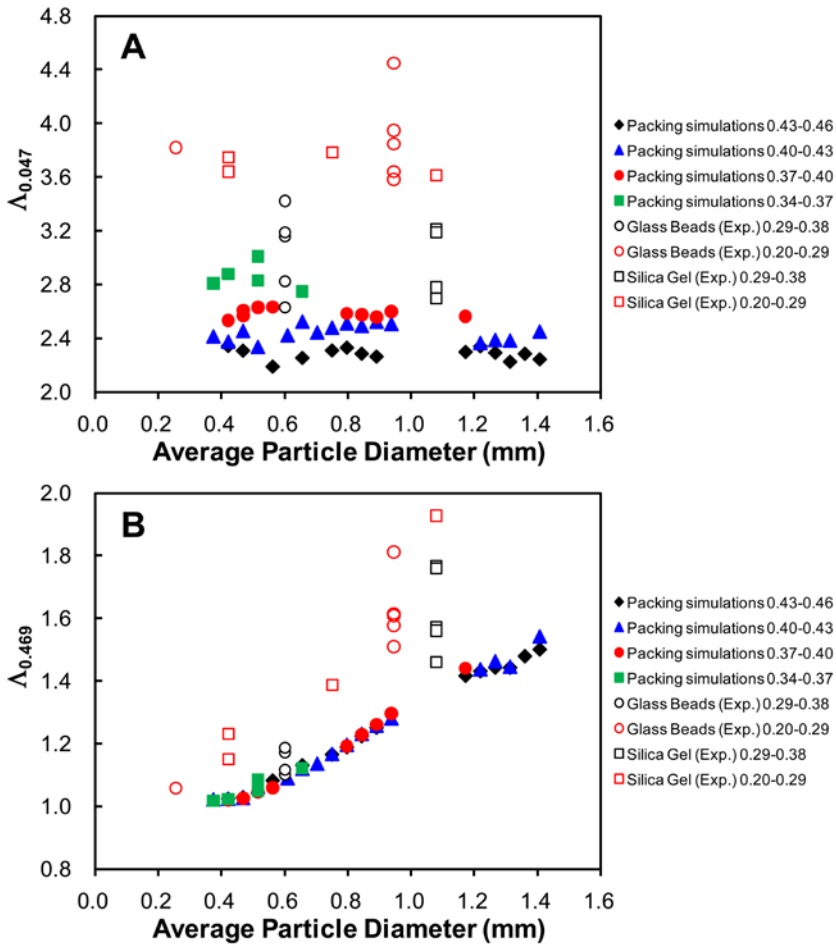

Figure 4-S7. (A) Relationship between lacunarity at the minimum box size (corresponding to a side length of 0.047 mm) and average particle diameter. (B) Relationship between lacunarity at a box size of 0.47 mm and average particle diameter.

4.S6. Effect of specific surface area and porosity on entropy length and maximum configurational entropy

Figure 4-S8 shows the relationship between entropy length and porosity. The trend for the relationship between entropy length and porosity is not clear while entropy length decreases with increasing specific surface area (Figure 4-13B). Figure 4-S9A shows the relationship between maximum configurational entropy and average particle diameter, and Figure 4-S9B shows the relationship between maximum configurational entropy and specific surface area. While maximum configurational entropy increases with increasing porosity (Figure 4-14), the trends for the relationships shown in Figure 4-S9 are not clear. These data indicate the characteristics of each parameter related with configurational entropy; entropy length depends on specific surface area, and maximum configurational entropy depends on porosity.

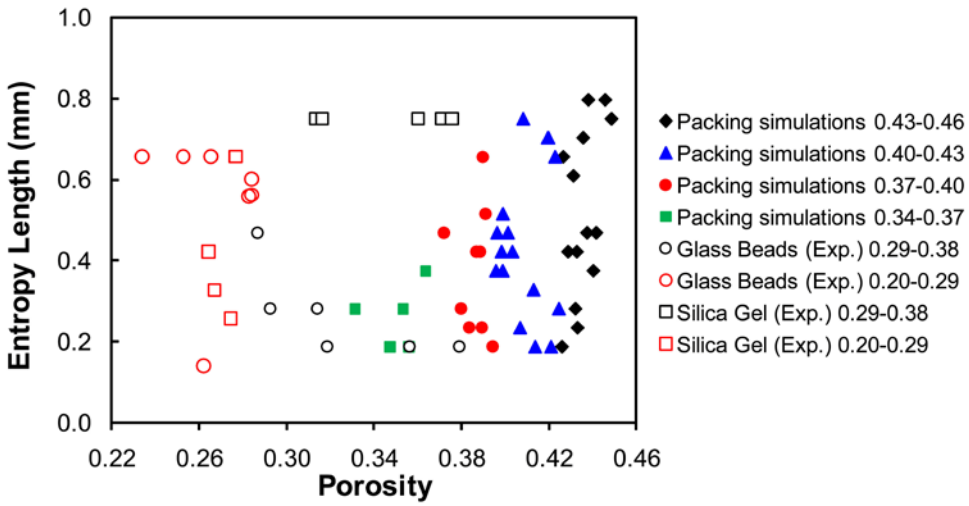

Figure 4-S8. Relationship between entropy length and porosity for porous networks obtained by random packing simulations and NMR micro-imaging experiments.

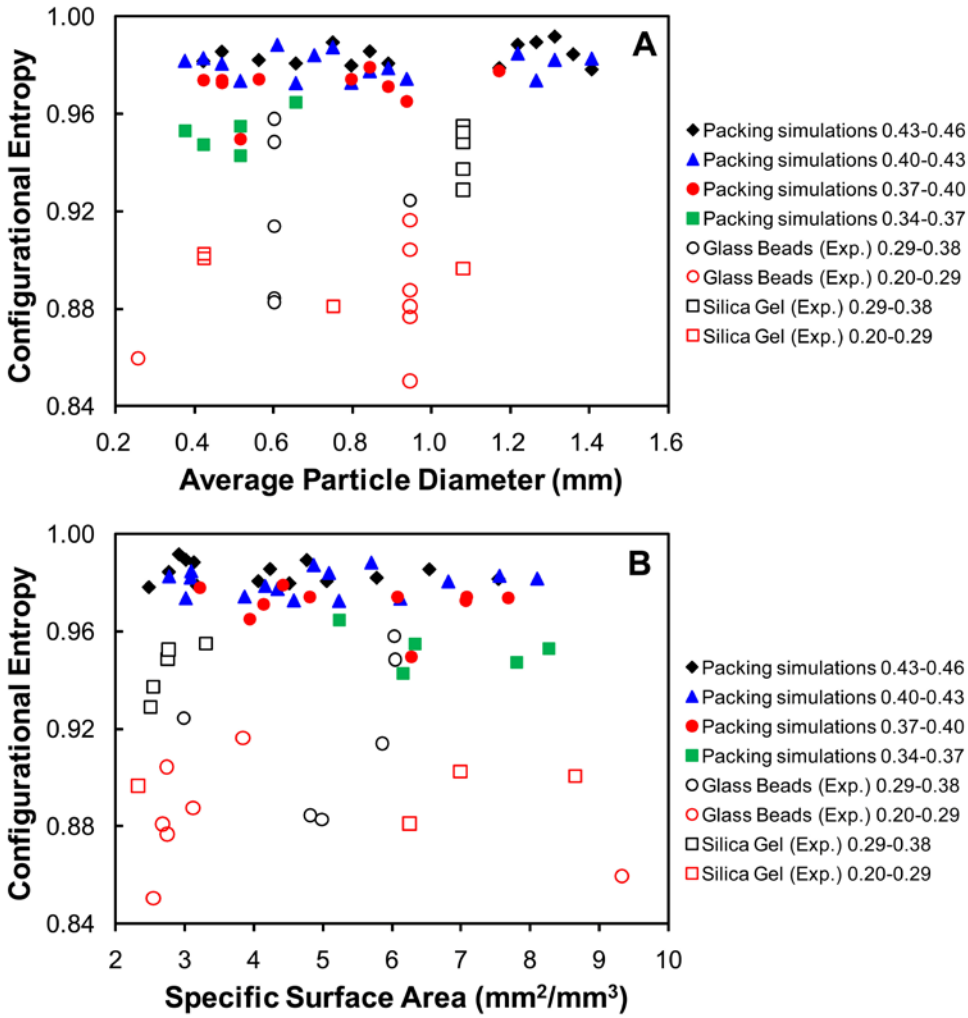

Figure 4-S9. (A) Relationship between maximum configurational entropy and average particle diameter. (B) Relationship between maximum configurational entropy and specific surface area for porous networks obtained by random packing simulations and NMR micro-imaging experiments.

δ

4.S7. Comparison between Kozeny equation and Kozeny-Carman equation

Figure 4-S10 shows the relationship between permeability and a factor obtained from the Kozeny equation (Carman, 1937; Bear, 1972):

$$k = \frac{\phi^3}{C_T T S^2}, \tag{4.S1}$$

where C_T is Kozeny's constant, and T is tortuosity. The results show that the relationships among permeability, porosity, and specific surface area for porous media composed of single-sized spheres were also well explained by the Kozeny equation. In contrast, the permeability for porous media composed of diverse grain shapes (e.g., single-sized spheres, glass beads, and silica gels with irregular shapes) and mixtures of grain sizes (GB2 and SG2) was better explained by factors of porosity and specific surface area from the Kozeny-Carman equation (4.11) than those from the Kozeny equation, which is consistent with previous reports (Carman, 1937).

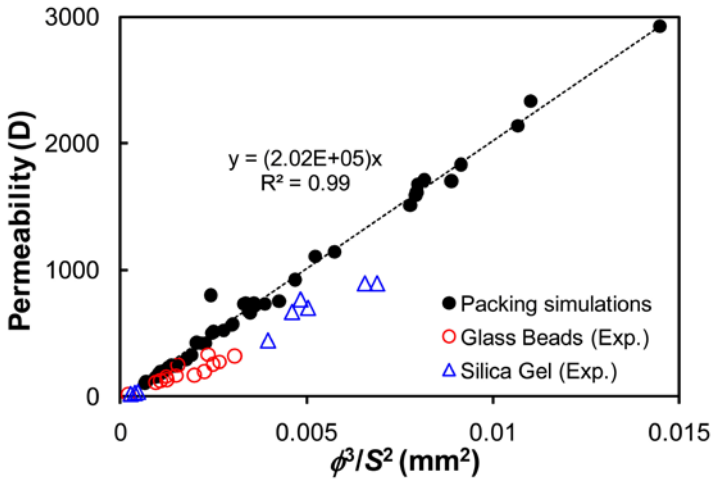

Figure 4-S10. Relationship between permeability and (porosity)^3/(specific surface area)^2 indicated by the Kozeny equation (4.S1). Black closed circles correspond to packing simulation data, and red open circles and blue open triangles correspond to experimental data for glass beads and silica gel samples, respectively.

4.S8. Relationship between surface area per unit bulk volume and surface area per unit solid volume

Figure 4-S11 shows the relationship between surface area per unit solid volume (S) and surface area per unit solid volume (S_0).

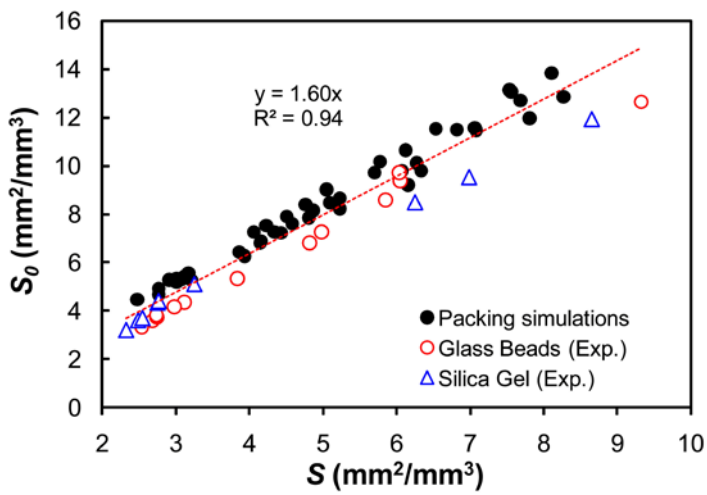

Figure 4-S11. Relationship between surface area per unit solid volume (S) and surface area per unit solid volume (S_0).

4.S9. Relationships between permeability and D_{cc} of solid mass and between permeability and D_{cc} of surface

Figure 4-S12 shows the relationships among permeability, porosity, and the D_{cc} of solid mass (Figure 4-S12A) and surface (Figure 4-S12B). Permeability tends to decrease with increasing D_{cc} at constant porosity and increase with increasing porosity at constant D_{cc}.

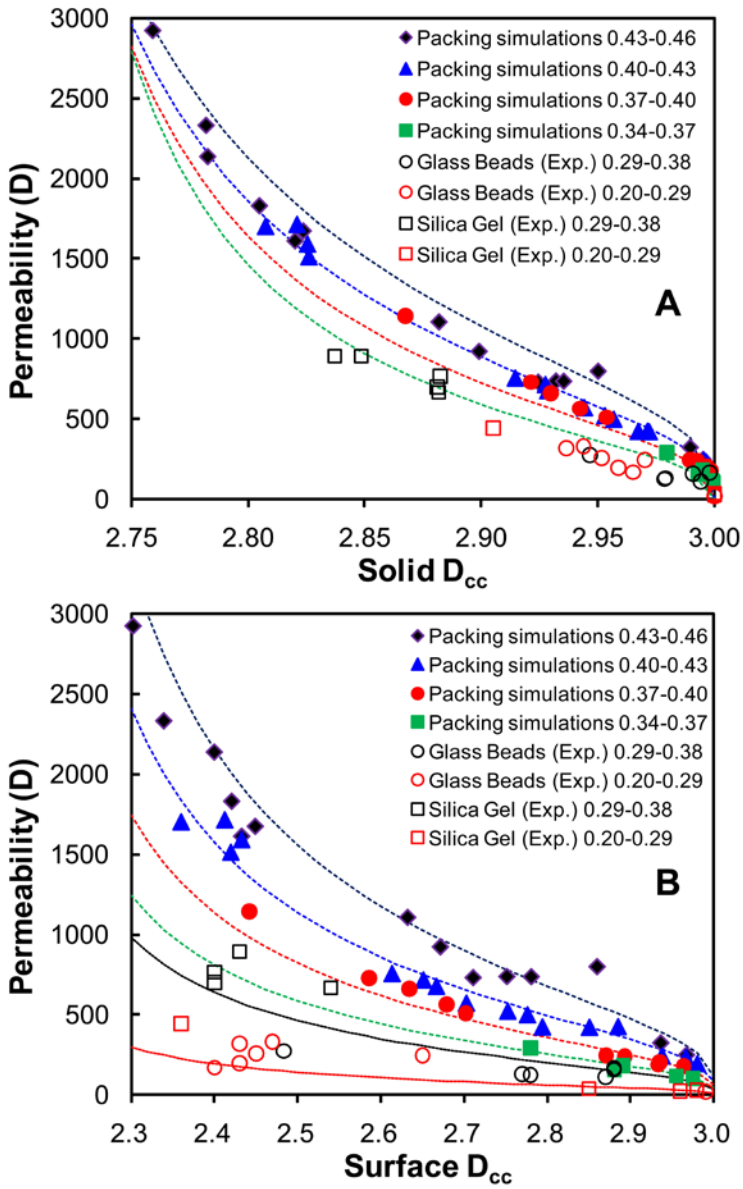

Figure 4-S12. (caption on next page)

Figure 4-S12. Effect of cube counting fractal dimension of (A) solid mass and (B) surface (interface) of model sands on permeability. The equation for each curve is shown as equation (4.12) in the text (coefficients *a, b, c,* and *d* for D_{cc} of solid mass are described in equation (4.8), and those for D_{cc} of surface are 3, 2, 3.455, and 1.28, respectively). Black diamonds, blue triangles, red circles, and green squares correspond to each group of simulation data for the porosities of 0.43–0.46, 0.40–043, 0.37–0.40, and 0.34–0.37, respectively. Black and red open circles correspond to glass bead samples for the porosities of 0.29–0.38 and 0.20–029, respectively. Black and red open squares correspond to silica gel samples for the porosities of 0.29–0.38 and 0.20–0.29, respectively. Black, blue, red, and green dashed lines, and black and red dotted lines are curves for equation (4.12) corresponding to the median porosities in each group: 0.445, 0.415, 0.385, 0.355, 0.335, and 0.245.

4.S10. Effect of (porosity)^3/(specific surface area)^2 and (porosity)^3/[(specific surface area)^2(1-porosity^2)] on cube counting fractal dimension, configurational entropy, and entropy length.

Figures 4-S13–15 show the effects of (porosity)^3/(specific surface area)^2 obtained from the Kozeny equation (4.S1) and (porosity)^3/[(specific surface area)^2(1-porosity^2)] obtained from the Kozeny-Carman equation (4.11) on cube-counting fractal dimension (Figure 4-S13), configurational entropy (Figure 4-S14), and entropy length (Figure 4-S15). Cube-counting fractal dimension decreases with increasing (porosity)^3/(specific surface area)^2 and (porosity)^3/[(specific surface area)^2(1-porosity^2)], and increases with increasing porosity, as shown in Figures 4-6 and 4-7. Maximum configurational entropy increases with increasing (porosity)^3/(specific surface area)^2, (porosity)^3/[(specific surface area)^2(1-porosity^2)], and porosity as shown in Figure 4-14. Entropy length increases with increasing (porosity)^3/(specific surface area)^2 and (porosity)^3/[(specific surface area)^2(1-porosity^2)]. Thus, cube-counting fractal dimension, maximum configurational entropy, and entropy length can also be used to explain permeability.

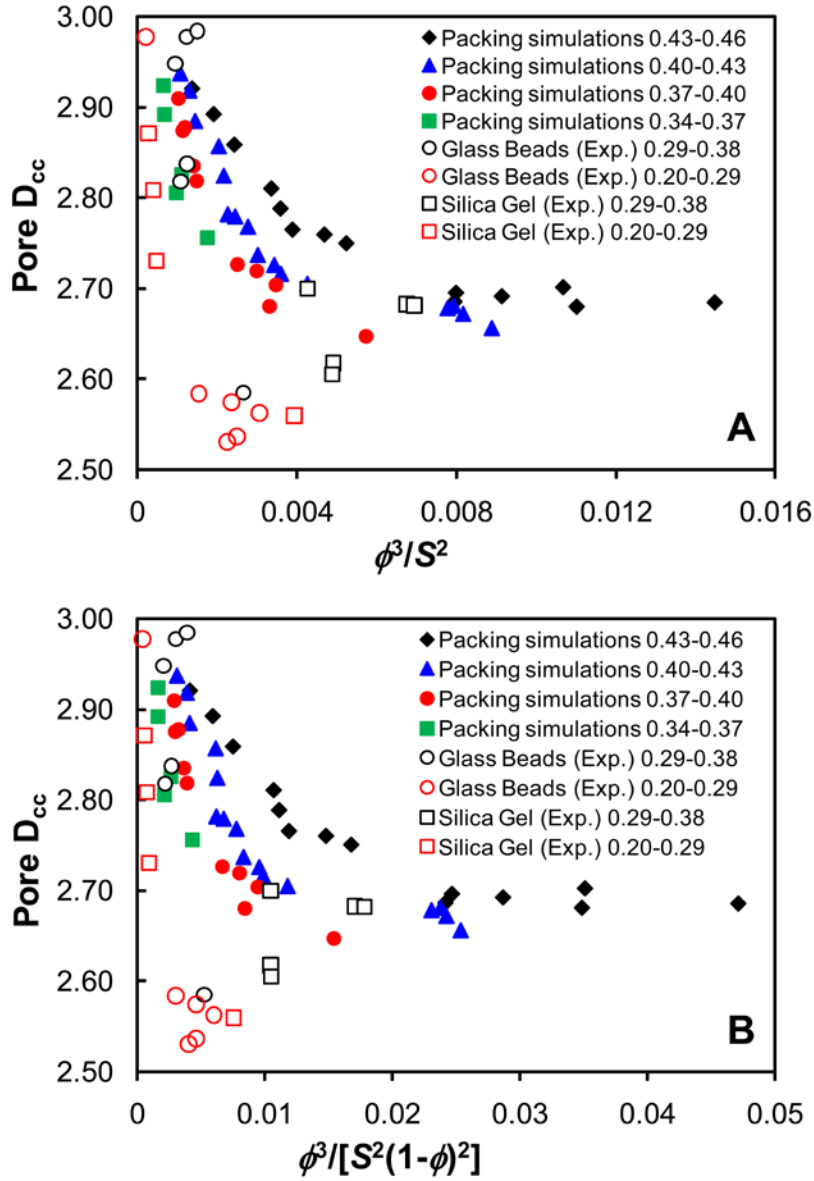

Figure 4-S13. (A) Relationship between cube-counting fractal dimension and (porosity)^3/(specific surface area)^2. (B) Relationship between cube-counting fractal dimension and (porosity)^3/[(specific surface area)^2(1-porosity^2)].

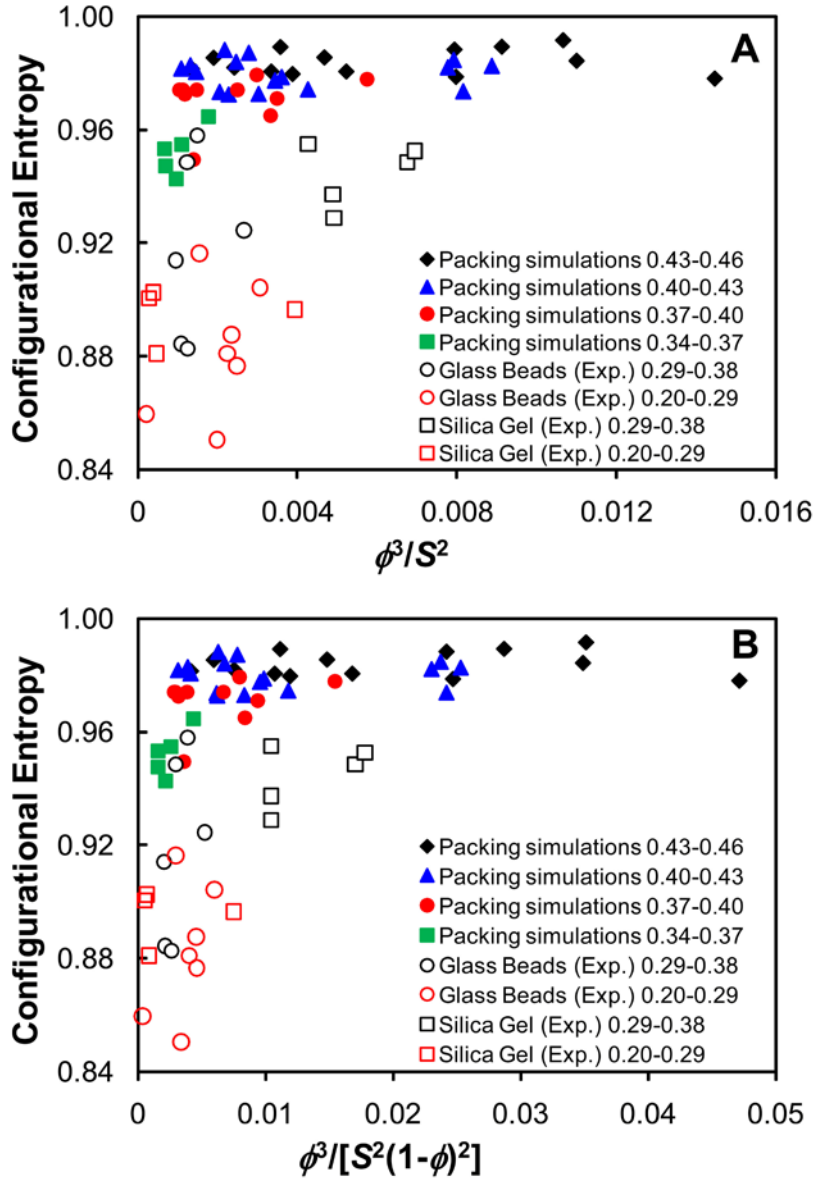

Figure 4-S14. (A) Relationship between maximum configurational entropy and (porosity)^3/(specific surface area)^2. (B) Relationship between maximum configurational entropy and (porosity)^3/[(specific surface area)^2(1-porosity^2)].

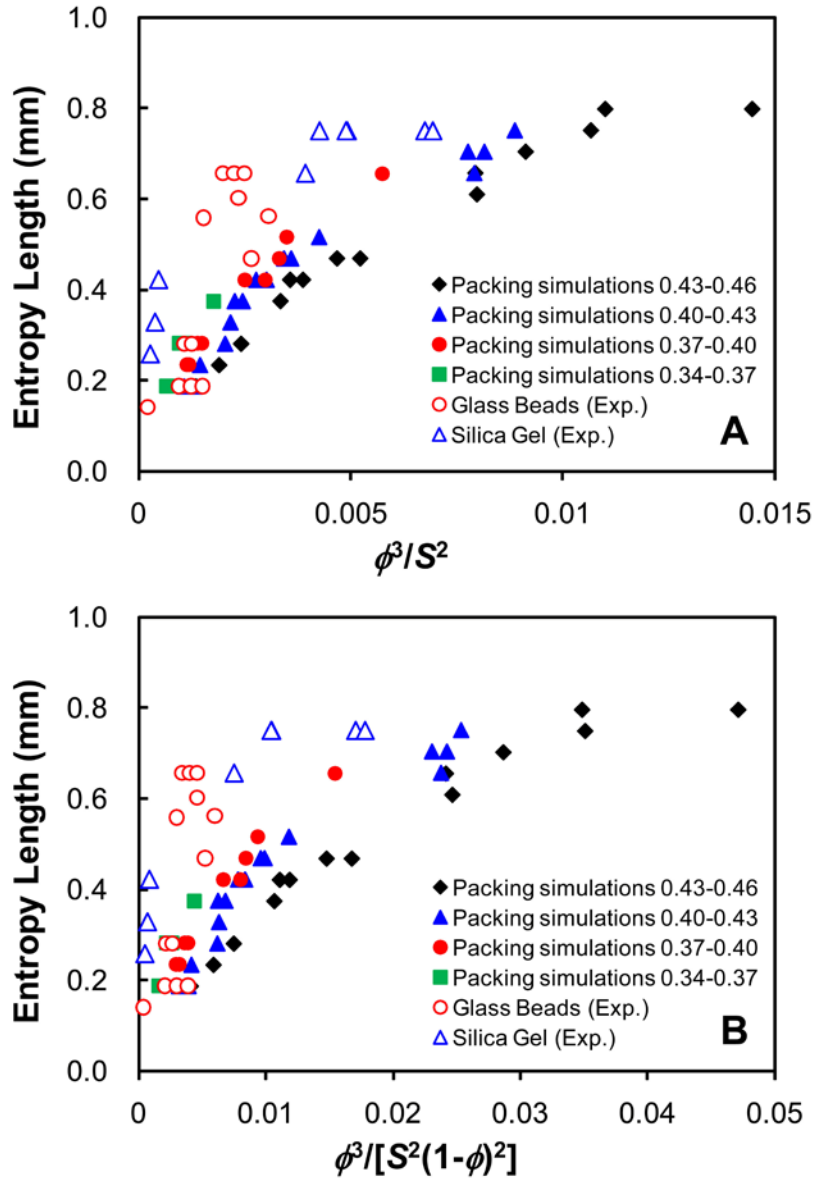

Figure 4-S15. (A) Relationship between entropy length and (porosity)^3/(specific surface area)^2. (B) Relationship between entropy length and (porosity)^3/[(specific surface area)^2(1-porosity^2)].

δ

4.S11. Structure-structure and structure-property relationships for the porous networks of model sands

Extensive analyses of all the structural parameters and permeability were performed to establish the structure-structure and structure-property relationships of porous networks of model sands. Structural parameters analyzed in this study include porosity (ϕ), average particle diameter (d_p), specific surface area (S), cube-counting fractal dimension (D_{cc}), lacunarity (Λ), entropy length (EL), and maximum configurational entropy (MCE). Table 4-S1 shows the figure numbers for the relationships between these parameters shown in this study.

Table 4-S1. Figure numbers for the relationships shown in this study.

	d_p	S	ϕ	ϕ^3/S^2	$\phi^3/S^2(1-\phi^2)$	D_{cc}
S	4-8B	-	4-8A	-	-	4-6, 7A, 7B
ϕ	4-S6	4-8A	-	-	-	4-7C
D_{cc}	4-8C	4-6, 7A, 7B	4-7C	4-S13A	4-S13B	-
$\Lambda_{0.047}$	4-S7A	-	4-11A			-
$\Lambda_{0.469}$	4-S7B	4-11B	-			-
EL	4-13A	4-13B	4-S8	4-S15A	4-S15B	-
MCE	4-S9A	4-S9B	4-14	4-S14A	4-S14B	-
Permeability	4-15A	4-15B	4-15C	4-S10	4-16	4-17

4.S12. Effect of the infiltrated silicone oil into the grain of silica gel on the NMR micro-imaging images

Figures 4-S16 shows the spin density image of silicone oil in the sample composed of silica gel and its binary image. Firure 4-S16A shows that the signal does not come from the infiltrated silicone oil into the grain of silica gel, probably because the amount of infiltrated silicone oil is much lower than that of saturated silicone oil outside the grains. Figure 4-S16B shows that data are not included in the grain of silica gel in binary image.

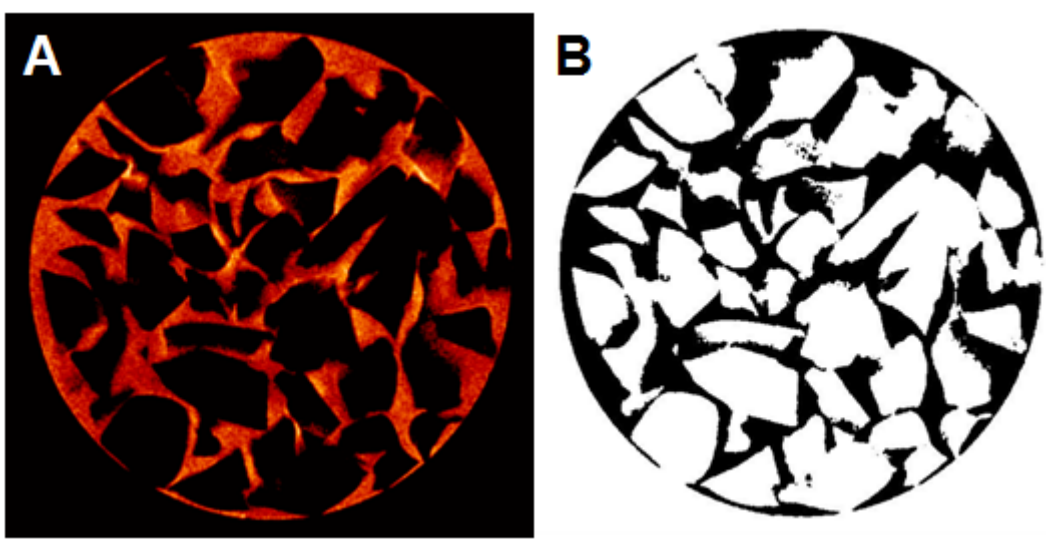

Figure 4-S16. (A) 2D spin density image of silicone oil in the sample composed of silica gel (SG1). (B) Binary image of (A) obtained from the threshold value.

4.S12. Maximum intensity projection images of 3D porous networks obtained by NMR micro-imaging

Figures 4-S17 shows maximum intensity projection images of 3D pore structure obtained by NMR micro-imaging. 3D binary image data of pore structures are obtained from these images using the threshold values.

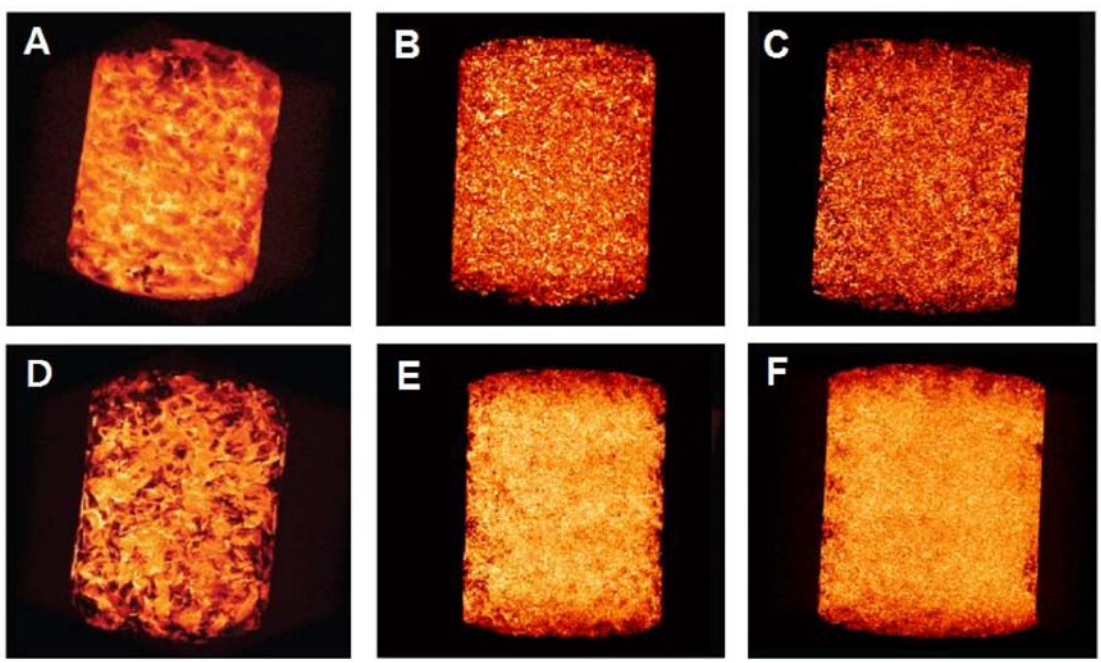

Figure 4-S17. Maximum intensity projection images of 3D pore structure obtained by NMR micro-imaging: (A) GB1, (B) GB2, (C) GB3, (D) SG1, (E) SG2, and (F) SG3.

References

Adam, G. and Gibbs, J. H. (1965) On the temperature dependence of cooperative relaxation properties in glass-forming liquids. J. Chem. Phys., 43, 139-146.

Allain, C. and Cloitre, M. (1991) Characterizing the lacunarity of random and deterministic fractal sets. Physical Review A, 44(6), 3552-3558.

Andraud, C., Beghdadi, A., Haslund, E., Hilfer, R., Lafait, J. and Virgin, B. (1997) Local entropy characterization of correlated random microstructures. Physica A, 235, 307-318.

Andraud, C., Beghdadi, A. and Lafait, J. (1994) Entropic analysis of random morphologies. Physica A, 207, 208-212.

Armatas, G. S., Kolonia, K. M. and Pomonis, P. J. (2002) Morphometry of porous solids: lacunarity, fractal dimensions, connectivity, and some topological similarities with neurons. Lanmuir, 18, 10421-10429.

Avnir, D., Farin, D. and Pfeifer, P. (1985) Surface geometric irregularity of particulate materials: The fractal approach. Journal of Colloid and Interface Science, 103, 112-123.

Balcom, B. J., Barrita, J. C., Choi, C., Beyea, S. D., Goodyear, D. J. and Bremner, T. W. (2003) Single-point magnetic resonance imaging (MRI) of cement based materials. Materials and Structures, 36(257), 166-182.

Bartoli, F., Bird, N. R. A., Gomendy, V., Vivier, H. and Niquet, S. (1999) The relation between silty soil structures and their mercury porosimetry curve counterparts: fractals and percolation. European Journal of Soil Science, 50, 9-22.

Bear, J. (1972) Dynamics of Fluids in Porous Media. New York, American Elsevier, 764 p.

Bird, N., Díaz, M. C., Saa, A. and Tarquis, A. M. (2006) Fractal and multifractal analysis of pore-scale images of soil. Journal of Hydrology, 322, 211-219.

Blümich, B. (2000) NMR Imaging of Materials. Oxford, Clarendon Press, 541 p.

Bourbié, T., Coussy, O. and Zinszner, B. (1987) Acoustics of Porous Media. Paris, Editions Technip, 334 p.

Buczkowski, S., Kyriacos, S., Nekka, F. and Cartilier, L. (1998) The modified box-counting method: Analysis of some characteristic parameters. Pattern Recognition, 31(4), 411-418.

Callaghan, P. T. (1991) Principles of Nuclear Magnetic Resonance Microscopy. Oxford, Clarendon Press, 492 p.

Carman, P. G. (1937) Fluid flow through granular beds. Transactions, Institution of Chemical Engineers (London), 15, 150-166.

Chen, S. and Doolen, G. D. (1998) Lattice Boltzmann method for fluid flows. Annual Reviews in Fluid Mechanics, 30, 329-364.

Chun, H. C., Giménez, D. and Yoon, S. W. (2008) Morphology, lacunarity and entropy of intra-aggregate pores: Aggregate size and soil management effects. Geoderma, 146, 83-93.

Ciccotti, M. and Mulargia, F. (2002) Pernicious effect of physical cutoffs in fractal analysis. Physical Review E, 65, 037201.

Coelho, D., Thovert, J. F. and Adler, P. M. (1997) Geometrical and transport properties of random packings of spheres and aspherical particles. Physical Review E, 55(2), 1959-1978.

Costa, A. (2006) Permeability-porosity relationship: A reexamination of the

Kozeny-Carman equation based on a fractal pore-space geometry assumption. Geophysical Research Letters, 33, L02318.

Crawford, J. W. and Matsui, N. (1996) Heterogeneity of the pore and solid volume of soil: distinguishing a fractal space from its non-fractal complement. Geoderma, 73, 183-195.

Dathe, A., Tarquis, A. M. and Perrier, E. (2006) Multifractal analysis of the pore- and solid-phases in binary two-dimensional images of natural porous structures. Geoderma, 134, 318-326.

Dathe, A. and Thullner, M. (2005) The relationship between fractal properties of solid matrix and pore space in porous media. Geoderma, 129, 279-290.

Davies, S., Hardwick, A., Robert, D., Spowage, K. and Packer, K. J. (1994) Quantification of oil and water in preserved reservoir rock by NMR spectroscopy and imaging. Magnetic Resonance Imaging, 12, 349-353.

de Marsily, G. (1986) Quantitative Hydrogeology. Orlando, Academic Press, Inc.

Dereppe, J. M., Moreaux, C. and Schenker, K. (1991) Chemical shift imaging of fluid filled porous rocks. Magnetic Resonance Imaging, 9, 809-813.

Doughty, D. A. and Tomutsa, L. (1996) Multinuclear NMR microscopy of two-phase fluid systems in porous rock. Magnetic Resonance Imaging, 14(7-8), 869-873.

Dullien, F. A. L. (1979) Porous Media: Fluid Transport and Pore Structure. London, Academic Press, 396 p.

Farmer, J. D., Ott, E. and York, J. A. (1983) The dimension of chaotic attractors. Physica D, 7, 153-180.

Faure, P., Care, S., Po, C. and Rodts, S. (2005) An MRI-SPI and NMR

relaxation study of drying-hydration coupling effect on microstructure of cement-based materials at early age. Magnetic Resonance Imaging, 23(2), 311-314.

Foroutan-pour, K., Dutilleul, P. and Smith, D. L. (1999) Advances in the implementation of the box-counting method of fractal dimension estimation. Applied Mathematics and Computation, 105, 195-210.

Garcia, X., Akanji, L. T., Blunt, M. J., Matthai, S. K. and Latham, J. P. (2009) Numerical study of the effects of particle shape and polydispersity on permeability. Physical Review E, 80, 021304.

Gefen, Y., Meir, Y., Mandelbrot, B. B. and Aharony, A. (1983) Geometric implementation of hypercubic lattices with noninteger dimensionality by use of low lacunarity fractal lattices. Physical Review Letters, 50(3), 145-148.

Ghilardi, P., Kai, A. K. and Menduni, G. (1993) Self-similar heterogeneity in granular porous media at the representative elementary volume scale. Water Resources Research, 29(4), 1205-1214.

Giménez, D., Allmaras, R. R., Nater, E. A. and Huggins, D. R. (1997) Fractal dimensions for volume and surface of interaggregate pores - scale effects. Geoderma, 77, 19-38.

Giménez, D., Perfect, E., Rawls, W. J. and Pachepsky, Y. (1997) Fractal models for predicting soil hydraulic properties: a review. Engineering Geology, 48, 161-183.

Gladden, L. F. (2003) Recent advances in MRI studies of chemical reactors: ultrafast imaging of multiphase flows. Topics in Catalysis, 24(1-4), 19-28.

Gladden, L. F., Buckley, C., Chow, P. S., Davidson, J. F., Mantle, M. D. and Sederman, A. J. (2004) 'Looking into' chemical products and

processes. Current Applied Physics, 4(2-4), 93-97.

Gladden, L. F., Hollewand, M. P. and Alexander, P. (1995) Characterization of structural inhomogeneities in porous-media. AIChE Journal, 41(4), 894-906.

Grau, J., Mendez, V., Tarquis, A. M., Diaz, M. C. and Saa, A. (2006) Comparison of gliding box and box-counting methods in soil image analysis. Geoderma, 134, 349-359.

Gussoni, A., Greco, F., Bonazzi, F., Vezzoli, A., Botta, D., Dotelli, G., Sora, I. N., Pelosato, R. and Zetta, L. (2004) H-1 NMR spin-spin relaxation and imaging in porous systems: an application to the morphological study of white Portland cement during hydration in the presence of organics. Magnetic Resonance Imaging, 22(6), 877-889.

Hamburger, D., Biham, O. and Avnir, D. (1996) Apparent fractality emerging from models of random distributions. Physical Review E, 53(4), 3342-3358.

Hansen, J. P. and Skjeltorp, A. T. (1988) Fractal pore space and rock permeability implications. Physical Review B, 38(4), 2635-2638.

Hentschel, H. G. E. and Procaccia, I. (1983) The infinite number of generalized dimensions of fractals and strange attractors. Physica D, 8(3), 435-444.

Jacquin, C. G. and Adler, P. M. (1987) Fractal porous media II: geometry of porous geological structures. Transport in Porous Media, 2, 571-596.

Jia, X. and Williams, R. A. (2001) A packing algorithm for particles of arbitrary shapes. Powder Technology, 120, 175-186.

Keehm, Y. (2003) Computational Rock Physics: Transport Properties in Porous Media and Applications. Geophysics, Stanford University, Doctor of Philosophy, 135 p.

δ

Keehm, Y., Mukerji, T. and Nur, A. (2004) Permeability prediction from thin sections: 3D reconstruction and Lattice-Boltzmann flow simulation. Geophysical Research Letters, 31(4), L04606.

Kim, J.-W., Perfect, E. and Choi, H. (2007) Anomalous diffusion in two-dimensional Euclidean and prefractal geometrical models of heterogeneous porous media. Water Resources Research, 43, W01405.

Kleinberg, R. L. (2001) NMR well logging at Schlumberger. Concepts in Magnetic Resonance, 13(6), 396-403.

Klemm, A., Kimmich, R. and Weber, M. (2001) Flow through percolation clusters: NMR velocity mapping and numerical simulation study. Physical Review E, 63(4), 041514.

Klemm, A., Müller, H.-P. and Kimmich, R. (1997) NMR microscopy of pore-space backbones in rock, sponge, and sand in comparison with random percolation model objects. Physical Review E, 55(4), 4413-4422.

Kossel, E. and Kimmich, R. (2005) Flow measurements below 50 μm: NMR microscopy experiments in lithographic model pore spaces. Magnetic Resonance Imaging, 23(2), 397-400.

Lee, S. K. (2005) Microscopic origins of macroscopic properties of silicate melts and glasses at ambient and high pressure: Implications for melt generation and dynamics. Geochimica et Cosmochimica Acta, 69(14), 3695-3710.

Lee, S. K., Kim, H. N., Lee, B. H., Kim, H. I. and Kim, E. J. (2010) Nature of chemical and topological disorder in borogermanate glasses: insights from B-11 and O-17 solid-state NMR and quantum chemical calculations. Journal of Physical Chemistry B, 114, 412-420.

Lee, S. K. and Stebbins, J. F. (1999) The degree of aluminum avoidance in aluminosilicate glasses. American Mineralogist, 84, 937-945.

Li, X., Zhong, L. and Pyrak-Nolte, L. J. (2001) Physics of partially saturated porous media: residual saturation and seismic-wave propagation. Annual Review of Earth and Planetary Sciences, 29, 419-460.

Lindquist, W. B., Lee, S. M., Coker, D. A., Jones, K. W. and Spanne, P. (1996) Medial axis analysis in three-dimensional tomographic images of porous media. Journal of Geophysical Research, 101, 8297-8310.

Lysova, A. A., Koptyug, I. V., Sagdeev, R. Z., Parmon, V. N., Bergwerff, J. A. and Weckhuysen, B. M. (2005) Noninvasive in situ vsualization of supported catalyst preparations using multinuclear magnetic resonance imaging. Journal of American Chemical Society, 127, 11916-11917.

Müller, H.-P., Weis, J. and Kimmich, R. (1995) Computer simulation and six-dimensional spin density and velocity NMR microimaging of lacunar systems: A comparative analysis of percolation properties. Physical Review E, 52(5), 5195-5204.

Mandelbrot, B. B. (1982) The Fractal Geometry of Nature. New York, Freeman, 468 p.

Manz, B., Gladden, L. F. and Warren, P. B. (1999) Flow and dispersion in porous media: Lattice-Boltzmann and NMR studies. AIChE Journal, 45(9), 1845-1854.

Maria, A. and Carey, S. (2002) Using fractal analysis to quantitatively characterize the shapes of volcanic particles. Journal of Geophysical Research, 107(B11), 2283.

McNamara, G. R. and Zanetti, G. (1988) Use of the Boltzmann equation to simulate lattice-gas automata. Physical Review Letters, 61(20), 2332-

2335.

Moreau, E., Velde, B. and Terribile, F. (1999) Comparison of 2D and 3D images of fractures in a Vertisol. Geoderma, 92, 55-72.

Muller, J. (1996) Characterization of pore space in chalk by multifractal analysis. Journal of Hydrology, 187, 215-222.

Muller, J., Huseby, O. K. and Saucier, A. (1995) Influence of multifractal scaling of pore geometry on permeabilities of sedimentary rocks. Chaos, Solitons and Fractals, 5(8), 1485-1492.

Muller, J. and McCauley, J. L. (1992) Implication of fractal geometry for fluid flow properties of sedimentary rocks. Transport in Porous Media, 8, 133-147.

Nesse, W. D. (2000) Introduction to Mineralogy. Oxford, Oxford University Press, 442 p.

Pendleton, D. E., Dathe, A. and Baveye, P. (2005) Influence of image resolution and evaluation algorithm on estimates of the lacunarity of porous media. Physical Review E, 72, 041306.

Perret, J. S., Prasher, S. O. and Kacimov, A. R. (2003) Mass fractal dimension of soil macropores using computed tomography: from the box-counting to the cube-counting algorithm. European Journal of Soil Science, 54, 569-579.

Plotnick, R. E., Gardner, R. H., Hargrove, W. W., Prestegaard, K. and Perlmutter, M. (1996) Lacunarity analysis: A general technique for the analysis of spatial patterns. Physical Review E, 53(5), 5461-5468.

Plotnick, R. E., Gardner, R. H. and O'Neill, R. V. (1993) Lacunarity indices as measures of landscape texture. Landscape Ecology, 8(3), 201-211.

Posadas, A. N. D., Giménez, D., Bittelli, M., Vaz, C. M. P. and Flury, M. (2001) Multifractal characterization of soil particle-size distributions.

Soil Science Society of America Journal, 65, 1361-1367.

Posadas, A. N. D., Giménez, D., Quiroz, R. and Protz, R. (2003) Multifractal characterization of soil pore systems. Soil Science Society of America Journal, 67, 1361-1369.

Pride, S. R. and Masson, Y. J. (2006) Acoustic attenuation in self-affine porous structures. Physical Review Letters, 97, 184301.

Rasband, W. S. (1997-2009) ImageJ. Bethesda, Maryland, USA, National Institutes of Health.

Richet, P. (1984) Viscosity and configurational entropy of silicate melts. Geochimica et Cosmochimica Acta, 48, 471-483.

Sahimi, M. (1993) Flow phenomena in rocks: from continuum models to fractals, percolation, cellular automata, and simulated annealing. Reviews of Modern Physics, 65(4), 1393-1534.

Saucier, A. and Muller, J. (1999) Textural analysis of disordered materials with multifractals. Physica A, 267, 221-238.

Schwartz, L. M. and Banavar, J. R. (1989) Transport properties of disordered continuum systems. Physical Review B, 39(16), 11965-11970.

Sederman, A. J., Alexander, P. and Gladden, L. F. (2001) Structure of packed beds probed by magnetic resonance imaging. Powder Technology, 117(3), 255-269.

Sederman, A. J., Johns, M. L., Bramley, A. S., Alexander, P. and Gladden, L. F. (1997) Magnetic resonance imaging of liquid flow and pore structure within packed beds. Chemical Engineering Science, 52(14), 2239-2250.

Song, S.-R., Jones, K. W., Lindquist, W. B., Dowd, B. A. and Sahagian, D. L. (2001) Synchrotron X-ray computed microtomography: studies on

vesiculated basaltic rocks. 63, 252-263.

Song, Y.-Q., Cho, H., Hopper, T., Pomerantz, A. E. and Sun, P. Z. (2008) Magnetic resonance in porous media: Recent progress. Journal of Chemical Physics, 128, 052212.

Stallmach, F., Vogt, C., Kärgar, J., Helbig, K. and Jacobs, F. (2002) Fractal geometry of surface areas of sand grains probed by pulsed field gradient NMR. Physical Review Letters, 88(10), 105505.

Takei, Y. (1998) Constitutive mechanical relations of solid-liquid composites in terms of grain-boundary contiguity. Journal of Geophysical Research, 103(B8), 18183-18203.

Takei, Y. (2002) Effect of pore geometry on V_P/V_S: From equilibrium geometry to crack Journal of Geophysical Research-Solid Earth, 107(B2), 2043.

Takei, Y. (2005) Deformation-induced grain boundary wetting and its effects on the acoustic and rheological properties of partially molten rock analogue. Journal of Geophysical Research-Solid Earth, 110, B12203.

Takei, Y. and Holtzman, B. K. (2009) Viscous constitutive relations of solid-liquid composites in terms of grain boundary contiguity: 1. Grain boundary diffusion control model. Journal of Geophysical Research, 114, B06205.

Tang, D. and Maragoni, A. G. (2008) Fractal dimensions of simulated and real fat crystal networks in 3D space. Journal of the American Oil Chemists' Society, 85, 495-499.

Tarquis, A. M., Heck, R. J., Andina, D., Alvarez, A. and Anton, J. M. (2009) Pore network complexity and thresholding of 3D soil images. Ecological Complexity, 6, 230-239.

Tarquis, A. M., Heck, R. J., Grau, J. B., Fabregat, J., Sanchez, M. E. and Anton, J. M. (2008) Influence of thresholding in mass and entropy dimension of 3-D soil images. Nonlinear Processes in Geophysics, 15, 881-891.

Tarquis, A. M., McInnes, K. J., Key, J. R., Saa, A., Garcia, M. R. and Diaz, M. C. (2006) Multiscaling analysis in a structured clay soil using 2D images. Journal of Hydrology, 322, 236-246.

Thompson, A. H. (1991) Fractals in rock physics. Annual Reviews in Earth and Planetary Sciences, 19, 237-262.

Xu, Y. F. and Dong, P. (2004) Fractal approach to hydraulic properties in unsaturated porous media. Chaos, Solitons and Fractals, 19, 327-337.

Xu, Y. F. and Sun, D. A. (2005) Correlation of surface fractal dimension with frictional angle at critical state of sands. Géotechnique, 55(9), 691-695.

Yu, B. and Cheng, P. (2002) A fractal permeability model for bi-dispersed porous media. International Journal of Heat and Mass Transfer, 45, 2983-2993.

Yu, B. and Liu, W. (2004) Fractal analysis of permeabilities for porous media. AIChE Journal, 50, 46-57.

δ

Chapter 5. Probing of water distribution in porous model sands with immiscible fluids: Nuclear magnetic resonance micro-imaging study

Abstract

NMR micro-imaging was used to obtain high-resolution (up to about 50 μm) images of the distribution of water injected for varying durations into porous media initially saturated with silicone oil, and thereby investigated the effect of the particle size and shape of the porous media on the distribution of water. The obtained 2D NMR chemical shift images can distinguish hydrogens in water and silicone oil and thus distinguish both phases with flow duration. The variations in volume fraction, specific surface area, and the cube counting fractal dimension of the water phase in each sample obtained from 3D spin echo images with increasing duration of water injection are well fitted with the single-exponential recovery functions. The asymptotic values for glass bead samples were much larger than those for silica gel samples. This is mostly due to the intrinsic differences in the porous networks and local arrangement of pore size distribution and connectivity of the two samples. In addition, this is partly because the interaction between silica gel and silicone oil is stronger than that between glass beads and silicone oil and the fact that silica gel has large mesoporosity whereas glass beads have no mesoporosity. The convergence rates of all the properties are inversely proportional to the permeability, indicating that the convergence rates are

correlated with the transport property of the porous media. The current results show that the types of particles consisting of porous networks play an important role in determining the water distribution in porous media that are initially saturated with an immiscible fluid.

5.1. Introduction

Understanding the nature of interstitial fluid flow through porous media containing an immiscible liquid is important in the development of methods for enhanced oil recovery (Taber, 1980) and underground disposal of CO_2 (Bachu, 2000). Probing of the distribution of two immiscible fluid phases in natural porous media can also provide improved understanding of the physical properties of complex soil systems and melt–fluids–rock composites in the Earth's interior. Despite its importance and implications, the effect of structural heterogeneity in the porous networks, such as particle size and shape on the water distribution in porous media initially saturated with the immiscible fluid with increasing duration of water injection and the effect of the rate of fluid saturation (the convergence rate, hereafter) in the relationship between oil recovery and time (Aronofsky et al., 1958) on the macroscopic properties of the porous media have not been systematically studied, mostly due to the lack of suitable experimental probes. The objective of this study is to obtain high resolution images of water distribution in porous media initially saturated with immiscible fluids using NMR micro-imaging, to quantify the water distribution with varying duration of water injection, and to explore the relationships

δ

between the convergence rates for the structural parameters and transport properties of porous networks.

NMR micro-imaging is one of the effective non-destructive experimental probes for the fluid distribution in networks, allowing detailed characterization of the connectivity of fluids (see Lee and Lee (submitted) and references therein). The NMR micro-imaging technique can be particularly useful in distinguishing fluid phases non-destructively because the differences in NMR chemical shifts between the molecular units in different fluids can be separately probed (Brown et al., 1982; Callaghan, 1991; Blümich, 2000). X-ray computed tomography (CT) has also been used for non-destructive pore-scale characterization of two fluid phases in porous media (e.g., Peters and Hardham, 1990; Wildenscheld et al., 2002; Culligan et al., 2006; Sukop et al., 2008) . Since x-ray CT affords high-resolution images, typically in the range of 1–10 μm, it has been used recently to quantitatively characterize the morphology of individual fluid bodies and determine the blob-size distribution (e.g., Al-Raoush and Willson, 2005; Schnaar and Brusseau, 2005; Prodanovic et al., 2006). Previous studies on two-phase flow using NMR micro-imaging include mapping of the oil phase in porous media initially saturated with water (Chen et al., 1988), monitoring the dissolution of hydrocarbon ganglia in beds comprised of ballotini saturated with water (Johns and Gladden, 2000), imaging of ^{19}F in a NAPL flow through water-saturated columns packed with angular silica gel (Zhang et al., 2002), observing the flow of dense and light NAPLs through a water saturated dolomite fracture (Becker et al.,

δ

2003), imaging of NAPL during vapor extraction in columns packed with silica gel (Chu et al., 2004), and imaging of the distribution of water (^{1}H) and model contaminants (^{19}F) in soil columns (Simpson et al., 2007). Furthermore, detailed mapping of the velocity distributions of two distinct fluid phases can be achieved using NMR micro-imaging (e.g., Okamoto et al., 2001; Sankey et al., 2009). However, these advances and developments in NMR micro-imaging are rather focused on networks with relatively large particle diameters and so may not have direct geological implications. Furthermore, despite many x-ray CT and NMR imaging studies for two phase flow in porous media, the systematic study for the effect of structural heterogeneity on the water distribution in porous media containing the immiscible fluids with varying the duration time of water flow and the effect of the convergence rates of the structural parameters for the networks of water distribution on the macroscopic properties of the porous media is lacking.

It is thus of crucial importance to explore the distribution of two fluid phases in porous media using NMR micro-imaging with a resolution of <100 μm. This would allow us to characterize the distribution of multi-phase fluids in porous networks corresponding to natural aquifers, sediments, and sandstones. It is attempted to obtain images of two fluid phases using the chemical shift imaging (CSI) method for 2D cross section images and the spin echo method with spoiler gradients for 3D images with a resolution below 100 μm. Combined with recent advances in high-resolution NMR micro-imaging, the water distribution in various porous

δ

media initially saturated with silicone oil can be explored with varying duration of water injection. Direct visualization of time-resolved water distribution in the model networks can thus yield insights into the relationship among porous networks, fluid distributions, and transport properties.

As the local structure of amorphous network in an atomic scale has strong implication for the macroscopic properties (e.g. Lee et al., 2008; Lee et al., 2010; Lee et al., 2010), similar progress have been made for the relationships between local structures of porous networks in a μm scale and the corresponding macroscopic properties. Diverse porous networks obtained by NMR micro-imaging and random packing simulations have been parameterized into cube counting fractal dimension and configurational entropy as a function of porosity and specific surface area (Lee and Lee, submitted). On the basis of this previous study, the distribution water into the pore network initially saturated with silicone oil with varying injection duration can be explored by quantitatively tracing the variation of the fractal dimension, specific surface area, and potentially configurational entropy.

In this study, convergence rates of these parameters with increasing the duration of water flow were obtained. Convergence rate was interpreted or used in many ways in previous studies, for example, to correlate with the imbibition parameters (Kazemi et al., 1992; Babadagli, 2002), to replace the viscosity term by the geometric mean of oil and water viscosities (Cil et al., 1998), and to propose an analytical model considering

δ

the matrix imbibition parameters and the fracture flow properties separately (Reis and Haq, 1999). However, the relationship between convergence rate and structural or transport properties of porous media has not been reported.

Here, 3D images were obtained by NMR micro-imaging with resolution below100 μm to explore the effect of particle size, and shape, and types of particles on the distribution of water injected for varying durations into porous media filled with silicone oil. Then, the networks of the water distribution were quantified by volume, specific surface, area, cube counting fractal dimension, and configurational entropy, and the relationships between the convergence rates of the parameters and the transport properties of the porous media were investigated.

d

5.2. Methods

Glass beads (GBs) and crushed silica gel (SG) particles with spherical and irregularly shaped grains, respectively, were used for investigating the effect of particle shape, heterogeneity, and diameter on the distribution of water in the porous media once they were initially saturated with silicone oil. The GB (Sigma, acid-washed) particle sizes (diameters) used in this study were 0.71–1.18 mm (GB1) and 0.21–0.30 mm (GB3). Those of the SG particles (Sigma-Aldrich) were 0.86–1.30 mm (SG1) and 0.25–0.60 mm (SG3). The diameter and length of the column containing the samples were 10 mm and 24 mm, respectively. The weights of the samples in the column were 2.78 g (GB1), 3.05 g (GB3), 1.47 g (SG1), and 1.30 g (SG3).

The column was saturated with silicone oil (polydimethylsiloxane, Baysilone M30000; density of 0.98 g/cm^3 and viscosity of 30000 mPa·s). A vacuum pump was used to saturate the pore space with silicone oil and to eliminate air bubbles. Both ends of the column were then covered with Teflon and membrane filters, and connected to a peristaltic pump. Distilled water with 0.1 wt% $CuSO_4 \cdot 5H_2O$, a paramagnetic impurity, was injected into the pre-saturated column at a pressure of 2 bar for each sample. Both ends were sealed with parafilms after water injection for the following durations: 10, 40, and 100 minutes (for GB1); 10, 30, and 195 minutes (for GB3); 75 and 195 minutes (for SG1); and 10, 40, and 195 minutes (for SG3). Each sample was loaded on the imaging probe for the micro-imaging experiment (see supplementary information for further details).

δ

The NMR micro-imaging experiments were performed using a Bruker Avance 400 NMR spectrometer with a 9.4-T, superconducting, vertical, and wide-bore magnet. A Micro2.5 probe head providing a gradient strength of 2.5 G cm^{-1} A^{-1} with a 25-mm NMR tube was used. 2D imaging of a specific fluid phase (i.e., silicon oil or water) was performed using a chemical shift selective (CHESS) imaging pulse sequence (Haase et al., 1985). The matrix size of the 2D cross section images was 256 × 256 and the field of view was 12 mm × 12 mm, resulting in a spatial resolution of 46.9 μm × 46.9 μm. The slice thickness was 0.4 mm. Images of three slices were collected. A frequency-selective excitation pulse with a Gaussian shape was used. The bandwidth and flip angle were 300 Hz and 90°, respectively. Imaging spoiler gradients with an amplitude of 30% and length of 1.0 ms were used in the x-, y-, and z- directions. The procedure leaves the spin system in a state where unwanted stimulated echoes are suppressed by spoiler gradients while the desired component remains entirely unaffected in the form of z-magnetization (Haase et al., 1985; Bernstein et al., 2004). The chemical shift for the imaging experiment was set to either water or silicone oil. The chemical shift difference between the two phases is 4.7 ppm (silicon oil is more shielded). 3D imaging for porous media saturated with silicone oil was performed with a 3D gradient echo (ge3D) imaging pulse sequence with a matrix size of the 3D images being 256 × 256 × 256. 3D imaging of the water distribution in the porous media initially saturated with silicone oil was performed with a spin echo 3D (se3D) imaging pulse sequence with image spoiler gradients with a 3D

d

image matrix size of 128 × 128 × 128. In 3D spectroscopic ^{1}H NMR imaging, a spin echo method was employed in which the 90° sinc-shaped excitation pulse is applied in the absence of magnetic field gradients for chemical shift selection (Rumpel and Pope, 1992). The field of view was 12 mm × 12 mm × 12 mm, thus the spatial resolution with a ge3D pulse sequence was 46.9 μm × 46.9 μm × 46.9 μm, and that with a se3D pulse sequence was 93.8 μm × 93.8 μm × 93.8 μm. For ge3D imaging, the sinc3-shaped pulse was used with an echo time of 1.781 ms and a repetition time of 1 s. For the se3D imaging, an excitation and a refocusing RF pulses were used with a rectangular shape and a pulse length of 0.128 ms. The echo time and repetition time were 4.145 ms and 1 s, respectively. Imaging spoiler gradients were used in all directions with an amplitude of 30% and length of 1.0 ms.

Volume, specific surface area, and cube counting fractal dimension were estimated for the water phase at each duration of water injection. The detailed method for estimating cube counting fractal dimension is described elsewhere (Lee and Lee, submitted). Briefly, to obtain D_{cc} from the 3D images for the water distribution, the fourfold expansion data of the original matrix were used, and D_{cc} analysis was conducted by covering the 3D water distribution data with increasing cube size (r) with the box sizes of the divisors of the matrix size to avoid border effects. Then, the number of cubes (N) required to cover the object completely was evaluated, and the slope of data points in the appropriate region for the estimation of the cube counting fractal dimension in the log (N)-log (r) plot was calculated.

δ

Permeability was estimated for 160 × 160 × 160 sub-volume data with the lattice Boltzmann method (LBM) using DigiFlow software (Structure Vision Ltd.). The D3Q18 scheme was applied in a 3D cubic lattice grid with each grid cell interacting with 18 (out of 26) of its closest neighbors (McNamara and Zanetti, 1988).

5.3. Results and Discussion

Figure 5-1 shows 2D binary images obtained by spin echo (first column) and chemical shift (second and third columns) pulse sequences. While water and silicone oil cannot be distinguished in the binary spin density images, the chemical shift images show that two immiscible fluid phases in porous media can be distinguished with a pixel resolution of ~50 μm. The sum of each phase in the CHESS images is slightly different from those of the spin density maps because each slice is 0.4 mm thick, thus water and silicone oil coexist in the 2D image of the same slice.

Figures 5-2 and 5-3 show 3D images of the distribution of water in the model sands consisting of GB and SG particles, respectively, with varying duration of water injection into the model porous networks. The results show that the water phase initially occupies the upper part of the column (note that water flows from the top to the bottom in the peristaltic pump) and that the total volume of the water phase apparently increases with increasing duration of water injection. The total volumes of water phase of GB1 and GB3 (Figure 5-2) are apparently larger than those of SG1 and SG3 (i.e., GB1 > SG1, GB3 > SG3), indicating the effect of particle shape

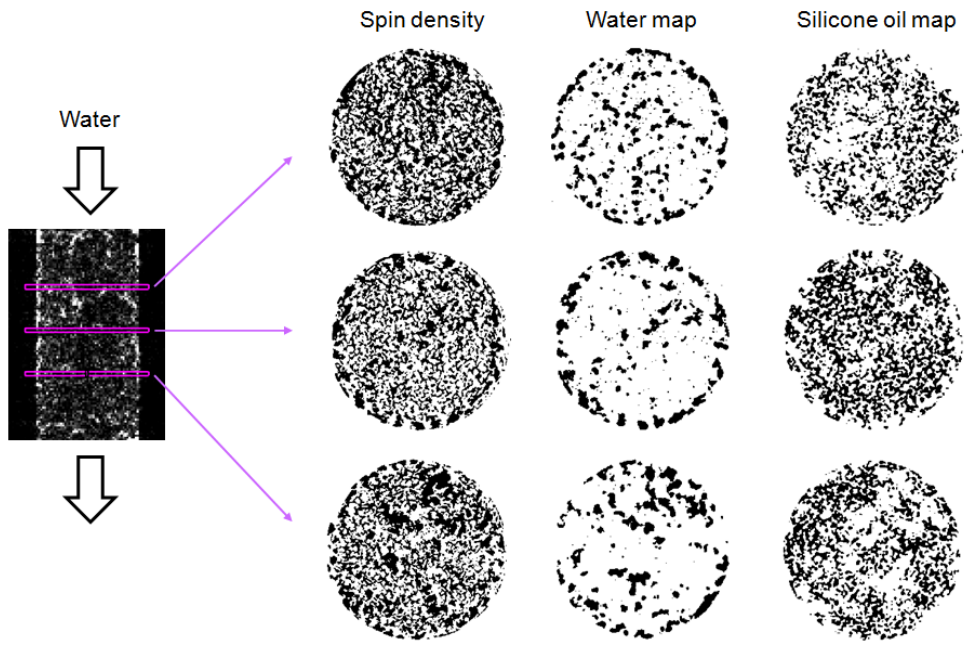

Figure 5-1. Binary 2D images for SG3 obtained at 40 minutes of duration of water injection. Each row corresponds to the same slice as depicted on the left. Each column corresponds to spin echo 2D images, chemical shift images for water phase, and chemical shift images for silicone oil phase, respectively.

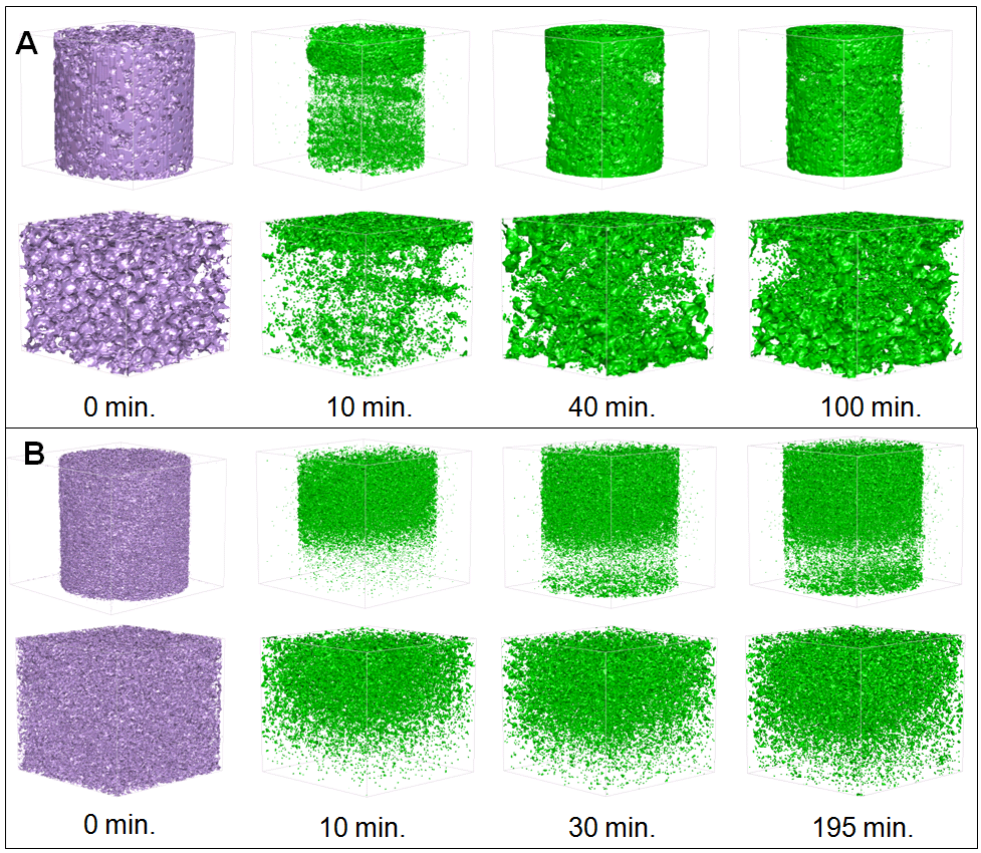

Figure 5-2. 3D binary images (A) for GB1 with varying duration of water injection: 0, 10, 40, and 100 minutes, and (B) for GB3 with varying duration of water injection: 0, 10, 30, and 195 minutes. In each image, above is the whole distribution of water, and below is the distribution in the cube where the data analysis was performed.

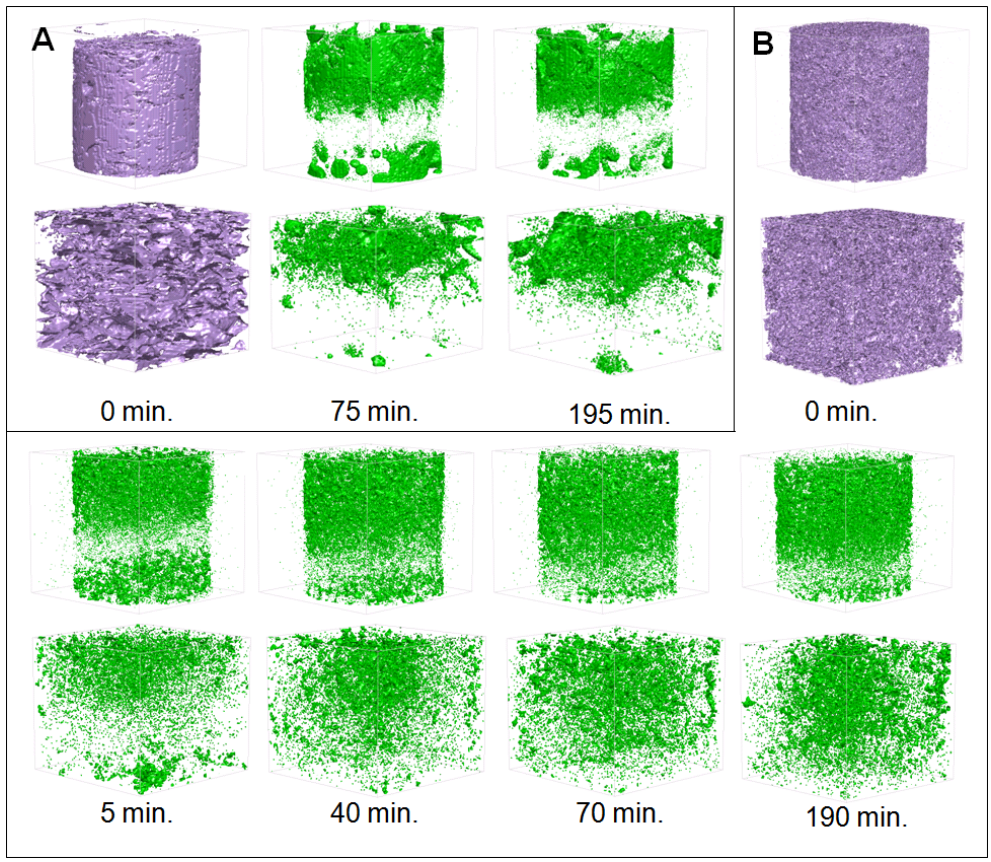

Figure 5-3. 3D binary images (A) for SG1 with varying duration of water injection: 0, 75 and 195 minutes, and (B) for SG3 with varying duration of water injection: 0, 5, 40, 70, and 190 minutes. In each image, above is the whole distribution of water, and below is the distribution in the cube where the data analysis was performed.

and porous networks on the degree of saturation in the model sands. Table 5-1 presents the porosity, specific surface area, and cube counting fractal dimension of each porous network saturated with silicon oil. Porous networks consisting of GB particles have lower specific surface area and cube counting fractal dimension than those of SG samples (i.e., GB1 < SG1, GB3 < SG3), indicating that porous networks of GB samples differ considerably from those of SG samples.

Figure 5-4 shows the volume fraction, specific surface area, and cube counting fractal dimension of water distribution in porous media with varying duration of water injection. Volumes of the water phase with increasing duration of water injection increased from 0 (0 minute) to 21.1 % (100 minutes, GB1), 8.5 % (195 minutes, GB3), 5.2 % (195 minutes, SG1), and 4.1 % (190 minutes, SG3), and the specific surface areas of water phase increased from 0 to 2.6 (100 minutes, GB1), 2.7 (195 minutes, GB3), 1.4 (195 minutes, SG1), and 1.5 mm^2/mm^3 (190 minutes, SG3). Note that the maximum volumes of water phase are smaller than the initial volumes of silicone oil for all samples because the remnant oil is entrapped in porous media.

The cube counting fractal dimension of the water phase with increasing duration of water injection increased from 0 (0 minute) to 2.49 (100 minutes, GB1), 2.57 (195 minutes, GB3), 1.96 (195 minutes, SG1), and 2.29 (195 min, SG3), respectively. The cube counting fractal dimension values of the SG samples are smaller than those of the GB samples due to the low volumes of water phase in the SG samples. The volume, specific

Table 5-1. Porosity, specific surface area, and cube counting fractal dimension of each sample before water flow.

	Porosity	Specific Surface Area (mm^2/mm^3)	Cube Counting Fractal Dimension
GB1	0.27	2.67	2.49
GB3	0.22	8.18	2.85
SG1	0.33	3.16	2.66
SG3	0.31	8.45	2.88

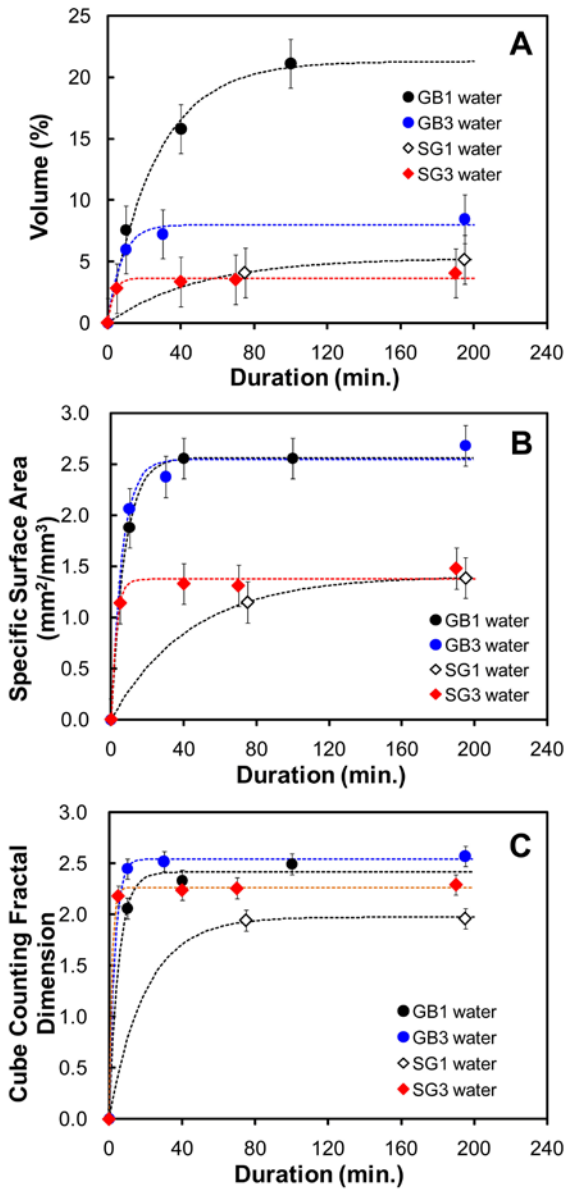

Figure 5-4. (A) Volume (%), (B) specific surface area (mm^2/mm^3), and (C) cube counting fractal dimension of water phase for all samples with varying duration of water injection.

δ

surface area, and cube counting fractal dimension increase rapidly, and then approach asymptotic values with increasing duration of water injection. These behaviors were fitted with the following single-exponential recovery function:

$$f(t) = a\left[1 - \exp(-\lambda t)\right] \qquad (5.1)$$

where *f(t)* is a recovered property of network such as volume (%), specific surface area (mm^2/mm^3), and cube counting fractal dimension, *a* is the asymptotic value of each property, *t* the duration of water injection (in minutes), and λ is a constant giving the rate of convergence. The trend of increasing volume fraction with increasing duration is similar to the empirical exponential recovery equation for predicting oil production in naturally-fractured reservoirs extracted by water (Aronofsky et al., 1958). Table 5-2 shows the fitting parameters for each property. The asymptotic values of volume and specific surface area for GB1 (21.1 % and 2.6 mm^2/mm^3, respectively) and GB3 (8.5 % and 2.7 mm^2/mm^3, respectively) are much larger than those for SG1 (5.2 % and 1.4 mm^2/mm^3, respectively) and SG3 (4.1 % and 1.5 mm^2/mm^3, respectively). The asymptotic values of cube counting fractal dimension for glass beads (2.49 for GB1 and 2.57 for GB3) are also larger than those for silica gel samples (1.96 for SG1 and 2.29 for SG3).

δ

Table 5-2. Fitting parameters and R^2 values for mono-exponential recovery equations for volume, specific surface area, and cube counting fractal dimension.

		a	λ	R^2
Volume (%)	GB1	21.28	0.038	0.99
	GB3	7.97	0.134	0.99
	SG1	5.28	0.020	1.00
	SG3	3.65	0.296	0.97
Specific Surface Area (mm^2/mm^3)	GB1	2.56	0.132	1.00
	GB3	2.55	0.162	0.99
	SG1	1.40	0.022	1.00
	SG3	1.37	0.355	0.99
Cube Counting Fractal Dimension	GB1	2.41	0.191	1.00
	GB3	2.54	0.328	1.00
	SG1	1.97	0.050	1.00
	SG3	2.26	0.665	1.00

δ

The manifested differences in the asymptotic values of volume, specific surface area, and cube counting fractal dimension are likely due to the differences in pore geometry and nature of particles in a 100 μm scale: porous networks of spherical grains (GB) and irregularly shaped grains (SG) have a moderate degree of clustering and a random distribution of pores, respectively, and the cube counting fractal dimension of pores for model sands composed of SG slightly increases with increasing specific surface area, whereas the cube counting fractal dimension for GBs increases rapidly and then increases gradually with increasing specific surface area (Lee and Lee, submitted). This could also be due to difference in nature of particles in a length scale less than 1μm: silica gel has larger mesoporosity while glass beads have no mesoporosity (Farrell et al., 1999). A mesopore is defined by pores that have a size of 20-500 Å on internal surfaces of solid grains (Huang et al., 1996). A previous experimental study of the adsorption-desorption of hydrophobic organic compounds from silica gels and glass beads showed that this difference of mesoporosity resulted in a larger amount of adsorbed trichloroethylene on silica gels than on glass beads (Farrell et al., 1999). This result indicates that the presence of mesopore leads to a stronger interaction between the surface of silica gel and fluids is likely to hamper the degree of saturation of porous network composed of silica gels. Note that mesopores do not appear on NMR micro-images because their size is smaller than the currently achievable resolution of the NMR micro-imaging. Finally note that the force balance of two immiscible fluids depends not only on the pore geometry, but also on the

δ

local fluid saturation (Keehm, 2003). Therefore, in order to investigate the exact origin of the observed distinct trends in water saturation, a visualization of the two phase flow with a higher resolution than that of the current study would be necessary.

The rates of convergence (λ in equation 5.1) of all properties for porous media composed of small grains (GB3 and SG3) are larger than those for large grains (GB1 and SG1). The rates of convergence of all the properties have the following order; from the largest to the smallest, SG3 > GB3 > GB1 > SG1. This indicates that the convergence rate exhibits the characteristics of the porous media: for small grains (GB3 and SG3), the convergence rate for silica gel is larger than that for glass beads whereas for large grains (GB1 and SG1), that for silica gel is smaller than that for glass beads

The relationships between convergence rates, parameters describing pore structures, and properties of porous media including configurational entropy and permeability were investigated. Figure 5-5 shows the relationship between the convergence rate of each property and permeability (k). The convergence rates (λ) of volume (%), specific surface area (mm^2/mm^3), and cube counting fractal dimension decrease with increasing permeability. The data were fitted with the following power law equation:

$$\lambda = pk^q + r \qquad (5.2)$$

where p, q, and r are the fitting parameters. Table 5-3 shows the fitting parameters for each relationship. The results show that the relationship

δ

Table 5-3. Fitting parameters and R^2 values for power law equations for the relationship between convergence rates and entropy length.

	p	q	r	R^2
λ-volume	0.74	-0.290	-0.096	0.67
λ-specific surface area	5.15	-0.013	-4.699	0.61
λ-cube counting fractal dimension	9.14	-0.014	-8.254	0.69

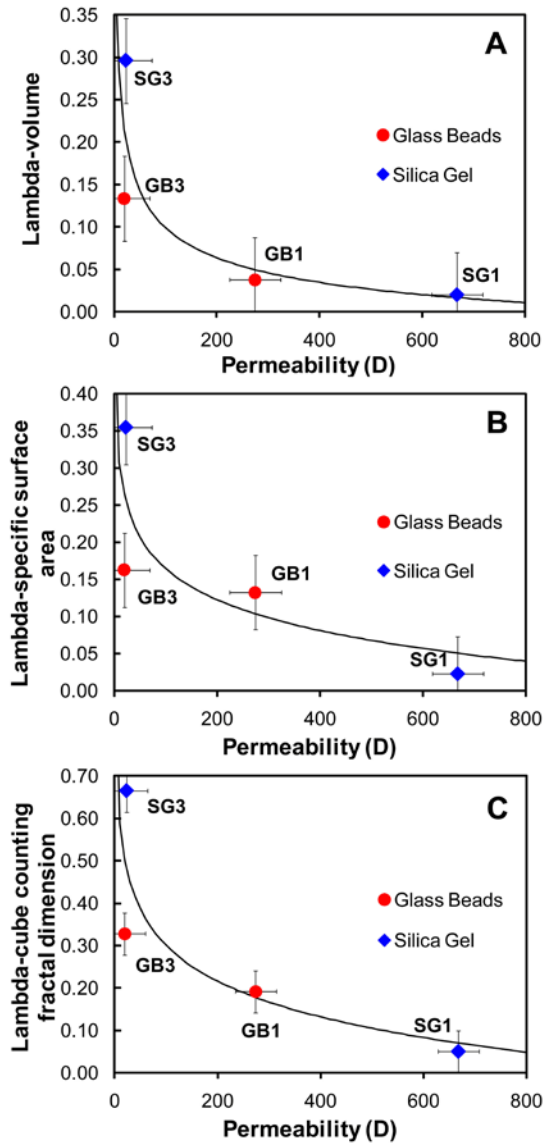

Figure 5-5. Relationship between convergence rates of (A) volume, (B) specific surface area, and (C) cube counting fractal dimension of water phase and the permeability. Each thick line is obtained from power law fitting function (Equation 5.2).

δ

between convergence rates and permeability fit well with the power-law equation, indicating that the convergence rate of any property can be explained by the transport property of the porous networks. Note that convergence rates are dependent on the flow pressure (i.e., injection rates) (Babadagli, 2002). Water was injected at a constant pressure (2 bar) for all samples, thus the results show the trend at a specific flow pressure while convergence rates would increase with increasing pressure. Therefore, in order to generalize equation (5.2), the convergence rates at varying flow pressures should be explored. Additional correlations can be found at sections 3 and 4 in Supplementary Information where the relationships between convergence rates and structural parameters including entropy length, porosity, specific surface area, cube counting fractal dimension, and configurational entropy are shown.

The current results show that NMR micro-imaging can also be used for obtaining pore scale resolution images (below 100 μm resolution) of two fluid phases in porous media. The current results also show that the network structures and the types of particles play crucial roles in the amount of permanent remnants of oil in oil sands and non aqueous phase liquids in sediments, and that the transport property of the porous networks determines the convergence rate of recovery.

d

Supplementary Information

5.S1. Validity of the experiments of this study

It was checked whether the distribution of water and silicone oil was affected by moving the sample. The procedure is as follows: 2D images were obtained, the sample was removed from the spectrometer, it was waited for 38 hours, the sample was set to the spectrometer, and 2D images were obtained again. Figure 5-S1 shows 2D images of SG3 samples at 40 minutes of duration of water injection. Figure 5-S1A was obtained before removing the sample from spectrometer, and Figure 5-S1B was obtained after setting the sample with the time interval of 38 hours. Figure 5-S1C is the difference image of the two images. Figure 5-S1C shows that the difference is not significant, and thus the distribution of water and silicone oil is almost constant in the resolution and time scale of this study before and after moving the sample. The insignificant changes of the distribution of two phases of fluid could be attributed to the fact that the viscosity of silicone oil is very large (30000 mPa·s), and the two fluids are immiscible and saturated in the column. The results show that the experiments are valid in the resolution and time scale of this study.

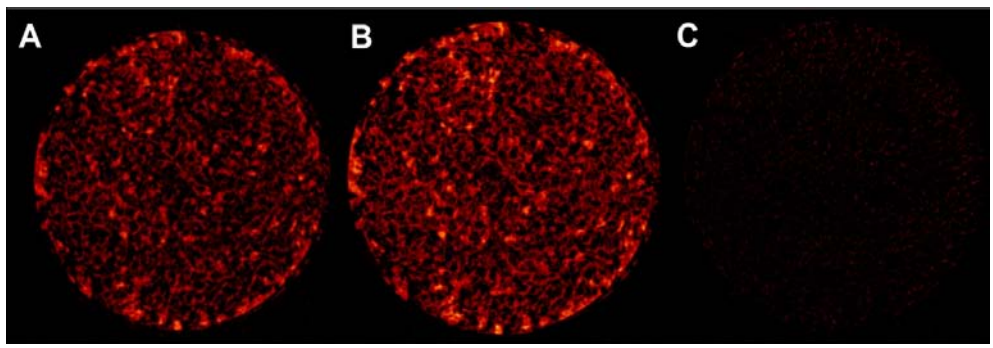

Figure 5-S1. (A) 2D image for SG3 obtained at 40 minutes of duration of water flow before removing the sample from spectrometer. (B) 2D image after 38 hours when the previous image was obtained. (C) Difference image between (A) and (B).

5.S2. 2D spin density maps and images obtained by chemical shift selective imaging method

Figure 5-S2 shows 2D spin density maps and images obtained by chemical shift selective imaging method for SG3 samples at 40 minutes of the duration of water flow.

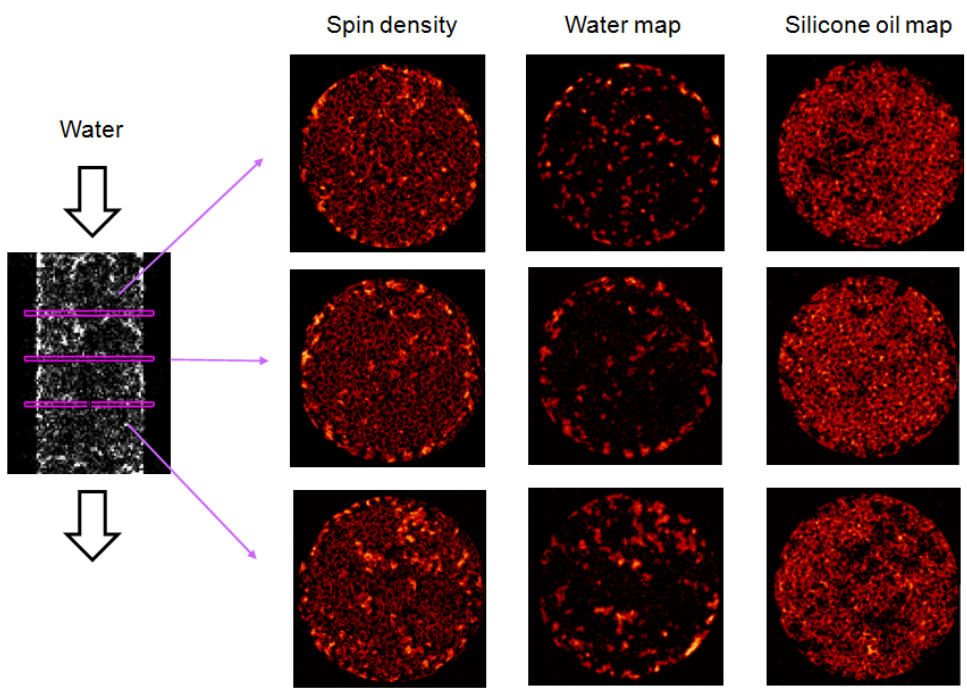

Figure 5-S2. Spin density maps and images obtained by chemical shift selective imaging method for SG3 obtained at 40 minutes of duration of water flow. The three columns correspond to spin echo 2D images, chemical shift images for water phase, and chemical shift images for silicone oil phase, respectively.

δ

5.S3. Effect of the entropy length on convergence rates

Configurational entropy analysis was estimated by the gliding-box algorithm (Andraud et al., 1994). Configurational entropy analyses were done for the 2D cross sections (slices) chosen from the 160 × 160 × 160 sub-volume data of each sample saturated with silicone oil (before the water flow). From this analysis, maximum configurational entropy and the corresponding entropy length can be obtained (Andraud et al., 1994). The entropy length is regarded as an accurate measure of the typical size of pores and/or constituent particles (Andraud et al., 1997). It was found that the entropy length is also strongly correlated with the convergence rates. Figure 5-S3 shows the effect of the entropy length on convergence rates. The results show that the convergence rates decrease with increasing the entropy length as well as permeability (Figure 5-5). The data was also fitted with the power law equation (Eq. 5.2) in which permeability is replaced with entropy length. Table 5-S1 shows the fitting parameters and R^2 values for each relationship. Permeability is proportional to the square of a representative grain diameter in Kozeny-Carman equation (Bear, 1972) and the entropy length is approximately 0.57 times of solid grains in porous media (Lee and Lee, submitted). Therefore, permeability and the entropy length are strongly correlated, and they have similar behavior for convergence rates. Note that the entropy length is a parameter characterizing porous networks and permeability is a transport property, and that both of them are well explained by the convergence rates of water distribution in initially saturated with silicone oil.

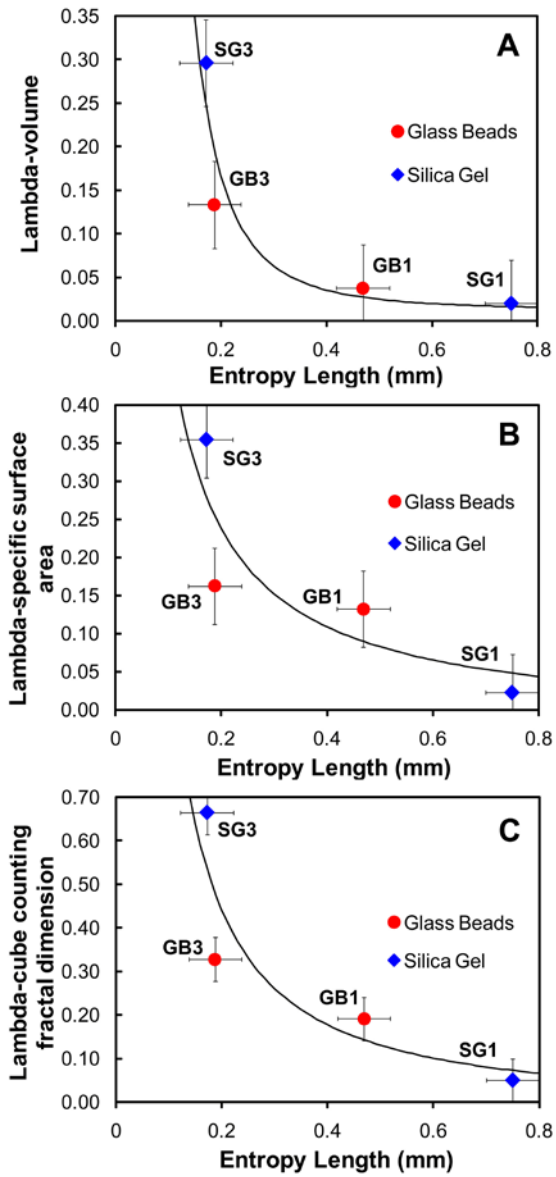

Figure 5-S3. Relationship between convergence rates of (A) volume, (B) specific surface area, and (C) cube counting fractal dimension of water phase and entropy length. Each thick line is obtained from power law fitting function (Equation 5.2).

δ

Table 5-S1. Fitting parameters and R^2 values for power law equations for the relationship between convergence rates and permeability.

	p	q	R	R^2
λ-volume	0.002	-2.749	0.012	0.863
λ-specific surface area	0.054	-0.985	-0.023	0.710
λ-cube counting fractal dimension	0.061	-1.250	-0.015	0.796

5.S4. Effect of structural parameters on convergence rates

Relationships between structural parameters and convergence rates were also investigated. This section describes relationships among various parameters and properties in which the correlations were not significant. Figure 5-S4-S7 show the relationships for porosity, specific surface area, cube counting fractal dimension, and configurational entropy, respectively with convergence rates. Convergence rates slightly decrease with increasing porosity (Figure 5-S4) and configurational entropy (Figure 5-S7), and slightly increase with increasing specific surface area (Figure 5-S5) and cube counting fractal dimension (Figure 5-S6). Compared to the relationships for permeability (Figure 5-5) and entropy length (Figure 5-S3), the trends for these relationships are not clear. The similar trend of porosity and maximum configurational entropy and that of specific surface area and cube counting fractal dimension are consistent with the results obtained for the model porous networks (Lee and Lee, submitted).

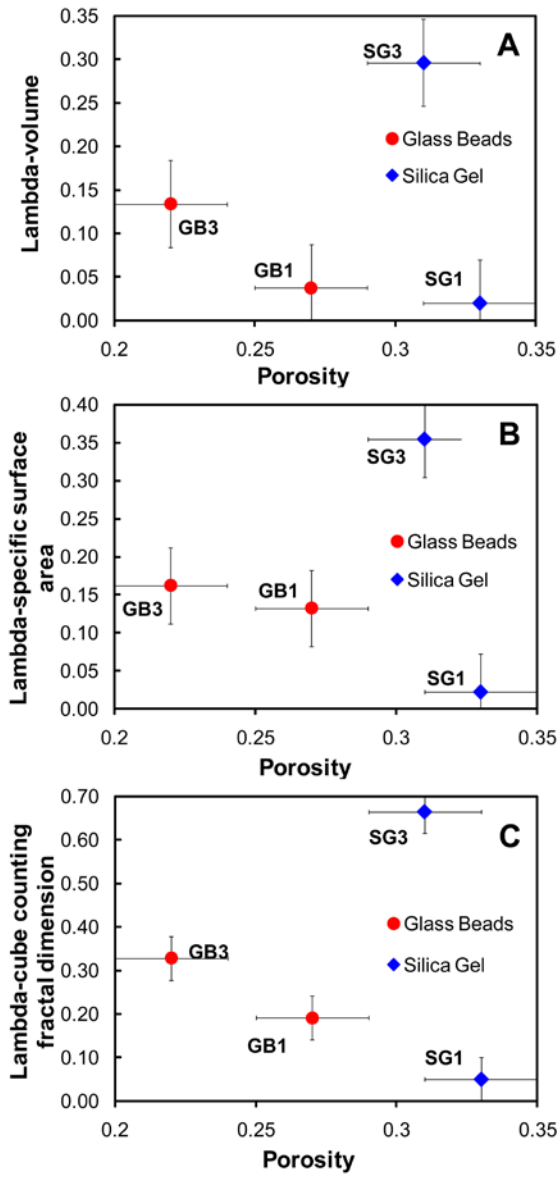

Figure 5-S4. Relationship between convergence rates of (A) volume, (B) specific surface area, and (C) cube counting fractal dimension of water phase and porosity.

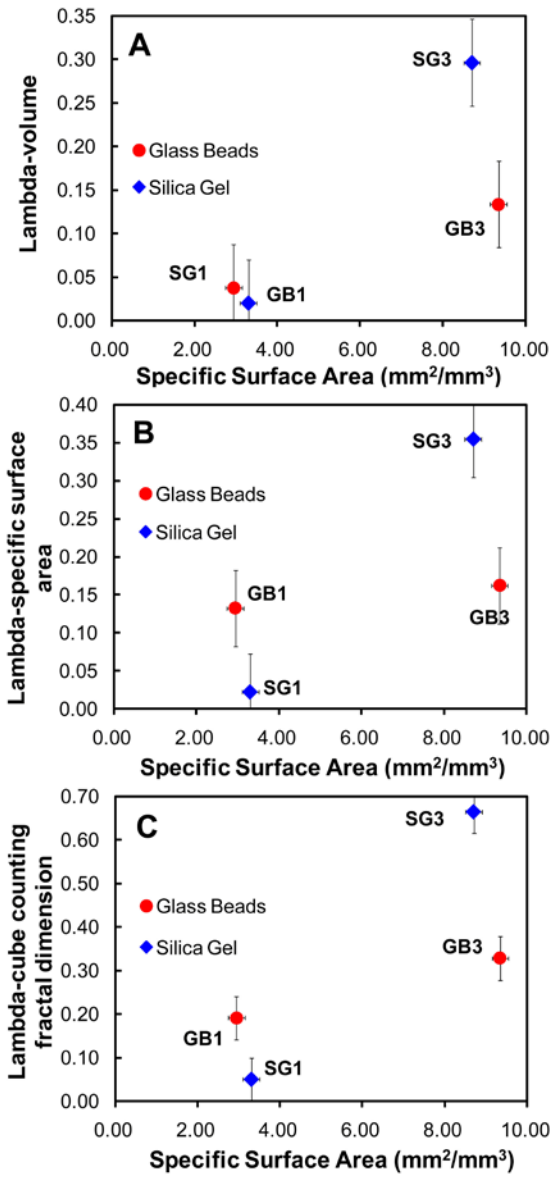

Figure 5-S5. Relationship between convergence rates of (A) volume, (B) specific surface area, and (C) cube counting fractal dimension of water phase and specific surface area (mm^2/mm^3).

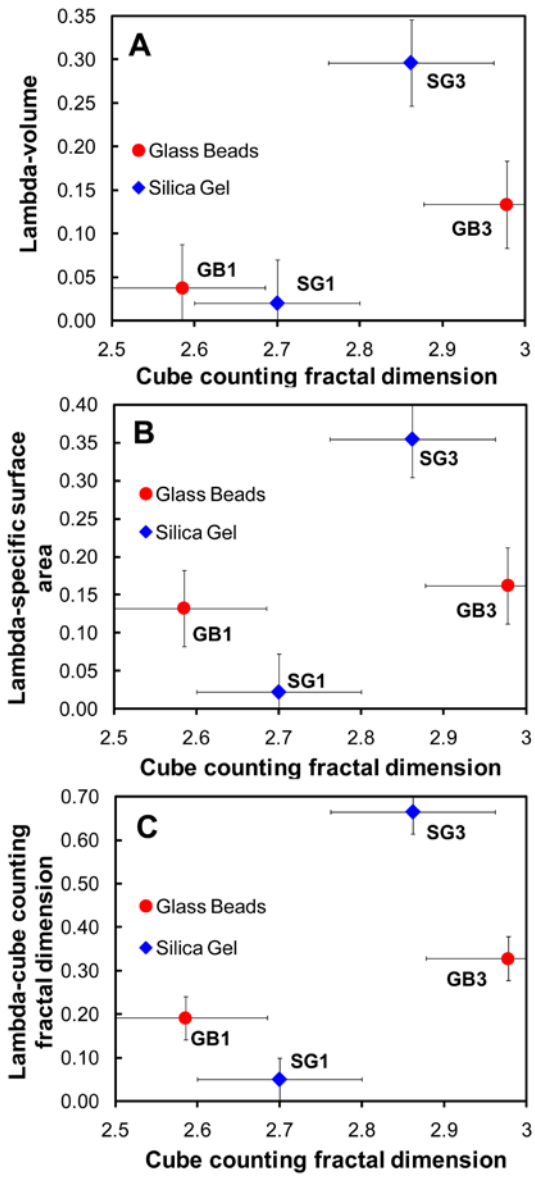

Figure 5-S6. Relationship between convergence rates of (A) volume, (B) specific surface area, and (C) cube counting fractal dimension of water phase and cube counting fractal dimension.

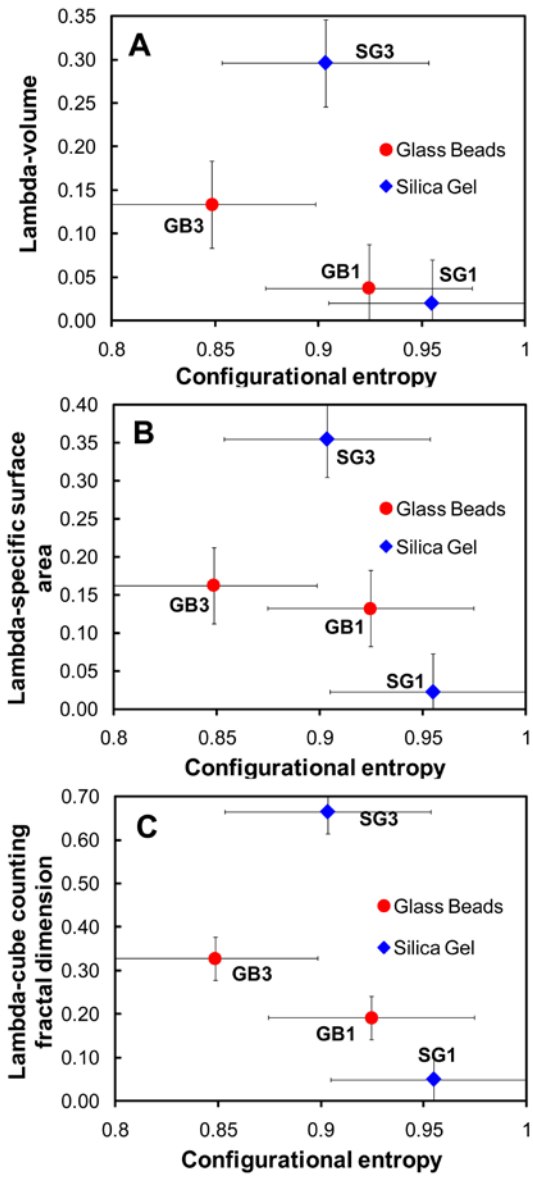

Figure 5-S7. Relationship between convergence rates of (A) volume, (B) specific surface area, and (C) cube counting fractal dimension of water phase and porosity.

References

Al-Raoush, R. I. and Willson, C. S. (2005) A pore-scale investigation of a multiphase porous media system. Journal of Contaminant Hydrology, 77, 67-89.

Andraud, C., Beghdadi, A., Haslund, E., Hilfer, R., Lafait, J. and Virgin, B. (1997) Local entropy characterization of correlated random microstructures. Physica A, 235, 307-318.

Andraud, C., Beghdadi, A. and Lafait, J. (1994) Entropic analysis of random morphologies. Physica A, 207, 208-212.

Aronofsky, J. S., Massé, L. and Natanson, S. G. (1958) A model for the mechanism of oil recovery from the porous matrix due to water invasion in fractured reservoirs. AIME Transactions, 213, 17-19.

Babadagli, T. (2002) Scaling capillary imbibition during static thermal and dynamic fracture flow conditions. Journal of Petroleum Science and Engineering, 33, 223-239.

Bachu, S. (2000) Sequestration of CO2 in geological media: criteria and approach for site selection in response to climate change. Energy Conversion and Management, 41(9), 953-970.

Barranco Jr., F. T., Dawson, H. E., Christener, J. M. and Honeyman, B. D. (1997) Influence of aqueous pH and ionic strength on the wettability of quartz in the presence of dense nonaqueous-phase liquids. Environmental Science & Technology, 31, 676-681.

Bear, J. (1972) Dynamics of Fluids in Porous Media. New York, American Elsevier, 764 p.

Becker, M. W., Pelc, M., Mazurchuk, R. V. and Spernyak, J. (2003) Magnetic resonance imaging of dense and light non-aqueous phase liquid in a

rock fracture. Geophysical Research Letters, 30(12), 1646.

Bernstein, M. A., King, K. F. and Zhou, X. J. (2004) Handbook of MRI Pulse Sequences. London, Elsevier Academic Press.

Blümich, B. (2000) NMR Imaging of Materials. Oxford, Clarendon Press, 541 p.

Brown, T. R., Kingaid, B. M. and Ugurbil, K. (1982) NMR chemical shift imaging in three dimensions. Proceedings of the National Academy of Sciences of the United States of America, 79, 3523-3526.

Callaghan, P. T. (1991) Principles of Nuclear Magnetic Resonance Microscopy. Oxford, Clarendon Press, 492 p.

Chen, J.-D., Dias, M. M., Patz, S. and Schwartz, L. M. (1988) Magnetic resonance imaging of immiscible-fluid displacement in porous media. Physical Review Letters, 61(13), 1489-1492.

Chu, Y. J., Werth, C. J., Valocchi, A. J., Yoon, H. and Webb, A. G. (2004) Magnetic resonance imaging of nonaqueous phase liquid during soil vapor extraction in heterogeneous porous media. Journal of Contaminant Hydrology, 73(1-4), 15-37.

Cil, M., Reis, J. C., Miller, M. A. and Misra, D. (1998) An examination of countercurrent capillary imbibition recovery from single matrix blocks and recovery predictions by analytical matrix/fracture transfer functions. SPE Annual Technical Conference and Exhibition. New Orleans, Louisiana, 49005 p.

Culligan, K. A., Wildenschild, D., Christensen, B. S. B., Gray, W. G. and Rivers, M. L. (2006) Pore-scale characteristics of multiphase flow in porous media: A comparison of air-water and oil-water experiments. Advances in Water Resources, 29(2), 227-238.

Farrell, J., Grassian, D. and Jones, M. (1999) Investigation of mechanisms

contributing to slow desorption of hydrophobic organic compounds from mineral solids. Environmental Science & Technology, 33, 1237-1243.

Haase, A., Frahm, J., Hanicke, W. and Matthaei, D. (1985) ^{1}H NMR chemical shift selective (CHESS) imaging. Physics in Medicine and Biology, 30, 341-344.

Huang, W., Schlautman, M. A. and Weber, J. W. J. (1996) A distributed reactivity model for sorption by soils and sediments. 5. The influence of near-surface characteristics in mineral domains. Environmental Science & Technology, 30(2993-3000).

Johns, M. L. and Gladden, L. F. (2000) Probing ganglia dissolution and mobilization in a water-saturated porous medium using MRI. Journal of Colloid and Interface Science, 225, 119-127.

Kazemi, H., Gilman, J. R. and Elsharkawy, A. M. (1992) Analytical and numerical solution of oil recovery from fractured reservoirs with empirical transfer functions. SPE Reservoir Engineering, 19849.

Keehm, Y. (2003) Computational Rock Physics: Transport Properties in Porous Media and Applications. Geophysics, Stanford University, Doctor of Philosophy, 135 p.

Lee, B. H. and Lee, S. K. (submitted) Effects of specific surface area and porosity on cube counting fractal dimension, lacunarity, and configurational entropy of porous networks of model sands: insights from random packing simulations and NMR micro-imaging. Journal of Geophysical Research.

Lee, S. K., Kim, H. N., Lee, B. H., Kim, H. I. and Kim, E. J. (2010) Nature of chemical and topological disorder in borogermanate glasses: insights from B-11 and O-17 solid-state NMR and quantum

chemical calculations. Journal of Physical Chemistry B, 114, 412-420.

Lee, S. K., Lin, J. F., Cai, Y. Q., Hiraoka, N., Eng, P. J., Okuchi, T., Mao, H. K., Meng, Y., Hu, M. Y., Chow, P., Shu, J. F., Li, B. S., Fukui, H., Lee, B. H., Kim, H. N. and Yoo, C. S. (2008) X-ray Raman scattering study of $MgSiO_3$ glass at high pressure: Implication for triclustered $MgSiO_3$ melt in Earth's mantle. Proceedings of the National Academy of Sciences, 105(23), 7925-7929.

Lee, S. K., Park, S. Y., S., Y. Y. and Moon, J. (2010) Structure and disorder in amorphous alumina thin films: insights from high-resolution solid-state NMR. Journal of Physical Chemistry C, 114(32), 13890-13894.

McNamara, G. R. and Zanetti, G. (1988) Use of the Boltzmann equation to simulate lattice-gas automata. Physical Review Letters, 61(20), 2332-2335.

Okamoto, I., Hirai, S. and Ogawa, K. (2001) MRI velocity measurements of water flow in porous media containing a stagnant immiscible liquid. Measurement Science & Technology, 12(9), 1465-1472.

Peters, E. J. and Hardham, W. D. (1990) Visualization of fluid displacements in porous media using computed tomography imaging. Journal of Petroleum Science and Engineering, 4(2), 155-168.

Prodanovic, M., Lindquist, W. B. and Seright, R. S. (2006) Porous structure and fluid partitioning in polyethylene cores from 3D X-ray microtomographic imaging. Journal of Colloid and Interface Sciences, 298, 282-297.

Reis, J. C. and Haq, S. A. (1999) Water advance in a single fracture in the presence of capillary imbibition into adjacent matrix blocks. In Situ, 23(3), 271-295.

Rumpel, H. and Pope, J. M. (1992) The application of 3D chemical shift microscopy to noninvasive histochemistry. Magnetic Resonance Imaging, 10, 187-194.

Sankey, M. H., Holland, D. J., Sederman, A. J. and Gladden, L. F. (2009) Magnetic resonance velocity imaging of liquid and gas two-phase flow in packed beds. Journal of Magnetic Resonance, 196, 142-148.

Schnaar, G. and Brusseau, M. L. (2005) Pore-scale characterization of organic immiscible-liquid morphology in natural porous media using synchrotron x-ray microtomography. Environmental Science & Technology, 39, 8403-8410.

Simpson, M. J., Simpson, A. J., Gross, D., Spraul, M. and Kingery, W. L. (2007) 1H and 19F nuclear magnetic resonance microimaging of water and chemical distribution in soil columns. Environmental Toxicology and Chemistry, 26(7), 1340-1348.

Sukop, M. C., Huang, H., Lin, C. L., Deo, M. D., Oh, K. and Miller, J. D. (2008) Distribution of multiphase fluids in porous media: Comparison between lattice Boltzmann modeling and micro-x-ray tomography. Physical Review E, 77(2), 026710.

Taber, J. J. (1980) Research on enhanced oil recovery: past, present and future. Pure and Applied Chemistry, 52(5), 1323—1347.

Wildenscheld, D., Hopmans, J. W., Vaz, C. M. P., Rivers, M. L. and Rikard, D. (2002) Using X-ray computed tomography in hydrology: systems, resolutions, and limitations. Journal of Hydrology, 267(3-4), 285-297.

Zhang, C. Y., Werth, C. J. and Webb, A. G. (2002) A magnetic resonance imaging study of dense nonaqueous phase liquid dissolution from angular porous media. Environmental Science & Technology, 36(15), 3310-3317.

δ

Chapter 6. High resolution NMR micro-imaging of fluids in porous media

Abstract

High resolution NMR micro-imaging of fluids in porous media may shed light on diverse applications in hydrogeology and geophysics. However, it is difficult to obtain high resolution images of fluids in porous media using NMR micro-imaging due to the low contents of fluids and short spin-spin relaxation times. Here, high resolution images of fluids in porous media including Mongolian desert sandstone, natural pisolite, and glass beads were obtained with relatively large porosity, small sample size, high magnetic field (18.8 T), and high gradient strength (300 G/cm). The results show that although signal to noise ratio is relatively low, NMR micro-imaging can be used to obtain the images of porous media composed of grain size down to 75 μm with the resolution of up to 19.5 μm/pixel for fluids in porous media.

6.1. Introduction

High resolution NMR micro-imaging of fluids in porous media with the resolution below 20 μm may allow us to study the pore-scale distribution and morphology of organic liquids at a fundamental level, which has the implication for the displacement and mass-transfer behavior of pollutant in porous media (Schnaar and Brusseau, 2005), and the connectivity of fluid and partial melt in rock, which has the implication for

δ

the seismic wave attenuation (Takei, 2002). However, it is difficult to obtain with the resolution below 20 μm using NMR micro-imaging because porous materials frequently possess low fluid contents and short spin–spin relaxation times, and both of which contribute to poor-quality NMR images (Callaghan, 1991; Blümich, 2000), and in addition, the difference in magnetic susceptibility between the pore fluid and the solid matrix leads to a large distribution of magnetic fields within the porous materials and correspondingly broad NMR line widths (Beyea et al., 2000). Here, it is attempted to obtain high resolution images of fluids in porous media including model sands, Mongolian sandstone, and natural pisolite filled with silicone oil with the resolution of up to 19.5 μm/pixel.

Before describing the limitation of NMR imaging and the strategy of this study for obtaining high resolution images, a brief introduction of imaging methods frequently used in porous media research is provided; optical imaging, confocal laser scanning microscopy, x-ray microtomography, and NMR imaging. Among them, optical imaging is the most straightforward method. Optical imaging methods include bright field microscopy, phase contrast microscopy, and reflected differential interference contrast microscopy (i.e., Nomarski microscopy) (Murphy, 2001). The advantages of optical imaging methods are their relative low cost, high-resolution, and fast acquisition time, and the disadvantage of optical imaging is that they are limited to a two dimensional acquisition (Werth et al., 2010).

Confocal laser scanning microscopy uses a laser to selectively

d

excite a narrow plane of light (Murphy, 2001). Images from multiple planes can be combined to create a three-dimensional image. In porous media research, the fluorescent resin impregnation method using confocal laser scanning microscopy was suggested (Fredrich et al., 1995) and has been successfully applied to porous sedimentary and crystalline rocks (Montoto et al., 1995; Fredrich and Lindquist, 1997; Onishi and Shimizu, 2005). The advantage of confocal laser scanning microscopy is that it covers a large area of sample surface with submicron resolution, and the disadvantage is that information from the interior of the samples is strongly restricted by decay of luminescent light through minerals (Onishi and Shimizu, 2005).

X-ray microtomography maps the absorption of x-rays passing through a sample (Flannery et al., 1987). The amount of absorption depends on sample composition and energy of the x-ray. In order to obtain a 3D spatially-distributed map of attenuation, the sample is rotated about the longitudinal axis (typically 0.5° to 1°) after an image is collected, and the image acquisition process is repeated until a total of 720 or 360 2D images of the sample are collected (Flannery et al., 1987). Recently, in order to obtain high resolution images, x-ray microtomography has been conducted at synchrotron sources and applied to unconsolidated (e.g., glass beads and soils) and consolidated (e.g., sandstone, limestone, and basaltic rocks) porous media (Spanne et al., 1994; Lindquist et al., 1996; Song et al., 2001; Arns et al., 2005; Øren et al., 2007). The advantage of x-ray microtomography is that it can produce high-resolution three-dimensional image, typically in the range of 1–10 μm, which is the greatest resolution

among the imaging methods that are applied to 3D systems, and the disadvantages include that a dopant is typically required, which may affect the fluid properties (Barranco Jr. et al., 1997; Wildenscheld et al., 2002), and that the dimensions of the sample are restricted to several millimeters, which is not sufficient to characterize the fracture patterns in coarse-grained rocks (Werth et al., 2010).

NMR imaging uses a field gradient for imaging the spins in fluids (Callaghan, 1991; Blümich, 2000). The linear relationship between NMR frequency and space coordinate is obtained by restricting the space dependence of the magnetic field to the field gradient (Levitt, 2001). To obtain an image, the gradient must be varied in such a way that all values of the wave vector that is the Fourier conjugate variable to the space coordinate are sampled. The image itself is then derived by Fourier transformation of the NMR signal. There are two ways to encode the space information to the NMR signal. First, the gradients can be turned on to a constant value of the gradient in x-direction during data acquisition. In this case, the wave vector scales with the acquisition time, and the space information in x-direction is frequency encoded. Second, the gradient in y-direction can be turned on for a fixed time before data acquisition to yield a certain value of the gradient integral at the start. In this case, the space information in y-direction is encoded in the phase of the signal acquired, and the experiment needs to be repeated for different initial phases obtained by varying the gradient. A 2D image is typically obtained by a combination of both phase encoding in one dimension and frequency

δ

encoding in the other. NMR imaging has many advantages (Callaghan, 1991; Blümich, 2000). Firstly, it can produce 3D images of pore structures non-destructively. Secondly, it can differentiate fluid phases in porous media at μm length scale. Thirdly, it can produce T_1 (spin-lattice relaxation time) and T_2 (spin-spin relaxation time) weighted imaging. Finally, it can produce velocity mapping. Recently, NMR imaging has been applied in many fields; for example, the controlled transport of polarized product in micro-reactors in chemical engineering (Bouchard et al., 2008), 3D structure of chick embryo in biochemistry (Goodall et al., 2009), temperature change in polymer in materials science (Small et al., 2009), water infiltration in sandstone in geology (Baraka-Lokmane et al., 2009), and NAPL distribution in the experimental aquifer in environmental sciences (Zhang et al., 2007).

The spatial resolution in the frequency encoding direction, $1/\Delta x$ is related to the width of the NMR absorption line, $\Delta\nu = \Delta\omega/2\pi$ by

$$\frac{1}{|\Delta x|} = \left|\frac{\gamma G_x}{2\pi\Delta\nu}\right|, \qquad (6.1)$$

where ω is the Larmor frequency and γ is the gyromagnetic ratio (Callaghan, 1991). This expression applies to direct detection of the NMR signal in the presence of a magnetic field gradient G_x. The digital resolution $1/\Delta y$ in the phase encoding direction is determined by the number n_y of complex signal values and by the k-space sampling interval $\Delta G_y t_1$,

$$\frac{1}{\Delta y} = \frac{n_y \Delta G_y t_1}{2\pi} \qquad (6.2)$$

where t_1 is the phase encoding time (Callaghan, 1991). As shown in

δ

equations (6.1) and (6.2), the spatial resolution is proportional to the magnetic field gradient. The most significant factor limiting the resolution is poor signal-to-noise ratio (SNR) of an NMR signal decreasing with voxel volume, because NMR signal amplitude is proportional to the number of nuclear spins in a voxel (Callaghan, 1991; Blümich, 2000). SNR is proportional to the 7/4th power of the static magnetic field (Hoult and Richards, 1976). Therefore, in order to increase SNR and voxel resolution, NMR micro-imaging experiments were performed at the high magnetic field (strength of 18.8 T) and high field gradient (300 G/cm) in this study.

Other limiting factors include the effects of diffusion, transverse relaxation, and susceptibility (Callaghan, 1991; Blümich, 2000). The transverse relaxation rate ($1/T_2$) is expressed as

$$\frac{1}{T_2} = \frac{1}{T_{2B}} + \rho_2 \frac{S}{V} + \frac{D}{12}\left(\gamma G t_E\right)^2, \qquad (6.3)$$

where ρ_2 is the transverse surface relaxivity, $1/T_{2B}$ is the relaxation rate of the bulk water, D is the self-diffusion coefficient of the water, and t_E is the echo-time (Brownstein and Tarr, 1979). Surface relaxivity is a geochemical property describing the capacity of the grain surface to enhance relaxation and generally increase with the concentration of paramagnetic impurities on a surface (Bryar et al., 2000). The product $\rho(S/V)$ reflects the effect of both pore geometry and geochemistry. Therefore, the transverse relaxation rate increases with increasing (S/V) (i.e., decreasing the grain size) and the echo time. In this study, in order to reduce these limiting factors, samples with high porosity were used and minimum echo time was applied.

δ

In the applications of NMR imaging to artificial phantoms or biological cells, there are two previous studies considered the highest resolutions to date (Lee et al., 2001; Ciobanu et al., 2003). In the former, 1×1 μm^2 at 75 μm slice thickness and, in the latter, 3.7×3.4×3.4 μm^3 were reported. In the applications to porous media research, NMR imaging has been mostly used to obtain images of multi phases of fluids or velocity vectors (Blümich, 2000), and obtaining high resolution images of fluids in porous media has not been much concerned. Therefore, as far as the author know, images obtained by NMR imaging with the resolution below 20 μm for fluids in porous media have not been reported previously.

Here, it was pursued to obtain high resolution images of fluids in porous media using NMR micro-imaging with the resolution of up to 19.5 μm/pixel . In order to enhance the resolution, high magnetic field (18.8 T), high field gradient (300 G/cm), highly porous sample, minimum echo time, and relatively small sample size were used.

6.2. Methods

Porous sandstone, natural pisolite, and glass beads were prepared for NMR micro-imaging experiments. The sandstone (late cretaceous, Cenomanian-Santonian) sample was taken at Khar Khutul area, East Gobi Basin, Mongolia. The grain size of the sandstone sample ranged from 0.12 mm to 0.43 mm (rarely up to 0.61 mm). The sandstone was composed of 52 % quartz, 39 % feldspar, and 9 % lithic fragment. Natural pisolite was comprised of spherical calcite grains in which the average grain diameter

d

was 2 mm. Average particle sizes (diameters) of the glass beads (Sigma, acid-washed) were 0.075 mm (GB4). Each sample was saturated with silicone oil (polydimethylsiloxane, Baysilone M30000, density of 0.98 g/cm^3 and viscosity of 30000 mPa·s). A vacuum pump with a pump pressure of 1.45 torr was used to saturate the pore space with silicone oil and to eliminate air bubbles. Each sample was sealed with parafilm after the saturation, and put into the 10 mm NMR tube (Wilmad).

The experiment was carried out at Korea Basic Science Institute, Ochang using a Bruker DMX 800 spectrometer equipped with a 18.8 T vertical bore magnet. Micro5.0 probehead was used and the gradient strength was 300 G/cm for DMX 800 spectrometer. Figure 6-1 shows the two dimensional spin echo pulse sequence used in the experiment. Minimum echo time (T_E) was used to reduce the signal attenuation due to T_2 relaxation and diffusion, which become more important as pixel size becomes smaller. Minimum echo time was 4.5 ms for 256 x 256 matrix, 12.335 ms for 512 x 512 matrix. Field of view, matrix size, and slice thickness varied with the sample. The sinc3-shaped excitation and refocusing pulses were used with a repetition time of 2 s. The number of scans varied from 1 to 4, depending on the signal-to-noise ratio of the spectra. After the image acquisition, binary images were obtained by threshold method using the pixel vs. intensity histogram showing a bimodal distribution.

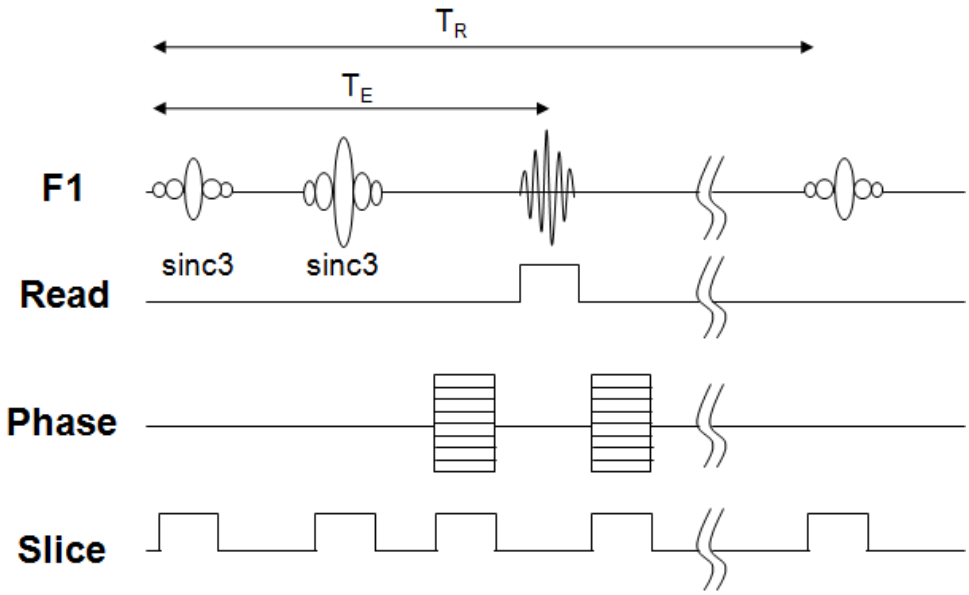

Figure 6.1. Timing diagram of two dimensional spin echo pulse sequence.

δ

6.3. Results and Discussion

Figure 6-2 shows the spin echo image (6-2A) and its binary image (6-2B) of Mongolian desert sandstone. Field of view was 9 mm x 9 mm, and matrix size was 256 x 256, and thus the resulting spatial resolution was 35 μm x 35 μm. The slice thickness was 0.5 mm. In spin density image, boundary of sandstone is distinctive due to the high intensity of silicone oil covered with the surface of sandstone. Note that the sample was covered by parafilm after the saturation of silicone oil by vacuum pump. In addition, signals from silicone oil infiltrated into the inside of sandstone can be seen. In binary image, the distribution of infiltrated silicone oil is more distinctive. Zoomed images show that the infiltrated silicone oil forms small blobs, and some blobs are interconnected. As mentioned above, it is difficult to obtain the detailed structure of infiltrated fluid in natural sandstone due to the low porosity and the large amount of paramagnetic impurities. Therefore, there has been previous NMR imaging studies for natural sandstones showing only the development of the fluid front during the imbibitions (e.g., Dijk et al., 1999; Baraka-Lokmane et al., 2001; Dijk et al., 2002; Baraka-Lokmane et al., 2009). Despite the difficulties, it was able to obtain the detailed distribution of silicone oil in sandstone.

Figure 6-3 shows two dimensional spin density images (6-3A and 3B) of pisolite filled with silicone oil, those with contour lines (6-3C and 3D), and their binary images (6-3E and 3F). Field of view was 10 mm x 10 mm, and matrix size was 512 x 512. Therefore, the spatial resolution was 19.5 μm x 19.5 μm. The slice thickness was 0.5 mm. Pisolite is composed of large

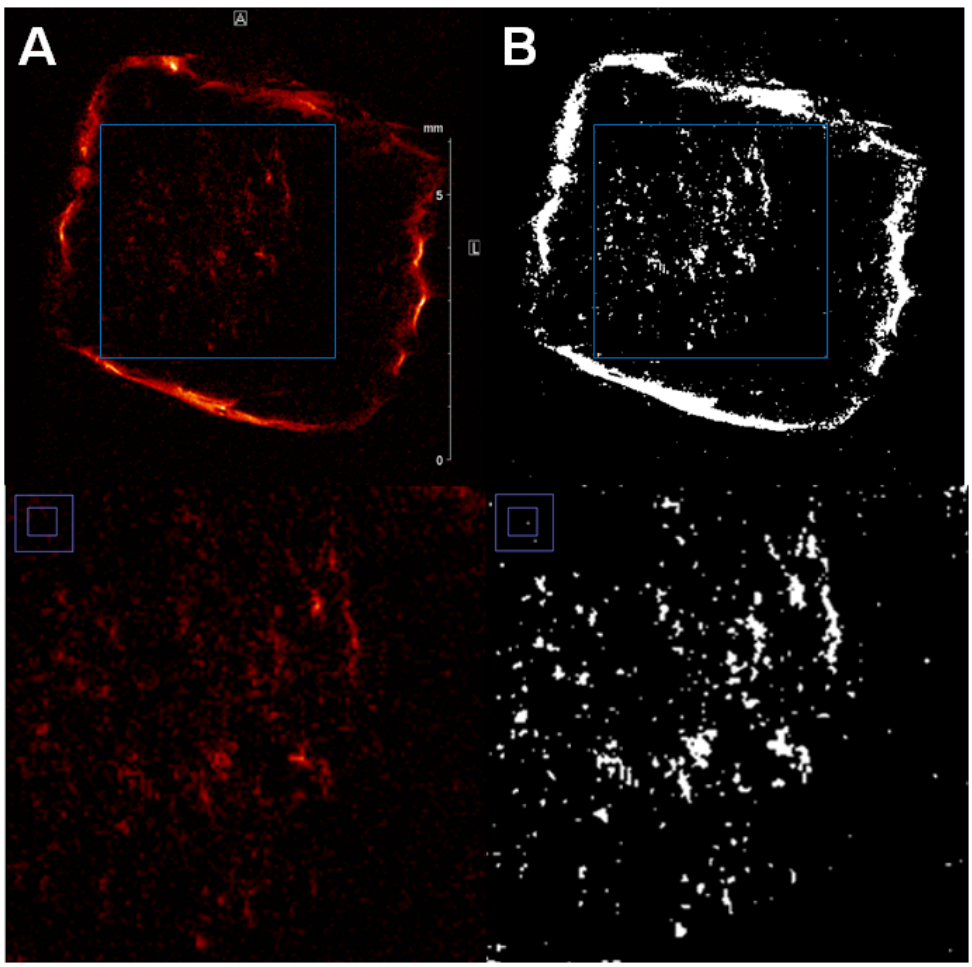

Figure 6-2. Two dimensional (A) spin density image and (B) binary image of Mongolian sandstone filled with silicone oil. Zoomed regions are indicated by squares in upper images and zoomed images of spin density and binary image are shown in below images.

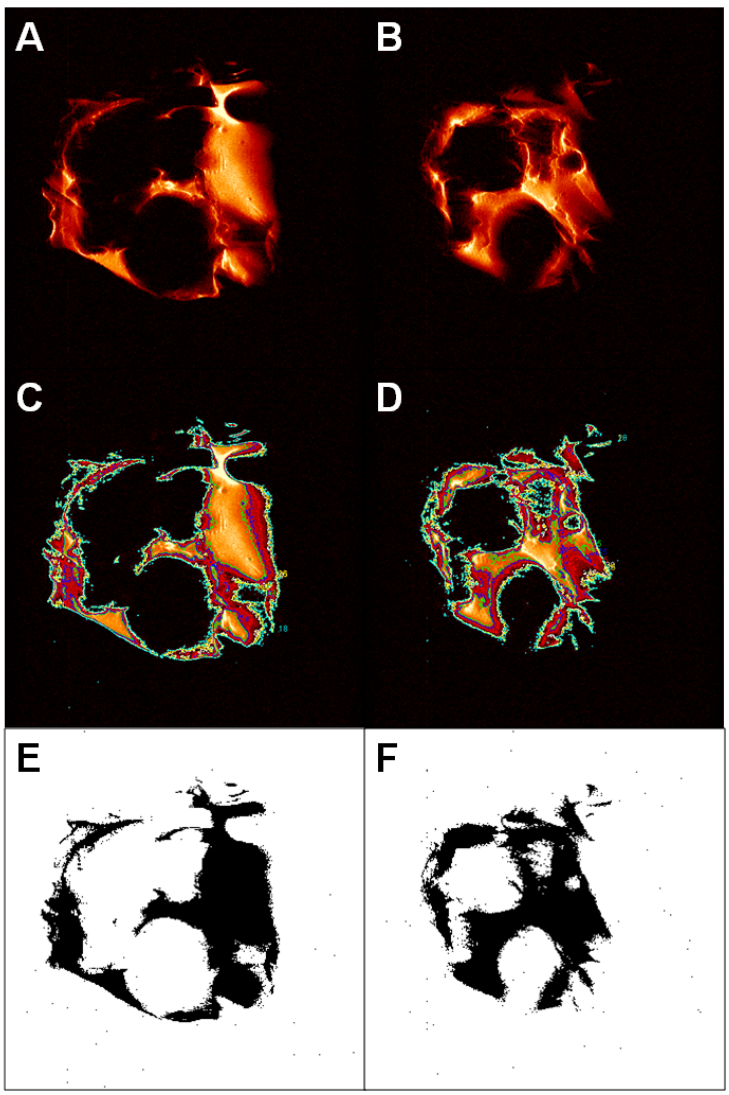

Figure 6-3. Two dimensional spin density images (A and B) of pisolite filled with silicone oil, those with contour lines (C and D), and their binary images (E and F). Each column belongs to the same slice. In (C) and (D), each contour line (color in parentheses) is drawn at 37.2 % (green), 29.4 % (blue), 21.6 % (red), 13.8 % (black), 11.8 % (white), 9.8 % (yellow), 7.8 % (orange), and 7.1 % (cyan) level of relative intensity.

δ

grains of calcite, and thus the pore size is relatively large, which allows us to make the voxel size small. Spin density images show that high intensities mostly come from silicone oil filled in the large pore. In spin density images with contour lines, one can see that the highest intensity is shown in the center of the pore, and the intensity becomes lower in the grain surfaces or inside the grains. High resolution images make one see the microstructure of infiltrated silicone oil into the grain. This is the highest resolution (i.e., the smallest pixel size, 19.5 μm) image of fluids in natural porous media, and it is noteworthy that the detailed structure of infiltrated fluid into the calcite grains was observed.

Figure 6-4 shows two dimensional spin density images of GB4 filled with silicone oil. Field of view was 6.5 mm x 6.5 mm, and matrix size was 256 x 256. Therefore, the spatial resolution was 25 μm x 25 μm. The slice thickness was 0.15 mm. Grain size of GB4 shown in this figure is the smallest size in the NMR imaging studies for porous media research. Spin density and binary images show that silicone oil structures filled in the pore space. The average particle size can be seen in the zoomed images with yellow circles. While the structure of silicone oil in small grains of glass beads is complex, the average size of the space where signals from silicone oil are not shown is comparable with the average particle size.

In order to obtain robust density images in porous media, the short encoding times, high magnetic field gradient strength, large filter widths, and low flip angle RF pulses are required. For that purpose, the spin-echo single point imaging (SE-SPI) technique was suggested with the

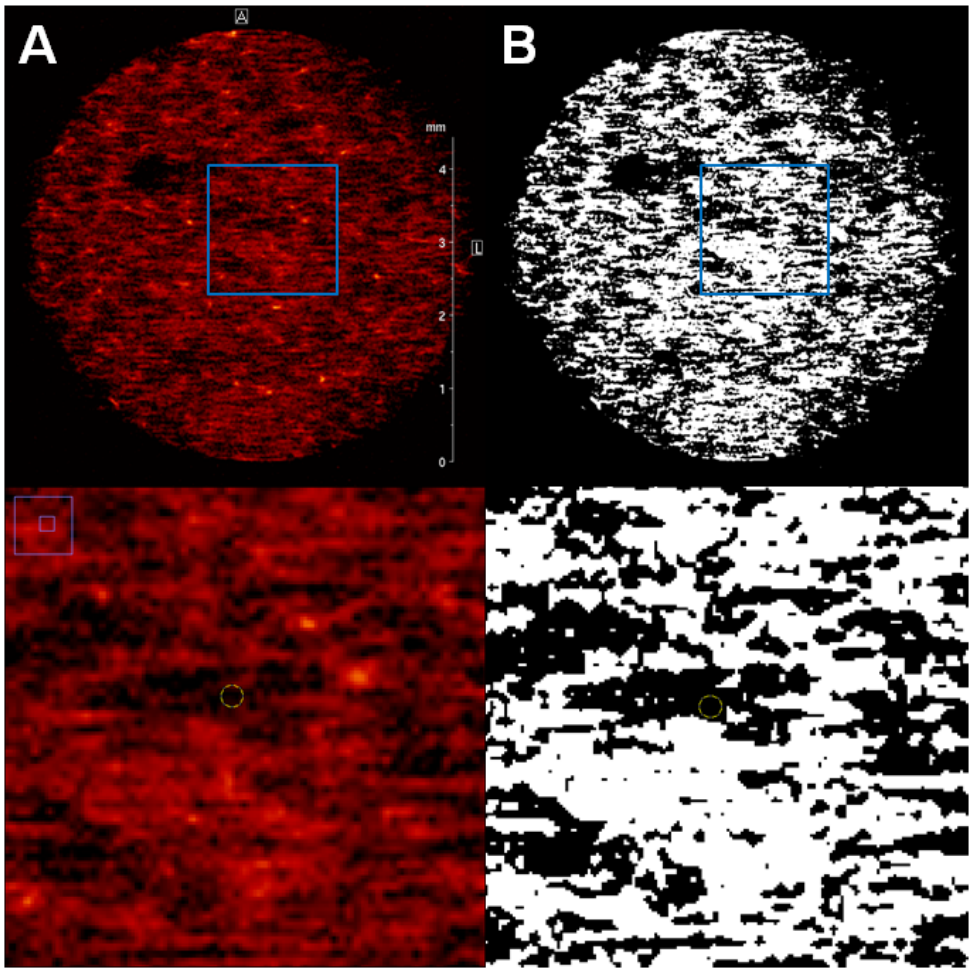

Figure 6-4. Two dimensional (A) spin density image and (B) binary image of GB4 filled with silicone oil. Zoomed regions are indicated by squares in upper images and zoomed images of spin density and binary image are shown in below images. Yellow circles in zoomed images indicate the average size of glass beads.

δ

achievement of true fluid content images through observing the signal intensity at near zero evolution time (Li et al., 2009). However, this method was tested for 1D imaging for rock core up to date. With the development of pulse sequences including SE-SPI for imaging fluids in porous media with short spin-spin relaxation time, it is expected that higher resolution images with below 10 μm pixel size can be obtained by using high magnetic field, high field gradient, and small sample size.

It was shown that high resolution NMR micro-imaging of fluids in porous media can be obtained with the resolution below 20 μm, which may enable us to study the connectivity of fluids and partial melts in rock at high pressures. Knowledge of the geometry of fluids and partial melts is essential for understanding the macroscopic properties of partially molten rocks (von Bargen and Waff, 1986; Takei, 2002). Three dimensional geometry of fluids and melts can be directly obtained by the advanced high resolution NMR micro-imaging with the resolution below 20 μm. However, this experiment requires in-situ high pressure and high temperature apparatus in imaging probe, which may be possible in the future.

References

Arns, C. H., Bauget, F., Limaye, A., Sakellariou, A., Senden, T. J., Sheppard, A. P., Sok, R. M., Pinczewski, W. V., Bakke, S., Berge, L. I., Oren, R. E. and Knackstedt, M. A. (2005) Pore-scale characterization of carbonates using X-ray microtomography. SPE Journal, 10(4), 475-484.

Baraka-Lokmane, S., Main, I. G., Ngwenya, B. T. and Elphick, S. C. (2009) Application of complementary methods for more robust characterization of sandstone cores. Marine and Petroleum Geology, 26(1), 39-56.

Baraka-Lokmane, S., Teutsch, G. and Maine, I. G. (2001) Influence of open and sealed fractures on fluid flow and water saturation in sandstone cores using Magnetic Resonance Imaging. Geophysical Journal International, 147(2), 263-271.

Barranco Jr., F. T., Dawson, H. E., Christener, J. M. and Honeyman, B. D. (1997) Influence of aqueous pH and ionic strength on the wettability of quartz in the presence of dense nonaqueous-phase liquids. Environmental Science & Technology, 31, 676-681.

Beyea, S. D., Balcom, B. J., Mastikhin, I. V., Bremner, T. W., Armstrong, R. L. and Grattan-Bellew, P. E. (2000) Imaging of heterogeneous materials with a turbo spin echo single-point imaging technique. Journal of Magnetic Resonance, 144(2), 255-265.

Blümich, B. (2000) NMR Imaging of Materials. Oxford, Clarendon Press, 541 p.

Bouchard, L. S., Burt, S. R., Anwar, M. S., Kovtunov, K. V., Koptyug, I. V.

and Pines, A. (2008) NMR imaging of catalytic hydrogenation in microreactors with the use of para-hydrogen. Science, 319(5862), 442-445.

Brownstein, K. R. and Tarr, C. E. (1979) Importance of classical diffusion in NMR studies of water in biological cells. Physical Review A, 19(6), 2446-2453.

Bryar, T. R., Daughney, C. J. and Knight, R. J. (2000) Paramagnetic effects of iron(III) species on nuclear magnetic relaxation of fluid protons in porous media. Journal of Magnetic Resonance, 142, 74-85.

Callaghan, P. T. (1991) Principles of Nuclear Magnetic Resonance Microscopy. Oxford, Clarendon Press, 492 p.

Ciobanu, L., Webb, A. G. and Pennington, C. H. (2003) Magnetic resonance imaging of biological cells. Progress in Nuclear Magnetic Resonance Spectroscopy, 42, 69-93.

Dijk, P., Berkowitz, B. and Bendel, P. (1999) Investigation of flow in water-saturated rock fractures using nuclear magnetic resonance imaging (NMRI). Water Resources Research, 35(2), 347-360.

Dijk, P. E., Berkowitz, B. and Yechieli, Y. (2002) Measurement and analysis of dissolution patterns in rock fractures. Water Resources Research, 38(2).

Flannery, B. P., Deckman, H. W., Roberge, W. G. and D'amico, K. L. (1987) Three-dimensional x-ray microtomography. Science, 237(4821), 1439-1444.

Fredrich, J. T. and Lindquist, W. B. (1997) Statistical characterization of the three-dimensional microgeometry of porous media and correlation with microscopic transport properties. International Journal of Rock Mechanics and Mining Sciences, 34, 3-4.

Fredrich, J. T., Menendez, B. and Wong, T.-F. (1995) Imaging the pore structure of geomaterials. Science, 268, 276-279.

Goodall, N., Kisiswa, L., Prashar, A., Faulkner, S., Tokarczuk, P., Singh, K., Erichsen, J. T., Guggenheim, J., Halfter, W. and Wride, M. A. (2009) 3-dimensional modelling of chick embryo eye development and growth using high resolution magnetic resonance imaging Experimental Eye Research, 89(4), 511-521.

Hoult, D. I. and Richards, R. E. (1976) The signal-to-noise ratio of the nuclear magnetic resonance experiment. Journal of Magnetic Resonance, 24, 71-85.

Lee, S.-C., Kim, K., Kim, J.-W., Lee, S. K., Yi, J. H., Kim, S. W., Ha, K.-S. and Cheong, C. (2001) One micrometer resolution NMR microscopy. Magnetic Resonance Imaging, 150, 207-213.

Levitt, M. H. (2001) Spin Dynamics. Chichester, John Wiley & Sons Ltd, 686 p.

Li, L., Han, H. and Balcom, B. J. (2009) Spin echo SPI methods for quantitative analysis of fluids in porous media. Journal of Magnetic Resonance, 198, 252-260.

Lindquist, W. B., Lee, S. M., Coker, D. A., Jones, K. W. and Spanne, P. (1996) Medial axis analysis in three-dimensional tomographic images of porous media. Journal of Geophysical Research, 101, 8297-8310.

Montoto, M., Martinez-Nistal, A., Rodriguez-Rey, A., Fernando-Merayo, N. and Soriano, P. (1995) Microfractography of granite rocks under confocal scanning laser microscopy. Journal of Microscopy, 177, 138-149.

Murphy, D. B. (2001) Fundamentals of Light Microscopy and Electronic Imaging. New York, Wiley-Liss, 368 p.

Onishi, C. T. and Shimizu, I. (2005) Microcrack networks in granite affected by a fault zone: visualization by confocal laser scanning microscopy. Journal of Structural Geology, 27, 2268-2280.

Øren, P. E., Bakke, S. and Held, R. (2007) Direct pore-scale computation of material and transport properties for North Sea reservoir rocks. Water Resources Research, 43(12), W12S04.

Schnaar, G. and Brusseau, M. L. (2005) Pore-scale characterization of organic immiscible-liquid morphology in natural porous media using synchrotron x-ray microtomography. Environmental Science & Technology, 39, 8403-8410.

Small, W., Gjersing, E., Herberg, J. L., Wilson, T. S. and Maitland, D. J. (2009) Magnetic resonance flow velocity and temperature mapping of a shape memory polymer foam device. Biomedical Engineering Online, 8(42).

Song, S.-R., Jones, K. W., Lindquist, W. B., Dowd, B. A. and Sahagian, D. L. (2001) Synchrotron X-ray computed microtomography: studies on vesiculated basaltic rocks. 63, 252-263.

Spanne, P., Thovert, J. F., Jacquin, C. J., Lindquist, W. B., Jones, K. W. and Adler, P. M. (1994) Synchrotron computed microtomography of porous media: Topology and transports. Physical Review Letters, 73(14), 2001-2004.

Takei, Y. (2002) Effect of pore geometry on V_P/V_S: From equilibrium geometry to crack Journal of Geophysical Research-Solid Earth, 107(B2), 2043.

von Bargen, N. and Waff, H. S. (1986) Permeabilities, interfacial areas and curvatures of partially molten systems: Results of computations of equilibrium microstructures. Journal of Geophysical Research, 91,

9261-9276.

Werth, C. J., Zhang, C., Brusseau, M. L., Oostrom, M. and Baumann, T. (2010) A review of non-invasive imaging methods and applications in contaminant hydrogeology research. Journal of Contaminant Hydrology, 113, 1-24.

Wildenscheld, D., Hopmans, J. W., Vaz, C. M. P., Rivers, M. L. and Rikard, D. (2002) Using X-ray computed tomography in hydrology: systems, resolutions, and limitations. Journal of Hydrology, 267(3-4), 285-297.

Zhang, C. Y., Werth, C. J. and Webb, A. G. (2007) Characterization of NAPL source zone architecture and dissolution kinetics in heterogeneous porous media using magnetic resonance imaging Environmental Science & Technology, 41(10), 3672-3678.

Chapter 7. Geophysical implications

One of the key issues in porous media research is to understand how the pore structure affects the transport processes of fluids in porous media. The zeroth order answer for this issue is characterizing the properties of porous media using porosity and specific surface area (Bear, 1972). However, porosity and specific surface area cannot provide further information about the morphology of the pore network. The first order answer is characterizing the properties of porous media by the statistical geometric methods. This approach includes multipoint correlation functions which analyze structural correlation between points belonging to the solid, interface or pore network (Reiss, 1992) and parameters analyzed in this study (cube counting fractal dimension, lacunarity, and configurational entropy). Configurational entropy and cube counting fractal dimension can be used in describing complex and disordered structures of fluids in rock-melt-fluid composites in the Earth's interior as well as porous networks shown by the interactions between earth materials and fluids in the Earth's surface.

Configurational entropy has been used to describe the degree of disorder in amorphous networks, including oxide glasses and melts with geophysical and geochemical implications (e.g. Lee and Stebbins, 1999; Lee, 2005; Lee et al., 2010). Adam and Gibbs (1965) defined configurational entropy (S^{config}) as follows:

δ

$$S^{config} = k \ln W_c , \tag{7.1}$$

where W_c is the number of configuration (individual arrangements into different configurations for microscopic cooperative regions). Based on the relaxation theory, liquid viscosity (η) is related to temperature and configurational entropy (Adam and Gibbs, 1965):

$$\log \eta = A + B \big/ TS^{config} . \tag{7.2}$$

where T is the temperature, and A and B are constants. Configurational entropy for aluminosilicate melts and glasses can be expressed as (Lee and Stebbins, 1999):

$$S^{config} = -R \sum X_{i-O-j} \ln X_{i-O-j} . \tag{7.3}$$

where R is the gas constant, and $X_{i\text{-}O\text{-}j}$ are the mole fractions of Si-O-Si, Al-O-Al, and Si-O-Al. With increasing chemical order, the configurational entropy decreases, which causes the viscosity of the melts to increase based on Adam-Gibbs theory (Richet, 1984; Lee, 2005).

Chapter 4 shows that the configurational entropy of total porosity is dependent on the porosity and explains the maximum configurational entropy well. The relationship between configurational entropy and porosity can be used to explain the properties of rock-melt-fluid composites. For example, macroscopic constitutive relations of solid-liquid composites are derived as functions of microscopic geometry described by grain-boundary contiguity (φ) which is defined by the portion of the grain surface being in contact with the neighboring grains, and takes a value between 0

δ

and 1 (Takei, 1998). Contiguity is the essential geometric factor that determines the macroscopic mechanical properties of the granular composites (Takei, 1998). Bulk modulus, shear modulus, and shear velocity of the composites comprised of spherical particles are explained by contiguity (Takei, 1998). In order to explain the macroscopic properties of solid-liquid composites, wetness ($\psi = 1 - \varphi$) is used rather than contiguity. Wetness represents interfacial geometry of the liquid phase (Takei, 1998). Wetness increases with increasing liquid volume fraction (ϕ), and the increase in the rate of wetness becomes faster when the dihedral angle (θ_d) gets smaller (von Barge and Waff, 1986). Therefore, wetness is given as a function of the liquid volume fraction and dihedral angle, and by substituting $\psi(\phi, \theta_d)$ into the macroscopic properties, including bulk modulus, shear modulus, bulk viscosity, and shear velocity, of the partially molten media under thermodynamic equilibrium, the macroscopic properties can be shown as a function of the liquid volume fraction and dihedral angle (Takei, 1998). For example, the shear wave velocity of partially molten media decreases with increasing liquid volume fraction, and the slope of the relationship between the shear wave velocity and liquid volume fraction becomes more negative when the dihedral angle gets smaller (Takei, 1998). The shear wave velocity of isotropic porous media in a low-frequency range, in which relative motion of the two phases is suppressed due to a viscous coupling, is given by:

$$\beta = \sqrt{(1-\phi)\,\mu_{sk}/\overline{\rho}}\,, \qquad (7.4)$$

δ

where μ_{sk} is the shear modulus of the solid skeleton, and $\bar{\rho}$ is the average density of the composites (Biot, 1956). Based on the correlation between configurational entropy and porosity (or liquid volume fraction), shear velocity can be expressed as:

$$\beta \propto \sqrt{\left(1 - S^{config}\right)\mu_{sk} / \bar{\rho}}\,. \qquad (7.5)$$

Furthermore, shear viscosity of rock-melt composites (η) in the earth's interior is inversely proportional to the liquid volume fraction (ϕ) in partially saturated porous media (e.g., $\eta^{-1} \propto \exp(\phi)$) (Takei, 1998; Takei, 2005; Takei and Holtzman, 2009). Therefore, on the basis of the inverse correlation between the liquid volume fraction (i.e., porosity) and configurational entropy, the shear viscosity in the melts can be expressed using the configurational entropy:

$$\eta^{-1} \propto \exp\left(S^{config}\right). \qquad (7.6)$$

The results suggest that shear viscosity decreases with increasing configurational entropy of the fluids that are partially saturated in rocks. Note that equation (7.6) shows remarkable similarity of the fundamental microscopic relationship between configurational entropy of supercooled liquids and the viscosity of melts on the basis of the Adam-Gibbs theory (equation 7.2) (Adam and Gibbs, 1965; Richet, 1984; Lee, 2005), suggesting that a relationship derived from equation (7.6) is robust and can be applied to diverse networks, regardless of the length scale of the constituent objects. A recent study on the elastic properties and viscosity of solid-liquid composites suggested that normalized bulk modulus, shear modulus, bulk

δ

viscosity, and shear viscosity exponentially increases with increasing contiguity, and the changes in viscosity are larger than those of elastic properties (Takei and Holtzman, 2009). Therefore, configurational entropy can be a complementary parameter for describing elastic properties and shear viscosity of porous media.

Fractal dimension analysis has been applied mainly to natural objects including porous media comprised of rocks and soils to describe hydrological processes. Recently, fractal dimension analysis has been applied to diverse geological processes. For example, it has been used to quantitatively characterize the shapes of volcanic particles that are not truly fractal and suggested that fractal dimensions are useful for understanding fragmentation and transport processes associated with volcanic eruptions (Maria and Carey, 2002). Fractal dimension analysis has been also applied to fracture networks with implications for the degree of fracture connectivity and the propensity for fracture flow and the transport of miscible or immiscible chemicals (Bonnet et al., 2001; Roy et al., 2007). As shown in previous studies, cube counting fractal dimension analyzed in this study can be applied to diverse processes including porous media shown in chapter 4. A recent study on the pore structure of volcanic clasts suggested that permeability can be expressed by electrical tortuosity (Wright et al., 2009) which is defined by:

$$\tau = L_e / L \,, \tag{7.7}$$

where L_e is the actual length followed by the flow path, and L is the sample length. Experimental results of this study showed that permeability can be

δ

expressed as (Wright et al., 2009):

$$k = b\tau^{d}, \tag{7.8}$$

where b is a scaling parameter reflecting the effects of both average hydraulic radius and porosity, and d determines the rate at which permeability decreases with
increasing tortuosity and likely reflects departure of the cross-flow path from that of simple straight tubes (Wright et al., 2009). It was shown that permeability can be expressed as a function of cube counting fractal dimension and porosity, and therefore the correlation among permeability, electric tortuosity, and cube counting fractal dimension can be found.

For the processes in the Earth's interior, cube counting fractal dimension can be applied to describe P-wave attenuation and velocity in partially molten rock. Seismic attributes like attenuation and velocity dispersion are sensitive to the pore- fluid distribution in the rocks. That is because seismic waves induce local pressure gradients between fluid patches of different elastic properties and consequently induce local fluid flows that are accompanied by internal friction (Pride and Masson, 2006; Müller et al., 2008). From the random patchy saturation model (Toms et al., 2007), P-wave modulus is expressed as:

$$\tilde{H}(\omega; S) = H^{W}\left(1 + \delta\left[\tau\xi^{2} + (\tau - 1)\xi\right]\right), \tag{7.9}$$

where ω is frequency; S is saturation; τ is a coefficient, and H^{W} is Wood's P-wave modulus (Müller et al., 2008). In this equation, the frequency dependent function ξ is given by:

δ

$$\xi(\omega;S) = 2\nu(ka)^2 \, {}_2F_1\left([1,\nu+1],\frac{1}{2},-k^2a^2\right) + i\sqrt{2}\pi^2 k^3 \Phi(k), \qquad (7.10)$$

where a is the correlation length; k is permeability; Φ(*k*) is the von Kármán spectrum function, and ν is the Hurst exponent which is related with fractal dimension of surface area (D = 3 - ν) (Müller et al., 2008). The P-wave modulus is connected to attenuation and phase velocity via (Pride and Masson, 2006; Müller et al., 2008):

$$Q^{-1}(\omega;S) = \frac{\mathrm{Im}\,\tilde{H}}{\mathrm{Re}\,\tilde{H}} \propto \omega^{-\nu}, \qquad (7.11)$$

$$v_P(\omega;S) = \sqrt{\frac{\mathrm{Re}\,\tilde{H}}{\overline{\rho}}}. \qquad (7.12)$$

These equations show that the fractal dimension of fluid patch is one of the parameters explaining P-wave attenuation. Fluid patches are distributed in three dimensional space in the Earth's interior whereas previous studies have used 2D images. Therefore, cube-counting fractal dimension for fluid patches would be a more accurate parameter for describing complex networks than the conventional fractal dimension obtained from 2D images.

References

Adam, G. and Gibbs, J. H. (1965) On the temperature dependence of cooperative relaxation properties in giass forming liquids. Journal of Chemical Physics, 43, 139-146.

Adam, G. and Gibbs, J. H. (1965) On the temperature dependence of cooperative relaxation properties in glass-forming liquids. J. Chem. Phys., 43, 139-146.

Bear, J. (1972) Dynamics of Fluids in Porous Media. New York, American Elsevier, 764 p.

Biot, M. A. (1956) Theory of propagation of elastic waves in a fluid-saturated porous solid, 1. Low-frequency range. Journal of the Acoustical Society of America, 28, 168-178.

Bonnet, E., Bour, O., Odling, N. E., Davy, P., Main, I., Cowie, P. and Berkowitz, B. (2001) Scaling of fracture systems in geological media. Reviews of Geophysics, 39(3), 347-383.

Lee, S. K. (2005) Microscopic origins of macroscopic properties of silicate melts and glasses at ambient and high pressure: Implications for melt generation and dynamics. Geochimica et Cosmochimica Acta, 69(14), 3695-3710.

Lee, S. K., Kim, H. N., Lee, B. H., Kim, H. I. and Kim, E. J. (2010) Nature of chemical and topological disorder in borogermanate glasses: insights from B-11 and O-17 solid-state NMR and quantum chemical calculations. Journal of Physical Chemistry B, 114, 412-420.

Lee, S. K. and Stebbins, J. F. (1999) The degree of aluminum avoidance in aluminosilicate glasses. American Mineralogist, 84, 937-945.

Müller, T. M., Toms-Stewart, J. and Wenzlau, F. (2008) Velocity-saturation

relation for partially saturated rocks with fractal pore fluid distribution. Geophysical Research Letters, 35, L09306.

Maria, A. and Carey, S. (2002) Using fractal analysis to quantitatively characterize the shapes of volcanic particles. Journal of Geophysical Research, 107(B11), 2283.

Pride, S. R. and Masson, Y. J. (2006) Acoustic attenuation in self-affine porous structures. Physical Review Letters, 97, 184301.

Reiss, H. (1992) Statistical geometry in the study of fluids and porous media. Journal of Physical Chemistry, 96, 4736-4747.

Richet, P. (1984) Viscosity and configurational entropy of silicate melts. Geochimica et Cosmochimica Acta, 48, 471-483.

Roy, A., Perfect, E., Dunne, W. M. and McKay, L. D. (2007) Fractal characterization of fracture networks: An improved box-counting technique. Journal of Geophysical Research, 112, B12201.

Takei, Y. (1998) Constitutive mechanical relations of solid-liquid composites in terms of grain-boundary contiguity. Journal of Geophysical Research, 103(B8), 18183-18203.

Takei, Y. (2005) Deformation-induced grain boundary wetting and its effects on the acoustic and rheological properties of partially molten rock analogue. Journal of Geophysical Research-Solid Earth, 110, B12203.

Takei, Y. and Holtzman, B. K. (2009) Viscous constitutive relations of solid-liquid composites in terms of grain boundary contiguity: 1. Grain boundary diffusion control model. Journal of Geophysical Research, 114, B06205.

Toms, J., Muller, T. M. and Gurevich, B. (2007) Seismic attenuation in porous rocks with random patchy saturation. Geophysical

Prospecting, 55(5), 671-678.

von Barge, N. and Waff, H. S. (1986) Permeabilities, interfacial areas and curvatures of partially molten systems: Results of computations of equilibrium microstructures. Journal of Geophysical Research, 91, 9261-9276.

Wright, H. M. N., Cashman, K. V., Gottesfeld, E. H. and Roberts, J. J. (2009) Pore structure of volcanic clasts: Measurements of permeability and electrical conductivity. Earth and Planetary Science Letters, 280, 93-104.

Appendix. Abstracts Published in Korean Journal

A1. The effect of lattice topology on benzyl alcohol adsorption on kaolinite surfaces: Quantum chemical calculations of Mulliken charges and magnetic shielding tensor

Bum Han Lee and Sung Keun Lee

Published in *Journal of Mineralogical Society of Korea*, 20, 313-325 (2007)

Abstract

In order to have better insights into adsorption of organic molecules on kaolinite surfaces, we performed quantum chemical calculations of interaction between three different model clusters of kaolinite siloxane surfaces and benzyl alcohol, with emphasis on the effect of size and lattice topology of the cluster on the variation of electron density and magnetic shielding tensor. Model cluster 1 is an ideal silicate tetrahedral surface that consists of 7 hexagonal rings, and model cluster 2 is composed of 7 ditrigonal siloxane rings with crystallographically distinct basal oxygen atoms in the cluster, and finally model cluster 3 has both tetrahedral and octahedral layers. The Mulliken charge analysis shows that siloxane surface of model cluster 3 undergoes the largest electron density transfer after the benzyl alcohol adsorption and that of model cluster 1 is apparently larger than that of model cluster 2. The difference of Mulliken

charges of basal oxygen atoms before and after the adsorption is positively correlated with hydrogen bond strength. NMR chemical shielding tensor calculation of clusters without benzyl alcohol shows that three different basal oxygen atoms (O3, O4, and O5) in model cluster 2 have the isotropic magnetic shielding tensor as 228.2 ± 3.9, 228.9 ± 3.4, and 222.3 ± 3.0 ppm, respectively. After the adsorption, the difference of isotropic chemical shift varies from 1 to 5.5 ppm for model cluster 1 and 2 while model cluster 2 apparently shows larger changes in isotropic chemical shift. The chemical shift of oxygen atoms is also positively correlated with electron density transfer. The current results show that the adsorption of benzyl alcohol on the kaolinite siloxane surfaces can largely be dominated by a weak hydrogen bonding and electrostatic force (charge-charge interaction) and demonstrate the importance of the cluster size and the lattice topology of surfaces on the adsorption behavior of the organic molecules on clay surfaces.

δ

A2. 3-Dimensional μm-scale pore structures of porous earth materials: NMR micro-imaging study

Bum Han Lee and Sung Keun Lee

Published in *Journal of Mineralogical Society of Korea*, 22, 313-324 (2009)

Abstract

We explore the effect of particle shape and size on 3-dimensional (3D) network and pore structure of porous earth materials composed of glass beads and silica gel using NMR micro-imaging in order to gain better insights into relationship between structure and the corresponding hydrologic and seismological properties. The 3D micro-imaging data for the model porous networks show that the specific surface area, porosity, and permeability range from 2.5 to 9.6 mm^2/mm^3, from 0.21 to 0.38, and from 11.6 to 892.3 D (Darcy), respectively, which are typical values for unconsolidated sands. The relationships among specific surface area, porosity, and permeability of the porous media are relatively well explained with the Kozeny equation. Cube counting fractal dimension analysis shows that fractal dimension increases from ~2.5-2.6 to 3.0 with increasing specific surface area from 2.5 to 9.6 mm^2/mm^3, with the data also suggesting the effect of porosity. Specific surface area, porosity, permeability, and cube counting fractal dimension for the natural mongolian sandstone are 0.33 mm^2/mm^3, 0.017, 30.9 mD, and 1.59, respectively. The current results highlight that NMR micro-imaging,

together with detailed statistical analyses can be useful to characterize 3D pore structures of various porous earth materials and be potentially effective in accounting for transport properties and seismic wave velocity and attenuation of diverse porous media in earth crust and interiors.

A3. Geophysical implications for configurational entropy and cube counting fractal dimension of porous networks: insights from random packing simulations

Bum Han Lee and Sung Keun Lee

Published in *Journal of Mineralogical Society of Korea*, 23, 367-375 (2010)

Abstract

Understanding the interactions between earth materials and fluids is essential for studying the diverse geological processes in the Earth's surface and interior. In order to better understand the interactions between earth materials and fluids, we explore the effect of specific surface area and porosity on structural parameters of pore structures. We obtained 3D pore structures, using random packing simulations of porous media composed of single sized spheres with varying the particle size and porosity, and then we analyzed configurational entropy for 2D cross sections of porous media and cube counting fractal dimension for 3D porous networks. The results of the configurational entropy analysis show that the entropy length decreases from 0.8 to 0.2 with increasing specific surface area from 2.4 to 8.3 mm^2/mm^3, and the maximum configurational entropy increases from 0.94 to 0.99 with increasing porosity from 0.33 to 0.46. On the basis of the strong correlation between the liquid volume fraction (i.e., porosity) and configurational entropy, we suggest that elastic properties and viscosity of mantle melts can be expressed using configurational entropy. The results of

the cube counting fractal dimension analysis show that cube counting fractal dimension increases with increasing porosity at constant specific surface area, and increases from 2.65 to 2.98 with increasing specific surface area from 2.4 to 8.3 mm^2/mm^3. On the basis of the strong correlation among cube counting fractal dimension, specific surface area, and porosity, we suggest that seismic wave attenuation and structural disorder in fluid-rock-melt composites can be described using cube counting fractal dimension.

요약 (국문초록)

지표 및 지구 내부에서 일어나는 다양한 지질학적 현상은 이를 구성하는 지구물질의 거시적 특성으로 설명되며 이는 원자 단위에서 마이크로미터 단위에 이르는 미시적 구조에 의해 결정된다. 따라서 지구물질의 미시적 구조를 관찰하고 이해하는 것은 다양한 지질학적 현상을 이해하는데 있어서 중요한 역할을 한다. 지구물질과 유체의 상호작용은 지표 및 지구 내부에서 일어나는 가장 중요한 현상 중 하나이다. 이를 이해하는 것은 지표에서 저류암 내 유류의 이동 및 추출, 퇴적물 내 오염물의 이동, 이산화탄소 저장 등과 같은 산업적, 환경적으로 중요한 문제들과 더불어 지구 내부에서 암석-부분 용융체-유체의 복합체에 의한 지진파 감쇠 등 지구물리적 현상들을 평가하고 예측하는 데 있어서 중요한 역할을 한다. 이러한 지구물질과 유체의 상호작용은 다양한 길이 단위에서 관찰이 가능하며 각각의 길이 단위에서 중요한 정보들을 얻을 수 있다. 본 연구에서는 원자 단위에서 일어나는 지구물질과 유체의 상호작용에 대해 양자화학계산을 이용하여 흡착 구조, 물성, 구조-물성 간 관계를 예측하고, 마이크로미터 단위에서 지구물질로 이루어진 다공성 매질 내 유체의 분포와 상호작용에 대해 핵자기공명 현미영상을 이용하여 관찰하였다.

양자화학계산 연구를 통해 비교적 간단한 구조의 유기 분자와 점토광물인 벤질 알코올의 캐올리나이트 표면 흡착에 대한 평형 상태의 구조, 결합 에너지, 핵자기공명 화학 차폐 텐서를 계산함으로써 원자

단위의 미시적 구조, 결합에서 예측할 수 있는 물성, 미시적 구조와 물성 간의 관계를 나타내는 변수를 이론적으로 예측하였다. 흡착 구조는 벤질 알코올이 약한 수소 결합과 분산력에 의해 캐올리나이트 사면체 표면에 흡착되며, 두 개의 수소 결합에 의해 캐올리나이트 팔면체 표면에 흡착되는 것을 보여준다. 결합 에너지는 벤질 알코올이 사면체 표면에 비해 팔면체 표면에 더 강하게 흡착되는 것을 보여준다. 결정학적 위상이 서로 다른 사면체 표면에 대한 결합 에너지는 비슷한 값을 갖지만 자세한 흡착 구조는 서로 다르게 나타나며 이는 결정학적 위상이 흡착에 미치는 영향을 보여준다. 사면체 표면의 산소에 대한 등방 자기 차폐는 흡착 후에 4-5 ppm 감소하는 것으로 예측되었고, 이는 산소 주변에 대한 고분해능 고상핵자기공명 분광분석을 통해 유기물과 규산염 표면의 흡착을 관찰할 수 있음을 제시한다.

첫 번째 핵자기공명 현미영상을 이용한 연구에서는 공극 구조와 공극 구조를 나타내는 매개 변수(상자집계 프랙탈 차원, 라쿠나리티, 구성 엔트로피), 그리고 매개 변수와 수리지질학적 특성의 관계를 정립하였다. 삼차원 공극 구조에 대한 상자집계 프랙탈 차원은 일정한 공극률에서 비표면적이 증가함에 따라 증가하고 일정한 비표면적에서 공극률이 증가함에 따라 증가한다. 약 0.47 mm에 해당하는 상자 크기에서의 라쿠나리티는 비표면적으로 잘 설명된다. 최대 구성 엔트로피는 공극률이 증가함에 따라 증가하고, 공극에 대한 엔트로피 길이는 비표면적이 증가함에 따라 감소하며 공극의 배위수 계산에 사용될 수 있다. 공극률, 비표면적, 투수율에 대한 관계는 코제니-카르만 식의 예측과 일치하며, 본 연구에서는 투수율을 상자집계 프랙탈 차원과

공극률의 함수로 나타낼 수 있음을 제시한다. 본 연구의 결과는 암석, 용융체, 유체로 이루어진 복합체의 탄성과 점성에 대한 지구물리학적 의의를 갖는다.

두 번째 핵자기공명 현미영상 연구에서는 실리콘 오일로 채워진 다공성 매질 내 물이 통과된 시간에 따라 물의 분포를 약 50 μm의 분해능으로 영상화하고, 다공성 매질을 구성하는 입자의 크기와 모양이 물의 분포에 미치는 영향을 조사하였다. 물의 부피, 비표면적, 상자집계 프랙탈 차원은 물이 주입된 시간에 따라 단일 지수형 회복 함수로 잘 설명된다. 글래스 비드로 이루어진 시료의 점근값은 실리카젤로 이루어진 시료에 비해 더 큰 값을 가지며 이는 두 시료의 공극 구조에 차이에 기인한다. 모든 매개 변수의 융합률은 투수율에 반비례하며 이는 융합률이 다공성 매질의 거동 특성과 관련됨을 의미한다. 본 연구는 서로 섞이지 않는 유체로 채워진 다공성 매질의 공극 구조에서 다공성 매질을 구성하는 입자가 물의 분포 특성에 중요한 역할을 하는 것을 보여준다.

다공성 매질 내 유체에 대한 고분해능 핵자기공명 현미영상은 수리지질학과 지구물리학 분야에서 다양한 적용이 가능할 것으로 예상된다. 그러나, 일반적으로 다공성 매질에 대해서는 유체의 양이 적고, 스핀-스핀 이완 시간이 빠르다는 단점 때문에 고분해능으로 영상을 얻기에 한계가 있다. 본 연구에서는 고자기장(18.8 T) 과 고구배(300 G/cm)의 핵자기공명 현미영상 기기를 이용해 비교적 유체의 양이 많이 포함된 몽고 사막의 사암, 두석, 글래스 비드로 이루어진 다공성 매질에 대해 고분해능 영상의 가능성을 조사하였다. 본 연구에서는 약 75 μm의

작은 입자로 이루어진 다공성 매질 내 유체의 영상을 얻었고, 공극률이 높은 시료에 대해 약 19.5 μm의 고분해능 영상을 얻었다. 이러한 핵자기공명 현미영상 기법의 발달에 따라 다공성 매질 내 기체, 액체 등 여러 종류의 유체를 다양한 핵종으로 영상화하는 등의 연구가 가능할 것으로 기대되며, 지구물질과 유체의 상호작용을 미시적으로 관찰하고 이해함으로써 거시적 성질을 예측하는데 도움을 줄 수 있을 것으로 보인다.

……

주요어: 양자화학계산, 핵자기공명 현미영상, 지구물질, 유체, 구조-물성 관계,

학번: 2000-20668

감사의 글

이 논문이 나오기까지 대학원 입학 이후 11 년이라는 긴 시간이 걸렸고 그만큼 저는 많은 분들께 신세를 졌습니다. 가장 먼저 지도교수이신 이성근 교수님께 깊이 감사 드립니다. 교수님께서는 진정한 연구자의 자세를 몸소 보여주셨고, 스승으로서 때로는 인생의 선배로서 귀한 가르침을 주셨습니다. 바쁘신 가운데에도 논문 심사를 위해 귀한 시간을 내어주시고 좋은 조언을 해주신 이용일 교수님, 유인석 교수님, 김준모 교수님, 김영석 교수님, 이강근 교수님께 감사 드립니다. 그리고 부족한 저를 제자로 받아주시고 연구자의 길로 이끌어주신 김수진 교수님께 감사 드립니다.

많은 시간을 함께 보내면서 동고동락했던 서울대학교 지구물질과학 연구실의 후배들에게 고마운 마음을 전합니다. 하나같이 착한 후배들은 부족한 선배의 고민을 함께 나누고 어려운 부탁을 묵묵히 들어주었습니다. 이제는 후배라기보다 친구 같은 현나, 어렵게 생각했던 문제들을 항상 쉽게 해결해주었던 유수, 인간 관계에 대해 배울 점이 많은 선영, 항상 밝은 미소로 기분 좋게 만들어주었던 효임, 막내라고 제일 많은 부탁을 했지만 불평 한 번 하지 않고 모두 들어주었던 은정, 함께 보낸 시간은 길지 않지만 어려운 시간 힘이 되어준 새봄이와 현진이, 모두 훌륭한 후배들인데 부족한 선배 만나서 고생이 많았습니다.

제 대학원 생활의 밑거름이 되고 든든한 버팀목이 되어준 광물학 연구실 선배님들께 감사 드립니다. 특히 광물학 연구실 대학원 생활 동안 저를 많이 챙겨주신 김정진 교수님, 이기무 선배님, 이승엽

박사님, 장세정 박사님, 권기덕 박사님께 감사 드립니다. 미국, 영국, 일본 등에서 실험과 학회 일로 만날 때마다 귀한 조언들을 해주시고 맛있는 것도 많이 사주신 이상수 박사님 감사 드립니다. 또한 연구와 직장 생활에 대해 많은 조언을 해주신 이성록 박사님, 장세원 박사님, 손병국 박사님, 최헌수 박사님, 권석기 선배님께 감사 드립니다.

제가 연구자의 길을 걸을 수 있도록 기회를 주시고 논문을 마무리할 수 있도록 배려해주신 한국지질자원연구원의 장호완 원장님, 정소걸 본부장님, 고상모 실장님과 해외광물자원연구실 선배님들, 지세정 실장님과 국내/북한자원연구실 선배님들께 감사 드립니다. 그리고 힘든 일정 중에도 저를 응원해주시고 여러모로 도와주셨던 윤소정 박사님, 강일모 박사님, 박계순 박사님, 오현주 박사님, 대학원 후배 광민이와 동기 분들께 감사의 말씀을 전합니다.

핵자기공명 현미영상 실험을 위해 불편함을 무릅쓰고 많이 도와주셨던 NICEM의 박미영 선생님, 김윤희 선생님, 기초과학지원 연구원의 조지현 선생님께 감사 드립니다. 양자화학계산을 위한 수퍼 컴퓨터 사용 시 항상 친절하게 도와주셨던 전산원의 정상혁 선생님께도 감사 드립니다. 영상 자료 처리를 위한 MATLAB 코딩을 도와준 후배 영균이에게도 고마움을 전합니다.

공부한다는 핑계로 자주 만나진 못했지만 친구들은 힘들고 어려울 때 아주 큰 힘이 되어 주었습니다. 멀리 떨어져 있지만 마음만은 가까운 남욱, 언제 만나도 며칠 만에 만난 것 같은 선영, 항상 내 일을 자신의 일처럼 생각해주는 승우, 고등학교, 대학교, 대학원, 직장까지 모두 동기이면서 고민을 함께 나누었던 희성, 그리고 한성과학고등학교

1기 동기들과 서울대학교 지질해양학과군 95학번 동기들 모두 고맙습니다.

부족한 저로 인해 마음 고생이 크셨지만 내색 한 번 하지 않으시고 저를 아들로 대해주시며 큰 사랑을 베풀어주신 장인 어른, 장모님께 깊이 감사 드립니다. 공부한다는 핑계로 제대로 한 번 챙겨주지도 못한 처제와 동서에게도 고마움을 전합니다. 그리고 제가 한참 바쁠 때 아내와 상준이를 잘 보살펴주신 외숙모님께도 감사 드립니다.

아들이 태어나고 나니 부모님의 사랑이 어떤 것인지 조금은 깨닫게 된 것 같습니다. 그러한 사랑으로 저를 길러주시고 지켜봐 주신 아버지, 어머니께 깊이 감사 드립니다. 주말에도 바쁘게 일하면서 가족에게 헌신하는 동생 도한에게도 고마움을 전합니다.

귀여운 나의 아들 상준이, 어려울 때마다 힘을 낼 수 있는 원동력이 되어 주었습니다. 고마운 아빠의 마음을 전하고 싶습니다.

무엇보다도, 이 논문을 마무리할 수 있도록 제 곁에서 오랜 시간 인내와 사랑으로 지켜봐 주고 도와준 아내에게 감사의 마음을 전합니다. 부족한 남편으로 인해 정말 고생이 많았는데, 아내에게 진 이 빚은 평생 갚으면서 살아도 모자랄 것 같습니다.

사랑하는 아내 지은에게 이 논문을 바칩니다.

이학박사학위논문

Probing interactions between earth materials and fluids at the atomic and micrometer scale: Insights from quantum chemical calculations and NMR micro-imaging

지구물질과 유체의 상호작용에 대한 원자 단위와 마이크로미터 단위의 관찰: 양자화학계산과 핵자기공명 현미영상 연구

A dissertation in partial fulfillment of the requirements for the degree of Doctor of Philosophy

2011년 2월

서울대학교 대학원
지구환경과학부

이 범 한

Abstract

Probing interactions between earth materials and fluids at the atomic and micrometer scale: Insights from quantum chemical calculations and NMR micro-imaging

Bum Han Lee
School of Earth and Environmental Sciences
The Graduate School
Seoul National University

Interactions between earth materials and fluids is one of the most important processes in the Earth's surface and interior, and thus, the probing and understanding the interaction play an important role in the estimation and prediction of industrial and environmental processes in the Earth's surface and geophysical processes in the Earth's interior. In this study, the structure, property, and structure-property relationships for interactions between earth materials and fluids were estimated by quantum chemical calculations at the atomic scale and probed by NMR micro-imaging at the micrometer scale.

In quantum chemical calculations study, the effect of the lattice topology (ideal hexagonal rings vs. ditrigonal rings) and cluster size of

model clusters (three-ring *vs.* seven-ring clusters) on the nature of benzyl alcohol adsorption on kaolinite surfaces were investigated with an emphasis on the equilibrium configuration, binding energy, and NMR chemical shielding tensors. The optimized structure of benzyl alcohol adsorbed on the tetrahedral layer of kaolinite is characterized by a weak hydrogen bond and dispersion force, and that on the octahedral layer of kaolinite is characterized by two hydrogen bonds. The results for the binding energies indicate a stronger binding energy between benzyl alcohol and octahedral surfaces than that between benzyl alcohol and tetrahedral layers. Although the calculated binding energies for seven-member rings with varying lattice topologies are rather similar, the detailed optimized structures are distinct, demonstrating the effect of lattice topology on the nature of adsorption. The calculated ^{17}O isotropic chemical shieldings of some basal oxygens decrease up to approximately 4–5 ppm after the adsorption, suggesting that the NMR technique may be useful in exploring the nature of adsorption between organic molecules and silicate surfaces.

In the first NMR micro-imaging study, relationships among porosity, specific surface area, structural parameters (D_{cc} and lacunarity), and the corresponding macroscopic properties (configurational entropy and permeability) were established. The D_{cc} of the 3D porous networks increases with increasing specific surface area at constant porosity and with increasing porosity at constant specific surface area. Lacunarity at the intermediate box size (~0.47 mm in the current model sands) was

δ

reproduced well with specific surface area. The maximum configurational entropy increases with increasing porosity, and the entropy length of the pores decreases with increasing specific surface area and was used to calculate the average connectivity among the pores. The correlation among porosity, specific surface area, and permeability is consistent with the prediction from the Kozeny-Carman equation. From the relationship between the permeability and the D_{cc} of pores, permeability can be expressed as a function of the D_{cc} of pores and porosity. This study provides improved insights into the nature of porous media and has useful geophysical implications for elasticity and shear viscosity of complex composites of rock, glasses, melt, and fluids.

In the second NMR micro-imaging study, high resolution images of water distribution in porous media initially saturated with silicone oil were obtained with varying durations of water flows using NMR micro-imaging with up to 50 μm resolution, and the effect of the size and shape of the particles which make up the porous media on the distribution of water was investigated. Volume fractions, specific surface areas, and cube counting fractal dimension of water phase for each sample obtained from 3D spin echo images with increasing duration of water injection and were well fitted to single-exponential recovery functions. Asymptotic values for the samples of glass beads were much larger than those for the silica gel samples, mostly because the pore structures of the silica gel are different from those of the glass beads. Convergence rates of all the properties were inversely proportional to the permeability, indicating that the convergence

δ

rates were correlated to the transport property of the porous media. This study shows that the pore structure of particles which make up the porous media plays an important role in the water distribution of porous media which was initially saturated with an immiscible fluid.

High resolution NMR micro-imaging of the fluids in porous media may shed some light on diverse applications in hydrogeology and geophysics. However, it is difficult to obtain high resolution images of fluids in porous media using NMR micro-imaging due to the low amounts of fluids and short spin-spin relaxation times. In the final NMR micro-imaging study, the possibility of high resolution images of fluids in porous media were investigated using Mongolian desert sandstone, natural pisolite, and samples of glass beads with a small sample size, high porosity, strong magnetic field (18.8 T), and strong field gradient (300 G/cm). The results show that NMR micro-imaging can be used to obtain images of the porous media comprised of grain sizes down to 75 μm with resolutions of up to 19.5 μm/pixel for highly porous media.

……

Keywords: quantum chemical calculations, NMR micro-imaging, earth materials, fluids, structure-property relationship,

Student Number: 2000-20668

Table of Contents

List of Figures

δ

List of Tables

δ

Chapter 1. Introduction

Diverse geological processes in the Earth's surface and interior depend on the macroscopic properties of earth materials which are determined by their microscopic scale (from Å to μm) local structures. For example, coordination environments and topological disorder of atoms in silicate melts and glasses play an crucial role in the generation, migration, and dynamics of magma (Lee, 2005; Lee et al., 2008), and those of germanate glasses may explain the large compressibility and nonlinear changes in density (Lee and Lee, 2006; Lee et al., 2010). Therefore, probing microscopic scale configuration is essential in understanding and predicting macroscopic properties and diverse geological processes.

The interactions between earth materials and fluids are one of the most important processes in the Earth's surface and interior. In the Earth's surface, the processes include pollutant migration, bioavailability, and biodegradation in soils (Knezovich et al., 1987; Kowalska et al., 1994), oil recovery from reservoir rocks (Lake, 1989), and underground storage of CO_2 and nuclear waste (Hendriks and Blok, 1993). In the Earth's interior, the processes take place in rock-melt-fluid composites (Takei, 1998), and affect the elastic properties, viscosity, and seismic wave attenuation of the composites. Therefore, probing and understanding these interactions play an important role in the estimation and prediction of processes in the Earth's surface and interior.

Interactions between earth materials and fluids can be probed at diverse length scales. For example, hydrologic cycle is estimated on a global length scale (hundreds of kilometers) (Dirmeyer and Brubaker, 2007), and the relationship between the variability of the topography, soil, and rainfalls and the storm response can be seen at the catchment scale (in the order of kilometers) (Wood et al., 1990). In this study, the interactions between earth materials and fluids were probed using quantum chemical calculations and NMR micro-imaging at the atomic and micrometer scale, respectively.

In the research area for silicate glasses and melts, there are three fundamental questions: the atomic and nano-scale structures and the extent of disorder of these systems, the effects of variation in atomic-scale disorder on the macroscopic properties of melts, and the effect of these properties on geological processes, such as generation, migration, and dynamics of magmas (Lee, 2005). The structure, the property, and the structure-property relationship are also key questions on the interactions between earth materials and fluids. This study's aim was for the systematic exploration of the structures, properties, and structure-property relationships for the interactions between earth materials and fluids from the information obtained at the atomic and micrometer scale.

This thesis is composed of 7 chapters including this introduction and appendix. In chapter 2, summary of the principles of quantum chemical calculations and NMR micro-imaging and pulse sequences of the NMR micro-imaging used in this study are presented. In chapter 3, probing

the interactions between kaolinite and benzyl alcohol at the atomic length scale using quantum chemical calculations and the detailed equilibrium configuration of the adsorption (for the microscopic structure), binding energies (for the macroscopic properties), and NMR parameters (for the parameter manifesting the structure-property relationship) are presented (Lee and Lee, 2009). In chapter 4, imaging of 3D porous networks filled with fluids at micrometer length scale using NMR micro-imaging (for the structure), quantifying them with parameters including cube counting fractal dimension, lacunarity, and configurational entropy (for the properties), and exploring the relationship between structural parameters and hydrological property such as permeability (for the structure-property relationship) are presented (Lee and Lee, submitted). In chapter 5, imaging of the water distribution in porous media initially saturated with silicone oil at the micrometer length scale using NMR micro-imaging (for the structure), quantification of the water distribution with structural parameters (for the property), and investigation of the relationship between a parameter characterizing the water distribution and permeability (for the structure-property relationship) are presented (Lee and Lee, in preparation). In chapter 6, in order to extend NMR micro-imaging to diverse applications in porous media research, high resolution images of fluid distribution in porous sandstone, natural pisolite, and glass beads column are presented (Lee et al., in preparation). In chapter 7, geophysical implications of this study are discussed. This thesis suggests that the parameters including configurational entropy and cube counting fractal dimension are also

useful in describing the processes in the Earth's interior in addition to the processes in the Earth's surface. Finally, in the appendix, abstracts of papers published in domestic journals are presented. They include a quantum chemical calculations study on Mulliken charges and magnetic shielding tensor for benzyl alcohol adsorption on kaolinite tetrahedral surfaces (Lee and Lee, 2007), a NMR micro-imaging study on porous media composed of glass beads, silica gel, and porous sandstone (Lee and Lee, 2009), and a random packing simulations study on geophysical implications for configurational entropy and cube counting fractal dimension of porous networks (Lee and Lee, 2010)..

d

References

Dirmeyer, P. A. and Brubaker, K. L. (2007) Characterization of the global hydrologic cycle from a back-trajectory analysis of atmospheric water vapor. Journal of Hydrometeorology, 8, 20-37.

Hendriks, C. A. and Blok, K. (1993) Underground storage of carbon dioxide. Energy Conversion and Management, 34, 945-957.

Knezovich, J. P., Harrison, F. L. and Wilhelm, R. G. (1987) The bioavailability of sediment-sorbed organic chemicals: A review. Water, Air, snd Soil Pollution, 32, 233-245.

Kowalska, M., Guler, H. and Cocke, D. L. (1994) Interactions of clay minerals with organic pollutants. The Science of the Total Environment, 141, 223-240.

Lake, L. W. (1989) Enhanced Oil Recovery. Old Tappan, Prentice Hall Inc.

Lee, B. H., Cho, J. H. and Lee, S. K. (in preparation) High resolution NMR micro-imaging of fluids in porous media.

Lee, B. H. and Lee, S. K. (2007) The effect of lattice topology on benzyl alcohol adsorption on kaolinite surfaces: Quantum chemical calculations of Mulliken charges and magnetic shielding tensor. Journal of Mineralogical Society of Korea, 20(4), 313-325.

Lee, B. H. and Lee, S. K. (2009) 3-dimensional μm-scale pore structures of porous earth materials: NMR micro-imaging study. Journal of Mineralogical Society of Korea, 22(4), 313-324.

Lee, B. H. and Lee, S. K. (2010) Geophysical implications for configurational entropy and cube counting fractal dimension of porous networks: insights from random packing simulations. Journal of Mineralogical Society of Korea, 23(4), 367-375.

Lee, B. H. and Lee, S. K. (2009) Effect of lattice topology on the adsorption of benzyl alcohol on kaolinite surfaces: Quantum chemical calculations of geometry optimization, binding energy, and NMR chemical shielding. American Mineralogist, 94, 1392-1404.

Lee, B. H. and Lee, S. K. (in preparation) Probing of water distribution in porous model sands with immiscible fluids: Nuclear magnetic resonance micro-imaging study.

Lee, B. H. and Lee, S. K. (submitted) Effects of specific surface area and porosity on cube counting fractal dimension, lacunarity, and configurational entropy of porous networks of model sands: insights from random packing simulations and NMR micro-imaging. Journal of Geophysical Research.

Lee, S. K. (2005) Microscopic origins of macroscopic properties of silicate melts and glasses at ambient and high pressure: Implications for melt generation and dynamics. Geochimica et Cosmochimica Acta, 69(14), 3695-3710.

Lee, S. K., Kim, H. N., Lee, B. H., Kim, H. I. and Kim, E. J. (2010) Nature of chemical and topological disorder in borogermanate glasses: insights from B-11 and O-17 solid-state NMR and quantum chemical calculations. Journal of Physical Chemistry B, 114, 412-420.

Lee, S. K. and Lee, B. H. (2006) Atomistic origin of germanate anomaly in GeO_2 and Na-germanate glasses: Insights from two-dimensional ^{17}O NMR and quantum chemical calculations. Journal of Physical Chemistry B, 110, 16408-16412.

Lee, S. K., Lin, J. F., Cai, Y. Q., Hiraoka, N., Eng, P. J., Okuchi, T., Mao, H. K., Meng, Y., Hu, M. Y., Chow, P., Shu, J. F., Li, B. S., Fukui, H., Lee, B. H., Kim, H. N. and Yoo, C. S. (2008) X-ray Raman scattering study

of $MgSiO_3$ glass at high pressure: Implication for triclustered $MgSiO_3$ melt in Earth's mantle. Proceedings of the National Academy of Sciences of the United States of America, 105(23), 7925-7929.

Takei, Y. (1998) Constitutive mechanical relations of solid-liquid composites in terms of grain-boundary contiguity. Journal of Geophysical Research, 103(B8), 18183-18203.

Wood, E. F., Sivapalan, M. and Beven, K. (1990) Similarity and scale in catchment storm response. Reviews of Geophysics, 28, 1-18.

δ

Chapter 2. Methods

2.1. Quantum Chemical Calculations

Quantum chemical calculations can provide complementary information to experiments or estimate data that cannot be obtained by experimental methods due to limitations. In quantum chemical calculations, the energy and other related properties of a system are obtained by solving the Schrödinger equation (Foresman and Frisch, 1996; McQuarrie and Simon, 1997);

$$H\Psi = E\Psi . \qquad (2.1)$$

where H is the Hamiltonian operator, E is the energy (an eigen value of the Hamiltonian operator), and Ψ is the wave function. However, exact solutions to the Schrödinger equation for a multi-electron molecule are not computationally practical, and therefore, quantum chemical calculations use approximation methods for its solutions (Foresman and Frisch, 1996; McQuarrie and Simon, 1997). One of the most popular approximation methods is the Hartree-Fock method where the solution is obtained by self-consistent field for multi-electron wave function (Fukutome, 1981). Another popular approximation method is the density functional theory where electron correlations are treated by density functional of electrons. Among density functional theory methods, B3LYP (Becke, 3 parameters, Lee-Yang-Parr) is the most frequently used method (Lee et al., 1988; Becke, 1993). By using these approximation methods, various properties including single

δ

point energy, optimized geometry, transitional state geometry, and vibrational frequency of a system can be obtained (Foresman and Frisch, 1996). With the improvement of computation speed, it can use large clusters with hundreds of atoms. Therefore, it might be a suitable tool for probing the interaction between earth materials and fluids at the atomic length scale.

2.2. NMR Micro-imaging

NMR micro-imaging refers to NMR imaging in which a high spatial resolution (100 μm <) is obtained. The difference between NMR micro-imaging and MRI (magnetic resonance imaging) which is widely used in clinical purposes is the size of the samples and the strength of the magnetic field; in MRI, human bodies and animals are objectives in which the diameters are generally tens of centimeters and the magnetic field generally ranges from 0.2 to 3 Tesla, and in NMR micro-imaging, the size of samples ranges from a few millimeters to a few centimeters and the magnetic field generally ranges from 4.7 to 21.1 Tesla.

2.2.1. Principles of NMR imaging

A key to understanding NMR imaging is a field gradient (Callaghan, 1991; Blümich, 2000). The linear relationship between NMR frequency and space coordinate is obtained by restricting the space dependence of the magnetic field to the field gradient (Levitt, 2001),

δ

$$G_x = \frac{\partial B_z}{\partial x}. \qquad (2.2)$$

In this case, each point along the x-axis of the sample is characterized by a different resonance frequency. Figure 2-1 shows the schematic diagram of field gradient in the x-direction and the corresponding NMR signals.

In general, the components $\boldsymbol{G}_{kl}$ of the magnetic-field gradient tensor **G** are defined as the spatial derivatives of the magnetic field,

$$G_{kl} = \frac{\partial B_k}{\partial x_l} \qquad (2.3)$$

Because the magnetic field $\boldsymbol{B}$ is a vector with components B_x, B_y, and B_z, the magnetic-field gradient is a second-rank tensor with nine components. It can be written as the dyadic product of the gradient operator ∇ and the magnetic field,

$$\mathbf{G} = \nabla B = \begin{bmatrix} G_{xx} & G_{xy} & G_{xz} \\ G_{yx} & G_{yy} & G_{yz} \\ G_{zx} & G_{zy} & G_{zz} \end{bmatrix} \qquad (2.4)$$

The gradient field is generated by an extra set of coils and is added to the homogeneous magnetic fields B_0 in the z-direction and the weak time-dependent field B_{rf} perpendicular to B_0,

$$B = B_0 + B_{rf} + \mathbf{G}r \qquad (2.5)$$

where r is the space vector with components x, y, and z. When $B_{rf} = 0$, the NMR frequency is dependent on space,

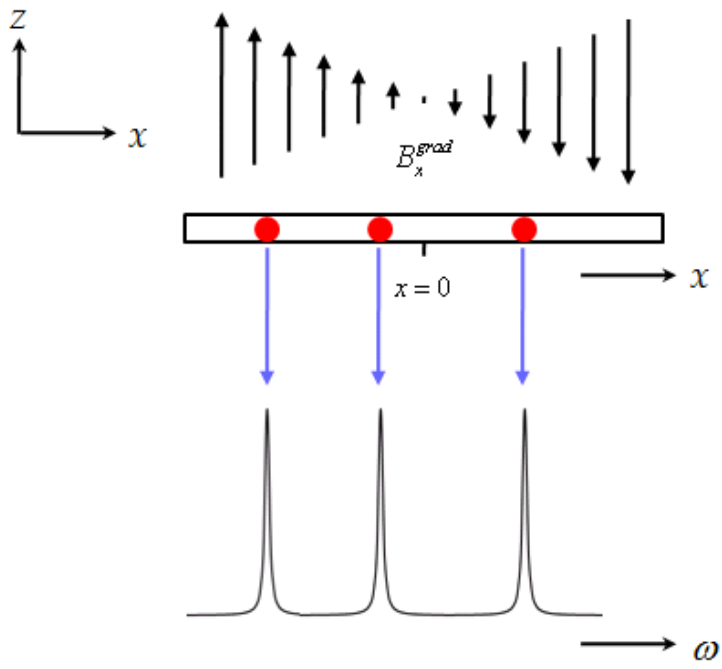

Figure 2-1. A diagram showing field gradient, nuclei lying in x-direction, and the corresponding NMR signals which are different in frequency domain because Larmor frequencies varied due to the field gradient (modified from Levitt (2001)).

δ

$$\begin{aligned}\varpi_0(r) &= \gamma\left|\boldsymbol{B}\right| = \gamma\left|B_0 + \mathbf{G}r\right| \\ &= \gamma[(B_{0x} + G_{xx}x + G_{xy}y + G_{xz}z)^2 \\ &+(B_{0y} + G_{yx}x + G_{yy}y + G_{yz}z)^2 \\ &+(B_{0z} + G_{zx}x + G_{zy}y + G_{zz}z)^2]^{1/2}\end{aligned} \tag{2.6}$$

Because $B_{0x} = B_{0y} = 0$, the terms dominating the resonance frequency are given in the last row. Thus only three elements of the gradient tensor determine the resonance frequency in first order. The three relevant terms are often used to form the gradient vector *G*,

$$\begin{pmatrix} G_{zx} \\ G_{zy} \\ G_{zz} \end{pmatrix} \equiv \boldsymbol{G} = \begin{pmatrix} G_x \\ G_y \\ G_z \end{pmatrix}. \tag{2.7}$$

In NMR imaging, the equilibrium magnetization M_0 depends on space *r*. For a 90 degree pulse, the magnetization from the volume element at position *r* is given by

$$M^+(t) = M_0(r)\exp\{\mathrm{i}\varpi_0(r)t\}, \tag{2.8}$$

where $\omega_0(r)$ is the space-dependent NMR frequency. The sum of signals originating from the nuclei at all position *r* is observed, so that Eq. (2.8) needs to be integrated,

$$M^+(t) = \int_{-\infty}^{\infty} M_0(r)\exp(\mathrm{i}\gamma \mathrm{G}rt)dr\,. \tag{2.9}$$

If in addition the gradient is time dependent, the phase of the exponential in (2.9) is determined by the time integral of G,

δ

$$M^{+}(t) = \int_{-\infty}^{\infty} M_0(r)\exp\left(\mathrm{i}\gamma r\int_0^t G(t')dt'\right)dr \equiv \int_{-\infty}^{\infty} M_0(r)\exp\{-\mathrm{i}k(t)r\}dr \tag{2.10}$$

where the wave vector k is the Fourier conjugate variable to the space coordinate r,

$$k(t) = -\gamma\int_0^t G(t')dt' . \tag{2.11}$$

Transverse magnetization will be in phase at all space coordinates immediately after the pulse. But in the presence of a magnetic field gradient the precession frequency varies in space, and a different precession phase is accumulated over time at each space coordinate.

To obtain an image, the gradient $G(t)$ must be varied in such a way that all values of k are sampled which are relevant to the image. The image itself is then derived by Fourier transformation of the NMR signal. There are two ways to encode the space information to the NMR signal. First, the gradients can be turned on to a constant value G_x during data acquisition (frequency encoding). In this case, k_x scales with the acquisition time t_2, and the space information in x-direction is frequency encoded. Second, the gradient G_y can be turned on for a fixed time t_1 before data acquisition to yield a certain value of the gradient integral k_y at the start (phase encoding). In this case, the space information in y-direction is encoded in the phase of the signal acquired during t_2, and the experiment needs to be repeated for different initial phases obtained by varying G for fixed t_1. A 2D image is typically obtained by a combination of both phase encoding in one

dimension and frequency encoding in the other.

2.2.2. Pulse sequences used in this study

Figure 2-2 shows a timing diagram of 3D imaging with the gradient echo method (GE3D) which is used in chapter 4 for obtaining various 3D pore structure data of the samples of glass beads and silica gel. In this method, echo signal is obtained by sinc3 shaped pulse in F1 channel and gradient echo in Phase direction. Frequency encoding is applied by a gradient in Phase direction during the acquisition of echo signal. Phase encoding is applied to two orthogonal directions; Phase and Slice directions. In this way, three orthogonal space information is obtained; frequency encoding in one direction, phase encoding in two directions. The two gradient pulses are applied at the same time and are cycled through all possible combinations. The frequency encoding gradient has its dephasing negative lobe to cause the spins to be in phase at the center of the acquisition, and then, the frequency encoding gradient is applied and a signal recorded

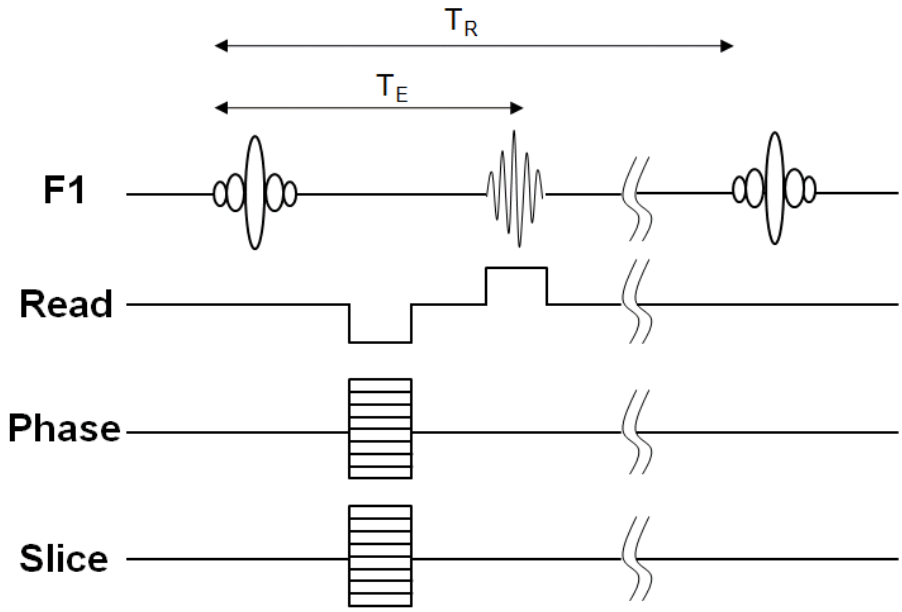

Figure 2-2. A timing diagram for 3D imaging with the gradient echo method (GE3D). Echo time (T_E) and repetition time (T_R) are also shown.

Figure 2-3 shows a timing diagram of chemical shift selective excitation pulse sequence (CHESS) used in chapter 5 for obtaining 2D images of two phase fluids. In this method, echo signal is obtained by Gaussian excitation and refocusing pulses in F1 channel. Gaussian excitation pulse with a flip angle of 90 degree is applied for excitation of a specific frequency, followed by a dephasing gradient (homogeneity spoiling gradient). The spoiling gradient leaves the spin system in a state where no net magnetization of the unwanted component remains entirely unaffected in the form of z-magnetization (Haase et al., 1985). A period of time equal to $T_E/2$ elapses and a 180 degree slice selective pulse is applied in conjunction with the slice selection gradient. Phase encoding gradients are applied after the 180 degree pulse, and after the echo signal. The frequency encoding gradient is applied in Read direction after the 180 degree pulse during the time that echo is collected.

Figure 2-4 shows a timing diagram of 3D imaging with the spin echo method (SE3D) used in chapter 5 for obtaining 3D images of water distribution in porous media comprised of glass beads and silica gel which are initially saturated with silicone oil. In this method, echo signal is obtained by sinc3 shaped excitation and refocusing pulses in F1 channel. A slice selective 90 degree RF pulse is applied, followed by a dephasing spoiler gradient which plays the same role in the CHESS protocol. A period of time equal to $T_E/2$ elapses and a 180 degree slice selective pulse is applied. Phase encoding is applied to two directions; Phase and Slice directions as in GE3D protocol. The frequency encoding gradient is applied

in Read direction after the 180 degree pulse during the time that echo is collected.

Figure 2-5 shows a timing diagram of 2D imaging with the spin echo method (SE2D) used in chapter 6 for obtaining high resolution images of porous media. In this method, echo signal is obtained by sinc3 shaped excitation and refocusing pulses in F1 channel. A slice selective 90 degree RF pulse is applied in conjunction with a slice selection gradient. A period of time equal to $T_E/2$ elapses and a 180 degree slice selective pulse is applied in conjunction with the slice selection gradient. Phase encoding gradients are applied after the 180 degree pulse, and after the echo signal. The frequency encoding gradient is applied in Read direction after the 180 degree pulse during the time that echo is collected.

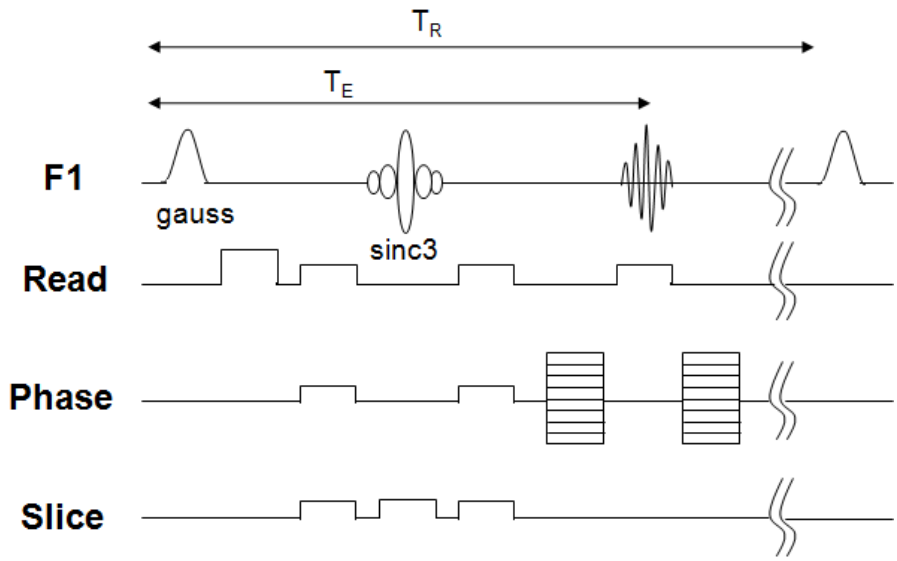

Figure 2-3. A timing diagram for chemical shift selective excitation pulse sequence (CHESS). Echo time (T_E) and repetition time (T_R) are also shown.

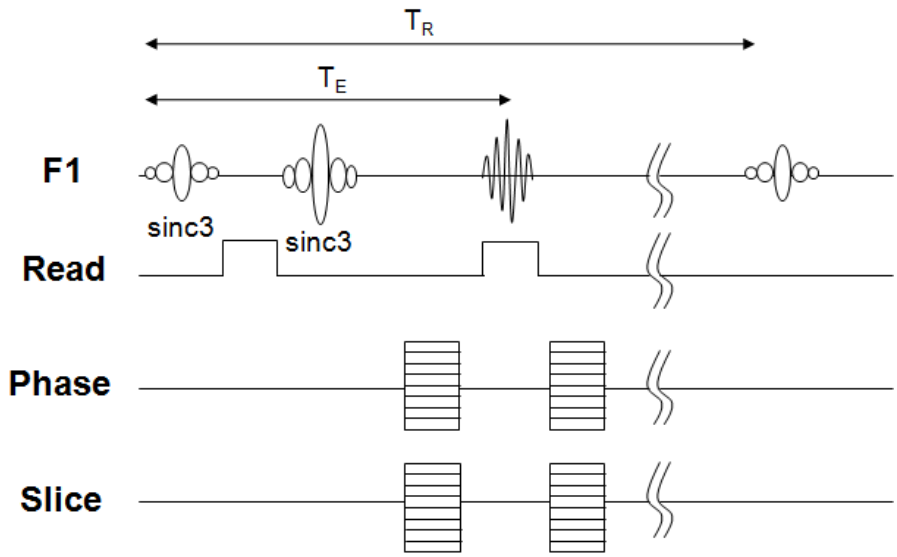

Figure 2-4. A timing diagram for spin echo 3D imaging pulse sequence (SE3D). Echo time (T_E) and repetition time (T_R) are also shown.

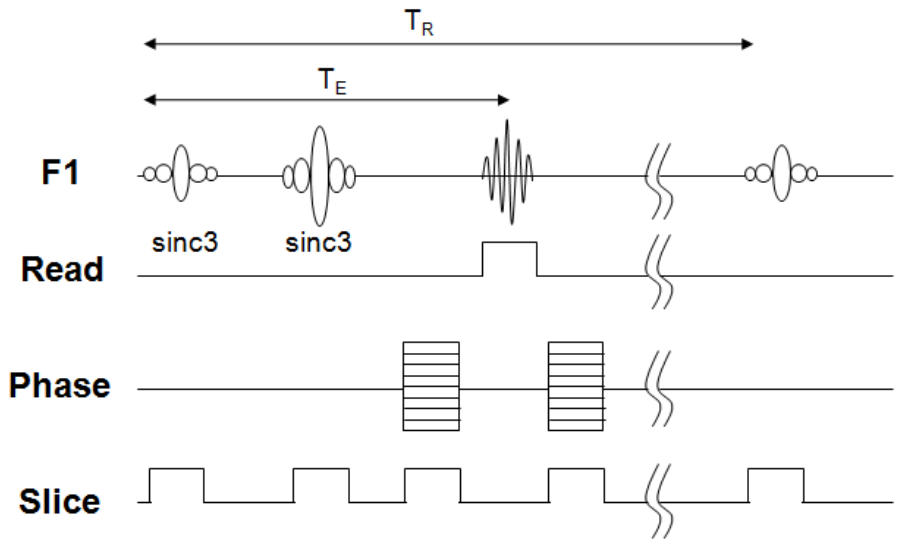

Figure 2-5. A timing diagram for spin echo 2D imaging pulse sequence (SE2D). Echo time (T_E) and repetition time (T_R) are also shown.

References

Becke, A. D. (1993) A new mixing of Hartree-Fock and local density-functional theories. Journal of Chemical Physics, 98(2), 1372-1377.

Blümich, B. (2000) NMR Imaging of Materials. Oxford, Clarendon Press, 541 p.

Callaghan, P. T. (1991) Principles of Nuclear Magnetic Resonance Microscopy. Oxford, Clarendon Press, 492 p.

Foresman, J. B. and Frisch, Æ. (1996) Exploring Chemistry with Electronic Structure Methods. Pittsburgh, PA, Gaussian, Inc., 302 p.

Fukutome, H. (1981) Unrestricted Hartree-Fock theory and its applications to molecules and chemical reactions. International Journal of Quantum Chemistry, 20, 955-1065.

Haase, A., Frahm, J., Hanicke, W. and Matthaei, D. (1985) ^{1}H NMR chemical shift selective (CHESS) imaging. Physics in Medicine and Biology, 30, 341-344.

Lee, C., Yang, W. and Parr, R. G. (1988) Development of the Colle-Salvetti correlation-energy formula into a functional of the electron density. Physical Review B, 37(2), 785-789.

Levitt, M. H. (2001) Spin Dynamics. Chichester, John Wiley & Sons Ltd, 686 p.

McQuarrie, D. A. and Simon, J. D. (1997) Physical Chemistry: A Molecular Approach. Sausalito, University Science Books, 1360 p.

Chapter 3. Effect of lattice topology on the adsorption of benzyl alcohol on kaolinite surfaces: Quantum chemical calculations of geometry optimization, binding energy, and NMR chemical shielding

Abstract

The effect of the lattice topology (ideal hexagonal rings vs. ditrigonal rings) and cluster size of model clusters (three-ring vs. seven-ring clusters) on the nature of benzyl alcohol adsorption on kaolinite surfaces using quantum chemical calculations were investigated with an emphasis on the equilibrium configuration, binding energy, and NMR chemical shielding tensors. The optimized structure of benzyl alcohol adsorbed on the tetrahedral layer of kaolinite varies according to the type and size of model cluster. While the calculated binding energy varies with the level of theory and the basis sets used for the calculations, the binding energies between benzyl alcohol and seven-ring clusters are smaller than those between benzyl alcohol and three-ring clusters partly due to the edge hydrogen for the latter. The results also indicate a stronger binding energy between benzyl alcohol and octahedral surfaces than that between benzyl alcohol and tetrahedral layers. Although the calculated binding energies for seven-member rings with varying lattice topologies are rather similar, the detailed optimized structures are distinct, demonstrating the effect of lattice topology on the nature of adsorption. The optimized structures and binding energies indicate that an intermediate degree of hydrogen bonding

is dominant for the three-member silicate rings and that the interaction between the benzene ring and basal oxygens in the seven-member rings is characterized by a weak hydrogen bond and dispersion force. The calculated ^{17}O isotropic chemical shieldings of some basal oxygens decrease up to approximately 4–5 ppm after the adsorption (with an estimated uncertainty of approximately 2 ppm). Since the high-resolution ^{17}O 3QMAS NMR spectroscopy of layer silicates yielded a resolution of 1–2 ppm for the basal oxygen sites in the layer silicates (e.g., Lee et al. 2003), the NMR technique may be useful in exploring the nature of adsorption between organic molecules and silicate surfaces, while further computational studies on the effect of the basis sets, the surface coverage, and the types of diverse organic molecules with larger model clusters for surfaces remain to be explored.

3.1. Introduction

Interactions between layer silicates and organic molecules play an important role in pollutant migration, bioavailability, and biodegradation in soils (Knezovich et al., 1987; Kowalska et al., 1994; Brown et al., 1999). The knowledge of their interactions can give improved insights into their applications as catalysts and nano-composites and into the enhanced oil recovery (Ogawa and Kuroda, 1995; Tunney and Detellier, 1996; Pinnavaia and Beall, 2000). An understanding of the process of benzyl alcohol adsorption on kaolinite surfaces can offer better insights into the adsorption of a benzene ring with alcohol functionality on mineral surfaces

and account for the wettability of reservoir rocks (Anderson, 1986; Madsen et al., 1996). The adsorption of benzyl alcohol on kaolinite surfaces renders the surfaces functional for many applications including polymer reinforcement (Bayer et al., 2010), and thus batch experiments were performed for the determination of the adsorption isotherm (Førland et al., 1995; Førland, 2001). Despite the importance and implications of this process, little is known about the detailed equilibrium configuration and binding energy for the adsorption of benzyl alcohol on kaolinite surfaces, which are essential to understand the nature of the interactions. The objective of this study is to investigate the nature of the interactions between kaolinite and benzyl alcohol theoretically using quantum chemical calculations.

Kaolinite is one of the dioctahedral 1:1 layer silicates. The nature of organic molecule adsorption on kaolinite has been studied using diverse experimental techniques, such as batch adsorption isotherm experiments (e.g., Førland 2001; Førland et al. 1995; Lee and Kim 2002; Li and Gupta 1994), X-ray absorption spectroscopy (e.g., Bantignies et al. 1998; Brown et al. 1988; Kelleher and O'Dwyer 2002; Olejnik et al. 1970), nuclear magnetic resonance (e.g., Feng et al. 2005; Jurkiewicz and Maciel 1995; Murray et al. 2005; Seger and Maciel 2006; Tao and Maciel 1998; Wang and Xing 2005; Xie and Hayashi 1999), and infrared and Raman spectroscopy (e.g., Johansson et al. 1999; Kubicki et al. 1999; Thomas and Kelley 2008; Yariv 1996; Yariv and Lapides 2000). Molecular dynamics (MD) simulation has also been useful in revealing the nature of the interactions between kaolinite and

organic molecules (e.g., Murgich et al. 1998; Teppen et al. 1998; Tunega et al. 2002a; Tunega et al. 2004; van Duin and Larter 2001). While these experimental and theoretical studies have provided insights into the nature of adsorption, the detailed atomic configuration of adsorbed molecules and the binding energies between the adsorbed molecules and surfaces have not yet been fully understood.

Quantum chemical calculations, which are effective tools for obtaining detailed microscopic information on the adsorption behavior of organic molecules, are complementary to other experimental and MD studies (Foresman and Frisch, 1996; Boulet et al., 2006), and have been utilized in diverse geological applications (e.g., see Cygan and Kubicki 2001 and the references therein). A few recent applications include studies of the atomic structures of silicate glasses and melts (e.g., Lee 2004; Lee 2006; Lee et al. 2001; Lee and Stebbins 2006; Tossell 2001; Xue and Kanzaki 1998), isotope fractionation in natural systems (Schauble et al., 2001; Schauble et al., 2003; Schauble et al., 2004; Ottonello and Zuccolini, 2005; Tossell, 2005; Suh et al., 2007), and the adsorption of organic species onto mineral surfaces (e.g., Aquino et al. 2007; Kwon et al. 2006; Plant et al. 2006; Viruela-Martín et al. 1993; Yoon et al. 2004; Zhanpeisov et al. 1999).

Quantum chemical calculations have been used to study the adsorption of various organic molecules on kaolinite surfaces, including formamide, N-methylformamide and dimethylsulfoxide (Michalkova et al., 2002), sarin and soman (Michalkova et al., 2004), thymine and uracil (Robinson et al., 2007), acetic acid and acetate ion (Tunega et al., 2002),

nitrobenzene (Pelmenschikov and Leszczynski, 1999; Michalkova et al., 2005; Gorb et al., 2006), and benzene (Castro and Martins, 2005) (see Table 3-1). Previous theoretical studies on the adsorption of organic molecules on kaolinite surfaces have reported that the more the hydrogen bonds formed between the surface oxygen and the hydrogen in organic molecules, the stronger the overall interaction between the organic molecules and the surfaces (Michalkova et al., 2002). It has also been shown that organic molecules on the octahedral layer are more strongly adsorbed than those on the tetrahedral layer of kaolinite (Michalkova et al., 2002; Tunega et al., 2002; Michalkova et al., 2004; Robinson et al., 2007).

Previous studies have often used relatively small clusters, and their results may have been somewhat affected by the terminal hydrogens (See Table 3-1 below). Although the actual lattice surfaces of layer silicates consist of ditrigonal rings, some of the previous studies have used ideal (hexagonal) rings (Pelmenschikov and Leszczynski, 1999; Hong et al., 2001; Hong et al., 2002; Gorb et al., 2006). Therefore, the effect of the cluster size and lattice topology of the model clusters on the binding energy and equilibrium configuration has not yet been fully understood. For example, previous quantum chemical calculations for the adsorption of sarin ($C_4H_{10}FO_2P$) and soman ($C_7H_{16}FO_2P$) on kaolinite (dickite) surfaces and the adsorption of 25 small organic molecules on zeolite surfaces showed that the optimized structures were not significantly affected by the size of the model clusters but the binding energy between the molecules and the surfaces increases with an increase in the size of the clusters, up to 33

kJ/mol (Michalkova et al., 2004; Solans-Monfort et al., 2005). However, the orientations of nitrobenzene molecules on layer silicates were found to be dependent on the surface area of the tetrahedral layers (Pelmenschikov and Leszczynski, 1999; Michalkova et al., 2004). Other earlier theoretical studies also showed that the lattice topology and the size of the model cluster affect the nature of the interaction: the enthalpy of hydrolysis for crystalline silicates was reported to significantly vary with the size and topology (bond angle) of the silicate clusters (Pelmenschikov et al., 2000). These studies suggest that the effects of cluster size (taking long-range interaction into consideration) and lattice topology on the equilibrium geometry and the strength of the interactions between organic molecules and mineral surfaces should be carefully examined. In this study, four different model clusters for kaolinite were prepared in order to improve our understanding of the interaction between benzyl alcohol and kaolinite and to systematically investigate the effects of the lattice topology and surface area of the model clusters on the atomic configuration and binding energy. NMR parameters, including chemical shielding, are effective in determining local electronic structures because the parameters are sensitive to changes in the electron distribution around the nuclides of interest (Mehring, 1983; Tossell, 2001). The NMR chemical shielding tensors of the nuclides (e.g., ^{1}H, ^{13}C, ^{15}N) in adsorbates have been estimated using quantum chemical calculations in order to give insights into the hydrogen bonding and van der Waals' bondings between organic molecules and inorganic substrates, such as zeolite (Haase and Sauer, 1994; Haase and

Sauer, 1995; Krossner and Sauer, 1996; Simperler et al., 2002; Simperler et al., 2004). Most NMR experiments have explored the adsorption of organic molecules on clay minerals by probing the atomic configurations around the nuclides in the adsorbates (Feng et al., 2005; Wang and Xing, 2005; Winkler et al., 2007). Because ^{17}O NMR chemical shielding is also sensitive to local electronic structures, and thus the atomic configuration around oxygen (see Stebbins 1995 and the references therein), the changes in atomic environments due to adsorption can potentially be investigated by exploring the changes in the ^{17}O NMR chemical shift for oxygens in the layer silicates before and after the adsorption. Recent ^{17}O triple-quantum magic-angle spinning (3QMAS) NMR studies have shown that in chemically distinct O environments, a resolution of up to several ppm can be achieved for phyllosilicates (e.g., ^{17}O enriched natural kaolinite and synthetic complex 2:1 layer silicates) (Lee and Stebbins, 2003; Lee et al., 2003; Lee and Weiss, 2008). Quantum chemical calculations of ^{17}O NMR chemical shielding for model layer silicates before and after adsorption can, therefore, test the utility of the 3QMAS NMR technique as an experimental probe of adsorption on kaolinite.

In this study, optimized structures, binding energies, and NMR chemical shieldings of the interactions between benzyl alcohol and kaolinite surfaces are estimated by performing quantum chemical calculations. Then, the nature of the interactions and the importance of model clusters used to simulate clay minerals are discussed.

Table 3-1. BSSE corrected binding energies (kJ/mol) between the tetrahedral layer (T) or octahedral layer (O) of kaolinite and other organic molecules, as reported in previous studies of quantum chemical calculations applying cluster approximation.

Model Cluster*	Organic Molecule†	Binding Energy‡	Level of Theory and Basis Set§	Reference‖
1 ring T + 1 ring O	Acetatic acid (T)	-17.2 ~ -10.9	B3LYP/SVP+sp:MNDO ~ B3LYP/SVP	(1)
	Acetate ion (O)	-280.9 ~ -305.6	B3LYP/SVP+sp ~ B3LYP/SVP:MNDO	
1 ring O	Formamide (O)	-60.9	B3LYP/3-21G*	(2)
	N-methylformamide (O)	-15.4	B3LYP/3-21G*	
	Dimethylsulfoxide (O)	-11.1	B3LYP/3-21G*	
7 ring T + 7 ring O	Sarin (T)	-31.0	B3LYP/6-31G(d,p):PM3	(3)
	Soman (T)	-38.1	B3LYP/6-31G(d,p):PM3	
	Sarin (O)	-69.1	B3LYP/6-31G(d,p):PM3	
	Soman (O)	-63.6	B3LYP/6-31G(d,p):PM3	
1 ring T + 1 ring O	Sarin (T)	-20.5 ~ -16.3	B3LYP/6-31G(d,p):HF/3-21G ~ B3LYP/6-31G(d,p):PM3	
	Soman (T)	-23.9 ~ -16.7	B3LYP/6-31G(d,p):HF/3-21G ~ B3LYP/6-31G(d,p):PM3	
	Sarin (O)	-54.4 ~ -53.6	B3LYP/6-31G(d,p):HF/3-21G ~ B3LYP/6-31G(d,p):PM3	
	Soman (O)	-41.4 ~ -31.0	B3LYP/6-31G(d,p):HF/3-21G ~ B3LYP/6-31G(d,p):PM3	
1 ring T	Thymine (T)	-17.2 ~ -5.9	B3LYP/6-31++G(d,p) ~ B3LYP/6-31G(d)	(4)
1 ring O	Thymine (O)	-88.3	B3LYP/6-31G(d)	
1 ring T	Uracil (T)	-17.6 ~ -15.1	B3LYP/6-31++G(d,p) ~ B3LYP/6-31G(d)	
1 ring O	Uracil (O)	-126.9	B3LYP/6-31G(d)	
ideal 1 ring T	1,3,5-trinitrotoluene (T)	-15	B3LYP//SCF/6-31G(d)	(5)
3 ring T + 3 ring O	1,3,5-trinitrotoluene (T)	-29.7 ~ -13.0	MP2/6-31G(d): HF/6-31G(d): HF/3-21G ~ HF/6-31+G(d):HF/6-31G(d):HF/3-21G	(6)
ideal 3 ring T	1,3,5-trinitrotoluene (T)	-60.7 ~ -16.3	MP2/6-31G(d)(0.25)//HF/6-31G(d) ~ B3LYP/6-31G(d)//HF/6-31G(d)	(6)
3 ring T	2,4-dinitrotoluene (T)	-27.2	HF/3-21G	(7)
1 ring O	2,4-dinitrotoluene (O)	-74.1	HF/3-21G	
1 ring T + 1 ring O	Benzene (O)	-19.0	RHF/3-21G* using the Morokuma–Kitaura correction	(8)
	Benzene (O)	-21.6	RHF/3-21G* using the Counterpoise correction	

* T and O refer to the tetrahedral layer and octahedral layer of kaolinite, respectively. The number refers to the number of tetrahedral or octahedral rings in each layer. Thus, "1 ring T + 1 ring O" indicates that the model cluster comprises a sheet of kaolinite on both layers. A model cluster represented as "ideal" indicates that the tetrahedral layer is an ideal hexagonal ring, and a model cluster not represented as "ideal" indicates that the atomic position of the model cluster is obtained from its structural data.

† T and O in parentheses refer to the tetrahedral and octahedral surfaces, respectively, on which the organic molecule is adsorbed.

‡ The lowest and highest energies, respectively, obtained in each study.

§ Each method refers to the level of theory and basis set used in the calculation of the binding energy. The method with a colon refers to ONIOM (high level: (medium level:) low level). The lower and upper limits correspond to the methods for determining the lowest and highest binding energies, respectively, in each study.

‖ (1) Tunega et al. 2002b; (2) Michalkove et al. 2002; (3) Michalkove et al. 2004; (4) Robinson et al. 2007; (5) Pelmenschikov and Leszczynski 1999; (6) Gorb et al. 2006; (7) Michalkove et al. 2005; (8) Castro and Martins 2005.

3.2. Methods

3.2.1. Model clusters

Figure 3-1 shows the model clusters used to simulate kaolinite surfaces. All of the dangling bonds were saturated with hydrogens for charge balance. Model cluster 1 ($Si_{24}O_{66}H_{36}$) consists of seven ideal (hexagonal) silicate rings (Figure 3-1A). Symmetry constraints in this model cluster are as follows: basal and apical Si-O bond lengths are fixed at 1.616 Å and 1.618 Å, respectively (Bish, 1993), and Si-O-Si and O-Si-O angles are maintained at 140° and 109.5°, respectively, which are the average values for silica (Sauer et al., 1994). The O-H bond length, Si-O-H angle, and O-Si-O-H dihedral angle for the dangling hydrogen atoms are fixed at 0.96 Å, 140°, and 0°, respectively (Pelmenschikov et al., 1992; Sauer et al., 1994; Zhanpeisov et al., 1999). Model cluster 2 ($Si_{24}O_{66}H_{36}$) is composed of seven ditrigonal silicate rings and the atomic positions are obtained from crystallographic data (Bish and von Dreele, 1989) (Figure 3-1B). Kaolinite has three distinct basal oxygen sites (O3, O4, and O5), as shown in Figure 3-1B, and two apical oxygen sites (O1 and O2). Model cluster 3 ($Al_{13}Si_{13}O_{63}H_{35}$) is a sheet of kaolinite that consists of three rings of tetrahedral silicate and octahedral aluminum layers (Figure 3-1C). This model cluster consists of seven inner hydrogens 19 interlayer hydrogens (Hobbs et al., 1997), and nine dangling hydrogens. Model cluster 4 ($Si_{13}O_{37}H_{22}$), which consists of three ditrigonal silicate rings, is obtained by removing the octahedral layer from model cluster 3 (Figure 3-1D).

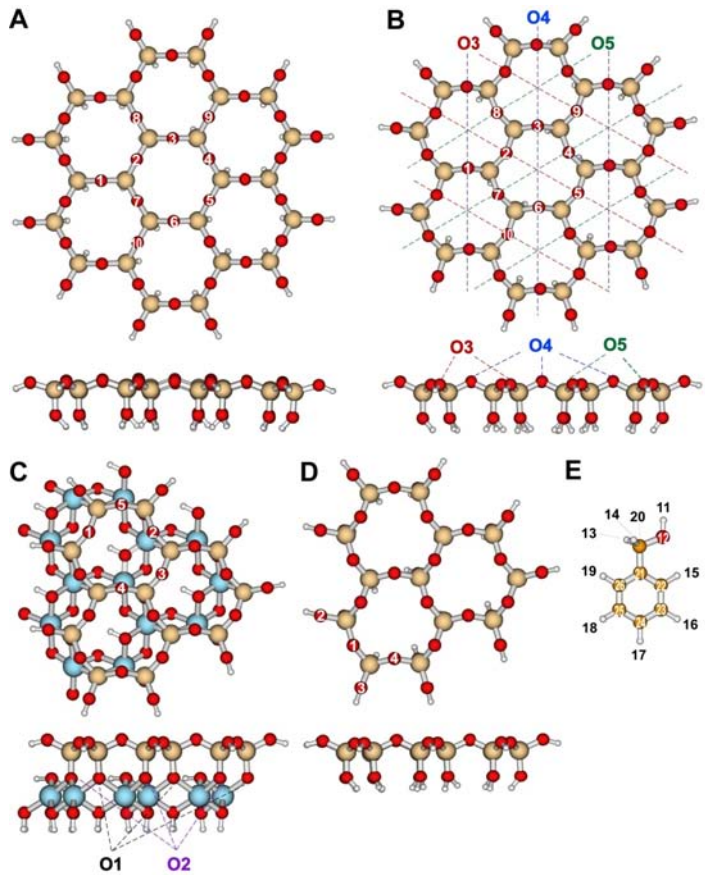

Figure 3-1. Four different model clusters for simulating kaolinite: (A) Model cluster 1; (B) model cluster 2 with three distinct basal oxygen sites—O3, O4, and O5 (indicated by red, blue, and green dashed lines, respectively); (C) model cluster 3 with two distinct apical oxygen sites—O1 and O2 (indicated by black and purple dashed lines, respectively); and (D) model cluster 4; and (E) the optimized molecular structure of benzyl alcohol calculated at the HF level with a 6-31G basis set. The top view (top) and side view (bottom) are shown in (A)-(D). In all of the clusters, the oxygen, silicon, hydrogen, aluminum, and carbon atoms are represented by red, wheat-colored, white, blue, and gold spheres, respectively.

It should be noted that a model cluster with a single siloxane ring is too small to be used for describing the interaction between the layer silicates and benzyl alcohol and that the results would be largely affected by the terminal hydrogens. Three-ring clusters have often been used to simulate layer silicate surfaces (e.g., Gorb et al. 2006; Michalkova et al. 2005). It would be difficult to carry out quantum chemical calculations for clusters larger than seven silicate rings without using the ONIOM method, which utilizes multilevel calculation for computational efficiency (Svensson et al., 1996). In this study, a seven member ring cluster without ONIOM, which was more thorough and precise in reproducing the potential energy of the electrons in the interaction between the silicates and organic molecules, but necessitated a moderate computational cost, was used. Thus, the three-ring cluster represents a relatively small silicate surface and seven-ring cluster a larger surface. This study serves as a starting point to explore the effects of cluster size and lattice topology on the adsorption of organic molecules on kaolinite surfaces. Surfaces with intermediate sizes (i.e., four, five, and six ring clusters) remain to be explored because the current study only provides the results for two model end members.

3.2.2. Computational methods

Geometry optimization, binding energy, and NMR chemical shielding calculations involving quantum chemical calculations were performed using Gaussian 03 (Frisch et al., 2004). Whereas a much larger cluster can be studied using MD simulations, the potential fields used for

MD simulations are greatly simplified compared with those based on the detailed electron interactions used in the current quantum chemical calculations. Quantum chemical calculations can be performed with either a Gaussian atomic orbital basis set or plane wave basis set. Quantum chemical calculations using Gaussian basis sets, where it is essential to select an appropriate cluster choice to obtain the desired results were performed.

A cluster of benzyl alcohol ($C_6H_5CH_2OH$) molecules was optimized without molecular symmetry constraints at the Hartree-Fock (HF) level of theory with a 6-31G basis set. Figure 3-1E shows the optimized molecular structure of benzyl alcohol. The geometry optimization of the intermolecular structure of benzyl alcohol adsorbed on each model cluster was performed at the HF level of theory with the 6-31G basis set, and additionally, on model clusters 1 and 2, at the Becke, three-parameter, Lee-Yang-Parr (B3LYP) hybrid functional level of theory with the 6-31G and 6-31G(d) basis sets (Lee et al., 1988; Becke, 1993; Becke, 1993). The benzyl alcohol molecule was located at the same position on each siloxane surface with the same initial configurations of inter-molecular distances, angles, and dihedral angles.

It should be noted that only the distances, angles, and dihedral angles between benzyl alcohol and each model cluster could be varied, while the internal variables for benzyl alcohol and each model cluster were fixed upon optimizing the geometry of benzyl alcohol adsorption on the tetrahedral layer of the model cluster. Because the orientation of the

δ

hydroxyl groups could play an important role in the adsorption of the kaolinite on the octahedral layer, the hydrogen atoms of the interlayer and inner hydroxyl groups of model cluster 3 were also varied upon geometry optimization.

Binding energy (E_{bind}) is defined as

$$E_{bind} = (E_A + E_B) - E_{AB} . \qquad (3.1)$$

where E_{AB} is the total energy of AB molecule, and E_A and E_B are the energies of molecules A and B, respectively. The binding energies between benzyl alcohol and model clusters 1 and 2 were calculated at the HF level with a 6-31G basis set; at the B3LYP level with 6-31G, 6-31G(d), and 6-311+G(2d,p) basis sets; and at the MP2 level with a 6-31G basis set for the optimized geometries at HF/6-31G. In addition to these, the binding energies between benzyl alcohol and model clusters 1 and 2 were also calculated at the B3LYP level with the 6-31G and 6-31G(d) basis sets for the optimized geometries determined at each level [i.e., B3LYP/6-31G//B3LYP/6-31G and B3LYP/6-31G(d)//B3LYP/6-31G(d)]. The binding energies between benzyl alcohol and model clusters 3 and 4 were calculated at the HF level with a 6-31G basis set and at the B3LYP level with 6-31G, 6-31G(d), and 6-311+G(2d,p) basis sets for the optimized geometries at HF/6-31G. Basis set superposition errors (BSSE) in the binding energies were corrected using the counterpoise method (Boys and Bernardi, 1970).

The NMR chemical shielding tensors of the hydrogens (^{1}H),

carbons (^{13}C) in benzyl alcohol, and basal oxygens (^{17}O) were calculated using the gauge-including atomic orbital (GIAO) method, the individual gauges for atoms in molecules (IGAIM) method, and the continuous set of gauge transformations (CSGT) method at the B3LYP level of theory with a 6-31G(d) basis set for benzyl alcohol and all model clusters before and after the adsorption. Because the calculated NMR chemical shielding tensors depend on the choice of basis sets, energy level of theory, and cluster size (Foresman and Frisch, 1996; Xue and Kanzaki, 1998; Tossell, 2001; Frisch et al., 2004)], the ^{17}O NMR chemical shielding tensors of the basal oxygens were also calculated at the B3LYP level with a 6-311+G(2d,p) basis set for model clusters 1 and 2 to check the effect of the basis sets. As for the ^{17}O chemical shielding tensors of the basal oxygens, the calculated ^{17}O NMR chemical shifts of the basal oxygens using the IGAIM and the CSGT methods ranged approximately from 20 to 34 ppm [referenced to $H_2O(l)$ with an absolute chemical shielding value of 287.5 $\pm$ 0.6 ppm, see Wasylishen and Bryce 2002], and are not consistent with the experimental ^{17}O NMR results for bridging oxygen in layer silicates [ranging from 43 to 56 ppm (Lee and Stebbins, 2003)] and in other silicates [ranging approximately from 40 to 87 ppm (Stebbins, 1995)]. The ^{17}O isotropic chemical shifts for basal oxygens [referenced to $H_2O(l)$], calculated using the GIAO method, range from 42.5 to 51.1 ppm [B3LYP/6-31G(d)] and from 58.6 to 68.5 ppm [B3LYP/6-311+G(2d,p)]; thus, the experimental ^{17}O isotropic chemical shifts were reasonably well-reproduced (see Results and Discussion below). As the GIAO method has also been successful in

δ

calculating the ^{17}O chemical shifts for diverse oxide materials (e.g., Lee 2004; Lee and Lee 2006; Xue and Kanzaki 1998), and the IGAIM and CSGT methods have been used mostly to calculate the ^{1}H and ^{13}C NMR chemical shielding tensors in organic molecules (e.g., Huang et al. 2005; Simion and Sorensen 1996; Wiberg et al. 1999), the O-17 NMR *chemical shieldings* that were found using the GIAO method are reported (see below for more discussion). The ^{17}O quadrupolar coupling constants (C_q) and asymmetry parameters (η) were calculated at the B3LYP level of theory with a 6-31G(d) basis set using the Gaussian 03 and were extracted using the EFGshield (Adiga et al., 2007).

3.3. Results and Discussion

3.3.1. Optimized structures

Figure 3-2 shows the optimized structures of benzyl alcohol adsorbed on model clusters; the structures are calculated at the HF level of theory with a 6-31G basis set. The optimized structures on the tetrahedral layer have various configurations depending on the topology and size of the model clusters. The planes of benzene rings on model clusters 1 and 2 are subparallel to the siloxane surfaces, with a slight inclination toward the center of the tetrahedral surface due to hydrogen bonding between alcohol hydrogen [H(11) in the benzyl alcohol molecule, Figure 3-1E] and basal oxygens and the dispersion forces between the benzene rings and basal oxygens (Figures 3-2A and 2B, see below for further discussion). Since the benzyl alcohol molecule is located at the center of the siloxane ring, it is

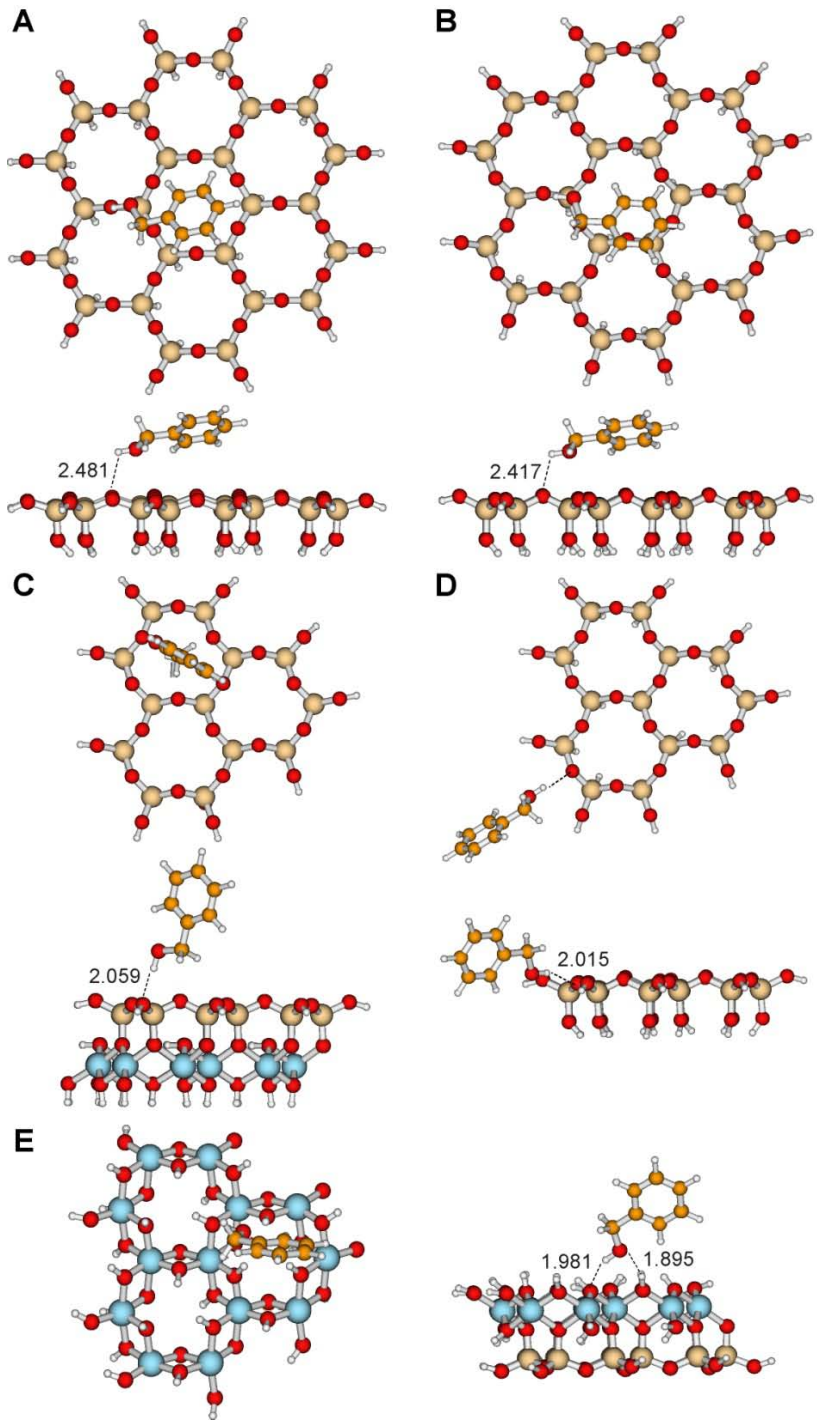

Figure 3-2. (caption on next page)

Figure 3-2. Optimized structures of benzyl alcohol adsorbed on (A) model cluster 1, (B) model cluster 2, (C) the tetrahedral layer of model cluster 3, (D) model cluster 4, and (E) the octahedral layer of model cluster 3, calculated at HF/6-31G. The top view and side view of the optimized structure are shown for each of the clusters. The oxygen, silicon, hydrogen, aluminum, and carbon atoms are represented by red, wheat-colored, white, blue, and gold spheres, respectively. In the top views of (C) and (E), the bottom layers [the octahedral layer in (C) and the tetrahedral layer in (E)] have been removed for visual clarity. Dashed lines indicate the hydrogen bonding in each model cluster and the numbers indicate the hydrogen bonding distances (the unit is Å).

unlikely that the optimized structures are significantly affected by the terminal hydrogens. The optimized structures of benzyl alcohol adsorbed on the tetrahedral layer of model clusters 3 and 4 are different from those on model clusters 1 and 2: the plane of the benzene ring is perpendicular to the siloxane surface for model cluster 3, and the benzyl alcohol molecule is located outside the basal surface of model cluster 4. The configurations for model clusters 3 and 4 are probably due to the small cluster size where the interaction between the terminal hydrogen and the hydrogens of the benzene ring is apparently dominant. The optimized geometries of clusters with (model cluster 3) and without (model cluster 4) the octahedral layer are also different, demonstrating the effect of the octahedral layer on the adsorption. Figure 3-2E shows the optimized structure of benzyl alcohol adsorbed on the octahedral layer of model cluster 3. The plane of the benzene ring is also normal to the octahedral surface of model cluster 3 (as is the case for the tetrahedral layer, as shown in Figure 3-2C): hydrogen bonds are formed between the oxygen in the alcohol group [O(12) in the benzyl alcohol molecule, Figure 3-1E] and the hydrogen in the hydroxyl group of the octahedral surface, and between the hydrogen in the alcohol group [H(11) in the benzyl alcohol molecule, Figure 3-1E] and the oxygen in the hydroxyl group of the octahedral surface. Note that the basal surface at the octahedral layer consists of only interlayer hydrogens, and therefore, the octahedral layer of model cluster 3 is free from perturbations caused by the terminal hydrogens. Figure 3-3 shows the optimized structures of benzyl alcohol adsorbed on model clusters 1and 2 calculated at the B3LYP

energy level of theory. Whereas the optimized structures are clearly dependent on the lattice topology, the optimized configurations at the B3LYP level of theory and varying basis sets are rather similar to those calculated at the HF level of theory (Figure 3-2), suggesting that the optimized geometry are not much dependent on the energy level of theory or the basis set [Figures 3-2A, 3- 3A, and 3-3C show model cluster 1 calculated at HF/6-31G, B3LYP/6-31G, and B3LYP/6-31G(d), respectively, and Figures 3-2B, 3-3B, and 3-3D show model cluster 2 calculated at HF/6-31G, B3LYP/6-31G, and B3LYP/6-31G(d), respectively]. Table 3-2 shows the interatomic distances between benzyl alcohol and the tetrahedral layer of each model cluster. Figure 3-2 (and Figure 3-3) further indicates that the detailed optimized structures of model clusters 1 and 2 are different. For instance, the distances between the hydrogen in the alcohol group [H(11) in Figure 3-1E] and the basal oxygen in model cluster 1 are longer than those in model cluster 2, regardless of the calculation method used [HF/6-31G, B3LYP/6-31G, and B3LYP/6-31G(d)]. The distances between the basal oxygens and the hydrogens in benzene ring [H(15), H(16), H(17), H(18), and H(19) in the benzyl alcohol molecule, Figure 3-1E] for model cluster 1 are generally shorter than those for model cluster 2 (Table 3-2).

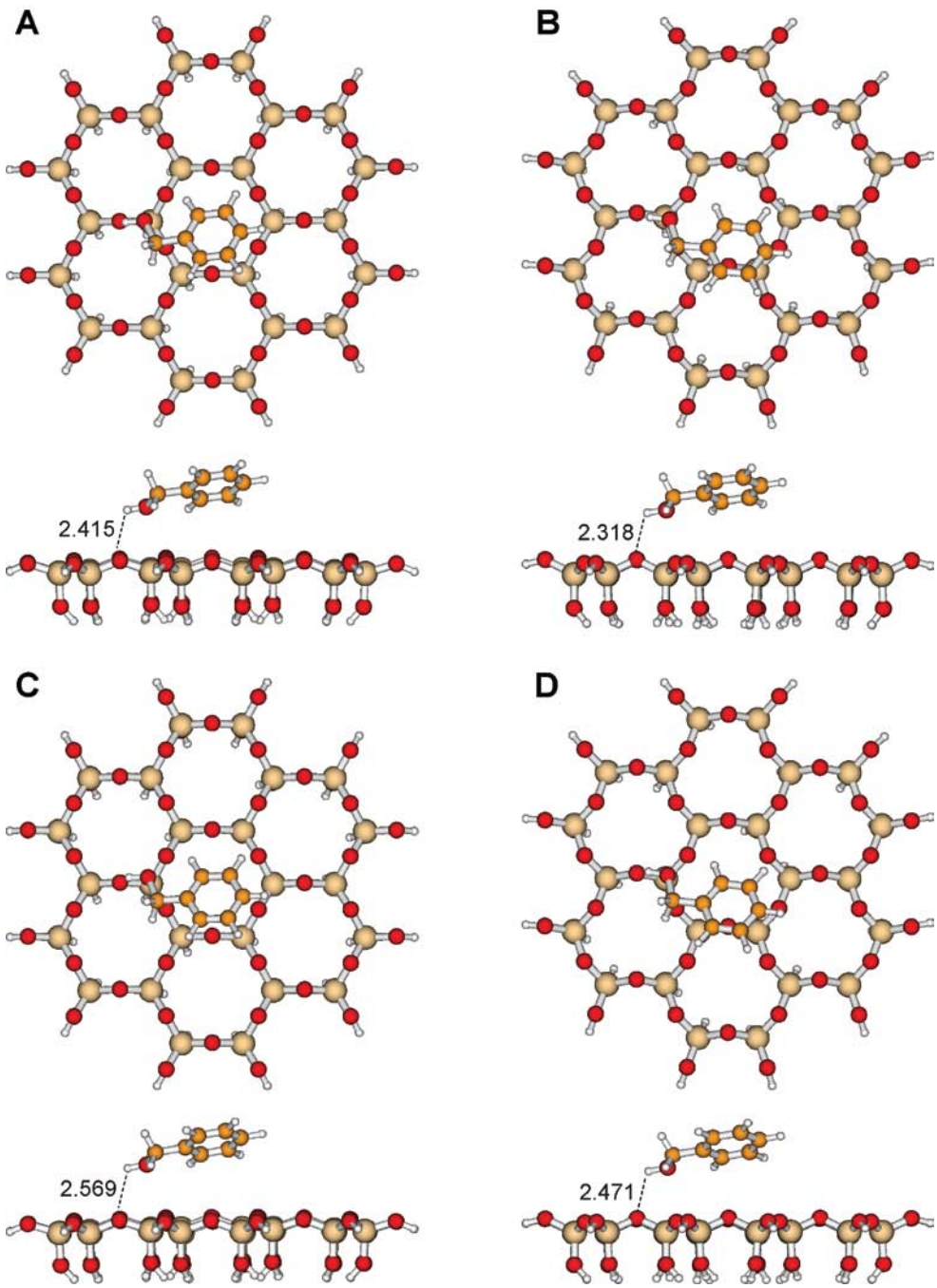

Figure 3-3. (caption on next page)

Figure 3-3. Optimized structures of benzyl alcohol adsorbed on (A) model cluster 1 and (B) model cluster 2, calculated at B3LYP/6-31G, and on (C) model cluster 1 and (D) model cluster 2, calculated at B3LYP/6-31G(d). The top view and side view of the optimized structure are shown for each of the clusters. The oxygen, silicon, hydrogen, aluminum, and carbon atoms are represented by red, wheat-colored, white, blue, and gold spheres, respectively. Dashed lines indicate the hydrogen bonding in each model cluster and the numbers indicate the hydrogen bonding distances (the unit is Å).

Table 3-2. Interatomic distances (Å) in the optimized structures of benzyl alcohol adsorbed on the tetrahedral layer of each model cluster of kaolinite; the distances are calculated at the HF (all clusters) and B3LYP (model clusters 1 and 2) levels of theory with 6-31G and 6-31G(d) basis sets.

Atom in kaolinite (atom number in Figures 3-1A-D) - Atom in benzyl alcohol (atom number in Figure 3-1E)	HF/6-31G (Å)		B3LYP/6-31G (Å)		B3LYP/6-31G(d) (Å)	
	Cluster 1	**Cluster 2**	**Cluster 1**	**Cluster 2**	**Cluster 1**	**Cluster 2**
O(1)-H(11)	2.481	2.417	2.415	2.318	2.569	2.471
O(2)-H(15)	2.746	2.896	2.702	2.890	3.044	3.194
O(4)-H(16)	3.089	3.215	2.930	2.994	3.296	3.425
O(5)-H(17)	4.112	4.451	3.890	3.926	4.174	4.417
O(6)-H(18)	4.976	5.059	4.796	4.706	4.948	5.084
O(6)-H(19)	4.459	4.318	4.360	4.388	4.557	4.713
O(7)-H(13)	2.789	2.755	2.716	2.694	2.828	2.881
O(7)-H(14)	4.264	4.268	4.183	4.212	4.330	4.418
	Cluster 3	**Cluster 4**				
O(1)-H(11)	2.059	2.015				
O(2)-H(13)	2.780	4.124				
O(3)-H(19)	4.038	3.144				
O(4)-H(14)	2.529					

The shortest distances between the hydrogen in the alcohol group [H(11) in Figure 3-1E] and the basal oxygen of the tetrahedral layer of model clusters 1, 2, 3, and 4, calculated at HF/6-31G, are 2.481 Å, 2.317 Å, 2.059 Å, and 2.015 Å, respectively, and the two hydrogen bond distances in the case of the octahedral layer of model cluster 3, calculated at HF/6-31G, are 1.895 Å and 1.981 Å (Figure 3-2). The relative strength of hydrogen bonding is estimated by considering the distance between hydrogen and the acceptor atom (i.e., oxygen); the distance ranges of 1.2–1.5, 1.5–2.2, and 2.2–3.0 Å correspond to strong, medium, and weak hydrogen bonds, respectively (Parthasarathi and Subramanian, 2006; Rozas, 2007). On the basis of this correspondence, the hydrogen bond for model clusters 1 and 2 can be categorized as weak (note that this classification was based on the interatomic distance only, see below for further discussion). The adsorption on the tetrahedral layer of model clusters 3 and 4 and on the octahedral layer of model cluster 3 are characterized by medium hydrogen bonding.

3.3.2. Binding energies

Table 3-3 and Figure 3-4 show the binding energies between each model cluster and benzyl alcohol. The binding energies calculated at the HF level of theory are larger than those calculated at the B3LYP level of theory and decrease with an increase in the number of basis set functions (Foresman and Frisch, 1996; Pelmenschikov and Leszczynski, 1999). The binding energies calculated at MP2/6-31G for model clusters 1 and 2 are smaller than those calculated at HF/6-31G, but larger than those based on

Table 3-3. BSSE corrected binding energies (kJ/mol) between each model cluster and benzyl alcohol. The BSSE values are shown in parentheses. BSSE uncorrected binding energies can be calculated by subtracting the BSSE values from the BSSE corrected binding energy values.

	Cluster 1	**Cluster 2**	**Cluster 3 (tetrahedral layer)**	**Cluster 3 (octahedral layer)**	**Cluster 4**
HF/6-31G	-33.4 (29.9)	-37.1 (26.8)	-52.8 (24.2)	-92.7 (22.1)	-71.3 (15.4)
B3LYP/6-31G//HF/6-31G	1.5 (26.7)	-0.6 (30.4)	-16.8 (19.0)	-62.7 (27.7)	-29.1 (17.3)
B3LYP/6-31G(d)//HF/6-31G	8.9 (25.4)	13.0 (30.4)	-1.2 (16.7)	-52.5 (23.8)	-19.8 (14.6)
B3LYP/6-311+G(2d,p)//HF/6-31G	9.4 (16.7)	7.5 (17.0)	-2.7 (11.4)	-43.9 (7.7)	-16.6 (5.1)
MP2/6-31G//HF/6-31G	-4.2 (42.4)	-8.6 (39.6)			
B3LYP/6-31G	3.3 (33)	3.4 (34.1)			
B3LYP/6-31G(d)	13.3 (30.7)	6.9 (25.4)			

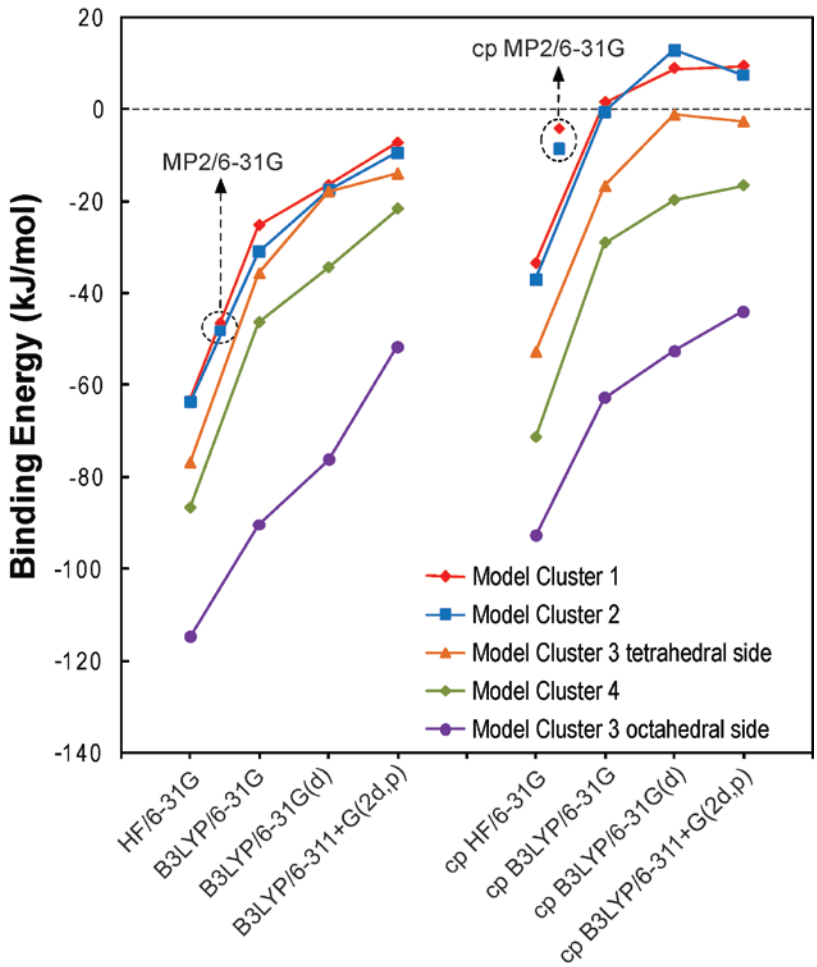

Figure 3-4. Binding energies between benzyl alcohol and each model cluster for the optimized structures at HF/6-31G. The level of theory and the basis set for each binding energy are given in the x-axis label. A basis set with the prefix "cp" indicates counterpoise correction. Dashed ellipses indicate binding energies calculated at MP2/6-31G for model clusters 1 and 2.

B3LYP/6-31G. The BSSE corrected binding energies are systematically smaller than the binding energies without counterpoise correction.

While the calculated binding energy varies significantly with the energy levels of theory and the types of basis sets, the binding energy differences among the clusters are fairly constant, regardless of the calculation method (from the weakest to the strongest binding energy: model cluster 1 < model cluster 2 < tetrahedral layer of model cluster 3 < model cluster 4 < octahedral layer of model cluster 3). The BSSE corrected binding energies (uncorrected values are shown in parentheses) are –33.4 to +9.4 (–63.3 to –7.3) kJ/mol (model cluster 1), –37.1 to +13.0 (–63.8 to -9.5) kJ/mol (model cluster 2), –52.8 to –1.2 (–77.0 to –14.0) kJ/mol (tetrahedral layer of model cluster 3), -92.7 to -43.9 (–114.8 to -51.6) kJ/mol (octahedral layer of model cluster 3), and –71.3 to –16.6 (–86.7 to –21.7) kJ/mol (model cluster 4). The basis set superposition error values range from 5.1 to 42.4 kJ/mol and are similar to the values reported for interactions between organic molecules and clay minerals or oxide fragments (Pelmenschikov and Leszczynski, 1999; Michalkova et al., 2002; Tunega et al., 2002; Castro and Martins, 2005; Gorb et al., 2006; Granqvist et al., 2007; Robinson et al., 2007). Whereas the BSSE is comparable to the calculated binding energy difference, it should be noted that the *differences* in the binding energies among the model clusters are rather constant regardless of the level of theory and the basis sets. At identical levels of theory and with similar basis sets, the differences between the binding energies for model cluster 1 and those for model cluster 2 are relatively insignificant (0.1 to 6.4 kJ/mol)

(Table 3-3). However, the optimized structures are rather different (Table 3-2 and Figures 3-2 and 3-3), which indicates the effect of the lattice topology (i.e., ideal hexagonal rings vs. ditrigonal rings) on the atomic arrangement of the molecules on the kaolinite surfaces.

As shown in Table 3-3 and Figure 3-4, the binding energies for model clusters 1 and 2 at the B3LYP level of theory are observed to be positive in the current study. A positive binding energy for the interactions between kaolinite and other organic molecules has not been reported in previous studies. However, positive binding energies have been reported for weakly bonded systems at the density functional theory, including B3LYP, after counterpoise corrections. Examples include diatomic rare gas molecules (Pérez-Jordá and Becke, 1995), van der Waals complexes between hydrogen peroxide and nitrogen, helium, neon, and argon (Molina et al., 2002), and $H_3C–H \cdots [NO]$ complexes (Crespo-Otero et al., 2005). Thus, the positive values may be due to the underestimation of the weak interatomic interactions, including dispersion forces, in the calculations based on B3LYP. Because the dispersion force arises from the correlation of excited electrons between molecules (i.e., inter-molecular electronic interaction) (Stone, 1996), molecular orbital methods involving electron correlation, such as the MP2 method, may better describe non-primary bonding, such as hydrogen bonding, and the dispersion force (Møller and Plesset, 1934; Cremer, 1998). This is because the second-order perturbation term explicitly includes a contribution from the dispersion force term (Stone, 1996). Because MP2 calculation for large clusters, as in the current

study, is computationally expensive, the binding energies were calculated using a relatively small basis set (i.e., 6-31G) for benzyl alcohols adsorbed on model clusters 1 and 2. Calculation with an extended basis set at the MP2 level needs to be examined.

The calculated binding energy at MP2/6-31G with counterpoise correction is found to be negative (–4.2 kJ/mol for model cluster 1 and –8.6 kJ/mol for model cluster 2). Therefore, the current results (weak positive or nearly zero binding energies calculated at the B3LYP level and weak negative binding energies at the MP2 level for model clusters 1 and 2) indicate that B3LYP may not completely reproduce weak interactions, such as dispersion force interactions, as suggested by other studies (Pérez-Jordá and Becke, 1995; Stone, 1996; Molina et al., 2002; Crespo-Otero et al., 2005). The results also indicate the contribution of the dispersion force potential to the interactions between the benzene ring and basal oxygens.

Table 3-1 shows the binding energies between kaolinite and other organic molecules reported in previous quantum chemical calculations using cluster approximation. The BSSE corrected binding energies for the octahedral layer of kaolinite are generally larger than those for the tetrahedral layer (in absolute value), which is consistent with the current results for benzyl alcohol. While a direct comparison would be difficult due to differences in the calculation methods and cluster sizes, the binding energy, which depends on the size of the clusters, the energy levels of theory, and the basis sets, calculated for benzyl alcohol on the tetrahedral layer of model clusters 1 and 2 is somewhat smaller than that calculated for

other molecules. The binding energy for benzyl alcohol on the octahedral layer of model cluster 3 is comparable to that calculated for other molecules.

3.3.3. NMR chemical shielding

Table 3-4 shows the isotropic magnetic shieldings of the hydrogens (^{1}H) and carbons (^{13}C) in benzyl alcohol. While the absolute isotropic magnetic shieldings calculated using the GIAO method are slightly larger than those estimated by the IGAIM and the CSGT methods, the differences in the chemical shielding before and after adsorption is largely identical regardless of the calculation method (Table 3-4). The calculated ^{1}H isotropic magnetic shielding for hydrogen forming a hydrogen bond with surface oxygen decreases upon adsorption. The isotropic magnetic shielding of the hydrogens forming hydrogen bonds [H(11) in Figure 3-1E], calculated using the GIAO method, decreases up to 0.31 ppm for model cluster 1, 0.49 ppm for model cluster 2, 1.14 ppm for model cluster 3, and 1.99 ppm for model cluster 4 after the adsorption (Table 3-4). This trend and the magnitude of the changes in the ^{1}H chemical shielding are consistent with the previous experimental and theoretical studies of organic molecule adsorption on layer silicate surfaces (e.g., Chu et al. 1990; Xie and Hayashi 1999; Yesinowski and Eckert 2009). While further study is necessary, a stronger hydrogen bond and thus a shorter H···O distance (cluster 4) apparently leads to a larger change in the isotropic chemical shielding after the adsorption.

Table 3-4. Isotropic magnetic shieldings (ppm) of hydrogens and carbons in benzyl alcohol before and after the adsorption on the tetrahedral surface of each model cluster.

	Atom in benzyl alcohol (atom number in Figure 3-1E)	Isotropic magnetic shielding (ppm)				
		before	after* (Cluster 1)	after* (Cluster 2)	after* (Cluster 3)	after* (Cluster 4)
GIAO	H(11)	32.71	32.40 (-0.31)	32.22 (-0.49)	31.56 (-1.14)	30.71 (-1.99)
	H(13,14)	27.55	27.46 (-0.08)	27.36 (-0.18)	26.95 (-0.60)	27.46 (-0.09)
	H(15,16,17,18,19)	25.24	25.07 (-0.17)	25.01 (-0.23)	25.00 (-0.24)	25.24 (0.00)
	C(20)	128.86	128.91 (0.05)	128.87 (0.02)	130.00 (1.15)	129.6 (0.72)
	C(21)	59.14	58.55 (-0.59)	58.47 (-0.68)	56.67 (-2.47)	56.7 (-2.44)
	C(22,26)	74.34	73.93 (-0.40)	73.8 (-0.54)	73.48 (-0.86)	73.9 (-0.46)
	C(23,24,25)	71.61	71.52 (0.09)	71.49 (-0.12)	72.37 (0.77)	72.1 (0.51)
IGAIM	H(11)	32.03	30.83 (-1.19)	30.82 (-1.21)	30.49 (-1.53)	30.29 (-1.73)
	H(13,14)	26.37	25.52 (-0.85)	25.54 (-0.92)	25.32 (-1.05)	26.13 (-0.23)
	H(15,16,17,18,19)	24.84	23.90 (-0.94)	-23.92 (-0.92)	24.18 (-0.66)	24.82 (0.02)
	C(20)	126.65	126.12 (-0.53)	126.32 (-0.33)	127.81 (1.15)	127.99 (1.33)
	C(21)	58.75	57.38 (-1.38)	57.42 (-1.33)	55.71 (-3.04)	56.28 (-2.48)
	C(22,26)	70.99	69.70 (-1.29)	69.79 (-1.20)	69.64 (-1.35)	70.58 (-0.41)
	C(23,24,25)	69.00	68.02 (-0.98)	68.08 (-0.92)	69.39 (0.39)	69.55 (0.56)
CSGT	H(11)	32.00	30.83 (-1.18)	30.81 (-1.20)	30.50 (-1.51)	30.29 (-1.71)
	H(13,14)	26.34	25.50 (-0.84)	25.53 (-0.81)	25.31 (-1.03)	26.11 (-0.23)
	H(15,16,17,18,19)	24.81	23.88 (-0.93)	23.91 (-0.91)	24.15 (-0.66)	24.79 (-0.02)
	C(20)	126.65	126.12 (-0.53)	126.33 (-0.32)	127.81 (1.16)	127.99 (1.33)
	C(21)	58.76	57.39 (-1.37)	57.44 (-1.32)	55.72 (-3.04)	56.28 (-2.48)
	C(22,26)	70.98	69.70 (-1.28)	69.79 (-1.19)	69.63 (-1.35)	70.56 (-0.41)
	C(23,24,25)	68.98	68.01 (-0.97)	68.07 (-0.91)	69.37 (0.39)	69.54 (0.55)

***** The number in parentheses is the difference in the isotropic magnetic shielding [(after the adsorption) – (before the adsorption)].

The calculated differences in the ^{13}C isotropic magnetic shielding for benzyl alcohol are insignificant, with the exception of those for C(21) (in Figure 3-1E) in model clusters 3 and 4, where the differences are approximately 2-3 ppm. While the ^{13}C isotropic magnetic shielding differences calculated using the GIAO method are slightly smaller than those estimated using the IGAIM and the CSGT methods (up to approximately 0.9 ppm), the differences in chemical shielding calculated using the IGAIM and the CSGT methods are almost identical. The relatively larger decrease in chemical shielding for C(21) in model clusters 3 and 4 may also stem from the stronger hydrogen bonding between benzyl alcohol and those clusters (Table 3-4).

The ^{17}O isotropic chemical shieldings of basal oxygens before the adsorption (without benzyl alcohol) in model cluster 1 calculated at B3LYP/6-31G(d), range from 243.8 ppm to 253.2 ppm, apparently depending on the distance from the center of the model cluster. They are also slightly affected by the configurations of dangling hydrogens attached to apical oxygens (note that the oxygen sites in model cluster 1 are not crystallographically distinct). These results demonstrate that the ^{17}O NMR chemical shielding strongly depends on the atomic configuration around the second and higher coordination environments as well as on the nearest-neighbor atomic arrangements (e.g., Lee 2004; Tossell 2001). The isotropic chemical shieldings of the basal oxygens in the other model clusters calculated at B3LYP/6-31G(d) range from 236.4 ppm to 245.0 ppm (for model cluster 2), from 242.7 ppm to 251.7 ppm (for model cluster 3), and

from 243.7 ppm to 250.2 ppm (for model cluster 4). Those of the oxygens in model cluster 2 are dependent on the crystallographic positions (i.e., O3, O4, and O5 in Figure 3-1B): the average Si-O-Si bond angles are 130.6° (O3), 142.6° (O4), and 132.6° (O5), and the average Si-O bond lengths are 1.608 and 1.614 Å (O3), 1.597 and 1.628 Å (O4), and 1.611 and 1.618 Å (O5) (Bish and von Dreele, 1989). The isotropic chemical shifts [referenced to $H_2O(l)$] for the O3, O4, and O5 sites in model cluster 2 calculated at B3LYP/6-31G(d) are 43.8 ± 1.2, 45.6 ± 0.7, and 49.9 ± 1.0 ppm, respectively. While there is a noticeable basis set effect (see Computational methods above), the ^{17}O chemical shielding calculated at B3LYP/6-311+G(2d,p) show a similar trend with respect to cluster size variation and crystallographically distinct oxygen environments. The trend in the average chemical shielding for oxygen sites in the current study is somewhat different from the trend suggested in a previous O-17 3QMAS NMR study of kaolinite, where the isotropic chemical shifts for the O3, O4, and O5 sites were 54.3 ± 1, 46.5 ± 1, and 51.3 ± 1 ppm, respectively (Lee and Stebbins, 2003), suggesting that a larger cluster may be necessary to reveal the relatively small difference in chemical shift in crystallographically distinct atomic sites.

Table 3-5 shows the calculated ^{17}O isotropic magnetic shieldings for the basal oxygens on the surfaces. Figure 3-5 (showing model clusters 1 and 2 only) also presents the isotropic magnetic shielding differences between the oxygen sites before and after the adsorption [(isotropic magnetic shielding after the adsorption) – (isotropic magnetic shielding before the adsorption)], where several oxygens close to benzyl alcohol are shown (see

Table 3-5. Isotropic magnetic shieldings (ppm) of several basal oxygens close to the benzyl alcohol.

	Cluster 1	Isotropic magnetic shielding (ppm)		Cluster 2	Isotropic magnetic shielding (ppm)	
	Atom*	before	after†	Atom*	before	after†
B3LYP/6-31G(d) GIAO	**O(1)**	**244.3**	**241.4 (-2.9)**	**O(1)**	**242.1**	**240.8 (-1.6)**
	O(2)	252.4	247.7 (-4.7)	O(2)	242.2	238.4 (-3.8)
	O(3)	252.7	252.2 (-0.5)	O(3)	245.0	245.0 (0)
	O(4)	252.8	251.4 (-1.4)	O(4)	238.1	236.5 (-1.6)
	O(5)	253.0	252.2 (-0.8)	O(5)	242.1	242.4 (0.3)
	O(6)	252.8	253.3 (0.6)	O(6)	243.7	244.0 (0.3)
	O(7)	252.7	251.2 (-1.5)	O(7)	238.7	238.6 (-0.1)
	O(8)	243.9	243.5 (-0.4)	O(8)	237.2	236.8 (-0.4)
	O(9)	243.9	243.1 (-0.8)	O(9)	242.4	242.2 (-0.2)
	O(10)	244.4	244.5 (0.1)	O(10)	241.0	241.3 (0.3)
B3LYP/6-311+G(2d,p) GIAO	**O(1)**	**230.4**	**226.7 (-3.7)**	**O(1)**	**226.2**	**224.7 (-1.5)**
	O(2)	239.1	233.7 (-5.4)	O(2)	227.6	222.1 (-5.5)
	O(3)	238.9	237.0 (-1.9)	O(3)	228.9	228.9 (0)
	O(4)	239.0	235.7 (-3.3)	O(4)	221.3	217.9 (-3.4)
	O(5)	239.7	237.7 (-2.0)	O(5)	227.9	228.1 (0.2)
	O(6)	239.0	237.5 (-1.5)	O(6)	226.8	225.6 (-1.2)
	O(7)	239.0	235.9 (-3.1)	O(7)	222.0	220.6 (-1.4)
	O(8)	229.9	228.4 (-1.5)	O(8)	220.5	218.9 (-1.6)
	O(9)	230.3	227.9 (-2.4)	O(9)	228.8	228.3 (-0.5)
	O(10)	230.8	228.5 (-2.3)	O(10)	225.2	225.3 (0.1)
	Cluster 3	Isotropic magnetic shielding (ppm)		Cluster 4	Isotropic magnetic shielding (ppm)	
	Atom*	before	after†	Atom*	before	after†
B3LYP/6-31G(d) GIAO	**O(1)**	**245.0**	**243.6 (-1.4)**	**O(1)**	**237.1**	**236.9 (-0.2)**
	O(4)	242.7	241.1 (-1.6)	O(4)	246.5	245.1 (-1.4)

* The number in parentheses refers to the atom number in model clusters 1, 2, 3, and 4, as indicated in Figures 3-1A, B, C, and D, respectively. O(1) forms the hydrogen bond. See Figure 3-5 for the position of each oxygen atom. Note that the atom number in Figure 3-1 (white font) is for labeling the basal oxygens only.

† The number in parentheses is the difference in the isotropic magnetic shielding [(after the adsorption) – (before the adsorption)].

δ

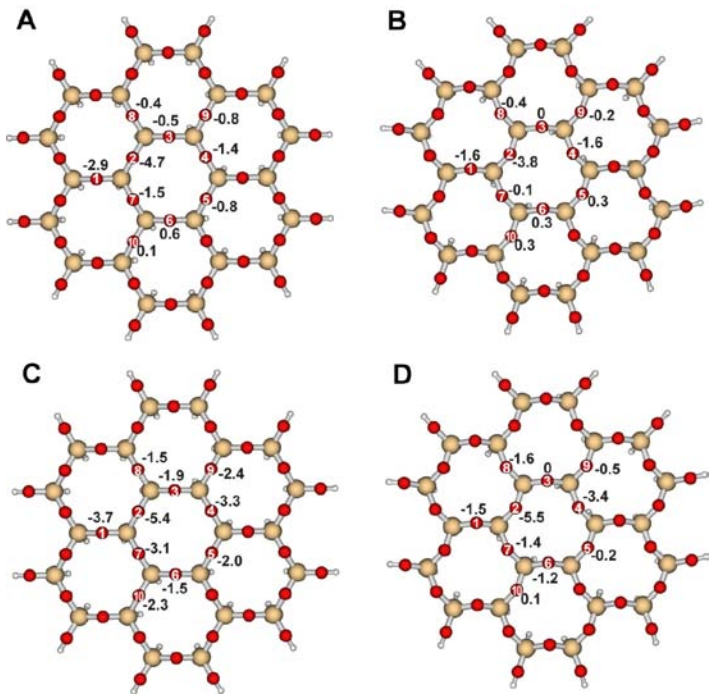

Figure 3-5. Model cluster 1 (A and C) and model cluster 2 (B and D) with the differences in chemical shielding for several oxygens close to benzyl alcohol. (A) and (B) are calculated at B3LYP/6-31G(d), and (C) and (D) are calculated at B3LYP/6-311+G(2d,p). The oxygen, silicon, and hydrogen are represented by red, wheat-colored, and white spheres, respectively. Refer to Figure 3-2 for the location of benzyl alcohol on each model cluster. The numbers on the oxygen atom are identical to those shown in Figure. 3-1. Note that the chemical shift in the oxygen site (δ_{shift}) can be described as follows: δ_{shift} = isotropic chemical shielding of oxygen in reference molecule (σ_{ref}) – isotropic chemical shielding of oxygen sites in layer silicates (σ_{oxy}). The chemical shift difference before and after the adsorption is $\Delta\delta_{shift} = \delta_{shift}$ (after adsorption) – δ_{shift} (before adsorption) = [$\sigma_{ref} - \sigma_{oxy}$ (after adsorption)] – [$\sigma_{ref} - \sigma_{oxy}$ (before adsorption)] = – [σ_{oxy} (after adsorption) - σ_{oxy} (before adsorption)] = - $\Delta\ \sigma_{oxy}$. Therefore, $\Delta\ \delta_{shift} = -\ \Delta\ \sigma_{oxy}$.

figure caption 3-5). Whereas the model clusters used in this study may not be sufficiently large to accurately estimate the NMR chemical shielding values for basal oxygens, *the differences* in the ^{17}O NMR chemical shieldings before and after the adsorption are important, revealing the effect of the adsorption. In systematically controlled calculations, as shown in the computational method section above, the difference in the chemical shift is due only to the adsorption of benzyl alcohol on the surfaces. The ^{17}O chemical shielding of the basal oxygens mostly decreases after the adsorption (see Table 3-5). The largest chemical shielding differences calculated at B3LYP/6-31G(d) are –4.7, –3.8, –1.6, and –1.4 ppm for model clusters 1, 2, 3, and 4, respectively, and those calculated at B3LYP/6-311+G(2d,p) are 5.4 and -5.5 ppm for model clusters 1 and 2, respectively. The ^{17}O chemical shift differences calculated at B3LYP/6-311+G(2d,p) are somewhat larger (from -0.1 to +2.4 ppm) than those calculated at B3LYP/6-31G(d) (Figure 3-5). This discrepancy indicates that the calculated uncertainty in the O-17 NMR chemical shielding could be as large as 2.4 ppm. Some of the oxygens in the model clusters [e.g., O(1) and O(2) in model cluster 1 and O(1) in model cluster 2] have chemical shielding differences that were larger than the maximum uncertainty, and these calculated differences stem from the adsorption. It should be noted that the oxygens that formed hydrogen bonds with benzyl alcohol did not show the largest chemical shielding differences after the adsorption [O(1) in Figure 3-5 and Table 3-1]. This may be due to the fact that the ^{17}O NMR chemical shielding is dependent, not only on the O···H distance but also on the

δ

atomic configurations beyond the first coordination environments (i.e., the entire atomic arrangement of the molecule on the surface) (Lee, 2004).

The calculated differences in the ^{17}O C_q and η of the key basal oxygen before and after the adsorption were 0.088 MHz and 0.015 [O(1) in Figure 3-1A] (model cluster 1), 0.081 MHz and 0.033 [O(1) in Figure 3-1B] (model cluster 2), 0.171 MHz and 0.024 [O(1) in Figure 3-1C] (model cluster 3), and 0.215 MHz and 0.125 [O(1) in Figure 3-1D] (model cluster 4), respectively. These differences, with the exception of the C_q for model clusters 3 and 4, are insignificant. Thus, it is difficult to investigate these changes experimentally. The relatively large changes in C_q for the oxygen sites in model cluster 4 may have resulted from the stronger hydrogen bond between the alcohol hydrogen and basal oxygen [O(1)] compared to the other clusters.

While additional theoretical NMR chemical shielding tensor calculations using larger coordination spheres for the model clusters for clay surfaces are certainly necessary, the calculated ^{17}O isotropic chemical shieldings of some basal oxygens generally decrease up to approximately 4–5 ppm after the adsorption. Since the experimental high-resolution ^{17}O 3QMAS NMR spectroscopy of layer silicates yielded a resolution of 1–2 ppm among the basal oxygen sites in the layer silicates (Lee and Stebbins, 2003; Lee et al., 2003; Lee and Weiss, 2008), the advanced ^{17}O 3QMAS may be useful in exploring the nature of the adsorption between organic molecules and silicate surfaces. Whereas the oxygen sites were well resolved in our previous ^{17}O NMR spectra for natural Georgia kaolinite

with negligible Fe content and synthetic 2:1 layer silicates without Fe (Lee and Stebbins, 2003; Lee et al., 2003; Lee and Weiss, 2008), the presence of paramagnetic impurity (e.g., Fe) in other natural layer silicates can broaden the NMR peaks. Also note that the adsorption of organic molecules may result in a broadening of the resonance peaks (in addition to the shift), making it difficult to resolve the adsorption induced changes in the chemical shift. As the current study only explores the effect of a single benzyl alcohol molecule on the surface, the additional effects of surface coverage and other diverse organic molecules on NMR chemical shielding remain to be investigated.

3.4. Conclusion

The effect of lattice topology and cluster size of four different kaolinite model clusters on the adsorption of benzyl alcohol were investigated by performing quantum chemical calculations of the optimized structure, binding energy, and NMR chemical shielding. The optimized geometry of benzyl alcohol adsorbed on the tetrahedral surface of kaolinite show that the adsorption on three-ring clusters is affected by the edge hydrogens due to relatively small surface area, while that on seven-ring clusters is not affected. The results also show that the geometry of adsorption on ideal hexagonal rings is different from that of adsorption on ditrigonal rings, demonstrating the topology dependence of adsorption. The optimized structure and binding energy calculations suggest that adsorption on the tetrahedral surface is dominated by weak hydrogen

bonding and dispersion force, while that on the octahedral surface is mostly governed by hydrogen bonding. The NMR chemical shielding calculations show that the weak interaction on the tetrahedral surface can be potentially resolved by high-resolution solid-state ^{17}O 2D NMR. The results obtained and trends observed in the present manuscript suggest that a model cluster simulating clay surfaces should be carefully designed using quantum chemical calculations, particularly when the adsorption is weak and the adsorbate is fairly large.

References

Adiga, S., Aebi, D. and Bryce, D. L. (2007) EFGShield - A program for parsing and summarizing the results of electric field gradient and nuclear magnetic shielding tensor calculations. Canadian Journal of Chemistry, 85, 496-505.

Anderson, W. G. (1986) Wettability literature survey - Part 1: Rock-oil-brine interactions and the effects of core handling on wettability. Journal of Petroleum Technology, 38(11), 1125-1144.

Aquino, A. J. A., Tunega, D., Haberhauer, G., Gerzabek, M. H. and Lischka, H. (2007) Quantum chemical adsorption studies on the (110) surface of the mineral goethite. Journal of Physical Chemistry C, 111(2), 877-885.

Bantignies, J. L., Moulin, C. C. D. and Dexpert, H. (1998) Asphaltene adsorption on kaolinite characterized by infrared and X-ray absorption spectroscopies. Journal of Petroleum Science and Engineering, 20(3-4), 233-237.

Bayer, I. S., Steele, A., Martorana, P. J. and Loth, E. (2010) Fabrication of superhydrophobic polyurethane/organoclay nano-structured composites from cyclomethicone-in-water emulsions. Applied Surface Science, 257, 823-826.

Becke, A. D. (1993) Density-functional thermochemistry. III. The role of exact exchange. Journal of Chemical Physics, 98, 5648-5652.

Becke, A. D. (1993) A new mixing of Hartree-Fock and local density-functional theories. Journal of Chemical Physics, 98(2), 1372-1377.

Bish, D. L. (1993) Rietveld refinement of the kaolinite structure at 1.5 K. Clays and Clay Minerals, 41, 738-744.

Bish, D. L. and von Dreele, R. B. (1989) Rietveld refinement of non-hydrogen atomic positions in kaolinite. Clays and Clay Minerals, 37, 289-296.

Boulet, P., Greenwell, H. C., Stackhouse, S. and Coveney, P. V. (2006) Recent advances in understanding the structure and reactivity of clays using electronic structure calculations. Journal of Molecular Structure: THEOCHEM, 762, 33-48.

Boys, S. F. and Bernardi, F. (1970) The calculation of small molecular interactions by the differences of separate total energies. Some procedures with reduced errors. Molecular Physics, 19, 553-566.

Brown, G. E. J., Calas, G., Waychunas, G. A. and Petiau, J. (1988) X-ray absorption-spectroscopy and its applications in mineralogy and geochemistry. Spectroscopic Methods in Mineralogy and Geology. F. C. Hawthorne. Chelsea, Michigan, Mineralogical Society of America, 18, 431-512 p.

Brown, G. E. J., Henrich, V. E., Casey, W. H., Clark, D. L., Eggleston, C., Felmy, A., D.W., G., Grätzel, M., Maciel, G., McCarthy, M. I., Nealson, K. H., Sverjensky, D. A., Toney, M. F. and Zachara, J. M. (1999) Metal oxide surfaces and their interactions with aqueous solutions and microbial organisms. Chemical Reviews, 99, 77-174.

Castro, E. A. S. and Martins, J. B. L. (2005) Theoretical study of benzene interaction on kaolinite. Journal of Computer-Aided Materials Design, 12, 121-129.

Chu, P.-J., Potrzebowski, M. J., Gao, Y. and Scott, A. I. (1990) Conformational studies of N-benzoyl-L-phenylalanine by combined rotation and multiple-pulse spectroscopy ^{1}H nuclear magnetic resonance. Journal of the American Chemical Society, 112, 881-883.

Cremer, D. (1998) Møller–Plesset Perturbation Theory. Encyclopedia of Computational Chemistry. P. von Rague-Schleyer. New York, John Wiley, 3, 1706-1735 p.

Crespo-Otero, R., Montero, L. A., Stohrer, W.-D. and de la Vega, J. M. G. (2005) Basis set superposition error in MP2 and density-functional theory: A case of methane-nitric oxide association. Journal of Chemical Physics, 123, 134107.

Cygan, R. T. and Kubicki, J. D., Eds. (2001) Molecular Modeling Theory: Applications in the Geosciences. Reviews in Mineralogy & Geochemistry. Washington DC, Mineralogical Society of America, 531 p.

Førland, G. M. (2001) Adsorption of benzyl alcohol onto alumina and kaolinite surfaces from a nonaqueous solution. Journal of Colloid and Interface Science, 242(2), 477-479.

Førland, G. M., Borve, K. J., Hoiland, H. and Skauge, A. (1995) Adsorption of short-chain alcohols from decane solutions onto kaolinite. Journal of Colloid and Interface Science, 171(2), 261-269.

Feng, X. J., Simpson, A. J. and Simpson, M. J. (2005) Chemical and mineralogical controls on humic acid sorption to clay mineral surfaces. Organic Geochemistry, 36(11), 1553-1566.

Foresman, J. B. and Frisch, Æ. (1996) Exploring Chemistry with Electronic Structure Methods. Pittsburgh, PA, Gaussian, Inc., 302 p.

Frisch, M. J., Trucks, G. W., Schlegel, H. B., Scuseria, G. E., Robb, M. A., Cheeseman, J. R., J.A. Montgomery, J., Vreven, T., Kudin, K. N., Burant, J. C., Millam, J. M., Iyengar, S. S., Tomasi, J., Barone, V., Mennucci, B., Cossi, M., Scalmani, G., Rega, N., Petersson, G. A., Nakatsuji, H., Hada, M., Ehara, M., Toyota, K., Fukuda, R.,

Hasegawa, J., Ishida, M., Nakajima, T., Honda, Y., Kitao, O., Nakai, H., Klene, M., Li, X., Knox, J. E., Hratchian, H. P., Cross, J. B., Bakken, V., Adamo, C., Jaramillo, J., Gomperts, R., Stratmann, R. E., Yazyev, O., Austin, A. J., Cammi, R., Pomelli, C., Ochterski, J. W., Ayala, P. Y., Morokuma, K., Voth, G. A., Salvador, P., Dannenberg, J. J., Zakrzewski, V. G., Dapprich, S., Daniels, A. D., Strain, M. C., Farkas, O., Malick, D. K., Rabuck, A. D., Raghavachari, K., Foresman, J. B., Ortiz, J. V., Cui, Q., Baboul, A. G., Clifford, S., Cioslowski, J., Stefanov, B. B., Liu, G., Liashenko, A., Piskorz, P., Komaromi, I., Martin, R. L., Fox, D. J., Keith, T., Al-Laham, M. A., Peng, C. Y., Nanayakkara, A., Challacombe, M., Gill, P. M. W., Johnson, B., Chen, W., Wong, M. W., Gonzalez, C. and Pople, J. A. (2004) Gaussian 03. Wallingford CT, Gaussian, Inc.

Gorb, L., Lutchyn, R., Zub, Y., Leszczynska, D. and Leszczynski, J. (2006) The origin of the interaction of 1,3,5-trinitrobenzene with siloxane surface of clay minerals. Journal of Molecular Structure: THEOCHEM, 766(2-3), 151-157.

Granqvist, B., Sandberg, T. and Hotokka, M. (2007) Adsorption of organic probes on silica through Lewis interactions: A comparison of experimental results and quantum chemical calculations. Journal of Colloid and Interface Science, 310, 369-376.

Haase, F. and Sauer, J. (1994) H-1 NMR chemical-shifts of ammonia, methanol, and water-molecules interacting with Brönsted acid sites of zeolite catalysts - Ab-initio calculations. Journal of Physical Chemistry, 98(12), 3083-3085.

Haase, F. and Sauer, J. (1995) Interaction of methanol with Brönsted acid sites of zeolite catalysts - An ab-initio study. Journal of the

American Chemical Society, 117(13), 3780-3789.

Hobbs, J. D., Cygan, R. T., Nagy, K. L., Schultz, P. A. and Sears, M. P. (1997) All-atom ab initio energy minimization of the kaolinite crystal structure. American Mineralogist, 82(7-8), 657-662.

Hong, H. L., Fu, Z. Y. and Min, X. M. (2001) The adsorption of $[Au(HS)_2]^-$ on kaolinite surfaces: Quantum chemistry calculations. Canadian Mineralogist, 39, 1591-1596.

Hong, H. L., Min, X. M. and Fu, Z. Y. (2002) Study on adsorption of submicrometer gold on kaolinite by quantum chemistry calculations. American Mineralogist, 87(1), 1-4.

Huang, M. J., Lee, K. S. and Hurley, S. J. (2005) Nuclear magnetic resonance spectral analysis and molecular properties of berberine. International Journal of Quantum Chemistry, 105(4), 396-409.

Johansson, U., Holmgren, A., Forsling, W. and Frost, R. L. (1999) Adsorption of silane coupling agents onto kaolinite surfaces. Clay Minerals, 34(2), 239-246.

Jurkiewicz, A. and Maciel, G. E. (1995) Solid-state ^{13}C NMR studies of the interaction of aceton, carbon tetrachloride and trichloroethylene with soil components. The Science of the Total Environment, 164, 195-202.

Kelleher, B. P. and O'Dwyer, T. F. (2002) Intercalation of benzamide into expanded kaolinite under ambient environmental conditions. Clays and Clay Minerals, 50(3), 331-335.

Knezovich, J. P., Harrison, F. L. and Wilhelm, R. G. (1987) The bioavailability of sediment-sorbed organic chemicals: A review. Water, Air, snd Soil Pollution, 32, 233-245.

Kowalska, M., Guler, H. and Cocke, D. L. (1994) Interactions of clay

minerals with organic pollutants. The Science of the Total Environment, 141, 223-240.

Krossner, M. and Sauer, J. (1996) Interaction of water with Brönsted acidic sites of zeolite catalysts. Ab initio study of 1:1 and 2:1 surface complexes. Journal of Physical Chemistry, 100(15), 6199-6211.

Kubicki, J. D., Schroeter, L., M., Itoh, M. J., Nguyen, B. N. and Apitz, S. E. (1999) Attenuated total reflectance Fourier-transform infrared spectroscopy of carboxylic acids adsorbed onto mineral surfaces. Geochimica et Cosmochimica Acta, 63(18), 2709-2725.

Kwon, K. D., Vadillo-Rodriguez, V., Logan, B. E. and Kubicki, J. D. (2006) Interactions of biopolymers with silica surfaces: Force measurements and electronic structure calculation studies. Geochimica et Cosmochimica Acta, 70(15), 3803-3819.

Lee, C., Yang, W. and Parr, R. G. (1988) Development of the Colle-Salvetti correlation-energy formula into a functional of the electron density. Physical Review B, 37(2), 785-789.

Lee, S. K. (2004) Structure of silicate glasses and melts at high pressure: Quantum chemical calculations and solid-state NMR. Journal of Physical Chemistry B, 108, 5889-5900.

Lee, S. K. and Lee, B. H. (2006) Atomistic origin of germanate anomaly in GeO_2 and Na-germanate glasses: Insights from two-dimensional ^{17}O NMR and quantum chemical calculations. Journal of Physical Chemistry B, 110, 16408-16412.

Lee, S. K., Musgrave, C. B., Zhao, P. and Stebbins, J. F. (2001) Topological disorder and reactivity of borosilicate glasses: Quantum chemical calculations and ^{17}O and ^{11}B NMR. Journal of Physical Chemistry B, 105, 12583-12595.

Lee, S. K. and Stebbins, J. F. (2003) O atom sites in natural kaolinite and muscovite: O-17 MAS and 3QMAS NMR study. American Mineralogist, 88(4), 493-500.

Lee, S. K. and Stebbins, J. F. (2006) Disorder and the extent of polymerization in calcium silicate and aluminosilicate glasses: O-17 NMR results and quantum chemical molecular orbital calculations. Geochimica et Cosmochimica Acta, 70, 4275-4286.

Lee, S. K., Stebbins, J. F., Weiss Jr., C. A. and Kirkpatrick, R. J. (2003) O-17 and Al-27 MAS and 3QMAS NMR study of synthetic and natural layer-silicates. Chemistry of Materials, 15, 2605-2613.

Lee, S. K. and Weiss, C. A. J. (2008) Multiple oxygen sites in synthetic phyllosilicates with expandable layers: ^{17}O solid-state NMR study. American Mineralogist, 93, 1066-1071.

Lee, S. Y. and Kim, S. J. (2002) Adsorption of naphtalene by HDTMA modified kaolinite and halloysite. Applied Clay Science, 22, 55-63.

Li, Y. C. and Gupta, G. (1994) Adsorption of hydrocarbons by clay-minerals from gasoline. Journal of Hazourdous Materials, 38(1), 105-112.

Møller, C. and Plesset, M. S. (1934) Note on an approximation treatment for many-electron systems. Physical Review 46, 618-622.

Madsen, L., Grahl-Madsen, L., C. Gron, Lind, I. and Engell, J. (1996) Adsorption of polar aromatic hydrocarbons on synthetic calcite. Organic Geochemistry, 24(12), 1151-1155.

Mehring, M. (1983) Principles of High Resolution NMR in Solids. Berlin Heidelberg New York, Springer-Verlag, 342 p.

Michalkova, A., Gorb, L., Ilchenko, M., Zhikol, O. A., Shishkin, O. V. and Leszczynski, J. (2004) Adsorption of sarin and soman on dickite: An ab initio ONIOM study. Journal of Physical Chemistry B, 108(6),

1918-1930.

Michalkova, A., Martinez, J., Zhikol, O. A., Gorb, L., Shishkin, O. V., Leszczynska, D. and Leszczynski, J. (2006) Theoretical study of adsorption of Sarin and Soman on tetrahedral edge clay mineral fragments. Journal of Physical Chemistry B, 110(42), 21175-21183.

Michalkova, A., Szymczak, I. J. and Leszczynski, J. (2005) Adsorption of 2,4-dinitrotoluene on dickite: The role of H-bonding. Structural Chemistry, 16(3), 325-337.

Michalkova, A., Tunega, D. and Nagy, L. T. (2002) Theoretical study of interactions of dickite and kaolinite with small organic molecules. Journal of Molecular Structure: THEOCHEM, 581, 37-49.

Molina, J. M., Dobado, J. A., Daza, M. C. and Villaveces, J. L. (2002) Structure and bonding of weak hydrogen peroxide complexes. Journal of Molecular Structure: THEOCHEM, 580, 117-126.

Murgich, J., Rodriguez M., J., Izquierdo, A., Carbognani, L. and Rogel, E. (1998) Interatomic interactions in the adsorption of asphaltenes and resins on kaolinite calculated by molecular dynamics. Energy & Fuels, 12, 339-343.

Murray, D. K., Harrison, J. C. and Wallace, W. E. (2005) A ^{13}C CP/MAS and ^{31}P NMR study of the interactions of dipalmitoylphosphatidylcholine with respirable silica and kaolin. Journal of Colloid and Interface Science, 288, 166-170.

Ogawa, M. and Kuroda, K. (1995) Photofunctions of intercalation compounds. Chemical Reviews, 95, 399-438.

Olejnik, S., Posner, A. M. and Quirk, J. P. (1970) The interaction of polar organic compounds into kaolinite. Clay Minerals, 8(4), 421-434.

Ottonello, G. and Zuccolini, M. V. (2005) Ab-initio structure, energy and

δ

stable Cr isotopes equilibrium fractionation of some geochemically relevant H-O-Cr-Cl complexes. Geochimica et Cosmochimica Acta, 69, 851-874.

Pérez-Jordá, J. M. and Becke, A. D. (1995) A density-functional study of van der Waals forces: rare gas diatomics. Chemical Physics Letters, 233, 134-137.

Parthasarathi, R. and Subramanian, V. (2006) Characterization of hydrogen bonding: From van der Waals interactions to covalency Hydrogen Bonding - New Insights. S. J. Grabowski. Dordrecht Springer, 3, 1-50 p.

Pelmenschikov, A. and Leszczynski, J. (1999) Adsorption of 1,3,5-trinitrobenzene on the siloxane sites of clay minerals: Ab initio calculations of molecular models. Journal of Physical Chemistry B, 103(33), 6886-6890.

Pelmenschikov, A., Strandh, H., Pettersson, L. G. M. and Leszczynski, J. (2000) Lattice resistance to hydrolysis of Si-O-Si bonds of silicate minerals: Ab initio calculations of a single water attack onto the (001) and (111) β-cristobalite surfaces. Journal of Physical Chemistry B, 104, 5779-5783.

Pelmenschikov, A. G., Morosi, G. and Gamba, A. (1992) Quantum chemical molecular models of oxides. 2. Methanol adsorption on silica and zeolites. Journal of Physical Chemistry, 96, 2241-2246.

Pinnavaia, T. J. and Beall, G. W., Eds. (2000) Polymer-clay nanocomposites. New York, John Wiley & Sons, 349 p.

Plant, D. F., Simperler, A. and Bell, R. G. (2006) Adsorption of methanol on zeolites X and Y. An atomistic and quantum chemical study. Journal of Physical Chemistry B, 110, 6170-6178.

Robinson, T. L., Michalkova, A., Gorb, L. and Leszczynski, J. (2007) Hydrogen bonding of thymine and uracil with surface of dickite: An ab initio study. Journal of Molecular Structure: THEOCHEM, 844-845, 48-58.

Rozas, I. (2007) On the nature of hydrogen bonds: An overview on computational studies and a word about patterns. Physical Chemistry Chemical Physics, 9, 2782-2790.

Sauer, J., Ugliengo, P., Garrone, E. and Saunders, V. R. (1994) Theoretical study of van der Waals complexes at surface sites in comparison with the experiment. Chemical Reviews, 94, 2095-2160.

Schauble, E. A., Rossman, G. R. and Taylor, J. H. P. (2001) Theoretical estimates of equilibrium Fe-isotope fractionation from vibrational spectroscopy. Geochimica et Cosmochimica Acta, 65(2487-2497).

Schauble, E. A., Rossman, G. R. and Taylor, J. H. P. (2003) Theoretical estimates of equilibrium chlorine-isotope fractionation. Geochimica et Cosmochimica Acta, 67, 3267-3281.

Schauble, E. A., Rossman, G. R. and Taylor, J. H. P. (2004) Theoretical estimates of equilibrium chromium-isotope fractionation. Chemical Geology, 205, 99-114.

Seger, M. R. and Maciel, G. E. (2006) NMR investigation of the behavior of an organothiophosphate pesticide, chlorpyrifos, sorbed on soil components. Environmental Science & Technology, 40, 791-796.

Simion, D. V. and Sorensen, T. S. (1996) A theoretical computation of the aromaticity of (benzene)Cr(CO)(3) compared to benzene using the exaltation of magnetic susceptibility criterion and a comparison of calculated and experimental NMR chemical shifts in these compounds. Journal of the American Chemical Society, 118(31),

7345-7352.

Simperler, A., Bell, R. G. and Anderson, M. W. (2004) Probing the acid strength of Brønsted acidic zeolites with acetonitrile: Quantum chemical calculaton of ^{1}H, ^{15}N, and ^{13}C NMR shift parameters. Journal of Physical Chemistry B, 108, 7142-7151.

Simperler, A., Bell, R. G., Philippou, A. and Anderson, M. W. (2002) Theoretical study of toluene adsorbed on zeolites X and Y: Calculation of ^{13}C NMR parameters. Journal of Physical Chemistry B, 106, 10944-10954.

Solans-Monfort, X., Sodupe, M., Mó, O., Yáñez, M. and Elguero, J. (2005) Hydrogen bond vs proton transfer in HZSM5 zeolite. A theoretical study. Journal of Physical Chemistry B, 109, 19301-19308.

Stebbins, J. F. (1995) Nuclear magnetic resonance spectroscopy of silicates and oxides in geochemistry and geophysics. Handbook of Physical Constants. T. J. Ahrens. Washington D.C., American Geophysical Union, 2, 303-332 p.

Stone, A. J. (1996) The Theory of Intermolecular Forces. Oxford, Clarendon Press, 264 p.

Suh, J. H., Lee, S. K. and Lee, I. (2007) Quantum chemical calculations of equilibrium copper (I) isotope fractionations in ore-forming fluids. Chemical Geology, 243, 225-237.

Svensson, M., Humbel, S., Froese, R. D. J., Matsubara, T., Sieber, S. and Morokuma, K. (1996) ONIOM: A multilayered integrated MO + MM method for geometry optimizations and single point energy predictions. A test for diels-alder reactions and $Pt(P(t\text{-}Bu)_3)_2 + H_2$ oxidative addition. Journal of Physical Chemistry 100, 19357-19363.

Tao, T. and Maciel, G. E. (1998) ^{13}C NMR study of co-contamination of clays

with carbon tetrachloride and benzene. Environmental Science & Technology, 32, 350-357.

Teppen, B. J., Yu, C. H., Miller, D. M. and Schafer, L. (1998) Molecular dynamics simulations of sorption of organic compounds at the clay mineral/aqueous solution interface. Jounal of Computational Chemistry, 19(2), 144-153.

Thomas, J. E. and Kelley, M. J. (2008) Interaction of mineral surfaces with simple organic molecules by diffuse reflectance IR spectroscopy (DRIFT) Journal of Colloid and Interface Science, 322(2), 516-526.

Tossell, J. A. (2001) Calculating the NMR properties of minerals, glasses, and aqueous species. Molecular Modeling Theory: Applications in the Geosciences. R. T. Cygan and J. D. Kubicki. Washington, DC, The Mineralogical Society of America, 42, 437-458 p.

Tossell, J. A. (2005) Calculating the partitioning of the isotopes of Mo between oxidic and sulfidic species in aqueous solution. Geochimica et Cosmochimica Acta, 69(2981-2993).

Tunega, D., Benco, L., Haberhauer, G., Gerzabek, M. H. and Lischka, H. (2002) Ab initio molecular dynamics study of adsorption sites on the (001) surfaces of 1 : 1 dioctahedral clay minerals. Journal of Physical Chemistry B, 106(44), 11515-11525.

Tunega, D., Haberhauer, G., Gerzabek, M. H. and Lischka, H. (2002) Theoretical study of adsorption sites on the (001) surfaces of 1 : 1 clay minerals. Langmuir, 18(1), 139-147.

Tunega, D., Haberhauer, G., Gerzabek, M. H. and Lischka, H. (2004) Sorption of phenoxyacetic acid herbicides on the kaolinite mineral surface - an ab initio molecular dynamics simulation. Soil Science, 169(1), 44-54.

Tunney, J. J. and Detellier, C. (1996) Aluminosilicate nanocomposite materials. Poly(ethylene glycol)-kaolinite intercalates. Chemistry of Materials, 8, 927-935.

van Duin, A. C. T. and Larter, S. R. (2001) Molecular dynamics investigation into the adsorption of organic compounds on kaolinite surfaces. Organic Geochemistry, 32, 143-150.

Viruela-Martín, P., Zicovich-Wilson, C. M. and Corma, A. (1993) Ab initio molecular orbital calculations of the protonation reaction of propylene and isobutene by acidic OH groups of isomorpbously substituted zeolites. Journal of Physical Chemistry, 97, 13713-13719.

Wang, K. J. and Xing, B. S. (2005) Structural and sorption characteristics of adsorbed humic acid on clay minerals. Journal of Environmental Quality, 34(1), 342-349.

Wasylishen, R. E. and Bryce, D. L. (2002) A revised experimental absolute magnetic shelding scale for oxygen. Journal of Chemical Physics, 117(22), 10061-10066.

Wiberg, K. B., Hammer, J. D., Zilm, K. W. and Cheeseman, J. R. (1999) NMR chemical shifts. 3. A comparison of acetylene, allene, and the higher cumulenes. Journal of Organic Chemistry, 64(17), 6394-6400.

Winkler, P., Novoszad, M., Gerzabek, M. H., Haberhauer, G., Tunega, D. and Lischka, H. (2007) Interaction of naphthalene derivatives with soil: an experimental and theoretical case study. European Journal of Soil Science, 58(4), 967-977.

Xie, X. and Hayashi, S. (1999) NMR study of kaolinite intercalation compounds with formamide and its derivatives. 1. Structure and orientation of guest molecules. Journal of Physical Chemistry B, 103, 5949-5955.

Xue, X. and Kanzaki, M. (1998) Correlations between ^{29}Si, ^{17}O and ^{1}H NMR properties and local structures in silicates: An ab initio calculation. Physics and Chemistry of Minerals, 26, 14-30.

Yariv, S. (1996) Thermo-IR-spectroscopy analysis of the interactions between organic pollutants and clay minerals Thermochimica Acta, 274, 1-35.

Yariv, S. and Lapides, I. (2000) The effect of mechanochemical treatments on clay minerals and the mechanochemical adsorption of organic materials onto clay minerals. Journal of Materials Synthesis and Processing, 8(3-4), 223-233.

Yesinowski, J. P. and Eckert, H. (2009) Hydrogen environments in calcium phosphates: ^{1}H MAS NMR at high spinning speeds. Journal of the American Chemical Society, 109(21), 6274-6282.

Yoon, T. H., Johnson, S. B., Musgrave, C. B. and Brown, G. E. (2004) Adsorption of organic matter at mineral/water interfaces: I. ATR-FTIR spectroscopic and quantum chemical study of oxalate adsorbed at boehmite/water and corundum/water interfaces. Geochimica et Cosmochimica Acta, 68(22), 4505-4518.

Zhanpeisov, N. U., Adams, J. W., Larson, S. L., Weiss, C. A., Zhanpeisova, B. Z., Leszczynska, D. and Leszczynski, J. (1999) Cluster quantum chemical study of triaminotoluene interaction with a model clay surface. Structural Chemistry, 10(4), 285-294.

Chapter 4. Effects of specific surface area and porosity on cube counting fractal dimension, lacunarity, and configurational entropy of porous networks of model sands: insights from random packing simulations and NMR micro-imaging

Abstract

Despite the importance of understanding and quantifying the microstructure of porous networks in diverse geologic settings, the effect of specific surface area and porosity on the key structural parameters of the networks have not been fully understood. Cube-counting fractal dimension (D_{cc}) and lacunarity analyses of 3D porous networks of model sands and configurational entropy analysis of 2D cross sections of model sands were performed using random packing simulations and nuclear magnetic resonance (NMR) micro-imaging. Relationships among porosity, specific surface area, structural parameters (D_{cc} and lacunarity), and the corresponding macroscopic properties (configurational entropy and permeability) were established. The D_{cc} of the 3D porous networks increases with increasing specific surface area at constant porosity and with increasing porosity at constant specific surface area. Predictive relationships correlating D_{cc}, specific surface area, and porosity were also obtained. Lacunarity at the minimum box size decreases with increasing porosity, and the calculated lacunarity at the intermediate box size (~470

δ

μm in the current model sands) was reproduced well with specific surface area. The maximum configurational entropy increases with increasing porosity, and the entropy length of the pores decreases with increasing specific surface area and was used to calculate the average connectivity among the pores. The correlation among porosity, specific surface area, and permeability is consistent with the prediction from the Kozeny-Carman equation. From the relationship between the permeability and the D_{cc} of pores, permeability can be expressed as a function of the D_{cc} of pores and porosity. The current methods and these newly identified correlations among structural parameters and properties provide improved insights into the nature of porous media and have useful geophysical implications for elasticity and shear viscosity of complex composites of rock, glasses, melt, and fluids.

4.1. Introduction

Quantification of the porous networks in porous media is important for understanding and predicting their macroscopic properties, including permeability of fluids in partially molten rocks (Takei and Holtzman, 2009), transport behavior of ground water (Sahimi, 1993; Gladden et al., 1995), and seismic wave attenuation (Bourbié et al., 1987; Li et al., 2001; Takei, 2002; Takei, 2005). Such quantification also provides essential information that can be used for improving oil recovery from reservoir rocks, predicting pollutant migration in soil, and underground storage of CO_2 and nuclear waste. To quantify and characterize irregular

and disordered porous networks, diverse structural parameters other than porosity have been introduced. These include fractal dimension (e.g., Hansen and Skjeltorp, 1988; Ghilardi et al., 1993; Giménez et al., 1997; Dathe and Thullner, 2005; Tarquis et al., 2008), generalized dimensions (multifractals) (e.g., Muller et al., 1995; Posadas et al., 2003), and lacunarity (e.g., Pendleton et al., 2005). Often, more than two parameters of the porous networks were used to gain insights into the nature of porous media. For example, fractal and multifractal (e.g., Bird et al., 2006), fractal and lacunarity (e.g., Armatas et al., 2002), multifractal and configurational entropy (e.g., Tarquis et al., 2006), and lacunarity and configurational entropy (e.g., Chun et al., 2008) analyses were used to characterize diverse natural porous networks. Despite these key previous studies, the systematic relationships among the structural parameters have not yet been established because most fractal, lacunarity, and configurational entropy analyses of porous networks have been carried out on natural systems (e.g., soil) characterized by intrinsic heterogeneity in density, composition, and phase. Consequently, the general relationship among these parameters for random networks with well-controlled particle sizes and shapes have not been available thus far. Studies of model porous networks prepared by random packing simulations or model glass beads can facilitate easy control of the diameter and shape of the particles in porous media (Schwartz and Banavar, 1989; Coelho et al., 1997; Garcia et al., 2009). The potential results enable us to establish the much anticipated systematic and quantitative relationships among these structural parameters. Furthermore,

macroscopic properties of porous media, such as permeability, depend on specific surface area (Bear, 1972; Dullien, 1979). Because previous studies often used 2D images of porous networks rather than complete 3D networks, the effect of specific surface area on these structural parameters remains unknown. The objective of this study is to investigate the relationships among 3D porous networks, structural parameters, and transport properties, such as permeability, with emphasis on the effect of specific surface area on these parameters.

Nuclear magnetic resonance (NMR) imaging or magnetic resonance imaging (MRI) is a nondestructive technique used to obtain 3D distributions of porous networks in porous media. NMR imaging enables imaging of different chemical species of fluid phases (as opposed to solid skeletons probed by X-ray based techniques), exploring species with varying relaxation times (e.g., spin-lattice relaxation time and spin-spin relaxation time), and mapping of the flow velocity vectors in porous media (see Callaghan, 1991; Blümich, 2000 and references therein). Hence, this method has been used for porous media research such as the distribution of fluids in rocks (e.g., Dereppe et al., 1991; Davies et al., 1994; Doughty and Tomutsa, 1996), chemical reactors (e.g., Gladden, 2003; Lysova et al., 2005, and cements (e.g., Balcom et al., 2003; Gussoni et al., 2004; Faure et al., 2005). NMR method including NML (NMR logging) also has been used to study the relationships between porous media and fluids. It measures relaxation times or diffusion coefficients of fluids in porous media (Kleinberg, 2001; Song et al., 2008). The major difference between NMR imaging and NMR

d

method for probing the porous media is that the former directly obtains the information of pore structure or fluid distribution from the imaging data and the latter indirectly obtains the information from the relaxation times or diffusion coefficients. While both methods enabled us to provide useful information of porous media, a link between the distribution of relaxation times and the measurements from the indirect method needs to be explored. The study will be possible with the ability of 3D imaging of relaxation times and the development of high resolution NMR imaging. NMR micro-imaging refers to NMR imaging in which a high spatial resolution (<100 μm) is obtained. A few NMR micro-imaging studies of porous media have been conducted, including flow velocity in computer-generated percolation clusters (Kossel and Kimmich, 2005), fluid flow and dispersion in random packing of spheres (Manz et al., 1999), self-diffusion maps through chemical products (Gladden et al., 2004), and a fixed bed of ion-exchange resin saturated with methanol (Gladden, 2003). However, little attention has been paid to 3D characterization of porous networks using NMR micro-imaging. It is demonstrated that NMR micro-imaging can be used to obtain 3D images of fluids in various porous media composed of model sands with a spatial resolution of less than ~50 μm. Model sands can also be generated using random packing simulations where the particle sizes, shapes, and packing density of porous networks can be controlled (Jia and Williams, 2001). This would allow us to systematically explore unambiguous relationships between changes in network structures and the corresponding macroscopic properties.

δ

In this study, the nature of diverse structural parameters, such as cube-counting fractal dimension, lacunarity of 3D model porous networks, and configurational entropy of model sands, is explored using their 2D cross-sectional porous network images from NMR micro-imaging and random packing simulations. On the basis of these analyses, the current results aim to provide the previously unknown systematic relationships among the porous networks, these key structural parameters, and the corresponding transport and macroscopic properties. Before describing the methods and discussing the results of this study, a brief introduction of the parameters considered in the current study in the following subsections is provided.

4.1.1. Cube-counting fractal dimension of model porous networks

Fractal dimension—a measure of the degree of complexity of an object—is a noninteger dimension that originates from the power-law relationship between the length scale and the types of objects (e.g., pore space, solid mass, and interface) (Mandelbrot, 1982). 3D box counting fractal dimension (D_{cc}) used in this study can be described as follows (Mandelbrot, 1982):

$$\ln N = D_{cc} \ln\left(1/r\right) + \ln k\,, \tag{4.1}$$

where N is the number of cubes covering the object, r is the side of a cube, and k is a constant. The absolute value of the slope of the linear part within the cutoff lengths in the log-log plot is estimated as D_{cc}.

In the percolation theory, the fractal dimension of the cluster is defined for the regime where the length scale is smaller than the correlation length (Sahimi, 1993). In this regime the cluster is statistically self similar, and its mass M scales with the length scale L as $M \sim L^{D_p}$, where D_p is the fractal dimension of the cluster (Sahimi, 1993). Previous studies assumed that this fractal dimension of the cluster is the same with the fractal dimension obtained by box counting method (Thompson, 1991; Sahimi, 1993). However, the relationship between the fractal dimension obtained from the percolation theory (mass-radius relation) and the cube counting fractal dimension for the 3D objects needs to be explored.

Table 4-1 presents the results of fractal dimension analysis obtained in previous studies for pore space in 3D images of various porous media. 3D images have been obtained mostly by X-ray computed tomography (CT) and NMR imaging. Fractal dimension values obtained for 3D images of soil ranged from 2.05 to 2.94 (Moreau et al., 1999; Perret et al., 2003; Tarquis et al., 2008), and those for glass beads, body-centered cubic (bcc) packed spheres, or glass ballotini ranged from 2.42 to 2.52 (Müller et al., 1995; Klemm et al., 1997; Sederman et al., 1997). Fractal dimension values obtained for 3D images for percolation clusters, pumice stone, and quartz sand were 2.53, 2.90, and 2.70, respectively (Müller et al., 1995; Klemm et al., 1997). It has been shown that an increase in the fractal dimension may indicate an increase in the complexity of the network structure (Perret et al., 2003), irregularity of the fractal objects (Muller and McCauley, 1992; Xu and Sun, 2005), porosity (pore fractal) or area fraction

Table 4-1. Fractal dimension of 3D images of various porous networks from previous studies.

Porous Media	Image Size	Grain Size	Analysis Method	Imaging Method	Fractal Dimension	Reference
soil	2 ~ 6 cm		box counting	Photograph	2.44 ~ 2.84	(Moreau et al., 1999)
soil	19.5 ~ 40 mm		box counting	CT	2.05 ~ 2.16	(Perret et al., 2003)
soil	11.5 mm		box counting	CT	2.20 ~ 2.94	(Tarquis et al., 2008)
sponge	8 mm		porosity-radius	MRI	2.91	(Müller et al., 1995)
sponge	4 mm		porosity-radius	MRI	2.90	(Klemm et al., 1997)
glass beads	8 mm	1 mm	porosity-radius	MRI	2.52	(Müller et al., 1995)
glass beads	4 mm	1 mm	porosity-radius	MRI	2.50	(Klemm et al., 1997)
bcc packed spheres			porosity-radius	Simulation	2.48	(Muller et al., 1995)
percolation cluster	16 mm		porosity-radius	MRI	2.53	(Muller et al., 1995)
pumice stone	13 mm		porosity-radius	MRI	2.90	(Klemm et al., 1997)
quartz sand	4 mm	0.45 ~ 1 mm	porosity-radius	MRI	2.70	(Klemm et al., 1997)
glass ballotini	4.6 cm	5 mm	volume-area	MRI	2.42 ~ 2.44	(Sederman et al., 1997)

(for solid mass fractal) (Perret et al., 2003; Yu and Liu, 2004; Tang and Maragoni, 2008), and the fraction of smaller grains (Avnir et al., 1985; Bartoli et al., 1999; Xu and Dong, 2004).

The fractal object was characterized by self-similarity. Natural objects (including porous media) exhibit linearity within the lower and upper cutoff lengths in log (box counts)-log (box size) plots (Foroutan-pour et al., 1999; Maria and Carey, 2002). Fractal dimension analysis can also be applied to simple structures without apparent self-similarity, such as dilute sets of single-sized spheres (Hamburger et al., 1996; Foroutan-pour et al., 1999; Ciccotti and Mulargia, 2002) and porous networks of model sands, including single-sized spheres (Müller et al., 1995; Klemm et al., 1997; Klemm et al., 2001; Sederman et al., 2001). In this study, D_{cc} analysis was applied to the porous networks of model sands without much pronounced self-similarity (for a network composed of single-sized spheres) and those model sands in which self-similarity existed within a relatively narrow range of cube sizes (see 4.2.4 below for further details).

4.1.2. Lacunarity of model porous networks

Lacunarity—a scale-dependent measure of heterogeneity or texture of an object— can indicate differences between structures that have the same fractal dimensions (Mandelbrot, 1982). In lacunarity analysis, a box (or a cube, as used in this study) of side r is allowed to move over the entire image, and the number of boxes [$n_k(r)$] is counted whenever the box mass

δ

equals k. This procedure is repeated by varying k from 0 to a value equal to the total number of boxes [$N(r)$]. Then, the probability distribution function, $Q(k, r)$, is defined as (Allain and Cloitre, 1991)

$$Q(k,r) = \frac{n_k(r)}{N(r)}. \tag{4.2}$$

The lacunarity [$\Lambda(r)$] is then defined as (Allain and Cloitre, 1991)

$$\Lambda(r) = \sum_{k=0}^{r^2} k^2 Q(k,r) \Bigg/ \left[\sum_{k=0}^{r^2} kQ(k,r) \right]^2, \tag{4.3}$$

where the denominator is the square of the first moment of the probability distribution, and the numerator is the second moment of the probability distribution, which is thus a measure of the variance to mean ratio of box mass (Plotnick et al., 1996).

Lacunarity analysis has recently been used to describe the 2D spatial distribution of natural soil systems (e.g., Pendleton et al., 2005; Kim et al., 2007; Chun et al., 2008). Because of the computational difficulties of lacunarity analysis using the gliding box algorithm, as far as I know, there have been no previous studies using lacunarity analysis in 3D porous networks. Thus the first lacunarity analysis of 3D porous networks of model sands is reported and the relationship among lacunarity, porosity, and specific surface area is explored.

4.1.3. Configurational entropy of model porous networks

Configurational entropy is effective in describing the degree of

δ

disorder in amorphous networks, including oxide glasses and melts with geophysical and geochemical implications (e.g. Lee and Stebbins, 1999; Lee, 2005; Lee et al., 2010). In the current image analysis, configurational entropy analysis was performed using the gliding box algorithm. The probability of a pore pixel number k, $p_k(r)$, is calculated as (Andraud et al., 1994)

$$p_k(r) = \frac{N_k(r)}{N}, \tag{4.4}$$

where $N_k(r)$ is the total number of boxes containing the number of pore pixels of k, and N is the total number of visited boxes. Configurational entropy is defined as

$$H^*(r) = \frac{H(r)}{H_M(r)} = \frac{1}{\log\left(r^2+1\right)} \sum_{k=0}^{r^2} p_k(r) \log p_k(r), \tag{4.5}$$

where $H_M(r) = \log(r^2 + 1)$ is the maximum possible entropy for boxes with an area of r^2. The entropy length refers to a box size at which the configurational entropy reaches its maximum value (i.e., maximum configurational entropy; see Section 3.3 for further details). Entropy length is regarded as an accurate measure of the characteristic size of pores and/or constituent particles (Andraud et al., 1997). Although the maximum configurational entropy is reported to be positively correlated with the porosity of soil networks (Chun et al., 2008), the configurational entropy of the porous networks of model sands and the relationship between configurational entropy and other pore-structure properties have not yet been systematically studied. In this study, the relationships among the

configurational entropy, entropy length, and other parameters of porous networks in model sands were explored.

4.2. Methods

4.2.1. Random packing simulations

Random packing simulations of single-sized spheres were performed using DigiPac software (Structure Vision Ltd.) where particles move according to a predefined stochastic settling process governed by the rebounding probability (Jia and Williams, 2001). The particles and the container were digitized and mapped onto a lattice grid, and then the particles moved on the grid. In the simulation process employed in this study, particles were added from randomly selected points to a circular area directly above the packing. Random packing of spheres was simulated under the influence of gravity. To reproduce a glass-bead packing in a column (see below for glass bead sample preparation for NMR micro-imaging experiment), a tube container and solid wall boundary conditions were used. At a constant tube container diameter of 252 pixels, the particle diameters of the porous media composed of single-sized spheres used for our simulations were varied from 8 to 20 pixels, which corresponded to the approximate diameters of the small and large grains of the glass beads, respectively (see Section 4.2.2 for details). The porous media with diameters ranging from 25 to 30 pixels that corresponded to approximately the maximum size of the sphere in the simulated box were also simulated. The

number of particles in the simulation box was set to decrease with increasing particle diameters; for example, 200, 100, 50, and 10 particles were used for sphere diameters of 8, 10, 15, and 20, respectively.

Porous media with varying porosities were prepared by increasing the number of particles in the fixed container volume while keeping the diameters of the spherical particles constant. The resulting porosity of the simulated porous media ranges from 0.34 to 0.46 (see Table 4-2 for the number of samples for the same sphere diameter and the porosity of each sample). Figure 4-1 shows the 3D isosurface images (Figures 4-1A, 1C, and 1E) and 2D cross-sectional images (Figures 4-1B, 1D, and 1F) of the porous networks of the porous media composed of single-sized spheres with diameters of 20 pixels (Figures 4-1A and 1B), 15 pixels (Figures 4-1C and 1D), and 10 pixels (Figures 4-1E and 1F) obtained by random packing simulations.

δ

Table 4-2. Structural parameters and properties for porous networks obtained by random packing simulations.

Sample name[a]	ϕ[b]	SSA[c]	Perm[d]	EL[e]	MCE[f]	$\Lambda_{0.047}$[g]	$\Lambda_{0.47}$[h]	D_{cc}[l]
8-1	0.41	8.11	194	0.19	0.98	2.41	1.02	2.94
8-2	0.36	8.27	103	0.19	0.95	2.81	1.02	2.93
9-1	0.42	7.56	233	0.19	0.98	2.38	1.02	2.93
9-2	0.43	7.54	250	0.19	0.98	2.34	1.03	2.93
9-3	0.35	7.81	116	0.19	0.95	2.88	1.02	2.90
9-4	0.39	7.69	179	0.19	0.97	2.53	1.02	2.92
10-1	0.43	6.53	325	0.23	0.99	2.31	1.03	2.88
10-2	0.39	7.06	204	0.23	0.97	2.57	1.03	2.87
10-3	0.38	7.08	188	0.23	0.97	2.61	1.03	2.87
10-4	0.41	6.82	242	0.23	0.98	2.45	1.03	2.88
11-1	0.38	6.27	240	0.28	0.95	2.63	1.04	2.82
11-2	0.35	6.33	182	0.28	0.96	2.83	1.05	2.81
11-3	0.42	6.12	425	0.28	0.97	2.34	1.06	2.84
11-4	0.33	6.16	153	0.28	0.94	3.01	1.08	2.79
12-1	0.38	6.07	245	0.28	0.97	2.63	1.06	2.79
12-2	0.43	5.77	801	0.28	0.98	2.19	1.08	2.84
13-1	0.41	5.70	421	0.33	0.99	2.42	1.09	2.81
14-1	0.40	5.23	423	0.38	0.97	2.52	1.12	2.76
14-2	0.36	5.23	291	0.38	0.97	2.75	1.12	2.73
14-3	0.44	5.05	738	0.38	0.98	2.25	1.13	2.79
15-1	0.40	5.09	499	0.38	0.98	2.44	1.14	2.76
16-1	0.40	4.87	521	0.42	0.99	2.48	1.17	2.75
16-2	0.43	4.76	739	0.42	0.99	2.31	1.17	2.77
17-1	0.39	4.81	510	0.42	0.97	2.58	1.19	2.72
17-2	0.40	4.58	571	0.42	0.97	2.51	1.20	2.73
17-3	0.43	4.51	732	0.42	0.98	2.33	1.19	2.75
18-1	0.40	4.34	676	0.47	0.98	2.49	1.23	2.72

δ

18-2	0.39	4.43	565	0.47	0.98	2.58	1.23	2.70
18-3	0.44	4.23	924	0.47	0.99	2.29	1.22	2.75
19-1	0.44	4.06	1108	0.47	0.98	2.26	1.25	2.74
19-2	0.39	4.14	662	0.47	0.97	2.56	1.26	2.70
19-3	0.40	4.16	715	0.47	0.98	2.52	1.26	2.71
20-1	0.40	3.86	755	0.52	0.97	2.51	1.28	2.71
20-2	0.37	3.94	730	0.47	0.97	2.60	1.30	2.68
25-1	0.39	3.21	1144	0.66	0.98	2.56	1.44	2.68
25-2	0.43	3.17	1675	0.61	0.98	2.30	1.42	2.71
26-1	0.42	3.09	1591	0.66	0.99	2.36	1.44	2.70
26-2	0.43	3.13	1613	0.66	0.99	2.34	1.43	2.71
27-1	0.44	3.01	1832	0.70	0.99	2.29	1.44	2.71
27-2	0.42	3.01	1714	0.70	0.97	2.39	1.46	2.69
28-1	0.45	2.91	2138	0.75	0.99	2.22	1.44	2.72
28-2	0.42	3.08	1512	0.70	0.98	2.38	1.44	2.71
29-1	0.44	2.76	2333	0.80	0.98	2.29	1.48	2.71
30-1	0.45	2.48	2924	0.80	0.98	2.24	1.50	2.72
30-2	0.41	2.77	1701	0.75	0.98	2.45	1.54	2.69

[a] The number in front of the hyphen indicates the sphere diameter (pixels), and the number behind the hyphen is used to differentiate the samples by different porosities with the same sphere diameter.

[b] Porosity

[c] Specific surface area (mm^2/mm^3)

[d] Permeability (Darcy, D)

[e] Entropy length

[f] Maximum configurational entropy

[g] Lacunarity value for a box size of 0.047 mm

[h] Lacunarity value for a box size of 0.47 mm

[l] Cube-counting fractal dimension of 3D porous networks

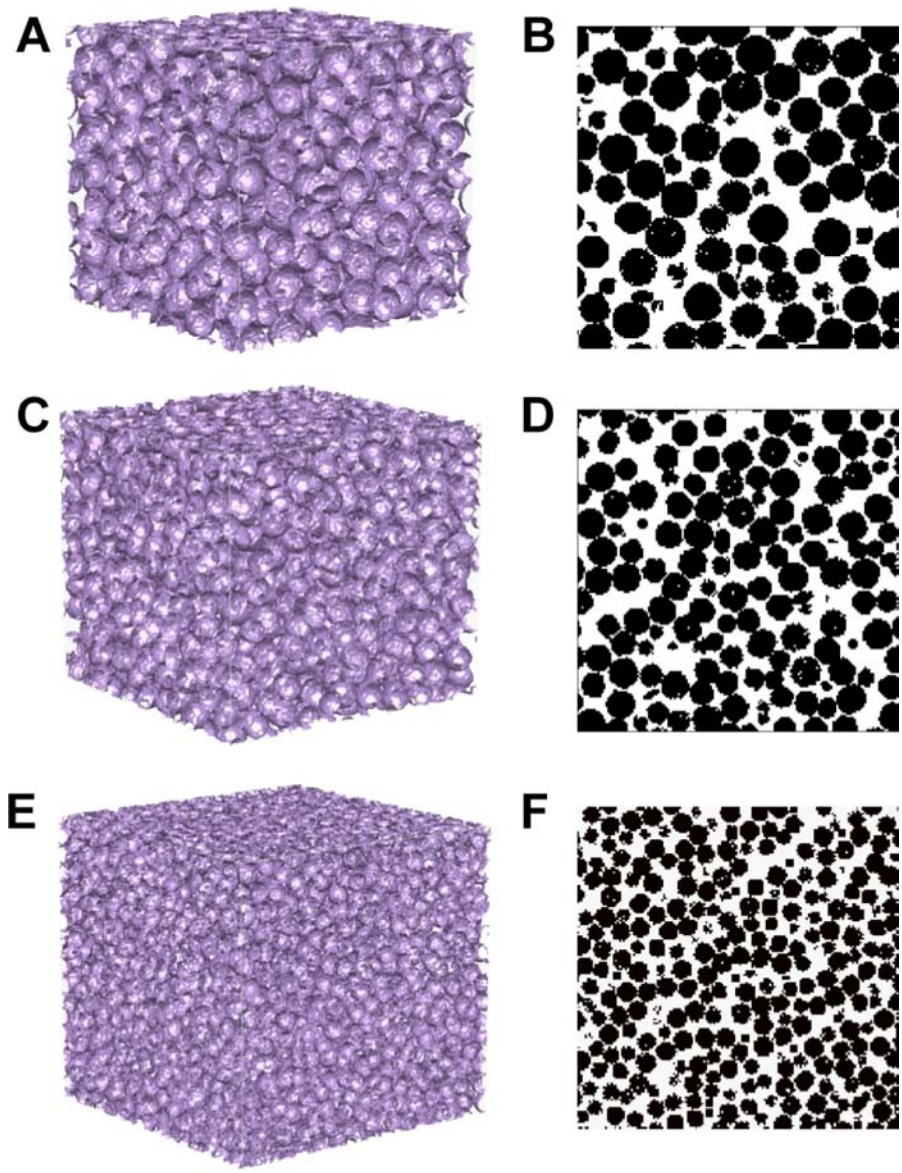

Figure 4-1. Isosurface images of 3D porous networks (A, C, and E) and 2D cross-sectional images (B, D, and F) of porous model sands composed of single-sized spheres with the diameter of 20 pixels (A and B), 15 pixels (C and D) and 10 pixels (E and F) obtained by random packing simulations.

4.2.2. Sample preparation

The glass beads (GBs) and crushed silica gel (SG) particles were spherical and irregularly shaped grains, respectively, and were used for investigating the effect of particle shape and diameter on the porous networks. The samples used for our NMR micro-imaging experiments were divided into six groups: GB1, GB2, GB3, SG1, SG2, and SG3, depending on the average particle size. The particle sizes (diameters) of the GBs (Sigma, acid-washed) were 0.71–1.18 mm (GB1, average 0.95 mm) and 0.21–0.30 mm (GB3, average 0.26 mm) and those of silica gels (SG) were 0.86–1.30 mm (SG1) and 0.25–0.60 mm (SG3). The values of the particle sizes were provided by vendors. It should be noted that the majority of the diameters of GB particles in GB1 and GB3 were mostly the average diameters of the groups and those for SG particles were randomly distributed within the ranges of particle diameters within the groups. Hybrid samples (GB2 and SG2 groups) were obtained by mixing two types of GBs or SG particles (weight ratio of GB1 and GB3 = 1:1 for GB2, and weight ratio of SG1 and SG3 = 1:1 for SG2) to investigate the effect of grain size heterogeneity and diameter on the porous networks and the corresponding properties. Each sample was put in a column that was 10.0 mm in diameter and 24.0 mm in length. Various samples with different porosities within a group by varying packing density of the grains were prepared (see Table 4-3 for the number of samples in each group and the porosity of each sample). Packing density was controlled by shaking the column filled with grains and subsequently checking the weight of the column. For example, the net weight of each

δ

Table 4-3. Structural parameters and properties for porous networks obtained by NMR micro-imaging.

Sample name[a]	ϕ[b]	SSA[c]	Perm[d]	EL[e]	MCE[f]	$\Lambda_{0.047}$[g]	$\Lambda_{0.47}$[h]	D_{cc}[l]
GB 1-1	0.29	2.98	274	0.47	0.93	3.64	1.51	2.60
GB 1-2	0.28	3.12	331	0.60	0.89	3.52	1.51	2.61
GB 1-3	0.28	2.74	318	0.56	0.90	3.58	1.58	2.61
GB 1-4	0.26	2.74	257	0.66	0.88	3.85	1.62	2.59
GB 1-5	0.25	2.68	196	0.66	0.88	3.95	1.61	2.58
GB 1-6	0.23	2.54	169	0.66	0.85	4.45	1.81	2.58
GB 1-7	0.28	3.84	247	0.56	0.92	3.54	1.46	2.55
GB 2-1	0.31	4.98	131	0.28	0.88	3.19	1.17	2.75
GB 2-2	0.29	4.82	125	0.28	0.88	3.42	1.19	2.71
GB 2-3	0.38	6.03	166	0.19	0.96	2.63	1.12	2.86
GB 2-4	0.36	6.05	158	0.19	0.95	2.83	1.10	2.86
GB 2-5	0.32	5.85	111	0.19	0.91	3.16	1.17	2.82
GB 3-1	0.26	9.33	19	0.14	0.86	3.82	1.06	2.90
SG 1-1	0.36	3.25	668	0.75	0.96	3.31	1.46	2.69
SG 1-2	0.31	2.48	700	0.75	0.93	3.19	1.76	2.67
SG 1-3	0.28	2.32	444	0.66	0.90	3.61	1.93	2.66
SG 1-4	0.37	2.76	593	0.75	0.95	3.70	1.56	2.71
SG 1-5	0.31	2.54	766	0.75	0.94	3.21	1.77	2.68
SG 1-6	0.37	2.75	892	0.75	0.95	4.45	1.81	2.71
SG 2-1	0.26	6.25	38	0.42	0.88	3.78	1.39	2.68
SG 3-1	0.27	6.99	30	0.33	0.90	3.75	1.23	2.67

[a] GB and SG indicate glass beads and silica gel samples, respectively. The number in front of the hyphen indicates the group with a similar average grain diameter (see Section 3.2), and the number behind the hyphen is used to differentiate the samples by different porosities within the same group (see text).

δ

[b] Porosity

[c] Specific surface area (mm^2/mm^3)

[d] Permeability (Darcy, D)

[e] Entropy length

[f] Maximum configurational entropy

[g] Lacunarity value for a box size of 0.047 mm

[h] Lacunarity value for a box size of 0.47 mm

[l] Cube-counting fractal dimension of 3D porous networks

d

sample in the column varied from 2.78 g to 3.12 g with decreasing porosity from 0.29 to 0.23 (GB1), from 3.05 g to 3.32 g with decreasing porosity from 0.38 to 0.29 (GB2), and from 1.42 g to 1.68 g with decreasing porosity from 0.36 to 0.28 (SG1). Both ends of the column were loosely covered during the mixing to provide space for grain mixing. The column was saturated with silicone oil (polydimethylsiloxane, Baysilone M30000, density of 0.98 g/cm^3 and viscosity of 30000 mPa·s). A vacuum pump was used to saturate the pore space with silicone oil and to eliminate air bubbles. Both ends of the column were covered with Teflon and membrane filters. Saturation time depended on the grain size. The time taken was approximately 5 min (GB1 and SG1 groups) to ~30 min (GB2, GB3, SG2, and SG3 groups) with a pump pressure of 1.45 torr to saturate the columns. Both ends of the column were sealed with parafilm after saturation.

4.2.3. NMR micro-imaging

NMR micro-imaging experiments were performed at Seoul National University using a Bruker DMX 400 NMR spectrometer with a 9.4 T vertical, wide-bore superconducting magnet, and Korea Basic Science Institute, Ochang using a Bruker DMX 600 NMR spectrometer with a 14.1 T vertical, standard bore superconducting magnet. A micro-2.5 probe head providing a gradient strength of 2.5 G/cm/A for DMX 400 NMR spectrometer and a micro-5 probe head providing a gradient strength of 5.0 G/cm/A for DMX 600 NMR spectrometer were used. As for the scan conditions for 3D volume imaging, a 3D gradient echo (ge3D) imaging

d

pulse sequence was used with a matrix size of the 3D images being 256 × 256 × 256, the field of view being 12 mm × 12 mm × 12 mm, and the spatial resolution being 46.9 μm × 46.9 μm × 46.9 μm. The sinc3-shaped pulse was used with an echo time of 1.781 ms and a repetition time of 1 s. The imaging time for one sample was approximately 18 h for one scan, and the number of scans varied from 1 to 4, depending on the signal-to-noise ratio of the spectra. Figures 4-2 and 4-3 show 3D isosurface images (Figures 4-2A, 2C, 2E, 3A, 3C, and 3E) and 2D cross-sectional images (Figures 4-2B, 2D, 2F, 3B, 3D, and 3F) of the porous networks of GBs (Figure 4-2) and SGs (Figure 4-3) obtained by NMR micro- imaging. Here, the differences in the porous networks among various porous media, such as GB1 (Figures 4-2A and 2B), GB2 (Figures 4-2C and 2D), GB3 (Figures 4-2E and 2F), SG1 (Figures 4-3A and 3B), SG2 (Figures 4-3C and 3D), and SG3 (Figures 4-3E and 3F), were clearly demonstrated. It should be noted that pores that were not accessible to silicone oil were not probed.

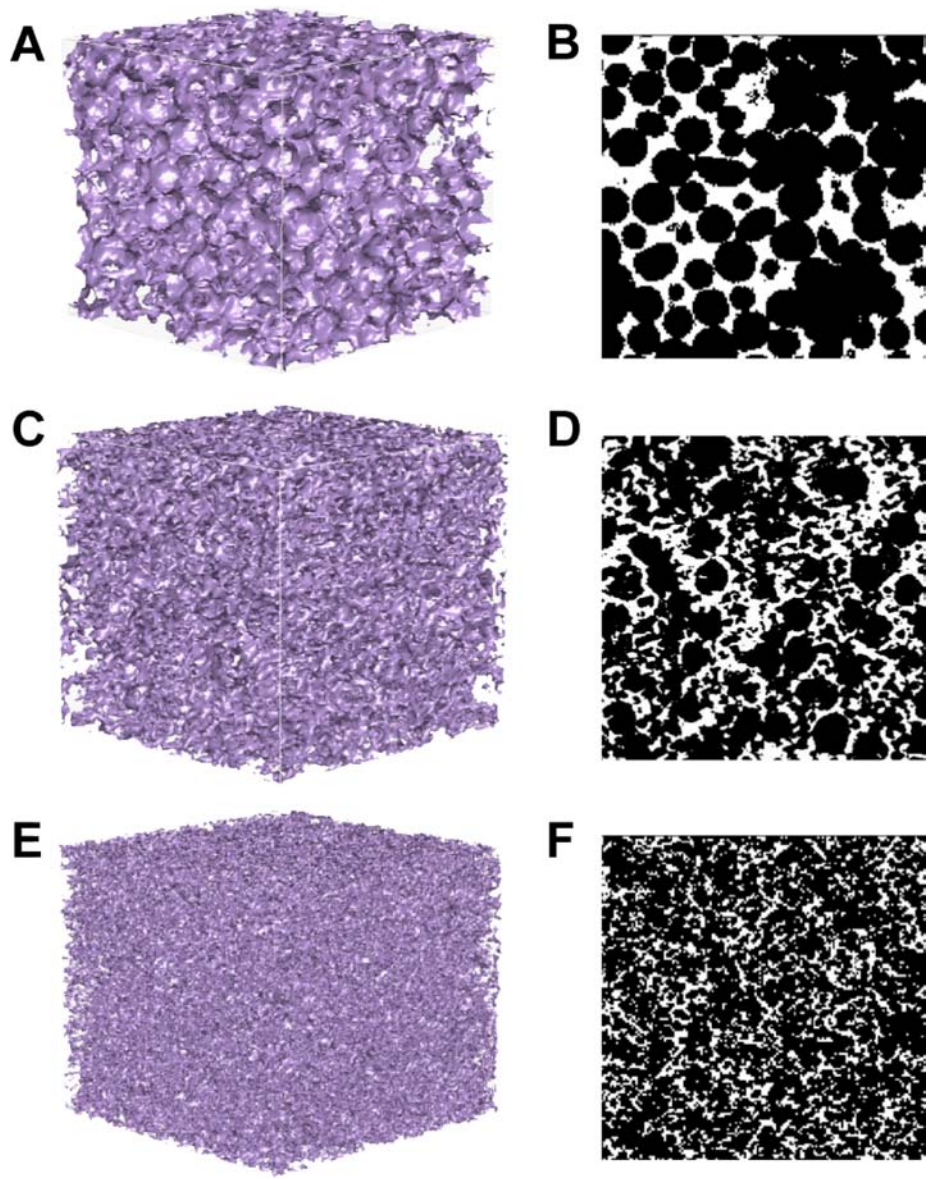

Figure 4-2. Isosurface images of 3D porous networks (A, C, and E) and 2D cross-sectional images (B, D, and F) of GB1 (A and B), GB2 (C and D) and GB3 (E and F) obtained by NMR micro-imaging experiments.

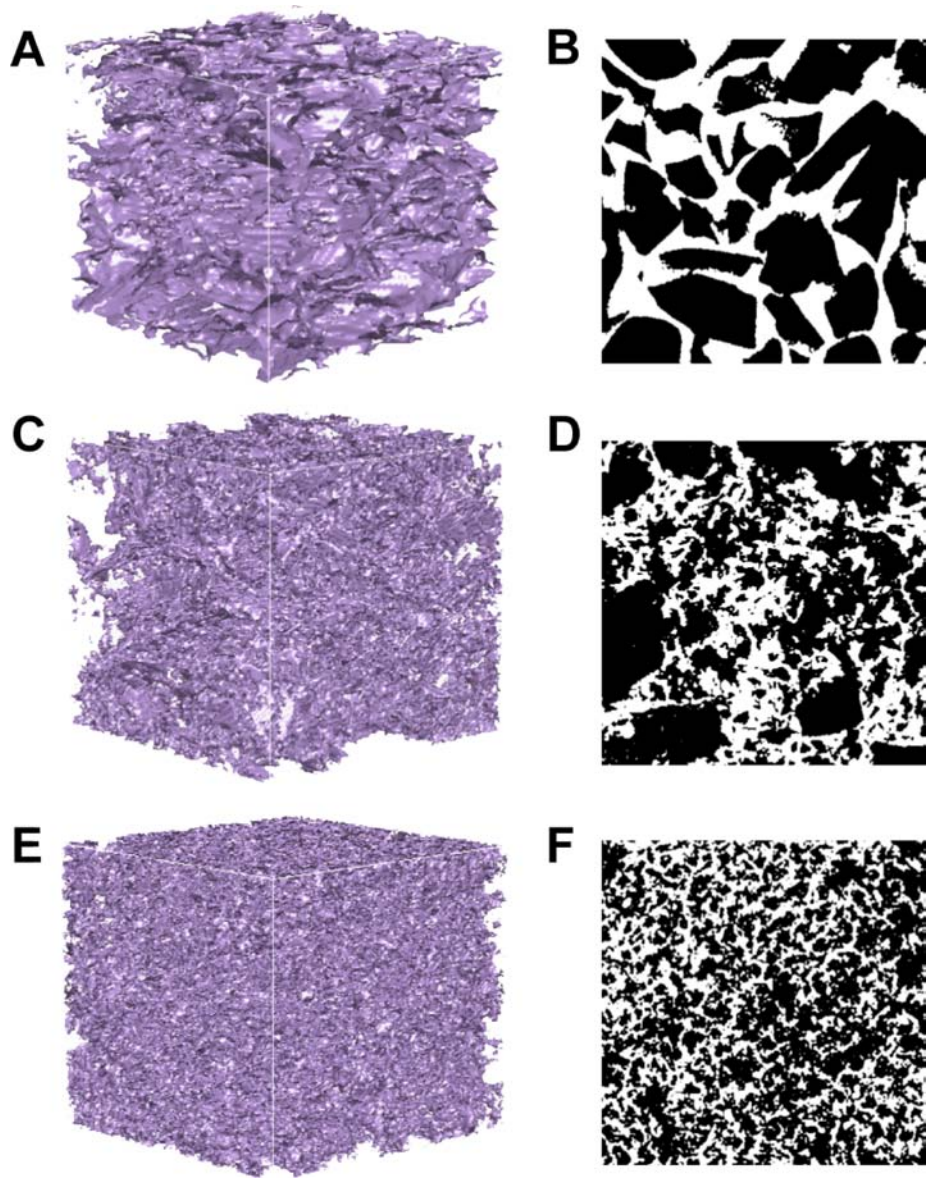

Figure 4-3. Isosurface images of 3D porous networks (A, C, and E) and 2D cross-sectional images (B, D, and F) of SG1 (A and B), SG2 (C and D) and SG3 (E and F) obtained by NMR micro-imaging experiments.

4.2.4. Data analysis

Data analysis of the porous networks was performed using the pixel vs. intensity histogram showing a bimodal distribution. The intensity value at the minimum point between the two peaks was set as the threshold value. Pixels having a larger value than the threshold were set to 1, and those having a smaller value than the threshold were set to 0. These resulting binary data were used for the analysis. To exclude the data outside the column and to suppress wall effects, a sub-volume dataset having a matrix size of 160 × 160 × 160 was extracted from the center of the 3D image having a matrix size of 256 × 256 × 256. The maximum cube size for the entire sample was ~178 × 178 × 178, and 9 pixels from the exterior were excluded.

4.2.4.1. Cube-counting fractal dimension of model porous networks

To obtain D_{cc} from the 3D images for the model porous networks, a 640 × 640 × 640 matrix obtained by fourfold expansion of the original 160 × 160 × 160 matrix was used; thus, the box sizes used for the assessment of D_{cc} were smaller than those for the original data matrix. D_{cc} analysis was conducted by covering the 3D pore volume data with increasing cube size (r). Then, box sizes of 1, 2, 4, 5, 8, 10, 16, 20, 32, 40, 80, 160, 320, and 640 (divisors of 640) were used to avoid border effects (Buczkowski et al., 1998). Then, the number of cubes (N) required to cover the object completely was evaluated. Figure 4-4 shows the log-log plots of box counts vs. box sizes for

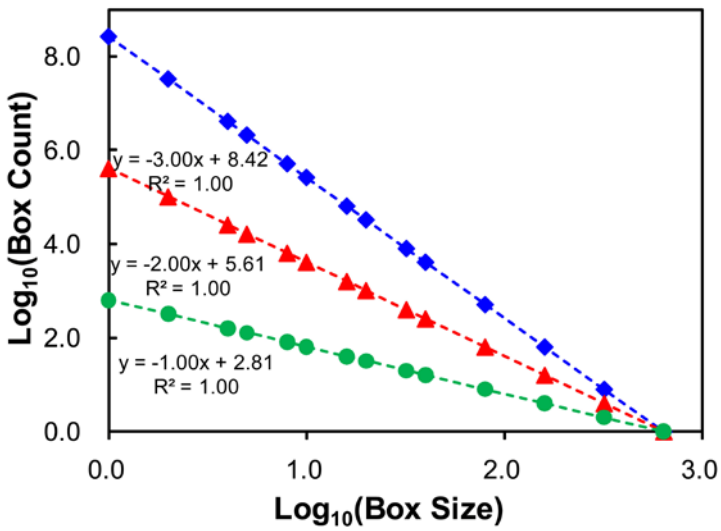

Figure 4-4. Relationship between box counts and box size in log-log plot for a straight line (green circles), a plane (red triangles), and a cube (blue diamonds).

a line, a plane, and a cube using the D_{cc} analysis. The calculated dimensions were the Euclidean dimensions for the line, plane, and cube (1, 2, and 3, respectively), and the data points fit perfectly on each straight line (R^2 = 1.00), indicating that the current cube-counting method with the aforementioned box size selection worked well.

Figure 4-5 shows the log-log plots of the relationship between box counts and box size for the simulated porous networks composed of randomly packed spheres (samples 8-1 and 30-2 had the minimum and maximum grain diameters, respectively; the number in front of the hyphen indicates the sphere diameter (pixels), and the number behind the hyphen refers to the samples with varying porosities for the same sphere diameter, as shown in Table 4-2). As shown in Figure 4-5A, data was grouped into 3 distinct regions with varying box size; the box size ranges for those regions were from 4 to 16 pixels, corresponding to 0.05-0.19 mm (for region I), from 16 to 40 pixels (for region II) pixels, corresponding to 0.19-0.47 mm, and from 40 to 80 pixels, corresponding to 0.47-0.94 mm (for region III), respectively. Region II was then used to estimate the D_{cc} value of the model sands: note that in order to determine the suitable region for the estimation of D_{cc}, the relationship between box counts and box size in log-log plot was plotted with varying box sizes from 4 to 128 pixels, and the region where the box counting is simply counting the object volume, and the region where boxes for counting the object covered the entire volume of the data matrix were excluded (*Bourke*, 2003) (see Supplementary Information 4-S1 for further details). The range of non-integer fractal dimension (i.e., cutoff

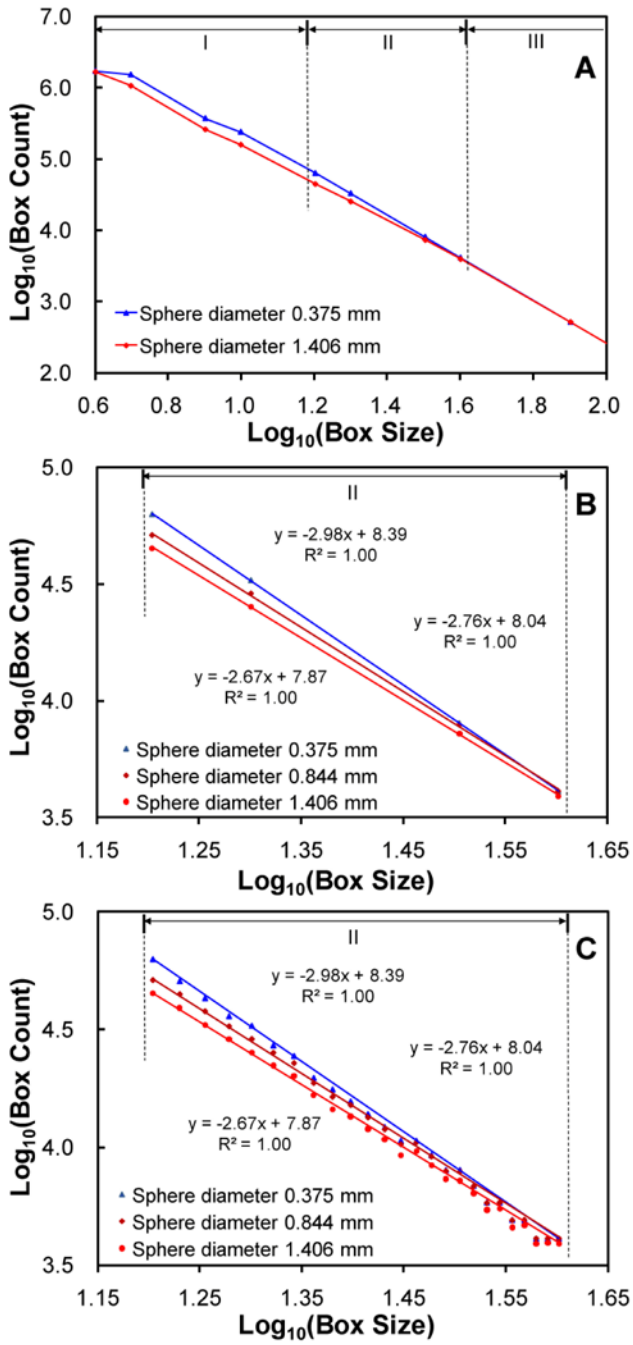

Figure 4-5. (caption on next page)

Figure 4-5. Relationship between box counts and box size in log-log plot for porous networks obtained by random packing simulations of single sized spheres. Each figure is grouped by the following box size ranges: (A) 4-80 pixels (corresponding to 0.047-0.94 mm) with the box sizes of 4, 5, 8, 10, 16, 20, 32, 40, and 80 (divisors of 640) to avoid border effects, (B) 16-40 pixels (corresponding to 0.19-0.47 mm) for sphere diameters of 8, 16, and 30 pixels (corresponding to 0.38, 0.75, and 1.41 mm) with the box sizes of 16, 20, 32, and 40, and (C) 16-40 pixels (corresponding to 0.19-0.47 mm) for sphere diameters of 8, 16, and 30 pixels (corresponding to 0.38, 0.75, and 1.41 mm) with the box sizes from 16 to 40 (16, 17, 18, ….40). In (A), Region I (from 4 to 16 pixels, corresponding to 0.047-0.19 mm), Region II (from 16 to 40 pixels, corresponding to 0.19-0.47 mm), and Region III (from 16 to 80 pixels, corresponding to 0.47-0.94 mm) are shown. Trend lines that are used to estimate the D_{cc} values are also shown in (B) and (C) (see supplementary information for further details).

lengths) in the porous networks may have varied with grain size, but the range for the estimation of D_{cc} in the current study did not vary significantly with grain size because the variation in grain size in this study was not significant within the range used for the estimation of D_{cc}. Thus, the self-similarity of the object was achieved within this relatively narrow range of box sizes that were characterized by power-law behavior in all the 3D porous network data of the model sands (see Supplementary Information 4-S1 for further details). Note that if the grain diameter becomes smaller and the voxel size can be more reduced than the current matrix, the range of the cutoff lengths in the porous networks will be shifted to the smaller scale of box sizes. Then, the corresponding fractal dimension can be different from that obtained from the current cutoff lengths. The estimated uncertainty of D_{cc} value is obtained by varying ranges of pixel size for estimation and is not larger than 0.07 (see Supplementary Information 4-S2 for further details).

The fractal dimension of porous media can be obtained by analyzing solid mass, pore volume, and surface area. The fractal dimension of soil has often shown that the values of the three abovementioned parameters are not identical because the analyzed objects differ from one another even in an image (Crawford and Matsui, 1996; Giménez et al., 1997; Giménez et al., 1997; Stallmach et al., 2002). The D_{cc} of pores, solid mass, and the surfaces of model sands prepared by simulations and experiments were analyzed. For the D_{cc} of solid mass, binary data were generated inversely by the threshold procedure in which values 1 and 0 were used for

solid mass and pores, respectively (see Supplementary Information , Figure 4-S2). For the D_{cc} of the surface, cubes covering only the interface between the pore and the solid mass were considered in box counting (see Supplementary Information , Figure 4-S3).

4.2.4.2. Other parameters

Lacunarity of the 3D porous networks was calculated for 160 × 160 × 160 sub-volume data by the gliding box algorithm by varying the box size from 1 to 48 pixels. The relationship between the lacunarity of all samples at a specific box size and porosity or specific surface area was investigated. Among the various algorithms used for estimating lacunarity (Gefen et al., 1983; Allain and Cloitre, 1991), the gliding box algorithm was suitable to 3D data analysis of porous networks.

Configurational entropy analysis was performed for the 2D cross sections (slices) chosen from the 160 × 160 × 160 sub-volume data; five slices perpendicular to the vertical z-direction (at z = 30, 60, 90, 120, and 150 from the top of the sub-volume data) were selected. The average of the configurational entropies of these five slices is reported. The estimated maximum error was ~0.05 for configurational entropy. Configurational entropy analysis was performed by the gliding box algorithm; the box sizes in this case ranged from 1 to 32 pixels.

Because the binary data was 0 for solid mass and 1 for pores, porosity was estimated by the sum of the pore data divided by the volume

of the matrix. Specific surface area can be defined as the total surface area of the interstitial voids divided by the total mass of the solid grains, total surface area divided by the volume of the solid grains, and that divided by the total bulk volume of the porous medium (Bear, 1972; de Marsily, 1986). In the current study, the third definition of specific surface area - sum of the surface area of clusters composed of connected pixels divided by the volume of the matrix – was used. Surface area was calculated by directly counting the number of pixels corresponding to interfaces from 3D images (Lindquist et al., 1996; Song et al., 2001). Then specific surface area is expressed as surface area (mm^2) divided by volume (mm^3). The unit of specific surface area ($pixel^2/pixel^3$) in the packing simulations was converted to mm^2/mm^3 by setting the field of view of the entire matrix size (256 × 256 × 256) to a dimension used for NMR micro-imaging experiments (12 mm × 12 mm × 12 mm). In the Appendix, the multi-fractal analysis of the model porous networks is described. Supplementary Information also describes relationships among various parameters and properties in which the correlations were not significant and were thus not included in the manuscript.

4.2.4.3. Permeability calculations

The lattice Boltzmann method (LBM) (McNamara and Zanetti, 1988) has been used for simulating fluid flow in porous media and for estimating the permeability of complex 3D porous networks (e.g., Keehm, 2003; Keehm et al., 2004, see Chen and Doolen, 1998 for more detailed

δ

information). In this study, the permeability of model sands was estimated using the LBM, and the relationships between the determined permeability and other structural parameters, including D_{cc}, were investigated. Permeability was estimated for 160 × 160 × 160 sub-volume data with the LBM using DigiFlow software (Structure Vision Ltd.). The D3Q18 scheme was applied in a 3D cubic lattice grid with each grid cell interacting with 18 (out of 26) of its closest neighbors.

4.3. Results and Discussion

Tables 4-2 and 4-3 summarize the calculated structural parameters for the simulated porous networks obtained by random packing simulations and the model sands made of glass beads and silica gel probed using NMR micro-imaging, respectively. Detailed interpretations of the characteristic features of these parameters and the relationships among these parameters are presented below.

4.3.1. Cube-counting fractal dimension of model porous networks

Figure 4-6 shows the relationships between the specific surface area and the D_{cc} of pores, solid mass, and surfaces for single-sized spheres obtained by random packing simulations. Our results indicate that D_{cc} is systematically correlated with the specific surface area (S) and porosity (ϕ) of the porous media. The D_{cc} of pores increases from 2.68 (±0.05) to 2.96 (±0.05) with increasing specific surface area (Figure 4-6A and Table 4-2).

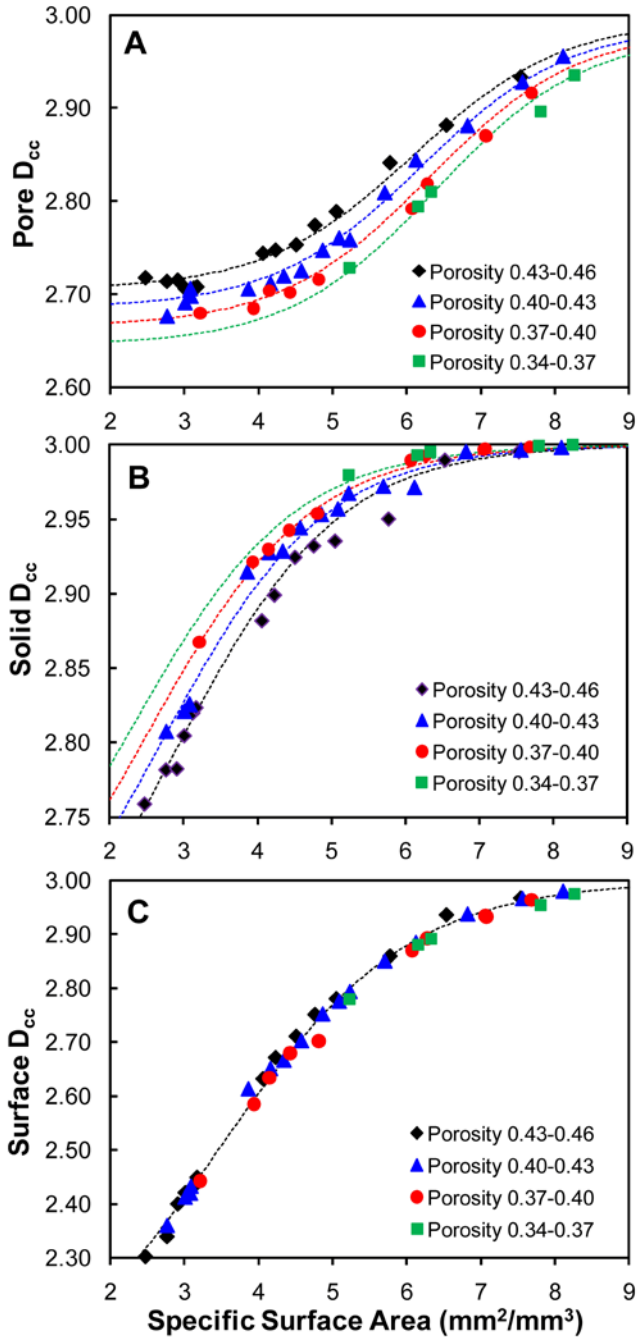

Figure 4-6. (caption on next page)

Figure 4-6. Relationships between cube counting fractal dimension of (A) pore, (B) solid mass, (C) and surface (interface) and specific surface area for porous networks obtained by random packing simulations. Black diamonds, blue triangles, red circles, and green squares correspond to each group of simulation data for porosities 0.43–0.46, 0.40–043, 0.37–0.40, and 0.34–0.37, respectively. Black, blue, red, and green dashed lines in (a) and (b) are obtained from equation (4.6) at the median of the corresponding range of porosity. Each median (the range of porosity is shown in the parentheses) is as follows; 0.445 (0.43-0.46), 0.415 (0.40-0.43), 0.385 (0.37-0.40), 0.355 (0.34-0.37). The fitting parameters for D_{cc} of pore and D_{cc} of solid mass are shown as equations (4.7) and (4.8), respectively, and a, b, c, and d (the fitting parameters) for D_{cc} of surface are 3, 2, 3.455, and 1.28, respectively.

δ

The available data in the figure based on the varying porosity ranges were grouped: 0.43 to 0.46 (group 1), 0.40 to 0.43 (group 2), 0.37 to 0.40 (group 3), and 0.34 to 0.37 (group 4) for visual clarity in the figure. To fit the data and demonstrate the correlation among D_{cc}, specific surface area, and porosity, the Boltzmann sigmoidal function was used as given below:

$$D_{cc}(S) = b + \frac{a-b}{1+\exp[-(S-c)/d)]}, \qquad (4.6)$$

where S is the specific surface area. a, b, c, and d are fitting parameters; a and b are the upper and lower limits of D_{cc}, respectively; c is the median specific surface area; d is a slope parameter. Each dashed line corresponds to the $D_{cc}(S)$ curve where the porosity is the median in each group. Table 4-4 shows the resulting fitting parameters and the corresponding coefficient of determination (R^2) for each group. The high R^2 values (0.99, 1.00, 0.99, and 0.95 for groups 1, 2, 3, and 4, respectively) indicate that the current Boltzmann sigmoidal functions reproduce the data well. From the fitting parameters of pore D_{cc}, the following relations were obtained:

$$a = \tfrac{1}{6}\phi + 2.9, \qquad (4.7a)$$

$$b = \tfrac{2}{3}\phi + 2.4, \qquad (4.7b)$$

$$c = -\tfrac{10}{3}\phi + 7.6, \text{ and} \qquad (4.7c)$$

$$d = 1.0 \quad \text{(constant)}. \qquad (4.7d)$$

δ

The D_{cc} of solid mass also increases from 2.76 (±0.05) to 3.00 (±0.05) with increasing specific surface area and decreasing porosity (Figure 4-6B), consistent with the trend observed for the D_{cc} of pores. Each dataset is fitted with equation (4.6) again. From the fitting parameters of solid mass D_{cc}, the following relations were established (Table 4-4):

$$a = 3.0 \text{ (constant)}, \tag{4.8a}$$

$$b = -\frac{1}{3}\phi + 1.7, \tag{4.8b}$$

$$c = \frac{20}{3}\phi, \text{ and} \tag{4.8c}$$

$$d = 1.1 \text{ (constant)}. \tag{4.8d}$$

The degree of space filling for the D_{cc} of pores and that of solid mass shows opposite signs for fitting parameters; for example, the coefficient of porosity for D_{cc} of pores and that of solid mass in b were 2/3 and -1/3, respectively, and those in c were -10/3 and 20/3, respectively.

The D_{cc} of surfaces increases from 2.30 (±0.05) to 2.98 (±0.05) with increasing specific surface area from 2.48 to 8.27 mm^2/mm^3 (Figure 4-6C). The D_{cc} of surfaces for the specific surface area of 2.48 mm^2/mm^3 (2.3) was much smaller than those for pores and solid mass (2.72 and 2.76, respectively) because the space filling of surfaces was intrinsically much smaller than that of pores and solid mass. Unlike the pores and solid mass, the D_{cc} of surfaces does not depend on the porosity, which is consistent with the previous study on soils (Dathe and Thullner, 2005).

Table 4-4. Parameters and coefficient of determination (R^2) values for fitting functions (equation 4.6) of the relationships between D_{cc} (of pore, solid mass, and surface) and specific surface area with varying porosities for sphere random packing.

	Porosity	a	B	x_0	W	R^2
Pore	0.43-0.46	2.995	2.705	6.1	1.0	0.99
	0.40-0.43	2.990	2.685	6.2	1.0	1.00
	0.37-0.40	2.985	2.665	6.3	1.0	0.99
	0.34-0.37	2.980	2.645	6.4	1.0	0.95
Solid mass	0.43-0.46	3.00	2.59	2.90	1.10	0.99
	0.40-0.43	3.00	2.60	2.70	1.10	0.99
	0.37-0.40	3.00	2.61	2.50	1.10	1.00
	0.34-0.37	3.00	2.62	2.30	1.10	0.96
Surface	-	3.00	2.00	3.455	1.28	1.00

Taking into consideration the experimental results obtained by NMR micro-imaging, Figure 4-7 shows the relationship between the D_{cc} of pore and specific surface area. D_{cc} increases from 2.54 (±0.05) to 2.99 (±0.05) with increasing specific surface area and depended on porosity (Figure 4-7A). Although experimental data showed a similar trend as compared to the results of random packing simulations with single-sized spheres, data for SG (black and red squares in Figures 4-7A and 7B) and hybrid samples of GB (black and red circles in Figures 4-7A and 7B) slightly deviates from the fitted lines (gray and red shaded areas that correspond to the $D_{cc}(S)$ where the porosity ranges from 0.29–0.38 and 0.20–0.29, respectively), indicating that the grain shape and the heterogeneity of the grain size affect the overall trend in $D_{cc}(S)$. Figure 4-7B also shows the D_{cc} of pores for model sands composed of SG (red circle) with heterogeneity in particle shape and size and those for GBs (blue circle) composed of spherical grains. The D_{cc} of pores for model sands composed of SG slightly increases from 2.66 (±0.05) to 2.79 (±0.05) with increasing specific surface area from 2.32 to 8.66 mm^2/mm^3. The D_{cc} for GBs increased rapidly from 2.58 (±0.05) to 2.86 (±0.05) with increasing specific surface area from 2.54 to 6.05 mm^2/mm^3 and then increased gradually to 2.90 (±0.05) with a further increase in specific surface area from 6.05 to 9.33 mm^2/mm^3. The results for GB1 and GB3, composed of uniform spherical grains, were reproduced well using equation (4.6), indicating that the trend obtained from random packing simulations can be extended to the lower porosity regime. The results for SG and GBs for D_{cc} of solid mass and surface were also reproduced well

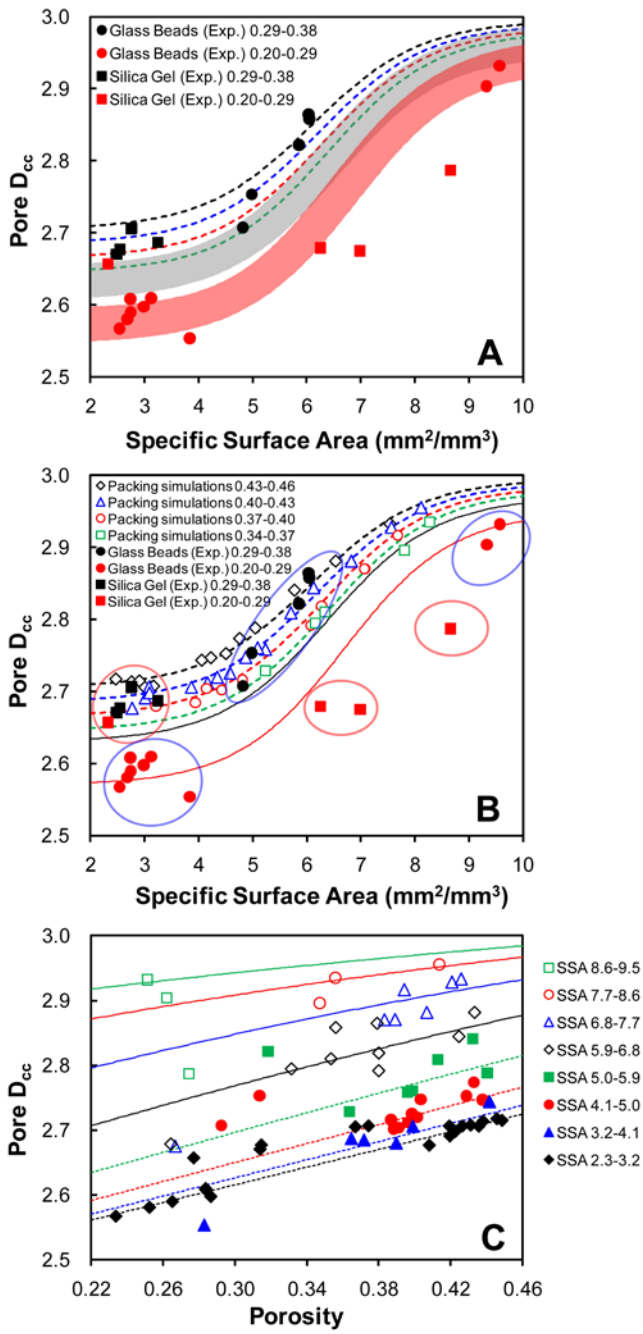

Figure 4-7. (caption on next page)

Figure 4-7. (A) Relationship between cube counting fractal dimension of pore and specific surface area for porous networks obtained by the NMR micro-imaging experiments only with sigmoidal curves for porosity of 0.20-0.29 (red shaded area) and 0.29-0.38 (gray shaded area). (B) Relationship between cube counting fractal dimension of pore and specific surface area for porous networks obtained by NMR micro-imaging experiments indicated by blue large circles for glass beads and red large circles for silica gel samples together with simulation data (open points). Black and red circles correspond to glass bead samples for the porosities of 0.29–0.38 and 0.20–029, respectively. Black and red squares correspond to silica gel samples for the porosities of 0.29–0.38 and 0.20–0.29, respectively. Black diamonds, blue triangles, red circles, and green squares correspond to each group of simulation data for the porosities of 0.43– 0.46, 0.40–043, 0.37–0.40, and 0.34–0.37, respectively. (C) Relationship between cube counting fractal dimension of pore and porosity for porous networks obtained by the random packing simulations and by the NMR micro-imaging experiments. Each line is obtained from equations (4.6) and (4.7) at the median of the corresponding range of specific surface area. Each median (the range of specific surface area is shown in the parentheses) is as follows; from bottom to top, 2.75 (2.3-3.2), 3.65 (3.2-4.1), 4.55 (4.1-5.0), 5.45 (5.0-5.9), 6.35 (5.9-6.8), 7.25 (6.8-7.7), 8.15 (7.7-8.6), and 9.05 (8.6-9.5).

using equation (4.6) (see Supplementary Information, Figure 4-S5). The model sands with pronounced heterogeneity in particle shapes and sizes (e.g. SGs and GB2) may slightly deviate from the prediction from equations (4.6). Figure 4-7C presents the relationship between the D_{cc} of pores and porosity. While the relationship among parameters can be complicated, the trend clearly shows that D_{cc} increases with increasing porosity if it is scaled with specific surface area of the networks. The overall trend is consistent with the trends reported previously (Perret et al., 2003; Yu and Liu, 2004; Tang and Maragoni, 2008).

These results suggest systematic relationships among specific surface area, porosity, the D_{cc} of pores, and average particle diameter. For example, Figure 4-8A shows that the specific surface area of the network decreases with increasing porosity at constant D_{cc} of pores. The D_{cc} does not linearly vary with porosity because of the non-linear relationships among the D_{cc} of pores, specific surface area, and porosity (Figures 4-6 and 4-7). Figures 4-8B and 4-8C show a variation in specific surface area and the D_{cc} of pores as a function of average particle diameter. Both the specific surface area and the D_{cc} of pore apparently decrease with increasing average particle diameter, particularly for the random packing simulations. Note that a variation in specific surface area and the D_{cc} of pore at a specific value of average particle diameter for glass beads and silica gels is also observed, as expected from the experimental condition of varied porosity with fixed diameters of spheres. The correlation between porosity and average particle diameter was weak (see Supplementary Information,

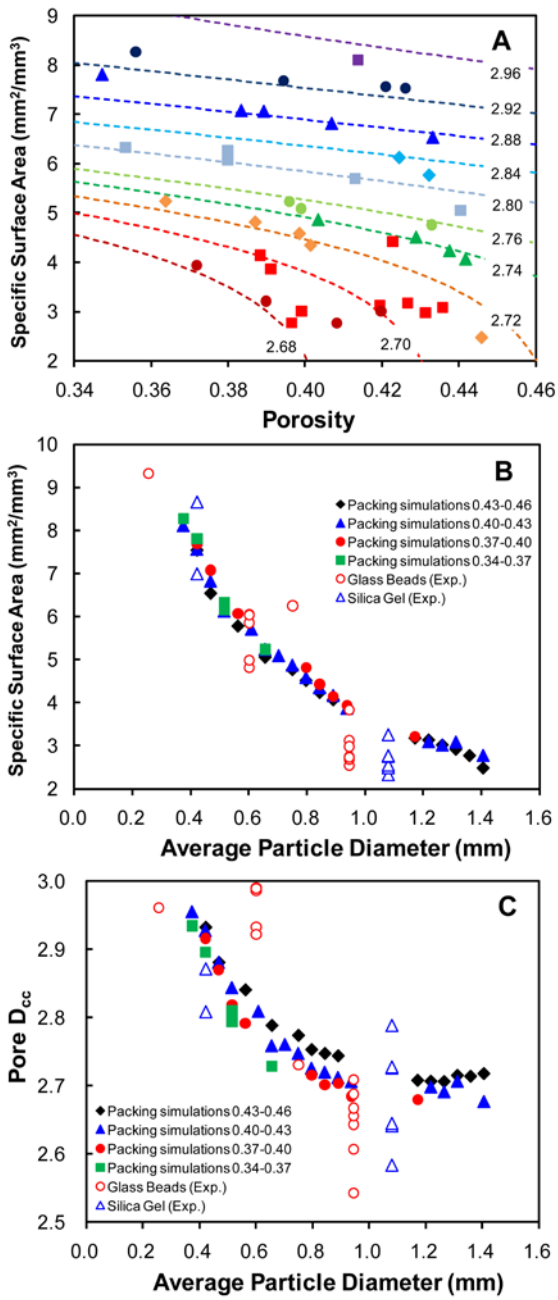

Figure 4-8. (caption on next page)

Figure 4-8. (A) Relationship between specific surface area (mm^2/mm^3) and porosity at identical cube-counting fractal dimension. Each cube-counting fractal dimension value is shown as the numeral on each corresponding dash-dot line obtained using equations (4.6) and (4.7). Data points represented by the same color as each dash-dot line were obtained by random packing simulations for the nearest cube-counting fractal dimension value of each dash-dot line. (B) Relationship between specific surface area (mm^2/mm^3) and average particle diameter. (C) Relationship between cube-counting fractal dimension of pores and average particle diameter. Data in (B) and (C) were obtained by random packing simulations and by NMR micro-imaging experiments.

Figure 4-S6); however, for random packing simulations, porosity increases slightly with increasing particle diameter.

4.3.2. Lacunarity of model porous networks

Figure 4-9 shows the effect of box size on the calculated lacunarity with varying porosity (0.26–0.27, 0.35–0.36, 0.41, and 0.43–0.44) of model porous networks in log (lacunarity)-log (box size) plots. The lacunarity at constant porosity decreases to zero with increasing box size in the log (lacunarity)-log (box size) plot. The log (lacunarity) values at constant box size decrease from ~0.6 to ~0.35 with increasing porosity from 0.26–0.27 to 0.43–0.44. The lacunarity for a porous network composed of larger particle diameters (e.g., GB1-4, 30-2) is larger than that for smaller particle diameters (e.g., GB3-1, 8-1). For porous networks composed of large particle diameters, including GB1-4 (Figure 4-9A), SG1-1 (Figure 4-9B), 30-2 (Figure 4-9C), and 29-1 (Figure 4-9D), the trend in the log (lacunarity)-log (box size) plot produces a peculiar pattern that was initially concave downward. Porous networks composed of intermediate and small particle diameters produce curves that are initially linear at smaller box sizes. The former and the latter corresponded to the moderately clustered pores and the randomly distributed pores in the lacunarity, respectively (Plotnick et al., 1993; Plotnick et al., 1996).

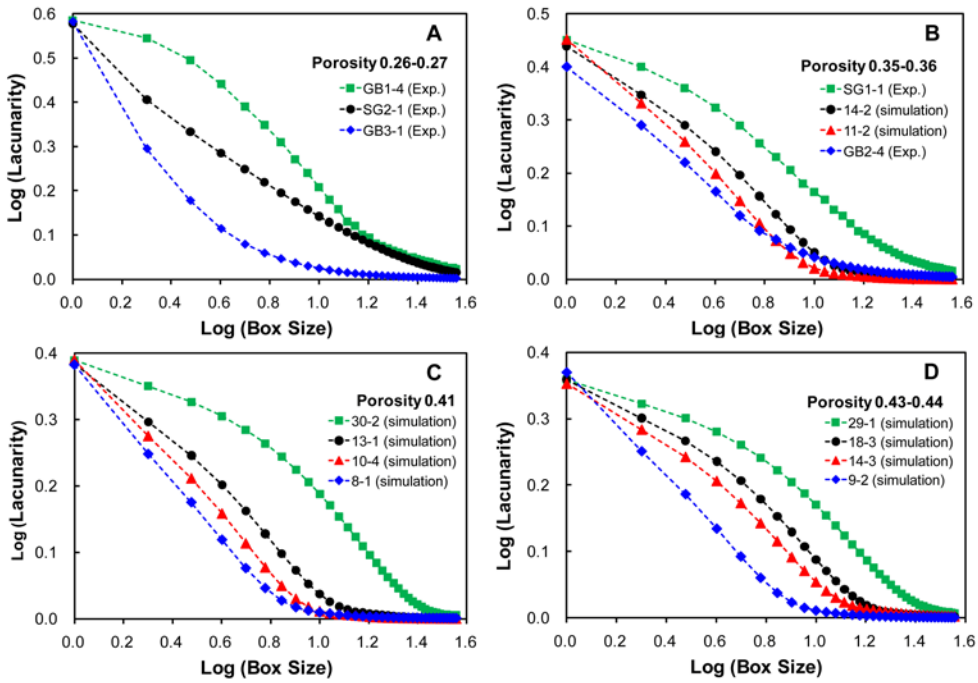

Figure 4-9. Relationship between lacunarity and box size in the log-log plot for porous networks obtained by random packing simulations and by NMR micro-imaging experiments. Each figure is grouped by the following porosity ranges: (A) 0.26–0.27, (B) 0.35–0.36, (C) 0.41, and (D) 0.43–0.44. Each legend indicates the sample names of corresponding data (refer to Tables 4-2 and 4-3).

Because lacunarity can bring out the differences between structures that have the same fractal dimension (Mandelbrot, 1982), the lacunarity of porous networks with identical cube-counting fractal dimension was investigated. Figure 4-10 shows that the effect of box size on lacunarity was distinct for porous networks with identical D_{cc} in the log (lacunarity)-log (box size) plot. In Figure 4-10A, although all porous networks have a D_{cc} of 2.68, the trend in the log (lacunarity)-log (box size) plot for SG2-1 and the trends of the simulation data (20-2 and 25-1) are classified into two distinct groups of networks (i.e., a random distribution of pores and a moderate degree of clustering) (Plotnick et al., 1996). Similarly, in Figure 4-10B, the porous networks have a D_{cc} of 2.79, but the trend in the log (lacunarity)-log (box size) plot for SG3-2 and the trends of the simulation data (12-1 and 14-3) are categorized into random and slightly clustered pores, respectively (Plotnick et al., 1996).

The current results show that the lacunarity of porous networks systematically depends on box size, sphere diameter, and porosity. Figure 4-11A shows the lacunarity of 3D porous networks at the minimum box size (corresponding to 0.047 mm in this study) as a function of porosity. As expected from the definition given in equation (4.3), lacunarity at the minimum box size (r = 1) is inversely proportional to the fraction of occupied sites (Plotnick et al., 1996). The current data (lacunarity vs. porosity) also clearly show that lacunarity decreases with increasing porosity. Figure 4-11B shows the lacunarity of 3D porous networks at a box size of 0.47 mm as a function of specific surface area. Lacunarity of 3D

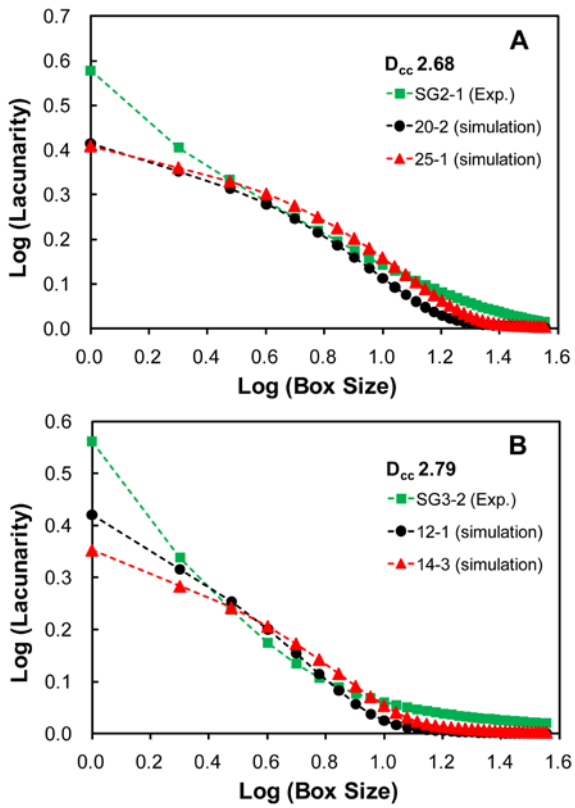

Figure 4-10. Relationship between lacunarity and box size in the log-log plot for porous networks with identical cube-counting fractal dimension (D_{cc}): (A) at D_{cc} = 2.68 and (B) at D_{cc} = 2.79. Each legend indicates the sample names for corresponding data (refer to Tables 4-2 and 4-3).

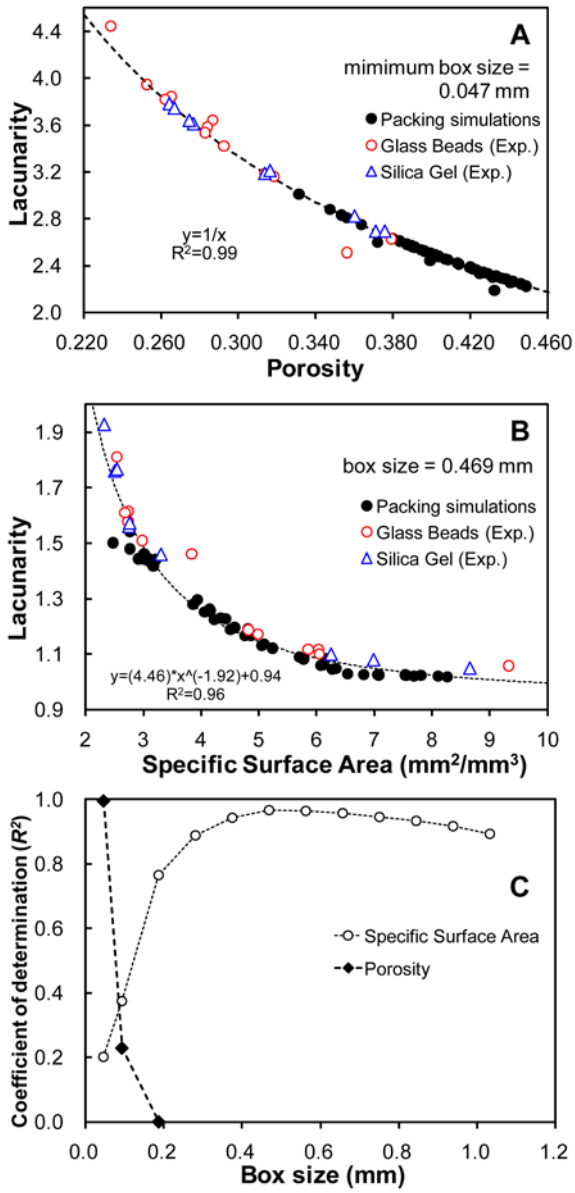

Figure 4-11. (caption on next page)

Figure 4-11. (A) Relationship between lacunarity at the minimum box size and porosity. (B) Relationship between lacunarity at a box size of 0.47 mm and specific surface area. (C) Relationship between coefficient of determination (R^2) and box size for porous networks obtained by random packing simulations and by NMR micro-imaging experiments. The R^2 value of each fitting curve was obtained for the relationship between lacunarity at a specific box size and porosity (black closed diamonds) and between lacunarity at a specific box size and specific surface area (black open circles). Each dashed line in (A) and (B) is a fitting curve obtained using the equation shown in each plot.

δ

porous networks decreases from 1.93 to 1.02 with increasing specific surface area from 2.32 to 8.27 mm^2/mm^3. The relationship between the calculated lacunarity at a box size of 0.47 mm and specific surface area ($\Lambda_{0.469}$) is fitted well with the simple power-law equation:

$$\Lambda_{0.47} = aS^b + c, \tag{4.9}$$

where $\Lambda_{0.469}$ is the lacunarity value at the box size of 0.469 mm, S is the specific surface area, and a, b, and c are fitting parameters and are shown in Figure 4-11B. Figure 4-11C shows R^2 values as a function of box size, showing the effect of box size on porosity and specific surface area; the R^2 values were obtained for lacunarity values of all samples at a specific box size as a function of porosity and specific surface area. Lacunarity at the minimum box size shows the best correlation with porosity (closed diamonds in Figure 4-11C), which is consistent with the correlation reported previously (Plotnick et al., 1996). Furthermore, lacunarity was well correlated with specific surface area when the box size ranged from 8 to 14 pixels (0.38 to 0.66 mm), with the best correlation at 0.47 mm (Figure 4-11B, Equation 4.9 above). The lacunarity at this intermediate box size also had a positive correlation with the average particle diameter (see Figure 4-S7B in Supplementary Information).

d

4.3.3. Configurational entropy of cross sections of model porous networks

Figure 4-12 shows the configurational entropy [$H^*(r)$] of porous networks as a function of box size, r. As previously mentioned (Section 4.1.3), the maximum configurational entropy and the corresponding entropy length can be obtained from $H^*(r)$ (see Figure 4-12A inset). For example, the calculated maximum configurational entropy and the entropy length for porous networks composed of single-sized spheres of diameter 0.656 mm are ~0.96 and 0.4 mm, respectively (Figure 4-12A). The configurational entropy apparently increases with increasing porosity from 0.34–0.37 (Figure 4-12A) to 0.43–0.46 (Figure 4-12D).

Figure 4-13 shows the entropy length of porous networks as a function of average particle diameter (d_p) and specific surface area. The entropy length of the network increased linearly with increasing average particle diameter with a slope of ~0.57 for porous networks obtained by random packing simulations of single-sized spheres and NMR micro-imaging of SG and GBs (red dashed line in Figure 4-13A) and a slope of ~0.54 for porous networks obtained by random packing simulations of single-sized spheres only (black dashed line in Figure 4-13A). Thus, entropy length = ~0.57 $d_p \approx (1/\sqrt{3})d_p$, indicating that the characteristic length of the porous network was ~0.57 times the average particle diameter of the solid grains comprising the porous media. Assuming that the entropy length measures the average diameter of the inscribed spheres in

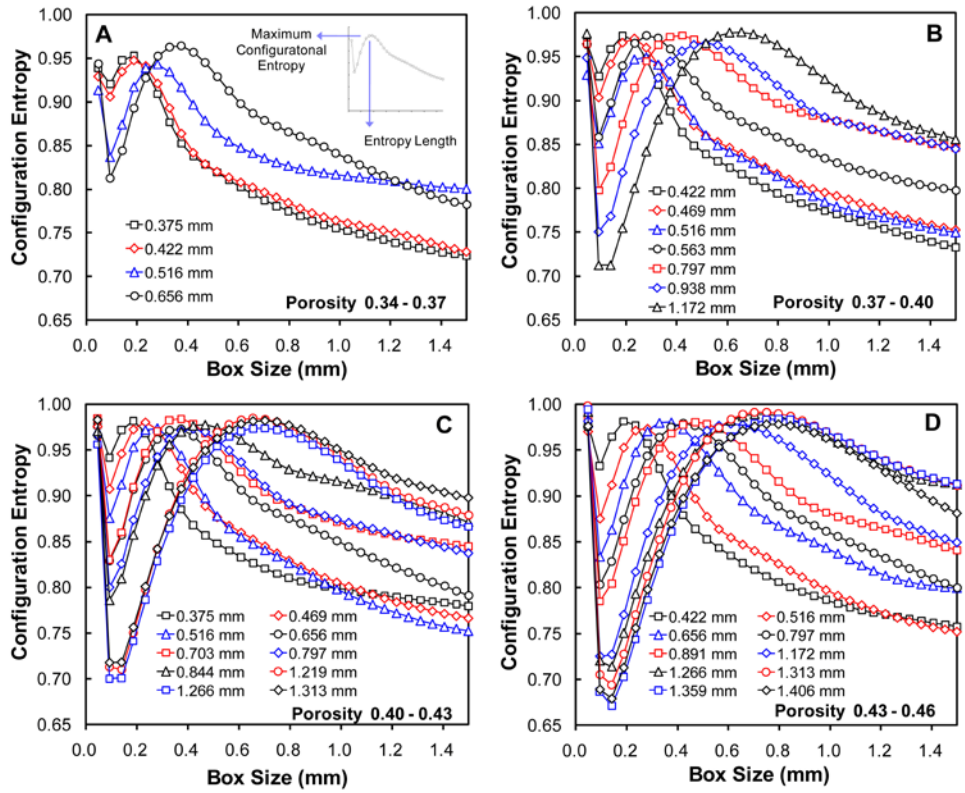

Figure 4-12. Relationship between configurational entropy and box size. Each plot corresponds to the following porosity ranges: (A) 0.34 to 0.37, (B) 0.37 to 0.40, (C) 0.40 to 0.43, and (D) 0.43 to 0.46. Inset in (A) shows the maximum configurational entropy and the corresponding entropy length.

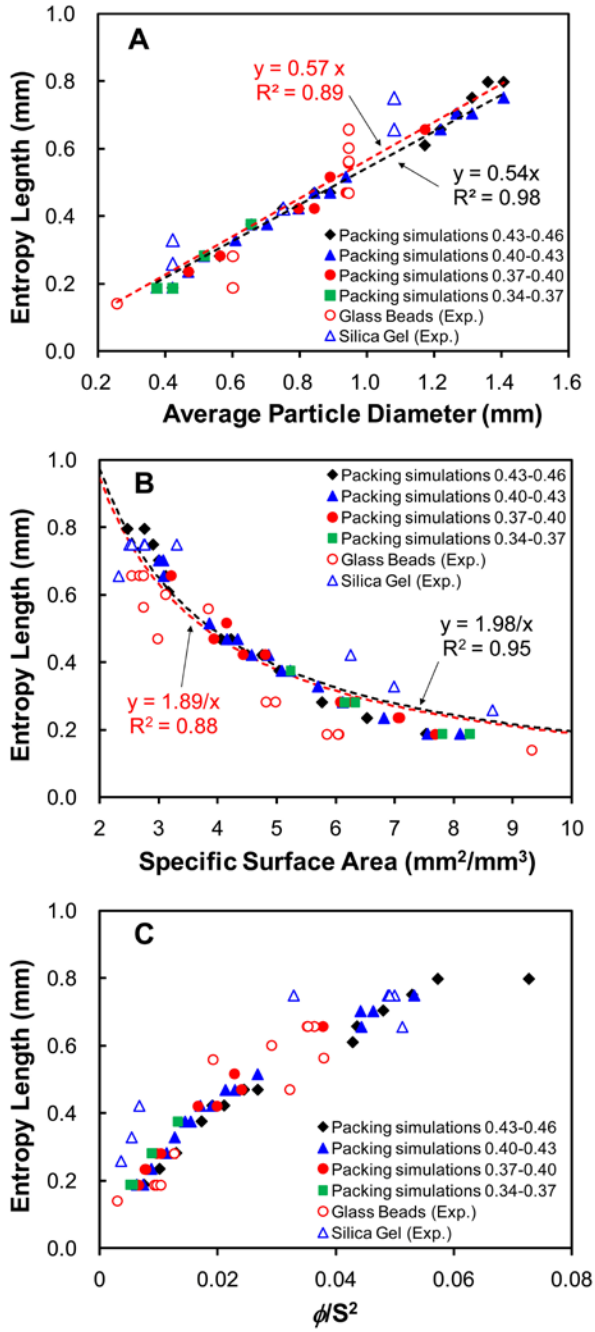

Figure 4-13. (caption on next page)

Figure 4-13. (A) Relationship between entropy length and average particle diameter (mm). (B) Relationship between entropy length and specific surface area (mm^2/mm^3). (C) Relationship between entropy length and (porosity)/(specific surface area)^2. Data in (A, B, and C) were obtained both experimentally and by calculations.

δ

pore bodies, the average coordination number of the pore body can be predicted and is likely to be ~6; the radius ratio of the coordination polyhedra for an octahedron ranges from 0.414 to 0.732 (Nesse, 2000). The current correlation between the average particle diameter and entropy length for porous networks has not been reported previously. As expected from the relationship between specific surface area and the D_{cc} of pores at an average particle diameter (e.g., Figures 4-8B and 8C), there is a variation in entropy length at a specific average particle diameter (Figure 4-13A). In particular, the variation is more significant for the SG than for GBs, indicating that entropy length is sensitive to the heterogeneity of grain size in porous media. Because the specific surface area decreases with increasing average particle diameter, entropy length also decreases (from 1.02 to 0.19 mm) with increasing specific surface area (from 2.32 to 8.27 mm^2/mm^3) (Figure 4-13B). Although the correlation between entropy length and porosity is not significant (see Figure 4-S8 in Supplementary Information) in the samples studied here, it is found that entropy length also increased with increasing (porosity)/(specific surface area)^2 (Figure 4-13C).

Figure 4-14 shows the effect of porosity (ϕ) on configurational entropy. The maximum configurational entropy increases from 0.85 to 0.99 with increasing porosity from 0.23 to 0.45. In addition to the maximum configurational entropy, configurational entropy due to total porosity (S^{config}) can also be calculated from the following simple expression:

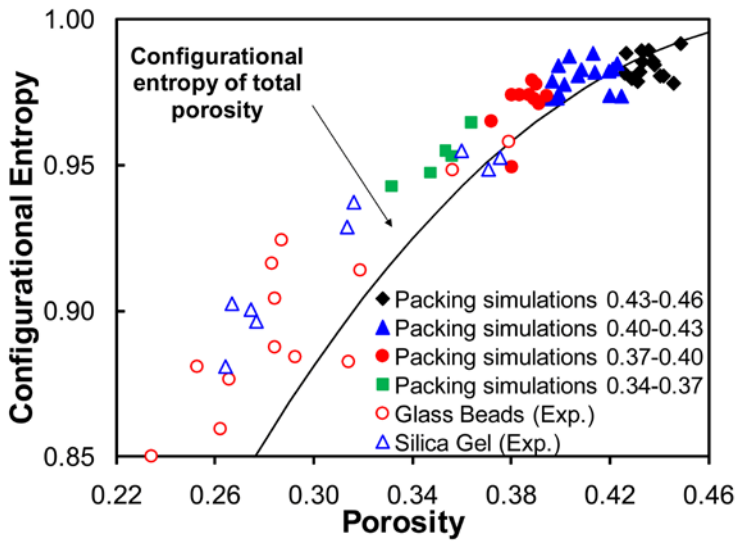

Figure 4-14. Relationship between maximum configurational entropy and porosity. The solid line denotes configurational entropy of total porosity (see text for details).

δ

$$S^{config} = k\left[\phi \ln \phi + (1-\phi)\ln(1-\phi)\right], \qquad (4.10)$$

where k is a constant used to normalize the S^{config} to be a maximum configurational entropy (=1) at $\phi = 0.5$ (In the current study, k = ~ -1.4, black curve in Figure 4-14). Equation (4.10) is equivalent to the configurational entropy, $H^*(r)$, at a box size of 1. Configurational entropy due to total porosity increases with increasing porosity up to 0.5. Although the overall trend is similar, the difference between the configurational entropy of total porosity and the maximum configurational entropy apparently decreases with decreasing porosity. The difference is due to the fact that the former is obtained from the total structure of porous media, whereas the latter is obtained from the local porous networks at the box size of maximum disorder (Andraud et al., 1994) and should thus be larger than the configurational entropy due to total porosity. The clear correlations between configurational entropy and average particle diameter and between configurational entropy and specific surface area were not demonstrated (see Figures 4-S9 in Supplementary Information). By considering the 1:1 correspondence between porosity and configurational entropy, the latter can be predicted and used for the modeling of properties of porous networks and multi-phase rock-melt-fluid composites (see further discussion below). The above correlations revealed the previously unknown nature of entropy length and configurational entropy and their relationships with other key structural parameters in porous networks. Configurational entropy analyses in the current analysis have been limited

δ

to cross sections of porous networks; however, it would be necessary to compare these analyses with future results of configurational entropy for 3D structures of porous networks.

4.3.4. Relationship among structural parameters, cube-counting fractal dimension, and permeability

Structural relationships allowed us to establish a link between the structure and properties of porous networks and conventional structural parameters such as specific surface area, porosity, and average diameter. Permeability for the current dataset was estimated and its relationship with other structural parameters was investigated. Figure 4-15 shows the effects of average particle diameter (Figure 4-15A), specific surface area (Figure 4-15B), and porosity (Figure 4-15C) on calculated permeability for the current dataset obtained by random packing simulations and NMR micro-imaging experiments. The calculated permeability shows a general trend of increasing with increasing average particle diameter and decreasing with increasing specific surface area. Permeability apparently increases with increasing porosity. Figure 4-16A also shows the relationships among permeability, specific surface area (S), and porosity (ϕ) of model sands. The results show that the relationships among the parameters for the model sands are well described with the Kozeny-Carman equation (e.g., de Marsily, 1986)

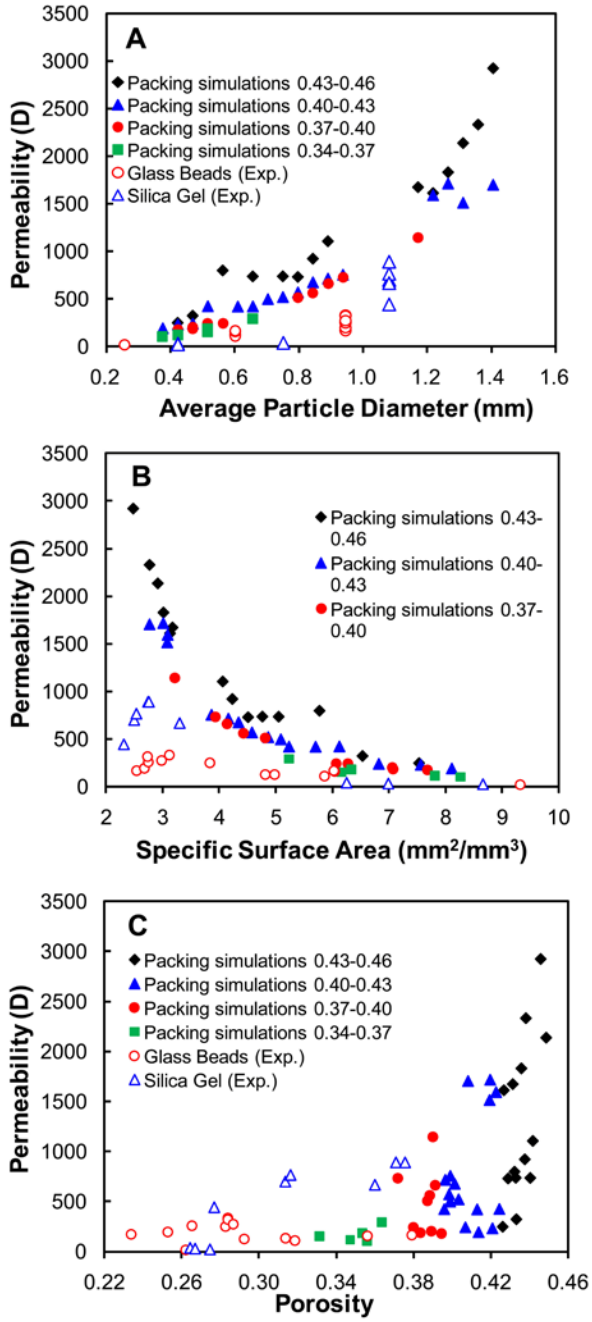

Figure 4-15. (caption on next page)

Figure 4-15. (A) Relationship between permeability and average particle diameter (mm). (B) Relationship between permeability and specific surface area (mm^2/mm^3). (C) Relationship between permeability and porosity. The data in this figure were obtained by random packing simulations and by NMR micro-imaging experiments.

δ

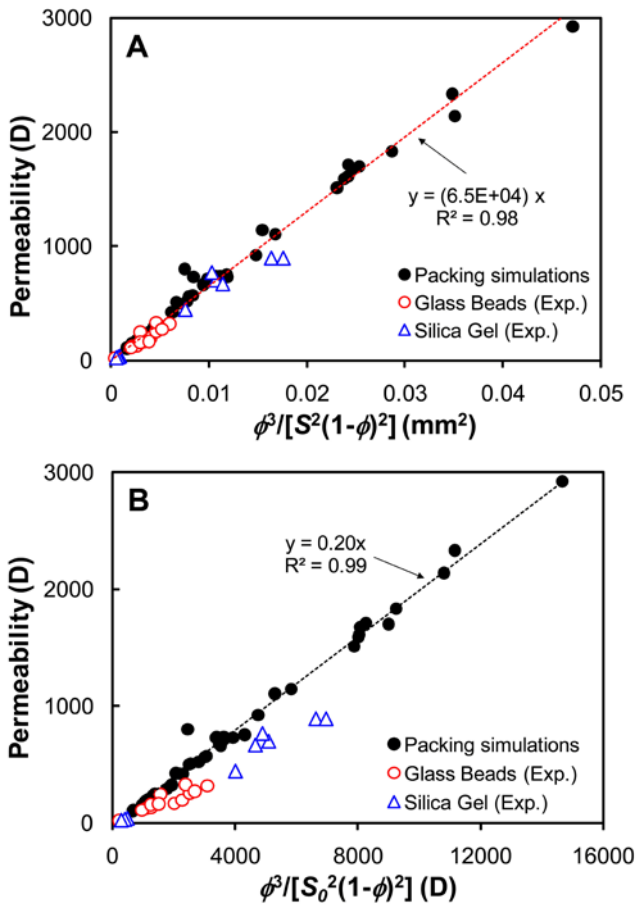

Figure 4-16. (A) Relationship between permeability and (porosity)^3/[(specific surface area)^2(1-porosity)^2] (unit in mm^2). Here the specific surface area refers to total surface area of the interstitial voids divided by the total bulk volume. (B) Relationship between permeability and $\phi^3/[S_0^2(1-\phi)^2]$ (unit in Darcy). Here, S_0 is the total surface area of the interstitial voids divided by the volume of the solid grains. Black closed circles correspond to packing simulation data, and red open circles and blue open triangles correspond to experimental data for glass beads and silica gel samples, respectively.

δ

$$k(\phi, S) = \frac{\phi^3}{C_0 S^2 (1-\phi)^2}, \qquad (4.11)$$

where C_0 is the pore shape factor. Permeability can be well explained by this equation, regardless of grain shape (e.g., sphere or shaped particles studied in the current study) and the heterogeneity in particle size (see Figure 4-S10 in Supplementary Information for correlations among the parameters based on the Kozeny equation).

Upon utilizing total surface area of the interstitial voids divided by the volume of the solid grains (S_0, see Section 4.2.4.2 above) instead of the current definition of the specific surface area, Figure 4-16B also shows the relationship between permeability and $\phi^3/[(S_0)^2 (1-\phi)^2]$ (unit in Darcy). The slope of the relationship for porous media composed of single-sized spheres is approximately 0.2, and that for porous media composed of diverse grain shapes and particle diameters (GB2 and SG2) is slightly smaller than 0.2. The correlation between surface area per unit bulk volume and surface area per unit solid volume is described in Supplementary Information, Figure 4-S11.

Previous studies have suggested that the fractal dimension of porous networks can be used to account for macroscopic transport properties of porous media. For instance, permeability has often been described as a function of porosity and fractal dimension (Jacquin and Adler, 1987; Hansen and Skjeltorp, 1988; Muller and McCauley, 1992; Ghilardi et al., 1993; Costa, 2006) and as a function of pore fractal

δ

dimension and tortuosity fractal dimension (Yu and Cheng, 2002). These results offer useful insights into the nature of permeability in porous networks. The relationships obtained in the current study can also provide further and improved generalization of the relationships between permeability, fractal dimension, and porosity on the basis of newly identified relationships among the structural parameters. For example, by combining equations (4.6) and (4.11) and replacing specific surface area in equation (4.11) with the D_{cc} of pores from equation (4.6), the following equation can be obtained:

$$k(\phi, D_{cc}) = \phi^3 / \left[C_0 \left\{ c - d \ln\left(\frac{a - D_{cc}}{D_{cc} - b} \right) \right\}^2 (1-\phi)^2 \right]. \qquad (4.12)$$

where coefficients *a, b,* and *c* are functions of porosity, as described in equation (4.7), and C_0 is the pore shape factor in the Kozeny-Carman equation. Figure 4-17 shows the relationships among permeability, the D_{cc} of pores, and porosity. Permeability decreases with increasing D_{cc} at constant porosity and increases with increasing porosity at constant D_{cc}. Thus, permeability can be expressed on the basis of the D_{cc} of pores and porosity in porous media composed of sand-sized particles. Note that D_{cc} of pore can be expressed as a function of specific surface area at constant porosity or a function of porosity at constant specific surface area (Figure 4-7). For the geophysical applications, it is more useful that specific surface area is replaced by D_{cc} of pore, and therefore equation (4.12) which is a function of porosity and D_{cc} of pore is suggested. Furthermore, because

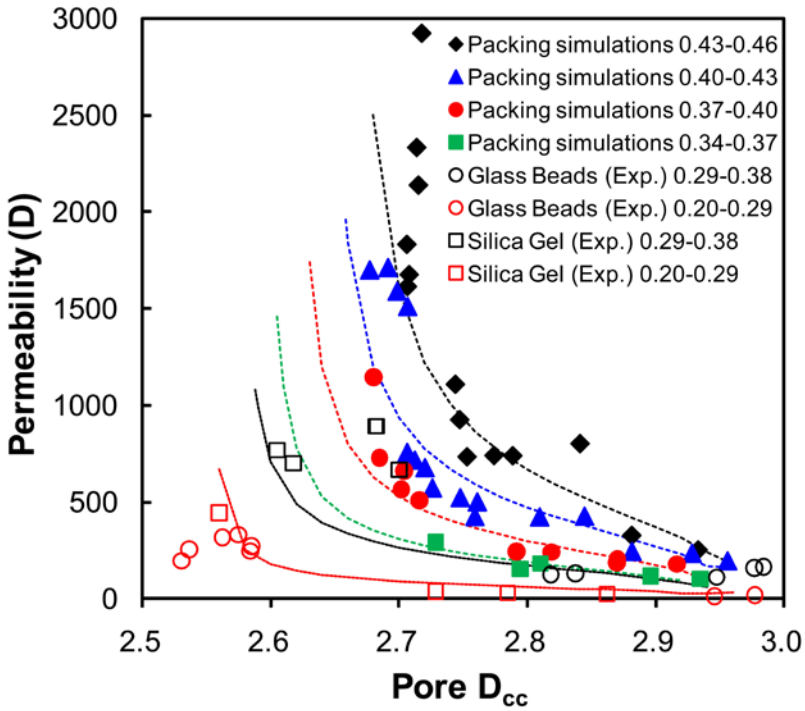

Figure 4-17. Relationship between permeability and cube-counting fractal dimension of porous networks. The equation for each curve is shown as equation (4.12) in the text. Black diamonds, blue triangles, red circles, and green squares correspond to each group of simulation data for porosities 0.43–0.46, 0.40–043, 0.37–0.40, and 0.34–0.37, respectively. Black and red open circles correspond to glass bead samples for porosities 0.29–0.38 and 0.20–029, respectively. Black and red open squares correspond to silica gel samples for the porosities 0.29–0.38 and 0.20–0.29, respectively. Black, blue, red, and green dashed lines and black and red dotted lines are curves for equation (4.12) corresponding to the median porosities in each group: 0.445, 0.415, 0.385, 0.355, 0.335, and 0.245, respectively.

δ

equation (4.12) yielded high correlations among the key structural parameters and properties, it can be applied to diverse natural porous networks (see Supplementary Information, Figure 4-S12 for relationship between permeability and D_{cc} of solid mass, and that between permeability and D_{cc} of surface). In order to generalize equation (4.12), a scaling factor that has the dimension of the square of the length should be included in equation (4.12) (note that permeability has the dimension of the square of the length). A scaling factor would be, for example, the volume of the object divided by the average cutoff lengths. However, as D_{cc} may depend on the length scale of observation, the investigation on D_{cc} for a wider range of volume is necessary for the estimation of the scaling factor. As shown in equation (4.11), permeability has been expressed as a function of porosity and specific surface area (i.e., $k = f(\phi)f(S)$) by Kozeny-Carman equation. In this study, it is suggested that permeabity can be expressed as a function of porosity and D_{cc} (i.e., $k = f(\phi)f(D_{cc})$) by equation (4.12). In Supplementary Information, the effects of $(\text{porosity})^3/(\text{surface area})^2$ and $(\text{porosity})^3/[(\text{surface area})^2(1\text{-porosity}^2)]$ on cube-counting fractal dimension (Figure 4-S13), configurational entropy (Figure 4-S14), and entropy length (Figure 4-S15) have been provided.

In addition to their obvious applications and implications for ground water transport and fluid distribution in natural porous networks, the newly identified relationships among structural parameters and properties may provide additional implications for characterizing and understanding fluid-rock-melts composites and glass-vesicles-rock

δ

composites regardless of the length scale of heterogeneity (from microscopic to mesoscopic). For example, previous studies have shown that shear viscosity of rock-melt composites (η) in the earth's interior is inversely proportional to the exponential of liquid volume fraction (ϕ) in partially saturated porous media [e.g., $\eta^{-1} \propto \exp(\phi)$] (Takei, 1998; Takei, 2005; Takei and Holtzman, 2009). Therefore, on the basis of the inverse correlation between the liquid volume fraction (i.e., porosity) and configurational entropy [equation 4.10], the shear viscosity (η) in the melts can be simply expressed using the configurational entropy (S_c)

$$\eta^{-1} \propto \exp(S_C). \qquad (4.13)$$

The results suggest that shear viscosity decreases with increasing configurational entropy of fluids that are partially saturated in rocks. Thus, configurational entropy can be a complementary parameter for describing elastic properties and shear viscosity of porous media. Note that equation (4.13) shows remarkable similarity to the fundamental microscopic relationship between configurational entropy of supercooled liquids and the viscosity of melts on the basis of the Adam-Gibbs theory (Adam and Gibbs, 1965; Richet, 1984; Lee, 2005), suggesting that a relationship derived from equation (4.13) is robust and can be applied to diverse networks, regardless of the length scale of the constituent objects.

Additionally, the 3D fractal dimension was used to describe P-wave attenuation and velocity in partially saturated rocks. For example, P-wave attenuation at high-frequencies is expressed as

δ

$$Q^{-1} \propto \omega^{-\nu}, \tag{4.14}$$

where Q^{-1} is the P-wave attenuation, and ν is a Hurst exponent (= 3 - fractal dimension of fluid patches in the mesoscopic scale) (Pride and Masson, 2006). Since the fractal dimension (3–Hurst exponent) can be directly calculated by considering fluid patches of partially saturated rocks, P-wave attenuation can also be estimated. 3D fractal dimension would be a more accurate parameter for describing complex networks than the conventional fractal dimension obtained from 2D images.

Although the current analyses are focused on simple porous networks to establish the correlations among the structural and transport properties, the results will be helpful for characterizing more complex porous networks with broader distributions of grain sizes and particle shapes. The methodology and results systematically analyze the structures of diverse porous networks and complex geologic media and have elucidated previously unknown details of the nature of those structural parameters. Further generalization of the relationships identified in the current study using diverse particle sizes and heterogeneity remains to be explored.

4.4. Conclusions

Relationships among the structural parameters and properties for porous media composed of model sands from random packing simulations and NMR micro-imaging experiments were established. The D_{cc} of 3D

δ

porous networks increases with increasing specific surface area at constant porosity and increases with increasing porosity at constant specific surface area. The first lacunarity of 3D porous networks was also reported. The lacunarity at intermediate box size (~ 0.469 mm in the current study) decreases with increasing specific surface area with data showing the power-law relationship between the two parameters. The entropy length of the porous networks decreases linearly with decreasing average particle diameter and can be used to constrain the characteristic length scale of the pores in the networks. The maximum configurational entropy increases with increasing porosity, showing a similar trend with the configurational entropy of the total porosity. Based on this newly identified correlation and the Kozeny-Carman equation, a predictive relationship among permeability as a function of porosity and D_{cc} was proposed. The correlations among the structural and transport parameters analyzed in this study are helpful for understanding complex porous networks and can be used to explain the geometrical and transport properties of porous media.

It was also demonstrated that 3D porous networks can be successfully obtained by NMR micro-imaging with a spatial resolution of ~50 μm, which allowed us to obtain 3D images of porous media composed of particles as small the silt-sized grains. The availability of high spatial resolution images together with other advantages highlighted by its capability of directly probing of fluid phases using NMR micro-imaging will be useful to visualize micrometer scale distributions of two-phase

δ

fluids in porous media and to image melts and fluids in rocks.

Appendix: Multifractal analysis of cross sections of model porous networks

Multifractal analysis of cross sections of porous networks has been applied to characterize the complex geometry that exhibits local fluctuations in density (see below). In that sense, the model sands studied here may not be a favorable system for the multifractal analysis. Multifractal analysis on relatively simple porous networks, however, can reveal useful correlations among their structural parameters and properties; thus, the analysis on porous networks composed of single-sized spheres or model sands was performed to reveal the relationships between generalized dimensions and other key structural parameters.

4.A.1. Summary of theoretical background and data analysis

In multifractal analysis, probability $\mu_i(r)$ in a box i of size r covering a pore space is defined as (Hentschel and Procaccia, 1983)

$$\mu_i(r) = \frac{M_i(r)}{M}, \qquad (4.A1)$$

where $M_i(r)$ is the number of pore pixels included in a square box, and M is the total mass of the object. For every box i, the partition function $[X(q.r)]$ was obtained for different moments q (varying from $-\infty$ to $+\infty$) using

$$X(q,r) = \sum_{i=1}^{N(r)} \mu_i^q(r) = r^{(q-1)D_q}, \qquad (4.A2)$$

δ

where $N(r)$ is the number of boxes covering the entire image. For each q, generalized dimensions (D_q) can be obtained from equation (4.A2) given by

$$D_q = \frac{1}{q-1}\lim_{r\to 0}\frac{\log X(q,r)}{\log r}. \qquad (4.A3)$$

The geometric meaning of D_q can be understood as the dimensions of the set, which leads to divergence of moments of the order of q or higher (Farmer et al., 1983). The generalized dimensions for q = 0, q = 1, and q = 2 (capacity, information, and correlation dimension, respectively), are often used to characterize complex porous networks (e.g., Muller and McCauley, 1992; Muller et al., 1995; Muller, 1996). Multifractal analysis of porous media has been extended to pore space in soils (e.g., Posadas et al., 2003; Bird et al., 2006; Dathe et al., 2006; Grau et al., 2006) and rocks (e.g., Muller and McCauley, 1992; Muller, 1996; Saucier and Muller, 1999). Recently, multifractal analysis was applied to characterize the 3D images of soil samples (Tarquis et al., 2009). Generalized dimensions of 2D cross-sectional images of the porous networks of model sands were calculated and the effect of specific surface area on the generalized dimensions was explored.

Multifractal analysis was carried out using a box-counting algorithm where 2D data with a matrix size of 160 × 160 were expanded to 400 × 400 data using ImageJ software (Rasband, 1997-2009). The box-counting algorithm was performed for every box size from 2 to 256 pixels in steps of 2^k. The generalized dimensions were estimated from the slope of the log-log plot of the partition function [$X(q,r)$] over box size (r).

4.A.2. Results and discussion

Figure 4-A1 shows partition functions [$X(q,r)$] over box sizes (r) in log-log plots ranging from 2 to 256 pixels for 2D cross-sectional images of model porous media by random packing simulations. For $q \geq 0$, the partition functions show linear relationships in the log-log plots. For $q < 0$, two distinct regions were distinguished by a breakpoint at ~log(r) of ~2.8 for [$X(q,r)$] for a sphere diameter of 468.75 mm [break points (BP) in Figure 4-A1]. The box size at the breakpoint increased with increasing grain size.

Figure 4-A2 shows the generalized dimensions of 2D model porous networks studied here as a function of q. The generalized dimension (D_q) was obtained from the trend line corresponding to each q value from –10 to +10 in log [$X(q,r)$] over log [box sizes (r)] (Figure 4-A1). For $q \leq 0$, D_q values decreased with increasing q. For $q > 0$, and they showed relatively constant D_q values. This behavior was consistent with the trend reported for the pore space of soils (Dathe et al., 2006; Grau et al., 2006; Tarquis et al., 2006). In general, D_q values increase with decreasing grain diameter.

Figure 4-A3 shows the relationship between generalized dimensions and specific surface area. Figures 4-A3A and 4-A3B were obtained from the porous networks composed of spheres grouped by porosity ranges of 0.40–0.46 and 0.34–0.40, respectively. Figures 4-A3C and 4-A3D were obtained from GBs and SG samples, respectively. Although it was not clear whether D_q (with varying specific surface area) was dependent on porosity or type of particles (SG or GB) generalized dimensions for $q \leq 0$ increases with increasing specific surface area for

δ

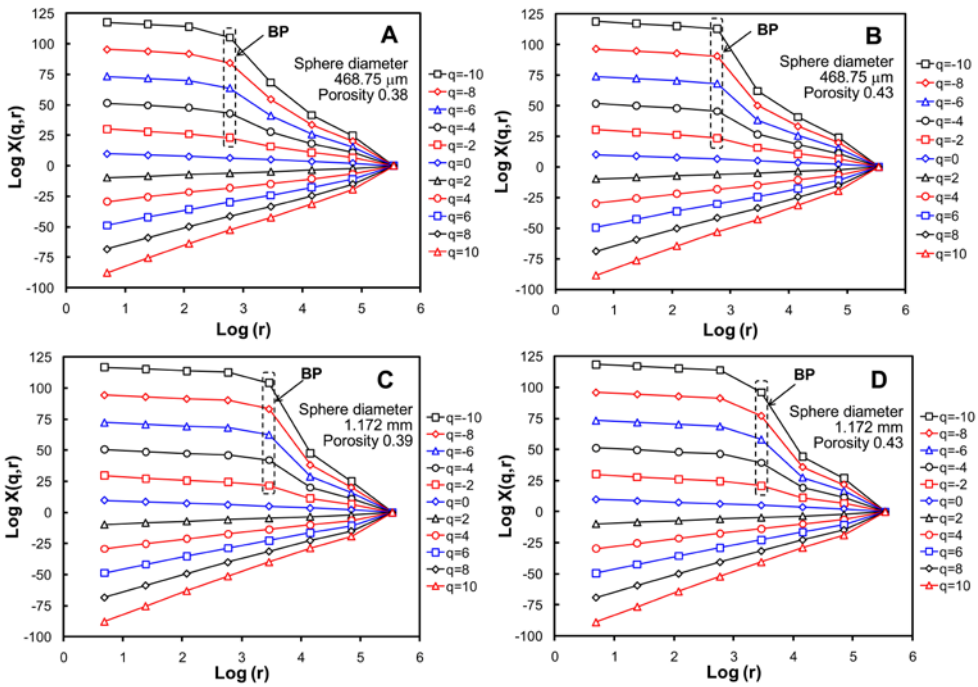

Figure 4-A1. Relationship between partition functions in multifractal analysis and box size in the log-log plots when moment q was varied from –10 to +10. (A) and (B) correspond to the porous networks obtained by random packing simulations for sphere diameters of 468.75 μm and porosities of 0.38 and 0.43, respectively, and (C) and (D) correspond to the porous networks obtained by random packing simulations for sphere diameters of 1.172 mm and porosities of 0.39 and 0.43, respectively.

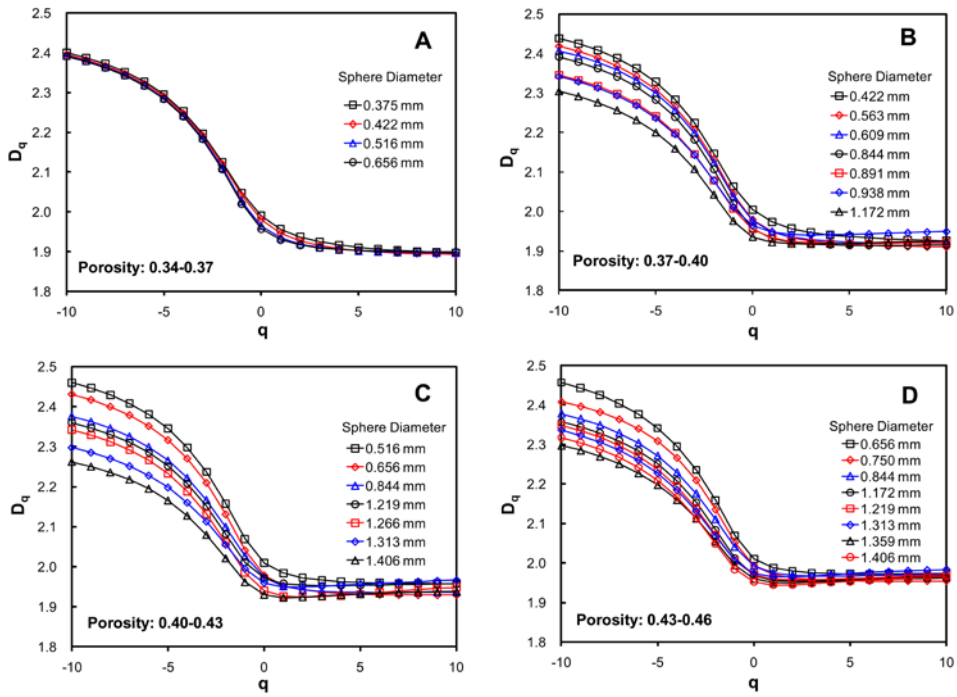

Figure 4-A2. Relationship between generalized dimensions and moment q. Each plot corresponds to the following porosity ranges: (A) 0.34 to 0.37, (B) 0.37 to 0.40, (C) 0.40 to 0.43, and (D) 0.43 to 0.46.

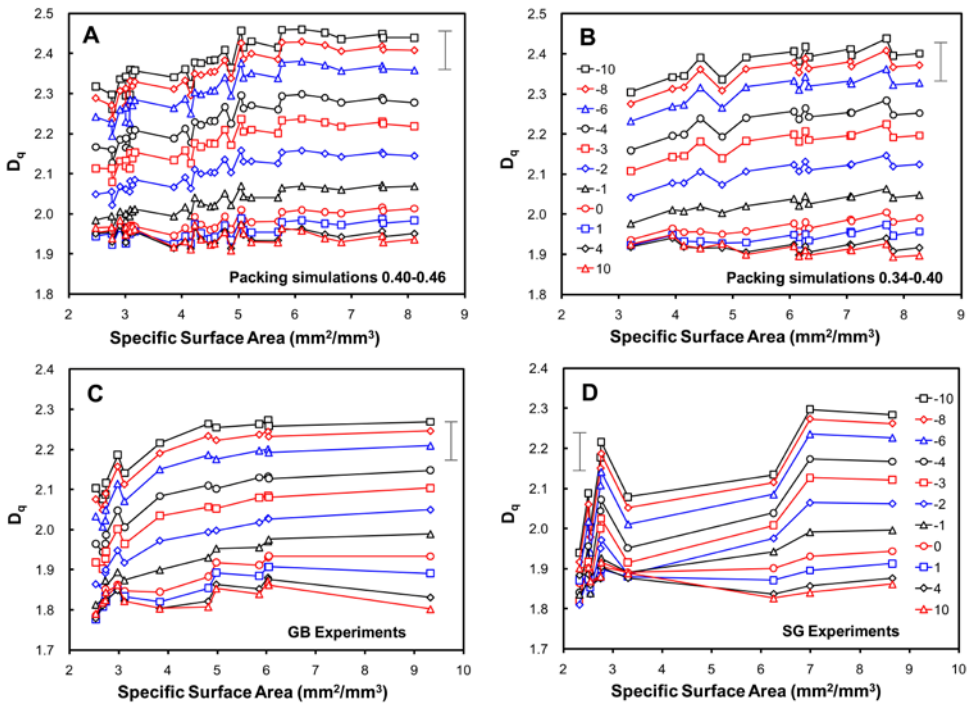

Figure 4-A3. Relationship between generalized dimensions and specific surface area (mm^2/mm^3) when moment q was varied from –10 to +10 (curves for q = –9, –7, –5, 2, 3, 5, 6, 7, 8, and 9 that had trends similar to the other curves are not shown for the sake of clarity). (A) and (B) correspond to the results obtained by random packing simulations of the following porosity ranges: (A) 0.34 to 0.40 and (B) 0.40 to 0.46. (C) and (D) correspond to the results obtained by NMR micro-imaging experiments; (C) glass beads and (D) silica gel. Maximum error is shown as an error bar in each plot. The legend for all figures is shown in (B) and (D).

every data group (Figures 4-A3A-A3D). The difference between the largest and the smallest generalized dimensions at a specific q value was as large as 0.2. The estimated maximum errors (depicted by error bars in Figures 4-A3A–A3D) were smaller than 0.1.

Figure 4-A4 shows the relationships among generalized dimensions, specific surface area, and porosity. While the relationship was not clear in Figure 4-A3, the generalized dimension at a constant specific surface area increases with increasing porosity. This trend is similar to the trends among D_{cc}, specific surface area, and porosity (see Section 4.3.1).

Figure 4-A5 shows the differences between D_0, D_1, and D_2 (i.e., D_0-D_2, D_0-D_1, and D_1-D_2) as a function of specific surface area. The difference functions increase with increasing specific surface area, whereas D_1 and D_2 are not correlated with specific surface area, as shown in Figures 4-A4E and A4F. Among the difference functions, D_0-D_2 shows the largest difference between the maximum and minimum differences between D_0, D_1, and D_2. It was previously reported that D_0-D_1 is a measure of the degree of heterogeneity of a particle size distribution (Posadas et al., 2001). The current relationship between D_0-D_2 and specific surface area has not been reported so far. The fine correlation between the difference function and specific surface area suggests that multifractal analysis may be useful to characterize relatively simple porous networks.

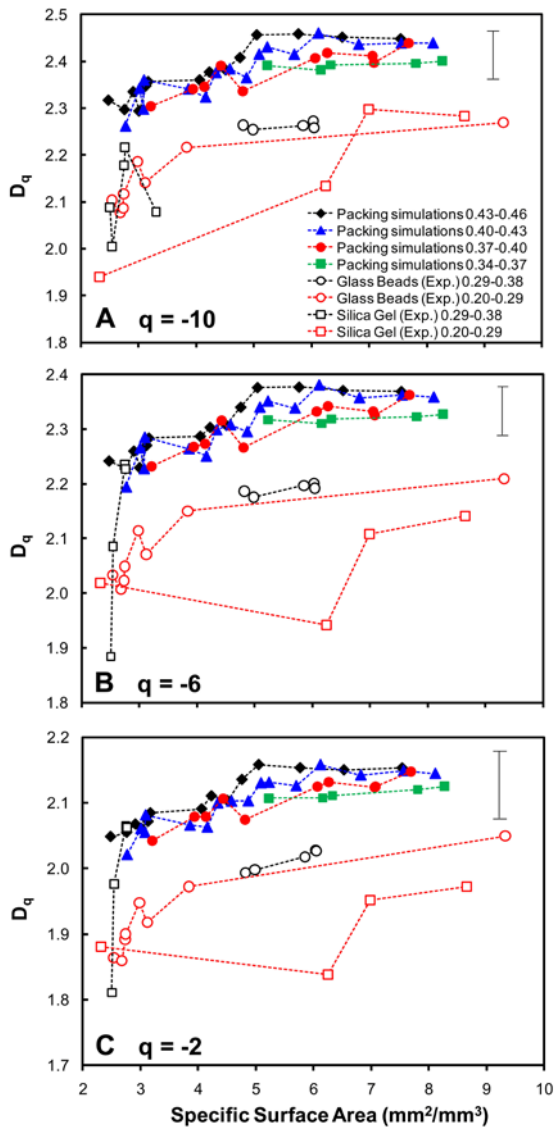

Figure 4-A4. Relationship between generalized dimension and specific surface area (mm^2/mm^3) at a specific moment, q. (A, B, C, D, E, and F) correspond to moment q of –10, –6, –2, 0, 1, and 2, respectively. Maximum error is shown as an error bar in each plot. The legend for all figures is shown in (A) and (D).

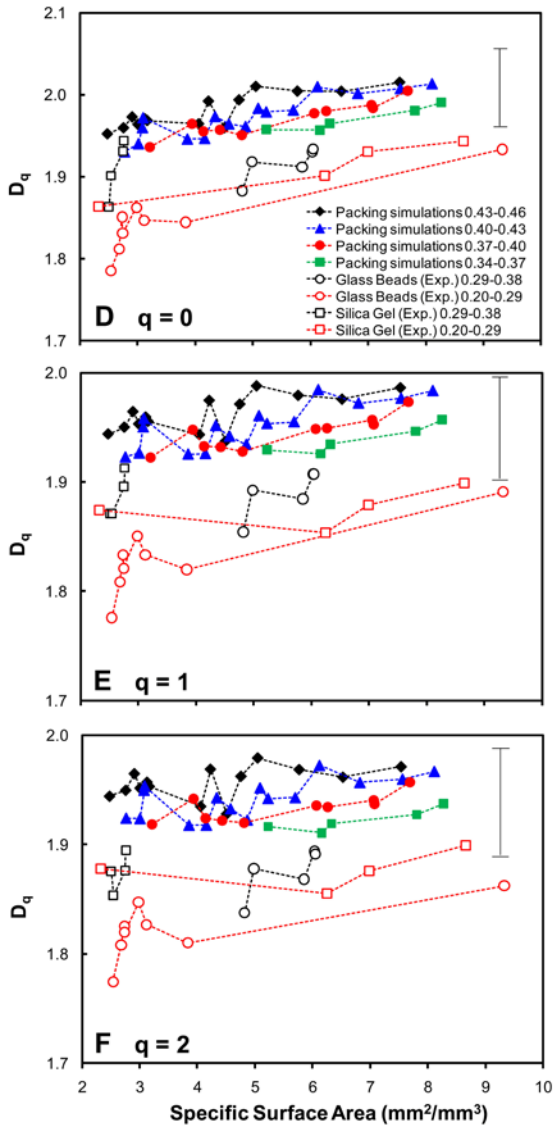

Figure 4-A4. (continued)

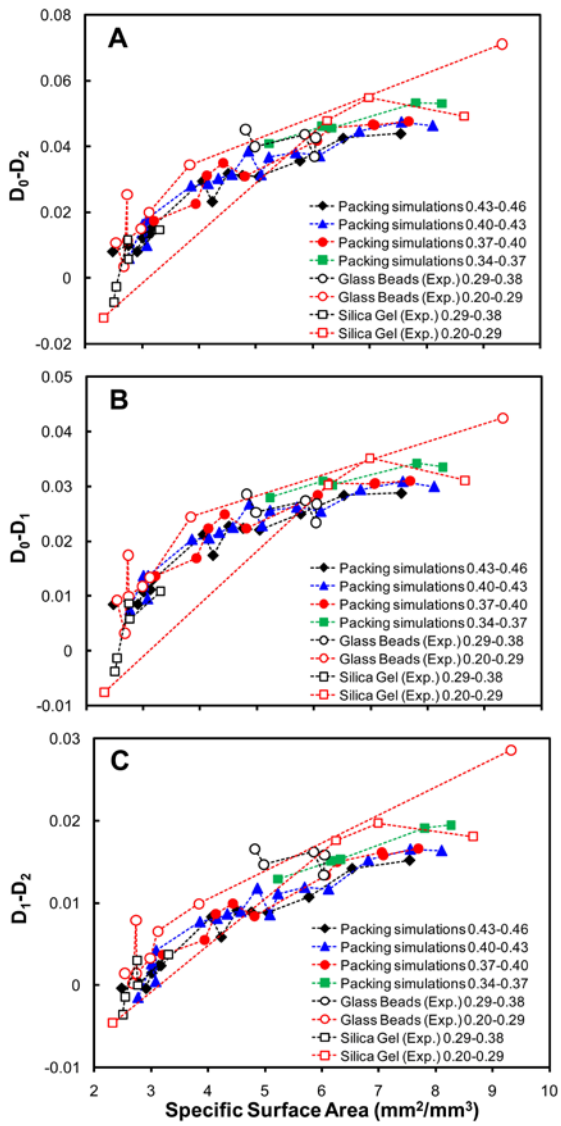

Figure 4-A5. (A) Relationship between D_0-D_2 and specific surface area (mm²/mm³). (B) Relationship between D_0-D_1 and specific surface area (mm²/mm³). (C) Relationship between D_1-D_2 and specific surface area (mm²/mm³).

Supplementary Information

4.S1. Selection of box sizes for estimation of D_{cc}

Figures 4-S1-3 show the relationship between box counts and box size for the simulated pores (Figure 4-S1), solid grains (Figure 4-S2), and surface (Figure 4-S3) composed of randomly packed spheres for sphere diameters of 8 pixels (0.38 mm) (Figure 4-S1A, 4-S2A, and 4-S3A), 15 pixels (0.70 mm) (Figure 4-S1B, 4-S2B, and 4-S3B), and 30 pixels (1.41 mm) (Figure 4-S1C, 4-S2C, and 4-S3C) with varying box size from 4 to 128 pixels (corresponding to 0.047-1.50 mm). Trend lines with three characteristic slopes can be drawn from ~4 to ~10 pixels (red line), from ~11 to ~40 pixels (dark blue line), and from ~40 to ~128 pixels (blue line). These ranges are roughly consistent with region I, II, and III, respectively (see Figure 4-5).

As specifically mentioned in the text, the box size range for non-integer fractal dimension in the porous networks only slightly varies with grain size because the variation in grain size in this study was not significant within the range used for the estimation of D_{cc}. The pixel sizes included in this range (among the divisors of 640) are 16, 20, 32, and 40 pixels (corresponding to 0.19, 0.23, 0.38, and 0.46 mm, respectively).

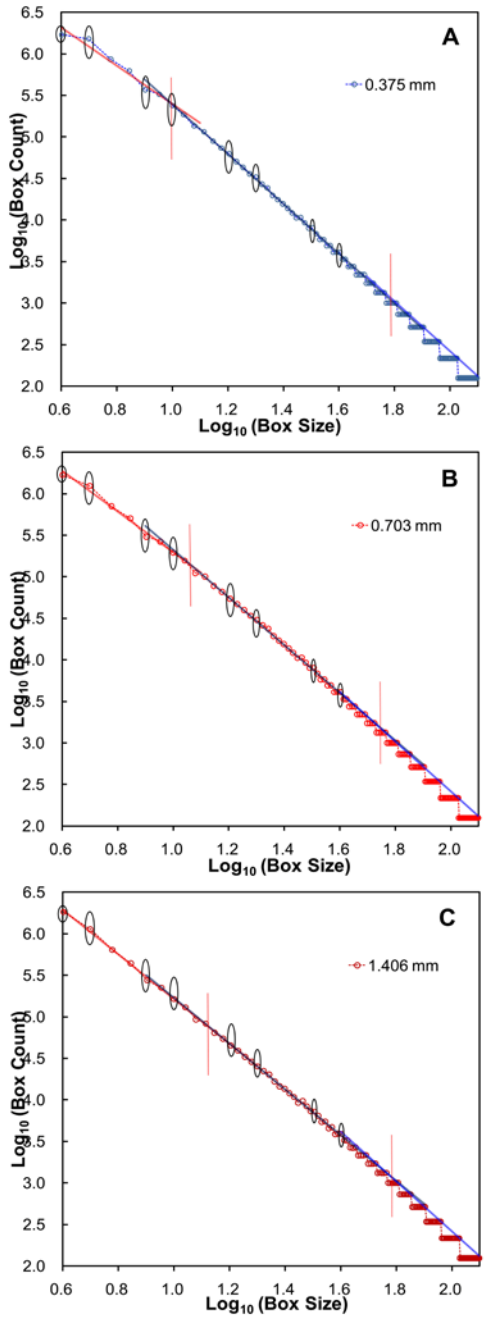

Figure 4-S1. (caption on next page)

Figure 4-S1. Relationship between box counts and box size (from 4 to 128 pixels, corresponding to 0.047-1.50 mm) in log-log plot for porous networks obtained by random packing simulations of single sized spheres with the diameters of (A) 8 pixels (corresponding to 0.38 mm), (B) 15 pixels (corresponding to 0.70 mm), and (C) 30 pixels (corresponding to 1.41 mm). Black ellipsoids indicate the data points that correspond to divisors of 640.

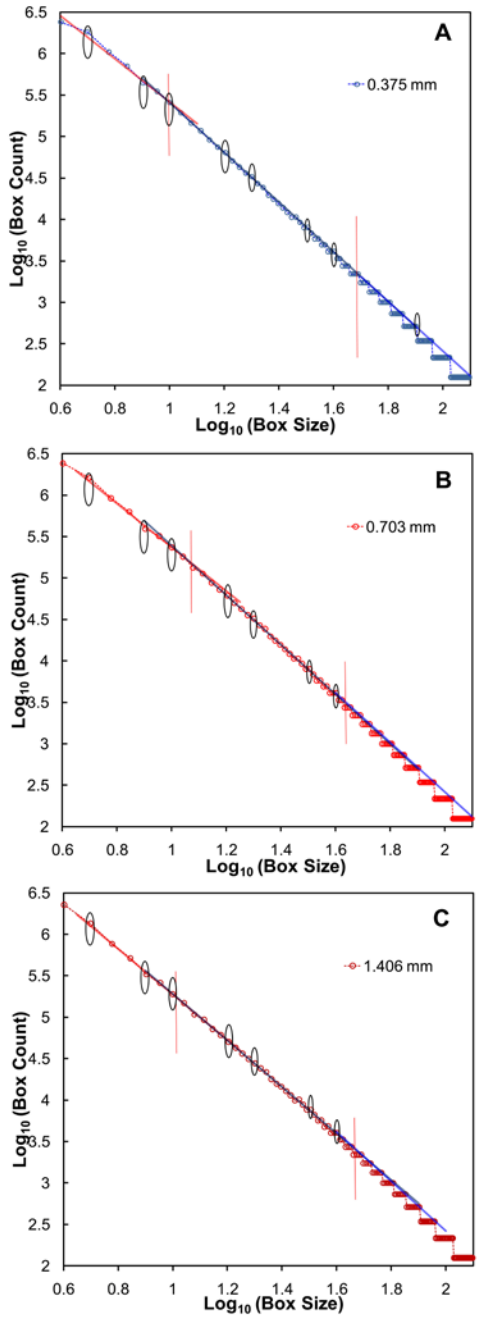

Figure 4-S2. (caption on next page)

Figure 4-S2. Relationship between box counts and box size (from 4 to 128 pixels, corresponding to 0.047-1.50 mm) in log-log plot for solid grains obtained by random packing simulations of single sized spheres with the diameters of (A) 8 pixels (corresponding to 0.38 mm), (B) 15 pixels (corresponding to 0.70 mm), and (C) 30 pixels (corresponding to 1.41 mm). Black ellipsoids indicate the data points that correspond to divisors of 640.

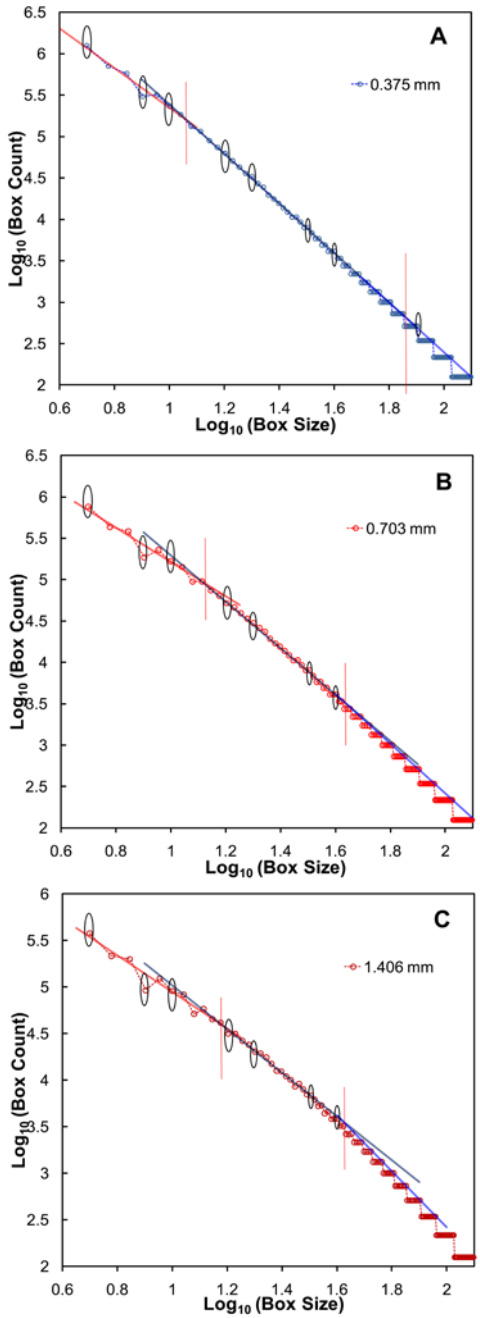

Figure 4-S3. (caption on next page)

Figure 4-S3. Relationship between box counts and box size (from 4 to 128 pixels, corresponding to 0.047-1.50 mm) in log-log plot for solid grains obtained by random packing simulations of single sized spheres with the diameters of (A) 8 pixels (corresponding to 0.38 mm), (B) 15 pixels (corresponding to 0.70 mm), and (C) 30 pixels (corresponding to 1.41 mm). Black ellipsoids indicate the data points that correspond to divisors of 640.

4.S2. Uncertainty in D_{cc}

The estimated D_{cc} in the current study may also depend on the choice of the ranges of box size. In order to estimate the uncertainty in the D_{cc} value, D_{cc} with two distinct box size ranges along the region II was estimated. Figure 4-S4 shows the log-log plots of the relationship between box counts and box size for the simulated porous networks composed of randomly packed spheres for sphere diameters of 8 pixels (0.38 mm) and 30 pixels (1.41 mm) with varying the box size. Two trend lines drawn from ~10 to ~32 pixels (blue line) and from 20 to 64 pixels (red line) for sphere diameters of 8 pixels (0.38 mm) and 30 pixels lead to similar D_{cc} values. The result shows that differences in the estimated D_{cc} are insignificant. The estimated uncertainty in D_{cc} value is thus smaller than ~ 0.07.

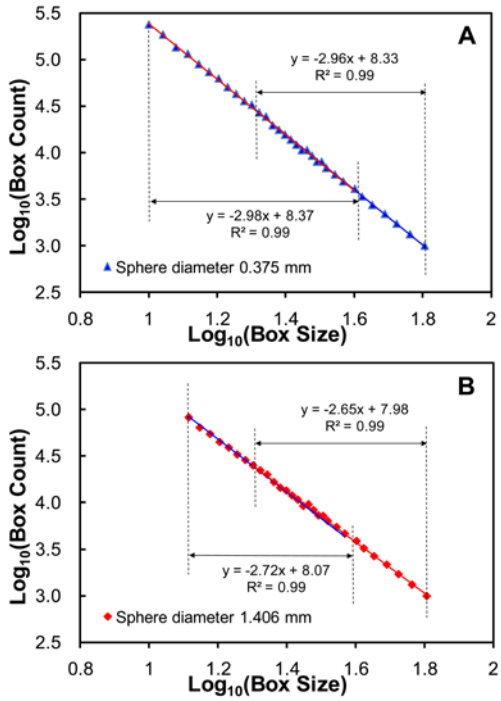

Figure 4-S4. Relationship between box counts and box size in log-log plot for porous networks obtained by random packing simulations of single sized spheres with the diameters of (A) 8 pixels, corresponding to 0.38 mm with the box sizes from 10 to 64 pixels (corresponding to 0.12-0.75 mm), and (B) 30 pixels, corresponding to 1.41 mm with the box sizes from 13 to 64 pixels (corresponding to 0.15-0.75 mm, respectively).

S3. The D_{cc} of solid mass, surface, and specific surface area

Taking into consideration the experimental results obtained by NMR micro-imaging, Figure 4-S5 shows the relationship between the D_{cc} of solid mass, surface, and specific surface area. Figure 4-S5A shows the D_{cc} of solid mass for model sands composed of SG (red circle) with heterogeneity in particle shape and size and those for GBs (blue circle) composed of spherical grains. The D_{cc} of solid mass for model sands composed of SG increases from 2.76 (±0.05) to 3.00 (±0.05) with increasing specific surface area from 2.84 to 8.66 mm^2/mm^3. The D_{cc} of solid mass for GBs increased slightly from 2.94 (±0.05) to 3.00 (±0.05) with increasing specific surface area from 2.74 to 9.57 mm^2/mm^3. Figure 4-S5B shows that D_{cc} of surface increases from 2.30 (±0.05) to 3.00 (±0.05) with increasing specific surface area and does not depend on porosity. The results for SG and GBs for D_{cc} of solid mass and surface were reproduced well using equation (4.6).

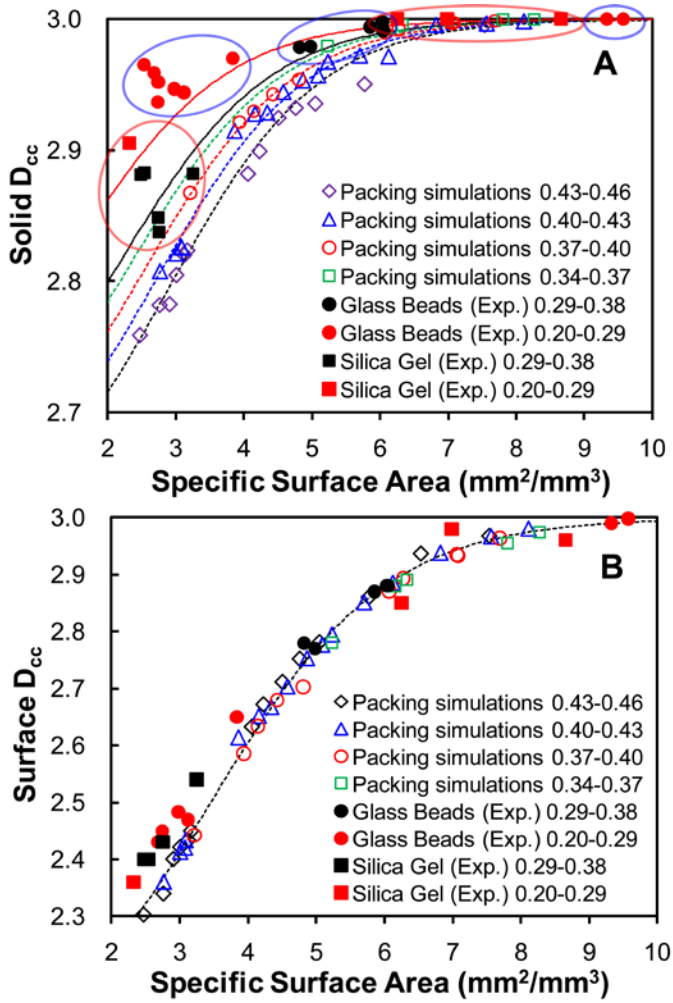

Figure 4-S5. (caption on next page)

Figure 4-S5. Effect of specific surface area on cube counting fractal dimension of (A) solid mass and (B) surface (interface) of model sands. Black and red circles correspond to glass bead samples for the porosities of 0.29–0.38 and 0.20–029, respectively. Black and red squares correspond to silica gel samples for the porosities of 0.29–0.38 and 0.20–0.29, respectively. Black diamonds, blue triangles, red circles, and green squares correspond to each group of simulation data for the porosities of 0.43– 0.46, 0.40–043, 0.37–0.40, and 0.34–0.37, respectively. Black, blue, red, and green dashed lines, and black and red dotted lines in (A) are curves for equation (4.6) corresponding to the median porosities in each group: 0.445, 0.415, 0.385, 0.355, 0.335, and 0.245. The coefficients *a, b, c,* and *d* for D_{cc} of solid mass are shown as equation (4.8). Black dashed line in (B) is curve for equation (4.6) with the coefficients *a, b, c,* and *d* for D_{cc} of surface of 3, 2, 3.455, and 1.28, respectively.

4.S4. Effect of average particle diameter on porosity

Figure 4-S6 shows the effect of average particle diameter on porosity. The general trend is increasing porosity with increasing average particle diameter. However, the trend is not clear because there are several values of porosity for a given average particle diameter used in the synthesis of GB and SG samples.

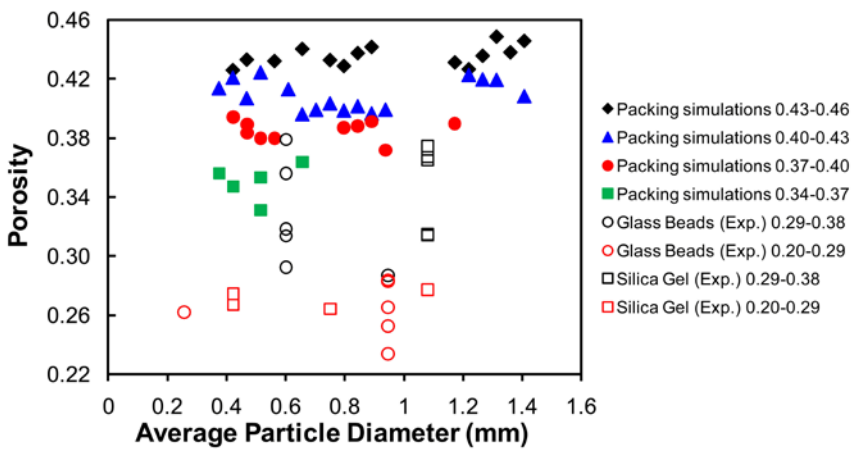

Figure 4-S6. Relationship between porosity and average particle diameter for porous networks obtained by random packing simulations and NMR micro-imaging experiments.

4.S5. Effect of average particle diameter on lacunarity

Figure 4-S7 shows the effect of average particle diameter on lacunarity. Although the lacunarity values at the minimum box size were grouped by their porosity range, the trend for the relationship between lacunarity at the minimum box size and the average particle diameter is not clear (Figure 4-S7A). The lacunarity values at a box size of 0.47 mm are also grouped by their porosity range. While the grouping for simulation data is not noticeable, the lacunariy values apparently increase with increasing average particle diameter (Figure 4-S7B).

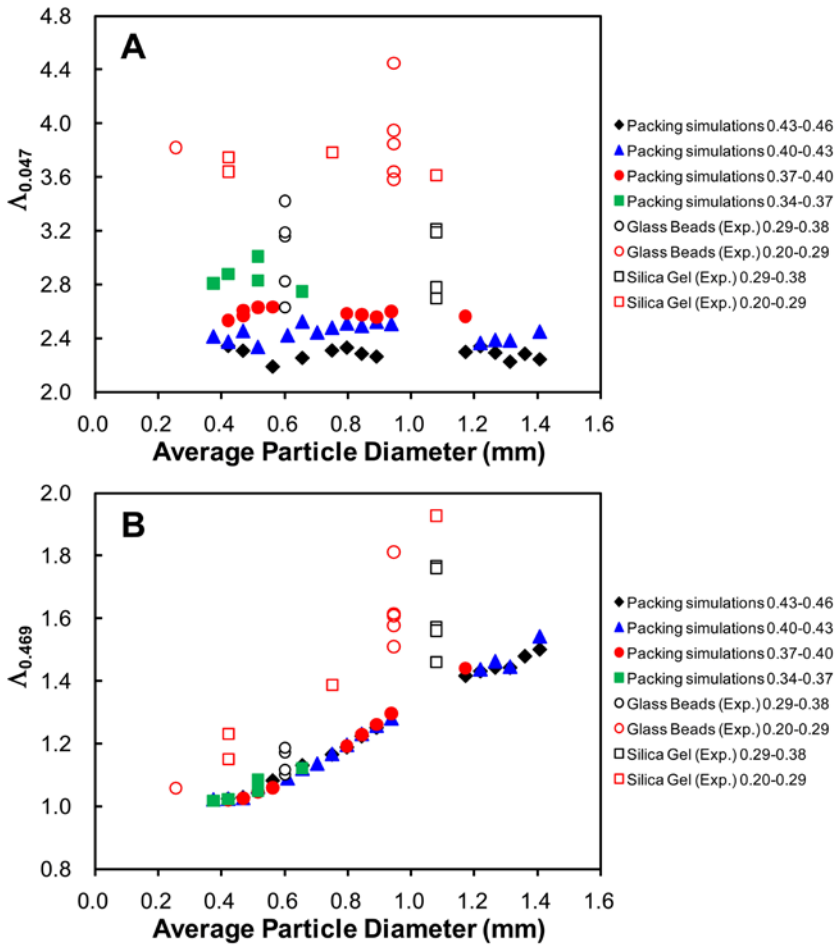

Figure 4-S7. (A) Relationship between lacunarity at the minimum box size (corresponding to a side length of 0.047 mm) and average particle diameter. (B) Relationship between lacunarity at a box size of 0.47 mm and average particle diameter.

4.S6. Effect of specific surface area and porosity on entropy length and maximum configurational entropy

Figure 4-S8 shows the relationship between entropy length and porosity. The trend for the relationship between entropy length and porosity is not clear while entropy length decreases with increasing specific surface area (Figure 4-13B). Figure 4-S9A shows the relationship between maximum configurational entropy and average particle diameter, and Figure 4-S9B shows the relationship between maximum configurational entropy and specific surface area. While maximum configurational entropy increases with increasing porosity (Figure 4-14), the trends for the relationships shown in Figure 4-S9 are not clear. These data indicate the characteristics of each parameter related with configurational entropy; entropy length depends on specific surface area, and maximum configurational entropy depends on porosity.

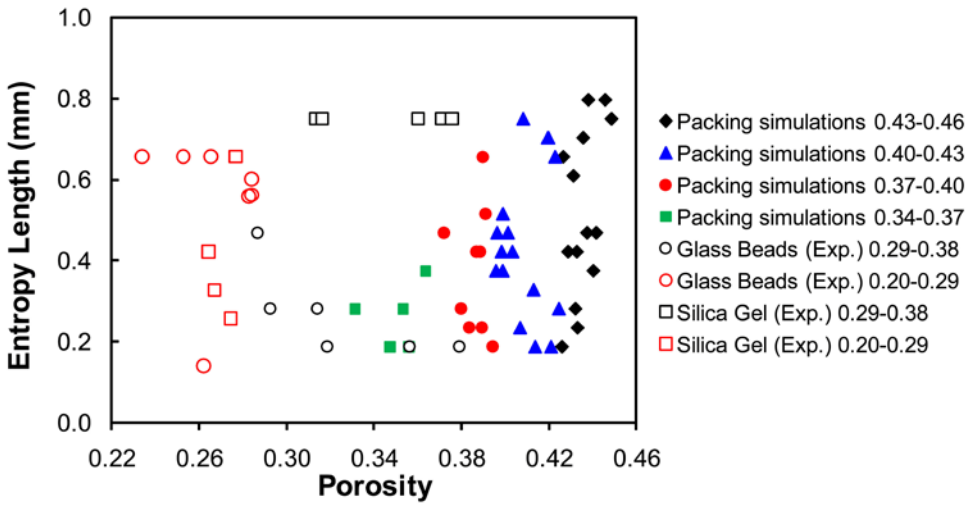

Figure 4-S8. Relationship between entropy length and porosity for porous networks obtained by random packing simulations and NMR micro-imaging experiments.

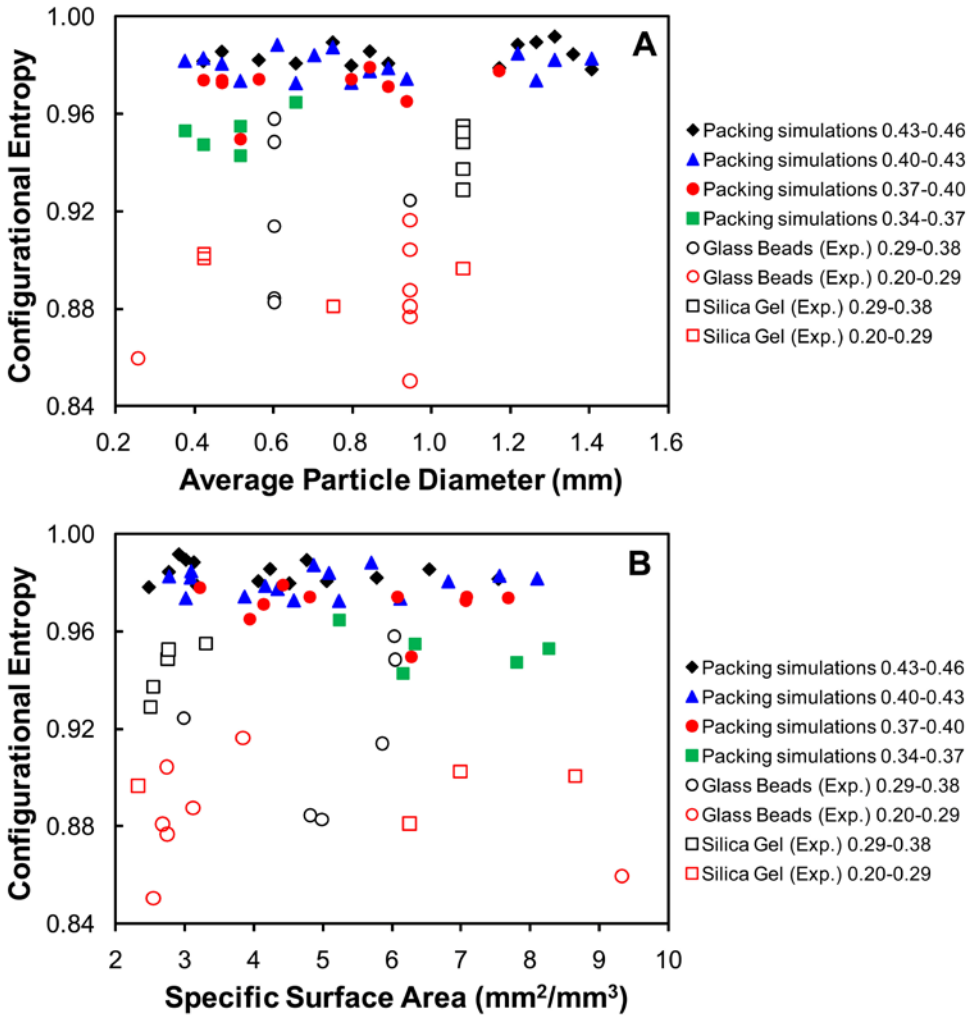

Figure 4-S9. (A) Relationship between maximum configurational entropy and average particle diameter. (B) Relationship between maximum configurational entropy and specific surface area for porous networks obtained by random packing simulations and NMR micro-imaging experiments.

δ

4.S7. Comparison between Kozeny equation and Kozeny-Carman equation

Figure 4-S10 shows the relationship between permeability and a factor obtained from the Kozeny equation (Carman, 1937; Bear, 1972):

$$k = \frac{\phi^3}{C_T T S^2}, \tag{4.S1}$$

where C_T is Kozeny's constant, and T is tortuosity. The results show that the relationships among permeability, porosity, and specific surface area for porous media composed of single-sized spheres were also well explained by the Kozeny equation. In contrast, the permeability for porous media composed of diverse grain shapes (e.g., single-sized spheres, glass beads, and silica gels with irregular shapes) and mixtures of grain sizes (GB2 and SG2) was better explained by factors of porosity and specific surface area from the Kozeny-Carman equation (4.11) than those from the Kozeny equation, which is consistent with previous reports (Carman, 1937).

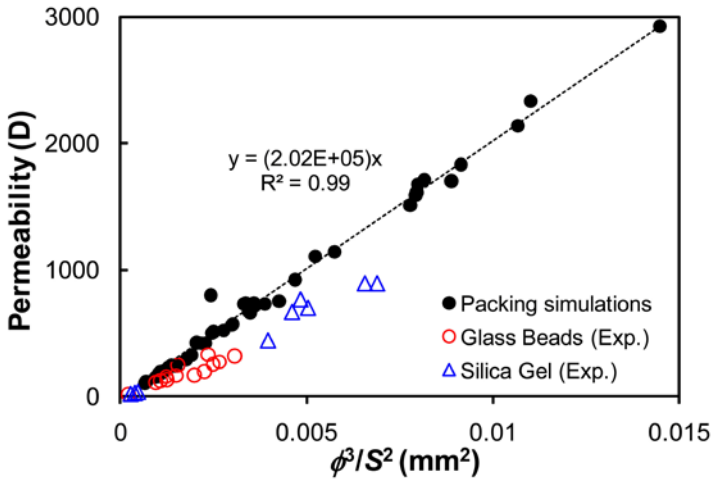

Figure 4-S10. Relationship between permeability and (porosity)^3/(specific surface area)^2 indicated by the Kozeny equation (4.S1). Black closed circles correspond to packing simulation data, and red open circles and blue open triangles correspond to experimental data for glass beads and silica gel samples, respectively.

4.S8. Relationship between surface area per unit bulk volume and surface area per unit solid volume

Figure 4-S11 shows the relationship between surface area per unit solid volume (S) and surface area per unit solid volume (S_0).

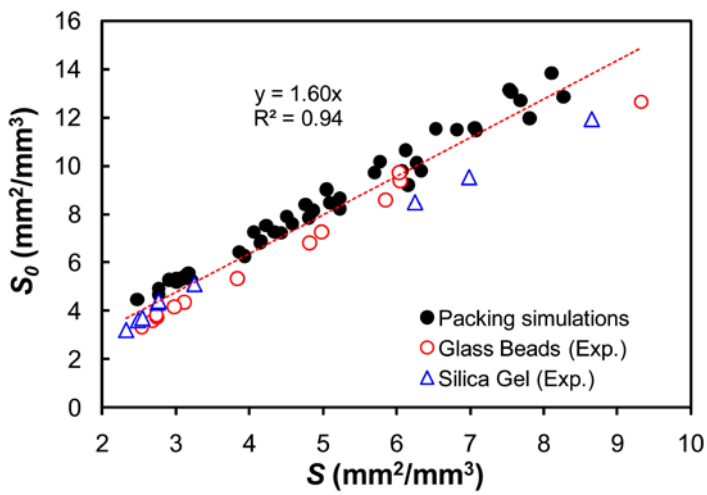

Figure 4-S11. Relationship between surface area per unit solid volume (S) and surface area per unit solid volume (S_0).

4.S9. Relationships between permeability and D_{cc} of solid mass and between permeability and D_{cc} of surface

Figure 4-S12 shows the relationships among permeability, porosity, and the D_{cc} of solid mass (Figure 4-S12A) and surface (Figure 4-S12B). Permeability tends to decrease with increasing D_{cc} at constant porosity and increase with increasing porosity at constant D_{cc}.

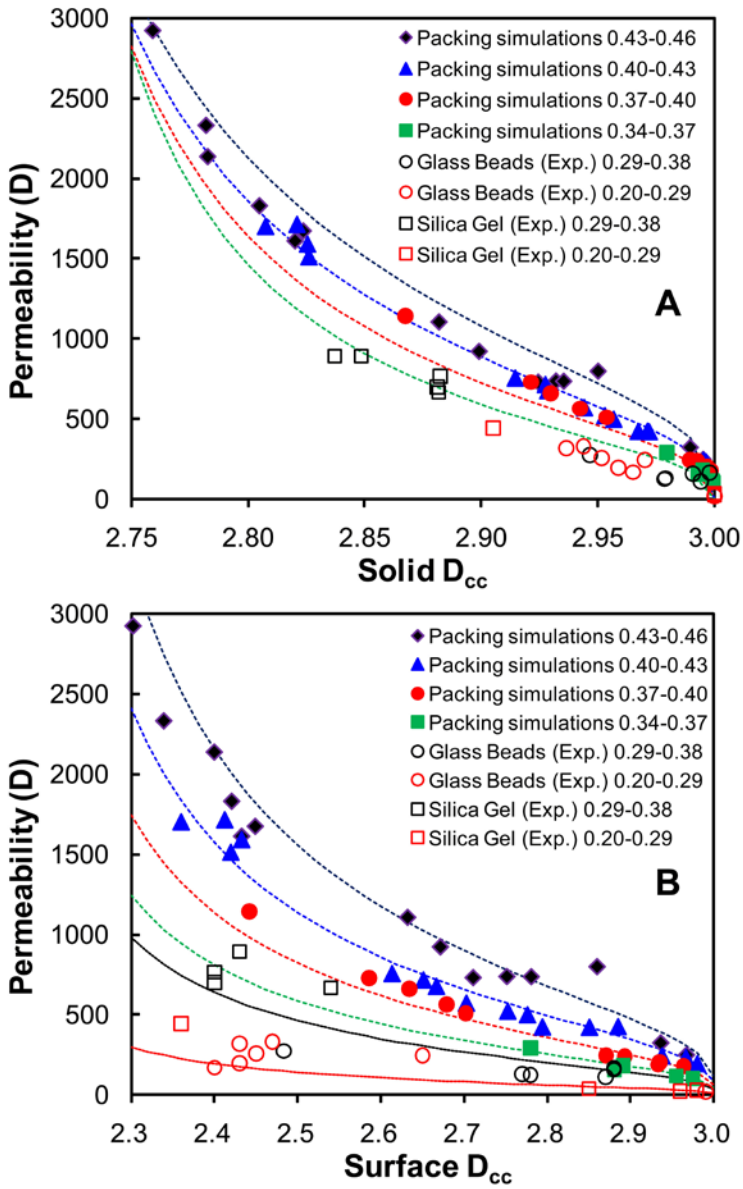

Figure 4-S12. (caption on next page)

Figure 4-S12. Effect of cube counting fractal dimension of (A) solid mass and (B) surface (interface) of model sands on permeability. The equation for each curve is shown as equation (4.12) in the text (coefficients *a, b, c,* and *d* for D_{cc} of solid mass are described in equation (4.8), and those for D_{cc} of surface are 3, 2, 3.455, and 1.28, respectively). Black diamonds, blue triangles, red circles, and green squares correspond to each group of simulation data for the porosities of 0.43–0.46, 0.40–043, 0.37–0.40, and 0.34–0.37, respectively. Black and red open circles correspond to glass bead samples for the porosities of 0.29–0.38 and 0.20–029, respectively. Black and red open squares correspond to silica gel samples for the porosities of 0.29–0.38 and 0.20–0.29, respectively. Black, blue, red, and green dashed lines, and black and red dotted lines are curves for equation (4.12) corresponding to the median porosities in each group: 0.445, 0.415, 0.385, 0.355, 0.335, and 0.245.

4.S10. Effect of (porosity)^3/(specific surface area)^2 and (porosity)^3/[(specific surface area)^2(1-porosity^2)] on cube counting fractal dimension, configurational entropy, and entropy length.

Figures 4-S13–15 show the effects of (porosity)^3/(specific surface area)^2 obtained from the Kozeny equation (4.S1) and (porosity)^3/[(specific surface area)^2(1-porosity^2)] obtained from the Kozeny-Carman equation (4.11) on cube-counting fractal dimension (Figure 4-S13), configurational entropy (Figure 4-S14), and entropy length (Figure 4-S15). Cube-counting fractal dimension decreases with increasing (porosity)^3/(specific surface area)^2 and (porosity)^3/[(specific surface area)^2(1-porosity^2)], and increases with increasing porosity, as shown in Figures 4-6 and 4-7. Maximum configurational entropy increases with increasing (porosity)^3/(specific surface area)^2, (porosity)^3/[(specific surface area)^2(1-porosity^2)], and porosity as shown in Figure 4-14. Entropy length increases with increasing (porosity)^3/(specific surface area)^2 and (porosity)^3/[(specific surface area)^2(1-porosity^2)]. Thus, cube-counting fractal dimension, maximum configurational entropy, and entropy length can also be used to explain permeability.

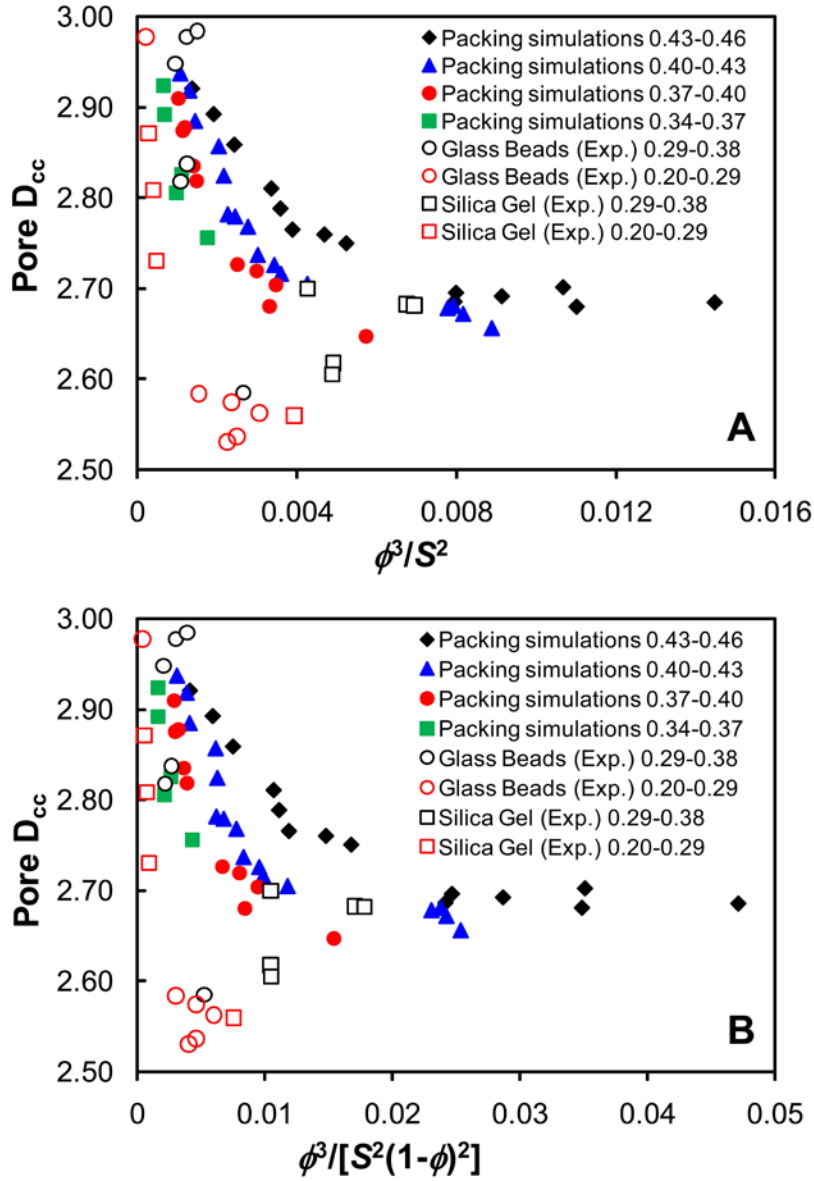

Figure 4-S13. (A) Relationship between cube-counting fractal dimension and (porosity)^3/(specific surface area)^2. (B) Relationship between cube-counting fractal dimension and (porosity)^3/[(specific surface area)^2(1-porosity^2)].

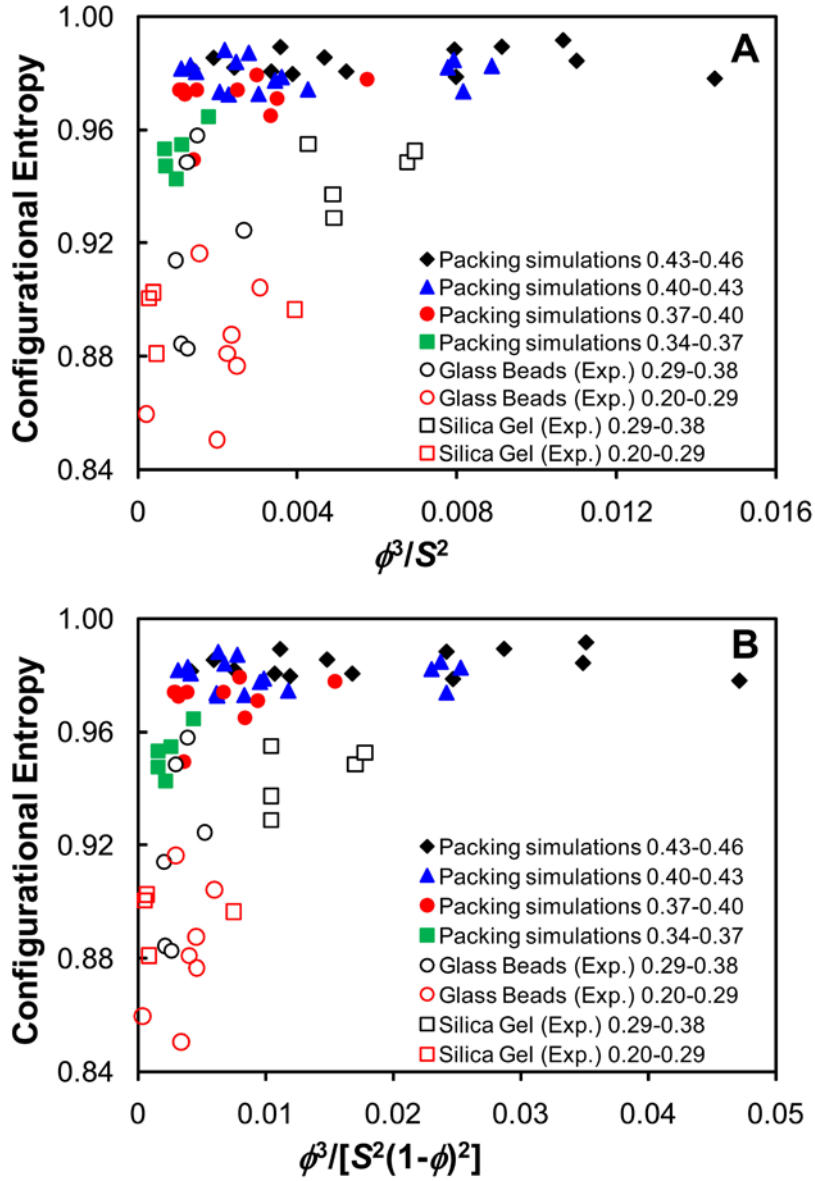

Figure 4-S14. (A) Relationship between maximum configurational entropy and (porosity)^3/(specific surface area)^2. (B) Relationship between maximum configurational entropy and (porosity)^3/[(specific surface area)^2(1-porosity^2)].

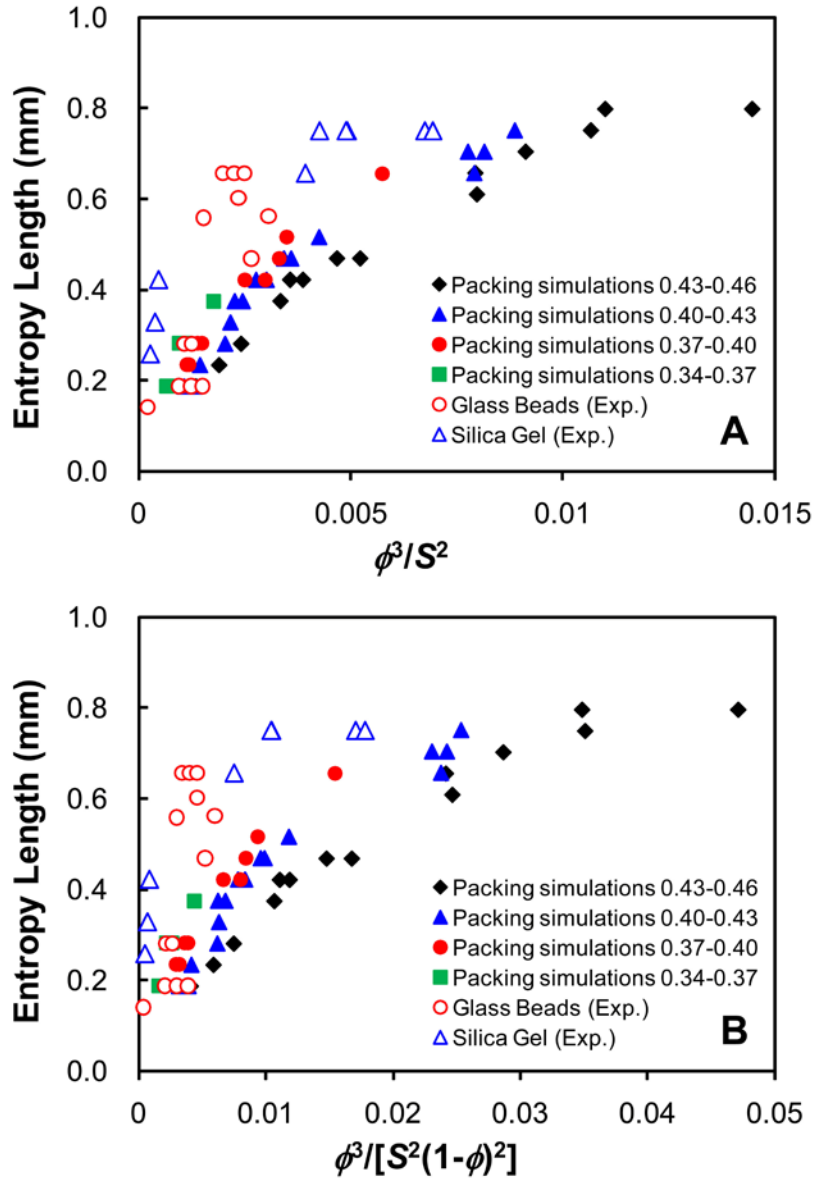

Figure 4-S15. (A) Relationship between entropy length and (porosity)^3/(specific surface area)^2. (B) Relationship between entropy length and (porosity)^3/[(specific surface area)^2(1-porosity^2)].

δ

4.S11. Structure-structure and structure-property relationships for the porous networks of model sands

Extensive analyses of all the structural parameters and permeability were performed to establish the structure-structure and structure-property relationships of porous networks of model sands. Structural parameters analyzed in this study include porosity (ϕ), average particle diameter (d_p), specific surface area (S), cube-counting fractal dimension (D_{cc}), lacunarity (Λ), entropy length (EL), and maximum configurational entropy (MCE). Table 4-S1 shows the figure numbers for the relationships between these parameters shown in this study.

Table 4-S1. Figure numbers for the relationships shown in this study.

	d_p	S	ϕ	ϕ^3/S^2	$\phi^3/S^2(1-\phi^2)$	D_{cc}
S	4-8B	-	4-8A	-	-	4-6, 7A, 7B
ϕ	4-S6	4-8A	-	-	-	4-7C
D_{cc}	4-8C	4-6, 7A, 7B	4-7C	4-S13A	4-S13B	-
$\Lambda_{0.047}$	4-S7A	-	4-11A			-
$\Lambda_{0.469}$	4-S7B	4-11B	-			-
EL	4-13A	4-13B	4-S8	4-S15A	4-S15B	-
MCE	4-S9A	4-S9B	4-14	4-S14A	4-S14B	-
Permeability	4-15A	4-15B	4-15C	4-S10	4-16	4-17

4.S12. Effect of the infiltrated silicone oil into the grain of silica gel on the NMR micro-imaging images

Figures 4-S16 shows the spin density image of silicone oil in the sample composed of silica gel and its binary image. Firure 4-S16A shows that the signal does not come from the infiltrated silicone oil into the grain of silica gel, probably because the amount of infiltrated silicone oil is much lower than that of saturated silicone oil outside the grains. Figure 4-S16B shows that data are not included in the grain of silica gel in binary image.

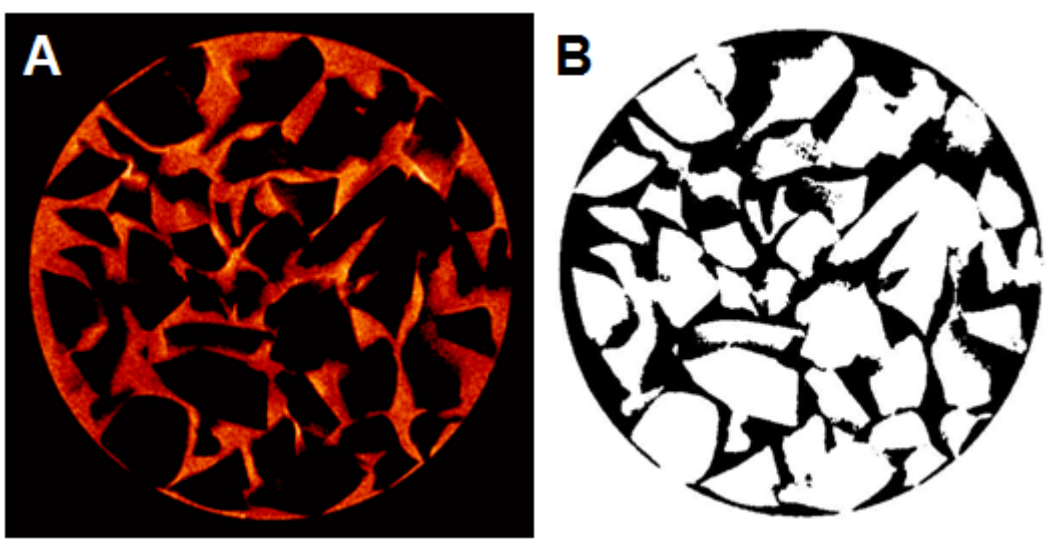

Figure 4-S16. (A) 2D spin density image of silicone oil in the sample composed of silica gel (SG1). (B) Binary image of (A) obtained from the threshold value.

4.S12. Maximum intensity projection images of 3D porous networks obtained by NMR micro-imaging

Figures 4-S17 shows maximum intensity projection images of 3D pore structure obtained by NMR micro-imaging. 3D binary image data of pore structures are obtained from these images using the threshold values.

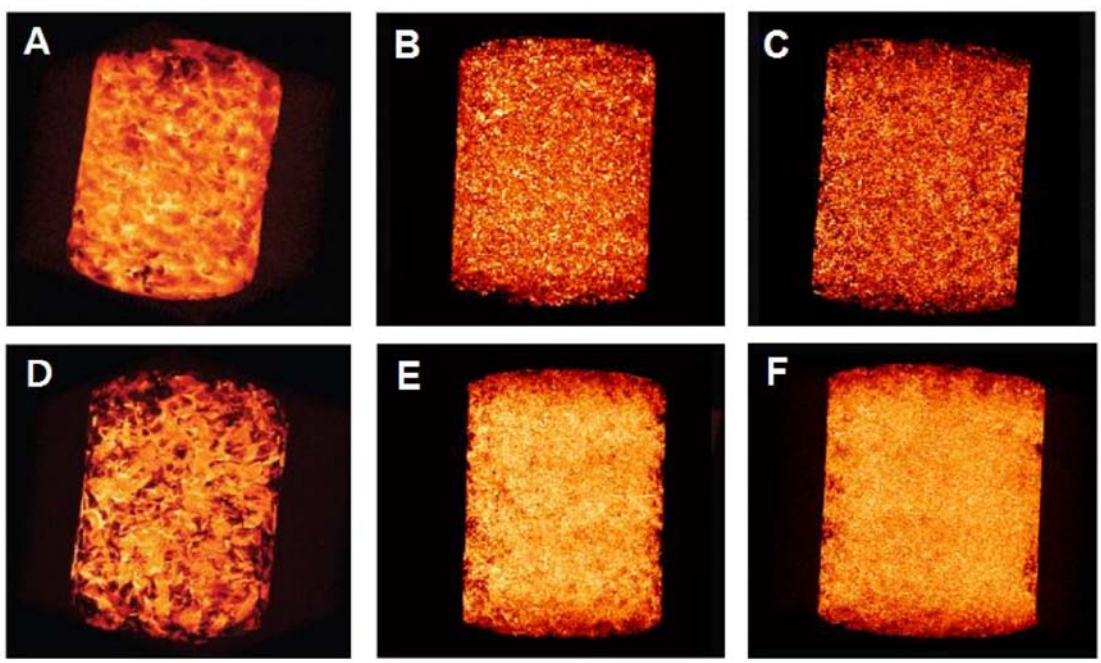

Figure 4-S17. Maximum intensity projection images of 3D pore structure obtained by NMR micro-imaging: (A) GB1, (B) GB2, (C) GB3, (D) SG1, (E) SG2, and (F) SG3.

References

Adam, G. and Gibbs, J. H. (1965) On the temperature dependence of cooperative relaxation properties in glass-forming liquids. J. Chem. Phys., 43, 139-146.

Allain, C. and Cloitre, M. (1991) Characterizing the lacunarity of random and deterministic fractal sets. Physical Review A, 44(6), 3552-3558.

Andraud, C., Beghdadi, A., Haslund, E., Hilfer, R., Lafait, J. and Virgin, B. (1997) Local entropy characterization of correlated random microstructures. Physica A, 235, 307-318.

Andraud, C., Beghdadi, A. and Lafait, J. (1994) Entropic analysis of random morphologies. Physica A, 207, 208-212.

Armatas, G. S., Kolonia, K. M. and Pomonis, P. J. (2002) Morphometry of porous solids: lacunarity, fractal dimensions, connectivity, and some topological similarities with neurons. Lanmuir, 18, 10421-10429.

Avnir, D., Farin, D. and Pfeifer, P. (1985) Surface geometric irregularity of particulate materials: The fractal approach. Journal of Colloid and Interface Science, 103, 112-123.

Balcom, B. J., Barrita, J. C., Choi, C., Beyea, S. D., Goodyear, D. J. and Bremner, T. W. (2003) Single-point magnetic resonance imaging (MRI) of cement based materials. Materials and Structures, 36(257), 166-182.

Bartoli, F., Bird, N. R. A., Gomendy, V., Vivier, H. and Niquet, S. (1999) The relation between silty soil structures and their mercury porosimetry curve counterparts: fractals and percolation. European Journal of Soil Science, 50, 9-22.

Bear, J. (1972) Dynamics of Fluids in Porous Media. New York, American Elsevier, 764 p.

Bird, N., Díaz, M. C., Saa, A. and Tarquis, A. M. (2006) Fractal and multifractal analysis of pore-scale images of soil. Journal of Hydrology, 322, 211-219.

Blümich, B. (2000) NMR Imaging of Materials. Oxford, Clarendon Press, 541 p.

Bourbié, T., Coussy, O. and Zinszner, B. (1987) Acoustics of Porous Media. Paris, Editions Technip, 334 p.

Buczkowski, S., Kyriacos, S., Nekka, F. and Cartilier, L. (1998) The modified box-counting method: Analysis of some characteristic parameters. Pattern Recognition, 31(4), 411-418.

Callaghan, P. T. (1991) Principles of Nuclear Magnetic Resonance Microscopy. Oxford, Clarendon Press, 492 p.

Carman, P. G. (1937) Fluid flow through granular beds. Transactions, Institution of Chemical Engineers (London), 15, 150-166.

Chen, S. and Doolen, G. D. (1998) Lattice Boltzmann method for fluid flows. Annual Reviews in Fluid Mechanics, 30, 329-364.

Chun, H. C., Giménez, D. and Yoon, S. W. (2008) Morphology, lacunarity and entropy of intra-aggregate pores: Aggregate size and soil management effects. Geoderma, 146, 83-93.

Ciccotti, M. and Mulargia, F. (2002) Pernicious effect of physical cutoffs in fractal analysis. Physical Review E, 65, 037201.

Coelho, D., Thovert, J. F. and Adler, P. M. (1997) Geometrical and transport properties of random packings of spheres and aspherical particles. Physical Review E, 55(2), 1959-1978.

Costa, A. (2006) Permeability-porosity relationship: A reexamination of the

Kozeny-Carman equation based on a fractal pore-space geometry assumption. Geophysical Research Letters, 33, L02318.

Crawford, J. W. and Matsui, N. (1996) Heterogeneity of the pore and solid volume of soil: distinguishing a fractal space from its non-fractal complement. Geoderma, 73, 183-195.

Dathe, A., Tarquis, A. M. and Perrier, E. (2006) Multifractal analysis of the pore- and solid-phases in binary two-dimensional images of natural porous structures. Geoderma, 134, 318-326.

Dathe, A. and Thullner, M. (2005) The relationship between fractal properties of solid matrix and pore space in porous media. Geoderma, 129, 279-290.

Davies, S., Hardwick, A., Robert, D., Spowage, K. and Packer, K. J. (1994) Quantification of oil and water in preserved reservoir rock by NMR spectroscopy and imaging. Magnetic Resonance Imaging, 12, 349-353.

de Marsily, G. (1986) Quantitative Hydrogeology. Orlando, Academic Press, Inc.

Dereppe, J. M., Moreaux, C. and Schenker, K. (1991) Chemical shift imaging of fluid filled porous rocks. Magnetic Resonance Imaging, 9, 809-813.

Doughty, D. A. and Tomutsa, L. (1996) Multinuclear NMR microscopy of two-phase fluid systems in porous rock. Magnetic Resonance Imaging, 14(7-8), 869-873.

Dullien, F. A. L. (1979) Porous Media: Fluid Transport and Pore Structure. London, Academic Press, 396 p.

Farmer, J. D., Ott, E. and York, J. A. (1983) The dimension of chaotic attractors. Physica D, 7, 153-180.

Faure, P., Care, S., Po, C. and Rodts, S. (2005) An MRI-SPI and NMR

relaxation study of drying-hydration coupling effect on microstructure of cement-based materials at early age. Magnetic Resonance Imaging, 23(2), 311-314.

Foroutan-pour, K., Dutilleul, P. and Smith, D. L. (1999) Advances in the implementation of the box-counting method of fractal dimension estimation. Applied Mathematics and Computation, 105, 195-210.

Garcia, X., Akanji, L. T., Blunt, M. J., Matthai, S. K. and Latham, J. P. (2009) Numerical study of the effects of particle shape and polydispersity on permeability. Physical Review E, 80, 021304.

Gefen, Y., Meir, Y., Mandelbrot, B. B. and Aharony, A. (1983) Geometric implementation of hypercubic lattices with noninteger dimensionality by use of low lacunarity fractal lattices. Physical Review Letters, 50(3), 145-148.

Ghilardi, P., Kai, A. K. and Menduni, G. (1993) Self-similar heterogeneity in granular porous media at the representative elementary volume scale. Water Resources Research, 29(4), 1205-1214.

Giménez, D., Allmaras, R. R., Nater, E. A. and Huggins, D. R. (1997) Fractal dimensions for volume and surface of interaggregate pores - scale effects. Geoderma, 77, 19-38.

Giménez, D., Perfect, E., Rawls, W. J. and Pachepsky, Y. (1997) Fractal models for predicting soil hydraulic properties: a review. Engineering Geology, 48, 161-183.

Gladden, L. F. (2003) Recent advances in MRI studies of chemical reactors: ultrafast imaging of multiphase flows. Topics in Catalysis, 24(1-4), 19-28.

Gladden, L. F., Buckley, C., Chow, P. S., Davidson, J. F., Mantle, M. D. and Sederman, A. J. (2004) 'Looking into' chemical products and

processes. Current Applied Physics, 4(2-4), 93-97.

Gladden, L. F., Hollewand, M. P. and Alexander, P. (1995) Characterization of structural inhomogeneities in porous-media. AIChE Journal, 41(4), 894-906.

Grau, J., Mendez, V., Tarquis, A. M., Diaz, M. C. and Saa, A. (2006) Comparison of gliding box and box-counting methods in soil image analysis. Geoderma, 134, 349-359.

Gussoni, A., Greco, F., Bonazzi, F., Vezzoli, A., Botta, D., Dotelli, G., Sora, I. N., Pelosato, R. and Zetta, L. (2004) H-1 NMR spin-spin relaxation and imaging in porous systems: an application to the morphological study of white Portland cement during hydration in the presence of organics. Magnetic Resonance Imaging, 22(6), 877-889.

Hamburger, D., Biham, O. and Avnir, D. (1996) Apparent fractality emerging from models of random distributions. Physical Review E, 53(4), 3342-3358.

Hansen, J. P. and Skjeltorp, A. T. (1988) Fractal pore space and rock permeability implications. Physical Review B, 38(4), 2635-2638.

Hentschel, H. G. E. and Procaccia, I. (1983) The infinite number of generalized dimensions of fractals and strange attractors. Physica D, 8(3), 435-444.

Jacquin, C. G. and Adler, P. M. (1987) Fractal porous media II: geometry of porous geological structures. Transport in Porous Media, 2, 571-596.

Jia, X. and Williams, R. A. (2001) A packing algorithm for particles of arbitrary shapes. Powder Technology, 120, 175-186.

Keehm, Y. (2003) Computational Rock Physics: Transport Properties in Porous Media and Applications. Geophysics, Stanford University, Doctor of Philosophy, 135 p.

δ

Keehm, Y., Mukerji, T. and Nur, A. (2004) Permeability prediction from thin sections: 3D reconstruction and Lattice-Boltzmann flow simulation. Geophysical Research Letters, 31(4), L04606.

Kim, J.-W., Perfect, E. and Choi, H. (2007) Anomalous diffusion in two-dimensional Euclidean and prefractal geometrical models of heterogeneous porous media. Water Resources Research, 43, W01405.

Kleinberg, R. L. (2001) NMR well logging at Schlumberger. Concepts in Magnetic Resonance, 13(6), 396-403.

Klemm, A., Kimmich, R. and Weber, M. (2001) Flow through percolation clusters: NMR velocity mapping and numerical simulation study. Physical Review E, 63(4), 041514.

Klemm, A., Müller, H.-P. and Kimmich, R. (1997) NMR microscopy of pore-space backbones in rock, sponge, and sand in comparison with random percolation model objects. Physical Review E, 55(4), 4413-4422.

Kossel, E. and Kimmich, R. (2005) Flow measurements below 50 μm: NMR microscopy experiments in lithographic model pore spaces. Magnetic Resonance Imaging, 23(2), 397-400.

Lee, S. K. (2005) Microscopic origins of macroscopic properties of silicate melts and glasses at ambient and high pressure: Implications for melt generation and dynamics. Geochimica et Cosmochimica Acta, 69(14), 3695-3710.

Lee, S. K., Kim, H. N., Lee, B. H., Kim, H. I. and Kim, E. J. (2010) Nature of chemical and topological disorder in borogermanate glasses: insights from B-11 and O-17 solid-state NMR and quantum chemical calculations. Journal of Physical Chemistry B, 114, 412-420.

Lee, S. K. and Stebbins, J. F. (1999) The degree of aluminum avoidance in aluminosilicate glasses. American Mineralogist, 84, 937-945.

Li, X., Zhong, L. and Pyrak-Nolte, L. J. (2001) Physics of partially saturated porous media: residual saturation and seismic-wave propagation. Annual Review of Earth and Planetary Sciences, 29, 419-460.

Lindquist, W. B., Lee, S. M., Coker, D. A., Jones, K. W. and Spanne, P. (1996) Medial axis analysis in three-dimensional tomographic images of porous media. Journal of Geophysical Research, 101, 8297-8310.

Lysova, A. A., Koptyug, I. V., Sagdeev, R. Z., Parmon, V. N., Bergwerff, J. A. and Weckhuysen, B. M. (2005) Noninvasive in situ vsualization of supported catalyst preparations using multinuclear magnetic resonance imaging. Journal of American Chemical Society, 127, 11916-11917.

Müller, H.-P., Weis, J. and Kimmich, R. (1995) Computer simulation and six-dimensional spin density and velocity NMR microimaging of lacunar systems: A comparative analysis of percolation properties. Physical Review E, 52(5), 5195-5204.

Mandelbrot, B. B. (1982) The Fractal Geometry of Nature. New York, Freeman, 468 p.

Manz, B., Gladden, L. F. and Warren, P. B. (1999) Flow and dispersion in porous media: Lattice-Boltzmann and NMR studies. AIChE Journal, 45(9), 1845-1854.

Maria, A. and Carey, S. (2002) Using fractal analysis to quantitatively characterize the shapes of volcanic particles. Journal of Geophysical Research, 107(B11), 2283.

McNamara, G. R. and Zanetti, G. (1988) Use of the Boltzmann equation to simulate lattice-gas automata. Physical Review Letters, 61(20), 2332-

2335.

Moreau, E., Velde, B. and Terribile, F. (1999) Comparison of 2D and 3D images of fractures in a Vertisol. Geoderma, 92, 55-72.

Muller, J. (1996) Characterization of pore space in chalk by multifractal analysis. Journal of Hydrology, 187, 215-222.

Muller, J., Huseby, O. K. and Saucier, A. (1995) Influence of multifractal scaling of pore geometry on permeabilities of sedimentary rocks. Chaos, Solitons and Fractals, 5(8), 1485-1492.

Muller, J. and McCauley, J. L. (1992) Implication of fractal geometry for fluid flow properties of sedimentary rocks. Transport in Porous Media, 8, 133-147.

Nesse, W. D. (2000) Introduction to Mineralogy. Oxford, Oxford University Press, 442 p.

Pendleton, D. E., Dathe, A. and Baveye, P. (2005) Influence of image resolution and evaluation algorithm on estimates of the lacunarity of porous media. Physical Review E, 72, 041306.

Perret, J. S., Prasher, S. O. and Kacimov, A. R. (2003) Mass fractal dimension of soil macropores using computed tomography: from the box-counting to the cube-counting algorithm. European Journal of Soil Science, 54, 569-579.

Plotnick, R. E., Gardner, R. H., Hargrove, W. W., Prestegaard, K. and Perlmutter, M. (1996) Lacunarity analysis: A general technique for the analysis of spatial patterns. Physical Review E, 53(5), 5461-5468.

Plotnick, R. E., Gardner, R. H. and O'Neill, R. V. (1993) Lacunarity indices as measures of landscape texture. Landscape Ecology, 8(3), 201-211.

Posadas, A. N. D., Giménez, D., Bittelli, M., Vaz, C. M. P. and Flury, M. (2001) Multifractal characterization of soil particle-size distributions.

Soil Science Society of America Journal, 65, 1361-1367.

Posadas, A. N. D., Giménez, D., Quiroz, R. and Protz, R. (2003) Multifractal characterization of soil pore systems. Soil Science Society of America Journal, 67, 1361-1369.

Pride, S. R. and Masson, Y. J. (2006) Acoustic attenuation in self-affine porous structures. Physical Review Letters, 97, 184301.

Rasband, W. S. (1997-2009) ImageJ. Bethesda, Maryland, USA, National Institutes of Health.

Richet, P. (1984) Viscosity and configurational entropy of silicate melts. Geochimica et Cosmochimica Acta, 48, 471-483.

Sahimi, M. (1993) Flow phenomena in rocks: from continuum models to fractals, percolation, cellular automata, and simulated annealing. Reviews of Modern Physics, 65(4), 1393-1534.

Saucier, A. and Muller, J. (1999) Textural analysis of disordered materials with multifractals. Physica A, 267, 221-238.

Schwartz, L. M. and Banavar, J. R. (1989) Transport properties of disordered continuum systems. Physical Review B, 39(16), 11965-11970.

Sederman, A. J., Alexander, P. and Gladden, L. F. (2001) Structure of packed beds probed by magnetic resonance imaging. Powder Technology, 117(3), 255-269.

Sederman, A. J., Johns, M. L., Bramley, A. S., Alexander, P. and Gladden, L. F. (1997) Magnetic resonance imaging of liquid flow and pore structure within packed beds. Chemical Engineering Science, 52(14), 2239-2250.

Song, S.-R., Jones, K. W., Lindquist, W. B., Dowd, B. A. and Sahagian, D. L. (2001) Synchrotron X-ray computed microtomography: studies on

vesiculated basaltic rocks. 63, 252-263.

Song, Y.-Q., Cho, H., Hopper, T., Pomerantz, A. E. and Sun, P. Z. (2008) Magnetic resonance in porous media: Recent progress. Journal of Chemical Physics, 128, 052212.

Stallmach, F., Vogt, C., Kärgar, J., Helbig, K. and Jacobs, F. (2002) Fractal geometry of surface areas of sand grains probed by pulsed field gradient NMR. Physical Review Letters, 88(10), 105505.

Takei, Y. (1998) Constitutive mechanical relations of solid-liquid composites in terms of grain-boundary contiguity. Journal of Geophysical Research, 103(B8), 18183-18203.

Takei, Y. (2002) Effect of pore geometry on V_P/V_S: From equilibrium geometry to crack Journal of Geophysical Research-Solid Earth, 107(B2), 2043.

Takei, Y. (2005) Deformation-induced grain boundary wetting and its effects on the acoustic and rheological properties of partially molten rock analogue. Journal of Geophysical Research-Solid Earth, 110, B12203.

Takei, Y. and Holtzman, B. K. (2009) Viscous constitutive relations of solid-liquid composites in terms of grain boundary contiguity: 1. Grain boundary diffusion control model. Journal of Geophysical Research, 114, B06205.

Tang, D. and Maragoni, A. G. (2008) Fractal dimensions of simulated and real fat crystal networks in 3D space. Journal of the American Oil Chemists' Society, 85, 495-499.

Tarquis, A. M., Heck, R. J., Andina, D., Alvarez, A. and Anton, J. M. (2009) Pore network complexity and thresholding of 3D soil images. Ecological Complexity, 6, 230-239.

Tarquis, A. M., Heck, R. J., Grau, J. B., Fabregat, J., Sanchez, M. E. and Anton, J. M. (2008) Influence of thresholding in mass and entropy dimension of 3-D soil images. Nonlinear Processes in Geophysics, 15, 881-891.

Tarquis, A. M., McInnes, K. J., Key, J. R., Saa, A., Garcia, M. R. and Diaz, M. C. (2006) Multiscaling analysis in a structured clay soil using 2D images. Journal of Hydrology, 322, 236-246.

Thompson, A. H. (1991) Fractals in rock physics. Annual Reviews in Earth and Planetary Sciences, 19, 237-262.

Xu, Y. F. and Dong, P. (2004) Fractal approach to hydraulic properties in unsaturated porous media. Chaos, Solitons and Fractals, 19, 327-337.

Xu, Y. F. and Sun, D. A. (2005) Correlation of surface fractal dimension with frictional angle at critical state of sands. Géotechnique, 55(9), 691-695.

Yu, B. and Cheng, P. (2002) A fractal permeability model for bi-dispersed porous media. International Journal of Heat and Mass Transfer, 45, 2983-2993.

Yu, B. and Liu, W. (2004) Fractal analysis of permeabilities for porous media. AIChE Journal, 50, 46-57.

δ

Chapter 5. Probing of water distribution in porous model sands with immiscible fluids: Nuclear magnetic resonance micro-imaging study

Abstract

NMR micro-imaging was used to obtain high-resolution (up to about 50 μm) images of the distribution of water injected for varying durations into porous media initially saturated with silicone oil, and thereby investigated the effect of the particle size and shape of the porous media on the distribution of water. The obtained 2D NMR chemical shift images can distinguish hydrogens in water and silicone oil and thus distinguish both phases with flow duration. The variations in volume fraction, specific surface area, and the cube counting fractal dimension of the water phase in each sample obtained from 3D spin echo images with increasing duration of water injection are well fitted with the single-exponential recovery functions. The asymptotic values for glass bead samples were much larger than those for silica gel samples. This is mostly due to the intrinsic differences in the porous networks and local arrangement of pore size distribution and connectivity of the two samples. In addition, this is partly because the interaction between silica gel and silicone oil is stronger than that between glass beads and silicone oil and the fact that silica gel has large mesoporosity whereas glass beads have no mesoporosity. The convergence rates of all the properties are inversely proportional to the permeability, indicating that the convergence rates are

correlated with the transport property of the porous media. The current results show that the types of particles consisting of porous networks play an important role in determining the water distribution in porous media that are initially saturated with an immiscible fluid.

5.1. Introduction

Understanding the nature of interstitial fluid flow through porous media containing an immiscible liquid is important in the development of methods for enhanced oil recovery (Taber, 1980) and underground disposal of CO_2 (Bachu, 2000). Probing of the distribution of two immiscible fluid phases in natural porous media can also provide improved understanding of the physical properties of complex soil systems and melt–fluids–rock composites in the Earth's interior. Despite its importance and implications, the effect of structural heterogeneity in the porous networks, such as particle size and shape on the water distribution in porous media initially saturated with the immiscible fluid with increasing duration of water injection and the effect of the rate of fluid saturation (the convergence rate, hereafter) in the relationship between oil recovery and time (Aronofsky et al., 1958) on the macroscopic properties of the porous media have not been systematically studied, mostly due to the lack of suitable experimental probes. The objective of this study is to obtain high resolution images of water distribution in porous media initially saturated with immiscible fluids using NMR micro-imaging, to quantify the water distribution with varying duration of water injection, and to explore the relationships

δ

between the convergence rates for the structural parameters and transport properties of porous networks.

NMR micro-imaging is one of the effective non-destructive experimental probes for the fluid distribution in networks, allowing detailed characterization of the connectivity of fluids (see Lee and Lee (submitted) and references therein). The NMR micro-imaging technique can be particularly useful in distinguishing fluid phases non-destructively because the differences in NMR chemical shifts between the molecular units in different fluids can be separately probed (Brown et al., 1982; Callaghan, 1991; Blümich, 2000). X-ray computed tomography (CT) has also been used for non-destructive pore-scale characterization of two fluid phases in porous media (e.g., Peters and Hardham, 1990; Wildenscheld et al., 2002; Culligan et al., 2006; Sukop et al., 2008) . Since x-ray CT affords high-resolution images, typically in the range of 1–10 μm, it has been used recently to quantitatively characterize the morphology of individual fluid bodies and determine the blob-size distribution (e.g., Al-Raoush and Willson, 2005; Schnaar and Brusseau, 2005; Prodanovic et al., 2006). Previous studies on two-phase flow using NMR micro-imaging include mapping of the oil phase in porous media initially saturated with water (Chen et al., 1988), monitoring the dissolution of hydrocarbon ganglia in beds comprised of ballotini saturated with water (Johns and Gladden, 2000), imaging of ^{19}F in a NAPL flow through water-saturated columns packed with angular silica gel (Zhang et al., 2002), observing the flow of dense and light NAPLs through a water saturated dolomite fracture (Becker et al.,

δ

2003), imaging of NAPL during vapor extraction in columns packed with silica gel (Chu et al., 2004), and imaging of the distribution of water (^{1}H) and model contaminants (^{19}F) in soil columns (Simpson et al., 2007). Furthermore, detailed mapping of the velocity distributions of two distinct fluid phases can be achieved using NMR micro-imaging (e.g., Okamoto et al., 2001; Sankey et al., 2009). However, these advances and developments in NMR micro-imaging are rather focused on networks with relatively large particle diameters and so may not have direct geological implications. Furthermore, despite many x-ray CT and NMR imaging studies for two phase flow in porous media, the systematic study for the effect of structural heterogeneity on the water distribution in porous media containing the immiscible fluids with varying the duration time of water flow and the effect of the convergence rates of the structural parameters for the networks of water distribution on the macroscopic properties of the porous media is lacking.

It is thus of crucial importance to explore the distribution of two fluid phases in porous media using NMR micro-imaging with a resolution of <100 μm. This would allow us to characterize the distribution of multi-phase fluids in porous networks corresponding to natural aquifers, sediments, and sandstones. It is attempted to obtain images of two fluid phases using the chemical shift imaging (CSI) method for 2D cross section images and the spin echo method with spoiler gradients for 3D images with a resolution below 100 μm. Combined with recent advances in high-resolution NMR micro-imaging, the water distribution in various porous

δ

media initially saturated with silicone oil can be explored with varying duration of water injection. Direct visualization of time-resolved water distribution in the model networks can thus yield insights into the relationship among porous networks, fluid distributions, and transport properties.

As the local structure of amorphous network in an atomic scale has strong implication for the macroscopic properties (e.g. Lee et al., 2008; Lee et al., 2010; Lee et al., 2010), similar progress have been made for the relationships between local structures of porous networks in a μm scale and the corresponding macroscopic properties. Diverse porous networks obtained by NMR micro-imaging and random packing simulations have been parameterized into cube counting fractal dimension and configurational entropy as a function of porosity and specific surface area (Lee and Lee, submitted). On the basis of this previous study, the distribution water into the pore network initially saturated with silicone oil with varying injection duration can be explored by quantitatively tracing the variation of the fractal dimension, specific surface area, and potentially configurational entropy.

In this study, convergence rates of these parameters with increasing the duration of water flow were obtained. Convergence rate was interpreted or used in many ways in previous studies, for example, to correlate with the imbibition parameters (Kazemi et al., 1992; Babadagli, 2002), to replace the viscosity term by the geometric mean of oil and water viscosities (Cil et al., 1998), and to propose an analytical model considering

δ

the matrix imbibition parameters and the fracture flow properties separately (Reis and Haq, 1999). However, the relationship between convergence rate and structural or transport properties of porous media has not been reported.

Here, 3D images were obtained by NMR micro-imaging with resolution below100 μm to explore the effect of particle size, and shape, and types of particles on the distribution of water injected for varying durations into porous media filled with silicone oil. Then, the networks of the water distribution were quantified by volume, specific surface, area, cube counting fractal dimension, and configurational entropy, and the relationships between the convergence rates of the parameters and the transport properties of the porous media were investigated.

d

5.2. Methods

Glass beads (GBs) and crushed silica gel (SG) particles with spherical and irregularly shaped grains, respectively, were used for investigating the effect of particle shape, heterogeneity, and diameter on the distribution of water in the porous media once they were initially saturated with silicone oil. The GB (Sigma, acid-washed) particle sizes (diameters) used in this study were 0.71–1.18 mm (GB1) and 0.21–0.30 mm (GB3). Those of the SG particles (Sigma-Aldrich) were 0.86–1.30 mm (SG1) and 0.25–0.60 mm (SG3). The diameter and length of the column containing the samples were 10 mm and 24 mm, respectively. The weights of the samples in the column were 2.78 g (GB1), 3.05 g (GB3), 1.47 g (SG1), and 1.30 g (SG3).

The column was saturated with silicone oil (polydimethylsiloxane, Baysilone M30000; density of 0.98 g/cm^3 and viscosity of 30000 mPa·s). A vacuum pump was used to saturate the pore space with silicone oil and to eliminate air bubbles. Both ends of the column were then covered with Teflon and membrane filters, and connected to a peristaltic pump. Distilled water with 0.1 wt% $CuSO_4 \cdot 5H_2O$, a paramagnetic impurity, was injected into the pre-saturated column at a pressure of 2 bar for each sample. Both ends were sealed with parafilms after water injection for the following durations: 10, 40, and 100 minutes (for GB1); 10, 30, and 195 minutes (for GB3); 75 and 195 minutes (for SG1); and 10, 40, and 195 minutes (for SG3). Each sample was loaded on the imaging probe for the micro-imaging experiment (see supplementary information for further details).

δ

The NMR micro-imaging experiments were performed using a Bruker Avance 400 NMR spectrometer with a 9.4-T, superconducting, vertical, and wide-bore magnet. A Micro2.5 probe head providing a gradient strength of 2.5 G cm^{-1} A^{-1} with a 25-mm NMR tube was used. 2D imaging of a specific fluid phase (i.e., silicon oil or water) was performed using a chemical shift selective (CHESS) imaging pulse sequence (Haase et al., 1985). The matrix size of the 2D cross section images was 256 × 256 and the field of view was 12 mm × 12 mm, resulting in a spatial resolution of 46.9 μm × 46.9 μm. The slice thickness was 0.4 mm. Images of three slices were collected. A frequency-selective excitation pulse with a Gaussian shape was used. The bandwidth and flip angle were 300 Hz and 90°, respectively. Imaging spoiler gradients with an amplitude of 30% and length of 1.0 ms were used in the x-, y-, and z- directions. The procedure leaves the spin system in a state where unwanted stimulated echoes are suppressed by spoiler gradients while the desired component remains entirely unaffected in the form of z-magnetization (Haase et al., 1985; Bernstein et al., 2004). The chemical shift for the imaging experiment was set to either water or silicone oil. The chemical shift difference between the two phases is 4.7 ppm (silicon oil is more shielded). 3D imaging for porous media saturated with silicone oil was performed with a 3D gradient echo (ge3D) imaging pulse sequence with a matrix size of the 3D images being 256 × 256 × 256. 3D imaging of the water distribution in the porous media initially saturated with silicone oil was performed with a spin echo 3D (se3D) imaging pulse sequence with image spoiler gradients with a 3D

d

image matrix size of 128 × 128 × 128. In 3D spectroscopic ^{1}H NMR imaging, a spin echo method was employed in which the 90° sinc-shaped excitation pulse is applied in the absence of magnetic field gradients for chemical shift selection (Rumpel and Pope, 1992). The field of view was 12 mm × 12 mm × 12 mm, thus the spatial resolution with a ge3D pulse sequence was 46.9 μm × 46.9 μm × 46.9 μm, and that with a se3D pulse sequence was 93.8 μm × 93.8 μm × 93.8 μm. For ge3D imaging, the sinc3-shaped pulse was used with an echo time of 1.781 ms and a repetition time of 1 s. For the se3D imaging, an excitation and a refocusing RF pulses were used with a rectangular shape and a pulse length of 0.128 ms. The echo time and repetition time were 4.145 ms and 1 s, respectively. Imaging spoiler gradients were used in all directions with an amplitude of 30% and length of 1.0 ms.

Volume, specific surface area, and cube counting fractal dimension were estimated for the water phase at each duration of water injection. The detailed method for estimating cube counting fractal dimension is described elsewhere (Lee and Lee, submitted). Briefly, to obtain D_{cc} from the 3D images for the water distribution, the fourfold expansion data of the original matrix were used, and D_{cc} analysis was conducted by covering the 3D water distribution data with increasing cube size (r) with the box sizes of the divisors of the matrix size to avoid border effects. Then, the number of cubes (N) required to cover the object completely was evaluated, and the slope of data points in the appropriate region for the estimation of the cube counting fractal dimension in the log (N)-log (r) plot was calculated.

δ

Permeability was estimated for 160 × 160 × 160 sub-volume data with the lattice Boltzmann method (LBM) using DigiFlow software (Structure Vision Ltd.). The D3Q18 scheme was applied in a 3D cubic lattice grid with each grid cell interacting with 18 (out of 26) of its closest neighbors (McNamara and Zanetti, 1988).

5.3. Results and Discussion

Figure 5-1 shows 2D binary images obtained by spin echo (first column) and chemical shift (second and third columns) pulse sequences. While water and silicone oil cannot be distinguished in the binary spin density images, the chemical shift images show that two immiscible fluid phases in porous media can be distinguished with a pixel resolution of ~50 μm. The sum of each phase in the CHESS images is slightly different from those of the spin density maps because each slice is 0.4 mm thick, thus water and silicone oil coexist in the 2D image of the same slice.

Figures 5-2 and 5-3 show 3D images of the distribution of water in the model sands consisting of GB and SG particles, respectively, with varying duration of water injection into the model porous networks. The results show that the water phase initially occupies the upper part of the column (note that water flows from the top to the bottom in the peristaltic pump) and that the total volume of the water phase apparently increases with increasing duration of water injection. The total volumes of water phase of GB1 and GB3 (Figure 5-2) are apparently larger than those of SG1 and SG3 (i.e., GB1 > SG1, GB3 > SG3), indicating the effect of particle shape

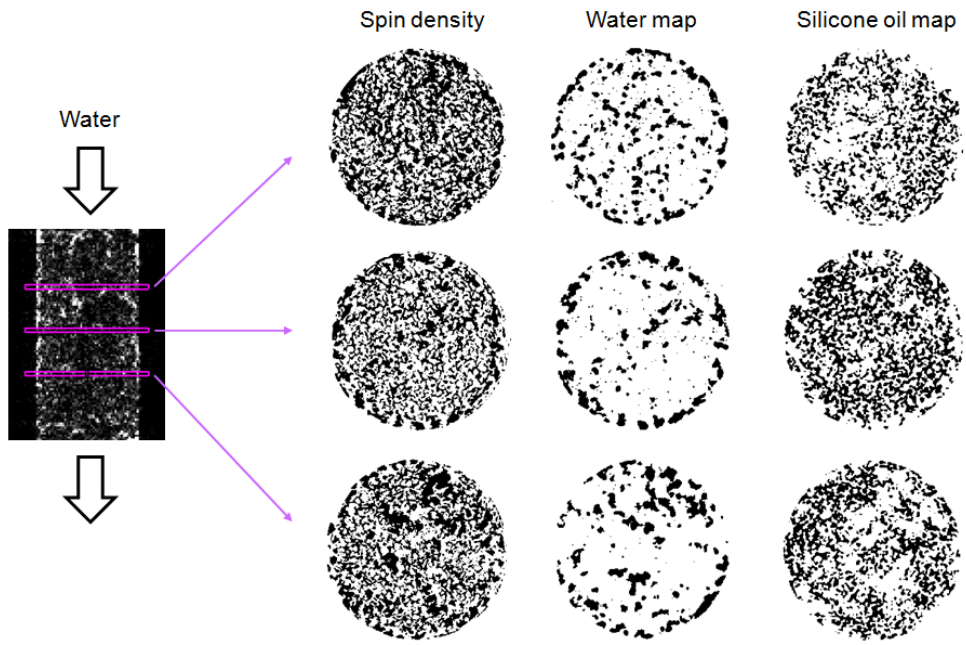

Figure 5-1. Binary 2D images for SG3 obtained at 40 minutes of duration of water injection. Each row corresponds to the same slice as depicted on the left. Each column corresponds to spin echo 2D images, chemical shift images for water phase, and chemical shift images for silicone oil phase, respectively.

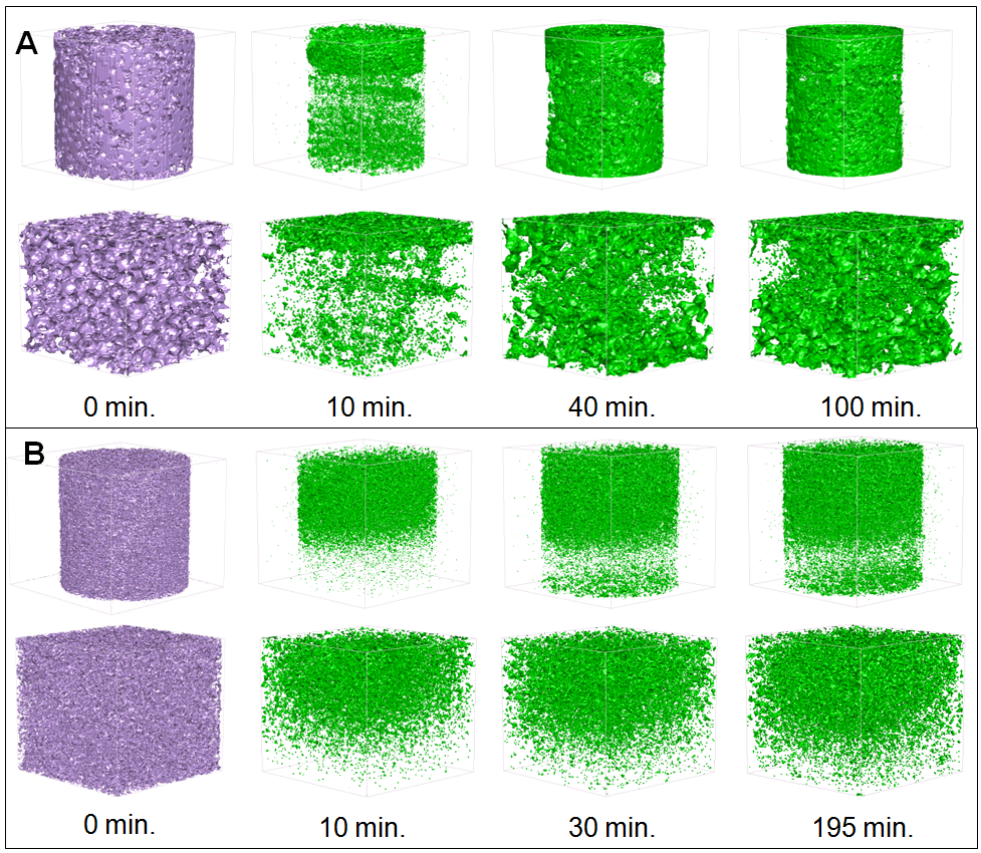

Figure 5-2. 3D binary images (A) for GB1 with varying duration of water injection: 0, 10, 40, and 100 minutes, and (B) for GB3 with varying duration of water injection: 0, 10, 30, and 195 minutes. In each image, above is the whole distribution of water, and below is the distribution in the cube where the data analysis was performed.

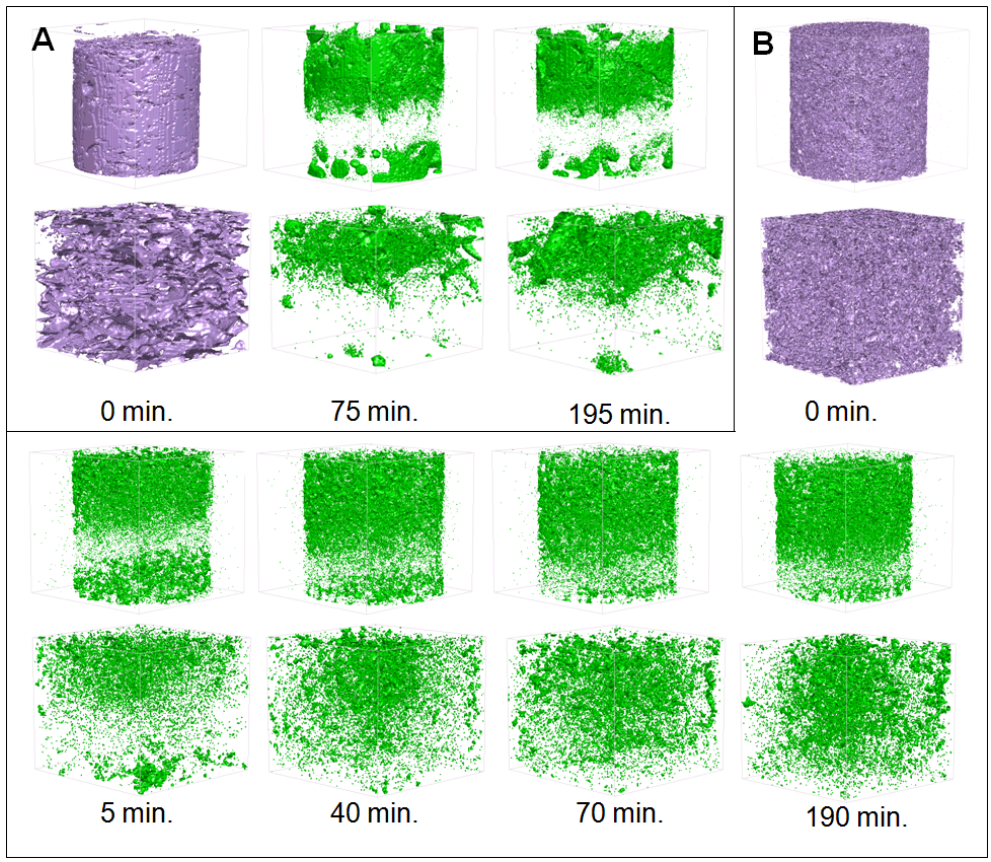

Figure 5-3. 3D binary images (A) for SG1 with varying duration of water injection: 0, 75 and 195 minutes, and (B) for SG3 with varying duration of water injection: 0, 5, 40, 70, and 190 minutes. In each image, above is the whole distribution of water, and below is the distribution in the cube where the data analysis was performed.

and porous networks on the degree of saturation in the model sands. Table 5-1 presents the porosity, specific surface area, and cube counting fractal dimension of each porous network saturated with silicon oil. Porous networks consisting of GB particles have lower specific surface area and cube counting fractal dimension than those of SG samples (i.e., GB1 < SG1, GB3 < SG3), indicating that porous networks of GB samples differ considerably from those of SG samples.

Figure 5-4 shows the volume fraction, specific surface area, and cube counting fractal dimension of water distribution in porous media with varying duration of water injection. Volumes of the water phase with increasing duration of water injection increased from 0 (0 minute) to 21.1 % (100 minutes, GB1), 8.5 % (195 minutes, GB3), 5.2 % (195 minutes, SG1), and 4.1 % (190 minutes, SG3), and the specific surface areas of water phase increased from 0 to 2.6 (100 minutes, GB1), 2.7 (195 minutes, GB3), 1.4 (195 minutes, SG1), and 1.5 mm^2/mm^3 (190 minutes, SG3). Note that the maximum volumes of water phase are smaller than the initial volumes of silicone oil for all samples because the remnant oil is entrapped in porous media.

The cube counting fractal dimension of the water phase with increasing duration of water injection increased from 0 (0 minute) to 2.49 (100 minutes, GB1), 2.57 (195 minutes, GB3), 1.96 (195 minutes, SG1), and 2.29 (195 min, SG3), respectively. The cube counting fractal dimension values of the SG samples are smaller than those of the GB samples due to the low volumes of water phase in the SG samples. The volume, specific

Table 5-1. Porosity, specific surface area, and cube counting fractal dimension of each sample before water flow.

	Porosity	Specific Surface Area (mm^2/mm^3)	Cube Counting Fractal Dimension
GB1	0.27	2.67	2.49
GB3	0.22	8.18	2.85
SG1	0.33	3.16	2.66
SG3	0.31	8.45	2.88

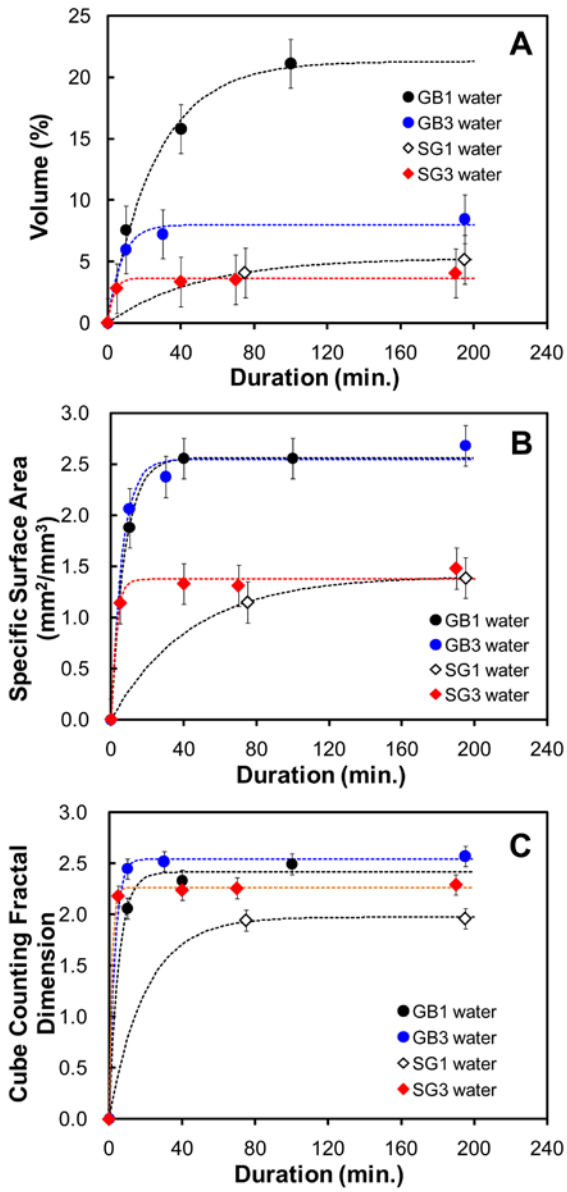

Figure 5-4. (A) Volume (%), (B) specific surface area (mm^2/mm^3), and (C) cube counting fractal dimension of water phase for all samples with varying duration of water injection.

δ

surface area, and cube counting fractal dimension increase rapidly, and then approach asymptotic values with increasing duration of water injection. These behaviors were fitted with the following single-exponential recovery function:

$$f(t) = a\left[1 - \exp(-\lambda t)\right] \qquad (5.1)$$

where *f(t)* is a recovered property of network such as volume (%), specific surface area (mm^2/mm^3), and cube counting fractal dimension, *a* is the asymptotic value of each property, *t* the duration of water injection (in minutes), and λ is a constant giving the rate of convergence. The trend of increasing volume fraction with increasing duration is similar to the empirical exponential recovery equation for predicting oil production in naturally-fractured reservoirs extracted by water (Aronofsky et al., 1958). Table 5-2 shows the fitting parameters for each property. The asymptotic values of volume and specific surface area for GB1 (21.1 % and 2.6 mm^2/mm^3, respectively) and GB3 (8.5 % and 2.7 mm^2/mm^3, respectively) are much larger than those for SG1 (5.2 % and 1.4 mm^2/mm^3, respectively) and SG3 (4.1 % and 1.5 mm^2/mm^3, respectively). The asymptotic values of cube counting fractal dimension for glass beads (2.49 for GB1 and 2.57 for GB3) are also larger than those for silica gel samples (1.96 for SG1 and 2.29 for SG3).

δ

Table 5-2. Fitting parameters and R^2 values for mono-exponential recovery equations for volume, specific surface area, and cube counting fractal dimension.

		a	λ	R^2
Volume (%)	GB1	21.28	0.038	0.99
	GB3	7.97	0.134	0.99
	SG1	5.28	0.020	1.00
	SG3	3.65	0.296	0.97
Specific Surface Area (mm^2/mm^3)	GB1	2.56	0.132	1.00
	GB3	2.55	0.162	0.99
	SG1	1.40	0.022	1.00
	SG3	1.37	0.355	0.99
Cube Counting Fractal Dimension	GB1	2.41	0.191	1.00
	GB3	2.54	0.328	1.00
	SG1	1.97	0.050	1.00
	SG3	2.26	0.665	1.00

δ

The manifested differences in the asymptotic values of volume, specific surface area, and cube counting fractal dimension are likely due to the differences in pore geometry and nature of particles in a 100 μm scale: porous networks of spherical grains (GB) and irregularly shaped grains (SG) have a moderate degree of clustering and a random distribution of pores, respectively, and the cube counting fractal dimension of pores for model sands composed of SG slightly increases with increasing specific surface area, whereas the cube counting fractal dimension for GBs increases rapidly and then increases gradually with increasing specific surface area (Lee and Lee, submitted). This could also be due to difference in nature of particles in a length scale less than 1μm: silica gel has larger mesoporosity while glass beads have no mesoporosity (Farrell et al., 1999). A mesopore is defined by pores that have a size of 20-500 Å on internal surfaces of solid grains (Huang et al., 1996). A previous experimental study of the adsorption-desorption of hydrophobic organic compounds from silica gels and glass beads showed that this difference of mesoporosity resulted in a larger amount of adsorbed trichloroethylene on silica gels than on glass beads (Farrell et al., 1999). This result indicates that the presence of mesopore leads to a stronger interaction between the surface of silica gel and fluids is likely to hamper the degree of saturation of porous network composed of silica gels. Note that mesopores do not appear on NMR micro-images because their size is smaller than the currently achievable resolution of the NMR micro-imaging. Finally note that the force balance of two immiscible fluids depends not only on the pore geometry, but also on the

δ

local fluid saturation (Keehm, 2003). Therefore, in order to investigate the exact origin of the observed distinct trends in water saturation, a visualization of the two phase flow with a higher resolution than that of the current study would be necessary.

The rates of convergence (λ in equation 5.1) of all properties for porous media composed of small grains (GB3 and SG3) are larger than those for large grains (GB1 and SG1). The rates of convergence of all the properties have the following order; from the largest to the smallest, SG3 > GB3 > GB1 > SG1. This indicates that the convergence rate exhibits the characteristics of the porous media: for small grains (GB3 and SG3), the convergence rate for silica gel is larger than that for glass beads whereas for large grains (GB1 and SG1), that for silica gel is smaller than that for glass beads

The relationships between convergence rates, parameters describing pore structures, and properties of porous media including configurational entropy and permeability were investigated. Figure 5-5 shows the relationship between the convergence rate of each property and permeability (k). The convergence rates (λ) of volume (%), specific surface area (mm^2/mm^3), and cube counting fractal dimension decrease with increasing permeability. The data were fitted with the following power law equation:

$$\lambda = pk^q + r \qquad (5.2)$$

where p, q, and r are the fitting parameters. Table 5-3 shows the fitting parameters for each relationship. The results show that the relationship

δ

Table 5-3. Fitting parameters and R^2 values for power law equations for the relationship between convergence rates and entropy length.

	p	q	r	R^2
λ-volume	0.74	-0.290	-0.096	0.67
λ-specific surface area	5.15	-0.013	-4.699	0.61
λ-cube counting fractal dimension	9.14	-0.014	-8.254	0.69

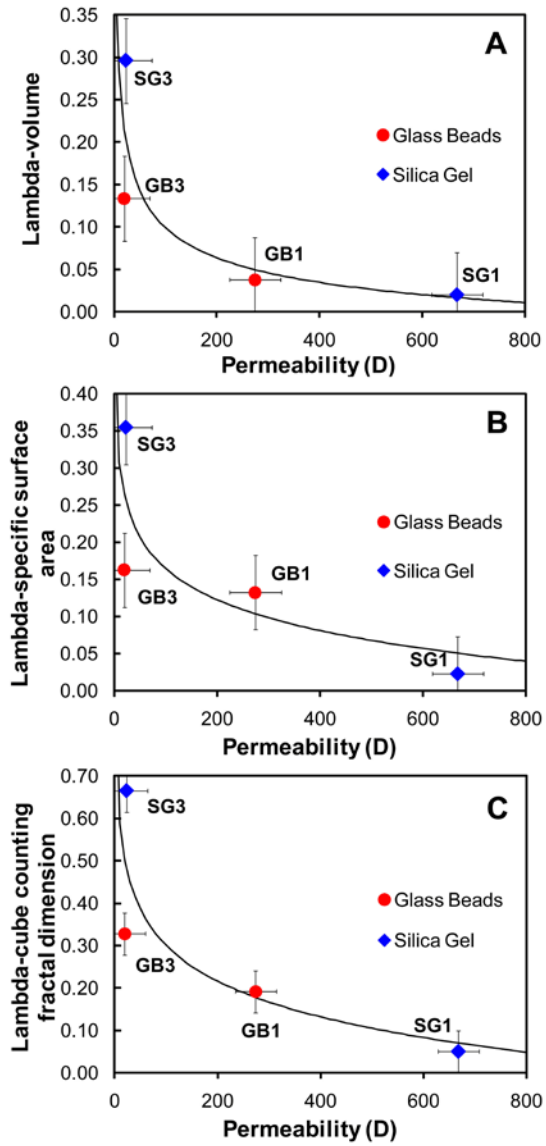

Figure 5-5. Relationship between convergence rates of (A) volume, (B) specific surface area, and (C) cube counting fractal dimension of water phase and the permeability. Each thick line is obtained from power law fitting function (Equation 5.2).

δ

between convergence rates and permeability fit well with the power-law equation, indicating that the convergence rate of any property can be explained by the transport property of the porous networks. Note that convergence rates are dependent on the flow pressure (i.e., injection rates) (Babadagli, 2002). Water was injected at a constant pressure (2 bar) for all samples, thus the results show the trend at a specific flow pressure while convergence rates would increase with increasing pressure. Therefore, in order to generalize equation (5.2), the convergence rates at varying flow pressures should be explored. Additional correlations can be found at sections 3 and 4 in Supplementary Information where the relationships between convergence rates and structural parameters including entropy length, porosity, specific surface area, cube counting fractal dimension, and configurational entropy are shown.

The current results show that NMR micro-imaging can also be used for obtaining pore scale resolution images (below 100 μm resolution) of two fluid phases in porous media. The current results also show that the network structures and the types of particles play crucial roles in the amount of permanent remnants of oil in oil sands and non aqueous phase liquids in sediments, and that the transport property of the porous networks determines the convergence rate of recovery.

d

Supplementary Information

5.S1. Validity of the experiments of this study

It was checked whether the distribution of water and silicone oil was affected by moving the sample. The procedure is as follows: 2D images were obtained, the sample was removed from the spectrometer, it was waited for 38 hours, the sample was set to the spectrometer, and 2D images were obtained again. Figure 5-S1 shows 2D images of SG3 samples at 40 minutes of duration of water injection. Figure 5-S1A was obtained before removing the sample from spectrometer, and Figure 5-S1B was obtained after setting the sample with the time interval of 38 hours. Figure 5-S1C is the difference image of the two images. Figure 5-S1C shows that the difference is not significant, and thus the distribution of water and silicone oil is almost constant in the resolution and time scale of this study before and after moving the sample. The insignificant changes of the distribution of two phases of fluid could be attributed to the fact that the viscosity of silicone oil is very large (30000 mPa·s), and the two fluids are immiscible and saturated in the column. The results show that the experiments are valid in the resolution and time scale of this study.

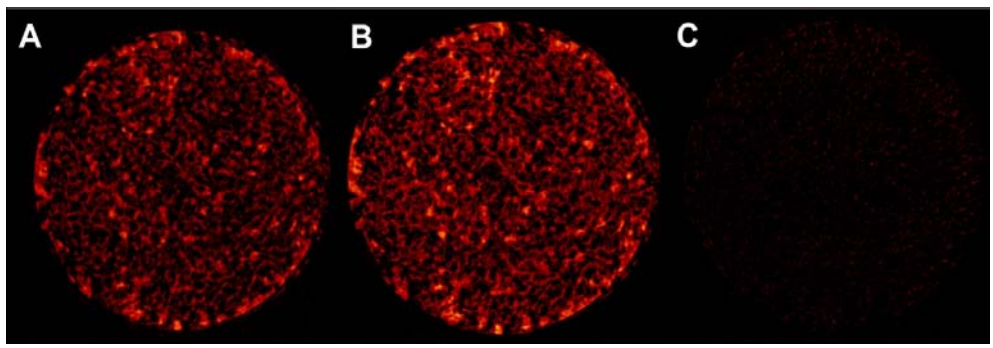

Figure 5-S1. (A) 2D image for SG3 obtained at 40 minutes of duration of water flow before removing the sample from spectrometer. (B) 2D image after 38 hours when the previous image was obtained. (C) Difference image between (A) and (B).

5.S2. 2D spin density maps and images obtained by chemical shift selective imaging method

Figure 5-S2 shows 2D spin density maps and images obtained by chemical shift selective imaging method for SG3 samples at 40 minutes of the duration of water flow.

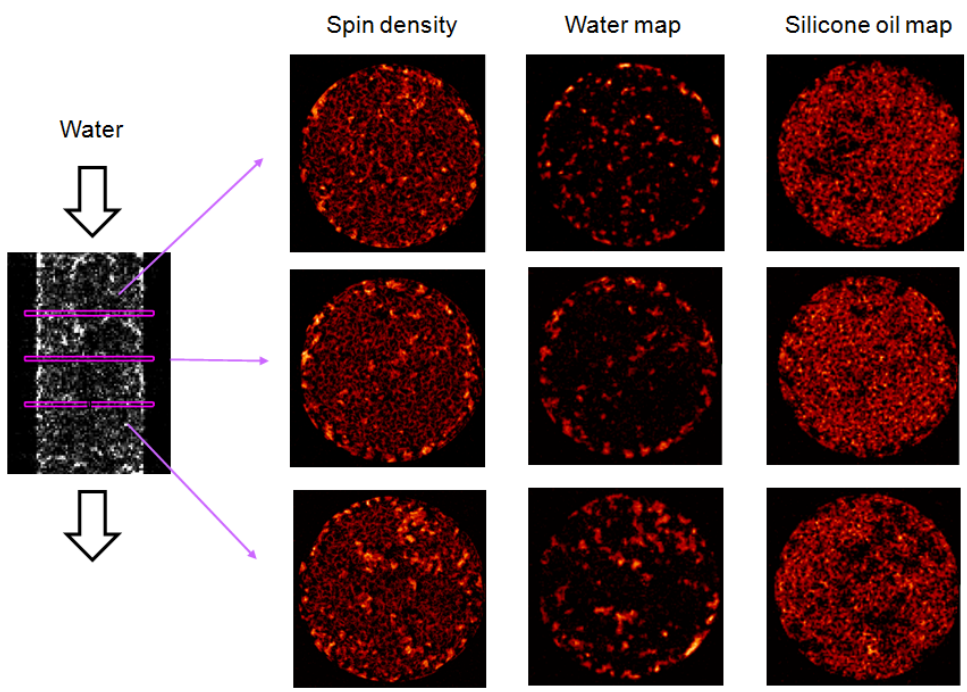

Figure 5-S2. Spin density maps and images obtained by chemical shift selective imaging method for SG3 obtained at 40 minutes of duration of water flow. The three columns correspond to spin echo 2D images, chemical shift images for water phase, and chemical shift images for silicone oil phase, respectively.

δ

5.S3. Effect of the entropy length on convergence rates

Configurational entropy analysis was estimated by the gliding-box algorithm (Andraud et al., 1994). Configurational entropy analyses were done for the 2D cross sections (slices) chosen from the 160 × 160 × 160 sub-volume data of each sample saturated with silicone oil (before the water flow). From this analysis, maximum configurational entropy and the corresponding entropy length can be obtained (Andraud et al., 1994). The entropy length is regarded as an accurate measure of the typical size of pores and/or constituent particles (Andraud et al., 1997). It was found that the entropy length is also strongly correlated with the convergence rates. Figure 5-S3 shows the effect of the entropy length on convergence rates. The results show that the convergence rates decrease with increasing the entropy length as well as permeability (Figure 5-5). The data was also fitted with the power law equation (Eq. 5.2) in which permeability is replaced with entropy length. Table 5-S1 shows the fitting parameters and R^2 values for each relationship. Permeability is proportional to the square of a representative grain diameter in Kozeny-Carman equation (Bear, 1972) and the entropy length is approximately 0.57 times of solid grains in porous media (Lee and Lee, submitted). Therefore, permeability and the entropy length are strongly correlated, and they have similar behavior for convergence rates. Note that the entropy length is a parameter characterizing porous networks and permeability is a transport property, and that both of them are well explained by the convergence rates of water distribution in initially saturated with silicone oil.

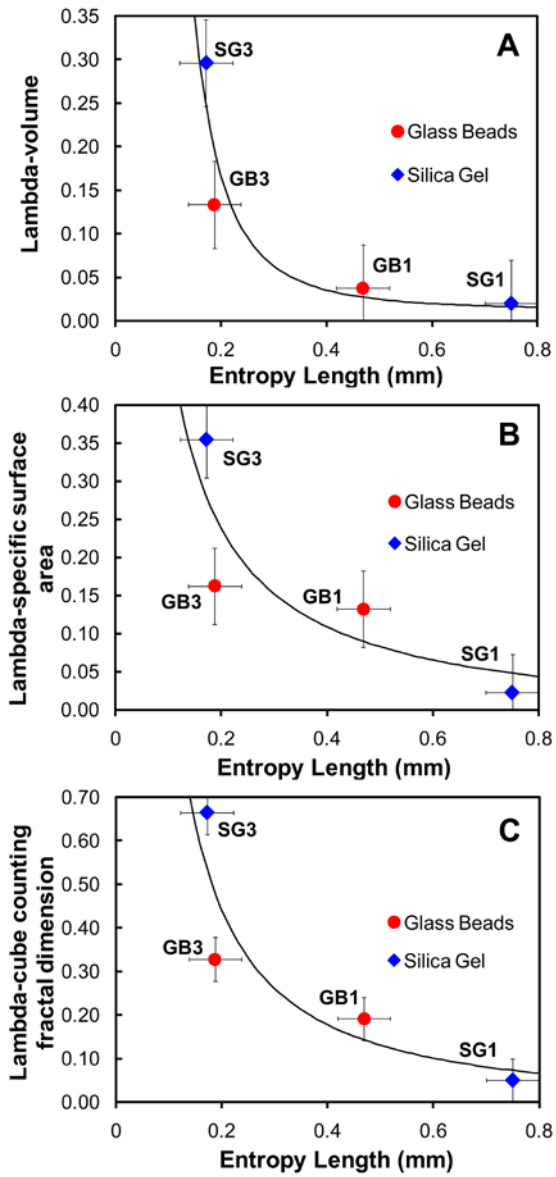

Figure 5-S3. Relationship between convergence rates of (A) volume, (B) specific surface area, and (C) cube counting fractal dimension of water phase and entropy length. Each thick line is obtained from power law fitting function (Equation 5.2).

δ

Table 5-S1. Fitting parameters and R^2 values for power law equations for the relationship between convergence rates and permeability.

	p	q	R	R^2
λ-volume	0.002	-2.749	0.012	0.863
λ-specific surface area	0.054	-0.985	-0.023	0.710
λ-cube counting fractal dimension	0.061	-1.250	-0.015	0.796

5.S4. Effect of structural parameters on convergence rates

Relationships between structural parameters and convergence rates were also investigated. This section describes relationships among various parameters and properties in which the correlations were not significant. Figure 5-S4-S7 show the relationships for porosity, specific surface area, cube counting fractal dimension, and configurational entropy, respectively with convergence rates. Convergence rates slightly decrease with increasing porosity (Figure 5-S4) and configurational entropy (Figure 5-S7), and slightly increase with increasing specific surface area (Figure 5-S5) and cube counting fractal dimension (Figure 5-S6). Compared to the relationships for permeability (Figure 5-5) and entropy length (Figure 5-S3), the trends for these relationships are not clear. The similar trend of porosity and maximum configurational entropy and that of specific surface area and cube counting fractal dimension are consistent with the results obtained for the model porous networks (Lee and Lee, submitted).

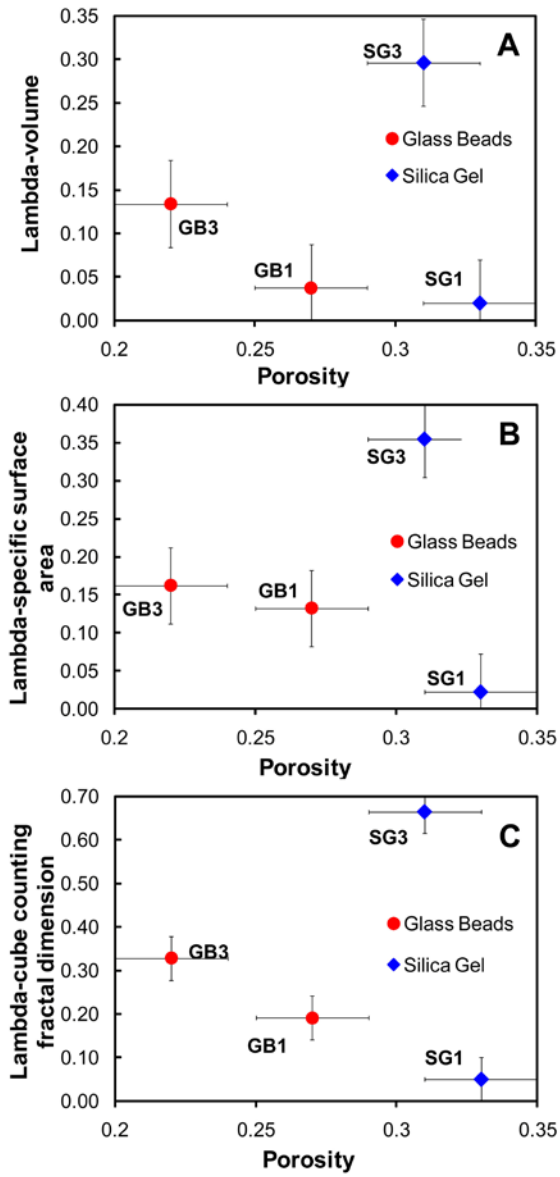

Figure 5-S4. Relationship between convergence rates of (A) volume, (B) specific surface area, and (C) cube counting fractal dimension of water phase and porosity.

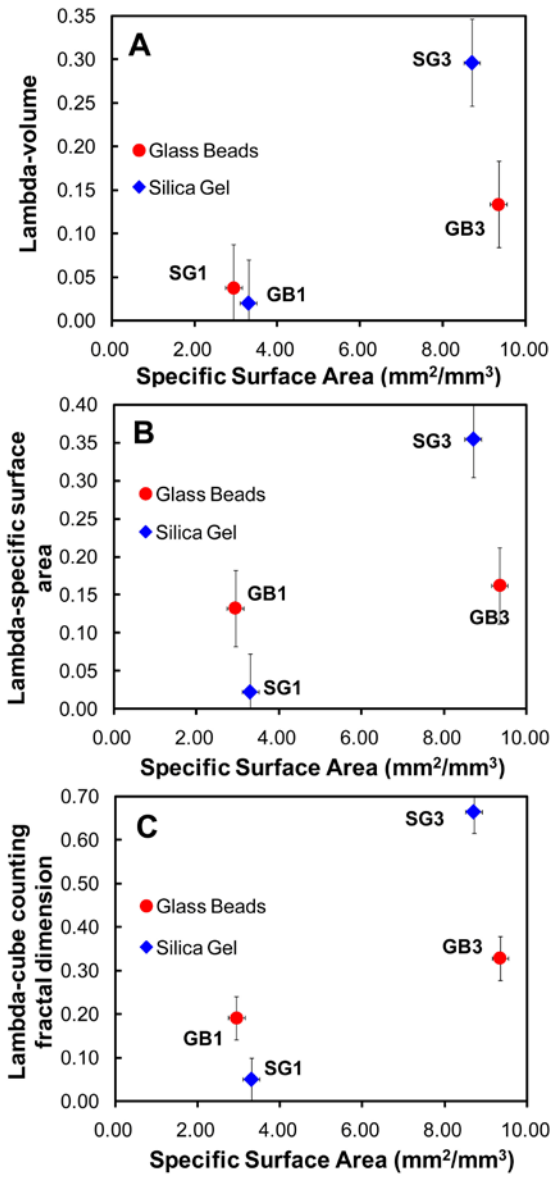

Figure 5-S5. Relationship between convergence rates of (A) volume, (B) specific surface area, and (C) cube counting fractal dimension of water phase and specific surface area (mm^2/mm^3).

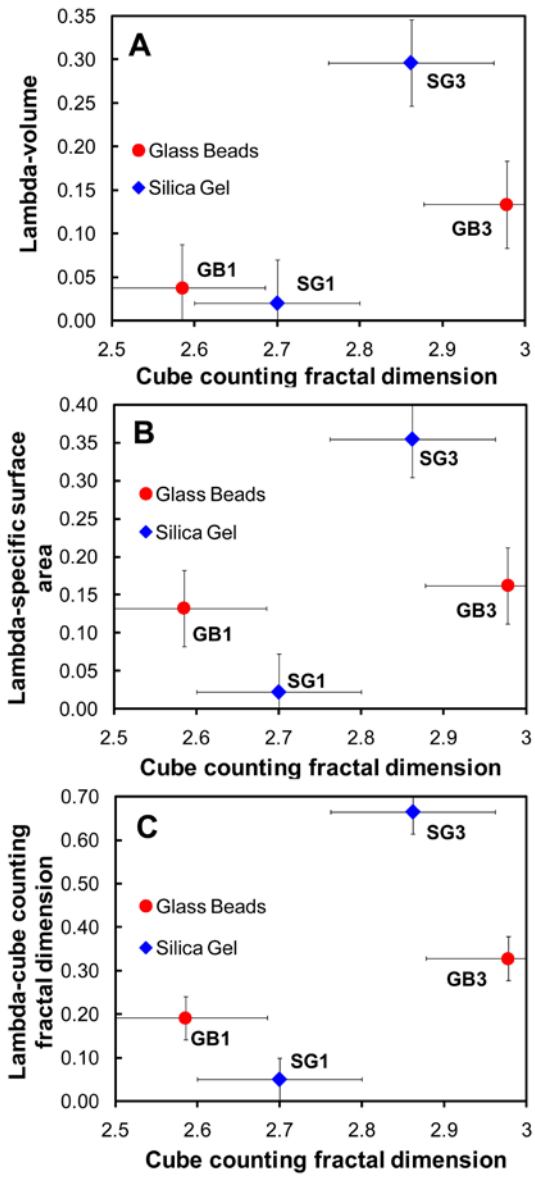

Figure 5-S6. Relationship between convergence rates of (A) volume, (B) specific surface area, and (C) cube counting fractal dimension of water phase and cube counting fractal dimension.

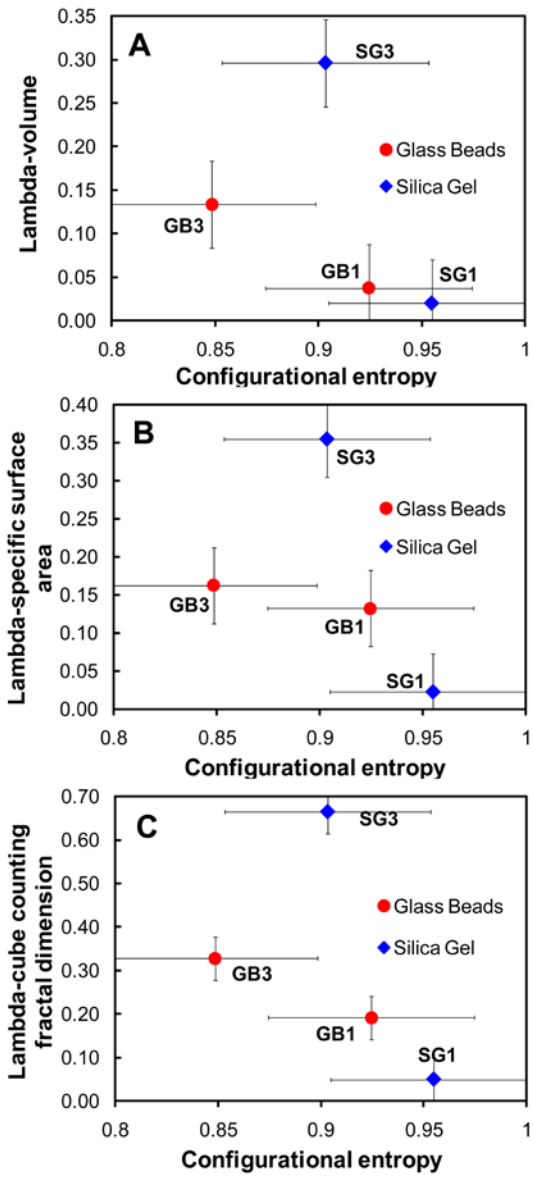

Figure 5-S7. Relationship between convergence rates of (A) volume, (B) specific surface area, and (C) cube counting fractal dimension of water phase and porosity.

References

Al-Raoush, R. I. and Willson, C. S. (2005) A pore-scale investigation of a multiphase porous media system. Journal of Contaminant Hydrology, 77, 67-89.

Andraud, C., Beghdadi, A., Haslund, E., Hilfer, R., Lafait, J. and Virgin, B. (1997) Local entropy characterization of correlated random microstructures. Physica A, 235, 307-318.

Andraud, C., Beghdadi, A. and Lafait, J. (1994) Entropic analysis of random morphologies. Physica A, 207, 208-212.

Aronofsky, J. S., Massé, L. and Natanson, S. G. (1958) A model for the mechanism of oil recovery from the porous matrix due to water invasion in fractured reservoirs. AIME Transactions, 213, 17-19.

Babadagli, T. (2002) Scaling capillary imbibition during static thermal and dynamic fracture flow conditions. Journal of Petroleum Science and Engineering, 33, 223-239.

Bachu, S. (2000) Sequestration of CO2 in geological media: criteria and approach for site selection in response to climate change. Energy Conversion and Management, 41(9), 953-970.

Barranco Jr., F. T., Dawson, H. E., Christener, J. M. and Honeyman, B. D. (1997) Influence of aqueous pH and ionic strength on the wettability of quartz in the presence of dense nonaqueous-phase liquids. Environmental Science & Technology, 31, 676-681.

Bear, J. (1972) Dynamics of Fluids in Porous Media. New York, American Elsevier, 764 p.

Becker, M. W., Pelc, M., Mazurchuk, R. V. and Spernyak, J. (2003) Magnetic resonance imaging of dense and light non-aqueous phase liquid in a

rock fracture. Geophysical Research Letters, 30(12), 1646.

Bernstein, M. A., King, K. F. and Zhou, X. J. (2004) Handbook of MRI Pulse Sequences. London, Elsevier Academic Press.

Blümich, B. (2000) NMR Imaging of Materials. Oxford, Clarendon Press, 541 p.

Brown, T. R., Kingaid, B. M. and Ugurbil, K. (1982) NMR chemical shift imaging in three dimensions. Proceedings of the National Academy of Sciences of the United States of America, 79, 3523-3526.

Callaghan, P. T. (1991) Principles of Nuclear Magnetic Resonance Microscopy. Oxford, Clarendon Press, 492 p.

Chen, J.-D., Dias, M. M., Patz, S. and Schwartz, L. M. (1988) Magnetic resonance imaging of immiscible-fluid displacement in porous media. Physical Review Letters, 61(13), 1489-1492.

Chu, Y. J., Werth, C. J., Valocchi, A. J., Yoon, H. and Webb, A. G. (2004) Magnetic resonance imaging of nonaqueous phase liquid during soil vapor extraction in heterogeneous porous media. Journal of Contaminant Hydrology, 73(1-4), 15-37.

Cil, M., Reis, J. C., Miller, M. A. and Misra, D. (1998) An examination of countercurrent capillary imbibition recovery from single matrix blocks and recovery predictions by analytical matrix/fracture transfer functions. SPE Annual Technical Conference and Exhibition. New Orleans, Louisiana, 49005 p.

Culligan, K. A., Wildenschild, D., Christensen, B. S. B., Gray, W. G. and Rivers, M. L. (2006) Pore-scale characteristics of multiphase flow in porous media: A comparison of air-water and oil-water experiments. Advances in Water Resources, 29(2), 227-238.

Farrell, J., Grassian, D. and Jones, M. (1999) Investigation of mechanisms

contributing to slow desorption of hydrophobic organic compounds from mineral solids. Environmental Science & Technology, 33, 1237-1243.

Haase, A., Frahm, J., Hanicke, W. and Matthaei, D. (1985) ^{1}H NMR chemical shift selective (CHESS) imaging. Physics in Medicine and Biology, 30, 341-344.

Huang, W., Schlautman, M. A. and Weber, J. W. J. (1996) A distributed reactivity model for sorption by soils and sediments. 5. The influence of near-surface characteristics in mineral domains. Environmental Science & Technology, 30(2993-3000).

Johns, M. L. and Gladden, L. F. (2000) Probing ganglia dissolution and mobilization in a water-saturated porous medium using MRI. Journal of Colloid and Interface Science, 225, 119-127.

Kazemi, H., Gilman, J. R. and Elsharkawy, A. M. (1992) Analytical and numerical solution of oil recovery from fractured reservoirs with empirical transfer functions. SPE Reservoir Engineering, 19849.

Keehm, Y. (2003) Computational Rock Physics: Transport Properties in Porous Media and Applications. Geophysics, Stanford University, Doctor of Philosophy, 135 p.

Lee, B. H. and Lee, S. K. (submitted) Effects of specific surface area and porosity on cube counting fractal dimension, lacunarity, and configurational entropy of porous networks of model sands: insights from random packing simulations and NMR micro-imaging. Journal of Geophysical Research.

Lee, S. K., Kim, H. N., Lee, B. H., Kim, H. I. and Kim, E. J. (2010) Nature of chemical and topological disorder in borogermanate glasses: insights from B-11 and O-17 solid-state NMR and quantum

chemical calculations. Journal of Physical Chemistry B, 114, 412-420.

Lee, S. K., Lin, J. F., Cai, Y. Q., Hiraoka, N., Eng, P. J., Okuchi, T., Mao, H. K., Meng, Y., Hu, M. Y., Chow, P., Shu, J. F., Li, B. S., Fukui, H., Lee, B. H., Kim, H. N. and Yoo, C. S. (2008) X-ray Raman scattering study of $MgSiO_3$ glass at high pressure: Implication for triclustered $MgSiO_3$ melt in Earth's mantle. Proceedings of the National Academy of Sciences, 105(23), 7925-7929.

Lee, S. K., Park, S. Y., S., Y. Y. and Moon, J. (2010) Structure and disorder in amorphous alumina thin films: insights from high-resolution solid-state NMR. Journal of Physical Chemistry C, 114(32), 13890-13894.

McNamara, G. R. and Zanetti, G. (1988) Use of the Boltzmann equation to simulate lattice-gas automata. Physical Review Letters, 61(20), 2332-2335.

Okamoto, I., Hirai, S. and Ogawa, K. (2001) MRI velocity measurements of water flow in porous media containing a stagnant immiscible liquid. Measurement Science & Technology, 12(9), 1465-1472.

Peters, E. J. and Hardham, W. D. (1990) Visualization of fluid displacements in porous media using computed tomography imaging. Journal of Petroleum Science and Engineering, 4(2), 155-168.

Prodanovic, M., Lindquist, W. B. and Seright, R. S. (2006) Porous structure and fluid partitioning in polyethylene cores from 3D X-ray microtomographic imaging. Journal of Colloid and Interface Sciences, 298, 282-297.

Reis, J. C. and Haq, S. A. (1999) Water advance in a single fracture in the presence of capillary imbibition into adjacent matrix blocks. In Situ, 23(3), 271-295.

Rumpel, H. and Pope, J. M. (1992) The application of 3D chemical shift microscopy to noninvasive histochemistry. Magnetic Resonance Imaging, 10, 187-194.

Sankey, M. H., Holland, D. J., Sederman, A. J. and Gladden, L. F. (2009) Magnetic resonance velocity imaging of liquid and gas two-phase flow in packed beds. Journal of Magnetic Resonance, 196, 142-148.

Schnaar, G. and Brusseau, M. L. (2005) Pore-scale characterization of organic immiscible-liquid morphology in natural porous media using synchrotron x-ray microtomography. Environmental Science & Technology, 39, 8403-8410.

Simpson, M. J., Simpson, A. J., Gross, D., Spraul, M. and Kingery, W. L. (2007) 1H and 19F nuclear magnetic resonance microimaging of water and chemical distribution in soil columns. Environmental Toxicology and Chemistry, 26(7), 1340-1348.

Sukop, M. C., Huang, H., Lin, C. L., Deo, M. D., Oh, K. and Miller, J. D. (2008) Distribution of multiphase fluids in porous media: Comparison between lattice Boltzmann modeling and micro-x-ray tomography. Physical Review E, 77(2), 026710.

Taber, J. J. (1980) Research on enhanced oil recovery: past, present and future. Pure and Applied Chemistry, 52(5), 1323—1347.

Wildenscheld, D., Hopmans, J. W., Vaz, C. M. P., Rivers, M. L. and Rikard, D. (2002) Using X-ray computed tomography in hydrology: systems, resolutions, and limitations. Journal of Hydrology, 267(3-4), 285-297.

Zhang, C. Y., Werth, C. J. and Webb, A. G. (2002) A magnetic resonance imaging study of dense nonaqueous phase liquid dissolution from angular porous media. Environmental Science & Technology, 36(15), 3310-3317.

δ

Chapter 6. High resolution NMR micro-imaging of fluids in porous media

Abstract

High resolution NMR micro-imaging of fluids in porous media may shed light on diverse applications in hydrogeology and geophysics. However, it is difficult to obtain high resolution images of fluids in porous media using NMR micro-imaging due to the low contents of fluids and short spin-spin relaxation times. Here, high resolution images of fluids in porous media including Mongolian desert sandstone, natural pisolite, and glass beads were obtained with relatively large porosity, small sample size, high magnetic field (18.8 T), and high gradient strength (300 G/cm). The results show that although signal to noise ratio is relatively low, NMR micro-imaging can be used to obtain the images of porous media composed of grain size down to 75 μm with the resolution of up to 19.5 μm/pixel for fluids in porous media.

6.1. Introduction

High resolution NMR micro-imaging of fluids in porous media with the resolution below 20 μm may allow us to study the pore-scale distribution and morphology of organic liquids at a fundamental level, which has the implication for the displacement and mass-transfer behavior of pollutant in porous media (Schnaar and Brusseau, 2005), and the connectivity of fluid and partial melt in rock, which has the implication for

δ

the seismic wave attenuation (Takei, 2002). However, it is difficult to obtain with the resolution below 20 μm using NMR micro-imaging because porous materials frequently possess low fluid contents and short spin–spin relaxation times, and both of which contribute to poor-quality NMR images (Callaghan, 1991; Blümich, 2000), and in addition, the difference in magnetic susceptibility between the pore fluid and the solid matrix leads to a large distribution of magnetic fields within the porous materials and correspondingly broad NMR line widths (Beyea et al., 2000). Here, it is attempted to obtain high resolution images of fluids in porous media including model sands, Mongolian sandstone, and natural pisolite filled with silicone oil with the resolution of up to 19.5 μm/pixel.

Before describing the limitation of NMR imaging and the strategy of this study for obtaining high resolution images, a brief introduction of imaging methods frequently used in porous media research is provided; optical imaging, confocal laser scanning microscopy, x-ray microtomography, and NMR imaging. Among them, optical imaging is the most straightforward method. Optical imaging methods include bright field microscopy, phase contrast microscopy, and reflected differential interference contrast microscopy (i.e., Nomarski microscopy) (Murphy, 2001). The advantages of optical imaging methods are their relative low cost, high-resolution, and fast acquisition time, and the disadvantage of optical imaging is that they are limited to a two dimensional acquisition (Werth et al., 2010).

Confocal laser scanning microscopy uses a laser to selectively

d

excite a narrow plane of light (Murphy, 2001). Images from multiple planes can be combined to create a three-dimensional image. In porous media research, the fluorescent resin impregnation method using confocal laser scanning microscopy was suggested (Fredrich et al., 1995) and has been successfully applied to porous sedimentary and crystalline rocks (Montoto et al., 1995; Fredrich and Lindquist, 1997; Onishi and Shimizu, 2005). The advantage of confocal laser scanning microscopy is that it covers a large area of sample surface with submicron resolution, and the disadvantage is that information from the interior of the samples is strongly restricted by decay of luminescent light through minerals (Onishi and Shimizu, 2005).

X-ray microtomography maps the absorption of x-rays passing through a sample (Flannery et al., 1987). The amount of absorption depends on sample composition and energy of the x-ray. In order to obtain a 3D spatially-distributed map of attenuation, the sample is rotated about the longitudinal axis (typically 0.5° to 1°) after an image is collected, and the image acquisition process is repeated until a total of 720 or 360 2D images of the sample are collected (Flannery et al., 1987). Recently, in order to obtain high resolution images, x-ray microtomography has been conducted at synchrotron sources and applied to unconsolidated (e.g., glass beads and soils) and consolidated (e.g., sandstone, limestone, and basaltic rocks) porous media (Spanne et al., 1994; Lindquist et al., 1996; Song et al., 2001; Arns et al., 2005; Øren et al., 2007). The advantage of x-ray microtomography is that it can produce high-resolution three-dimensional image, typically in the range of 1–10 μm, which is the greatest resolution

among the imaging methods that are applied to 3D systems, and the disadvantages include that a dopant is typically required, which may affect the fluid properties (Barranco Jr. et al., 1997; Wildenscheld et al., 2002), and that the dimensions of the sample are restricted to several millimeters, which is not sufficient to characterize the fracture patterns in coarse-grained rocks (Werth et al., 2010).

NMR imaging uses a field gradient for imaging the spins in fluids (Callaghan, 1991; Blümich, 2000). The linear relationship between NMR frequency and space coordinate is obtained by restricting the space dependence of the magnetic field to the field gradient (Levitt, 2001). To obtain an image, the gradient must be varied in such a way that all values of the wave vector that is the Fourier conjugate variable to the space coordinate are sampled. The image itself is then derived by Fourier transformation of the NMR signal. There are two ways to encode the space information to the NMR signal. First, the gradients can be turned on to a constant value of the gradient in x-direction during data acquisition. In this case, the wave vector scales with the acquisition time, and the space information in x-direction is frequency encoded. Second, the gradient in y-direction can be turned on for a fixed time before data acquisition to yield a certain value of the gradient integral at the start. In this case, the space information in y-direction is encoded in the phase of the signal acquired, and the experiment needs to be repeated for different initial phases obtained by varying the gradient. A 2D image is typically obtained by a combination of both phase encoding in one dimension and frequency

δ

encoding in the other. NMR imaging has many advantages (Callaghan, 1991; Blümich, 2000). Firstly, it can produce 3D images of pore structures non-destructively. Secondly, it can differentiate fluid phases in porous media at μm length scale. Thirdly, it can produce T_1 (spin-lattice relaxation time) and T_2 (spin-spin relaxation time) weighted imaging. Finally, it can produce velocity mapping. Recently, NMR imaging has been applied in many fields; for example, the controlled transport of polarized product in micro-reactors in chemical engineering (Bouchard et al., 2008), 3D structure of chick embryo in biochemistry (Goodall et al., 2009), temperature change in polymer in materials science (Small et al., 2009), water infiltration in sandstone in geology (Baraka-Lokmane et al., 2009), and NAPL distribution in the experimental aquifer in environmental sciences (Zhang et al., 2007).

The spatial resolution in the frequency encoding direction, $1/\Delta x$ is related to the width of the NMR absorption line, $\Delta\nu = \Delta\omega/2\pi$ by

$$\frac{1}{|\Delta x|} = \left|\frac{\gamma G_x}{2\pi\Delta\nu}\right|, \qquad (6.1)$$

where ω is the Larmor frequency and γ is the gyromagnetic ratio (Callaghan, 1991). This expression applies to direct detection of the NMR signal in the presence of a magnetic field gradient G_x. The digital resolution $1/\Delta y$ in the phase encoding direction is determined by the number n_y of complex signal values and by the k-space sampling interval $\Delta G_y t_1$,

$$\frac{1}{\Delta y} = \frac{n_y \Delta G_y t_1}{2\pi} \qquad (6.2)$$

where t_1 is the phase encoding time (Callaghan, 1991). As shown in

δ

equations (6.1) and (6.2), the spatial resolution is proportional to the magnetic field gradient. The most significant factor limiting the resolution is poor signal-to-noise ratio (SNR) of an NMR signal decreasing with voxel volume, because NMR signal amplitude is proportional to the number of nuclear spins in a voxel (Callaghan, 1991; Blümich, 2000). SNR is proportional to the 7/4th power of the static magnetic field (Hoult and Richards, 1976). Therefore, in order to increase SNR and voxel resolution, NMR micro-imaging experiments were performed at the high magnetic field (strength of 18.8 T) and high field gradient (300 G/cm) in this study.

Other limiting factors include the effects of diffusion, transverse relaxation, and susceptibility (Callaghan, 1991; Blümich, 2000). The transverse relaxation rate ($1/T_2$) is expressed as

$$\frac{1}{T_2} = \frac{1}{T_{2B}} + \rho_2 \frac{S}{V} + \frac{D}{12}\left(\gamma G t_E\right)^2, \qquad (6.3)$$

where ρ_2 is the transverse surface relaxivity, $1/T_{2B}$ is the relaxation rate of the bulk water, D is the self-diffusion coefficient of the water, and t_E is the echo-time (Brownstein and Tarr, 1979). Surface relaxivity is a geochemical property describing the capacity of the grain surface to enhance relaxation and generally increase with the concentration of paramagnetic impurities on a surface (Bryar et al., 2000). The product $\rho(S/V)$ reflects the effect of both pore geometry and geochemistry. Therefore, the transverse relaxation rate increases with increasing (S/V) (i.e., decreasing the grain size) and the echo time. In this study, in order to reduce these limiting factors, samples with high porosity were used and minimum echo time was applied.

δ

In the applications of NMR imaging to artificial phantoms or biological cells, there are two previous studies considered the highest resolutions to date (Lee et al., 2001; Ciobanu et al., 2003). In the former, 1×1 μm^2 at 75 μm slice thickness and, in the latter, 3.7×3.4×3.4 μm^3 were reported. In the applications to porous media research, NMR imaging has been mostly used to obtain images of multi phases of fluids or velocity vectors (Blümich, 2000), and obtaining high resolution images of fluids in porous media has not been much concerned. Therefore, as far as the author know, images obtained by NMR imaging with the resolution below 20 μm for fluids in porous media have not been reported previously.

Here, it was pursued to obtain high resolution images of fluids in porous media using NMR micro-imaging with the resolution of up to 19.5 μm/pixel . In order to enhance the resolution, high magnetic field (18.8 T), high field gradient (300 G/cm), highly porous sample, minimum echo time, and relatively small sample size were used.

6.2. Methods

Porous sandstone, natural pisolite, and glass beads were prepared for NMR micro-imaging experiments. The sandstone (late cretaceous, Cenomanian-Santonian) sample was taken at Khar Khutul area, East Gobi Basin, Mongolia. The grain size of the sandstone sample ranged from 0.12 mm to 0.43 mm (rarely up to 0.61 mm). The sandstone was composed of 52 % quartz, 39 % feldspar, and 9 % lithic fragment. Natural pisolite was comprised of spherical calcite grains in which the average grain diameter

d

was 2 mm. Average particle sizes (diameters) of the glass beads (Sigma, acid-washed) were 0.075 mm (GB4). Each sample was saturated with silicone oil (polydimethylsiloxane, Baysilone M30000, density of 0.98 g/cm^3 and viscosity of 30000 mPa·s). A vacuum pump with a pump pressure of 1.45 torr was used to saturate the pore space with silicone oil and to eliminate air bubbles. Each sample was sealed with parafilm after the saturation, and put into the 10 mm NMR tube (Wilmad).

The experiment was carried out at Korea Basic Science Institute, Ochang using a Bruker DMX 800 spectrometer equipped with a 18.8 T vertical bore magnet. Micro5.0 probehead was used and the gradient strength was 300 G/cm for DMX 800 spectrometer. Figure 6-1 shows the two dimensional spin echo pulse sequence used in the experiment. Minimum echo time (T_E) was used to reduce the signal attenuation due to T_2 relaxation and diffusion, which become more important as pixel size becomes smaller. Minimum echo time was 4.5 ms for 256 x 256 matrix, 12.335 ms for 512 x 512 matrix. Field of view, matrix size, and slice thickness varied with the sample. The sinc3-shaped excitation and refocusing pulses were used with a repetition time of 2 s. The number of scans varied from 1 to 4, depending on the signal-to-noise ratio of the spectra. After the image acquisition, binary images were obtained by threshold method using the pixel vs. intensity histogram showing a bimodal distribution.

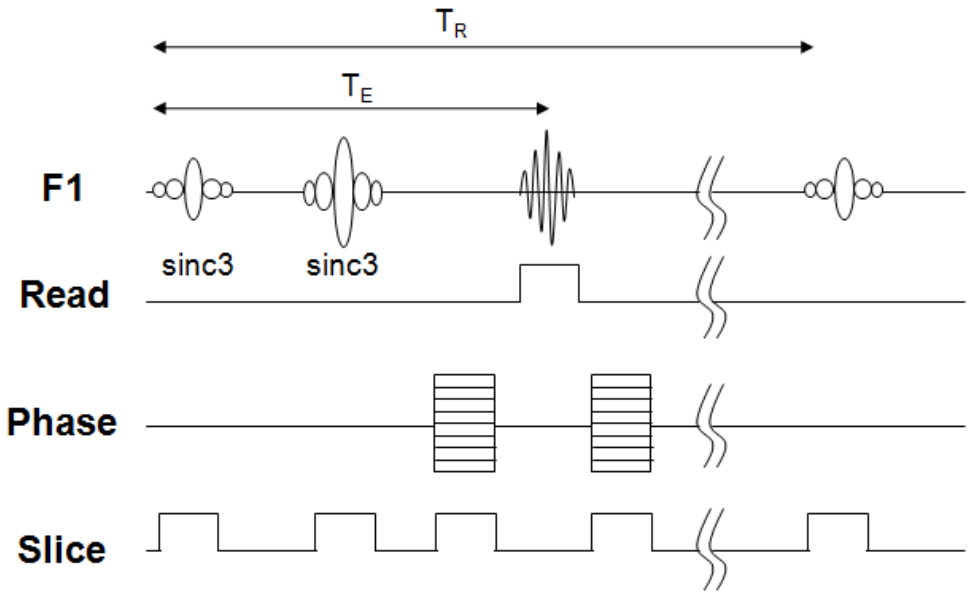

Figure 6.1. Timing diagram of two dimensional spin echo pulse sequence.

δ

6.3. Results and Discussion

Figure 6-2 shows the spin echo image (6-2A) and its binary image (6-2B) of Mongolian desert sandstone. Field of view was 9 mm x 9 mm, and matrix size was 256 x 256, and thus the resulting spatial resolution was 35 μm x 35 μm. The slice thickness was 0.5 mm. In spin density image, boundary of sandstone is distinctive due to the high intensity of silicone oil covered with the surface of sandstone. Note that the sample was covered by parafilm after the saturation of silicone oil by vacuum pump. In addition, signals from silicone oil infiltrated into the inside of sandstone can be seen. In binary image, the distribution of infiltrated silicone oil is more distinctive. Zoomed images show that the infiltrated silicone oil forms small blobs, and some blobs are interconnected. As mentioned above, it is difficult to obtain the detailed structure of infiltrated fluid in natural sandstone due to the low porosity and the large amount of paramagnetic impurities. Therefore, there has been previous NMR imaging studies for natural sandstones showing only the development of the fluid front during the imbibitions (e.g., Dijk et al., 1999; Baraka-Lokmane et al., 2001; Dijk et al., 2002; Baraka-Lokmane et al., 2009). Despite the difficulties, it was able to obtain the detailed distribution of silicone oil in sandstone.

Figure 6-3 shows two dimensional spin density images (6-3A and 3B) of pisolite filled with silicone oil, those with contour lines (6-3C and 3D), and their binary images (6-3E and 3F). Field of view was 10 mm x 10 mm, and matrix size was 512 x 512. Therefore, the spatial resolution was 19.5 μm x 19.5 μm. The slice thickness was 0.5 mm. Pisolite is composed of large

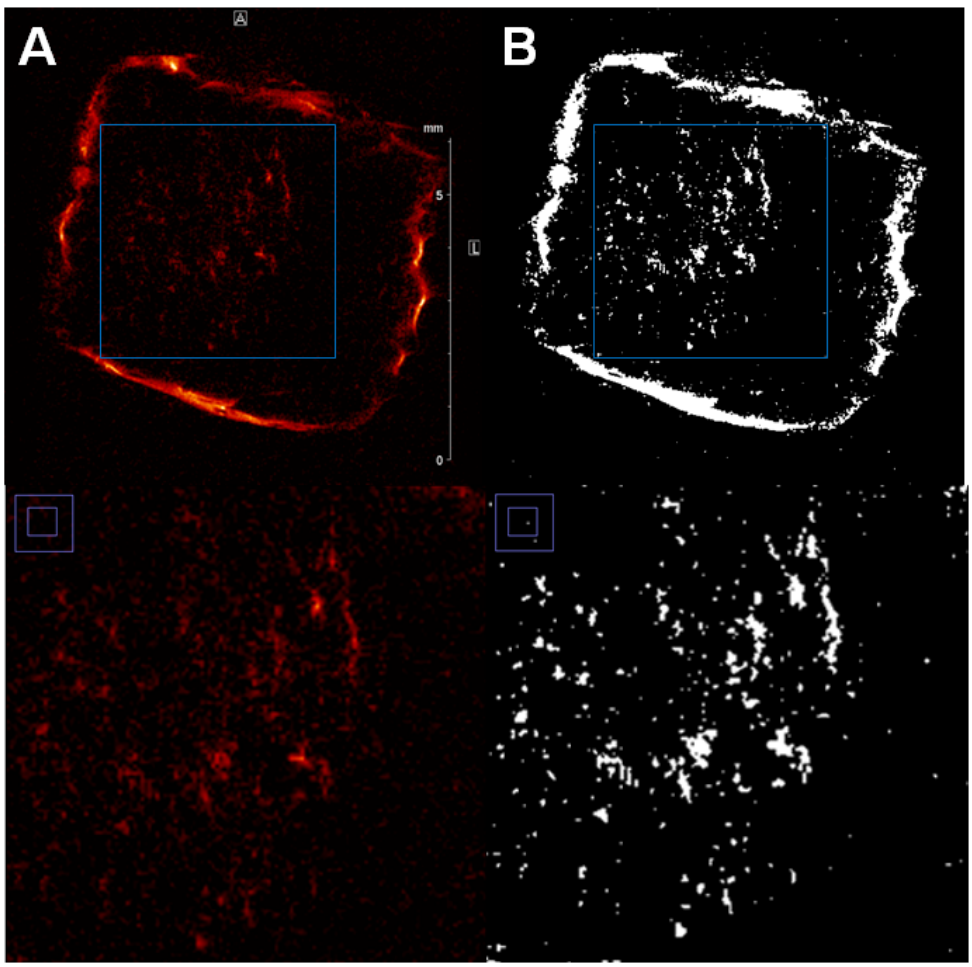

Figure 6-2. Two dimensional (A) spin density image and (B) binary image of Mongolian sandstone filled with silicone oil. Zoomed regions are indicated by squares in upper images and zoomed images of spin density and binary image are shown in below images.

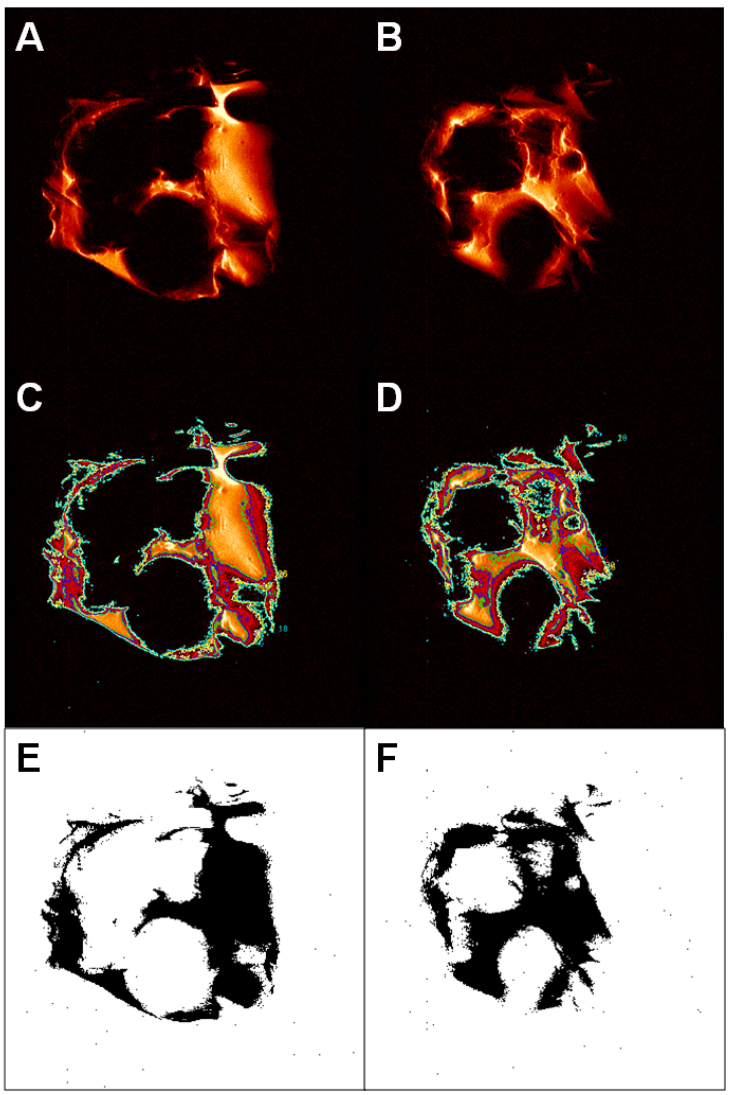

Figure 6-3. Two dimensional spin density images (A and B) of pisolite filled with silicone oil, those with contour lines (C and D), and their binary images (E and F). Each column belongs to the same slice. In (C) and (D), each contour line (color in parentheses) is drawn at 37.2 % (green), 29.4 % (blue), 21.6 % (red), 13.8 % (black), 11.8 % (white), 9.8 % (yellow), 7.8 % (orange), and 7.1 % (cyan) level of relative intensity.

δ

grains of calcite, and thus the pore size is relatively large, which allows us to make the voxel size small. Spin density images show that high intensities mostly come from silicone oil filled in the large pore. In spin density images with contour lines, one can see that the highest intensity is shown in the center of the pore, and the intensity becomes lower in the grain surfaces or inside the grains. High resolution images make one see the microstructure of infiltrated silicone oil into the grain. This is the highest resolution (i.e., the smallest pixel size, 19.5 μm) image of fluids in natural porous media, and it is noteworthy that the detailed structure of infiltrated fluid into the calcite grains was observed.

Figure 6-4 shows two dimensional spin density images of GB4 filled with silicone oil. Field of view was 6.5 mm x 6.5 mm, and matrix size was 256 x 256. Therefore, the spatial resolution was 25 μm x 25 μm. The slice thickness was 0.15 mm. Grain size of GB4 shown in this figure is the smallest size in the NMR imaging studies for porous media research. Spin density and binary images show that silicone oil structures filled in the pore space. The average particle size can be seen in the zoomed images with yellow circles. While the structure of silicone oil in small grains of glass beads is complex, the average size of the space where signals from silicone oil are not shown is comparable with the average particle size.

In order to obtain robust density images in porous media, the short encoding times, high magnetic field gradient strength, large filter widths, and low flip angle RF pulses are required. For that purpose, the spin-echo single point imaging (SE-SPI) technique was suggested with the

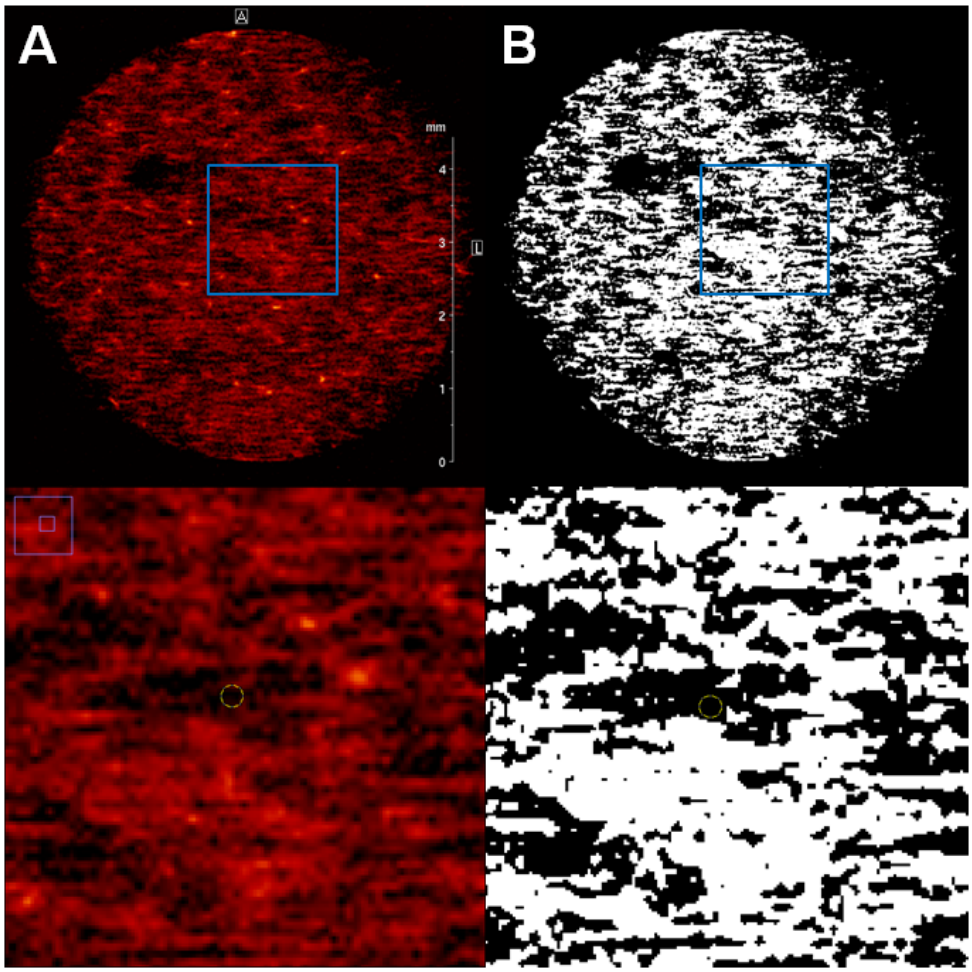

Figure 6-4. Two dimensional (A) spin density image and (B) binary image of GB4 filled with silicone oil. Zoomed regions are indicated by squares in upper images and zoomed images of spin density and binary image are shown in below images. Yellow circles in zoomed images indicate the average size of glass beads.

δ

achievement of true fluid content images through observing the signal intensity at near zero evolution time (Li et al., 2009). However, this method was tested for 1D imaging for rock core up to date. With the development of pulse sequences including SE-SPI for imaging fluids in porous media with short spin-spin relaxation time, it is expected that higher resolution images with below 10 μm pixel size can be obtained by using high magnetic field, high field gradient, and small sample size.

It was shown that high resolution NMR micro-imaging of fluids in porous media can be obtained with the resolution below 20 μm, which may enable us to study the connectivity of fluids and partial melts in rock at high pressures. Knowledge of the geometry of fluids and partial melts is essential for understanding the macroscopic properties of partially molten rocks (von Bargen and Waff, 1986; Takei, 2002). Three dimensional geometry of fluids and melts can be directly obtained by the advanced high resolution NMR micro-imaging with the resolution below 20 μm. However, this experiment requires in-situ high pressure and high temperature apparatus in imaging probe, which may be possible in the future.

References

Arns, C. H., Bauget, F., Limaye, A., Sakellariou, A., Senden, T. J., Sheppard, A. P., Sok, R. M., Pinczewski, W. V., Bakke, S., Berge, L. I., Oren, R. E. and Knackstedt, M. A. (2005) Pore-scale characterization of carbonates using X-ray microtomography. SPE Journal, 10(4), 475-484.

Baraka-Lokmane, S., Main, I. G., Ngwenya, B. T. and Elphick, S. C. (2009) Application of complementary methods for more robust characterization of sandstone cores. Marine and Petroleum Geology, 26(1), 39-56.

Baraka-Lokmane, S., Teutsch, G. and Maine, I. G. (2001) Influence of open and sealed fractures on fluid flow and water saturation in sandstone cores using Magnetic Resonance Imaging. Geophysical Journal International, 147(2), 263-271.

Barranco Jr., F. T., Dawson, H. E., Christener, J. M. and Honeyman, B. D. (1997) Influence of aqueous pH and ionic strength on the wettability of quartz in the presence of dense nonaqueous-phase liquids. Environmental Science & Technology, 31, 676-681.

Beyea, S. D., Balcom, B. J., Mastikhin, I. V., Bremner, T. W., Armstrong, R. L. and Grattan-Bellew, P. E. (2000) Imaging of heterogeneous materials with a turbo spin echo single-point imaging technique. Journal of Magnetic Resonance, 144(2), 255-265.

Blümich, B. (2000) NMR Imaging of Materials. Oxford, Clarendon Press, 541 p.

Bouchard, L. S., Burt, S. R., Anwar, M. S., Kovtunov, K. V., Koptyug, I. V.

and Pines, A. (2008) NMR imaging of catalytic hydrogenation in microreactors with the use of para-hydrogen. Science, 319(5862), 442-445.

Brownstein, K. R. and Tarr, C. E. (1979) Importance of classical diffusion in NMR studies of water in biological cells. Physical Review A, 19(6), 2446-2453.

Bryar, T. R., Daughney, C. J. and Knight, R. J. (2000) Paramagnetic effects of iron(III) species on nuclear magnetic relaxation of fluid protons in porous media. Journal of Magnetic Resonance, 142, 74-85.

Callaghan, P. T. (1991) Principles of Nuclear Magnetic Resonance Microscopy. Oxford, Clarendon Press, 492 p.

Ciobanu, L., Webb, A. G. and Pennington, C. H. (2003) Magnetic resonance imaging of biological cells. Progress in Nuclear Magnetic Resonance Spectroscopy, 42, 69-93.

Dijk, P., Berkowitz, B. and Bendel, P. (1999) Investigation of flow in water-saturated rock fractures using nuclear magnetic resonance imaging (NMRI). Water Resources Research, 35(2), 347-360.

Dijk, P. E., Berkowitz, B. and Yechieli, Y. (2002) Measurement and analysis of dissolution patterns in rock fractures. Water Resources Research, 38(2).

Flannery, B. P., Deckman, H. W., Roberge, W. G. and D'amico, K. L. (1987) Three-dimensional x-ray microtomography. Science, 237(4821), 1439-1444.

Fredrich, J. T. and Lindquist, W. B. (1997) Statistical characterization of the three-dimensional microgeometry of porous media and correlation with microscopic transport properties. International Journal of Rock Mechanics and Mining Sciences, 34, 3-4.

Fredrich, J. T., Menendez, B. and Wong, T.-F. (1995) Imaging the pore structure of geomaterials. Science, 268, 276-279.

Goodall, N., Kisiswa, L., Prashar, A., Faulkner, S., Tokarczuk, P., Singh, K., Erichsen, J. T., Guggenheim, J., Halfter, W. and Wride, M. A. (2009) 3-dimensional modelling of chick embryo eye development and growth using high resolution magnetic resonance imaging Experimental Eye Research, 89(4), 511-521.

Hoult, D. I. and Richards, R. E. (1976) The signal-to-noise ratio of the nuclear magnetic resonance experiment. Journal of Magnetic Resonance, 24, 71-85.

Lee, S.-C., Kim, K., Kim, J.-W., Lee, S. K., Yi, J. H., Kim, S. W., Ha, K.-S. and Cheong, C. (2001) One micrometer resolution NMR microscopy. Magnetic Resonance Imaging, 150, 207-213.

Levitt, M. H. (2001) Spin Dynamics. Chichester, John Wiley & Sons Ltd, 686 p.

Li, L., Han, H. and Balcom, B. J. (2009) Spin echo SPI methods for quantitative analysis of fluids in porous media. Journal of Magnetic Resonance, 198, 252-260.

Lindquist, W. B., Lee, S. M., Coker, D. A., Jones, K. W. and Spanne, P. (1996) Medial axis analysis in three-dimensional tomographic images of porous media. Journal of Geophysical Research, 101, 8297-8310.

Montoto, M., Martinez-Nistal, A., Rodriguez-Rey, A., Fernando-Merayo, N. and Soriano, P. (1995) Microfractography of granite rocks under confocal scanning laser microscopy. Journal of Microscopy, 177, 138-149.

Murphy, D. B. (2001) Fundamentals of Light Microscopy and Electronic Imaging. New York, Wiley-Liss, 368 p.

Onishi, C. T. and Shimizu, I. (2005) Microcrack networks in granite affected by a fault zone: visualization by confocal laser scanning microscopy. Journal of Structural Geology, 27, 2268-2280.

Øren, P. E., Bakke, S. and Held, R. (2007) Direct pore-scale computation of material and transport properties for North Sea reservoir rocks. Water Resources Research, 43(12), W12S04.

Schnaar, G. and Brusseau, M. L. (2005) Pore-scale characterization of organic immiscible-liquid morphology in natural porous media using synchrotron x-ray microtomography. Environmental Science & Technology, 39, 8403-8410.

Small, W., Gjersing, E., Herberg, J. L., Wilson, T. S. and Maitland, D. J. (2009) Magnetic resonance flow velocity and temperature mapping of a shape memory polymer foam device. Biomedical Engineering Online, 8(42).

Song, S.-R., Jones, K. W., Lindquist, W. B., Dowd, B. A. and Sahagian, D. L. (2001) Synchrotron X-ray computed microtomography: studies on vesiculated basaltic rocks. 63, 252-263.

Spanne, P., Thovert, J. F., Jacquin, C. J., Lindquist, W. B., Jones, K. W. and Adler, P. M. (1994) Synchrotron computed microtomography of porous media: Topology and transports. Physical Review Letters, 73(14), 2001-2004.

Takei, Y. (2002) Effect of pore geometry on V_P/V_S: From equilibrium geometry to crack Journal of Geophysical Research-Solid Earth, 107(B2), 2043.

von Bargen, N. and Waff, H. S. (1986) Permeabilities, interfacial areas and curvatures of partially molten systems: Results of computations of equilibrium microstructures. Journal of Geophysical Research, 91,

9261-9276.

Werth, C. J., Zhang, C., Brusseau, M. L., Oostrom, M. and Baumann, T. (2010) A review of non-invasive imaging methods and applications in contaminant hydrogeology research. Journal of Contaminant Hydrology, 113, 1-24.

Wildenscheld, D., Hopmans, J. W., Vaz, C. M. P., Rivers, M. L. and Rikard, D. (2002) Using X-ray computed tomography in hydrology: systems, resolutions, and limitations. Journal of Hydrology, 267(3-4), 285-297.

Zhang, C. Y., Werth, C. J. and Webb, A. G. (2007) Characterization of NAPL source zone architecture and dissolution kinetics in heterogeneous porous media using magnetic resonance imaging Environmental Science & Technology, 41(10), 3672-3678.

Chapter 7. Geophysical implications

One of the key issues in porous media research is to understand how the pore structure affects the transport processes of fluids in porous media. The zeroth order answer for this issue is characterizing the properties of porous media using porosity and specific surface area (Bear, 1972). However, porosity and specific surface area cannot provide further information about the morphology of the pore network. The first order answer is characterizing the properties of porous media by the statistical geometric methods. This approach includes multipoint correlation functions which analyze structural correlation between points belonging to the solid, interface or pore network (Reiss, 1992) and parameters analyzed in this study (cube counting fractal dimension, lacunarity, and configurational entropy). Configurational entropy and cube counting fractal dimension can be used in describing complex and disordered structures of fluids in rock-melt-fluid composites in the Earth's interior as well as porous networks shown by the interactions between earth materials and fluids in the Earth's surface.

Configurational entropy has been used to describe the degree of disorder in amorphous networks, including oxide glasses and melts with geophysical and geochemical implications (e.g. Lee and Stebbins, 1999; Lee, 2005; Lee et al., 2010). Adam and Gibbs (1965) defined configurational entropy (S^{config}) as follows:

δ

$$S^{config} = k \ln W_c , \tag{7.1}$$

where W_c is the number of configuration (individual arrangements into different configurations for microscopic cooperative regions). Based on the relaxation theory, liquid viscosity (η) is related to temperature and configurational entropy (Adam and Gibbs, 1965):

$$\log \eta = A + B \big/ TS^{config} . \tag{7.2}$$

where T is the temperature, and A and B are constants. Configurational entropy for aluminosilicate melts and glasses can be expressed as (Lee and Stebbins, 1999):

$$S^{config} = -R \sum X_{i-O-j} \ln X_{i-O-j} . \tag{7.3}$$

where R is the gas constant, and $X_{i\text{-}O\text{-}j}$ are the mole fractions of Si-O-Si, Al-O-Al, and Si-O-Al. With increasing chemical order, the configurational entropy decreases, which causes the viscosity of the melts to increase based on Adam-Gibbs theory (Richet, 1984; Lee, 2005).

Chapter 4 shows that the configurational entropy of total porosity is dependent on the porosity and explains the maximum configurational entropy well. The relationship between configurational entropy and porosity can be used to explain the properties of rock-melt-fluid composites. For example, macroscopic constitutive relations of solid-liquid composites are derived as functions of microscopic geometry described by grain-boundary contiguity (φ) which is defined by the portion of the grain surface being in contact with the neighboring grains, and takes a value between 0

δ

and 1 (Takei, 1998). Contiguity is the essential geometric factor that determines the macroscopic mechanical properties of the granular composites (Takei, 1998). Bulk modulus, shear modulus, and shear velocity of the composites comprised of spherical particles are explained by contiguity (Takei, 1998). In order to explain the macroscopic properties of solid-liquid composites, wetness ($\psi = 1 - \varphi$) is used rather than contiguity. Wetness represents interfacial geometry of the liquid phase (Takei, 1998). Wetness increases with increasing liquid volume fraction (ϕ), and the increase in the rate of wetness becomes faster when the dihedral angle (θ_d) gets smaller (von Barge and Waff, 1986). Therefore, wetness is given as a function of the liquid volume fraction and dihedral angle, and by substituting $\psi(\phi, \theta_d)$ into the macroscopic properties, including bulk modulus, shear modulus, bulk viscosity, and shear velocity, of the partially molten media under thermodynamic equilibrium, the macroscopic properties can be shown as a function of the liquid volume fraction and dihedral angle (Takei, 1998). For example, the shear wave velocity of partially molten media decreases with increasing liquid volume fraction, and the slope of the relationship between the shear wave velocity and liquid volume fraction becomes more negative when the dihedral angle gets smaller (Takei, 1998). The shear wave velocity of isotropic porous media in a low-frequency range, in which relative motion of the two phases is suppressed due to a viscous coupling, is given by:

$$\beta = \sqrt{(1-\phi)\,\mu_{sk}/\overline{\rho}}\,, \qquad (7.4)$$

δ

where μ_{sk} is the shear modulus of the solid skeleton, and $\bar{\rho}$ is the average density of the composites (Biot, 1956). Based on the correlation between configurational entropy and porosity (or liquid volume fraction), shear velocity can be expressed as:

$$\beta \propto \sqrt{\left(1 - S^{config}\right)\mu_{sk} / \bar{\rho}}\,. \qquad (7.5)$$

Furthermore, shear viscosity of rock-melt composites (η) in the earth's interior is inversely proportional to the liquid volume fraction (ϕ) in partially saturated porous media (e.g., $\eta^{-1} \propto \exp(\phi)$) (Takei, 1998; Takei, 2005; Takei and Holtzman, 2009). Therefore, on the basis of the inverse correlation between the liquid volume fraction (i.e., porosity) and configurational entropy, the shear viscosity in the melts can be expressed using the configurational entropy:

$$\eta^{-1} \propto \exp\left(S^{config}\right). \qquad (7.6)$$

The results suggest that shear viscosity decreases with increasing configurational entropy of the fluids that are partially saturated in rocks. Note that equation (7.6) shows remarkable similarity of the fundamental microscopic relationship between configurational entropy of supercooled liquids and the viscosity of melts on the basis of the Adam-Gibbs theory (equation 7.2) (Adam and Gibbs, 1965; Richet, 1984; Lee, 2005), suggesting that a relationship derived from equation (7.6) is robust and can be applied to diverse networks, regardless of the length scale of the constituent objects. A recent study on the elastic properties and viscosity of solid-liquid composites suggested that normalized bulk modulus, shear modulus, bulk

δ

viscosity, and shear viscosity exponentially increases with increasing contiguity, and the changes in viscosity are larger than those of elastic properties (Takei and Holtzman, 2009). Therefore, configurational entropy can be a complementary parameter for describing elastic properties and shear viscosity of porous media.

Fractal dimension analysis has been applied mainly to natural objects including porous media comprised of rocks and soils to describe hydrological processes. Recently, fractal dimension analysis has been applied to diverse geological processes. For example, it has been used to quantitatively characterize the shapes of volcanic particles that are not truly fractal and suggested that fractal dimensions are useful for understanding fragmentation and transport processes associated with volcanic eruptions (Maria and Carey, 2002). Fractal dimension analysis has been also applied to fracture networks with implications for the degree of fracture connectivity and the propensity for fracture flow and the transport of miscible or immiscible chemicals (Bonnet et al., 2001; Roy et al., 2007). As shown in previous studies, cube counting fractal dimension analyzed in this study can be applied to diverse processes including porous media shown in chapter 4. A recent study on the pore structure of volcanic clasts suggested that permeability can be expressed by electrical tortuosity (Wright et al., 2009) which is defined by:

$$\tau = L_e / L \,, \tag{7.7}$$

where L_e is the actual length followed by the flow path, and L is the sample length. Experimental results of this study showed that permeability can be

δ

expressed as (Wright et al., 2009):

$$k = b\tau^{d}, \tag{7.8}$$

where b is a scaling parameter reflecting the effects of both average hydraulic radius and porosity, and d determines the rate at which permeability decreases with
increasing tortuosity and likely reflects departure of the cross-flow path from that of simple straight tubes (Wright et al., 2009). It was shown that permeability can be expressed as a function of cube counting fractal dimension and porosity, and therefore the correlation among permeability, electric tortuosity, and cube counting fractal dimension can be found.

For the processes in the Earth's interior, cube counting fractal dimension can be applied to describe P-wave attenuation and velocity in partially molten rock. Seismic attributes like attenuation and velocity dispersion are sensitive to the pore- fluid distribution in the rocks. That is because seismic waves induce local pressure gradients between fluid patches of different elastic properties and consequently induce local fluid flows that are accompanied by internal friction (Pride and Masson, 2006; Müller et al., 2008). From the random patchy saturation model (Toms et al., 2007), P-wave modulus is expressed as:

$$\tilde{H}(\omega; S) = H^{W}\left(1 + \delta\left[\tau\xi^{2} + (\tau - 1)\xi\right]\right), \tag{7.9}$$

where ω is frequency; S is saturation; τ is a coefficient, and H^{W} is Wood's P-wave modulus (Müller et al., 2008). In this equation, the frequency dependent function ξ is given by:

δ

$$\xi(\omega;S) = 2\nu(ka)^2 \, {}_2F_1\left([1,\nu+1],\frac{1}{2},-k^2a^2\right) + i\sqrt{2}\pi^2 k^3 \Phi(k), \qquad (7.10)$$

where a is the correlation length; k is permeability; Φ(*k*) is the von Kármán spectrum function, and ν is the Hurst exponent which is related with fractal dimension of surface area (D = 3 - ν) (Müller et al., 2008). The P-wave modulus is connected to attenuation and phase velocity via (Pride and Masson, 2006; Müller et al., 2008):

$$Q^{-1}(\omega;S) = \frac{\mathrm{Im}\,\tilde{H}}{\mathrm{Re}\,\tilde{H}} \propto \omega^{-\nu}, \qquad (7.11)$$

$$v_P(\omega;S) = \sqrt{\frac{\mathrm{Re}\,\tilde{H}}{\overline{\rho}}}. \qquad (7.12)$$

These equations show that the fractal dimension of fluid patch is one of the parameters explaining P-wave attenuation. Fluid patches are distributed in three dimensional space in the Earth's interior whereas previous studies have used 2D images. Therefore, cube-counting fractal dimension for fluid patches would be a more accurate parameter for describing complex networks than the conventional fractal dimension obtained from 2D images.

References

Adam, G. and Gibbs, J. H. (1965) On the temperature dependence of cooperative relaxation properties in giass forming liquids. Journal of Chemical Physics, 43, 139-146.

Adam, G. and Gibbs, J. H. (1965) On the temperature dependence of cooperative relaxation properties in glass-forming liquids. J. Chem. Phys., 43, 139-146.

Bear, J. (1972) Dynamics of Fluids in Porous Media. New York, American Elsevier, 764 p.

Biot, M. A. (1956) Theory of propagation of elastic waves in a fluid-saturated porous solid, 1. Low-frequency range. Journal of the Acoustical Society of America, 28, 168-178.

Bonnet, E., Bour, O., Odling, N. E., Davy, P., Main, I., Cowie, P. and Berkowitz, B. (2001) Scaling of fracture systems in geological media. Reviews of Geophysics, 39(3), 347-383.

Lee, S. K. (2005) Microscopic origins of macroscopic properties of silicate melts and glasses at ambient and high pressure: Implications for melt generation and dynamics. Geochimica et Cosmochimica Acta, 69(14), 3695-3710.

Lee, S. K., Kim, H. N., Lee, B. H., Kim, H. I. and Kim, E. J. (2010) Nature of chemical and topological disorder in borogermanate glasses: insights from B-11 and O-17 solid-state NMR and quantum chemical calculations. Journal of Physical Chemistry B, 114, 412-420.

Lee, S. K. and Stebbins, J. F. (1999) The degree of aluminum avoidance in aluminosilicate glasses. American Mineralogist, 84, 937-945.

Müller, T. M., Toms-Stewart, J. and Wenzlau, F. (2008) Velocity-saturation

relation for partially saturated rocks with fractal pore fluid distribution. Geophysical Research Letters, 35, L09306.

Maria, A. and Carey, S. (2002) Using fractal analysis to quantitatively characterize the shapes of volcanic particles. Journal of Geophysical Research, 107(B11), 2283.

Pride, S. R. and Masson, Y. J. (2006) Acoustic attenuation in self-affine porous structures. Physical Review Letters, 97, 184301.

Reiss, H. (1992) Statistical geometry in the study of fluids and porous media. Journal of Physical Chemistry, 96, 4736-4747.

Richet, P. (1984) Viscosity and configurational entropy of silicate melts. Geochimica et Cosmochimica Acta, 48, 471-483.

Roy, A., Perfect, E., Dunne, W. M. and McKay, L. D. (2007) Fractal characterization of fracture networks: An improved box-counting technique. Journal of Geophysical Research, 112, B12201.

Takei, Y. (1998) Constitutive mechanical relations of solid-liquid composites in terms of grain-boundary contiguity. Journal of Geophysical Research, 103(B8), 18183-18203.

Takei, Y. (2005) Deformation-induced grain boundary wetting and its effects on the acoustic and rheological properties of partially molten rock analogue. Journal of Geophysical Research-Solid Earth, 110, B12203.

Takei, Y. and Holtzman, B. K. (2009) Viscous constitutive relations of solid-liquid composites in terms of grain boundary contiguity: 1. Grain boundary diffusion control model. Journal of Geophysical Research, 114, B06205.

Toms, J., Muller, T. M. and Gurevich, B. (2007) Seismic attenuation in porous rocks with random patchy saturation. Geophysical

Prospecting, 55(5), 671-678.

von Barge, N. and Waff, H. S. (1986) Permeabilities, interfacial areas and curvatures of partially molten systems: Results of computations of equilibrium microstructures. Journal of Geophysical Research, 91, 9261-9276.

Wright, H. M. N., Cashman, K. V., Gottesfeld, E. H. and Roberts, J. J. (2009) Pore structure of volcanic clasts: Measurements of permeability and electrical conductivity. Earth and Planetary Science Letters, 280, 93-104.

Appendix. Abstracts Published in Korean Journal

A1. The effect of lattice topology on benzyl alcohol adsorption on kaolinite surfaces: Quantum chemical calculations of Mulliken charges and magnetic shielding tensor

Bum Han Lee and Sung Keun Lee

Published in *Journal of Mineralogical Society of Korea*, 20, 313-325 (2007)

Abstract

In order to have better insights into adsorption of organic molecules on kaolinite surfaces, we performed quantum chemical calculations of interaction between three different model clusters of kaolinite siloxane surfaces and benzyl alcohol, with emphasis on the effect of size and lattice topology of the cluster on the variation of electron density and magnetic shielding tensor. Model cluster 1 is an ideal silicate tetrahedral surface that consists of 7 hexagonal rings, and model cluster 2 is composed of 7 ditrigonal siloxane rings with crystallographically distinct basal oxygen atoms in the cluster, and finally model cluster 3 has both tetrahedral and octahedral layers. The Mulliken charge analysis shows that siloxane surface of model cluster 3 undergoes the largest electron density transfer after the benzyl alcohol adsorption and that of model cluster 1 is apparently larger than that of model cluster 2. The difference of Mulliken

charges of basal oxygen atoms before and after the adsorption is positively correlated with hydrogen bond strength. NMR chemical shielding tensor calculation of clusters without benzyl alcohol shows that three different basal oxygen atoms (O3, O4, and O5) in model cluster 2 have the isotropic magnetic shielding tensor as 228.2 ± 3.9, 228.9 ± 3.4, and 222.3 ± 3.0 ppm, respectively. After the adsorption, the difference of isotropic chemical shift varies from 1 to 5.5 ppm for model cluster 1 and 2 while model cluster 2 apparently shows larger changes in isotropic chemical shift. The chemical shift of oxygen atoms is also positively correlated with electron density transfer. The current results show that the adsorption of benzyl alcohol on the kaolinite siloxane surfaces can largely be dominated by a weak hydrogen bonding and electrostatic force (charge-charge interaction) and demonstrate the importance of the cluster size and the lattice topology of surfaces on the adsorption behavior of the organic molecules on clay surfaces.

δ

A2. 3-Dimensional μm-scale pore structures of porous earth materials: NMR micro-imaging study

Bum Han Lee and Sung Keun Lee

Published in *Journal of Mineralogical Society of Korea*, 22, 313-324 (2009)

Abstract

We explore the effect of particle shape and size on 3-dimensional (3D) network and pore structure of porous earth materials composed of glass beads and silica gel using NMR micro-imaging in order to gain better insights into relationship between structure and the corresponding hydrologic and seismological properties. The 3D micro-imaging data for the model porous networks show that the specific surface area, porosity, and permeability range from 2.5 to 9.6 mm^2/mm^3, from 0.21 to 0.38, and from 11.6 to 892.3 D (Darcy), respectively, which are typical values for unconsolidated sands. The relationships among specific surface area, porosity, and permeability of the porous media are relatively well explained with the Kozeny equation. Cube counting fractal dimension analysis shows that fractal dimension increases from ~2.5-2.6 to 3.0 with increasing specific surface area from 2.5 to 9.6 mm^2/mm^3, with the data also suggesting the effect of porosity. Specific surface area, porosity, permeability, and cube counting fractal dimension for the natural mongolian sandstone are 0.33 mm^2/mm^3, 0.017, 30.9 mD, and 1.59, respectively. The current results highlight that NMR micro-imaging,

together with detailed statistical analyses can be useful to characterize 3D pore structures of various porous earth materials and be potentially effective in accounting for transport properties and seismic wave velocity and attenuation of diverse porous media in earth crust and interiors.

A3. Geophysical implications for configurational entropy and cube counting fractal dimension of porous networks: insights from random packing simulations

Bum Han Lee and Sung Keun Lee

Published in *Journal of Mineralogical Society of Korea*, 23, 367-375 (2010)

Abstract

Understanding the interactions between earth materials and fluids is essential for studying the diverse geological processes in the Earth's surface and interior. In order to better understand the interactions between earth materials and fluids, we explore the effect of specific surface area and porosity on structural parameters of pore structures. We obtained 3D pore structures, using random packing simulations of porous media composed of single sized spheres with varying the particle size and porosity, and then we analyzed configurational entropy for 2D cross sections of porous media and cube counting fractal dimension for 3D porous networks. The results of the configurational entropy analysis show that the entropy length decreases from 0.8 to 0.2 with increasing specific surface area from 2.4 to 8.3 mm^2/mm^3, and the maximum configurational entropy increases from 0.94 to 0.99 with increasing porosity from 0.33 to 0.46. On the basis of the strong correlation between the liquid volume fraction (i.e., porosity) and configurational entropy, we suggest that elastic properties and viscosity of mantle melts can be expressed using configurational entropy. The results of

the cube counting fractal dimension analysis show that cube counting fractal dimension increases with increasing porosity at constant specific surface area, and increases from 2.65 to 2.98 with increasing specific surface area from 2.4 to 8.3 mm^2/mm^3. On the basis of the strong correlation among cube counting fractal dimension, specific surface area, and porosity, we suggest that seismic wave attenuation and structural disorder in fluid-rock-melt composites can be described using cube counting fractal dimension.

요약 (국문초록)

지표 및 지구 내부에서 일어나는 다양한 지질학적 현상은 이를 구성하는 지구물질의 거시적 특성으로 설명되며 이는 원자 단위에서 마이크로미터 단위에 이르는 미시적 구조에 의해 결정된다. 따라서 지구물질의 미시적 구조를 관찰하고 이해하는 것은 다양한 지질학적 현상을 이해하는데 있어서 중요한 역할을 한다. 지구물질과 유체의 상호작용은 지표 및 지구 내부에서 일어나는 가장 중요한 현상 중 하나이다. 이를 이해하는 것은 지표에서 저류암 내 유류의 이동 및 추출, 퇴적물 내 오염물의 이동, 이산화탄소 저장 등과 같은 산업적, 환경적으로 중요한 문제들과 더불어 지구 내부에서 암석-부분 용융체-유체의 복합체에 의한 지진파 감쇠 등 지구물리적 현상들을 평가하고 예측하는 데 있어서 중요한 역할을 한다. 이러한 지구물질과 유체의 상호작용은 다양한 길이 단위에서 관찰이 가능하며 각각의 길이 단위에서 중요한 정보들을 얻을 수 있다. 본 연구에서는 원자 단위에서 일어나는 지구물질과 유체의 상호작용에 대해 양자화학계산을 이용하여 흡착 구조, 물성, 구조-물성 간 관계를 예측하고, 마이크로미터 단위에서 지구물질로 이루어진 다공성 매질 내 유체의 분포와 상호작용에 대해 핵자기공명 현미영상을 이용하여 관찰하였다.

양자화학계산 연구를 통해 비교적 간단한 구조의 유기 분자와 점토광물인 벤질 알코올의 캐올리나이트 표면 흡착에 대한 평형 상태의 구조, 결합 에너지, 핵자기공명 화학 차폐 텐서를 계산함으로써 원자

단위의 미시적 구조, 결합에서 예측할 수 있는 물성, 미시적 구조와 물성 간의 관계를 나타내는 변수를 이론적으로 예측하였다. 흡착 구조는 벤질 알코올이 약한 수소 결합과 분산력에 의해 캐올리나이트 사면체 표면에 흡착되며, 두 개의 수소 결합에 의해 캐올리나이트 팔면체 표면에 흡착되는 것을 보여준다. 결합 에너지는 벤질 알코올이 사면체 표면에 비해 팔면체 표면에 더 강하게 흡착되는 것을 보여준다. 결정학적 위상이 서로 다른 사면체 표면에 대한 결합 에너지는 비슷한 값을 갖지만 자세한 흡착 구조는 서로 다르게 나타나며 이는 결정학적 위상이 흡착에 미치는 영향을 보여준다. 사면체 표면의 산소에 대한 등방 자기 차폐는 흡착 후에 4-5 ppm 감소하는 것으로 예측되었고, 이는 산소 주변에 대한 고분해능 고상핵자기공명 분광분석을 통해 유기물과 규산염 표면의 흡착을 관찰할 수 있음을 제시한다.

첫 번째 핵자기공명 현미영상을 이용한 연구에서는 공극 구조와 공극 구조를 나타내는 매개 변수(상자집계 프랙탈 차원, 라쿠나리티, 구성 엔트로피), 그리고 매개 변수와 수리지질학적 특성의 관계를 정립하였다. 삼차원 공극 구조에 대한 상자집계 프랙탈 차원은 일정한 공극률에서 비표면적이 증가함에 따라 증가하고 일정한 비표면적에서 공극률이 증가함에 따라 증가한다. 약 0.47 mm에 해당하는 상자 크기에서의 라쿠나리티는 비표면적으로 잘 설명된다. 최대 구성 엔트로피는 공극률이 증가함에 따라 증가하고, 공극에 대한 엔트로피 길이는 비표면적이 증가함에 따라 감소하며 공극의 배위수 계산에 사용될 수 있다. 공극률, 비표면적, 투수율에 대한 관계는 코제니-카르만 식의 예측과 일치하며, 본 연구에서는 투수율을 상자집계 프랙탈 차원과

공극률의 함수로 나타낼 수 있음을 제시한다. 본 연구의 결과는 암석, 용융체, 유체로 이루어진 복합체의 탄성과 점성에 대한 지구물리학적 의의를 갖는다.

두 번째 핵자기공명 현미영상 연구에서는 실리콘 오일로 채워진 다공성 매질 내 물이 통과된 시간에 따라 물의 분포를 약 50 μm의 분해능으로 영상화하고, 다공성 매질을 구성하는 입자의 크기와 모양이 물의 분포에 미치는 영향을 조사하였다. 물의 부피, 비표면적, 상자집계 프랙탈 차원은 물이 주입된 시간에 따라 단일 지수형 회복 함수로 잘 설명된다. 글래스 비드로 이루어진 시료의 점근값은 실리카젤로 이루어진 시료에 비해 더 큰 값을 가지며 이는 두 시료의 공극 구조에 차이에 기인한다. 모든 매개 변수의 융합률은 투수율에 반비례하며 이는 융합률이 다공성 매질의 거동 특성과 관련됨을 의미한다. 본 연구는 서로 섞이지 않는 유체로 채워진 다공성 매질의 공극 구조에서 다공성 매질을 구성하는 입자가 물의 분포 특성에 중요한 역할을 하는 것을 보여준다.

다공성 매질 내 유체에 대한 고분해능 핵자기공명 현미영상은 수리지질학과 지구물리학 분야에서 다양한 적용이 가능할 것으로 예상된다. 그러나, 일반적으로 다공성 매질에 대해서는 유체의 양이 적고, 스핀-스핀 이완 시간이 빠르다는 단점 때문에 고분해능으로 영상을 얻기에 한계가 있다. 본 연구에서는 고자기장(18.8 T) 과 고구배(300 G/cm)의 핵자기공명 현미영상 기기를 이용해 비교적 유체의 양이 많이 포함된 몽고 사막의 사암, 두석, 글래스 비드로 이루어진 다공성 매질에 대해 고분해능 영상의 가능성을 조사하였다. 본 연구에서는 약 75 μm의

작은 입자로 이루어진 다공성 매질 내 유체의 영상을 얻었고, 공극률이 높은 시료에 대해 약 19.5 μm의 고분해능 영상을 얻었다. 이러한 핵자기공명 현미영상 기법의 발달에 따라 다공성 매질 내 기체, 액체 등 여러 종류의 유체를 다양한 핵종으로 영상화하는 등의 연구가 가능할 것으로 기대되며, 지구물질과 유체의 상호작용을 미시적으로 관찰하고 이해함으로써 거시적 성질을 예측하는데 도움을 줄 수 있을 것으로 보인다.

……

주요어: 양자화학계산, 핵자기공명 현미영상, 지구물질, 유체, 구조-물성 관계,

학번: 2000-20668

감사의 글

이 논문이 나오기까지 대학원 입학 이후 11 년이라는 긴 시간이 걸렸고 그만큼 저는 많은 분들께 신세를 졌습니다. 가장 먼저 지도교수이신 이성근 교수님께 깊이 감사 드립니다. 교수님께서는 진정한 연구자의 자세를 몸소 보여주셨고, 스승으로서 때로는 인생의 선배로서 귀한 가르침을 주셨습니다. 바쁘신 가운데에도 논문 심사를 위해 귀한 시간을 내어주시고 좋은 조언을 해주신 이용일 교수님, 유인석 교수님, 김준모 교수님, 김영석 교수님, 이강근 교수님께 감사 드립니다. 그리고 부족한 저를 제자로 받아주시고 연구자의 길로 이끌어주신 김수진 교수님께 감사 드립니다.

많은 시간을 함께 보내면서 동고동락했던 서울대학교 지구물질과학 연구실의 후배들에게 고마운 마음을 전합니다. 하나같이 착한 후배들은 부족한 선배의 고민을 함께 나누고 어려운 부탁을 묵묵히 들어주었습니다. 이제는 후배라기보다 친구 같은 현나, 어렵게 생각했던 문제들을 항상 쉽게 해결해주었던 유수, 인간 관계에 대해 배울 점이 많은 선영, 항상 밝은 미소로 기분 좋게 만들어주었던 효임, 막내라고 제일 많은 부탁을 했지만 불평 한 번 하지 않고 모두 들어주었던 은정, 함께 보낸 시간은 길지 않지만 어려운 시간 힘이 되어준 새봄이와 현진이, 모두 훌륭한 후배들인데 부족한 선배 만나서 고생이 많았습니다.

제 대학원 생활의 밑거름이 되고 든든한 버팀목이 되어준 광물학 연구실 선배님들께 감사 드립니다. 특히 광물학 연구실 대학원 생활 동안 저를 많이 챙겨주신 김정진 교수님, 이기무 선배님, 이승엽

박사님, 장세정 박사님, 권기덕 박사님께 감사 드립니다. 미국, 영국, 일본 등에서 실험과 학회 일로 만날 때마다 귀한 조언들을 해주시고 맛있는 것도 많이 사주신 이상수 박사님 감사 드립니다. 또한 연구와 직장 생활에 대해 많은 조언을 해주신 이성록 박사님, 장세원 박사님, 손병국 박사님, 최헌수 박사님, 권석기 선배님께 감사 드립니다.

제가 연구자의 길을 걸을 수 있도록 기회를 주시고 논문을 마무리할 수 있도록 배려해주신 한국지질자원연구원의 장호완 원장님, 정소걸 본부장님, 고상모 실장님과 해외광물자원연구실 선배님들, 지세정 실장님과 국내/북한자원연구실 선배님들께 감사 드립니다. 그리고 힘든 일정 중에도 저를 응원해주시고 여러모로 도와주셨던 윤소정 박사님, 강일모 박사님, 박계순 박사님, 오현주 박사님, 대학원 후배 광민이와 동기 분들께 감사의 말씀을 전합니다.

핵자기공명 현미영상 실험을 위해 불편함을 무릅쓰고 많이 도와주셨던 NICEM의 박미영 선생님, 김윤희 선생님, 기초과학지원 연구원의 조지현 선생님께 감사 드립니다. 양자화학계산을 위한 수퍼 컴퓨터 사용 시 항상 친절하게 도와주셨던 전산원의 정상혁 선생님께도 감사 드립니다. 영상 자료 처리를 위한 MATLAB 코딩을 도와준 후배 영균이에게도 고마움을 전합니다.

공부한다는 핑계로 자주 만나진 못했지만 친구들은 힘들고 어려울 때 아주 큰 힘이 되어 주었습니다. 멀리 떨어져 있지만 마음만은 가까운 남욱, 언제 만나도 며칠 만에 만난 것 같은 선영, 항상 내 일을 자신의 일처럼 생각해주는 승우, 고등학교, 대학교, 대학원, 직장까지 모두 동기이면서 고민을 함께 나누었던 희성, 그리고 한성과학고등학교

1기 동기들과 서울대학교 지질해양학과군 95학번 동기들 모두 고맙습니다.

부족한 저로 인해 마음 고생이 크셨지만 내색 한 번 하지 않으시고 저를 아들로 대해주시며 큰 사랑을 베풀어주신 장인 어른, 장모님께 깊이 감사 드립니다. 공부한다는 핑계로 제대로 한 번 챙겨주지도 못한 처제와 동서에게도 고마움을 전합니다. 그리고 제가 한참 바쁠 때 아내와 상준이를 잘 보살펴주신 외숙모님께도 감사 드립니다.

아들이 태어나고 나니 부모님의 사랑이 어떤 것인지 조금은 깨닫게 된 것 같습니다. 그러한 사랑으로 저를 길러주시고 지켜봐 주신 아버지, 어머니께 깊이 감사 드립니다. 주말에도 바쁘게 일하면서 가족에게 헌신하는 동생 도한에게도 고마움을 전합니다.

귀여운 나의 아들 상준이, 어려울 때마다 힘을 낼 수 있는 원동력이 되어 주었습니다. 고마운 아빠의 마음을 전하고 싶습니다.

무엇보다도, 이 논문을 마무리할 수 있도록 제 곁에서 오랜 시간 인내와 사랑으로 지켜봐 주고 도와준 아내에게 감사의 마음을 전합니다. 부족한 남편으로 인해 정말 고생이 많았는데, 아내에게 진 이 빚은 평생 갚으면서 살아도 모자랄 것 같습니다.

사랑하는 아내 지은에게 이 논문을 바칩니다.